Finite Antenna Arrays
and FSS

Finite Antenna Arrays and FSS

Ben A. Munk

◆IEEE

IEEE PRESS

WILEY-INTERSCIENCE

A John Wiley & Sons, Inc., Publication

To the increasing number of my friends who realize that computer power is a supplement, not a substitute, for brain power.
The constant support of the Electroscience Laboratory and my family—in particular, my wife Aase—is deeply appreciated.

B. A. M.

Contents

Foreword

It has often been said that a good teacher must have a number of attributes, among which are true expertise in the subject to be taught, and, just as important, the ability to put the subject across to the students, regardless of its complexity. We have all suffered under instructors who got straight A's as students, but who never understood how their own students did not do as well because the material was presented as if it should be obvious. Professor Ben Munk has no problems in either regard.

In this book, Ben treats a number of subjects related to antennas and both their intended usage as transmission or reception devices, as well as the important (these days) radar cross section (RCS) that they can contribute. A constant theme behind the presented results is how often investigators approach the problem with no apparent understanding of the real-world factors that bear heavily on the practicality and/or quality of the result. He takes issue with those who have become so enchanted with high-powered computers that they simply feed the machine some wonderful equations and sit back while it massages these and "optimizes" a result. Sad to say, Ben has been able to document all too many examples to prove his point.

All this is not intended in any way to say that powerful computers are useless. Far from it. Without the use of such machines, much of the work described herein could not have been done in a lifetime, but the approach has to be controlled by investigators who understand the physics and electromagnetic realities that make a solution truly optimal and practical.

Throughout this book, Ben makes excellent use of the work he described in his first book, *Frequency Selective Surfaces*, in which he demonstrated how what he called the "Periodic Moment Method" could be used to obtain excellent results for problems previously hampered by "micro" calculation methods. His array

theory approach, combined appropriately with the detailed "method of moments," produced successful solutions to a number of critical problems.

Here he further applies this approach and gives many examples of problems solved by himself and his graduate associates, with the goal of teaching by practical example. This is done by walking the reader, case by case, through the basic technology that applies, then to a logical solution. He then gives hard results to validate what was done, and then, to quickly bring the reader up to speed, he provides a problem or two for solution without further guidance.

Throughout all this, Ben uses his wonderful sense of humor to make various points, which goes a long way in making this book anything but tedious. Saying that about a book on heavy electromagnetic theory and design is certainly a far cry from the usual. His sections on "Common Misconceptions" are his way of highlighting how often "results" are developed and publicized without the necessary understanding of the basic rules of the game. He calls a spade a spade, for sure, and there may well be some who, though unnamed, might feel a twinge after reading these sections. All in all, this is an excellent book that will certainly benefit any serious investigator in the technology areas it discusses. Highly recommended!

WILLIAM F. BAHRET

Mr. W. Bahret was with the United States Air Force but is now retired. From the early 1950s he sponsored numerous projects concerning radar cross section of airborne platforms—in particular, antennas and absorbers. Under his leadership grew many of the concepts used extensively today—for example, the metallic radome. In fact he is considered by many to be the father of stealth technology.

BEN MUNK

Wow!! The former student (now a professor emeritus) has succeeded in advancing the former teacher's (an even older professor emeritus) knowledge of array design tremendously.

The information contained in this book is going to change the way that large, broadbanded arrays are designed. This also leads to new insights in the area of antenna scattering. I strongly recommend it to the designers of such arrays. The concept of starting a finite array design from an infinite array is a remarkable one.

A simple example of why I make this comment comes to mind. I was reading the papers in the December 2002 *IEEE Magazine* which discuss the transmission of power to earth from space. Several problems with interference created by reradiation of energy at harmonic frequencies were discussed. I could see potential cures simply from scanning the initial chapters. I would also be interested in applying these concepts to my current research namely, time-domain ground-penetrating radar (GPR). Some neat antennas may become practical.

Those who have read Ben's first book, *Frequency Selective Surfaces, Theory and Design*, will recall that I also wrote the Foreword to it. I was his teacher,

project supervisor, and later co-worker on much of that material. In reading it, I would turn pages and simply agree with many of the concepts.

At this time I have only scanned some of the chapters of the present book. For what I have seen thus far, I would scan a part of it and simply say, "Wow." The reader should understand that there were points where I would have said, "Bet a Coke" (Ben and I used to bet a Coke every time we disagreed. Neither of us ever paid up.). These points are provocative to those readers with an interest in antenna scattering and should make those readers think carefully about them but most of them are resolved when one recalls that the emphasis of this book is on arrays.

This book is a must for anyone involved in the design of large arrays. I fully intend to read it very carefully after it is published.

Finally, I would observe that Ben's comments about the review of journal papers are borne out of frustration. While Ben has worked in these areas throughout his career, most of his work was at that time classified. Thus when a paper in these general areas was published, he saw various flaws because of his experience but he could not comment. Neither the paper's author nor the reviewers, not having Ben's unique background, would see these flaws. The problem is in reality created by the necessity of security. This same factor has led to the very interesting sections he has titled "Common Misconceptions."

Columbus, Ohio   LEON PETERS, JR.

Leon Peters, Jr., was a professor at the Ohio State University but is now retired. From the early 1960s he worked on, among many other things, RCS problems involving antennas and absorbers. In fact, he became my supervisor when I joined the group in the mid-1960s.

BEN MUNK

Preface

Why did I write this book?

The approach to engineering design has changed considerably over the last decades.

Earlier, it was of utmost importance to first gain insight into the physics of the problem. You would then try to express the problem in mathematical form. The beauty here was, of course, that it then often was quite simple to determine the location of the extreme values such as the maxima and minima as well as nulls and asymptotic behavior. You would then, in many cases, be able to observe which parameters were pertinent to your problem and in particular which were not. It was then followed by actual calculations and eventually by a meaningful parametric study that took into account what was already observed earlier.

The problem with this approach was, of course, that it required engineers and scientists with considerable insight and extensive training (I deliberately did not say experience, although it helps). However, not everyone that started down this road would finish and not without a liberal dose of humiliation.

It is therefore quite understandable that when the purely numerical approaches appeared on the scene, they soon became quite popular. Most importantly, only a minimum of physical insight was required (or so it was thought). The computers would be so fast that they would be able to calculate all the pertinent cases. These would then be sorted out by using a more or less sophisticated optimization scheme, and the results would be presented on a silver platter completely untouched by the human mind.

It would be incorrect to state that the numerical approach has failed. It has in many cases produced remarkable results. However, the author is keenly aware of several cases that have been the subject of intense investigation for years and still have not produced a satisfactory solution, although some do exist—most often

because the computer has been directed to incorporate all kinds of parameters that are alien to this particular problem. Or lack of physical insight has prevented the operator from obtaining a meaningful parametric study—for example, in cases where a solution does not exist in the parametric space considered.

The author has watched this development with considerable concern for several years. One of his colleagues stated recently that a numerical solution to a somewhat complex problem of his could only be used to check out specific designs. An actual optimization was not possible because of the excessive computer time involved.

That almost sounds like an echo of other similar statements coming from the numerical camp.

A partial remedy for this calamity would be, of course, to give the students a better physical understanding. However, a fundamental problem here is that many professors today are themselves lacking in that discipline. The emphasis in the education of the younger generation is simply to write a computer program, run it, and call themselves engineers! The result is that many educators and students today simply are unaware of the most basic fundamentals in electromagnetics. Many of these shortcomings have been exposed at the end of each chapter of this book, in a section titled "Common Misconceptions." Others are so blatantly naive that I am embarrassed to even discuss them. What is particularly disturbing is the fact that many pursue these erroneous ideas and tales for no other reason than when "all the others do it, it must be OK!"

Neither this book nor my earlier one, *Frequency Selective Surfaces, Theory and Design*, make any claims to having the answers to all problems. However, there are strong signals from the readers out there that they more and more appreciate the analytic approach based on physical understanding followed up by a mathematical analysis. It is hoped that this second book will be appreciated as well.

The author shared this preface with some of his friends in the computational camp. All basically agreed with his philosophy, although one of them found the language a bit harsh!

However, another informed him before reading this preface that design by optimization has lately taken a back seat as far as he was concerned. Today, he said, there is a trend toward understanding the underlying mathematics and physics of the problem.

Welcome to the camp of real engineering. As they say, "there is greater joy in Heaven over one sinner who makes penance than over ninety-nine just ones."

Columbus, Ohio   BEN MUNK

Acknowledgments

As in my first book, *Frequency Selective Surfaces, Theory and Design*, three of my many mentors stand out: Mr. William Bahret, Professor Leon Peters, Jr., and Professor Robert Kouyoumjian. They were always ready with consultation and advice. That will not be forgotten.

Further support and interest in my work was shown by Dr. Brian Kent, Dr. Stephen Schneider, and Mr. Ed Utt from the U.S. Air Force. After completion of the development of the Periodic Method of Moments, the PMM code, the Hybrid radome, low RCS antennas, and more, the funding from the Air Force shifted into more hardware-oriented programs. Fortunately, the U.S. Navy needed our help in designing very broadbanded bandstop panels. Ultimately, this work resulted in the discovery of surface waves unique to finite periodic structures, which are treated in great detail in this book. The help and advice from Mr. Jim Logan, Dr. John Meloling, and Dr. John Rockway is deeply appreciated.

However, the most discussed subject was the Broadband Array Concept. It was set in motion by two of the author's oldest friends, namely Mr. William Croswell and Mr. Robert Taylor from the Harris Corporation. This relationship resulted in many innovative ideas as well as support. So did my cooperation with Mission Research (home of many of the author's old students). My deep-felt thanks goes to all who participated in particular Errol English who wrote Section 9.6 about Tapered Periodic Surfaces, and Peter Munk who supplied Section 3.7 investigating Periodic Surfaces with arbitrary oriented elements.

My good friend and mentor, Professor John Kraus, once stated that students really are at the university to "straighten" the professors out, not the other way around. I whole-heartedly agree. In fact, had it not been for my last two students, Dr. Dan Janning and Jonothan Pryor, this book would not have been written. I am particularly indebted to Jonothan, who tirelessly ran computer programs and

Symbols and Definitions

a	horizontal distance between column q and point of observation $\overline{R}$
a, a_1	wire radius of elements
a	side length of square elements
$d\overline{A}$	vector potential for double infinite array of Hertzian elements
$d\overline{A}_q$	vector potential of Hertzian elements located in column q
$d\overline{A}_{qm}$	vector potential of a single Hertzian element located in column q and row m
b_{m-1}	location of the front face of dielectric slab m in dipole case
b_m	location of the back face of dielectric slab m in dipole case
C_p	equivalent shunt capacitance from the orthogonal elements in a CA absorber
d	diameter of circular plate element
d_m	thickness of dielectric slab in dipole case
D_N	determinant of admittance matrix for N slot arrays
D_x	interelement spacings in the X direction
D_z	interelement spacings in the Z direction
$\overline{e} = [\hat{p} \times \hat{r}] \times \hat{r}$ $= {}_\perp\hat{n}_\perp e + {}_\parallel \hat{n}_\parallel e$	field vector for infinite array of Hertzian elements
$\overline{E}_m(\overline{R})$	electric field at $\overline{R}$ in medium m

$\overline{E}_m^i(\overline{R})$	incident electric field at $\overline{R}$ in medium m
$\overline{E}_m^{(R)}$	reflected electric field of $\overline{R}$ in medium m
f	frequency
f_g	onset frequency of grating lobe
$F(w)$	Fourier transform of $f(t)$, not necessarily a function of time
$\overline{H}_m(\overline{R})$	magnetic field of $\overline{R}$ in medium m
$\overline{H}_m^i(\overline{R})$	incident magnetic field at $\overline{R}$ in medium m
$\overline{H}_m^r(\overline{R})$	reflected magnetic field at $\overline{R}$ in medium m
$H_n^{(2)}(x)$	Hankels function of the second kind, order n and argument x
$I_{qm}(l)$	current along element in column q and row m
k, n	indices for the spectrum of plane, inhomogeneous waves from an infinite array
l	distance from a reference point to an arbitrary point on the element
$2l_1$	total element length
dl	infinitesimal element length
Δl	element length of Hertzian dipoles
$\overline{m}_\pm = \overline{E} \times \hat{n}_{D\pm}$	magnetic current density
$\overline{M}_\pm$	total magnetic current in slots
$\hat{n}_D$	unit vector orthogonal to dielectric interface pointing into the dielectric medium in question
$_\perp\hat{n}_m = \dfrac{\overline{n}_D \times \hat{r}}{\lvert n_D \times \hat{r}\rvert}$	unit vector(s) orthogonal to the planes of incidence or reradiation in medium m
$_\parallel\hat{n}_m = {}_\perp\hat{n}_m \times \overline{r}$	unit vector(s) parallel to the planes of incidence or reradiation in medium m
$n, n_0, n_1, n_2, \ldots$	integers
$\hat{p}$	orientation vector for elements
$\hat{p}^{(p)}$	orientation vector for element section p
$\hat{p}^{p,n}$	orientation vector for element section p in array n
$P^{(p)}$	scattering pattern function associated with element section p
$P^{(p)t}$	transmitting pattern function associated with element section p
$P_m^{(p)}$	scattering pattern function associated with element section p in medium m
${}_\parallel^\perp P_{m\pm}^{(p)}$ $= \hat{p}^{(p)} \cdot {}_\parallel^\perp \hat{n}_{m\pm} P_{m\pm}^{(p)}$	orthogonal and parallel pattern components of scattering pattern in medium m
$P_m^{(p)t}$	transmitting pattern function associated with element section p in medium m

$\perp_{\parallel} P_m^{(p)t}$ $= \hat{p}^{(p)} \cdot \perp_{\parallel} \hat{n}_{m\pm} P_{m\pm}^{(p)t}$	orthogonal and parallel pattern components of transmitting pattern in medium m
$\mathcal{P}_n$	polynomial for a bandpass filter comprised of n slot arrays
q, m	the position of a single element in column q and row m
$\hat{r}_\pm = \hat{x} r_x \pm \hat{y} r_y + \hat{z} r_z$	direction vectors of the plane wave spectrum from an infinite array
$\hat{r}_{m\pm}$ $= \hat{x} r_{mx} \pm \hat{y} r_{my} + \hat{z} r_{mz}$	direction vectors in medium m of the plane wave spectrum from an infinite array
$r_\rho = \sqrt{1 - \left(s_z + n \dfrac{\lambda}{D_z} \right)^2}$	the ρ component of $\hat{r}_\pm$
$\hat{s} = \hat{x} s_x + \hat{y} s_y + \hat{z} s_z$	direction of incident field
$\hat{s}_m = \hat{x} s_{mx} + \hat{y} s_{my} + \hat{z} s_{mz}$	direction of incident field in medium m
t	variable used in Poisson's sum formula
$\perp_{\parallel} T_m$	orthogonal and parallel transformation functions for single dielectric slab of thickness d_m
$\perp_{\parallel}^{E} T_m$	orthogonal and parallel transformation function for the E field in a single dielectric slab of thickness d_m
$\perp_{\parallel}^{H} T_m$	orthogonal and parallel transformation function for the H field in a single dielectric slab of thickness d_m
$\perp_{\parallel} T_{m-m'}$	orthogonal and parallel generalized transformation function when going from one dielectric slab of thickness d_m to another of thickness $d_{m'}$, both of which are located in a general stratified medium
$T.C._{\pm 1}$	transmission coefficient at the roots $Y_{1\pm}$, etc.
$V^{1,'1}$	induced voltage in an external element with reference point $\overline{R}^{(1')}$ caused by all the currents from an array with reference element at $\overline{R}^{(1)}$
$V_{Di\pm}^{(1')}$	induced voltage in an external element with reference point $\overline{R}^{(1')}$ caused by a direct wave only from the entire array
$V_{D\pm}^{(1')}$	induced voltage in an external element with reference point $\overline{R}^{(1')}$ caused by double bounded modes ending in the $\pm$ direction
$V_{S\pm}^{(1')}$	induced voltage in an external element with reference point $\overline{R}^{(1')}$ caused by a single bounded mode ending up in the $\pm$ direction
w	dipole or slot width

$\perp \!\!\!\! \parallel W_m$	orthogonal and parallel components for the Wronskian for a single dielectric slab of thickness d_m
$\perp \!\!\!\! \parallel W_m^e$	orthogonal and parallel components for the effective Wronskian for a single dielectric slab of thickness d_m and located in a general stratified medium
Y	intrinsic admittance
$Y_{1\pm}, Y_{2\pm}, \ldots$	roots of polynomial for bandpass filter
Y_A	scan admittance as seen at the terminals of an element in the array
Y_L	load admittance at the terminals of the elements
$Y_0 = \dfrac{1}{Z_0}$	intrinsic admittance of free space
$Y_m = 1/Z_m$	intrinsic admittance of medium m
$Y^{1,2}$	array mutual admittance between array 1 and 2
Z	intrinsic impedance
$Z = \dfrac{a + bz}{c + dz}$	the dependent variable as a function of the independent variable z in a bilinear transformation
$Z_0 = 1/Y_0$	intrinsic impedance of free space
$Z_A = R_A + jX_A$	scan impedance as seen at the terminals of an element in the array
Z_L	load impedance at the terminals of the elements
$Z_m = 1/Y_m$	intrinsic impedance of medium m
$Z^{n,n'}$	array mutual impedance between a reference element in array n and double infinite array n'
$Z^{q,q'}$	column mutual impedance between a reference element in column q and an infinite line array at q'
$Z_{q,q'm}$	mutual impedance between reference element in column q and element m in column q'
α	angle between plane of incidence and the xy plane
$\beta_m = \dfrac{2\pi}{\lambda_m}$	propagation constant in medium m.
Δl	total element length of Hertzian dipole
ε	dielectric constant
ε_{eff}	effective dielectric constant of a thin dielectric slab as it affects the resonant frequency
ε_m	dielectric constant in medium m
ε_{rm}	relative dielectric constant in medium m
η	angle of incidence from broadside
η_g	angle of grating lobe direction from broadside
θ_m	angle of incidence from broadside in medium m

$^E_{\perp\parallel}\Gamma_{m+} = ^E_{\perp\parallel}\Gamma_{m,m+1}$	orthogonal and parallel Fresnel reflection coefficient for the E field when incidence is from media m to $m+1$
$^H_{\perp\parallel}\Gamma_{m+} = ^H_{\perp\parallel}\Gamma_{m,m+1}$	orthogonal and parallel Fresnel reflection coefficient for the H field when incidence is from media m to $m+1$
$^E_{\perp\parallel}\Gamma^e_{m+} = ^E_{\perp\parallel}\Gamma^e_{m+1}$	orthogonal and parallel effective reflection coefficient for the E field when incidence is form media m to $m+1$
$^H_{\perp\parallel}\Gamma^e_{m+} = ^H_{\perp\parallel}\Gamma^e_{m,m+1}$	orthogonal and parallel effective reflection coefficient for the H field when incidence is from media m to $m+1$
λ_m	wavelength in medium m
μ_m	permeability in medium m
μ_{rm}	relative permeability in medium m
$^E_{\perp\parallel}\tau_{m+} = ^E_{\perp\parallel}\tau_{m,m+1}$	orthogonal and parallel Fresnel transmission coefficient for the E field when incidence is from media m to $m+1$
$^H_{\perp\parallel}\tau_{m+} = ^H_{\perp\parallel}\tau_{m,m+1}$	orthogonal and parallel Fresnel transmission coefficient for the H field when incidence is from media m to $m+1$
$^E_{\perp\parallel}\tau^e_{m+} = ^E_{\perp\parallel}\tau^e_{m,m+1}$	orthogonal and parallel effective transmission coefficient for the E field when incidence is from media m to $m+1$
$^H_{\perp\parallel}\tau^e_{m+} = ^H_{\perp\parallel}\tau^e_{m,m+1}$	orthogonal and parallel effective transmission coefficient for the H field when incidence is from media m to $m+1$
$\omega = 2\pi f$	angular frequency
$\omega_1\omega_0$ and ω_1	variables used in Poisson's sum formula (not angular frequencies)

1

Introduction

1.1 WHY CONSIDER FINITE ARRAYS?

The short answer to this question is, Because they are the only ones that really exist.

However, there are more profound reasons. Consider, for example, the infinite × infinite array shown in Fig. 1.1. It consists of straight elements of length $2l$, and the interelement spacings are denoted D_x and D_z as shown. Such an infinite periodic structure was investigated in great detail in my earlier book, *Frequency Selective Surfaces, Theory and Design* [1]. There the underlying theory and notation for the Periodic Moment Method (PMM) is described. It became the basis for the computer program PMM written by Dr. Lee Henderson as part of his doctoral dissertation in 1983 [2, 3].

In the intervening years it has stood its test and has become the standard in the industry.

Consider next the finite × infinite array shown in Fig. 1.2. It consists, like the infinite × infinite case in Fig. 1.1, of columns that are infinite in the Z direction, however, there is only a finite number of these columns in the X direction. Such arrays have been investigated by numerous researchers [4–23]—in particular, by Usoff, who wrote the computer program SPLAT (Scattering from a Periodic Linear Array of Thin wire elements) as part of his doctoral dissertation in 1993 [24, 25].

Let us now apply the PMM program to obtain the element currents for an infinite × infinite FSS array of dipoles with $D_x = 0.9$ cm and $D_z = 1.6$ cm, while

Incident wave in
direction $\hat{s} = \hat{x}s_x + \hat{y}s_y + \hat{z}s_z$:

$$I_{qm} = I_0\, e^{-j\beta qD_x s_x} e^{-j\beta mD_z s_z}$$

Floquet's Theorem

Infinite x Infinite Array
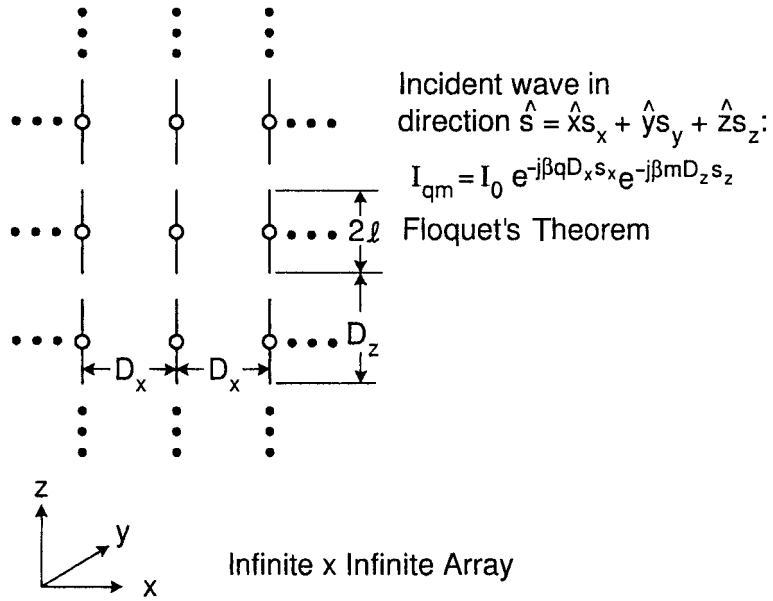
Fig. 1.1 An "infinite × infinite" truly periodic structure with interelement spacing D_x and D_z and element length 2l.

Incident wave in
direction $\hat{s}$

Floquet's Theorem valid
in infinite direction:

$$I_{1m} = I^{(1)}e^{-j\beta mD_z s_z}$$
$$I_{2m} = I^{(2)}e^{-j\beta mD_z s_z}$$
$$I_{3m} = I^{(3)}e^{-j\beta mD_z s_z}$$

Finite x Infinite Array
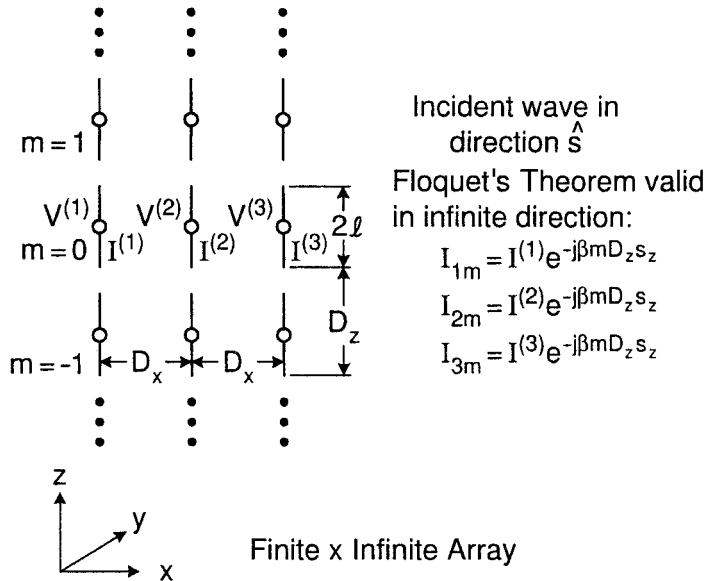
Fig. 1.2 An array that has a finite number of element columns in the X direction and is infinite in the Z direction. It is truly periodic in the latter direction but not in the former. Thus, Floquet's Theorem applies only to the Z direction, not the X direction.
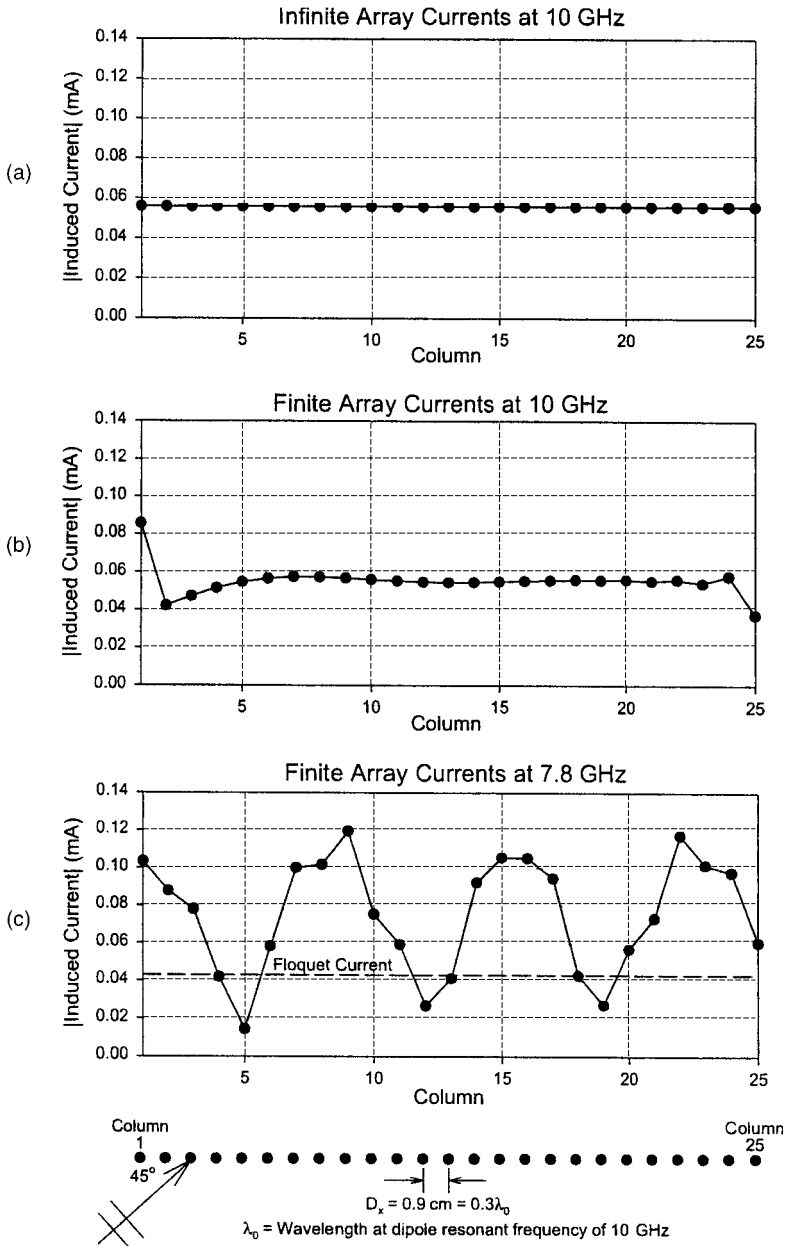
Fig. 1.3 *Various cases of a plane wave incident upon infinite as well as finite arrays at 45° from normal in the H plane. Element length 2l = 1.5 cm, load impedance $Z_L = 0$ and frequencies as indicated. (a) Element currents for an infinite × infinite array at 10 GHz as obtained by the PMM program (close to resonance). (b) Element currents for a finite × infinite array of 25 columns at 10 GHz (close to resonance). (c) Element currents for a finite × infinite array of 25 columns at 7.8 GHz (~25% below resonance).*

the element length $2l = 1.5$ cm; that is, the array will resonate around 10 GHz. The angle of incidence is 45° in the orthogonal plane (H plane). The current magnitudes are plotted column by column in Fig. 1.3a at $f = 10$ GHz.

Similarly we apply the SPLAT program to obtain the current magnitudes in an finite × infinite array of 25 columns as depicted in Fig. 1.3b. We notice that the infinite case in Fig. 1.3a agrees pretty well with the finite case in Fig. 1.3b, except for the very ends of the finite array. This observation is typical in general for large arrays and is simply the basis for using the infinite array program to solve large finite array problems as encountered in practice. The deviation between the two cases (namely the departure from Floquet's theorem [26] in the finite case) is usually of minor importance as long as the array is used as a frequency selective surface (FSS) like here [27]. However, if the array instead is designed to be an active array in front of a groundplane and each element is loaded with identical load resistors (representing the receiver or transmitter impedances), the situation may change dramatically. As shown in Chapters 2 and 5, we can in that case adjust the load impedances such that no reradiation takes place in the specular direction from all the elements except the edge elements. However, as also discussed in Chapter 5, we may change the loads for the edge elements such that no scattering in the specular direction takes place from these as well.

So far we have merely tacitly approved of the standard practice, namely the use of infinite array theory to solve finite periodic structure problems, at least in the case of an FSS with no loads and no groundplane. However, even in that case we may encounter a strong departure from the infinite array approach. In short, we may encounter phenomena that shows up only in a finite periodic structure and never in an infinite as will be discussed next.

1.2 SURFACE WAVES UNIQUE TO FINITE PERIODIC STRUCTURES

We have calculated the element currents only at $f = 10$ GHz—that is, close to the resonant frequency of the array. Let us now explore the situation at a frequency approximately 25% lower, namely at $f = 7.8$ GHz. From the SPLAT program we obtain the element currents shown in Fig. 1.3c, while the PMM program gives us element currents equal to 0.045 mA as shown in Fig. 1.3c, close to what would be expected based on the resonant value of 0.055 mA (see Fig. 1.3a).

We observe in Fig. 1.3c that the element currents for the finite array not only fluctuate dramatically from column to column but also exhibit an average current that can be estimated to be somewhat higher than the currents even for resonance condition (0.055 mA).

We shall investigate this phenomena in detail in Chapter 4. It will there be shown that the element currents are composed of three components:

1. The Floquet currents as observed in an infinite × infinite array—that is, currents with equal magnitude and a phase matching that of the incident plane wave.

2. Two surface waves, each of them propagating in opposite directions along the x axis. They will in general have different amplitudes but the same phase velocities that differ greatly from those of the Floquet currents. Thus, the surface waves and the Floquet currents will interfere with each other, resulting in strong variations of the current amplitudes as seen in Fig. 1.3c.

3. The so-called end currents. These are prevalent close to the edges of the finite array and are usually interpreted as reflections of the two surface waves as they arrive at the edges.

We emphasize that these surface waves are unique for finite arrays. They will not appear on an infinite array and will consequently not be printed out by, for example, the PMM program that deals strictly with infinite arrays. Nor should they be confused with what is sometimes referred to as edge waves [28]. The propagation constant of these equals that of free space, and they die out as you move away from the edges. See also Section 1.5.3.

Furthermore, the surface waves here are not related to the well-known surface waves that can exist on infinite arrays in a stratified medium next to the elements. These will readily show up in PMM calculations. These are simply grating lobes trapped in the stratified medium and will consequently show up only at higher frequencies, typically above resonance but not necessarily so in a poorly designed array. In contrast, the surface waves associated with finite arrays will typically show up below resonance (20–30%) and only if the interelement spacing D_x is $<0.5\lambda$.

From a practical point of view, the question is of course whether these surface waves can hurt the performance of a periodic structure when used either passively as an FSS or actively as a phased array. And if so, what can be done about it.

We will discuss these matters next and in more detail in Chapters 4 and 5.

1.3 EFFECTS OF SURFACE WAVES

The most prevalent effects of the new type of surface waves associated with finite periodic structures depend to an extent upon whether they are used passively as an FSS or actively as a phased array.

In the first case we will observe a significant increase in the bistatic scattering. In the second case we will observe a variation of the terminal impedance as we move from column to column. Let us look upon these two phenomena separately.

1.3.1 Surface Wave Radiation from an FSS

Surface waves on a finite FSS will radiate just like the Floquet currents will radiate. These matters—and, in particular, how they are being excited—will be the subject of detailed discussions in Chapter 4. It suffices in this introduction to present a typical example as shown in Fig. 1.4. We show here 25 columns with the same element dimension as earlier (see insert). The angle of incidence is
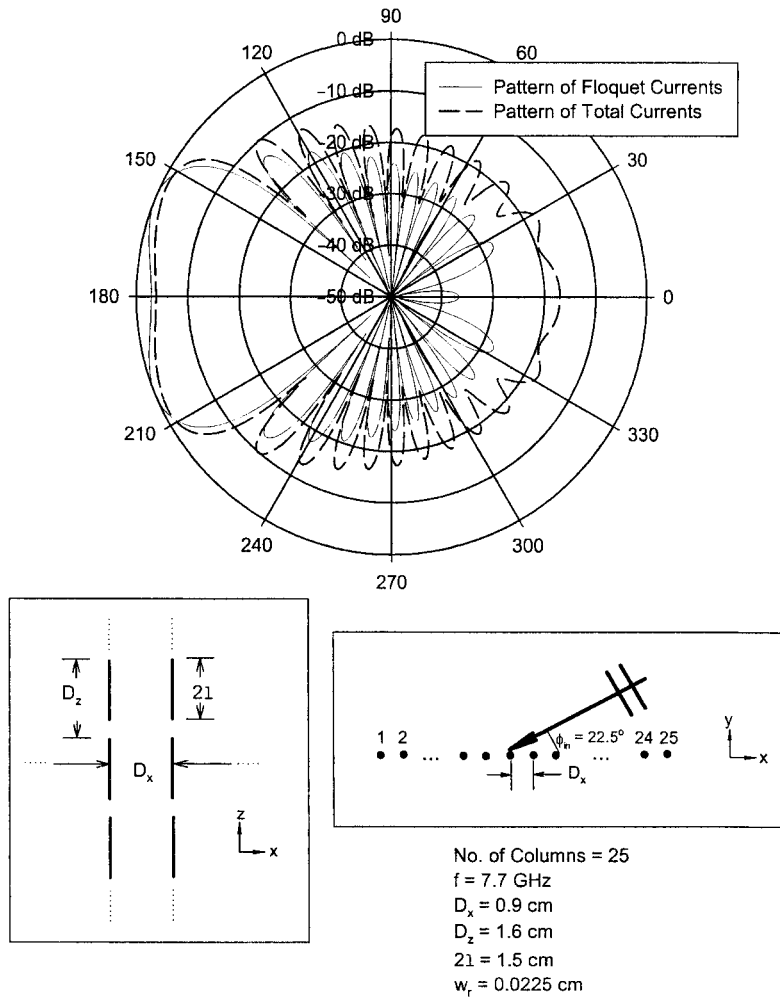
Fig. 1.4 The bistatic scattered field in the H plane from a finite × infinite array of 25 columns at f = 7.7 GHz. (———) Scattering pattern calculated by using merely the Floquet currents—that is, simply by truncating an infinite structure. (−−−) Scattering pattern calculated by using the actual element currents (exact).

$67.5°$ as also indicated in the insert. The Floquet currents alone are producing a bistatic scattering pattern as indicated by the full line in Fig. 1.4 (this corresponds to simple truncation of an infinite FSS). Also shown is the bistatic scattering pattern as obtained by using the total currents on the finite FSS—that is, the sum of the Floquet currents, the two surface waves, and the end currents as obtained by direct calculation from the SPLAT program (see the broken line pattern). The pattern obtained from the Floquet currents only are of course merely a pattern of the $\sin x/x$ type. However, when using the total calculated current we observe

no perceptible change of the two main beams while the sidelobe level in this case is raised by about 10 dB (the exception is the sector between the two main beams where it actually is lower than the Floquet pattern). Later in Chapter 4 we will show more examples where the sidelobe level can be raised by more than 10 dB. In other words, the RCS of a finite FSS could be raised by that amount unless treated.

The encouraging conclusion is of course that even if the surface waves might actually be stronger than the Floquet currents (see, for example, Fig. 1.3c), they apparently radiate less efficiently than the Floquet currents. These facts will be discussed in detail in Chapter 4.

1.3.2 Variation of the Scan Impedance from Column to Column

If our periodic structure is fed as a phased array from constant voltage generators without generator impedances, the relative current magnitudes at the terminals will be like those shown in Fig. 1.3. Since the scan impedance is equal to the terminal voltage (namely the constant generator voltages) divided by the terminal currents, it is clear that the scan impedance will vary inversely to the currents in Figs. 1.3b and 1.3c.

Obviously it would be too much of a challenge to match an impedance with precision to the fluctuating scan impedance of Fig. 1.3c—in particular, when we realize that the maximum and minimum will start moving around with scan angle and frequency. Thus, we must simply look for ways to get rid of the surface waves or at least reduce them. We will discuss these matters next and in more detail in Chapter 4.

1.4 HOW DO WE CONTROL THE SURFACE WAVES?

1.4.1 Phased Array Case

In the previous section we considered phased arrays fed from constant voltage generators with the generator impedance equal to zero. We saw how this scenario could lead to disastrous variations in the scan impedance. Fortunately, a more realistic situation would be to feed the individual elements from constant voltage generators with generator impedances similar to the scan impedances as obtained from the infinite array case (i.e., approximating conjugate match). Thus, we show in Fig. 1.5a the same case as shown earlier in Fig. 1.3c but with load resistors equal to 100 ohms in order to simulate the generator impedances.

Several features are worth observing. First of all the fluctuations from element to element have been greatly reduced but obviously not completely eradicated. Second, the Floquet currents in Fig. 1.3c have been reduced from 0.045 mA to ∼0.032 in Fig. 1.5a—that is, a reduction of approximately $0.032/0.045 = 0.71$.

This reduction is easy to explain by inspection of the equivalent circuit shown in Fig. 1.6a.

Here the voltage generator V^g is connected in series with its generator impedance Z_G and the scan impedance Z_A. The ratio between the currents

Fig. 1.5 The actual element currents in each column of a finite array of 25 columns when exposed to an incident plane wave at 45° from normal or fed like a phased array from individual voltage generators with a linear phase delay. (a) All elements loaded with $R_L = 100$ ohms. (b) Only the outer columns (each side) are loaded with 200 ohms, the next inner columns with 100 ohms and finally the third inner ones with 50 ohms. All other elements have no load resistances. (c) All elements loaded with $R_L = 20$ ohms.

Fig. 1.6   *The approximate equivalent circuit for an infinite periodic structure when used as: (a) A phased array with the individual elements fed from generators V^g with generator impedances Z_G. (b) A frequency selective surface when a voltage V^i is induced by an incident wave and Z_L is a load impedance (in general purely reactive).*

without and with the generator impedance is seen to be $Z_A/(Z_A + Z_G)$. For the array considered here a rough estimate of the average Z_A would be around 200 ohms. Thus, for $Z_G = 100$ ohms the reduction would be approximately $200/(200 + 100) = 0.67$, which is in fair engineering agreement with the observation above (namely 0.71).

We emphasize that this reduction is by no means "embarrassing." It is in basic agreement with the conjugate matched case where the current ratio would be 0.50 and the efficiency 50%. See also the discussion in Appendix B.9.

But how do we explain the much stronger reduction of the ripples associated with the surface waves? Well, we shall later in Chapter 4 investigate surface waves in much more detail. It will there be shown that the terminal impedance associated with the surface waves is quite low, say of the order of $Z_{surf} \sim$ 10 ohms for each of the two surface waves. Thus, by the same reasoning as for the Floquet currents above, we find for each surface wave a reduction equal to $10/(10 + 100) = 0.091$. This is of course an average value but explains the strong ripple reduction observed in Fig. 1.5a.

This observation is quite noteworthy. It shows that by matching an antenna in the neighborhood of maximum power transfer (i.e., conjugate matching) we obtain an added benefit, namely a potential strong reduction of the ripples of the scan impedance even at a frequency where the surface waves are dominating.

Incidentally, the low value of the terminal surface impedance Z_{surf} is just another manifest of what has been observed earlier (see Fig. 1.4)—namely, that in spite of the fact that the surface wave currents may be stronger than the Floquet currents (see Fig. 1.3c), their radiation intensity will in general be considerably below that of the Floquet currents. Several actual calculated examples illustrating this statement will be given in Chapter 4.

1.4.2   The FSS Case

When a periodic structure is intended to work as a wire FSS, it would lead to unacceptably high reflection loss if each element was loaded with resistors

comparable to the terminal impedance Z_A (about 3 dB). To gain further insight, let us consider the equivalent circuit for an FSS as shown in Fig. 1.6b. Here the generator voltages V^i are no longer produced by man-made generators V^g but are instead induced by the incident plane wave. The objective at resonance is now simply to get as high a current as possible to flow through Z_A and Z_L in order to obtain lossless reflection from the surface. Thus, any load impedance Z_L should ideally be purely imaginary and serve merely to cancel any imaginary components of Z_A.

So how do we control surface waves on an FSS?

One approach is to simply have no resistors anywhere over the entire surface, with the exception of a few columns at the edges. An example is shown in Fig. 1.5b, where the two outer columns have been loaded with 200 ohms, the next ones toward the center with 100 ohms, and finally the third column with 50 ohms. We observe a significant reduction of the ripple amplitudes as compared to the unloaded case in Fig. 1.3c. It should be noted that no parametric study was done on the resistive values of the loads at this point. More in Chapter 4.

We also show in Fig. 1.5c a case where each element over the entire surface has been loaded very lightly, namely with 20 ohms. We observe a strong reduction of the ripples from column to column—in particular, in the right half of the array.

The transmission loss at resonance due to the 20-ohm load resistors is obtained from the equivalent circuit in Fig. 1.6b. The reduction of current is equal to $Z_A/(Z_A + Z_L) = 200/(200 + 20) = 0.9$, or about 1 dB (just barely permissible).

Alternatively we may instead of the 20-ohm loss resistors obtain a moderate loss by simply using a slightly lossy dielectric next to the elements or simply a resistive sheet close to the elements.

Finally, many possibilities are open by combinations of the various approaches listed above. More about this in Chapter 4.

1.5   COMMON MISCONCEPTIONS

1.5.1   On Common Misconceptions

In my first book, *Frequency Selective Surfaces, Theory and Design* [1], I introduced at the end of each chapter a section called *Common Misconceptions*. It was intended to eradicate some of the many myths and misunderstandings that seem so prevalent "out there." It was also intended to form the basis for further discussion in class. It soon became very popular. In fact, I became aware that these sections were often read with great glee before the text preceding them. This was manifested in well-meaning comments like: "Well, it is fine that you tell us what will and will not work. But you must also tell us why." It slowly dawned on me that a new misconception had arrived: You just had to read the sections about common misconceptions and you would be up to speed and not make a fool out of yourself.

Furthermore, it was often implied that the design examples were the results of either a parametric study or an optimization process or were based on "many years of experience."

While I will admit to some parametric observations where no specific theoretical background could be established right away, we are basically using an analytic approach[1] that not only leads to a clear understanding of the problems but also establishes whether solutions exist and what they are.

I think it was Edison that once stated, "There is no substitute for hard work."

1.5.2 On Radiation from Surface Waves

This title will undoubtedly raise a few eyebrows. As stated in many respectable textbooks, surface waves do not radiate—period. What is not always emphasized is the fact that the theory for surface waves in general is based on a two-dimensional model like for example an infinitely long dielectric coated wire. And as discussed in this chapter infinite array theory may reveal many fundamental properties about arrays in general but there are phenomena that occur only when the array is finite. The fact is that surfaces waves are associated with element currents. They will radiate on a finite structure in the same manner an antenna radiates, namely by adding the fields from each column in an endfire array. Numerous examples of this kind of radiation pattern will be shown in Chapter 4. They are typically characterized by having a "mainbeam" in the direction of the X axis that is lower than the "sidelobe" level. The reason for this "abnormality" is simply that the phase delay from column to column exceeds that of the Hansen–Woodyard condition by a considerable amount [29]. They also have a much lower radiation resistance.

An alternative approach is to assume that the radiation from a finite array is associated entirely with the edge currents. While Maxwell's equations do not state specifically that radiation or scattering takes place from neither edges or element tips, it is nevertheless an observation that has proven valuable in classical electromagnetic theory. It is a convenient way to handle scattering properties from perfectly conducting half-planes, strips, wedges, and more, even when made of dielectric.

However, in the case of finite arrays of loaded wire elements the approach loses some of its appeal by the fact that surface waves exist only in a limited frequency range inside which the amplitude and phase vary considerably with frequency. Consequently, the scattering properties must be calculated numerically at each frequency and will actually also depend on array size in a somewhat complicated way.

At this point, this approach therefore is primarily of academic interest.

1.5.3 Should the Surface Waves Encountered Here Be Called Edge Waves?

It has been suggested to denote the surface waves introduced in this chapter as "edge waves" for no reason other than they originate at the edges of the array. This confronts us with certain problems.

---

[1] By analytic we mean to separate a problem into components and study each of these individually before we put them back together.

First of all, the term edge wave has been used to denote a wave that propagates along and not orthogonal to an edge [30]. In other words, we are talking about two entirely different kinds of waves.

Second, the term *edge wave* has been used by Ufimtsev and many others to denote waves that originate on the edges and propagate orthogonal to these all right [28]. However, that kind of edge wave dies down as you move away from the edge and their propagation constant is that of free space. The surface waves encountered here are basically not attenuated (except by radiation and ohmic losses) as they move away from the edge and propagate over the entire array.

Furthermore, the propagation constants of the waves encountered have been determined in Chapter 4 to be precisely equal to that of surface waves propagating along arrays of dipoles. These propagation constants are of course vastly different than that of free space. Thus, the surface waves encountered here should be called surface waves because that is what they are.

One is of course entitled to wonder why this phenomenon has gotten so sparse attention in the literature if any. The main reason is probably that the interelement spacing should be less than 0.5λ and the frequency $\sim 20-30\%$ below resonance (see Chapter 4 for details). Typically, many researchers choose a borderline spacing of $D_x = 0.5\lambda$ and concentrate their attention around the resonance frequency [31–33]. As can be seen in Fig. 1.3, this basically precludes the existence of any strong surface waves.

1.6 CONCLUSION

We have demonstrated the presence of surface waves that can exist only on a finite periodic structure. It is quite different from the well-known types of surface waves that can exist in a stratified medium next to a periodic structure often referred to as Type 1. These merely represent grating lobes trapped inside the stratified medium. Thus, they will readily manifest themselves in computations based on infinite array theory at frequencies so high that grating lobes can be launched.

In contrast, the new type of surface wave (Type 2) can exist only if the interelement spacing D_x is so small that no grating lobe can exist. In addition, the frequency must typically be 20–30% below the resonance frequency of the periodic structure.

The presence of this new type of surface wave manifests itself in various ways:

1. If used as an FSS, it can lead to a significant increase in the bistatic scattering. In particular, we may observe a sizeable increase in the RCS of objects comprised of FSS without treatment.

2. If the structure is used as a phased array, it can lead to dramatic variations of the terminal or scan impedance from column to column. Under these circumstances it would be very difficult to design a high-quality matching network in particular since the maximas and minimas of the scan impedance will move significantly with frequency and scan angle.

We also indicated that this type of surface wave could be controlled in various ways. One approach is to load each element resistively. If used as an FSS, the resistors should have a low value in order not to significantly attenuate the reflected signal. In case of phased arrays a resistive loading could be obtained by simply feeding the elements from constant voltage generators with realistic generator impedances.

Alternatively, we could use no resistors at any of the elements across the surface but only at a few columns at the edges of the periodic structure. Slightly lossy dielectric slabs or even resistive sheets can also be used.

Finally, many possibilities are left open by combinations of some or all of the approaches above. See also Chapter 4 for details.

One might well ask the question, Why not just operate in a frequency range between the two types of surface waves? Well, in the case of an FSS it has been demonstrated numerous times that stability with angle of incidence can be obtained only for small interelement spacings (see, for example, reference 34). And basically the same is true for phased arrays in particular if designed for broad bandwidth. See Chapter 6 for details.

This introduction has merely pointed out the presence and treatment of surface waves that may exist below resonance for finite periodic structures. An in-depth investigation will be given in Chapter 4 where we will rely entirely on rigorously calculated examples.

PROBLEMS

1.1 Consider a phased array with scan impedance $Z_A = 200$ ohms. It is being fed from a generator with impedance Z_G as shown in Fig. 1.6a. Assume conjugate match—that is, $Z_G = Z_A = 200$ ohms.

As shown in Chapter 4, each of the two surface waves are generated from semi-infinite arrays located adjacent to the finite array. We will assume the equivalent circuit to consist of surface wave generators at each end of the finite array with surface wave generator impedances for the left- and right-going surface wave denoted $Z_{SW\ L}$ and $Z_{SW\ R}$, respectively. We will assume that these impedances depend on angle of incidence.

Furthermore, we will assume that the generator impedances Z_G are connected in series with $Z_{SW\ L}$ and $Z_{SW\ R}$, separately; that is, Z_G will reduce the surface waves as observed for example in Fig. 1.5a.

Given the surface wave impedances $Z_{SW\ L}$ and $Z_{SW\ R}$ and the generator impedance Z_G:

1. Find the reduction of the surface waves compared to the no-load case $Z_G = 0$ for $Z_G = 200$ ohms, in decibels for $Z_{SW\ L}$ equal to

   (a)   2.5 ohms

   (b)   5.0 ohms

   (c)   10.0 ohms

(d) 20.0 ohms

(e) 40.0 ohms

2. If the generator loads are increased to 400 ohms, state approximately how many decibels the reduction will change (up, down?).

2

On Radar Cross Section of Antennas in General

2.1 INTRODUCTION

It is well known that the RCS of any antenna can be significantly reduced by placing a suitably shaped bandpass radome in front of it [35]. When the radome is opaque, the incident signal will primarily be reflected in the specular direction while the backscattered signal will be low as illustrated in Fig. 2.1. However, when the radome is transparent, no significant reduction of the antenna RCS will take place. Thus, the observable RCS will depend primarily on the antenna per se and whatever is behind the radome—for example, the back wall. It therefore becomes important to ask the scientifically very interesting question, "Is it possible to design an antenna that basically is invisible over a broad band in the backward sector without sacrificing its efficiency?"

Most readers will say no. They typically base their answer on well-documented facts about the most commonly used antennas such as a single dipole or monopole, the horn, the flat spiral, the corner reflector, the polyrod, the patch, the log periodic, the helical with a groundplane, and many more. These are all lacking in their ability to produce a low RCS over a broad frequency range when properly matched. Thus, we shall in this chapter instead concentrate on one of the few concepts that can truly produce invisibility in the backward sector, namely the large flat aperture in the form of an array backed by a groundplane and with uniform aperture illumination. The tapered case will also be discussed; and it will be shown that also in that case, invisibility is conceptually compatible with 100% efficiency.
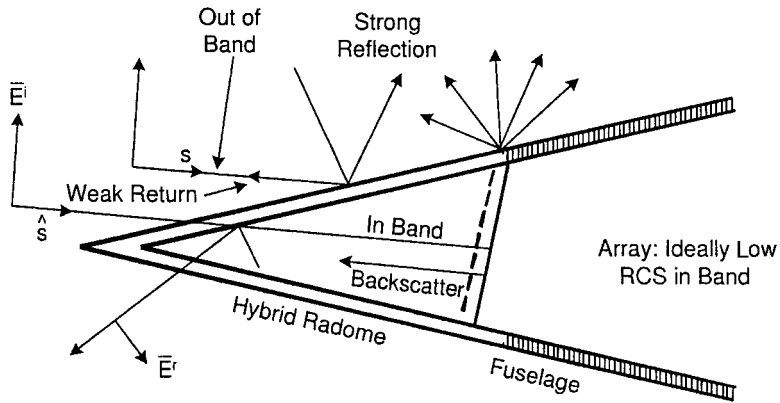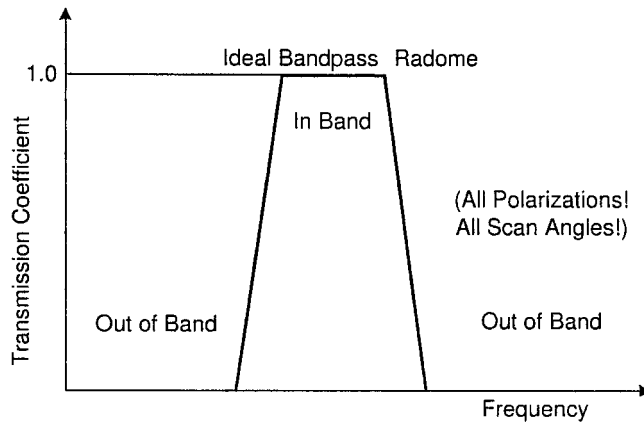
Fig. 2.1   Use of a hybrid radome with bandpass characteristic to reduce the antenna RCS out of band.

A large flat aperture is most often associated with a narrow pencil beam. However, we shall in Chapter 7 consider antennas with omnidirectional pattern and low visibility in the backward direction over a broad band. Further discussed in Chapter 8 is how to design a feed for a parabolic cylinder that will produce an RCS about 6 dB lower than with no feed at all. The design of such a feed is closely related to the omnidirectional design. We emphasize, however, that parabolic systems never can attain the inherently low RCS level encountered for the flat aperture over a broad frequency band.

In the next section we will present the classical fundamentals of antenna RCS valid for all antennas. They are important in order to better understand the intricacies of antenna RCS.

2.2 FUNDAMENTALS OF ANTENNA RCS

In this section we shall show that the field scattered (reradiated) from an antenna is comprised of two components:

1. The **antenna mode** component depending on the gain G, the load impedance Z_L, the polarization, the angle of incidence and the frequency.
2. The **residual mode** component representing whatever must be added to the antenna mode component to obtain the total RCS. It may or may not depend on the gain G, the polarization, the frequency, and the angle of incidence, but never on the load impedance Z_L.

The definition of the residual mode admittedly violates a fundamental scientific principle: Never explain something unknown by something else unknown. Nevertheless, the concept is extremely useful for understanding antenna scattering.

Thus, we shall show several important examples where the residual scattering component is determined and illustrate how it relates to the antenna mode component.

An alternative and somewhat older nomenclature for the residual component is the structural scattering. We do not particularly recommend this nomenclature because it is somewhat misleading. For example, large arrays of dipoles without a groundplane will be shown later (see Section 2.6) to have as much residual scattering as antenna mode scattering. However, when we add a groundplane (yes, add more structure) the antenna mode is increased by a factor of four while the residual scattering simply as shown later is equal to zero. Thus, we avoid the word "structure" because it is burdened by the misconception that more structure means more scattering due to the structure. It may or it may not. See also Sections 2.14.1 and 2.14.2.

2.2.1 The Antenna Mode

More specifically, let us now consider an antenna exposed to an incident plane wave propagating in the direction $\hat{s}_i$ and with power density Φ_i as shown in Fig. 2.2. If the load impedance Z_L is conjugate-matched to the antenna impedance Z_A, the received power is maximum and given by [36]

$$P_{rec}^i = \frac{\lambda^2}{4\pi} G_i \Phi_i p_i, \tag{2.1}$$

where G_i is the antenna gain in the direction of incidence $\hat{s}_i$ and p_i is the polarization mismatch factor between the incident E-field and the polarization of the antenna, that is, $0 \leq p_i \leq 1$.

We next seek the reflection coefficient Γ between the antenna impedance Z_A and Z_L. If one of them is real, the usual simple expression for Γ is valid (see later). However, if they are both complex as shown in Fig. 2.3, top, we
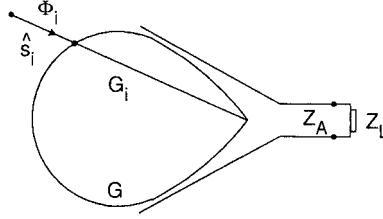
Fig. 2.2   *An antenna with gain G_i being exposed to an incident plane wave with power density Φ_i and direction $\hat{s}_i$ will receive the power $P^i_{rec} = \dfrac{\lambda^2}{4\pi} G_i \Phi_i p_i$, where p_i represent the polarization mismatch between the antenna and the plane wave.*

Original Problem: Determine the best match (i.e., maximum real power transfer) between the two complex impedances Z_A and Z_L.

Modified Problem: The match between the *real* impedance R_A and the complex impedance $R_L + j(X_A + X_L)$ is well known.
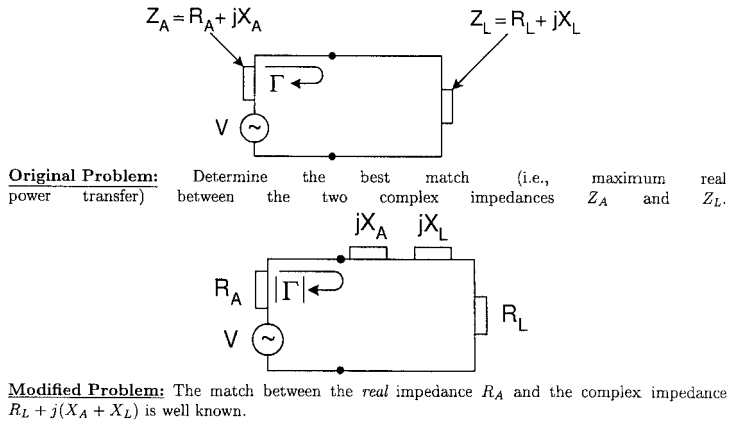
Fig. 2.3   *How the reflection coefficient Γ between two complex impedance $Z_A = R_A + jX_A$ and $Z_L = R_L + jX_L$ is reduced to the simpler problem between the real impedance R_A and the complex load $R_L + j(X_A + X_L)$.*

must modify the original problem to the one shown in Fig. 2.3, bottom. This is based on the simple fact that for a two-port lossless circuit the magnitude (not the complex value) of Γ will remain the same no matter where we place the terminals in the circuit. From the modified circuit the magnitude of the reflection coefficient between the real impedance R_A and the complex impedance $R_L + j(X_L + X_A)$ is readily obtained as

$$|\Gamma| = \left| \frac{R_L + j(X_L + X_A) - R_A}{R_L + j(X_L + X_A) + R_A} \right|. \tag{2.2}$$

The received power P_{rec} given by (2.1) will be partly absorbed by the load impedance Z_L and partly reflected back toward the antenna as reflected power given by

$$P_{refl} = P_{rec}|\Gamma|^2, \tag{2.3}$$

where $|\Gamma|$ is given by (2.2).
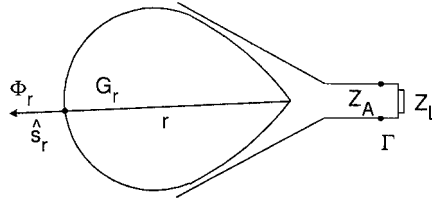
Fig. 2.4   The power P_{rec} received by the antenna will be reradiated as $P_{refl} = P_{rec}|\Gamma|^2$. In the bistatic direction $\hat{s}_r$ the antenna gain is G_r and we obtain a power density $\Phi_r = P_{refl}/4\pi r^2 G_r p_r$, where p_r is the polarization mismatch between the antenna and a receiving antenna.

The reflected power P_{refl} will now be radiated (or rather reradiated) by the antenna like any other signal impressed at its terminals.

If the antenna had been isotropic, the power P_{refl} would at a distance r be uniformly distributed over a sphere with surface area $4\pi r^2$. Thus, the power density at distance r would be $P_{refl}/4\pi r^2$. However, if the antenna has a gain G_r in the direction of radiation $\hat{s}_r$ as shown in Fig. 2.4, the power density in that direction and at distance r will be

$$\Phi_r = \frac{P_{refl}}{4\pi r^2} G_r p_r, \tag{2.4}$$

where p_r is the polarization mismatch factor between the scattering antenna and a receiving antenna located in the far field, that is, $0 \leq p_r \leq 1$.

Substituting (2.1) and (2.3) in (2.4), we obtain

$$\Phi_r = \frac{\lambda^2}{16\pi^2 r^2} G_i G_r p_i p_r |\Gamma|^2 \Phi_i. \tag{2.5}$$

The definition of the radar cross section (RCS) is illustrated in Fig. 2.5. Here a fictitious flat plate, with area σ_{ant}, intercepts an incident plane wave with power density Φ_i—that is, the intercepted power is $\sigma_{ant}\Phi_i$.

If this power is spread uniformly in space at distance r, the power density Φ_{ant} is

$$\Phi_{ant} = \frac{\sigma_{ant}\Phi_i}{4\pi r^2},$$

or

$$\sigma_{ant} = 4\pi r^2 \frac{\Phi_{ant}}{\Phi_i}. \tag{2.6}$$

The radar cross section of the antenna mode component is now defined as an area σ_{ant} so large that the power density Φ_{ant} associated with the fictitious plate is the same as the power density Φ_r associated with the antenna mode component; that is, we set

$$\Phi_{ant} = \Phi_r. \tag{2.7}$$
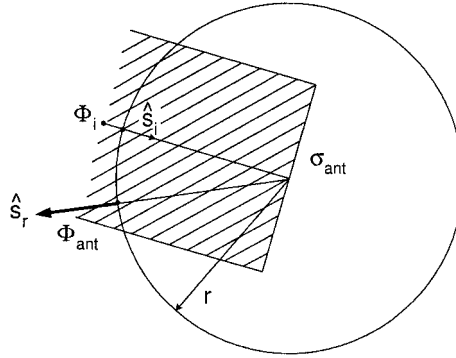
Fig. 2.5   The power intercepted by a fictitious flat plate with area σ_{ant} is $\sigma_{ant}\Phi_i$. When spread uniformly in space, it produces at distance r the power density $\Phi_{ant} = \sigma_{ant}\Phi_i/4\pi r^2$ or $\sigma_{ant} = 4\pi r^2 \Phi_{ant}/\Phi_i$. We define σ_{ant} such that $\Phi_{ant} = \Phi_r$ — that is, equal to the power density produced by the antenna. Thus, from earlier, $\sigma_{ant} = \dfrac{\lambda^2}{4\pi}G_iG_rp_ip_r|\Gamma|^2$.

Substituting (2.5) and (2.7) into (2.6) yields the radar cross section of the antenna mode:

$$\sigma_{ant} = \frac{\lambda^2}{4\pi}G_i\,G_r\,p_i\,p_r\,|\Gamma|^2. \tag{2.8}$$

2.2.2   The Residual Mode

Expression (2.8) will in general not constitute the entire RCS of an antenna. In fact, it is only a component of the total radar cross section, which implies that there may be something else. This is usually called the residual (or structural) component σ_{res}. It was defined earlier as "whatever must be added to the field associated with σ_{ant} as given by (2.8) in order to obtain the field associated with the total antenna RCS," that is,

$$\sigma_{tot} \equiv \frac{\lambda^2}{4\pi}G_i\,G_r\,p_i\,p_r\,|\Gamma + C|^2 \tag{2.9}$$

and the Residual scattering cross section is defined as

$$\sigma_{res} \equiv \frac{\lambda^2}{4\pi}G_i\,G_r\,p_i\,p_r\,|C|^2. \tag{2.10}$$

Note: $\sigma_{tot} \neq \sigma_{ant} + \sigma_{res}$ in general.

Inspection of (2.10) might seem to imply that σ_{res} is proportional to $G_iG_rp_ip_r$. This is not necessarily the case. In general it is a more intricate function. In fact, the only reason we write it on the form in (2.10) is that it enables us to add
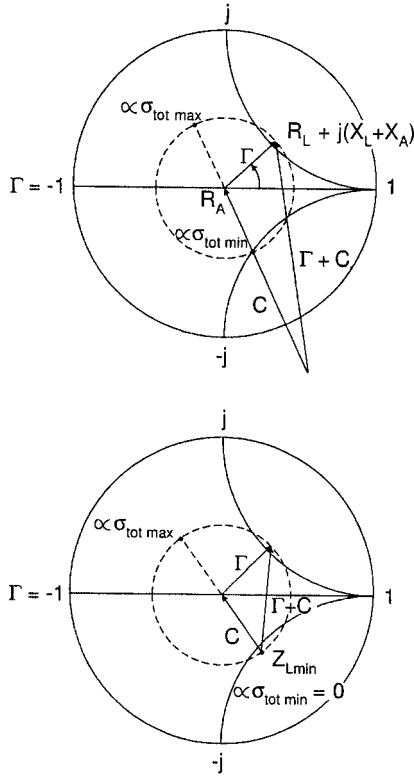
Fig. 2.6   Antenna mode: $\sigma_{ant} = \frac{\lambda^2}{4\pi}G^2|\Gamma|^2$. Residual mode: $\sigma_{res} = \frac{\lambda^2}{4\pi}G^2|C|^2$. Total antenna RCS: $\sigma_{tot} = \frac{\lambda^2}{4\pi}G^2|\Gamma + C|^2$. All antenna RCS can be envisioned as made up of the antenna mode component σ_{ant} and the residual component σ_{res}. The antenna mode component is proportional to $|\Gamma|$ and can therefore be depicted in a Smith chart. The residual component represented by C can be larger than Γ (top) or smaller (bottom).

it to σ_{ant} to obtain σ_{tot} as given by (2.9). However, it does not depend on Z_L. Otherwise it would have been part of σ_{ant}.

More specifically, consider Fig. 2.6, top. We show here a Smith chart normalized to R_A. Recall further that one of the unique features of the Smith chart is that the reflection coefficient Γ as given by (2.2) is a phasor measured from the center R_A of the Smith chart to the modified load impedance $R_L + j(X_L + X_A)$ as shown in the Smith chart. The magnitude of the field associated with the antenna mode component is proportional to $|\Gamma|$ [see (2.8)], while the magnitude of the field associated with the residual mode component is proportional to $|C|$ [see (2.10)]. Thus, according to (2.9) the field associated with σ_{tot} is proportional to the magnitude of the phasor sum $(\Gamma + C)$ as also shown in the same Smith chart.

The beauty of this representation is that it clearly shows how σ_{tot} varies with the load impedance Z_L (as mentioned above, C does not depend on Z_L). For example, we may let Z_L vary in such a way that the VSWR is constant. In

that case the tip of Γ will move along a circle with radius $|\Gamma| \leq 1$ as shown in Fig. 2.6, top. We can in that way obtain a maximum $\sigma_{tot\ max}$ as well as a minimum $\sigma_{tot\ min}$ as shown. For conjugate match $Z_L = Z_A^*$ and $\Gamma = 0$; that is, σ_{tot} is proportional to $|C|^2$. Thus, for matching the load to maximum power transfer, σ_{tot} can be substantial if $|C|$ is large; and what is worse, if $|C| > |\Gamma|$ as is the case in Fig. 2.6, top, we can never obtain $\sigma_{tot} = 0$ for any load.

2.3   HOW TO OBTAIN A LOW σ_{tot} BY CANCELLATION (NOT RECOMMENDED)

We considered above the case where the residual component C was bigger than Γ. We found that σ_{tot} could never become zero no matter how we chose our load impedance Z_L. However, if we instead considered an antenna where $|C| < 1$ as shown in Fig. 2.6, bottom (there are no particular limitations on C), we readily observe that we can choose the load impedance Z_L such that $C + \Gamma = 0$; that is, $\sigma_{tot\ min} = 0$. This technique is referred to as RCS control by cancellation.

There are two strikes against this approach. First of all the load impedance Z_L is not necessarily adjusted for conjugate match; that is, the power transfer is not perfect. But the biggest flaw is that the cancellation is in general very frequency-sensitive—that is, narrowbanded (Z_L and Z_A will in general change significantly and differently with frequency). And as if that is not enough, the cancellation condition changes in general with angle of incidence and polarization.

Therefore this approach should in general be discarded as being primarily of academic interest. See also Sections 2.14.1, 2.14.4, and 2.14.7, as well as Section 2.9 and Problem 2.2.

2.4   HOW DO WE OBTAIN LOW σ_{tot} OVER A BROAD BAND?

The answer to that question should by now be fairly obvious: Choose an antenna with a residual scattering close to zero (i.e., $C \sim 0$) and keep Γ as low as possible over as a broad a band as possible as illustrated in Fig. 2.7. That will ensure maximum power transfer (or almost) and low σ_{tot} at the same time.

The reaction to this suggestion is typically something like: Well, we have measured dipoles, horns, parabolic dishes, flat spirals as well as helical antennas with groundplane, and what not, and we have never come across an antenna with no residual scattering. In fact we are not even sure whether an antenna without residual scattering violates certain fundamental rules!

Actually, they are almost correct, but it is bad science to generalize based on a limited number of cases. The fact is that antenna configurations without residual scattering do not violate any fundamental law and that they do indeed exist. These will be discussed in Sections 2.6 and 2.7. However, let us first pay homage to some of the key people who pioneered the theory about antenna scattering.
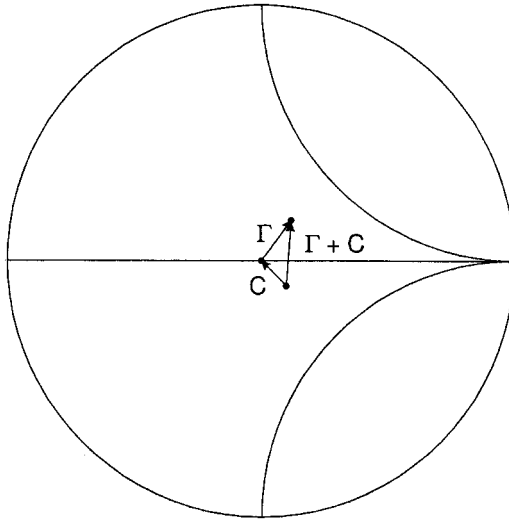
Fig. 2.7 *To obtain a low RCS over a broad band an antenna ideally should have (a) as low a residual scattering as possible (i.e., C ∼ 0) and (b) a broadband match yielding Γ ∼ 0.*

2.5   A LITTLE HISTORY

When the author joined the group of Professor Leon Peters, Jr., at the Ohio State University Antenna Laboratory (currently ElectroScience Laboratory) in the mid-1960s as a graduate student, he was considered a competent antenna engineer with a good industrial background. He had a good knowledge of antenna impedance and considerable experience in matching and he knew how to obtain a radiation pattern from a complex antenna system. However, he had not even heard about antenna radar cross section. And that was typical for most antenna engineers at that time.

He was first introduced to the mysteries of antenna scattering during a short course given at Ohio State University in 1966. One of the sessions was devoted to the RCS of antennas [37] and conducted by Professor Robert Garbacz, at that time a graduate student of Professor Edward Kennaugh. Furthermore, some time before in 1963 another graduate student and a close friend of Garbacz, namely Robert B. Green, wrote his dissertation that dealt exclusively with RCS of antennas [38]. It was that work that became the foundation for Section 2.2 in this chapter.

However, it appears that the concept describing how the scattering from an antenna is made up of two components was presented for the first time in an OSU report by McEntee [39]. He clearly recognized that the scattering (reradiation) is coming from the mismatch between antenna and load impedance(s) (the antenna mode), and, in addition, a scattering component comes from somewhere else associated with the antenna (the residual or structural component). He did not actually call these components by these names. Apparently that came later. All

of this activity did of course take place under the watchful eyes of Professors Peters and Kennaugh, who provided many of the basic ideas and concepts.

However, there were other important contributions. Hansen discussed the relationship between antennas as scatterers and as radiators [40]. Garbacz discussed measurement techniques [41], and so did Appel-Hansen [42], Wang et al. [43] and King [44]. Several oral papers about measurements were presented by Heidrich and Wiesbeck [45–48], culminating with the dissertation by Heidrich [49].

2.6 ON THE RCS OF ARRAYS

In the world of antennas, arrays of wires or dipoles have a unique position. They can be designed to have very large bandwidth ($>7:1$ with VSWR <2); see Chapter 6. They can be designed to have very low radar return, possibly the only concept available at this point in time. Finally they constitute a periodic structure and are therefore properly discussed in this book.

In many respects it makes a significant difference whether the array has a groundplane or not. Thus we shall look in detail at each of these cases separately.

Note that the discussion to follow serves merely the purpose of explaining the physics of antenna scattering. Actual rigorous calculations are obtained from either the PMM or the SPLAT program. Numerous rigorous calculated examples are given in Chapter 5. It has been the author's experience that while most scientists can use a computer program, only a minority understand "what goes on" and are lacking in design ability. Thus, although our presentation is based on approximate ideas, they are very important to the serious researcher.

2.6.1 Arrays of Dipoles without a Groundplane

Basically we will consider arrays of infinite extent in both the X and Z directions. However, the fundamental concept discussed here will also apply to very large arrays (in terms of wavelength) as long as we disregard edge effects. These will be discussed later in Chapter 5 and focus on the variation of the element impedance.

In Fig. 2.8 we show a dipole array seen edge-on under three different load conditions. The element lengths are $\sim\lambda/2$. In the case to the left the terminals are open-circuited. Thus, looking into the antenna terminals we observe a reflection coefficient $\Gamma = +1$ as also shown in the Smith chart underneath the array.

However, we can also consider such a structure as a frequency selective surface. When exposed to an incident plane wave the reflection coefficient $\Gamma_{FSS} \sim 0$. (From this viewpoint we have assumed here that the total scattering from $\lambda/4$ segments is negligible compared to that from $\lambda/2$ dipoles. While this is an approximation depending on wire radius, it does not alter the fundamental approach.)

$\Gamma_{FSS} \sim 0$ simply implies that $\sigma_{tot} \sim 0$, and from (2.9) we then obtain

$$C \sim -\Gamma = -1 \tag{2.11}$$

as also indicated in the Smith chart below the array.
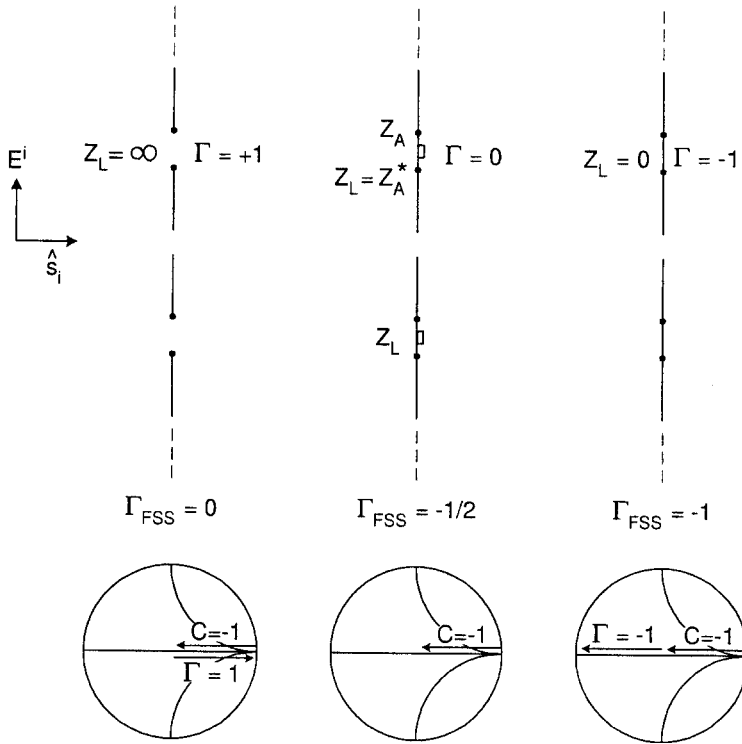
Fig. 2.8   A large array without a groundplane seen edge-on for three load conditions. Left: The terminals are open-circuited, that is, $\Gamma = +1$. Middle: The terminals are loaded with a conjugate match, that is, $\Gamma = 0$. Right: the terminals are short-circuited, that is, $\Gamma = -1$.

Obviously, (2.11) supports the statement made several times earlier (see Section 2.2), namely that an array without a groundplane has about as much residual as antenna mode scattering.

Next we consider the case where Z_L is conjugate-matched to the antenna impedance Z_A. Thus, the reflection coefficient at the array terminals is $\Gamma = 0$, and the backscatter from the array is simply proportional to $C = -1$.

Finally we consider the case to the right in Fig. 2.8. We have here loaded the array at its terminals with short circuits; thus $\Gamma = -1$ as indicated in the Smith chart underneath the array. The total backscattered field is proportional to $\Gamma + C \sim -1 - 1 = -2$ [see (2.9)]. However, when viewed as an FSS of elements with length $2l \sim \lambda/2$, we also know that such a surface reflects as a groundplane. Thus the reflection coefficient for an incident wave is $\Gamma_{FSS} = -1$. In other words, $\Gamma + C = -2$ produces a reflection coefficient equal to $\Gamma_{FSS} = -1$, and consequently the matched case in the middle with $C = -1$ will produce a reflection coefficient equal to $\Gamma_{FSS} = -1/2$.

The observation that loading an array with load impedances $Z_L = Z_A^*$ produces a backscattered radar cross section 6 dB below the backscatter obtained for the

short-circuited case is often referred to as the "6-dB Rule." It is characteristic for a class of antennas usually referred to as minimum scattering antennas (MSA) (according to the classical definition as will be discussed in Section 2.10). It is often falsely assumed that this rule pertains to all antennas. It does not. In fact, we shall in the next section consider arrays with a groundplane and observe that the 6-dB Rule fails completely as it does for many of the most important antenna configurations. And thank heaven for that! (See also Problem 2.3.)

2.6.2 Arrays of Dipoles Backed by a Groundplane

We now add a groundplane to our array of dipoles as shown in Fig. 2.9. This will distinctly change the antenna impedance Z_A, but that is of no particular concern for our present purpose.

An incident plane wave with direction of propagation $\hat{s}_i$ will induce currents on the elements as discussed in reference 50. They in turn will radiate a spectrum of plane inhomogeneous waves. The zero-order mode will always propagate in the specular direction $\hat{s}_r$ and is denoted by "1" in Fig. 2.9. Similarly, another plane wave will be radiated symmetrically to "1" and then be reflected in the
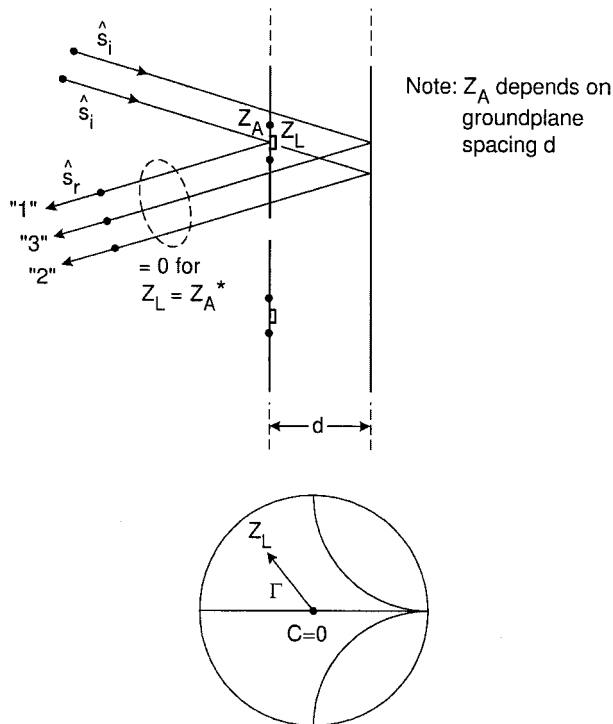
Fig. 2.9   A large array with a groundplane seen edge-on. It can be shown that for conjugate match the three plane waves denoted by their directions "1," "2," and "3" will add up to zero; that is, everything is absorbed.

groundplane such that it also propagates in the specular direction. It is denoted "2." Finally, the incident field will go straight through the elements and be reflected as "3" (remember in our model we substitute the conducting elements for just electric currents. These are always "transparent)."

We now observe the scattered field at a distance so large that all the evanescent waves have practically died out (typically that would be any distance from the dipoles exceeding about $\lambda/4$ unless the interelement spacings D_x and D_z are large). We also assume D_x and D_z to be so small that no grating lobes can exist. It is now left as an exercise for the students to show (see Problem 2.4) that if the load impedance Z_L is conjugate-matched to Z_A the sum of the three plane waves "1," "2," and "3" will add up to zero (we assume that our point of observation is beyond the extent of the evanescent waves). Thus, the incident field must be totally absorbed since nothing is reflected for conjugate match; that is, the residual scattering is zero, or $C = 0$. Obviously this constitutes the ideal situation as illustrated in Fig. 2.7: If the antenna is conjugate-matched, $\Gamma = 0$ and the antenna is invisible in the backward sector.

This result is surprising to many readers. However, it has actually been known by implication for at least half a century. As any classical textbook about antennas will tell you [51], the receiving area of a large array with uniform aperture distribution and no groundplane is half its physical size. Thus, when conjugate-matched, such an array will receive half the power incident upon it. The other half (i.e., down 3 dB) will be radiated equally in the forward and backward directions—that is, down another 3 dB. Thus we have simply verified the "6-dB Rule" introduced earlier.

Furthermore, it is also well known that if a large array is provided with a groundplane, the receiving area is simply equal to the physical area [52]. In other words, an array with a groundplane and conjugate match will receive *all* the energy incident upon it and will consequently not scatter any energy in the backward direction (*Remember*: Only for uniform aperture distribution. The tapered aperture distribution is discussed in Section 2.11.2).

As an antenna engineer these facts were well known to the author early on in his work with the RCS of antennas. In fact, they quickly became the guiding light in the pursuit of the invisible antenna concept. In all research it is a tremendous help if you know the final result ahead of time!

2.7   AN ALTERNATIVE APPROACH: THE EQUIVALENT CIRCUIT

The approach taken above is a good illustration of the scattering theory valid for all antennas. However, when we work with large flat arrays as above, it is actually considerably easier to simply consider an equivalent circuit. Note, however, that the primary purpose of such a circuit is to gain understanding and guidance in the design of arrays. It is never used to obtain actual numerical results. These are obtained from the PMM or similar programs.

The equivalent circuit was developed earlier [53] and is actually used extensively in Chapter 6 of this book for understanding large arrays designed for a
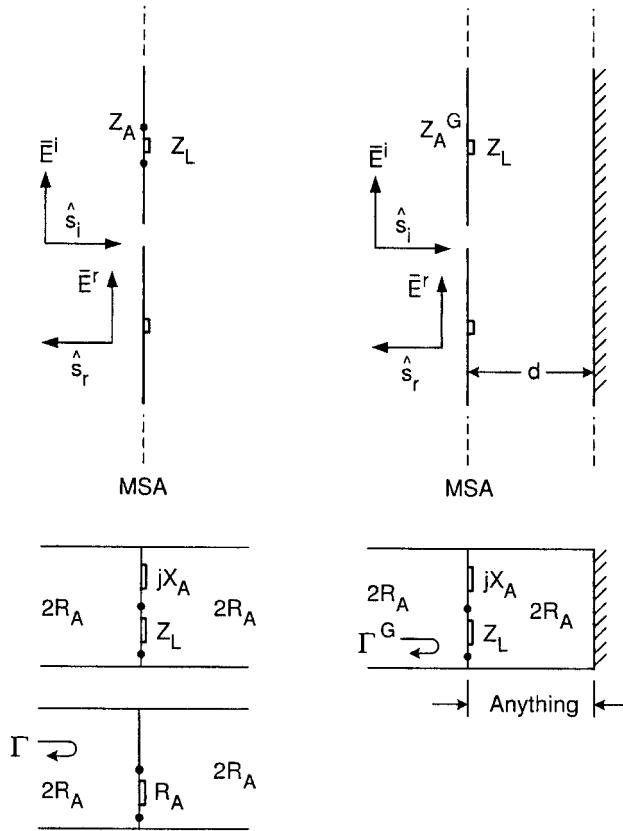
Fig. 2.10   *Left: A plane wave is incident upon a large array without a groundplane. As seen from the equivalent circuit below, it will have no backscatter only for $Z_L = \infty$; that is, we will receive no power. For Z_L conjugate matched, $\Gamma = -1/2$ [see (2.12)]. Right: Same situation as before but the array has a groundplane. When Z_L is conjugate-matched, the incident wave is completely absorbed; that is, the RCS equals zero. Note: These equivalent circuits are valid only in the principal planes.*

broad band. Thus, it suffices here simply to show the equivalent circuit for an array without a groundplane (see Fig. 2.10, left) and similarly an array with groundplane (see Fig. 2.10, right). In the first case we observe that it consists of an infinite transmission line with characteristic impedance $2R_A$ shunted with the antenna reactance jX_A in series with the load impedance Z_L. For conjugate match we obtain the equivalent circuit shown at the bottom. The reflection coefficient for a signal incident from left or right is then

$$\Gamma = \frac{R_A\|2R_A - 2R_A}{R_A\|2R_A + 2R_A} = -\frac{1}{2}, \tag{2.12}$$

that is, we observe the "6-dB Rule" as discussed above. See also Problem 2.5.

We now add a groundplane as shown in Fig. 2.10, right. This will change the original antenna impedance to Z_A^G, and the effect of the groundplane is taken into account by a transmission line in parallel with $jX_A^G + Z_L$ and terminated in a short (the groundplane). If the load impedance Z_L is conjugate-matched to whatever impedance is observed at the terminals, all available power will be absorbed. Since the groundplane case to the right is a lossless two-port device connected to Z_L (see Fig. 2.3), we may conclude that a signal incident along the transmission line from the left will also be completely absorbed; that is, $\Gamma^G = 0$ or the residual scattering is zero. In other words, the signal reflected from an array with a groundplane is ∞ dB below the incident signal if conjugate matched. This is sometimes referred to as the "∞-dB Rule." Obviously, the 6-dB Rule does not hold at all in the groundplane case. One substantial difference between the two cases is that the former is a three-port device, whereas the latter is a lossless two-port. Only for $Z_L = \infty$ could the array without groundplane be "invisible;" and since the power received in that case would be zero, it is primarily of academic interest only. See also Section 5.3.

Note that the spacing d between array and groundplane can be anything but $n\lambda/2$. See also discussion about this subject in Section 6.12.2.

We finally note that an array with a groundplane and resistive loads actually belongs to a simple form of circuit analog absorbers. This relationship was pointed out in reference 54 and is also discussed in a different context in Section 6.12.1.4.

2.8 ON THE RADIATION FROM INFINITE VERSUS FINITE ARRAYS

2.8.1 Infinite Arrays

It is well known that the field radiated from an infinite array can be written as a sum of a finite number of propagating waves (the principal term corresponding to k, $n = 0$, 0 plus grating waves if any) and an infinite number of evanescent waves [50]. An example is shown in Fig. 2.11, top, where the direction of the principal propagating wave is denoted $\hat{r}(0, 0)$ and where no grating waves are encountered. Also indicated are the evanescent waves. They will typically die out as the point of observation moves beyond a distance $\sim\lambda/4$ from the array at which point only the propagating waves will exist. Thus, when dealing with infinite arrays we will always be in the "near field" as far as the radiation pattern is concerned; the concept "far field" simply does not exist for an infinite array.

2.8.2 Finite Array

The field radiated from a finite array is shown quantitatively in Fig. 2.11, bottom. Close to the array the field looks approximately as for the infinite array except for some ripples. These are merely caused by the same type of surface waves encountered in Chapter 1 and discussed in more detail in Chapters 4 and 5. They typically occur every time a general aperture is finite rather than infinite.
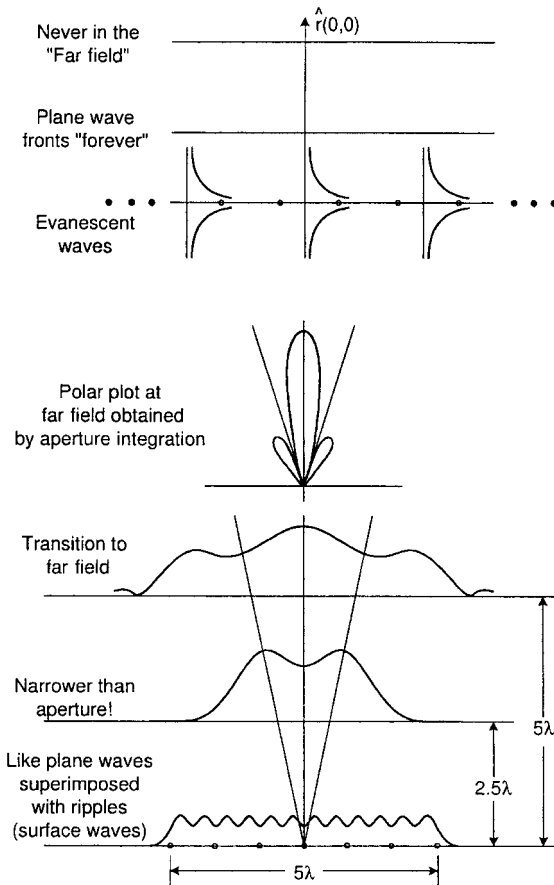
Fig. 2.11   Top: The field from an infinite array consists of a finite number of propagating plane waves and an infinite number of evanescent waves. The sum of the evanescent waves essentially constitutes the near field of the array. Bottom: The field from a finite array at various distances as shown.

As we move away from the finite array to a distance about half the size of the aperture we observe that the extent of the field becomes narrower than the aperture. And at a distance about the size of the aperture it has an extent about the size of the aperture. These observations are typical.

Finally, we show a polar plot of the far field obtained by simple aperture integration. Comparing the infinite and finite cases we observe that the former has an "infinite narrow" beam (like a Dirac-Delta function) in the direction $\hat{r}(0, 0)$ while the latter exhibits the well known far field pattern. At the array elements they both look similar except that the finite case shows ripples along the aperture as caused by the presence of surface waves as discussed in Chapters 1, 4 and 5.

We emphasize again: Fig. 2.11 is merely meant to be qualitative, not quantitative.

2.9 ON TRANSMITTING, RECEIVING, AND SCATTERING RADIATION PATTERN OF FINITE ARRAYS

In the last section we introduced the radiation pattern concept for finite arrays. We shall in this section consider in more detail what happens under transmitting versus receiving or scattering conditions.

Consider a finite array being fed from a single pair of terminals via some kind of harness. If we transmit from those terminals it is a conceptually simple process to obtain a far field transmit pattern Pat^{tr} based on the element currents under transmitting condition.

If we instead receive an incident signal at the same pair of terminals as above and rotate the antenna around its center we will record the receiving pattern Pat^{rec}. From the law of reciprocity we know that the transmit and receiving pattern will always be identical, i.e.

$$Pat^{tr} \equiv Pat^{rec}. \tag{2.13}$$

However, as also stated in the law of reciprocity, this fact does by no means imply that the currents under transmit and receiving conditions are identical. In fact, while they in some cases may be similar, they will in general be different.

Furthermore, if we evaluate the radiation pattern based on the receiving (i.e., scattering) currents, we will obtain the so-called scattering pattern Pat^{scat}. Obviously, based on our observation above concerning currents under receiving conditions, we can state that Pat^{scat} in some cases may be similar to $Pat^{tr} \equiv Pat^{rec}$, but it will in general be different, that is,

$$Pat^{scat} \neq Pat^{tr} \equiv Pat^{rec}. \tag{2.14}$$

We will now illustrate these statements by various examples.

2.9.1 Example I: Large Dipole Array without Groundplane

A large array of dipoles without a groundplane is shown in Fig. 2.12 top. Although not shown in the figure it is assumed that each dipole is fed via a harness containing hybrids as discussed later in Section 2.12. It will then be shown that as far as scattering is concerned, it is equivalent to loading each element with identical load impedances Z_L. And since we at present are most interested in the scattering aspect of such an array, this is quite sufficient for now.

If we impress a voltage at each terminal, we will obtain an element current under transmitting condition. For a total element length equal to $\sim\lambda/2$ or shorter, it will be approximately sinusoidal. However, if we instead expose the array to an incident plane wave we will obtain the element currents under receiving or scattering condition. They are not identical; in fact they are in general different, but if the total element length is $\sim\lambda/2$ or shorter, they will be similar (see also Section 2.11.1 dealing with full-wave dipoles). Now, the transmitting pattern Pat^{tr} is obtained based on the transmitting current. Similarly the scattering pattern
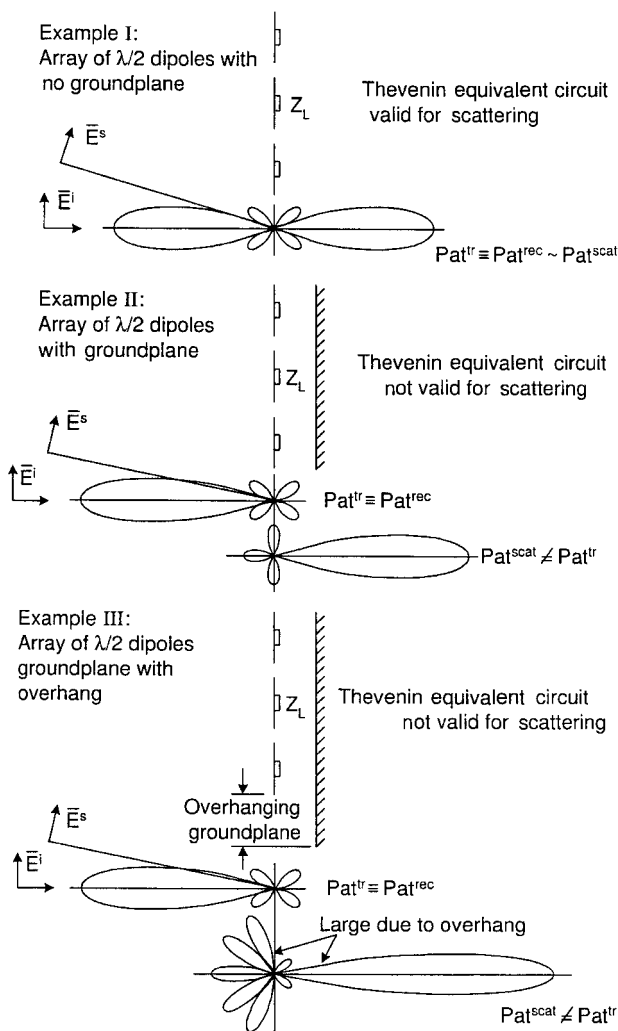
Fig. 2.12   The transmitting, receiving, and scattering pattern. Top: An array of dipoles without a groundplane. Middle: An array of dipoles with a groundplane. Bottom: An array of dipoles with an oversized groundplane.

Pat^{scat} is obtained from the receiving or scattering currents. And since the two current distributions are similar in this case (for element length $\sim\lambda/2$ or shorter), we may conclude that

$$Pat^{tr} \sim Pat^{scat}. \tag{2.15}$$

Note: For the receiving pattern Pat^{rec} we always have from the law of reciprocity $Pat^{rec} \equiv Pat^{tr}$ in spite of the fact that the current distributions in the two cases in general are different.

Based on this observation many assume that the scattering pattern is in general almost the same as the transmitting (or receiving) pattern. However, the next example will illustrate that this is a completely erroneous assumption.

2.9.2 Example II: Large Dipole Array with Groundplane

In Fig. 2.12, middle, we show a large finite array of dipoles backed by a finite groundplane as large as the array. When fed from constant current generators, we obtain the currents under transmitting condition, and the transmit pattern Pat^{tr} is obtained in the traditional way based on these currents and their approximate images in the finite groundplane.

Similarly to Example I above, we shall feed these elements via a harness containing hybrids in order to decouple the elements internally from each other (see Section 2.12). Thus, our scattering model will merely consist of elements loaded with identical load impedances Z_L as shown. We seek the bistatic scattering pattern Pat^{scat} based on the element currents when exposed to an incident plane wave. At this point we shall do so by estimating the scattering pattern in the backward and forward sectors separately (an example of exact calculation is given in Section 5.3).

Let us first examine the backward sector. If we assume that the load impedance Z_L is conjugate-matched to the antenna impedance Z_A, all the energy incident upon this array with a groundplane will (as shown in Section 2.6.2) basically be absorbed. Thus, for this load condition the scattering pattern will simply be given by a number of low-level sidelobes due to the finiteness of the array. For an actual calculated example of what happened when $Z_L \neq Z_A^*$, see Section 5.3.

And now for the forward sector. Right behind the groundplane (i.e., in the forward sector) we realize that the total field to a good approximation is equal to zero over the whole groundplane. We further recall that the total field is given as the sum of the incident field $\overline{E}^i$ and the scattered field $\overline{E}^s$. Thus we readily conclude that $\overline{E}^s \sim -\overline{E}^i$ right behind the groundplane. Furthermore, since the scattering pattern Pat^{scat} is obtained by aperture integration of $\overline{E}^s$ over the back of the groundplane, we may conclude that the scattering pattern in the forward direction is obtained simply as the negative of the incident field $\overline{E}^i$ integrated over the entire groundplane. Thus, the scattering pattern Pat^{scat} has in the forward direction a large mainbeam and in the backward sector some small sidelobes as indicated in Fig. 2.12, middle. In fact, one might be tempted to assume that Pat^{scat} is merely equal to the transmit pattern Pat^{tr} reversed. This is not the case. First of all, recall that the scattering pattern Pat^{scat} in the backward sector is highly dependent on the load impedance Z_L. In fact for Z_L imaginary we will obtain another main beam in the back. This is in sharp contrast to the transmit and receiving pattern that is completely independent of any generator or receiver impedance. Furthermore, while it is true that the main beams for Pat^{tr} and Pat^{scat} for this case are almost identical except for their opposite directions, this will in general not necessarily be the case. The next example will illustrate this point.

2.9.3   Example III: Large Dipole Array with Oversized Groundplane

Let us finally consider an array with the same number of elements as in Examples I and II but where the finite groundplane is somewhat larger than the dipole area as shown in Fig. 2.12, bottom.

The transmit pattern Pat^{tr} will essentially be as for Example II above except for the sidelobe region. Thus, we can immediately conclude that the power received for conjugate match will essentially be the same as for Example II. The energy scattered in the backward sector will, however, be quite different. When conjugate-matched we may think of the scattering area as an absorber (the dipole area) surrounded by a perfectly conducting "ring area," namely the overhanging groundplane. Thus, the scattering in the backward sector is essentially given by the scattering from the ring-shaped area and will consequently consist of many large "sidelobes" with a level depending on the size of the ring-shaped area.

Furthermore, the forward scattering is, as explained earlier, given by integration of the incident field over the entire groundplane—that is, including the overhang. Thus, the forward scattering will essentially consist of a mainbeam that is narrower and larger than the one observed in Example II above.

2.9.4   Final Remarks Concerning Transmitting, Receiving, and Scattering Radiation Pattern of Finite Arrays

Example I illustrated that the scattering pattern Pat^{scat} could essentially have the same shape as the transmit pattern Pat^{tr}, but the amplitude of the former depended on Z_L while the latter was independent of Z_L.

Example II showed that the transmit and scattering pattern in general are quite different and complicated by the fact that the backscatter section is highly dependent on Z_L while the forward sector is basically independent of Z_L.

Examples II and III showed that two antennas can basically have the same transmit pattern but significantly different scattering patterns.

We should finally note that the antenna in Example III could in some cases produce zero backscatter in a few directions by adjusting Z_L. As noted in Section 2.3, this destructive interference method is not recommended.

To many people it is counterintuitive that the transmit and the scattering patterns point in opposite directions. In Problem 2.6 you are asked to find these patterns by direct calculation for a single dipole (or column of dipoles) backed by a single parasitic dipole reflector (or column of parasitic dipoles).

Nothing brings home a point better than simply working it out.

2.10   MINIMUM VERSUS NONMINIMUM SCATTERING ANTENNAS

The *classical definition* of a minimum scattering antenna (MSA) is one that:

1. Scatters as much total power as it absorbs for conjugate match.
2. Has identical transmitting and scattering patterns.

   3. Radiates the same fields in the forward and backward directions.

   4. Is "invisible" when its terminals are "open-circuited."

Consequence: Only 6-dB reduction in RCS for conjugate match, see Example I above.

This definition has been known at least since World War II [55] and has been widely quoted eversince [37, 38, 56–58]. What is more, it has often been implied that this class of antenna represents the ultimate as far as low radar cross section is concerned and, consequently, should be treated with great respect!

However, this may not be quite the case (another case of bad notation). In fact, the author suggests a relaxed condition for an MSA, namely one that scatters (in total) only as much as it absorbs—that is, one that is constrained only by condition 1 above (most antennas scatter more in total than they absorb, never less). As we shall see, this relaxed condition leads to a much broader class of antennas, some of which are truly noteworthy. The three examples presented above are excellent illustrations of these concepts. However, let us briefly remind the reader about the Thevenin equivalent circuit as it applies to receiving antennas.

2.10.1   The Thevenin Equivalent Circuit

It is well known that any receiving antenna can be described by a Thevenin equivalent circuit, shown in Fig. 2.13. Here the power delivered to the load impedance Z_L will always correctly represent the power being absorbed by the antenna, while the power being lost in Z_A represents power being reradiated somewhere in space by the antenna. However, the antenna may actually scatter considerably more power than is being lost in Z_A.

2.10.2   Discussion

Let us consider Example I above first. We already established earlier that for conjugate match, half the incident power will be absorbed in Z_L, while the other half will be scattered with one quarter going in the forward direction and another
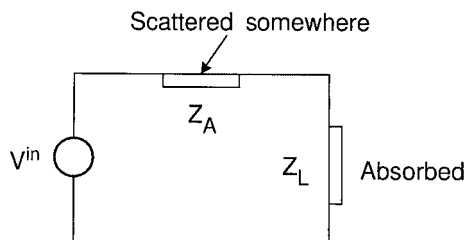
Fig. 2.13   *The Thevenin equivalent circuit for a receiving antenna always yields the correct power delivered to the load impedance Z_L. The power lost in the antenna impedance Z_A represents power scattered somewhere, not necessarily in the back direction. Additional scattering not accounted for by Z_A will in general take place.*

quarter in the backward sector (i.e., we observe the 6-dB Rule). Furthermore, the transmitting and scattering patterns are basically identical and we obtain as strong a signal in the forward as in the backward direction. Finally, the antenna is basically "invisible" only when $Z_L = \infty$.

Thus, this antenna is truly an MSA in the rigorous classical sense. In addition, the Thevenin equivalent circuit will correctly describe all of these features as far as the array in Example I is concerned.

Similarly, the antenna in Example II will for conjugate match absorb all the energy incident upon it while next to nothing is being scattered in the backward sector. However, as we saw earlier, we will in the forward sector observe a strong scattering pattern obtained by integration of the incident field across the ground-plane, which is basically identical to how we obtain the transmitting pattern in the backward direction. Thus, this antenna will scatter as much energy in the forward sector as it absorbs for conjugate match.

However, the transmitting (or receiving) pattern is radically different from the scattering pattern, and it radiates more in the backward than in the forward direction. And when open-circuited an incident field will essentially see just the groundplane and consequently exhibit a very large RCS. Thus, for conjugate match the Thevenin circuit will correctly account for the absorbed and scattered power but fail completely for $Z_L = \infty$. See also Figs. 5.2 and 5.3 for exact calculations.

Thus, this antenna will satisfy only condition 1 above and none of the other three and is therefore not an MSA in the classical sense.

Nevertheless, as we saw earlier, the antenna in Example II can for conjugate match produce a backscatter that is basically ∞ dB below the power scattered when $Z_L = 0$ while the MSA antenna in Example I has a backscatter only 6 dB below the case $Z_L = 0$.

To put it bluntly: The antenna in Example II is the only type that has a "shot" at invisibility when conjugate-matched in spite of the fact that it is not "pedigreed" as is the antenna in Example I.

Finally, the antenna in Example III will, for conjugate match, always scatter more total energy than it absorbs and in addition it will, like the antenna in Example II, not satisfy requirements 2, 3, or 4; that is, it is not an MSA even in the relaxed sense.

2.11   OTHER NONMINIMUM SCATTERING ANTENNAS

We demonstrated above without actual proof that to obtain zero backscatter for an antenna, it should scatter no more total energy than it absorbs when conjugate matched. Very few antennas belong to this elite class in fact most antennas do not. Let us illustrate these statements with some examples.

2.11.1   Large Array of Full-Wave Dipoles

A large array of full-wave dipoles without a groundplane will scatter approximately as much power as it receives when conjugate-matched (for no grating
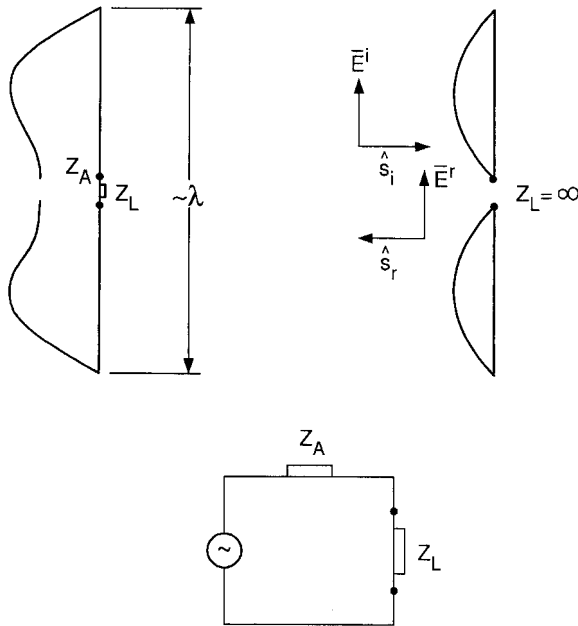
Fig. 2.14 An array of full-wave dipoles without a groundplane will have transmitting and scattering patterns that look alike and scatters the same amount in front and back. However, when $Z_L = \infty$ it will scatter like an array of $\lambda/2$ dipoles; that is, it yields a strong backscatter like a groundplane. Thus, the Thevenin circuit will not predict the correct scattering since no current flows through it. It is therefore not an MSA in the classical sense but it is in the relaxed sense.

lobes). However, for $Z_L = \infty$ it is merely an array of $\lambda/2$ dipoles (see Fig. 2.14), and will consequently exhibit strong scattering in the forward as well as the backward directions. Thus, the Thevenin equivalent circuit does not predict the correct scattering of an array of full-wave dipoles and is thus not an MSA in the classical sense, but it is in the relaxed sense. Furthermore, if backed by a groundplane, we can, as it was the case for the array of $\lambda/2$ dipoles, observe no backscatter for conjugate match (no grating lobes); that is, it is an MSA in the relaxed sense. See also Problem 2.3.

2.11.2 Effect of a Tapered Aperture

A uniform aperture with groundplane can basically absorb all the incident energy and will consequently have no backscatter (see Section 2.6.2). In contrast, a tapered aperture is capable of absorbing only part of the incident energy. Thus, some of the power not being absorbed by Z_L will be either reradiated, most likely in the backscatter direction but not necessarily so, or absorbed by some other absorbing mechanism (see Section 2.13).

This situation is summarized for planar apertures in Fig. 2.15, where we show the uniform aperture at the top and the tapered aperture at the bottom.
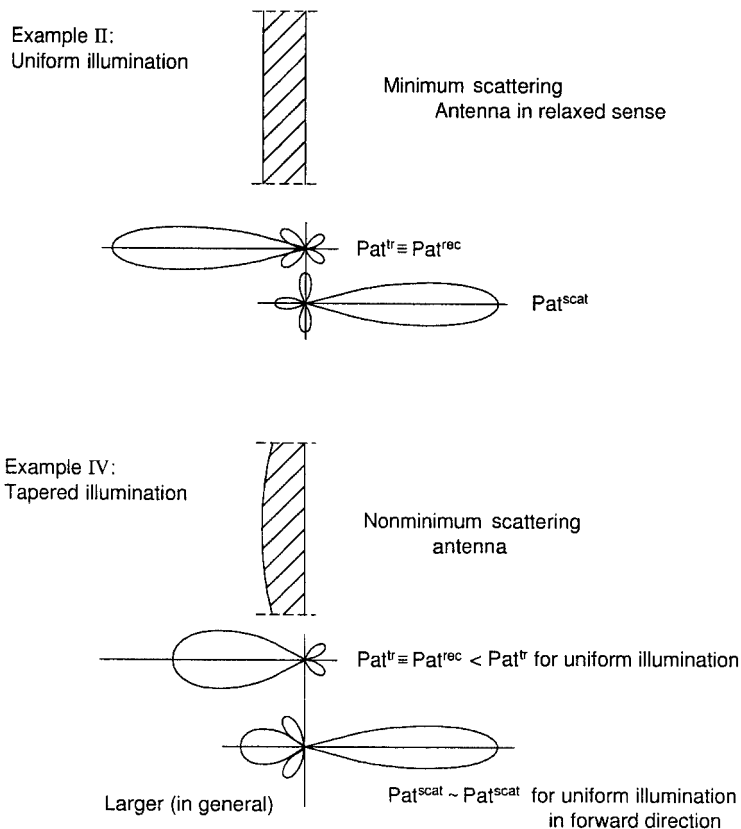
Fig. 2.15 Top: A uniform aperture with a groundplane similar to Example II in Fig. 2.12. Bottom: A tapered aperture will absorb less power than the uniform case, above; however, the scattering in the forward direction will basically be the same. Thus, it scatters more than it absorbs and is thus not an MSA.

We assume that the physical size of the two apertures is the same; that is, the beamwidth of the tapered aperture is somewhat larger and the gain somewhat smaller than for the uniform distribution. Furthermore, the backscatter is larger for the tapered aperture. However, the scattering pattern in the forward direction is essentially the same in the two cases. Thus, while the uniform aperture scatters as much energy as it absorbs, the tapered will scatter more and is consequently not an MSA, not even in the relaxed sense. The discussion above has tacitly assumed that all elements have the same scan impedance. This is not quite the case. A more rigorous and detailed investigation is given in Chapter 5.

The power scattered in the backward sector as a result of the tapered distribution can be absorbed if we work with arrays (see Section 2.13). However, most antennas with tapered aperture distribution are bad candidates for low RCS antennas. Horns, for example, always have a tapered aperture distribution because

of the boundary conditions at the walls, and not much can be done about it (see also Chapters 7 and 8). However, an array of horns still has no backscatter for conjugate match, provided that we have no grating lobes (an individual dipole element does not have a "uniform taper" either but is perfect when placed in an array with a groundplane).

2.11.3 The Parabolic Antenna

Typically, a parabolic dish is fed from a horn as shown in Fig. 2.16, top, resulting in a tapered aperture distribution with an aperture efficiency $\eta < 1$. This will produce a transmitting pattern with lower sidelobes, which might be highly desirable for many applications. However, as discussed in the previous section, it will also
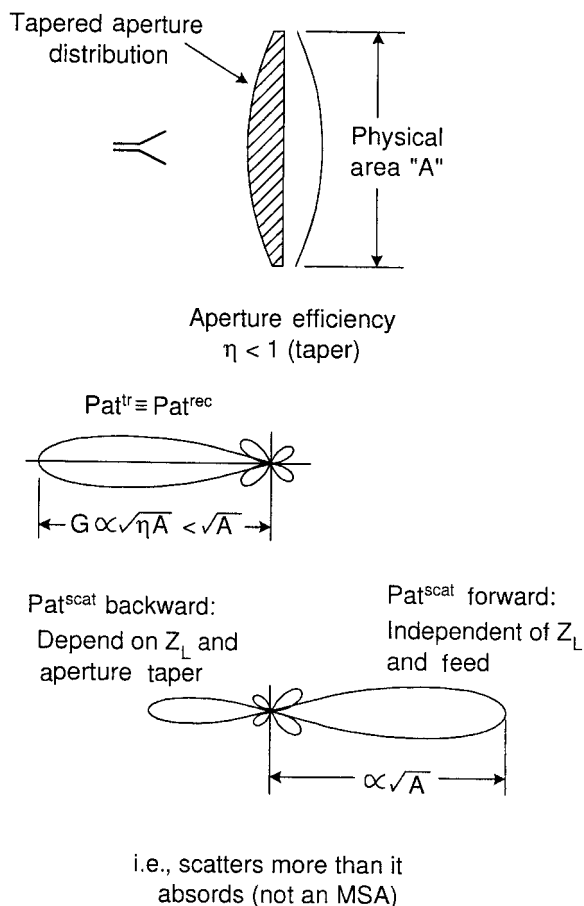
Fig. 2.16 *A parabolic antenna has a tapered aperture distribution and will therefore scatter more in the forward scattering direction than it absorbs. Thus, it is not an MSA even in the relaxed sense.*

for conjugate match produce an undesirable high level of backscatter; that is, it is not an MSA. However, the highest contribution to the backscatter may actually occur when the incident field is focused on one of the edges of the horn when slightly off boresight as discussed in detail in Chapter 8. Other related subjects will be discussed in Section 2.14.

2.12   HOW TO PREVENT COUPLING BETWEEN THE ELEMENTS THROUGH THE FEED NETWORK

2.12.1   Using Hybrids

The elements in an array will usually be fed via a harness of one sort or another. That opens up the possibility of reradiation via the feed cables unless special precautions are taken. As a simple but very fundamental example, consider Fig. 2.17. Here two subarrays are fed via a simple parallel T connector. Note that the characteristic impedance of the main feed line is Z_0 and how it splits up into two branchlines each with characteristic impedance $2Z_0$ and terminated with the subarrays each with input impedance $2Z_0$. Thus, we will have a perfect match at all frequencies whether we transmit or receive.

In particular, there will be no reradiation from the two subarrays when a signal is incident from broadside (top). However, if a signal is incident at an oblique angle such that the spatial delay between the two subarrays is $(2n + 1)\lambda/2$, the signals from the two subarrays will arrive at the T connector out of phase; that is, they will not continue into the mainline but instead be reflected back to the subarrays where reradiation will take place (bottom). The result is that the backscattering pattern will consist of several very strong lobes (actually there may be other scattering patterns from the subarrays themselves superimposed on these lobes).

We may interpret the backscattering above as caused by a mismatch at the T connector for certain angles of incidence. A very effective way to remedy this dilemma is to use one or more hybrids as shown for example in Fig. 2.18.

Hybrids can be considered as the "fulfillment of the antenna engineer's dream." They come in various types. The one considered here consists of a box with four input ports. When a signal is impressed at port 1, it will emerge at ports 2 and 3 with equal amplitude and $180°$ out of phase but not at port 4. Similarly, if a signal is impressed at port 2, it will emerge at ports 1 and 4 only, not at port 3. However, if signals of equal amplitude and phase are impressed at ports 2 and 3 simultaneously, a signal will emerge only at port 1, nothing at port 4. Furthermore, if the impressed signals at ports 2 and 3 are equal in amplitude but $180°$ out of phase, a signal will emerge at port 4 only, nothing at port 1.

From a backscattering point of view, the important feature is that the input impedances at ports 2 and 3 always will be perfectly matched to the subarrays. If the signals from the two subarrays are in phase, a signal will go to port 1—and if out of phase, to port 4—but the input impedances at ports 2 and 3 will always
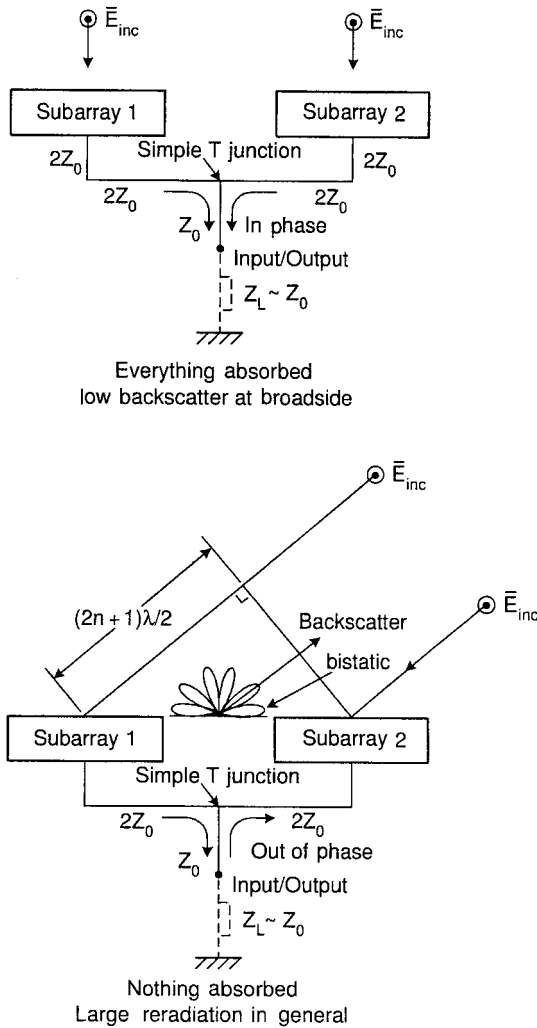
Fig. 2.17   Top: The power to the two subarrays is divided by a simple but perfectly matched T connector. A signal incident at broadside will be perfectly absorbed with basically no backscatter. Bottom: At oblique incidence the two subarrays can be excited out of phase as shown. Thus, the signals from the two subarrays will in that case be reflected at the T connector, resulting in a large backscatter.

be Z_0 regardless of the phase difference between the signals from the subarrays. This is one of the unique features of hybrids.

Thus, all signals incident from any direction will be absorbed by using hybrids resulting in a low backscattering.

The phases of the two subarrays may be controlled by individual phase shifters ϕ_1 and ϕ_2. Still, it has no bearing on the backscatter.
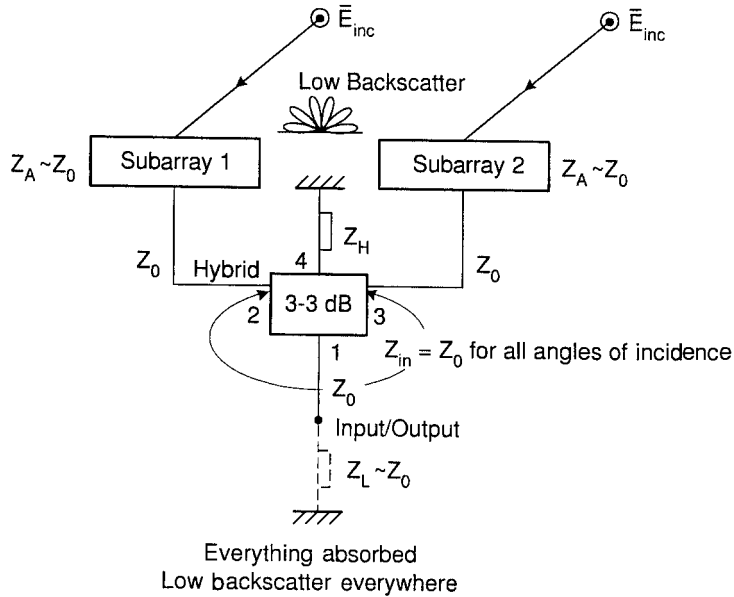
Fig. 2.18   By using a hybrid instead of a T connector as shown above, we can direct the signals from two subarrays into the input impedance when they are in phase and into the hybrid load Z_L when out of phase. In either case (and everything in between) the hybrid input impedance at ports 2 and 3 will be perfectly matched and no significant backscatter will take place.

2.12.2   Using Circulators

Another approach is to use a circulator as shown in Fig. 2.19. Here the transmitter with internal impedance Z_G is connected to port 1, the antenna with antenna impedance Z_A to port 2, and finally the receiver with input impedance Z_R to port 3. The workings of a circulator is now such that a signal applied to port 1 will occur only at port 2, while a signal applied to ports 2 and 3 will occur only on ports 3 and 1, respectively. Thus a signal incident upon the antenna will see only the receiver input impedance Z_R rather than the transmitter impedance Z_G. Since the former in general is matched well to the antenna impedance Z_A, a low reradiation will occur in contrast to seeing Z_G that may be quite different from Z_A (see Section B.9.1).

2.12.3   Using Amplifiers

We saw in the previous section how hybrids and circulators could be applied to prevent coupling between the elements via the feed cables. Another alternative is simply to connect each element to its own individual amplifier. The load impedances then simply become the input impedances of the amplifiers and the isolation from element to element will be high indeed. Furthermore, this approach has the added advantage that the loss in the feed lines can be alleviated by the
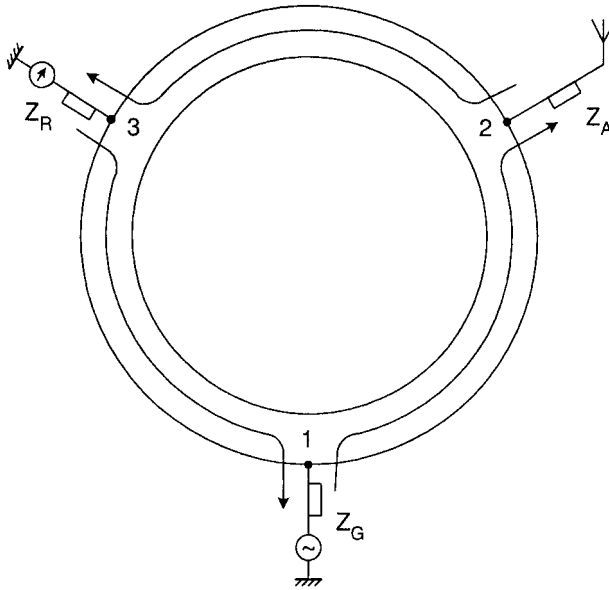
Fig. 2.19 Alternatively we may use circulators as shown above. A generator with impedance Z_G at port 1 delivers a signal only to the antenna Z_A at port 2. However, an incident signal upon the antenna will be directed only to the receiver at port 3. Since in general the receiver impedance Z_R is $\sim Z_A$ while $Z_G \neq Z_A$, we obtain a low backscatter by using a circulator.

amplifiers if their noise figure is low. Also, we can perform any processing after the receivers or amplifiers without worrying about the backscatter.

2.13 HOW TO ELIMINATE BACKSCATTER DUE TO TAPERED APERTURE ILLUMINATION

We saw earlier in Section 2.9.2 that a large uniform aperture backed by a ground-plane was capable of absorbing an incident plane wave entirely, resulting in very low backscattering. Furthermore, we saw in Section 2.11.2 how a tapered aperture always would backscatter unless special precautions are taken. We will discuss these in this section.

Consider Fig. 2.20, top, where we depict an array where the elements are fed via a simple harness with 3-dB T connectors. Clearly, this will lead to a uniform aperture illumination and consequently to a low backscattering, but only at broadside and certain other angles of incidence as discussed in Section 2.12.1.

Let us next consider the same array; but as shown in Fig. 2.20, middle, this time we feed the elements via a harness with T connectors arranged to give a tapered aperture illumination as indicated by the cross-hatched area. We will now receive less energy in Z_L while the excess energy between uniform and tapered illumination will be reradiated, resulting in a high backscatter level.
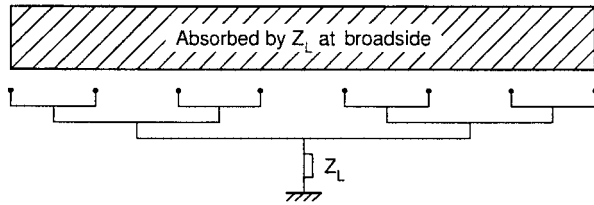
Uniform aperture illumination using simple harness with T connectors.
Absorbs everything at broadside and for some oblique angles of incidence
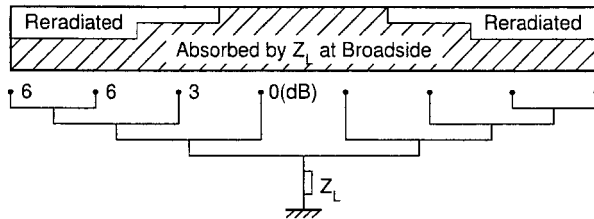
Tapered illumination by using T connectors. Absorbs some at broadside
and reradiates some.
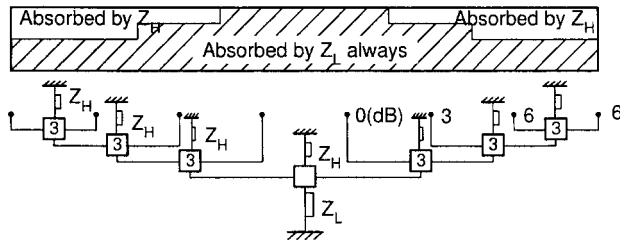
Tapered illumination using hybrids. Absorbs everything. No reradiation.

Fig. 2.20   Top: A uniform aperture illumination backed by a groundplane can absorb all the incident energy. Middle: A tapered illuminated aperture can absorb only a part of the incident energy. The other part will be reradiated if we use simple T connectors. Bottom: By substituting the T connectors with hybrids, the excess power can be absorbed in the hybrid loads Z_H rather than reradiated.

We finally in Fig. 2.20, bottom, show the same array as in the middle, but this time we have replaced all the T connectors with the same type of hybrids as used earlier in Fig. 2.18. We will receive the same amount of energy in the load impedance Z_L as in the middle case above; however, the excess energy will be absorbed by the hybrid loads Z_H rather than being reradiated (*Recall*: The antenna sections will always be matched so nothing can be reradiated.).

This conclusion is perhaps best understood if we at first transmit from the main terminal. That will readily produce the tapered aperture distribution as shown. Let us next receive an incident plane wave resulting in equal power delivered
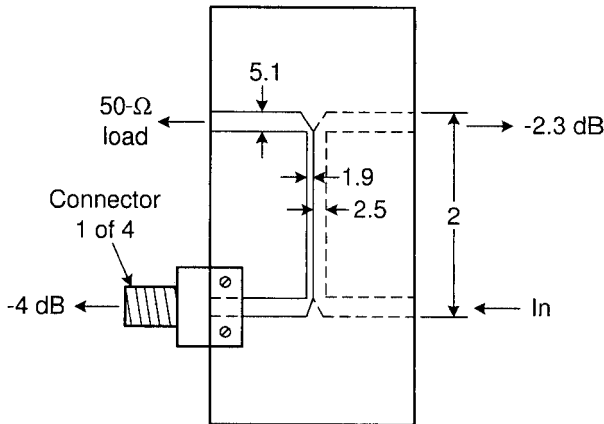
Fig. 2.21 *A specially designed hybrid with a power split 4.0/2.3 dB rather than 3/3 dB. All dimensions are in millimeters. (After Larson, private communication).*

from each element to the matched input terminals of the hybrids. Thus, no energy can be reflected and reradiated. However, the aperture taper must be the same whether we receive or transmit (reciprocity). This proves our case.

Note: The discussion above assumes that the hybrids are ideal—that is, nothing is being reflected. For a discussion where the hybrid is reflecting a small signal, see reference 59.

The examples above are only typical. Endless variations are possible. For example, the hybrids are not restricted to be merely of the 3-dB type. An example is shown in Fig. 2.21 with a power split of 2.3/4.0 dB. A former Ph.D. student Clayton Larson (now a successful "Big Shot") and the author needed such a hybrid for a very special antenna. Not being an off-the-shelf item, we had to either order one custom-made or make one ourselves. Clay those the latter approach (he was never too keen on telephone negotiations). Overnight he designed, cut the design with an exacto knife and assembled such a hybrid. The next morning we checked it out on the special antenna. It worked flawlessly. Thank you Clay.

2.14 COMMON MISCONCEPTIONS

2.14.1 On Structural Scattering

It has been said several times earlier that what we today prefer to call residual scattering used to be called structural scattering. As one might suspect, this resulted in numerous erroneous ideas. The author remembers in particular one time when he gave a lecture to a group of engineers in industry about RCS of antennas. After the talk one comment was, "We liked your lecture very much and it seems to make a lot of sense. However, we are confused because last week we had a talk from another professor and he told us that the first thing to do to

lower the RCS of an antenna is to get rid of the groundplane. You seem to say that the groundplane is our friend. Who is right?"

Well, based on the discussion earlier in Section 2.9, we do of course now know that removing the groundplane simply means that the RCS can get no more than 6 dB below maximum when conjugate-matched. In contrast, when leaving the groundplane in place, the RCS reduction can in principle be infinite! The misconception is of course rooted in the fact that the groundplane constitutes a significant "structure" and the more structure we can get rid of the better! Obviously this is not true.

Another variation on the same theme consists in substituting the groundplane with an absorber (i.e., essentially free space). Well, from an RCS point of view we are of course right back into the 6-dB case (e.g., see Fig. 2.10, left). Furthermore, if you have a transmitting power of 1 kW, you will have about 500 W transformed into heat. That should be enough to fry an omelet.

Then there is of course the case where the groundplane "moves" with frequency. That scam is discussed in Section 6.12.1.3.

2.14.2   On RCS of Horn Antennas

The classical horn antenna has been popular in the microwave community for years. It is therefore only natural that its RCS has been the subject of many investigations. Sadly, it has never emerged as a prime candidate for stealth applications.

This lack of performance is quite often attributed to "structural" scattering. And many designers associate this with scattering from the edges of the horn. Consequently these are "attacked" with all kinds of imaginative treatments ranging from edge cards, serrations, and other loss mechanisms of one kind or another. Although some improvement might be observed in some cases, they must usually be classified as insufficient and often result in some loss of antenna efficiency. The real problem is of course that all horn antennas inherently have a tapered aperture illumination. And as shown in Section 2.11.2, this simply means that a super-low RCS will never emerge for the conjugate-matched classical horn antenna.

However, as also mentioned in Section 2.11.2, this lack of performance of a horn as "soloist" does not prevent it from sounding pretty good in an "orchestra," namely, in an array of horns, as long as no grating lobes are encountered.

For an in-depth discussion of the scattering from horns when used as a feed antenna in a parabolic cylinder, see Chapter 8. There you will also find ways demonstrating how to alleviate some of the problems.

2.14.3   On the Element Pattern: Is It Important?

Based on our discussion in Section 2.9, it should be obvious that the radiation pattern of the individual elements plays almost no role in the array RCS. In fact, as illustrated in Fig. 2.22, top, the total antenna pattern is for no grating lobes so completely dominated by the array factor that any change in the element

pattern as indicated by Cases I and II is almost completely drowned out in the total pattern (no grating lobes please—not even close). Thus, the total pattern and consequently the directivity will remain essentially unchanged; that is, we will receive all the incident energy and have no backscatter for uniform aperture illumination (for tapered illumination see Section 2.13). Nevertheless, not everyone is familiar with the content of Section 2.6. Sometimes modifications of the elements are suggested as shown, for example, in Fig. 2.22, bottom. Here to the right we have used slotted waveguides with triangular cross sections rather than the usual square ones shown to the left. Although this idea might look appealing at first glance, the fallacy is of course that the difference in element pattern for the triangular and square cross section is merely of academic interest in this setting. Furthermore, for typical waveguide dimensions required here, the backscatter is not at all as expected from physical optics (a common "sin" committed quite often). At much higher frequencies, this approach makes some sense; however, using a hybrid radome instead will in general be more effective.
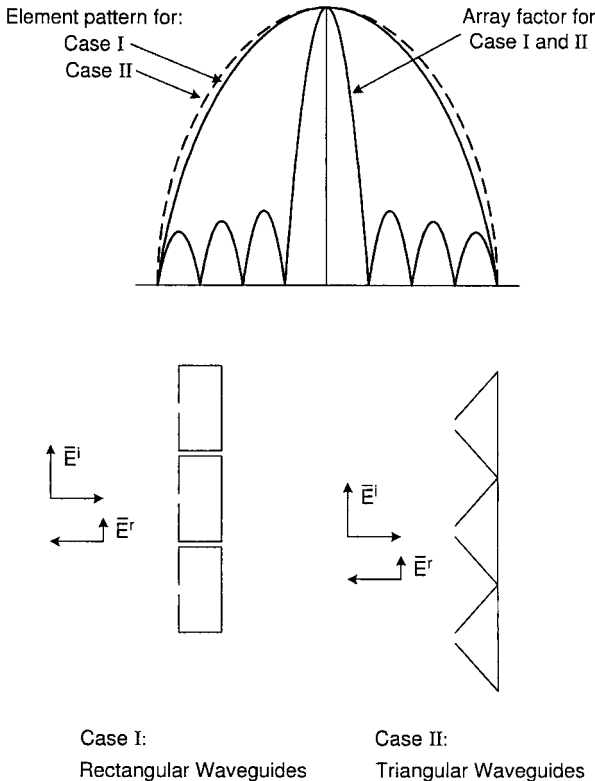
Fig. 2.22 *Top: The effect of the element pattern will usually "drown" in the array factor as long as we stay far away from onset of grating lobes. Bottom: Whether you make the array of slotted square waveguides (Case I) or triangular waveguides (Case II), it has very little effect on the scattering in-band. At much higher frequencies, Case II may be superior.*

2.14.4 Are Low RCS Antennas Obtained by Fooling Around on the Computer?

It is not unusual to hear the notion that low RCS antennas are obtained by a more or less systematic approach based entirely on computation. This is of course possible. In fact, we addressed this problem in Section 2.3 where we pointed out that any antenna with a residual component $|C| < 1$ could indeed produce a low RCS by simply adjusting the load impedance Z_L in such a way that cancellation between the antenna mode and the residual mode would occur. As also pointed out, this condition is not compatible with maximum power transfer, and perhaps worst of all it is usually narrowbanded, sensitive to the angle of incidence and polarization. Thus, these types of solutions are primarily of academic interest and should not be propagated as anything else when teaching antenna scattering theory on a practical level.

2.14.5 How Much Can We Conclude from the Half-Wave Dipole Array?

Short answer: Not much!

Although it has been stated several times earlier as well as in the summary, we strongly emphasize that the results observed to be true for an array of half-wave dipoles without a groundplane are not necessarily valid for antennas in general. Most notorious is probably the fact that the backscatter for such an antenna when conjugate-matched is reduced 6 dB compared to the maximum return (when short-circuited). This is only true for minimum scattering antennas in the classical sense. If we restrict ourselves merely to consider antennas that do not scatter more than they absorb, we are led for example to arrays of dipoles with a groundplane where for conjugate match we can observe a reduction of ∞ dB. This type is of the MSA type with relaxed conditions. They have certain "flaws;" for example, their Thevenin equivalent circuit does not predict the scattered power for all load conditions. However, they are infinitely more interesting from a practical point of view.

Also, while a dipole array without a groundplane has the same scattering as transmitting pattern, this is far from the case in most of the more interesting cases. See also Chapter 7, Section 7.6.

2.14.6 Do "Small" Antennas Have Lower RCS Than Bigger Ones?

It is well known that the RCS of a large flat plate with physical area A is at broadside proportional to A^2. What is perhaps less well known is the fact that the RCS of the same plate at oblique incidence is basically independent of A (at least in the principal planes). Thus, when it comes to RCS of an object in general, its size may or may not be an issue.

Whatever thought process goes through some people's minds (or lack thereof) it is sometimes suggested that a small antenna in terms of wavelength has a smaller RCS than a larger one. As an example, consider a dipole of total length

$\lambda/2$ and one of length 0.1λ. Now, let there be no doubt that the RCS of the $\lambda/2$-long rod is $\sim 0.8\lambda^2$ whereas it is $5-15\,\text{dB}$ lower for the short rod, depending on its wire radius.[1] However, we are of course more interested in the RCS of the two "rods" when they act like dipoles—that is, when they are provided with suitable terminals where we insert a short-circuit for the $\lambda/2$ dipole and a suitable inductance for the 0.1λ dipole that tunes it to resonance. We then merely note that the gains in the two cases are practically the same and consequently according to Section 2.2 will have about the same RCS.

But is there no difference between the two cases at all? Certainly: Namely their bandwidth. The RCS of the short dipole will simply deteriorate faster from its maximum value than will the longer one as a function of frequency. See also Chapter 7.

2.14.7   And the Worst Misconception of All: Omitting the Loads!

We devoted considerable time developing the general scattering theory for antennas, see Section 2.2. We showed that the total RCS of any antenna depends in general strongly on the load impedance Z_L. We further demonstrated these concepts by numerous cases; see, for example, Section 2.9.

Nevertheless, it is not uncommon to encounter presentations that completely ignore the effect of the antenna loads. One paper in particular stands out in my recollection. There the author claimed to have calculated the RCS of a patch antenna. His model was comprised of merely a single patch suspended somewhere in a dielectric slab over an infinite groundplane. No lead-in wire and obviously no loads. When I pointed the deficiency out to him he merely shrugged his shoulders and said, "OK, but this is so hard to do (!)." (Concerning "hard to do," see Appendix D.)

Many other types of antennas have been evaluated typically when their terminals were, for example, short-circuited. This is merely a calculation of an "object," not an antenna (it could of course be part of an important introduction to the antenna problem).

In other words, antennas should not be treated merely as scattering objects with undetermined loads located, for example, in a cavity or elsewhere. The load is extremely important and must always be incorporated to yield meaningful results. Omission of this fact represents in the author's opinion the worst misconception in the entire theory of antenna scattering.

2.15   SUMMARY

We opened this chapter with a review of the classical theory of antenna scattering. The total RCS of any antenna could be written as the phasor addition of two components, namely the *antenna* and the *residual* mode components. The first of these was clearly and precisely defined by the antenna gain G, the reflection

---

[1] Note that the wire radius affects the bandwidth.

coefficient Γ, and the polarization. The second, however, was more vaguely defined as whatever should be added to the antenna component to obtain the total antenna RCS.

Although this definition sounded somewhat ambiguous, it was nevertheless extremely useful in understanding the complexities of antenna scattering and we were in several important cases able to determine the residual as well as the antenna scattering.

The term residual scattering has also been denoted structural scattering. However, we demonstrated by several examples that this nomenclature was somewhat misleading. We found, for example, that adding a groundplane (i.e., adding structure) to an array of dipoles could reduce the residual scattering to practically nothing rather than increase it. Similarly, a flush-mounted antenna of slots may or may not have any structural scattering even if no structure is visible above the groundplane.

We further considered a very "classical" concept, namely the minimum scattering antenna. Originally it was defined as an antenna that did not scatter more (in total) than it absorbed when conjugate-matched. Furthermore, the scattering pattern should basically be identical to the transmitting pattern with the same amount being scattered in the forward and backward directions. For this class of antennas a Thevenin equivalent circuit would not only predict the correct received power in the load impedance Z_L (always valid) but would also predict the total scattered power as being associated only with the antenna impedance Z_A for all load conditions. Unfortunately, these constraints led to a class of antennas where the RCS for conjugate match is only 6 dB below the maximum RCS (not very impressive indeed).

It was further demonstrated that if we relaxed the conditions above to merely the first, namely that the antenna should scatter no more total energy than it absorbs, it could lead to antennas with virtually no residual scattering (but not necessarily so). An interesting feature of this class of antenna is that the Thevenin equivalent circuit may no longer correctly predict that the total scattered power as merely associated with Z_A under all load conditions. This should be accepted as a fact of life, and failing to realize this can lead to fatal mistakes.

To summarize: By requiring only that the total scattered power does not exceed the absorbed power, we expanded the original minimum scattering antennas with only 6-dB reduction from maximum into a new class of antennas where the reduction could be ∞ dB. Much "respect" has been bestowed upon the classical MSA over the years. However, in this writer's opinion, there is no question what antenna has the real "pedigree."

We also investigated in great detail the effect of aperture illumination upon the RCS of antennas. It was determined that only a uniform aperture illumination was capable of absorbing all the energy incident upon it, resulting in practically no backscatter. If the aperture illumination was tapered, only part of the incident energy could be absorbed. The surplus could be disposed of in basically two different ways. It could be reradiated, resulting in a significant backscatter. Or in case of arrays we could feed each element via appropriate hybrids and lose

the excess energy in the hybrid loads, resulting in practically no backscatter. Circulators also serve this purpose.

Alternatively, we could connect each element to its individual amplifier. This would be equivalent to all elements being connected to the same matched load (the input impedances of the amplifiers), resulting in practically no backscatter similar to uniform illumination. The actual aperture tapering or any processing in general could then conveniently be done at the outputs of the amplifiers.

Horn antennas were considered briefly, not so much for their merit as for their imaginative treatment of their edges that seems so fascinating to some. However, as pointed out, the real problem is that horns have an inherent tapered aperture illumination leading to substantial backscatter.

We shall return in much greater detail to feeding parabolic antennas in Chapter 8 and advise alternate ways to alleviate scattering problems. In Chapter 7 we present invisible antennas with omnidirectional radiation patterns.

PROBLEMS

2.1 Consider an array with uniform aperture distribution and assume that the residual scattering as well as edge effects are negligible.

A plane wave is incident upon this array at broadside where it is reflected in the backscattering direction with a reflection coefficient Γ.

Find the upper limits of the VSWR as seen at the array terminals if we require the reflection coefficient magnitude $|\Gamma|$ to be less than

1. 10 dB
2. 26 dB
3. 32 dB
4. 40 dB

This is a very easy, but important, problem.
See also Sections 5.8 and 5.9.

2.2 Show that

$$\sqrt{\sigma_{ant}} = \tfrac{1}{2}(\sqrt{\sigma_{tot\,max}} - \sqrt{\sigma_{tot\,min}})$$

$$\sqrt{\sigma_{res}} = \tfrac{1}{2}(\sqrt{\sigma_{tot\,max}} + \sqrt{\sigma_{tot\,min}})$$

These equations can be very helpful in determining σ_{ant} and σ_{res} experimentally.

2.3 Consider an array of full-wave dipoles without a groundplane rather than half-wave dipoles as shown in Fig. 2.8.

Find the component C associated with the residual scattering and show that this array obeys the 6-dB Rule (approximately).

You may assume that $\Gamma_{FSS} = -1$ when open-circuited and $\Gamma_{FSS} \sim 0$ when short-circuited, The last approximation actually becomes basically

exact at a frequency somewhat higher than the full-wave frequency (normal angle of incidence). Does the Thevenin equivalent circuit hold for all load conditions?

2.4 Consider an infinite array of half-wave dipoles with a groundplane at arbitrary distance as shown in Fig. 2.9.

Show that the sum of the three plane waves marked "1," "2," and "3" does indeed add up to zero for conjugate match.

To the instructor: This is a somewhat lengthy problem that should be assigned only as punishment! In fact, it is much simpler to use the equivalent circuit shown in Fig. 2.10, right.

2.5 Consider the equivalent circuit for an array of half-wave dipoles without a groundplane as shown in Fig. 2.10, left.

Show that the signal transmitted in the forward direction as well as the reflected signal are both 6 dB below the incident signal when conjugate-matched.

Also verify the conservation of power.

2.6 Single Dipole with Parasitic Dipole Reflector.

In Fig. P2.6 we show a single dipole with self-impedance $Z_{1,1}$ backed by a single parasitic element with self-impedance $Z_{2,2}$ and load impedance $Z_L^{(2)}$. Their mutual impedances are denoted $Z_{1,2} = Z_{2,1}$.

You are asked to find the transmitting, receiving, and scattering patterns for this antenna configuration.

Transmitting Case: The active element is fed from a voltage generator V_g as shown in Fig. P2.6, top. The element currents under transmitting condition are denoted $I_t^{(1)}$ and $I_t^{(2)}$ for the active and parasitic element, respectively.

The generalized Ohm's Law for the system then becomes

$$V_g = Z_{1,1}I_t^{(1)} + Z_{1,2}I_t^{(2)}$$

$$0 = Z_{2,1}I_t^{(1)} + (Z_{2,2} + Z_L^{(2)})I_t^{(2)}$$

a. Find the input impedance $Z_{in} = \dfrac{V_g}{I_t^{(1)}}$ for the antenna system.

b. Find the relative transmit pattern Pat^{tr} as indicated in Fig. P2.6, top, expressed by $I_t^{(1)}$, $Z_{2,1}$, $Z_{2,2} + Z_L^{(2)}$ and the distance d between the two elements. Sketch the transmit pattern Pat^{tr} based on your expression.

Receiving Case: We now remove the generator V_g from the antenna terminals and expose it instead to an incident plane wave $\overline{E}^i$ with direction of propagation $\hat{s}$ as shown in Fig. P2.6, bottom. The terminals are loaded with the load impedance $Z_L^{(1)}$ and the induced voltages in the active and passive element are called $V^{(1)}$ and $V^{(2)}$, respectively (we need not actually
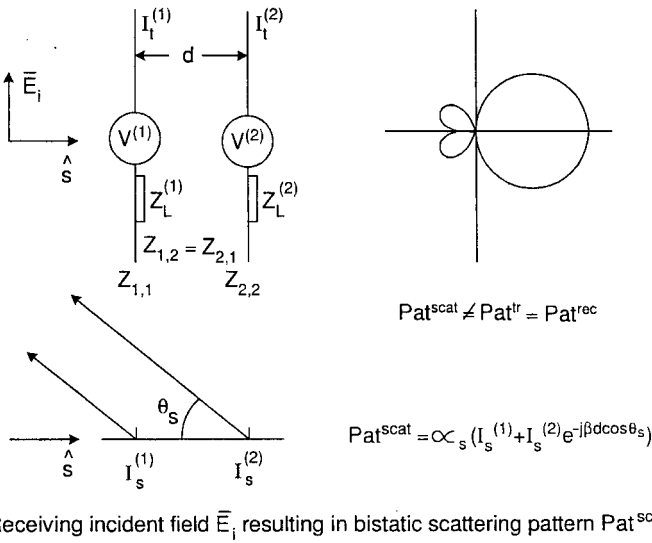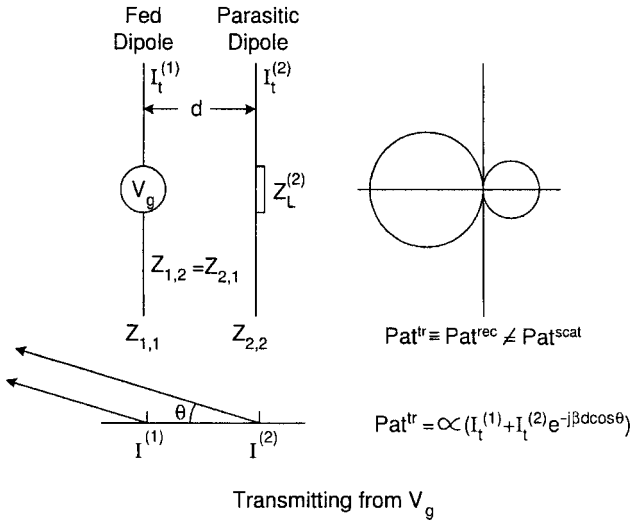
Fig. P2.6 Determination of the transmitting, receiving, and scattering patterns for an antenna comprised of one driven element (or column) and one parasitic element (or column).

calculate these voltages but in case you are curious; see reference 60). Thus, the generalized Ohm's Law for the receiving case becomes

$$V^{(1)} = (Z_{1,1} + Z_L^{(1)})I_s^{(1)} + Z_{1,2}I_s^{(2)}$$

$$V^{(2)} = Z_{2,1}I_s^{(1)} + (Z_{2,2} + Z_L^{(2)})I_s^{(2)}$$

where $I_s^{(1)}$ and $I_s^{(2)}$ denote the element currents under scattering (receiving) conditions.

c. You may now assume that the length of the two elements are the same (we can always tune the parasitic element by adjusting $Z_L^{(2)}$). Thus,

$$V^{(2)} = V^{(1)}e^{-j\beta d}$$

Find the relative scattering pattern Pat^{scat} as expressed by $V^{(1)}$ and all the appropriate impedance terms as well as the bistatic angle θ_s and the element spacing d. Sketch the pattern Pat^{scat} based on your expression.

d. Find the load impedance $Z_{L\ BS}^{(1)}$ that produces zero backscattering.

e. Find the load impedance $Z_{L\ max}^{(1)}$ that will absorb most of the incident power. Compare $Z_{L\ BS}^{(1)}$ to $Z_{L\ max}^{(1)}$ and estimate the power loss by using $Z_{L\ BS}^{(1)}$ instead of $Z_{L\ max}^{(1)}$.

f. Which one of the two patterns above (if any!) represents the receiving pattern Pat^{rec}?

2.7 Consider an array of four elements with individual reflectors fed from a corporate feed network as shown in Fig. P2.7. The two subarrays are fed via two simple T connectors with characteristic impedances as shown. However, the two T connectors are fed from an ideal hybrid as also shown. An incident plane wave $\overline{E}^i$ is incident upon this array at an angle η. Due to mismatch between the antenna impedance Z_A and the feed cables, we will
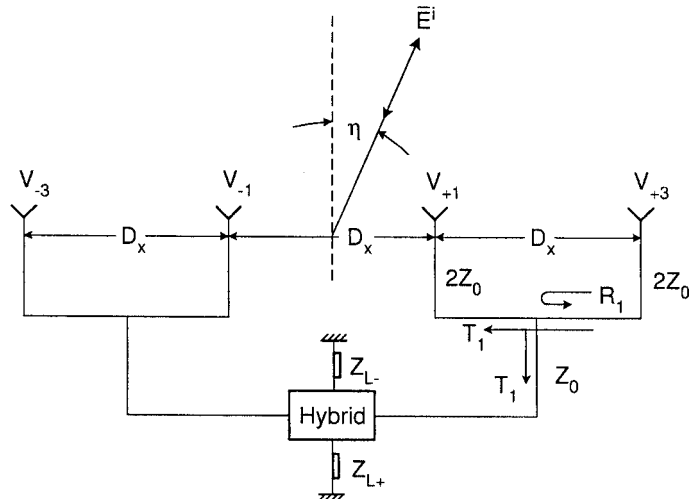
Fig. P2.7 A simple array of four elements fed via a harness comprised of two simple T connectors fed via a simple hybrid.

experience a mainbeam in the bistatic direction and some smaller sidelobes in the backscatter directions. However, you are only required to find the scattering pattern due to reflections from the two T connectors at oblique angle of incidence η. Estimate the magnitude of the backscattered field.

Hint: In general,

$$G = \frac{4\pi}{\lambda^2} A,$$

that is, (2.8) can for $G_i = G_r$ and $p_i = p_r = 1$ be written as

$$\sigma_{ant} = \frac{4\pi}{\lambda^2} A^2 \Gamma^2$$

where $\dfrac{4\pi}{\lambda^2} A^2$ is the RCS of a flat plate with physical area A.

3

Theory

3.1 INTRODUCTION

In Chapter 1 we introduced the fundamental concepts concerning a new type of surface wave that can be excited only on finite periodic structures. It was pointed out that radiation could occur from such surface waves and therefore could lead to an increase in the RCS level in the backward direction. Similarly, if the structure was active—as, for example, for a phased array—this type of surface wave could lead to a very significant variation of the terminal impedance form element to element. This could make precise matching difficult, if not impossible.

Furthermore, in Chapter 2 we presented the theory for the RCS of antennas in general. In particular, it was shown that the scattering from antennas can be decomposed into two components, namely the antenna mode component being proportional to the square of the reflection coefficient observed at the antenna terminals and another called for the residual component (also earlier denoted structural). Although the precise definition of the second was somewhat illusive, we nevertheless demonstrated that it was equal to zero for large flat apertures with uniform illumination. The most prominent member of that family was without a doubt the antenna array. In fact it has a very unique position in the world of radiators.

So far our mode of attack has been mostly based on physical insight. That pointed us in the right direction without going through an enormous amount of tedious calculations that might have led us into dead ends.

In my first book [61] we investigated primarily structures of infinite × infinite extent. However, in this chapter we shall primarily develop the mathematical tools that will enable us to investigate the finite × infinite case.

More specifically, we shall investigate arrays comprised of infinitely long columns along the z axis, where the elements have arbitrary orientation $\hat{p} = \hat{x}p_x + \hat{y}p_y + \hat{z}p_z$. Such single-column arrays are often called stick arrays. They are simply the building blocks for more complicated arrays and are therefore extremely important to investigate.

3.2 THE VECTOR POTENTIAL AND THE *H* FIELD FOR COLUMN ARRAYS OF HERTZIAN ELEMENTS

Consider an array of Hertzian elements with length dl and arbitrary orientation $\hat{p}$ as shown in Fig. 3.1. The reference element is located at $(0, 0, z')$ while the element current are assumed to be

$$I_m = I_0 \, e^{-j\beta m D_z s_z}, \tag{3.1}$$

where m denotes the element number along the z axis and I_0 denotes the current in reference element $m = 0$.

In fact, when the reference element is located at the origin (i.e., $z' = 0$), we have already determined the vector potential $d\overline{A}_q$ for this case in reference 62 as

$$d\overline{A}_q = \hat{p}\frac{\mu I_0 \, dl}{4jD_z} \sum_{n=-\infty}^{\infty} e^{-j\beta z r_z} H_0^{(2)}(\beta r_\rho \rho), \tag{3.2}$$

where

$$r_z = s_z + n\frac{\lambda}{D_z}, \tag{3.3}$$
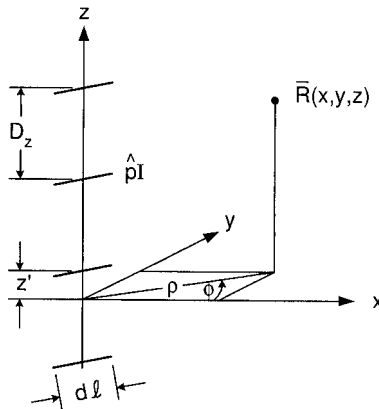
Fig. 3.1 *Infinite stick array of Hertzian dipoles with arbitrary orientation $\hat{p} = \hat{x}p_x + \hat{y}p_y + \hat{z}p_z$ and element currents $I_m = I_0 \, e^{-j\beta m D_z r_z}$. The reference element is located at (0, 0, z').*

$$r_\rho = \sqrt{1 - r_z^2} = \sqrt{1 - \left(s_z + n\frac{\lambda}{D_z}\right)^2}. \tag{3.4}$$

We shall next generalize to the case where the reference element 0 is located at $(0, 0, z')$ as shown in Fig. 3.1. This situation corresponds to keeping the reference element at the origin and lowering $\overline{R}$ to the new position $(0, 0, z - z')$. According to (3.2), we then find the vector potential for the general case to be

$$d\overline{A}_q = \hat{p}\frac{\mu I_0\, dl}{4jD_z}\sum_{n=-\infty}^{\infty} e^{-j\beta(z-z')r_z} H_0^{(2)}(\beta r_\rho \rho). \tag{3.5}$$

for reference element at $(0, 0, z')$.

Next we obtain the H field at the point of observation R from

$$d\overline{H} = \frac{1}{\mu}\nabla \times d\overline{A}. \tag{3.6}$$

Substituting (3.5) into (3.6), we obtain

$$d\overline{H}_q = \frac{I_0\, dl}{4jD_z}\sum_{n=-\infty}^{\infty} \nabla \times [\hat{p}\, e^{-j\beta(z-z')r_z} H_0^{(2)}(\beta r_\rho \rho)].$$

Further applying the vector identity

$$\nabla \times (\hat{p}\phi) = \phi\nabla \times \hat{p} - \hat{p} \times \nabla\phi$$

(where we note that the first term on the right-hand side is zero because $\hat{p}$ is a constant), we obtain

$$d\overline{H}_q = -\frac{I_0\, dl}{4jD_z}\sum_{n=-\infty}^{\infty} \hat{p} \times \nabla[e^{-j\beta(z-z')r_z} H_0^{(2)}(\beta r_\rho \rho)]. \tag{3.7}$$

In *cylindrical coordinates* we obtain from (3.7)

$$d\overline{H}_q = -\frac{I_0\, dl}{4jD_z}\sum_{n=-\infty}^{\infty} \hat{p}$$

$$\times \left[\hat{\rho}\frac{\partial}{\partial\rho} + \hat{\phi}\frac{1}{\rho}\frac{\partial}{\partial\phi} + \hat{z}\frac{\partial}{\partial z}\right][e^{-j\beta(z-z')r_z} H_0^{(2)}(\beta r_\rho \rho)]$$

$$d\overline{H}_q = -\frac{\beta I_0\, dl}{4jD_z}\sum_{n=-\infty}^{\infty} e^{-j\beta(z-z')r_z}$$

$$\cdot [\hat{p} \times \hat{\rho} r_\rho H_0^{(2)'}(\beta r_\rho \rho) - j\hat{p} \times \hat{z} r_z H_0^{(2)}(\beta r_\rho \rho)]. \tag{3.8}$$

In *rectangular coordinates* we obtain from (3.7)

$$d\overline{H}_q = -\frac{I_0\,dl}{4jD_z}\sum_{n=-\infty}^{\infty}e^{-j\beta(z-z')r_z}$$

$$\cdot\,\hat{p}\times\left[\hat{x}\frac{\partial}{\partial x}H_0^{(2)}(\beta r_\rho\sqrt{x^2+y^2})+\hat{y}\frac{\partial}{\partial y}H_0^{(2)}(\beta r_\rho\sqrt{x^2+y^2})\right.$$

$$\left.-\,j\hat{z}\beta r_z H_0^{(2)}(\beta r_\rho\sqrt{x^2+y^2})\right]. \tag{3.9}$$

Equations (3.8) and (3.9) are valid for arbitrary $\hat{p}$. However, in the following investigation we shall specialize to:

I: Longitudinal case where $\hat{p}$ is parallel with the array axis; that is, in our case $\hat{p}=\hat{z}$.

II: Transverse case where $\hat{p}$ is orthogonal to the array axis. In our case we will further specialize to $\hat{p}=\hat{x}$.[1]

3.3 CASE I: LONGITUDINAL ELEMENTS

For $\hat{p}=\hat{z}$ we obtain from (3.8) for Hertzian elements

$$d\overline{H}_q = -\frac{\beta I_0\,dl}{4jD_z}\sum_{n=-\infty}^{\infty}e^{-j\beta(z-z')r_z}\hat{\phi}r_\rho H_0^{(2)'}(\beta r_\rho\rho). \tag{3.10}$$

Furthermore,

$$\overline{E}_q = \frac{1}{j\omega\varepsilon}\nabla\times\overline{H}_q$$

$$=\frac{1}{j\omega\varepsilon}\left[\hat{\rho}\left[\frac{1}{\rho}\frac{\partial H_z}{\partial\phi}-\frac{\partial H_\phi}{\partial z}\right]+\hat{\phi}\left[\frac{\partial H_\rho}{\partial z}-\frac{\partial H_z}{\partial\rho}\right]\right.$$

$$\left.+\,\hat{z}\left[\frac{1}{\rho}\frac{\partial}{\partial\rho}(\rho H_\phi)-\frac{1}{\rho}\frac{\partial H_\rho}{\partial\phi}\right]\right]. \tag{3.11}$$

Substituting (3.10) into (3.11), we obtain

$$d\overline{E}_q = \frac{-1}{j\omega\varepsilon}\frac{\beta I_0\,dl}{4jD_z}\sum_{n=-\infty}^{\infty}e^{-j\beta(z-z')r_z}$$

$$\cdot\left[j\hat{\rho}r_\rho r_z\beta H_0^{(2)'}(\beta r_\rho\rho)+\hat{z}r_\rho^2\beta\left[\frac{1}{\rho}\rho H_0^{(2)''}(\beta r_\rho\rho)+\frac{1}{\beta r_\rho\rho}H_0^{(2)'}(\beta r_\rho\rho)\right]\right]. \tag{3.12}$$

---

[1] This choice in no way limits the generality of our investigation since our point of observation $\overline{R}(x,y,z)$ is arbitrary.

Applying $\beta = \omega\sqrt{\mu\varepsilon}$, $Z = \sqrt{\mu/\varepsilon}$, and the recursive relationship

$$H_0^{(2)''}(\beta r_\rho \rho) + \frac{1}{\beta r_\rho \rho} H_0^{(2)'}(\beta r_\rho \rho) = -H_0^{(2)}(\beta r_\rho \rho),$$

we can write (3.12) as

$$d\overline{E}_q = \frac{\beta Z I_0 \, dl}{4 D_z} \sum_{n=-\infty}^{\infty} e^{-j\beta(z-z')r_z}$$

$$\cdot [-j\hat{\rho} r_\rho r_z H_0^{(2)'}(\beta r_\rho \rho) + \hat{z} r_\rho^2 H_0^{(2)}(\beta r_\rho \rho)], \tag{3.13}$$

where $\hat{p} = \hat{z}$ and the reference element is located at $(0, 0, z')$.

3.3.1 Total Field from Infinite Column Array of *z*-Directed Elements of Arbitrary Length 2*l*

Equation (3.13) yields the entire field from an infinite array of z-directed (collinear) elements of length dl and the constant current I_0. In other words, the expression is essentially a dyadic Green's function.

Thus, we can use this expression to obtain the total field $\overline{E}_q$ of an infinite collinear array of elements of arbitrary length as well as arbitrary currents $I(z')$ simply by integrating $d\overline{E}^{(q)}$ given by (3.13) over a single element as discussed in reference 63.

More specifically, let the endpoints of the reference element be denoted by the points "a" and "b" as illustrated in Fig. 3.2. Further noting that $H_0^{(2)'}(\beta r_\rho \rho) =$
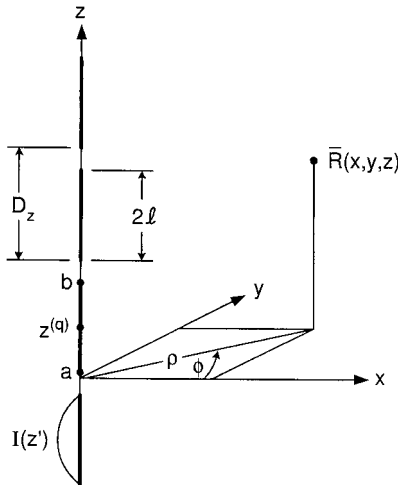
Fig. 3.2 Infinite collinear array of z-directed elements of length 2l and current distribution I(z'). The reference element is located at (0, 0, z^(q)).

$-H_1^{(2)}(\beta r_\rho \rho)$, we obtain the total field $\overline{E}^{(q)}$

$$\overline{E}^q = -\frac{\beta Z}{4D_z} \sum_{n=-\infty}^{\infty} \int_{z'=a}^{b} I(z') \, e^{-j\beta(z-z')r_z} \, dz'$$

$$\cdot \, [-j\hat{\rho} r_\rho r_z H_1^{(2)}(\beta r_\rho \rho) + \hat{z} r_\rho^2 H_0^{(2)}(\beta r_\rho \rho)]. \tag{3.14}$$

The integral in (3.14) can be better managed if we express the source point z' with respect to a reference point $z^{(q)}$ that basically can be chosen anywhere on the reference element. It is natural to choose it as the midpoint of an element of length $2l$, that is

$$z' = z^{(q)} + z'', \qquad -l < z'' < l. \tag{3.15}$$

Substituting (3.15) into (3.14), we obtain

$$\overline{E}^q = -\frac{\beta Z I^{(q)}}{4D_z} \sum_{n=-\infty}^{\infty} e^{-j\beta(z-z^{(q)})r_z} P_z^{(q)}$$

$$\cdot \, [j\hat{\rho} r_\rho r_z H_1^{(2)}(\beta r_\rho \rho) + \hat{z} r_\rho^2 H_0^{(2)}(\beta r_\rho \rho)], \tag{3.16}$$

where the pattern factor $P_z^{(q)}$ normalized to the reference current $I^{(q)}(z)$ at the reference point $z^{(q)}$ is defined as

$$P_z^{(q)} = \frac{1}{I^{(q)}} \int_{-l}^{l} I^{(q)}(z'') \, e^{j\beta z'' r_z} \, dz.'' \tag{3.17}$$

Equation (3.16) gives us the total E field of an infinite collinear column array of z-directed elements of length $2l$, the arbitrary current distribution $I^{(q)}(z)$, and the reference point of the reference element located at $z^{(q)}$.

3.3.2   The Voltage Induced in an Element by an External Field

Ultimately we are going to determine the mutual impedance $Z^{q,'q}$ between a collinear array q and the reference element of another array q'. It will be recalled that the mutual impedance in general is merely defined as the negative of the voltage induced in the external element q' by the entire line array divided by the current on the reference element of array q. The voltage induced at the terminals of a single element by an arbitrary field $\overline{E}$ is given by [64]

$$V^{(q')} = \frac{1}{I^{q't}} \int \overline{E} \cdot \hat{p}^{(q')} I^{q't}(l) \, dl, \tag{3.18}$$

where $\hat{p}^{(q')}$ is the direction of element in question, $I^{q't}(l)$ is the current distribution of the element q' when transmitting from its terminals, and $I^{q't}(0)$ is the current at the terminals of q'.

In the present case of interest we are considering two collinear arrays in which case

$$\hat{p}^{q'} = \hat{z} \quad \text{and} \quad \rho \to \rho'. \tag{3.19}$$

Substituting (3.16) and (3.19) into (3.18) yields

$$V^{(q')} = -\frac{\beta Z I^{(q)}}{4 D_z} \sum_{n=-\infty}^{\infty} P_z^{(q)} \frac{1}{I^{q't}} \int_{\text{Element } q'} I^{q't} \, e^{-j\beta(z-z^{(q)})r_z} \, dz \, r_\rho^2 H_0^{(2)}(\beta r_\rho \rho)'. \tag{3.20}$$

Similar to earlier [see (3.15)], we now express the arbitrary point z on the external element q' with respect to a reference point $z^{(q')}$:

$$z = z^{(q')} + z'', \qquad -l' < z'' < l'. \tag{3.21}$$

Substituting (3.21) into (3.20), we obtain

$$V^{(q')} = -\frac{\beta Z I^{(q)}}{4 D_z} \sum_{n=-\infty}^{\infty} e^{-j\beta(z^{(q')}-z^{(q)})r_z} P_z^{(q)} P^{q't} r_\rho^2 H_0^{(2)}(\beta r_\rho \rho'), \tag{3.22}$$

where the normalized transmitting pattern function for the external element q' is given by

$$P^{q't} = \frac{1}{I^{q't}(z^{q'})} \int_{-l'}^{l} I^{q't}(z'') \, e^{-j\beta z'' r_z} \, dz''. \tag{3.23}$$

3.3.3 The Mutual Impedance $Z^{q',q}$ Between a Column Array q and an External Element q'

As indicated above, the mutual impedance between a column array q and a single external element (namely the reference element of another array q') is simply defined as

$$Z^{q',q} = -\frac{V^{(q')}}{I^{(q)}}. \tag{3.24}$$

Substituting (3.22) into (3.24) yields

$$Z^{q',q} = \frac{\beta Z}{4 D_z} \sum_{n=-\infty}^{\infty} e^{-j\beta(q'-q)r_z} r_\rho^2 P_z^{(q)} P_z^{q't} H_0^{(2)}(\beta r_\rho \rho'), \tag{3.25}$$

where the two pattern functions $P_z^{(q)}$ and $P_z^{q't}$ are defined by (3.17) and (3.23), respectively.
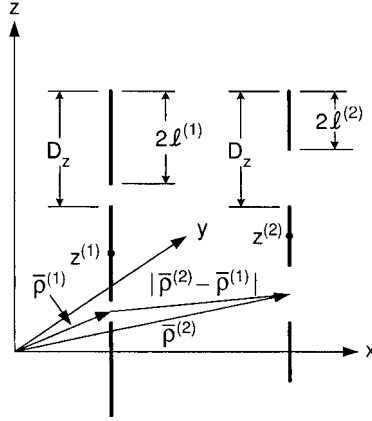
Fig. 3.3 Two infinite arrays of z-directed elements with length $2l^{(1)}$ and $2l^{(2)}$ and the reference points at $(\overline{\rho}^{(1)}, Z^{(1)})$ and $(\overline{\rho}^{(2)}, Z^{(2)})$, respectively.

In the case as shown in Fig. 3.3, it is easy to generalize (3.25) to

$$Z^{q',q} = \frac{\beta Z}{4D_z} \sum_{n=-\infty}^{\infty} e^{-j\beta(q'-q)r_z} r_\rho^2 P_z^{(q)} P_z^{q't} H_0^{(2)}(\beta r_\rho |\overline{\rho}' - \overline{\rho}|) \qquad (3.26)$$

where the two pattern functions are unchanged.

Let us finally consider the more general case where the reference points of the column arrays are given by $(\overline{\rho}^{(1)}, Z^{(1)})$ and $(\overline{\rho}^{(2)}, Z^{(2)})$, respectively, as shown in Fig. 3.3. By generalization of (3.25) we then readily obtain

$$Z^{2,1} = \frac{\beta Z}{4D_z} \sum_{n=-\infty}^{\infty} e^{-j\beta(Z^{(2)}-Z^{(1)})r_z} r_\rho^2 P_z^{(2)t} P_z^{(1)} H_0^{(2)}(\beta r_\rho |\overline{\rho}^{(2)} - \overline{\rho}^{(1)}|), \qquad (3.27)$$

where the two pattern functions are unchanged as defined by (3.17) and (3.23).

Equation (3.26) for the mutual impedance $Z^{2,1}$ between a *column* array at $\overline{\rho}^{(1)}, Z^{(1)}$ and the reference element of another array at $\overline{\rho}^{(2)}, Z^{(2)}$ should be compared to an earlier result for the mutual impedance $Z^{2,1}$ between a *planar* array and the reference element of another array found to be [65]

$$Z^{2,1} = \frac{Z}{2D_x D_z} \sum_{k=-\infty}^{\infty} \sum_{n=-\infty}^{\infty} \frac{e^{-j\beta(\overline{R}^{(2)} - \overline{R}^{(1)})\cdot\hat{r}}}{r_y} [\perp P^{(2)t} \perp P^{(1)} + \parallel P^{(2)t} \parallel P^{(1)}], \quad (3.28)$$

where

$$\begin{aligned} {}_\parallel^\perp P^{(1)} &= \hat{p}^{(1)} \cdot {}_\parallel^\perp \hat{n} P^{(1)}, \\ {}_\parallel^\perp P^{(2)t} &= \hat{p}^{(2)} \cdot {}_\parallel^\perp \hat{n} P^{(2)t}, \end{aligned}$$

If we limit ourselves to scan the yz plane, the orthogonal terms $_\perp P^{(1)}$ are either zero or cancel when k varies. We then note that (3.27) and (3.28) are similar as far as variation in the z direction is concerned, which should not surprise us since Floquet's theorem is valid for both cases in this direction. However, their behavior in the xy plane clearly indicates a planar wave in the double infinite case and a cylindrical wave in the collinear case.

Note further that for $\hat{p}^{(1)} = \hat{p}^{(2)} = \hat{z}$ we have

$$\hat{p}^{(1)} \cdot {}_\perp\hat{n} = \hat{p}^{(2)} \cdot {}_\perp\hat{n} = 0,$$

$$\hat{p}^{(1)} \cdot {}_\parallel\hat{n} = \hat{p}^{(2)} \cdot {}_\parallel\hat{n} = -r_\rho.$$

3.4 CASE II: TRANSVERSE ELEMENTS

We shall next investigate the transverse case, in particular where the line array is oriented in the x direction and the reference element located at $\overline{R}'(0, 0, z')$ while the point of observation is $\overline{R}(x, y, z)$, as shown in Fig. 3.4.

From (3.9) we obtain for $\hat{p} = \hat{x}$ and $dl \to dx'$

$$d\overline{H}_q = -\frac{I_0 \, dx'}{4 j D_z} \sum_{n=-\infty}^{\infty} e^{-j\beta(z-z')r_z} \left[\hat{z} \frac{\partial}{\partial y} H_0^{(2)}(\beta r_\rho \sqrt{x^2 + y^2}) \right.$$

$$\left. + j\hat{y}\beta r_z H_0^{(2)}(\beta r_\rho \sqrt{x^2 + y^2}) \right]. \tag{3.29}$$

Furthermore, we have in general

$$\overline{E}_q = \frac{1}{j\omega\varepsilon} \nabla \times \overline{H}_q$$
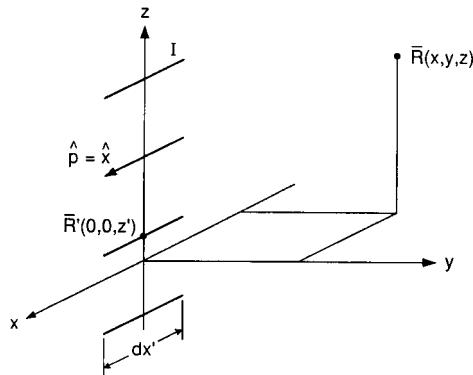
Fig. 3.4   An infinite array of transverse Hertzian dipoles with orientation $\hat{p} = \hat{x}$. The reference element is located at $\overline{R}'(0, 0, z')$ while the point of observation is at $\overline{R}(x, y, z)$.

$$= \frac{1}{j\omega\varepsilon}\left[\hat{x}\left(\frac{\partial H_z}{\partial y} - \frac{\partial H_y}{\partial z}\right) + \hat{y}\left(\frac{\partial H_x}{\partial z} - \frac{\partial H_z}{\partial x}\right) + \hat{z}\left(\frac{\partial H_y}{\partial x} - \frac{\partial H_x}{\partial y}\right)\right].$$
(3.30)

Substituting (3.29) into (3.30):

$$d\overline{E}_q = -\frac{1}{j\omega\varepsilon}\frac{I_0\,dx'}{4jD_z}\sum_{n=-\infty}^{\infty}e^{-j\beta(z-z')r_z}$$

$$\cdot\left[\hat{x}\left[\frac{\partial^2}{\partial y^2}H_0^{(2)}(\beta r_\rho\sqrt{x^2+y^2}) - \beta^2 r_z^2 H_0^{(2)}(\beta r_\rho\sqrt{x^2+y^2})\right]\right.$$

$$\left. - \hat{y}\frac{\partial^2}{\partial x\partial y}H_0^{(2)}(\beta r_\rho\sqrt{x^2+y^2}) + j\hat{z}\beta r_z\frac{\partial}{\partial x}H_0^{(2)}(\beta r_\rho\sqrt{x^2+y^2})\right]. \quad (3.31)$$

We are next going to investigate the *x, y,* and *z* components separately.

3.4.1 The *x* Component of $\overline{E}_q$

In order to reduce the *x* component of (3.31), consider for a moment the ∇^2 operator in cylindrical coordinates:

$$\nabla^2 = \frac{1}{\rho}\frac{\partial}{\partial\rho}\left(\rho\frac{\partial}{\partial\rho}\right) + \frac{1}{\rho^2}\frac{\partial^2}{\partial\phi^2} + \frac{\partial^2}{\partial z^2}.$$

Operating on $H_0^{(2)}(\beta r_\rho\rho)$ we obtain

$$\nabla^2 H_0^{(2)}(\beta r_\rho\rho) = \frac{1}{\rho}\frac{\partial}{\partial\rho}\left(\rho\frac{\partial H_0^{(2)}(\beta r_\rho\rho)}{\partial\rho}\right)$$

$$= (\beta r_\rho)^2\left[H_0^{(2)''}(\beta r_\rho\rho) + \frac{1}{\beta r_\rho\rho}H_0^{(2)'}(\beta r_\rho)\right].$$

Furthermore, by applying the recursive formula

$$H_0^{(2)''} + \frac{1}{x}H_0^{(2)'} = -H_0^{(2)}$$

we obtain

$$\nabla^2 H_0^{(2)}(\beta r_\rho\rho) = -(\beta r_\rho)^2 H_0^{(2)}(\beta r_\rho\rho). \quad (3.32)$$

Expressed in rectangular coordinates we have

$$\nabla^2 H_0^{(2)}(\beta r_\rho\rho) = \frac{\partial^2 H_0^{(2)}(\beta r_\rho\rho)}{\partial x^2} + \frac{\partial^2 H_0^{(2)}(\beta r_\rho\rho)}{\partial y^2}. \quad (3.33)$$

Equating (3.32) and (3.33), we obtain

$$\frac{\partial^2 H_0^{(2)}(\beta r_\rho \rho)}{\partial y^2} = -\frac{\partial^2 H_0^{(2)}(\beta r_\rho \rho)}{\partial x^2} - (\beta r_\rho)^2 H_0^{(2)}(\beta r_\rho \rho). \qquad (3.34)$$

Substituting (3.34) into (3.31) and assuming current distribution $I(x')$ on all the elements, we obtain the total x component of the E field by integrating over the reference element:

$$\overline{E}_q^{x,x'} = -\hat{x}\frac{1}{\omega \varepsilon}\frac{1}{4D_z}\sum_{n=-\infty}^{\infty} e^{-j\beta(z-z')r_z}$$

$$\times \int_{\text{Ref. ele.}} I(x')\left[\frac{\partial^2}{\partial x^2} + (\beta r_\rho)^2 + (\beta r_z)^2\right] H_0^{(2)}(\beta r_\rho \rho)\, dx',$$

where ρ now is

$$\rho = \sqrt{(x - x')^2 + y^2}.$$

Further noting that $r_\rho^2 + r_z^2 = 1$ and $\dfrac{\partial^2}{\partial x'^2} = \dfrac{\partial^2}{\partial x^2}$, we obtain

$$\overline{E}_q^{x,x'} = -\hat{x}\frac{\sqrt{\mu/\varepsilon}}{\omega\sqrt{\varepsilon\mu}4D_z}\sum_{n=-\infty}^{\infty} e^{-j\beta(z-z')r_z}$$

$$\times \int_{\text{Ref. ele.}} I(x')\left[\frac{\partial^2}{\partial x'^2} + \beta^2\right] H_0^{(2)}(\beta r_\rho \rho)\, dx'. \qquad (3.35)$$

Integrating the first term in the integral of (3.35) twice by parts, we obtain

$$\overline{E}_q^{x,x'} = -\hat{x}\frac{Z}{\beta 4D_z}\sum_{n=-\infty}^{\infty} e^{-j\beta(z-z')r_z}\left[I(x')\frac{\partial}{\partial x'}H_0^{(2)}(\beta r_\rho \rho)\Big|_{\text{Ref. ele. endpts.}}\right.$$

$$\left. - \int_{\text{Ref. ele.}} I'(x')\frac{\partial}{\partial x'}H_0^{(2)}(\beta r_\rho \rho) - \beta^2 I(x')H_0^{(2)}(\beta r_\rho \rho)\, dx'\right]$$

$$= -\hat{x}\frac{Z}{\beta 4D_z}\sum_{n=-\infty}^{\infty} e^{-j\beta(z-z')r_z}\left[\left[I(x')\frac{\partial}{\partial x'}H_0^{(2)}(\beta r_\rho \rho)\right.\right.$$

$$\left.\left. - I'(x')\, H_0^{(2)}(\beta r_\rho \rho)\right]\right|_{\text{Ref. ele. endpts.}}$$

$$+ \int_{\text{Ref. ele.}} [I''(x') + \beta^2 I(x')]\Big] H_0^{(2)}(\beta r_\rho \rho)\, dx. \qquad (3.36)$$

If the current distribution $I(x')$ is sinusoidal with propagation constant β, we note that the integrand in (3.36) equals zero. Furthermore, the current $I(x')$ at

the endpoints of the reference element must equal zero (boundary condition). Thus, the first term in (3.36) is also zero and we finally have

$$\overline{E}_q^{x,x'} = \hat{x}\frac{Z}{\beta 4 D_z}\sum_{n=-\infty}^{\infty} e^{-j\beta(z-z')r_z}[I'(x')H_0^{(2)}(\beta r_\rho \rho)]_{\text{Ref. ele. endpts.}} \quad (3.37)$$

for sinusoidal current with propagation constant β. Specifically for a sinusoidal current distribution

$$I(x') = I_a \sin\beta(l' - |x'|) \qquad \text{for} - l' < x' < l' \quad (3.38)$$

comprised of two sections with endpoint at $x' = \pm l'$ and 0. We obtain from (3.37)

$$\overline{E}_q^{x,x'} = -\hat{x}\frac{Z I_a}{4 D_z}\sum_{n=-\infty}^{\infty} e^{-j\beta(z-z')r_z}[H_0^{(2)}(\beta r_\rho \rho_+) + H_0^{(2)}(\beta r_\rho \rho_-)$$

$$- 2\cos\beta l' H_0^{(2)}(\beta r_\rho \rho_0)], \quad (3.39)$$

where $\rho_\pm = \sqrt{(x \pm l')^2 + y^2}$ and $\rho_0 = \sqrt{x^2 + y^2}$ as illustrated in Fig. 3.5.

The voltage $V_q^{x,x'}$ induced at the terminals of an x-directed element with current distribution $I_x(x)$ is given by (see Fig. 3.6, top)

$$V_q^{x,x'} = \frac{1}{I_x(0)}\int_{\text{Ext. ele.}} I_x(x)\,\overline{E}_q^{x,x'}\,dx. \quad (3.40)$$
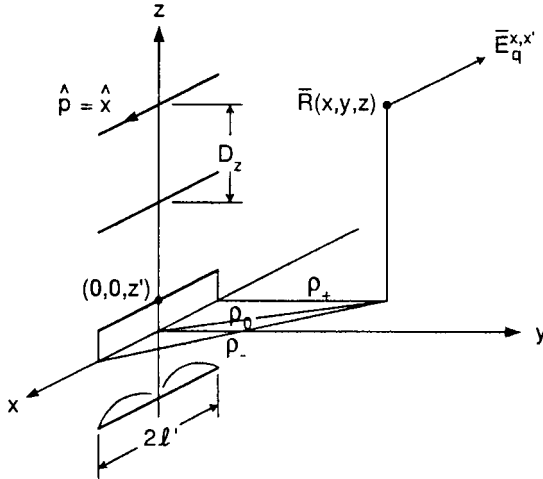
Fig. 3.5 *The x component of the E field at point $\overline{R}(x, y, z)$ from a transverse array with element orientation $\hat{p} = \hat{x}$ and sinusoidal current distribution can be expressed by an infinite series of three Hankel functions with radii ρ_+, ρ_- and ρ_0 as shown in the figure. See (3.39) for details.*
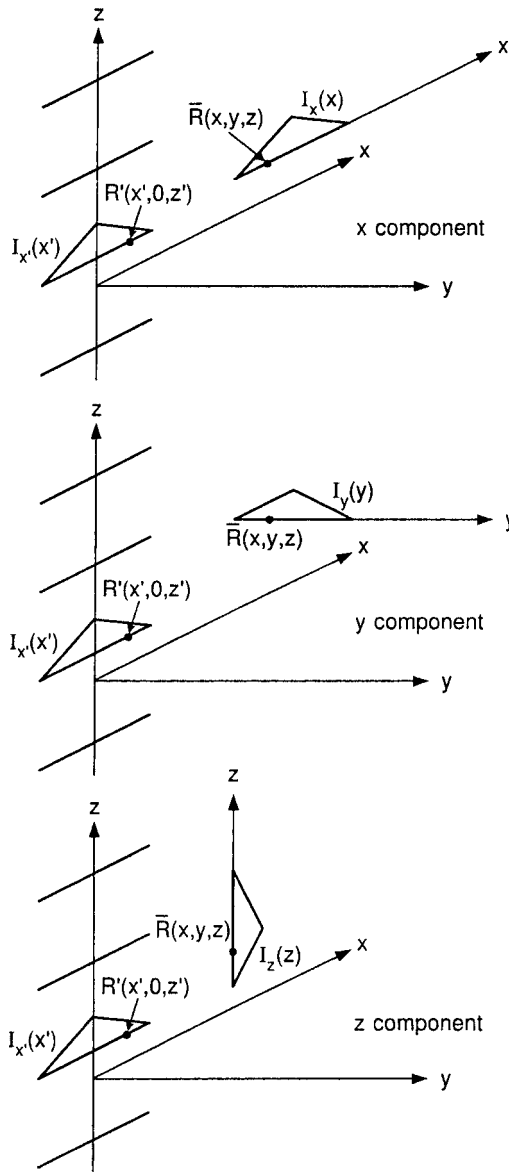
Fig. 3.6 An infinite line array with transverse x-directed elements of length 2l with current distribution $I_{x'}(x')$ induces a voltage in a single dipole with current distribution oriented along the x axis with $I_x(x)$ (top), y axis with $I_y(y)$ (middle), and z axis with $I_z(z)$ (bottom).

Finally, the mutual impedance $Z_q^{x,x'}$ between a stick array with an external element is defined as

$$Z_q^{x,x'} = -\frac{V_q^{x,x'}}{I(0)}, \tag{3.41}$$

where from (3.38)

$$I(0) = I_a \sin \beta l'. \tag{3.42}$$

Substituting (3.39), (3.40), and (3.42) into (3.41), we obtain

$$Z_q^{x,x'} = \frac{Z}{\beta 4D_z} \frac{1}{\sin \beta l'} \sum_{n=-\infty}^{\infty} e^{-j\beta(z-z')r_z} \frac{1}{I_x(0)} \int_{\text{Ext. ele.}} I_x(x)$$

$$\cdot [H_0^{(2)}(\beta r_\rho \rho_+) + H_0^{(2)}(\beta r_\rho \rho_-) - 2\cos \beta l' H_0^{(2)}(\beta r_\rho \rho_0)]\, dx. \tag{3.43}$$

For further discussion of (3.43), see Section 3.5.

3.4.2 The *y* Component of $\overline{E}_q$

The *y* component $\overline{E}_q^{y,x'}$ of the total field $\overline{E}_q$ from a line array with current distribution $I_{x'}(x')$ is readily obtained from (3.31) by integration of the *y* component over the reference element with current distribution $I_{x'}(x')$:

$$\overline{E}^{y,x'} = \hat{y} \frac{\sqrt{\mu/\varepsilon}}{\omega\sqrt{\varepsilon\mu}4D_z} \sum_{n=-\infty}^{\infty} e^{-j\beta(z-z')r_z}$$

$$\cdot \frac{\partial}{\partial y} \int_{\text{Ref. ele.}} I_{x'}(x') \frac{\partial}{\partial x'} H_0^{(2)}(\beta r_\rho \sqrt{(x-x')^2 + y^2})\, dx', \tag{3.44}$$

where we have used $\dfrac{\partial}{\partial x} = -\dfrac{\partial}{\partial x'}$. Integration by parts once with respect to x' gives

$$\overline{E}_q^{y,x'} = \hat{y}\frac{Z}{\beta 4D_z} \sum_{n=-\infty}^{\infty} e^{-j\beta(z-z')r_z}$$

$$\cdot \frac{\partial}{\partial y}\left[I_{x'}(x') H_0^{(2)}(\beta r_\rho \sqrt{(x-x')^2 + y^2})\, dx' \;|_{\text{Ref. ele. endpts.}} \right.$$

$$\left. - \int_{\text{Ref. ele.}} *I_{x'}'(x') H_0^{(2)}(\beta r_\rho \sqrt{(x-x')^2 + y^2})\, dx \right].' \tag{3.45}$$

Since $I_{x'}(x') = 0$ at the endpoints of the reference element, the first term in (3.45) must equal zero. Thus, the total *y* component at $\overline{R}(x, y, z)$ of the E field from the line array with transverse elements is

$$\overline{E}_q^{y,x'} = -\hat{y}\frac{Z}{\beta 4D_z} \sum_{n=-\infty}^{\infty} e^{-j\beta(z-z')r_z}$$

$$\cdot \frac{\partial}{\partial y} \int_{\text{Ref. ele.}} I_{x'}'(x') H_0^{(2)}(\beta r_\rho \sqrt{(x-x')^2 + y^2})\, dx.' \tag{3.46}$$

The voltage induced in a y-directed element with current $I_y(y)$ is now given by (see Fig. 3.6, middle):

$$V_q^{y,x'} = \frac{1}{I_y(0)} \int_{\text{Ext. ele.}} I_y(y) \, E_q^{y,x'} \, dy. \tag{3.47}$$

Substituting (3.46) into (3.47), we obtain

$$V_q^{y,x'} = -\frac{Z}{\beta 4 D_z} \sum_{n=-\infty}^{\infty} e^{-j\beta(z-z')r_z} \frac{1}{I_y(0)} \int_{\text{Ref. ele.}} I_{x'}'(x') \, dx'$$

$$\cdot \int_{\text{Ext. ele.}} I_y(y) \, \frac{\partial}{\partial y} H_0^{(2)}(\beta r_\rho \sqrt{(x-x')^2 + y^2}) \, dy. \tag{3.48}$$

Integrating the y integral once by parts, we get

$$V_q^{y,x'} = -\frac{Z}{\beta 4 D_z} \sum_{n=-\infty}^{\infty} e^{-j\beta(z-z')r_z} \frac{1}{I_y(0)} \int_{\text{Ref. ele.}} I_{x'}'(x') \, dx'$$

$$\cdot \left[I_y(y) H_0^{(2)}(\beta r_\rho \sqrt{(x-x')^2 + y^2})|_{\text{Ref. ele. endpts.}} \right.$$

$$\left. - \int_{\text{Ext. ele.}} I_y'(y) H_0^{(2)}(\beta r_\rho \sqrt{(x-x')^2 + y^2}) dy \right]. \tag{3.49}$$

Since $I_y(y) = 0$ at the endpoints of the external element, the first term in (3.49) equals zero. Thus, (3.49) reduces to just the last term and for the mutual impedance between the line array and an external element we find

$$\overline{Z}_q^{y,x'} = -\frac{\overline{V}_q^{y,x'}}{I_{x'}(0)}$$

$$= -\frac{Z}{\beta 4 D_z} \sum_{n=-\infty}^{\infty} e^{-j\beta(z-z')r_z} \frac{1}{I_{x'}(0) I_y(0)}$$

$$\cdot \int_{\text{Ref. ele.}} I_{x'}'(x') \, dx' \int_{\text{Ext. ele.}} I_y'(y) H_0^{(2)}(\beta r_\rho \sqrt{(x-x')^2 + y^2}) \, dy. \tag{3.50}$$

For sinusoidal current distribution as given by (3.38) we find

$$I_{x'}'(x') = \pm \beta I_a \cos \beta(l' - |x'|) \qquad \text{for} -l' < x' < l',$$

$$I_{x'}(0) = I_a \sin \beta l'.$$

Thus

$$Z_q^{y,z'} = \frac{Z}{4D_z \sin \beta l'} \sum_{n=-\infty}^{\infty} e^{-j\beta(z-z')r_z} \frac{1}{I_y(0)} \int_{\text{Ref. ele.}} \text{sign } x \cos \beta(l' - |x'|) \, dx'$$

$$\cdot \int_{\text{Ext. ele.}} I_y'(y) H_0^{(2)}(\beta r_\rho \sqrt{(x - x')^2 + y^2}) \, dy. \tag{3.51}$$

Alternatively, we can simply in (3.44) carry out the differentiation $H_0^{(2)}$ with respect to x' and y as follows:

$$\frac{\partial}{\partial x'} H_0^{(2)}(\beta r_\rho \sqrt{(x - x')^2 + y^2})$$

$$= -\beta r_\rho H_0^{(2)'}(\beta r_\rho \sqrt{(x - x')^2 + y^2}) \frac{x - x'}{\sqrt{(x - x')^2 + y^2}}$$

$$\frac{\partial}{\partial y} \left[\frac{\partial}{\partial x'} H_0^{(2)}(\beta r_\rho \sqrt{(x - x')^2 + y^2}) \right]$$

$$= -\beta r_\rho \left[\beta r_\rho H_0^{(2)''}(\beta r_\rho \sqrt{(x - x')^2 + y^2}) \cdot \frac{y}{\sqrt{(x - x')^2 + y^2}} \frac{x - x'}{\sqrt{(x - x')^2 + y^2}} \right]$$

$$- H_0^{(2)'}(\beta r_\rho \sqrt{(x - x')^2 + y^2}) \frac{(x - x')y}{[(x - x')^2 + y^2]^{3/2}}$$

$$= -(\beta r_\rho)^2 \frac{(x - x')y}{(x - x')^2 + y^2} \left[H_0^{(2)''}(\beta r_\rho \sqrt{(x - x')^2 + y^2}) \right.$$

$$\left. - \frac{1}{\beta r_\rho \sqrt{(x - x')^2 + y^2}} H_0^{(2)'}(\beta r_\rho \sqrt{(x - x')^2 + y^2}) \right] \tag{3.52}$$

Use of the recursive formulas

$$H_n^{(2)'}(x) - \frac{n}{x} H_n^{(2)}(x) = -H_{n+1}^{(2)}(x)$$

yields

$$H_0^{(2)'} = -H_1^{(2)} \quad \text{and thus} \quad H_0^{(2)''} = -H_1^{(2)'}.$$

That is,

$$H_0^{(2)''} - \frac{1}{x} H_0^{(2)'} = -H_1^{(2)'} + \frac{1}{x} H_1^{(2)} = H_2^{(2)}. \tag{3.53}$$

Substituting (3.53) into (3.52), we get

$$\frac{\partial^2}{\partial x' \partial y} H_0^{(2)}(\beta r_\rho \sqrt{(x - x')^2 + y^2})$$

$$= -(\beta r_\rho)^2 \frac{(x - x')y}{(x - x')^2 + y^2} H_2^{(2)}(\beta r_\rho \sqrt{(x - x')^2 + y^2}). \qquad (3.54)$$

Substituting (3.54) into (3.44), we obtain

$$\overline{E}_q^{y,x'} = -\hat{y} \frac{\beta Z}{4D_z} \sum_{n=-\infty}^{\infty} e^{-j\beta(z-z')r_z} r_\rho^2$$

$$\cdot \int_{\text{Ref. ele.}} I_{x'}(x') \frac{(x - x')y}{(x - x')^2 + y^2} H_2^{(2)}(\beta r_\rho \sqrt{(x - x')^2 + y^2}) \, dx.' \quad (3.55)$$

Substituting (3.55) into (3.47), we find for the voltage induced in a y-oriented element with current distribution $I_y(y)$:

$$V_q^{y,x'} = -\frac{\beta Z}{4D_z} \sum_{n=-\infty}^{\infty} e^{-j\beta(z-z')r_z} r_\rho^2 \int_{\text{Ext. ele.}} \frac{I_y(y)}{I_y(0)} \, dy$$

$$\cdot \int_{\text{Ref. ele.}} I_{x'}(x') \frac{(x - x')y}{(x - x')^2 + y^2} H_2^{(2)}(\beta r_\rho \sqrt{(x - x')^2 + y^2}) \, dx'. \quad (3.56)$$

Finally, for the mutual array impedance we have

$$Z_q^{y,x'} = -\frac{V_q^{y,x'}}{I_{x'}(0)}$$

$$= \frac{\beta Z}{4D_z} \sum_{n=-\infty}^{\infty} e^{-j\beta(z-z')r_z} r_\rho^2 \int_{\text{Ext. ele.}} \frac{I_y(y)}{I_y(0)} \, dy$$

$$\cdot \int_{\text{Ref. ele.}} \frac{I_{x'}(x')}{I_{x'}(0)} \frac{(x - x')y}{(x - x')^2 + y^2} H_2^{(2)}(\beta r_\rho \sqrt{(x - x')^2 + y^2}) \, dx'. \quad (3.57)$$

For further discussion see Section 3.5.

3.4.3 The z Component of $\overline{E}_q$

The z component $E_q^{z,x'}$ of the total field E_q from a line array with current distribution $I(x')$ is readily obtained from (3.31) by integration of the z component over the reference element:

$$\overline{E}_q^{z,x'} = \hat{z} \frac{j\beta}{\omega\varepsilon 4D_z} \sum_{n=-\infty}^{\infty} e^{-j\beta(z-z')r_z} r_z$$

$$\int_{\text{Ref. ele.}} I_{x'}'(x') \frac{\partial}{\partial x'} H_0^{(2)}(\beta r_\rho \sqrt{(x - x')^2 + y^2}) \, dx'.$$

Noticing that $\dfrac{\partial}{\partial x} = -\dfrac{\partial}{\partial x'}$ and $\beta/\omega\varepsilon = Z$, we obtain

$$\overline{E}_q^{z,x'} = -\hat{z}\frac{jZ}{4D_z} \sum_{n=-\infty}^{\infty} e^{-j\beta(z-z')r_z} r_z$$

$$\times \int_{\text{Ref. ele.}} I_{x'}(x')\frac{\partial}{\partial x'} H_0^{(2)}(\beta r_\rho \sqrt{(x-x')^2 + y^2})\, dx'. \qquad (3.58)$$

Integrating by parts, we obtain

$$\overline{E}_q^{z,x'} = -\hat{z}\frac{jZ}{4D_z} \sum_{n=-\infty}^{\infty} e^{-j\beta(z-z')r_z} r_z \left[I_{x'}(x') H_0^{(2)}\left(\beta r_\rho \sqrt{(x-x')^2 + y^2}\right) \right]\Bigg|_{\text{Ref. ele. endpt.}}$$

$$- \int_{\text{Ref. ele.}} I'_{x'}(x') H_0^{(2)}\left(\beta r_\rho \sqrt{(x-x')^2 + y^2}\right)\Bigg]\, dx'. \qquad (3.59)$$

As noted earlier, $I'_x(x') = 0$ at the endpoints of the reference elements [i.e., the first term in (3.59) is equal to zero], and we then obtain

$$\overline{E}_q^{z,x'} = \hat{z}\frac{jZ}{4D_z} \sum_{n=-\infty}^{\infty} e^{-j\beta(z-z')r_z} r_z \int_{\text{Ref. ele.}} I'_{x'}(x') H_0^{(2)}(\beta r_\rho \sqrt{(x-x')^2 + y^2})\, dx'.$$

$$(3.60)$$

The voltage induced in a z-directed element with current $I_z(z)$ is now given by

$$V_q^{y,x'} = \frac{1}{I_z(0)} \int_{\text{Ext. ele.}} I_z(z)\, E_q^{z,x'}\, dz. \qquad (3.61)$$

Substituting (3.60) into (3.61), we get

$$V_q^{z,x'} = \frac{jZ}{4D_z} \sum_{n=-\infty}^{\infty} \frac{r_z}{I_z(0)} \int_{\text{Ext. ele.}} I_z(z)\, e^{-j\beta(z-z')r_z}\, dz$$

$$\cdot \int_{\text{Ref. ele.}} I'_{x'}(x') H_0^{(2)}(\beta r_\rho \sqrt{(x-x')^2 + y^2})\, dx'. \qquad (3.62)$$

The first integral in (3.62) is managed as usual by expressing z by a reference point $z^{(q)}$:

$$z = z^{(q)} + z'', \qquad -l_z < z < l_z. \qquad (3.63)$$

Substituting (3.62) into (3.63) and noting that z' is a constant during the z integration, we obtain for the mutual impedance:

$$Z_q^{z,x'} = -\frac{V^{z,x'}}{I_{x'}(0)}$$

$$= -\frac{jZ}{4D_z} \sum_{n=-\infty}^{\infty} e^{-j\beta(z^{(q)}-z')r_z} r_z P_z$$

$$\cdot \frac{1}{I_{x'}(0)} \int_{\text{Ref. ele.}} I'_{x'}(x') H_0^{(2)}(\beta r_\rho \sqrt{(x-x')^2 + y^2}) \, dx', \quad (3.64)$$

where the pattern function P_z is defined [similar to (3.24)] by

$$P_z = \frac{1}{I_{z''}(0)} \int_{\text{Ext. ele.}} I_z(z'') e^{-j\beta z'' r_z} \, dz''. \quad (3.65)$$

3.5 DISCUSSION

We recall from (3.4) that

$$r_\rho = \sqrt{1 - r_z^2} = \sqrt{1 - \left(s_z + n\frac{\lambda}{D_z}\right)^2}.$$

For the principal mode $n = 0$ and the incident field in real space (i.e., $|s_z| < 1$) we observe that r_ρ is always real. However, as $n \to \infty$ we also observe that r_ρ becomes imaginary, namely,

$$r_\rho = \begin{array}{c} (+) \\ - \end{array} j \sqrt{\left(s_z + n\frac{\lambda}{D_z}\right)^2 - 1} \quad (3.66)$$

[The choice of sign in (3.66) will soon become clear.]

For r_ρ imaginary the arguments in the Hankel functions become imaginary; that is, they are modified Hankel functions. Examples of the second kind of order 0 and 1, respectively, are shown in Fig. 3.7 for negative imaginary arguments. We observe a fast fall-off as the magnitude of the negative argument increases. In fact, the asymptotic value is given by

$$H_v^{(2)}(x) \xrightarrow[x \to \infty]{} \sqrt{\frac{2j}{\pi x}} j^v e^{-jx}, \quad (3.67)$$

that is, it drops off somewhat faster than an exponential term when x is negative imaginary.

Thus, the infinite series (3.27) will in spite of the term $r_\rho^2 \sim (s_z + n\lambda/D_z)^2$ for n large converge very fast. In fact, in Problem 3.3 you are asked to compare the convergence of the impedance of an infinitely long column array given by (3.27)
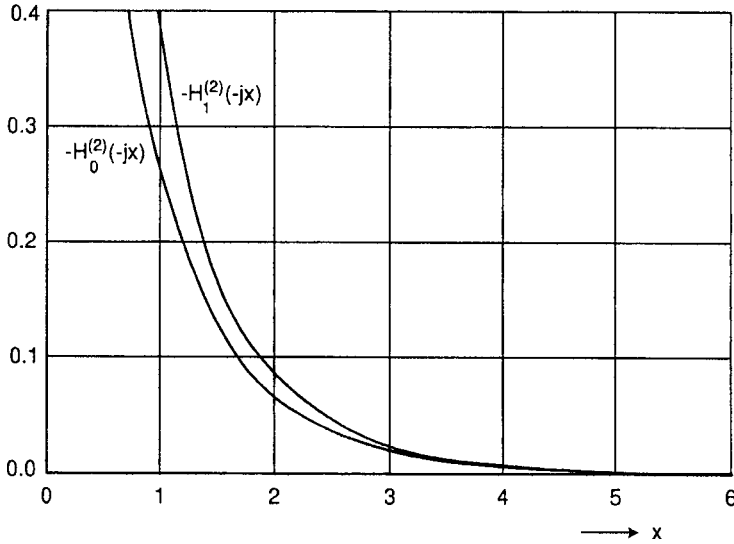
Fig. 3.7   *The Hankel function of the second kind and orders 0 and 1, respectively, for negative imaginary argument. For asymptotic approximation, see (3.67).*

with the impedance of an infinite × infinite array given by (3.28). The latter is of course known to converge very fast as observed in the PMM code.

Let us summarize our investigation so far.

In the *longitudinal* case we found that both the z and ρ components of the field could be expressed by a single fast convergent series of Hankel functions [see (3.16)]. Furthermore, the mutual impedance between the collinear array and external element parallel with the array elements (i.e., z-directed in our case) could also be expressed by a simple fast convergent series [see (3.27)]. However, if the external element was ρ-directed, simple integration was not possible.

In the *transverse* case we found that the field parallel with the array elements (i.e., x-directed in our case) could be expressed by a simple fast convergent infinite series containing three Hankel functions [see (3.39)]. However, to find the mutual impedance as given by (3.43), numerical integration will be necessary.

Furthermore, the field components orthogonal to the x-directed elements, namely the y- and z-directed components as expressed for example by (3.55) and (3.60), respectively, has so far not been possible to integrate into a simpler form.

It was primarily for that reason that Usoff decided to work in the spatial domain when he wrote the SPLAT program. He further used a shanks transform to obtain faster convergence [24]. It became a most wonderful and versatile program. In fact, it is the workhorse for our research into finite arrays.

However, it was always the author's dream to work in the spectral domain similar to the PMM program that is very fast converging and gives us the real part of the impedance as one term if no grating lobes are present. Thus, if anyone ever pulls it off, the author would appreciate to hear about it.

3.6   DETERMINATION OF THE ELEMENT CURRENTS

When all the mutual and the self-impedances of an assembly of stick arrays as shown in Fig. 3.8 has been determined, it is a relatively simple matter to find the currents on the elements. In fact, it was already discussed in my earlier book [62] and need therefore only to be restated here for easy reference.

Let the stick arrays in Fig. 3.8 be exposed to an incident plane wave with direction of propagation equal to $\hat{s}$. The voltages induced in the reference element of the three or more stick arrays are denoted $V^{(1)}$, $V^{(2)}$, and $V^{(3)}$, respectively. They are easily determined by application of (3.18). Similarly, the currents on each reference element are denoted by $I^{(1)}$, $I^{(2)}$, and $I^{(3)}$, respectively.

Then from the generalized Ohm's Law we obtain the following matrix equation:

$$
\begin{bmatrix} V^{(1)} \\ V^{(2)} \\ V^{(3)} \end{bmatrix} = \begin{bmatrix} [Z^{1,1} + Z_{L1}] & Z^{1,2} & Z^{1,3} \\ Z^{2,1} & [Z^{2,2} + Z_{L2}] & Z^{2,3} \\ Z^{3,1} & Z^{3,2} & [Z^{3,3} + Z_{L3}] \end{bmatrix} \begin{bmatrix} I^{(1)} \\ I^{(2)} \\ I^{(3)} \end{bmatrix}. \quad (3.68)
$$
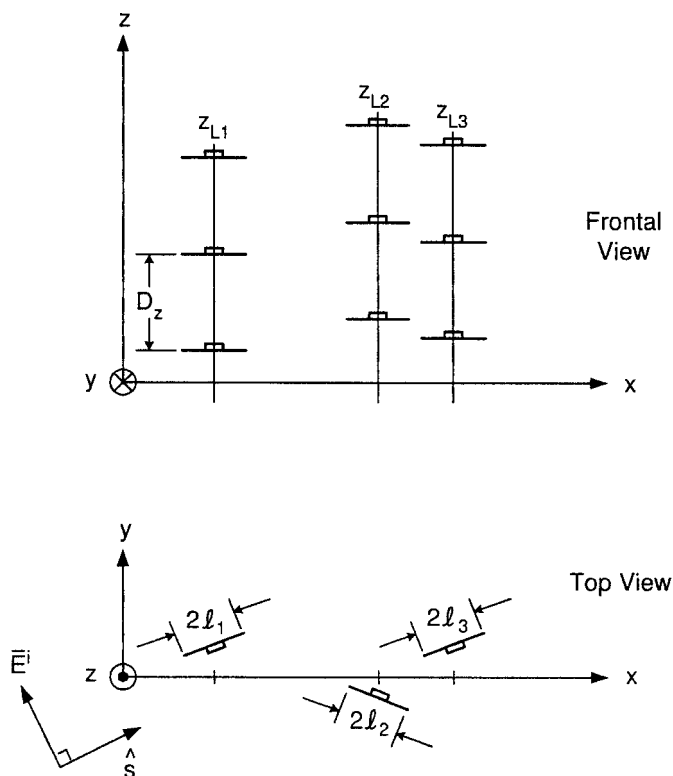
Fig. 3.8   An arbitrary but finite number of infinitely long stick arrays with the same interelement spacing D_z is exposed to an incident plane wave $\overline{E}_i$. Element orientation and length may vary from stick array to stick array.

Here $Z^{k,m}$ denotes the mutual array impedances between the reference element in array k and all the elements in array m while Z_{L1}, Z_{L2}, and Z_{L3} denote the load impedances in the respective array elements.

Note that the element orientation can vary from stick to stick while the interstick spacing can be arbitrary. Only the element spacing D_z in the z direction must be the same from stick to stick. Otherwise, Floquet's Theorem will be violated.

3.7 THE DOUBLE INFINITE ARRAYS WITH ARBITRARY ELEMENT ORIENTATION

In my first book we found the vector potential as well as the magnetic and electric fields for double infinite arrays of arbitrarily oriented Hertzian elements of length *dl* [63]. However, our investigation of elements of arbitrary length was basically limited to elements contained in the plane of the array (but of arbitrary shape and orientation in that plane).

It was also pointed out that several of the author's former students and others have tackled that problem [66–71]. The reason for not considering it further in my first book was that it leads to a very messy nested integration that could lead to certain convergence problems. The following derivation by Peter Munk avoids this problem, and we therefore find it appropriate to present it here.[2]

3.7.1 How to Get Well-Behaved Expressions

Consider an infinite array of elements oriented in the $\hat{p}^{(1)}$ direction located in slab m of a stratified dielectric medium as shown in Fig. 3.9. As throughout [61], the elements are assumed to be excited by an external plane wave. The plane wave spectrum generated by this array can be decomposed into five wave modes as described in references 66–71. Four of these modes involve the reflection coefficient from the dielectric interfaces bounding the m_{th} slab, while the fifth mode does not and is referred to as the "direct mode." It is this mode that requires special treatment and is the reason it is revisited in detail here. The direct mode field at some point $\overline{R}$ on a test element also located entirely in slab m and oriented in the $\hat{p}$ direction may be written [66, 68]

$$\overline{E}(\overline{R}) = \frac{Z_m}{2D_x D_z} \sum_{k=-\infty}^{+\infty} \sum_{n=-\infty}^{+\infty} \left\{ \frac{e^{-j\beta_m(\overline{R}-\overline{R}^{(1)})\cdot \hat{r}_{m+}}}{r_{my}} \right.$$

---

[2] While a graduate student at OSU, Peter took all the courses offered by the author. He was never a student of his since that would have been inappropriate. However, unofficially a good deal of consultation took place. Someone once stated that a good teacher at some point starts learning from his students. While the author never made any claims of being a particularly good teacher, he can at least testify to the fact that he learned a lot from all his students.
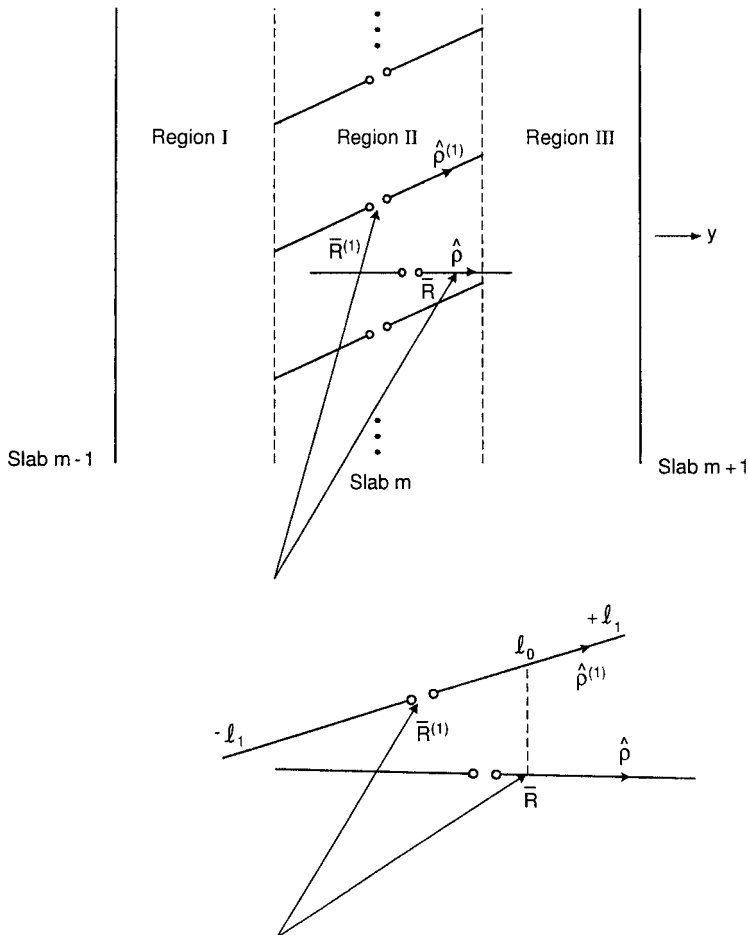
Fig. 3.9   Top: An array of arbitrarily oriented dipoles located in the dielectric slab m sandwiched between slab m − 1 and m + 1. Regions I, II, and III are defined by the tips of the dipoles as shown in the figure. Bottom: Detail of the element geometry.

$$\cdot \overline{e}_+ U(l_1 + l_o) \int_{-l_1}^{l_o} I_o^{(1)}(l) \, e^{j\beta_m l \hat{p}^{(1)} \cdot \hat{r}_{m+}} \, dl$$

$$+ \frac{e^{-j\beta_m (\overline{R} - \overline{R}^{(1)}) \cdot \hat{r}_{m-}}}{r_{my}} \cdot \overline{e}_- U(l_1 - l_o) \cdot \int_{l_o}^{l_1} I_o^{(1)}(l) \, e^{j\beta_m l \hat{p}^{(1)} \cdot \hat{r}_{m-}} dl \bigg\} , \quad (3.69)$$

where the Heavyside unit step functions $U(l_1 - l_o)$ and $U(l_1 + l_o)$ illustrate that if $\overline{R}$ is located in either region I or III, only the $\hat{r}_{m-}$ or $\hat{r}_{m+}$ waves are observed, respectively. In addition, l_o is defined as the y projection of the field point $\overline{R}$

onto the reference element and may be expressed as [66,68]

$$l_o = \frac{1}{p_y^{(1)}}(R_y - R_y^{(1)}),$$
(3.70)

where

$$\overline{R} \equiv R_x \hat{x} + R_y \hat{y} + R_z \hat{z},$$
(3.71)

and the point $\overline{R}'$ along the reference element is given by

$$\overline{R}' = \overline{R}^{(1)} + l\hat{p}^{(1)},$$
(3.72)

for $-l_1 \leq l \leq +l_1$, where

$$\overline{R}^{(1)} \equiv R_x^{(1)}\hat{x} + R_y^{(1)}\hat{y} + R_z^{(1)}\hat{z}.$$
(3.73)

Examining the first integral in (3.69) and employing integration by parts, one may write

$$\int_{-l_1}^{l_o} I_o^{(1)}(l)\, e^{j\beta_m l \hat{p}^{(1)} \cdot \hat{r}_{m+}} dl = \frac{I_o^{(1)}}{j\omega_+} e^{j\omega_+ l}\bigg|_{-l_1}^{l_o} - \frac{1}{j\omega_+}\int_{-l_1}^{l_o} \frac{\partial I_o^{(1)}(l)}{\partial l} e^{j\omega_+ l}\, dl, \quad (3.74)$$

where $\omega_\pm = \beta_m \hat{p}^{(1)} \cdot \hat{r}_{m\pm}$. The second integral may be treated similarly, yielding the expression

$$\int_{l_o}^{l_1} I_o^{(1)}(l) e^{j\beta_m l \hat{p}^{(1)} \cdot \hat{r}_{m-}} dl = \frac{I_o^{(1)}}{j\omega_-} e^{j\omega_- l}\bigg|_{l_o}^{l_1} - \frac{1}{j\omega_-}\int_{l_o}^{l_1} \frac{\partial I_o^{(1)}(l)}{\partial l} e^{j\omega_- l}\, dl. \quad (3.75)$$

Both integrals in (3.74) and (3.75) are well-behaved and will converge rapidly inside the double infinite summation, as will the terms evaluated at $+l_1$ and $-l_1$. However, these same two terms evaluated at l_o will exhibit convergence problems and must therefore be treated separately. It is beneficial at this point to decompose these two terms into their respective x, y, and z components. Making use of the fact that $\overline{e}_\pm$ may be written [64]

$$\overline{e}_\pm = \hat{x}\left(\frac{\omega_\pm r_{mx}}{\beta_m} - p_x^{(1)}\right) + \hat{y}\left(\frac{\pm\omega_\pm r_{my}}{\beta_m} - p_y^{(1)}\right) + \hat{z}\left(\frac{\omega_\pm r_{mz}}{\beta_m} - p_z^{(1)}\right), \quad (3.76)$$

the $\hat{x}$ components of the two terms may be combined, resulting in

$$\frac{I_o^{(1)}(l_o)\Lambda_o p_x^{(1)}}{j\omega_- r_{my}} - \frac{I_o^{(1)}(l_o)\Lambda_o p_x^{(1)}}{j\omega_+ r_{my}},$$
(3.77)

where

$$\Lambda_o \equiv e^{-j\beta_m[(R_x - R_x^{(1)} - p_x^{(1)}l_o)r_{mx} + (R_z - R_z^{(1)} - p_z^{(1)}l_o)r_{mz}]}.$$
(3.78)

Likewise, combining the $\hat{z}$ components yields

$$\frac{I_o^{(1)}(l_o)\Lambda_o p_z^{(1)}}{j\omega_- r_{my}} - \frac{I_o^{(1)}(l_o)\Lambda_o p_z^{(1)}}{j\omega_+ r_{my}}. \tag{3.79}$$

Examining (3.77) and (3.79) reveals that both expressions converge nicely in the double infinite summation over k and n. Combining the $\hat{y}$ components, on the other hand, results in an expression that differs in form from the combined $\hat{x}$ and $\hat{z}$ components and may be expressed instead as

$$-j\Lambda_o I_o^{(1)}(l_o) \cdot \left\{ \frac{2}{\beta_m} + \frac{p_y^{(1)}}{\omega_-} - \frac{p_y^{(1)}}{\omega_+} \right\}. \tag{3.80}$$

The second and third terms in (3.80) are identical in form to those found in (3.77) and (3.79), and likewise they converge rapidly in the double infinite summation. The convergent nature of the first term, however, is not immediately apparent. Employing the same mathematical identity used in references 66 and 68, the double infinite summation of the first term in (3.80) involving Λ_o may be written

$$\frac{-j2I_o^{(1)}(l_o)}{\beta_m} \cdot \sum_{k=-\infty}^{+\infty} \sum_{n=-\infty}^{+\infty} \Lambda_o$$

$$= \frac{-j2I_o^{(1)}(l_o)}{\beta_m} \cdot e^{-j\beta_m[s_{mx}(R_x - R_x^{(1)} - p_x^{(1)}l_o) + s_{mz}(R_z - R_z^{(1)} - p_z^{(1)}l_o)]}$$

$$\cdot D_x D_z \cdot \sum_{k=-\infty}^{+\infty} \sum_{n=-\infty}^{+\infty} \delta[(R_x - R_x^{(1)} - p_x^{(1)}l_o) - kD_x]$$

$$\cdot \delta[(R_z - R_z^{(1)} - p_z^{(1)}l_o) - nD_z]. \tag{3.81}$$

The dirac delta functions in (3.81) are identically zero unless

$$R_x - R_x^{(1)} - p_x^{(1)} \cdot l_o = kD_x, \tag{3.82}$$

for $k = 0, \pm1, \pm2, \ldots$, and

$$R_z - R_z^{(1)} - p_z^{(1)} \cdot l_o = nD_z, \tag{3.83}$$

for $n = 0, \pm1, \pm2, \ldots$.

Considering only the cases where the Heavyside unit step functions in (3.69) differ from zero (i.e., the nontrivial case where $\bar{r}$ overlaps in the $\hat{y}$ direction with the reference element), it is observed that (3.82) and (3.83) can never be true unless the test element is in contact with one (or more) of the reference array elements. Since this is not the case, the first term in (3.80) may be dropped.

Recombining the individual *x, y,* and *z* components then yields this new, "well-behaved" *E*-field equation

$$
\overline{E}(\overline{R}) = \frac{jZ_m}{2D_x D_z} \sum_{k=-\infty}^{+\infty} \sum_{n=-\infty}^{+\infty} \left\{ \frac{e^{-j\beta_m(\overline{R}-\overline{R}^{(1)})\cdot \hat{r}_{m+}}}{r_{my}\omega_+} \left[I_o^{(1)}(-l_1)e^{-j\omega_+ l_1} \right. \right.
$$

$$
\left. + \int_{-l_1}^{l_o} \frac{\partial I_o^{(1)}(l)}{\partial l} e^{j\omega_+ l} dl \right] \overline{e}_+ + \frac{I_o^{(1)}(l_o)\Lambda_o}{r_{my}\omega_+} \hat{p}^{(1)}
$$

$$
- \frac{e^{-j\beta_m(\overline{R}-\overline{R}^{(1)})\cdot \hat{r}_{m-}}}{r_{my}\omega_-} \left[I_o^{(1)}(l_1)e^{j\omega_- l_1} - \int_{l_o}^{l_1} \frac{\partial I_o^{(1)}(l)}{\partial l} e^{j\omega_- l} dl \right] \overline{e}_-
$$

$$
\left. - \frac{I_o^{(1)}(l_o)\Lambda_o}{r_{my}\omega_-} \hat{p}^{(1)} \right\}. \tag{3.84}
$$

Thus, the *E* field written in the form of (3.84) does not have the convergence problems observed earlier and should consequently be used in the architecture for a future PMM program with arbitrarily oriented nonplanar elements.

3.8 CONCLUSIONS

In this chapter we have obtained the *E* field from stick arrays composed of longitudinal or transverse elements of arbitrary length 2*l*.

In the *longitudinal* case we found that the field could always be expressed by a single infinite series of Hankel functions multiplied with a simple pattern functions [see (3.17)]. Similarly, the mutual impedance between the array and an external element parallel to the longitudinal elements could be obtained by further multiplication of a pattern function associated with the external element [see (3.27)]. If the external element was orthogonal to the longitudinal elements, the mutual impedance could be obtained by numerical integration of the orthogonal fields along the external elements.

In the *transverse* case we found that the electric fields parallel to the elements could be expressed by a single infinite series as the sum of just three Hankel functions emanating from the endpoints and the center of the elements, respectively. The mutual impedance to an external element could then be obtained by numerical integration of these three Hankel functions.

For the mutual impedance between an array of transverse elements and an external orthogonal element we found that a numerical double integration was necessary.

The computational advantage of using the Hankel functions is that they contain the argument $\beta r_\rho \rho$. Thus, as we enter the imaginary space, r_ρ would become imaginary (see Section 3.4), leading to modified Hankel functions that fall off exponentially as ρ or n increase (see Fig. 3.7). Thus, we could obtain the mutual impedances between arrays with elements of arbitrary orientation. Once these

were determined, it was a relatively simple matter to obtain the element currents (see Section 3.6).

Most of these expressions were not available to Usoff when he was given the task to write a program for finite arrays. He therefore chose to stay mostly in the spatial domain except for the longitudinal case. The result was a program that was extremely versatile and became the workhorse for our finite array research. It was later given a "face lift" by Dan Janning and other students that reduced the run time and made it more user friendly.

It is doubtful whether any of the author's students will ever attempt to write a program in the spectral domain for finite arrays like originally envisioned (I am running out of time, students, and money!). But if anyone out there does, please let me hear about it.

PROBLEMS

3.1 Consider a stick array with longitudinal elements as shown in Fig. 3.2 with element lengths $2l = 1.5$ cm and $D_z = 1.6$ cm. The incident field is arriving at broadside with $\hat{s} = \hat{y}$ and $\overline{E}^i = \hat{z}E^i$. Furthermore, the wire radius a is 0.1 cm. Assume sinusoidal current distribution.

   1. At $f = 10$ GHz evaluate the terms $n = 0, \pm1, \pm2,$ and ±3 in (3.26).
   2. How many of these terms contain a real part?
   3. At what value of D_z do we encounter the first grating lobe?
   4. If D_z is so small that no grating lobes are encountered, how does the radiation resistance R_A vary with D_z (constant frequency).
   5. Does the radiation resistance R_A vary significantly with the wire radius "a," if at all?
   6. Does the $n = 0$ term depend on the wire radius "a"?

3.2 An infinite $\times$ infinite array has the elements oriented along $\hat{p} = \hat{z}$ with interelement spacings $D_x = 0.8$ cm and $D_z = 1.6$ cm. The total length of the elements are $2l = 1.5$ cm and the wire radius $a = 0.1$ cm. An electromagnetic wave is incident upon this array at broadside; that is, $\hat{s} = \hat{y}$, while $\overline{E}^i = \hat{z}E^i$. Assume sinusoidal current distribution.

   1. For $f = 10$ GHz, evaluate the terms in (3.28) for $n = 0, \pm1, \pm2, \pm3$ and $k = 0$.
   2. How many of these terms are real?
   3. If we assume that D_x and D_z are so small that no grating lobes exist, how does the radiation resistance R_A vary with these interelement spacings?
   4. Does R_A depend strongly on the wire radius "a," if at all?

3.3 Compare the convergence properties for the stick array in Problem 3.1 with that of the infinite $\times$ infinite array in Problem 3.2.

3.4 A stick array with transverse elements as shown in Fig. 3.4 has the interelement spacing $D_z = 0.8\,\text{cm}$ and the reference element located at the origin. The total length of the elements are $2l = 1.5\,\text{cm}$, and the wire radius a is $0.1\,\text{cm}$. An EM field is incident at broadside with $\hat{s} = \hat{y}$ and $\overline{E}^i = \hat{x}E^i$.

Evaluate the terms $n = 0, \pm 1, \pm 2$ and ± 3 in (3.39) when the point of observation is located at

1. $\overline{R} = (0, 1, 0)\,\text{cm}$
2. $\overline{R} = (\pm 1.5, 1, 0)\,\text{cm}$

3.5 The E field for an infinite $\times$ infinite array with $\hat{p} = \hat{x}$ is given in reference 63 by

$$\overline{E}(\overline{R}) = I(\overline{R}^{(1)})\frac{Z}{2D_x D_z} \sum_{k=-\infty}^{\infty} \sum_{n=-\infty}^{\infty} \frac{e^{-j\beta(\overline{R}-\overline{R}^{(1)})}}{r_y}\overline{e}_{\pm}P,$$

where
$$\overline{e}_{\pm} = (\hat{p} \times \hat{r}_{\pm}) \times \hat{r}_{\pm},$$

$$P = \frac{1}{I(\overline{R}^{(1)})} \int_{\text{Ref. Ele.}} I(l)\,e^{j\beta l\hat{p}\cdot\hat{r}_{\pm}}\,dl,$$

$$r_y = \sqrt{1 - \left(s_x + k\frac{\lambda}{D_x}\right)^2 - \left(s_z + n\frac{\lambda}{D_z}\right)^2}.$$

An E field is incident at broadside with $\overline{E}^i = \hat{x}E^i$, $D_x = 1.6\,\text{cm}$, and $D_z = 0.8\,\text{cm}$. The total element length $2l$ is $1.5\,\text{cm}$, and the wire radius a is $0.1\,\text{cm}$.

Compare the convergence properties of the E field for the stick array in Problem 3.4 with that of the infinite $\times$ infinite array in this problem.

4

Surface Waves on Passive Surfaces of Finite Extent

4.1 INTRODUCTION

Different kinds of surface waves can propagate along periodic structures. Most familiar is the type attached to a periodic structure situated in a stratified medium. It was shown in reference 72 that as the frequency increases, grating waves will eventually start to propagate along the structure inside the dielectric. If these plane waves are incident upon the dielectric interfaces at angles of incidence larger than the critical angle(s), they will be totally reflected and thus remain inside the stratified medium. The combination of these crisscrossing plane waves looks similar to the well-known surface waves encountered in dielectric slabs; that is, they look like standing waves inside the slab and are evanescent outside. However, these surface waves must in general be sustained by voltages impressed at the terminals of the elements. Furthermore, since no energy escapes from the structure into free space, no energy is delivered to the terminals; that is, the particular impedance term associated with the surface wave will be purely imaginary. Such surface waves are called *forced surface waves*. If the particular impedance term happened to be zero, no impressed terminal voltages are needed to sustain propagation of the surface wave. In that case we have a *free surface wave*. This is the type usually encountered in the classical textbooks [73]. Whether forced or free, this type of surface wave will readily be observed with computer programs based on infinite array theory like, for example, the PMM program. It will be referred to here as Type I.

In contrast, the new type of surface wave introduced in Chapter 1 (Type II) can be encountered whether a dielectric substrate is present or not, but the structure

must be finite at least in one dimension as illustrated in Fig. 4.1. While the first kind typically shows up only at higher frequencies (in order for grating lobes to exist), the second occurs only at the lower frequencies such as 20–30% below resonance and only if the interelement spacing D_x is $<0.5\lambda$; that is, there must not even be a hint of grating lobes.

The presence of surface waves on finite periodic structures is of concern primarily for two reasons:

1. If used as an FSS to reduce the backscattering, the reradiation from the surface waves can lead to an increase in the total RCS.
2. If used as a phased array, surface waves can lead to a significant variation in scan impedance from element to element, making precise matching difficult (see Figs. 1.3 and 1.5).

In this chapter we shall study the FSS case in more detail and in particular how to control the surface waves. The phased array case will be discussed in Chapter 5.

4.2   MODEL

The finite array will be modeled by a finite number of infinitely long column arrays (also called stick arrays; see Fig. 4.1). This approach has been widely used by several researchers [74–80]. One of them, Usoff, wrote as part of his dissertation [24] the computer program "Scattering from a Periodic Array of Thin Wire Elements" (SPLAT). The excitation can be either in the form of an incident plane wave propagating in the direction $\hat{s} = \hat{x}s_x + \hat{y}s_y + \hat{z}s_z$ (passive case). Or it can be in the form of generators connected to the elements individually (active case). The program can then calculate the bistatic scattered field as well as the scan impedance of each column, to mention just a few features.

Basically the approach is a combination of the plane wave expansion (spectral) and the mutual impedance approach as explained in Chapter 3 and also reference 62.

4.3   THE INFINITE ARRAY CASE

When analyzing the finite array, it is advisable first to review the infinite array case; that is, the finite number of columns shown in Fig. 4.1 becomes infinite as shown earlier in Fig. 1.1. As discussed for example in reference 62 or Chapter 3, infinite arrays are significantly simpler to analyze than finite arrays. In particular, if exposed to an incident plane wave with direction of propagation equal to $\hat{s}$, the element currents are all related to each other by Floquet's Theorem:

$$I_{qm} = I_{00}e^{-j\beta q D_x s_x}e^{-j\beta m D_z s_z}, \tag{4.1}$$

where q equals the column number and m equals the row number (see Fig. 1.1).
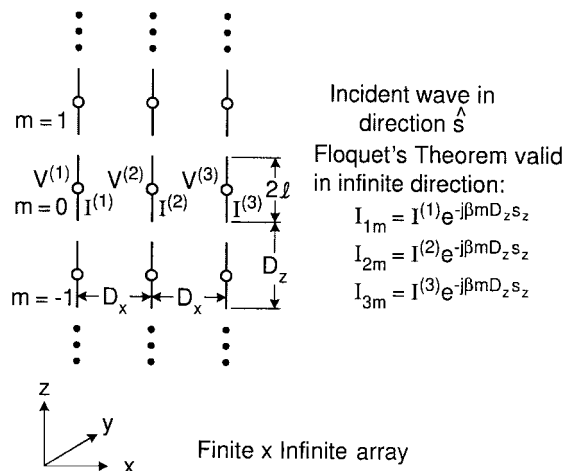
Fig. 4.1 *The array considered here consists of a finite number of infinitely long columns (stick arrays) with axial elements. Voltages are induced in all elements by an incident plane wave propagating in the direction $\hat{s} = \hat{x}s_x + \hat{y}s_y + \hat{z}s_z$. We seek the bistatic scattered pattern.*

However, when the array has only a finite number of columns as shown in Fig. 4.1, the column currents $I^{(q)}$ differ from column to column in amplitude as well as phase. Only along the infinite Z dimension does Floquet's Theorem apply as indicated in Fig. 4.1.

A typical idealized example of the scan impedance for an infinite array with interelement spacing $D_x/\lambda \sim 0.24$ at $f = 8\,\text{GHz}$ is shown in Fig. 4.2. The total length of the elements is $2l = 1.5\,\text{cm}$; that is, the array will resonate around $10\,\text{GHz}$. Thus, we observe that the scan impedance Z_A at $f = 8\,\text{GHz}$ will be located in the capacitive part of the complex plane as also seen in Fig. 4.2.

Furthermore, from (4.1) we observe that the phases of the element currents are determined by the direction cosines s_x and s_z. For example, if $s_x = s_z = 0$, all element currents are in phase and the main beam will point in the broadside direction. Similarly, if $s_z = 0$, the beam will scan only in the XY plane or the H plane. And if furthermore $s_x = 0.5$ or $\sqrt{3}/2$, the beam will be scanned to $30°$ or $60°$ from boresight, respectively. These typical cases are illustrated in Fig. 4.2 by small inserts adjacent to the various scan impedances $Z_A = R_A + jX_A$. Note in particular that while X_A remains fairly constant with scan angle,[1] R_A increases significantly. In fact, at grazing for $s_x = 1$ or $\eta = 90°$, R_A becomes singular (*Note*: There is no groundplane).

Had we excited the elements passively by an incident plane wave, the entire scan range would be limited to be between $s_x = 0(0°)$ and $s_x = \pm1(\pm90°)$. However, if we instead excite the array actively by driving the elements by individual voltage generators, the scan range can be extended into the imaginary (or invisible) space.

[1] True only for small D_x/λ.
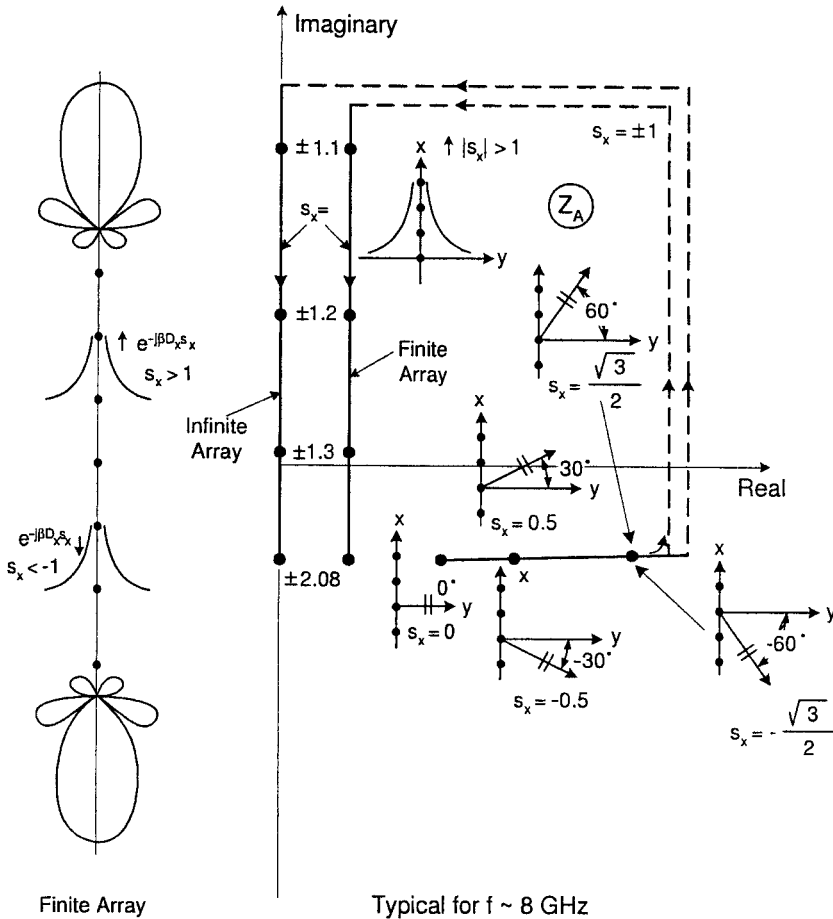
Fig. 4.2 Typical scan impedance for an infinite and a finite array at the fixed frequency 8 GHz (i.e., below resonance) as a function of scan angle. Note: By feeding the elements with actual voltage generators like a phased array, we can scan the "beam" beyond endfire into the imaginary space where $|s_x| > 1$ and only evanescent waves are possible, provided that the interelement spacing D_x is $< 0.5\, \lambda$.

For example, if the interelement spacing $\beta D_x = \pi/2$, then endfire condition is obtained when the phase increment between adjacent elements is equal to 90°. But since the individual generator voltages are controlled entirely by the "operator," he can choose the phase increment to exceed 90° corresponding to $s_x > 1$.

We now recall [61]

$$r_y^2 = 1 - \left(s_x + k\frac{\lambda}{D_x} \right)^2 - \left(s_z + n\frac{\lambda}{D_z} \right)^2. \tag{4.2}$$

We have propagating waves when $0 < r_y^2 < 1$ and evanescent when $r_y^2 < 0$. Thus, the transition between propagating and evanescent waves is determined by $r_y^2 = 0$; that is, from (4.2) we have

$$\left(s_x + k\frac{\lambda}{D_x}\right)^2 + \left(s_z + n\frac{\lambda}{D_z}\right)^2 = 1. \tag{4.3}$$

In the s_x, s_z plane (4.3) depicts unit circles with centers at $k\lambda/D_x, n\lambda/D_z$ as shown in Fig. 4.3.

Every time we are inside one of the unit circles, we are in visible space where we observe propagating modes. When outside, we are in invisible space where the modes are evanescent. For more about the grating lobe diagram, see reference 61.

If $D_x/\lambda = 0.5$ or smaller, we readily see that the unit circles will never touch each other; that is, we will never have a grating lobe, but will have only one propagating wave when particular values of s_x, s_z puts us inside one of the unit circles.
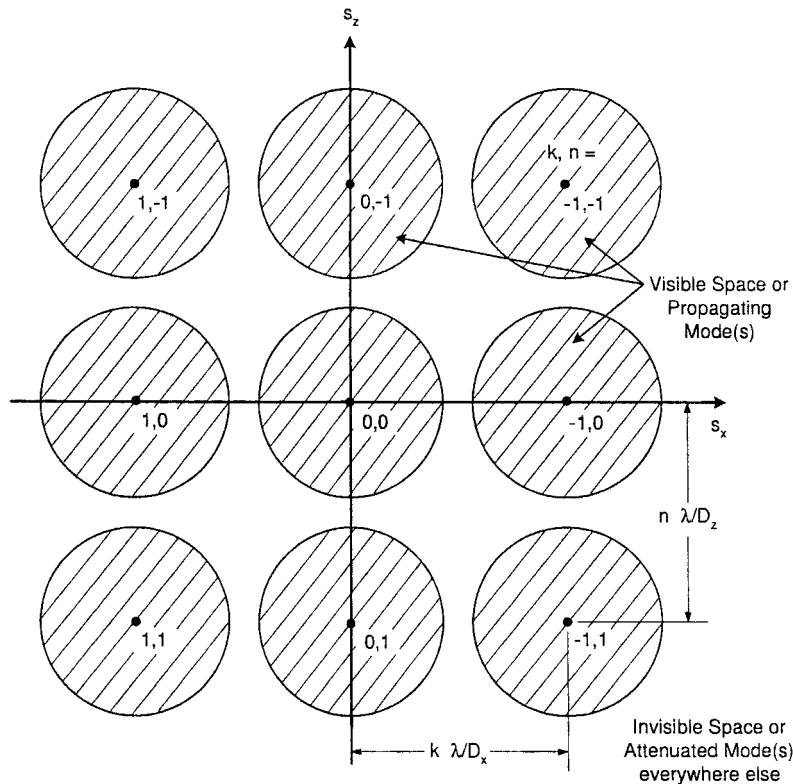
Fig. 4.3   *Grating lobe diagram plotted in the* (s_x, s_z) *plane. If* (s_x, s_z) *falls inside any of the unit circles, we have propagating mode(s). Otherwise, we have evanescent modes.*

The typical example in Fig. 4.2 has $D_x/\lambda = 0.24$ (or $\lambda/D_x = 4.15$). Thus, when s_x increases from $s_x = 1$, the scan impedance Z_A will be located on the imaginary axis and reach the most negative imaginary value for $s_x = \frac{1}{2}\lambda/D_x = 2.08$. Further increase of s_x to $s_x = \lambda/D_x - 1 = 4.15 - 1$ (equivalent to $s_x = -1$; see Fig. 4.3) leads Z_A back up along the imaginary axis the same way it came down as illustrated in Fig. 4.2.

Note in particular that $Z_A = 0$ for $s_x = \pm 1.32$. This case is particularly interesting because this constitutes the condition for a free surface wave as discussed earlier. In other words, a surface wave will propagate even when the impressed voltage is zero. Also note that it is the sum of the individual evanescent waves that constitutes a surface wave that is unique and satisfies the boundary condition at the elements of the array, not the individual modes.

4.4 THE FINITE ARRAY CASE EXCITED BY GENERATORS

We now turn our attention to the finite array shown in Fig. 4.1. We shall at first obtain an *approximation* of this case simply by truncation of the infinite array considered above. We will assume that waves similar to the surface waves on the infinite array can exist on the finite array. However, a significant difference between the two cases is that while no energy is radiated when the array is infinite, radiation will take place in the finite case similar to a finite array with a progressive current radiating in the endfire mode. Typically a free surface wave is encountered at this frequency in the neighborhood of $s_x = \pm 1.32$, where the positive sign produces a pattern radiating upward and the negative sign produces an identical pattern radiating downward (see Fig. 4.2, left). This radiated energy in the finite case must be accounted for by supplying energy to the individual elements using voltage generators. This in turn implies that the scan impedance for $|s_x| > 1$ no longer can be purely imaginary but must contain a real component as indicated in Fig. 4.2 and labeled as "Finite Array."

To summarize: No energy is radiated from the infinite array, only from the finite. Thus, a test antenna located a reasonably large distance from the array will pick up a signal only from the finite array, not the infinite. Furthermore, from the law of reciprocity we may conclude that a signal from the test antenna cannot produce a surface wave on the infinite array but can readily do so on the finite array.

Because of the lossy component of the scan impedance, the waves on the finite array can be considered as being surface waves for a slightly lossy periodic structure.

4.5 THE ELEMENT CURRENTS ON A FINITE ARRAY EXCITED
BY AN INCIDENT WAVE

We now return to our original problem, namely, where a finite array is exposed to an incident field rather than fed by voltage generators at each terminal.

When a plane wave with direction of propagation $\hat{s} = \hat{x}s_x + \hat{y}s_y + \hat{z}s_z$ is incident upon a periodic structure, we would expect to see strong currents of the Floquet type, namely the type given by (4.1). Thus, they all have the same amplitude and a relative phase which matches that of the incident plane wave.

When the array is infinite, these Floquet currents are the *only* ones present. This is a direct consequence of Floquet's Theorem, which basically states that for a periodic structure, the phases of the element currents must match those of the incident field. However, when the structure becomes finite, it is no longer periodic and Floquet's Theorem simply does not apply.

For a *finite* × *infinite* array as shown in Fig. 4.1, we will now show that the current will be:

1. The Floquet type as found on an infinite periodic structure—that is, of the form given by (4.1).
2. Traveling waves with $|s_x| > 1$ propagating in each direction along the array. Each of these will produce an end-fire radiation pattern. They are very similar to surface waves on an infinite periodic structure except that these waves have a loss component due to radiation (see Fig. 4.2).
3. Finally, there will be an end effect associated with the reflection of the three traveling waves at the edges of the array.

While it is easy to accept that the currents on a finite array will be of the Floquet type like they are on an infinite structure, it is more difficult to accept that the two traveling waves exist ONLY on the finite and not on the infinite array. The following discussion will hopefully clarify this problem.

4.6 HOW THE SURFACE WAVES ARE EXCITED ON A FINITE ARRAY

Consider an infinite array exposed to an incident plane wave $\overline{E}^i$ with the direction of propagation being $\hat{s}$, as shown in Fig. 4.4, top. From the basic theory for periodic structures we know that the reradiated (scattered) field consists of plane waves propagating in the directions $\hat{s} = \hat{x}s_x \pm \hat{y}s_y + \hat{z}s_z$ and, eventually, a finite number of grating lobes, as also illustrated in Fig. 4.4, top. Furthermore, there will be an infinite number of evanescent waves that die out quickly as we move away from the array.

Let us next consider a finite array as illustrated in Fig. 4.4, middle. When exposed to the same incident plane wave with the direction of propagation $\hat{s}$, the element currents will again, to a first-order *approximation*, be the Floquet currents as given by (4.1).

It is a simple matter to find the *far* field from these currents as a function of the continuous radiation direction $\hat{r}_c$. We show a typical example in Fig. 4.4, bottom. However, rather than plotting it as a function of radiation angle, it is plotted as a function of r_{cx}; see Fig. 4.4 middle. This makes it more compatible with our choice of variable s_x for the incident wave and the plane wave expansion in general. We obtain mainbeams at $r_{cx} = s_x$ and we also note that the visible
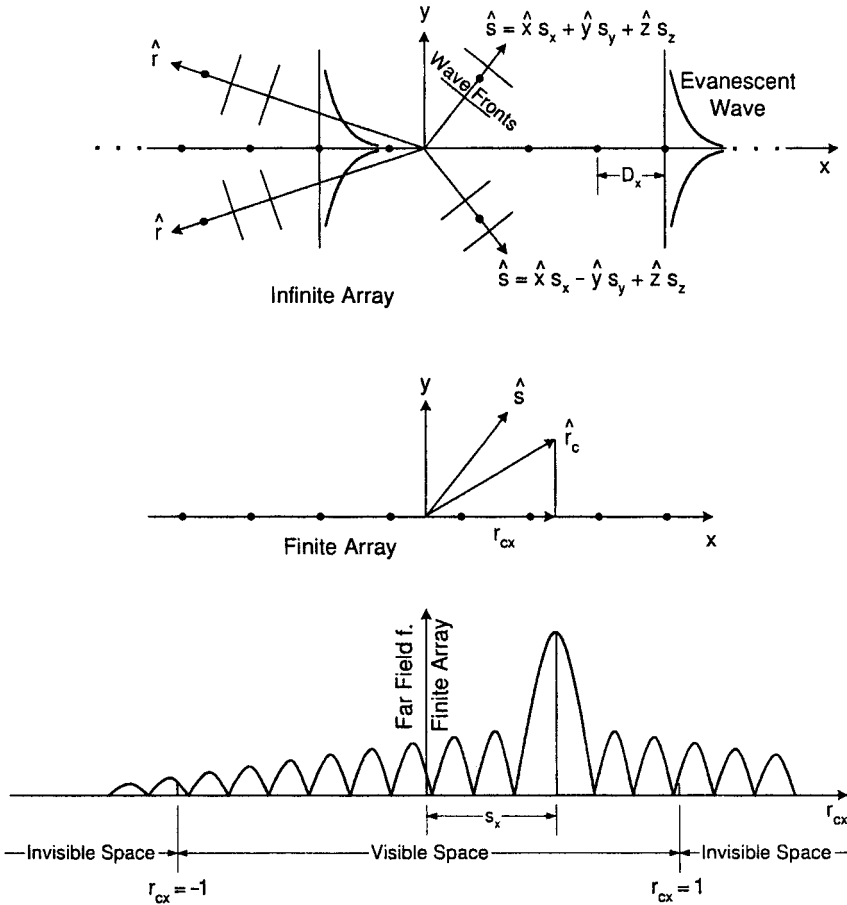
Fig. 4.4 Top: If an infinite array is exposed to an incident plane wave propagating in the directions, ŝ, it will reradiate propagating plane waves in the directions $\hat{s} = \hat{x}s_x \pm \hat{y}s_y + \hat{z}s_z$ and eventually a finite number of grating waves. In addition, evanescent waves are always present. Middle: A finite array with only Floquet currents will produce a continuous spectrum $\hat{r}_c$ with a mainbeam and sidelobes as shown at the bottom. Note that we use the x component r_{cx} of $\hat{r}$ as our variable. This is consistent with using s_x from the direction $\hat{s}$ of the incident plane wave. Bottom: Far field from Floquet currents as a function of the continuous radiation direction $\hat{r}_c$.

space runs from $r_{cx} = -1$ to $r_{cx} = +1$ as indicated in Fig. 4.4, bottom, while the invisible space is given by $|r_{cx}| > 1$, as shown.

Note also that as we continue into the invisible space for $r_{cx} < -1$ and $r_{cx} > 1$ there is no profound change in the general character of the radiation pattern.

However, the radiation pattern in Fig. 4.4 bottom is only a first-order approximation. To see what really goes on, consider Fig. 4.5. At the very top (Fig. 4.5a) we show an infinite periodic structure being exposed to an incident plane wave with direction of propagation $\hat{s}$. The element currents will be of the Floquet type only as we saw earlier in Fig. 4.4. In Fig. 4.5b we create a finite array by
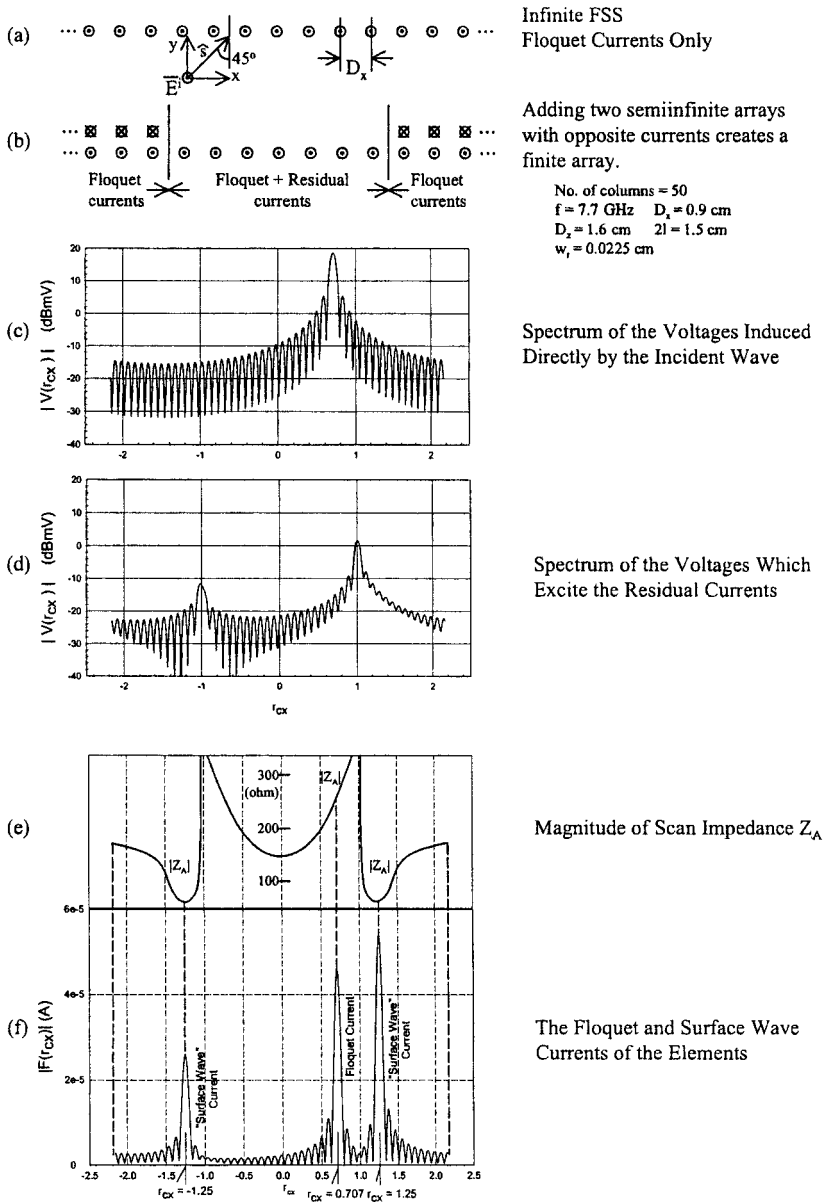
Fig. 4.5   (a) An infinite array exposed to an incident plane wave has only Floquet currents.
(b) Adding two semi-infinite arrays with negative Floquet currents creates a finite array with
actual currents (Floquet and residual currents). (c) Spectrum of the voltages induced in the
finite array by the incident wave. (d) Spectrum of the voltages in the finite array by the two
semi-infinite arrays. Note the two peaks in the endfire directions $r_{cx} = \pm 1$. (e) The magnitude of
the scan impedance Z_A as a function of r_{cx}. Note the minima at $r_{cx} = \pm 1.25$. (f) The spectrum
of the element currents as a function of r_{cx}. Note the surface waves where $|Z_A|$ is minimum is at
$r_{cx} = \pm 1.25$, not at $r_{cx} = \pm 1.0$.

superimposing two semi-infinite arrays with Floquet currents that are negatives of the original Floquet currents in the infinite case. Note that the currents on the two semi-infinite arrays are given rigorously by the Floquet currents only [i.e., (4.1)]; however, the currents on the finite array in the middle will, as we shall see, deviate for this simple form.[2] This becomes clear when we realize that the voltages induced in the elements of the finite array have two sources:

1. The incident plane wave
2. The two semi-infinite arrays

The voltage spectrum of the incident wave taken over the finite array is shown in Fig. 4.5c. It contains mainbeams in the forward and specular directions corresponding to the Floquet currents only (see Fig. 4.4).

Similarly, the voltage spectrum from the two semi-infinite arrays is shown in Fig. 4.5d. We observe two smaller beams at $r_{cx} = \pm 1$, that is, in the endfire directions. Thus, the two semi-infinite arrays will try to propagate waves along the array structure. However, as illustrated in Fig. 4.2, many evanescent waves with different $r_{cx}(s_x)$ are capable of propagating. They are distinguished by the magnitude of their scan impedance Z_A depicted in Fig. 4.2 and shown specifically in Fig. 4.5e.

4.7   HOW TO OBTAIN THE ACTUAL CURRENT COMPONENTS

The discussion above served primarily to explain how surface waves are established on a finite periodic surface, namely as the ratio between the voltages induced by the two semi-infinite arrays and the impedances of possible surface waves.

This is not necessarily the way we actually calculate the element currents. In fact this was done by direct calculations of the currents in the finite array in question by using the SPLAT program discussed in Chapter 3. Typical examples have already been presented in Figs. 1.3b and 1.3c. Clearly the currents in Fig. 1.3c are seen to be highly erratic. To find out what current components actually are contained in such a distribution, we simply ran a Fourier analysis and obtained the current spectrum shown in Fig. 4.5f. While the current spike at $r_{cx} = 0.707$ is easy to associate with the Floquet currents obtained for an infinite array exposed to a plane wave incident at $45°$, the two other spikes at $r_{cx} = \pm 1.25$ remained somewhat of a mystery until the explanation in Section 4.6 above was introduced.

Finally, the Fourier analysis shows that we in addition to the Floquet and surface waves also obtain a small amount of additional currents at the edges of the array. They are usually associated with reflections of the two surface waves and the Floquet currents at the edges of the array. We have denoted them "end currents."

---

[2] See also Common Misconceptions, Section 4.19.

It is interesting to observe that the amplitude of one of the surface waves actually is larger than the Floquet current. Inspection of Fig. 1.3c strongly suggests that it may indeed be the case. However, the impact of the surface waves should not be judged by their amplitude only. Both the Floquet and the surface wave currents will radiate (scatter) and we shall see in the next section that the former in general is a far more efficient radiator than the latter.

Note: Sometimes the reader perceives the introduction of the two semi-infinite arrays with negative Floquet currents as an inadequate approximation. As discussed in detail in Section 4.19 (Common Misconceptions), this is not the case. However, even if some inaccuracies were present in our explanation, it really would not matter since the currents in Fig. 4.5f were obtained by direct calculation of the actual currents obtained from the SPLAT program applied to a finite array.

4.8   THE BISTATIC SCATTERED FIELD FROM A FINITE ARRAY

In the previous section we gave a physical explanation of how various current components on finite arrays came about. Furthermore, we used the SPLAT program in conjunction with a Fourier analysis to determine the actual element currents on a finite array. We decomposed these according to their phase velocities and found one strong component at $r_{cx} = s_x = 0.707$ for $45°$ angle of incidence corresponding to the Floquet currents present on an infinite array while we observed the surface wave currents propagating in opposite directions along the array at $r_{cx} = \pm 1.25$. Finally, there was a component that we associated with reflections from the edges of the finite array (we are not entirely sure about this interpretation at this point). We will refer to them as "end currents."

Furthermore, it is often convenient to introduce the concept of "residual currents," defined as the difference between the actual currents on the finite array and the Floquet currents. In other words, the residual currents are simply here defined as the sum of the two surface waves and the end currents.

These current components will radiate. Their radiation patterns are obtained simply by considering the entire periodic structure as an antenna (the notion that surface waves do not radiate is true only if they are associated with an infinite structure. This is usually the case as presented in most textbooks).

Thus, based on the current components obtained rigorously in the previous section, we shall next present the radiation pattern associated with these components.

First we show in Fig. 4.6 the bistatic scattering pattern of the Floquet currents only when a signal is incident upon an array of 50 columns at $45°$ angle of incidence. We obtain main beams in the forward as well as the specular directions and note that the sidelobe level looks "clean" as expected (sin *x/x* function).

This is also an opportune time to remind the reader that the total field in the forward direction is given by the sum of the scattered and the incident field. Since these two components are basically out of phase and have similar magnitudes, the total field in the forward direction is about zero except for some minor sidelobes. Thus, we observe a shadow in the forward direction as we would expect.
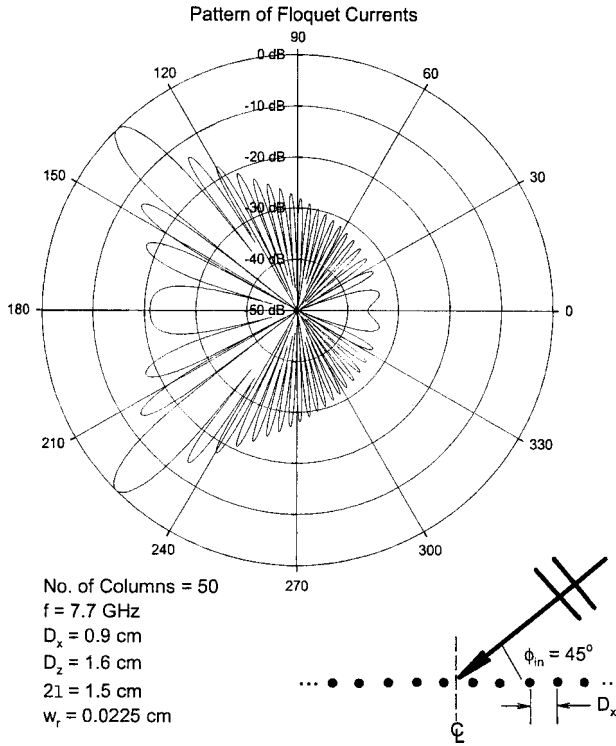
Fig. 4.6 *The bistatic scattering pattern for the Floquet currents only. Angle of incidence is 45°.*

Furthermore, we show in Fig. 4.7 the bistatic scattering pattern of the two surface waves. We observe that they are identical except for amplitude and direction of propagation. Note that the ratio between the pattern amplitudes of the two surface waves is close to the ratio between the two surface waves' amplitudes given in Fig. 4.5.

However, perhaps the most noteworthy is that in spite of the fact that one of the surface waves has a peak exceeding that of the Floquet currents peak by about 5 dB, the highest value of the scattering pattern is almost 20 dB below the peak of the Floquet pattern. In other words, the radiation efficiency of the surface waves is considerably lower than that of the Floquet currents. Or we may alternatively state that the radiation resistances associated with the surface waves are considerably lower than the one associated with the Floquet mode. Inspection of Fig. 4.5e shows this statement to be correct. This observation will later prove crucial when we try to control the radiation from the surface waves without significantly attenuating the one from the Floquet mode.

Furthermore, we show in Figs. 4.8 and 4.9 the bistatic scattering pattern associated with the end currents only and the residual currents, respectively. Comparing Figs. 4.7 and 4.8 with their sum in Fig. 4.9 indicates that the surface and end currents are basically out of phase. However, see also Section 4.9.

Pattern of SW$_L$ Currents (Dashed)
Pattern of SW$_R$ Currents (Solid)

No. of Columns = 50
f = 7.7 GHz
D_x = 0.9 cm
D_z = 1.6 cm
2l = 1.5 cm
w_r = 0.0225 cm

ϕ_{in} = 45°
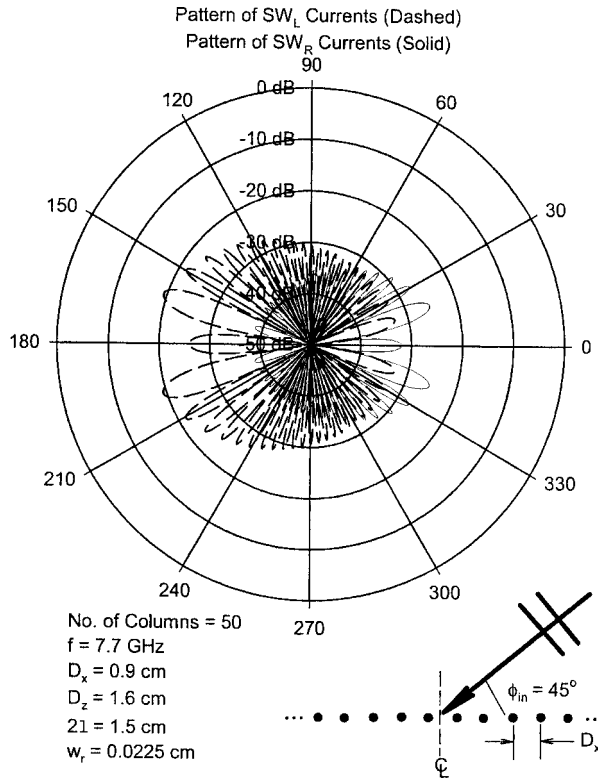
Fig. 4.7   The bistatic scattering pattern for the left- and right-going surface wave. Angle of incidence is 45°.

Finally, we show in Fig. 4.10 (broken line) the bistatic scattering pattern of the actual current on the finite array as obtained from the SPLAT program—that is, the sum of the Floquet currents, the surface waves, and the end currents. This pattern should be compared with the Floquet pattern shown in Fig. 4.6. It has been redrawn in Fig. 4.10 (solid line) for easy comparison. We readily observe that the main beams are unaffected and so is the *location* of the sidelobes. However, the sidelobe level is 5–7 dB higher when we include the radiation from the residual currents.

4.9   PARAMETRIC STUDY

Any periodic structure, whether infinite or finite, will in general change its properties considerably with angle of incidence. Furthermore, if the surface is of finite extent, we would expect its characteristic to depend to a degree on its size. Finally, surface waves are, as seen earlier, only prevalent in a certain frequency band.

Thus, in the following we shall examine some of these features in more detail.

Pattern of "End" Currents

No. of Columns = 50
f = 7.7 GHz
D_x = 0.9 cm
D_z = 1.6 cm
$2l$ = 1.5 cm
w_r = 0.0225 cm

ϕ_{in} = 45°
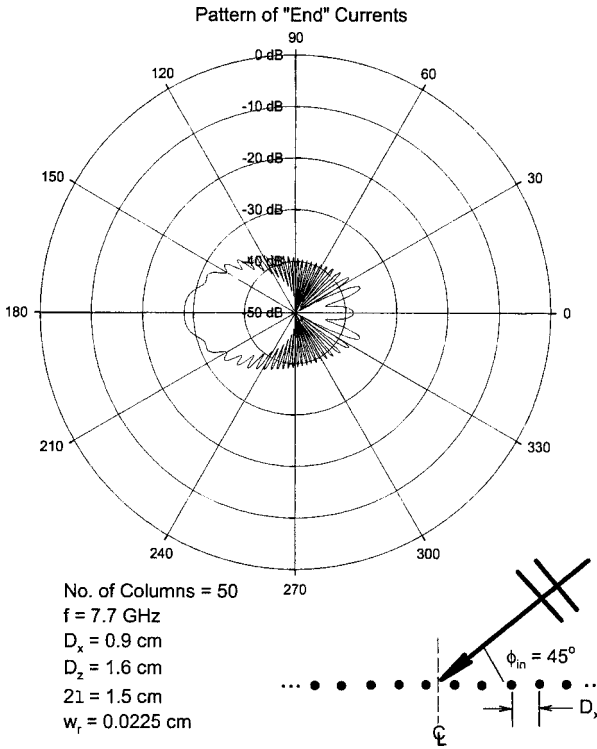
Fig. 4.8   The bistatic scattering pattern of the "end" currents. Angle of incidence is 45°.

4.9.1   Variation of the Angle of Incidence

First, for general orientation, we show in Fig. 4.11 the same case as shown in Fig. 4.10 except that the angle of incidence is now 67.5° (or 22.5° from grazing) instead of 45°. We observe only minor changes in the mainlobes while the location and level of the sidelobes has changed somewhat. However, as we shall see next, it actually takes only a small variation of the angle of incidence to obtain significant changes of the bistatic scattering pattern.

We have already illustrated in Figs. 4.5a and 4.5d how two semi-infinite arrays at each end of the finite array launches surface waves along the finite structure. In Fig. 4.12a we show this scenario in more detail. The semi-infinite arrays at the right of the finite array produces a field essentially pointing to the left. It will launch a left-going surface wave. Similarly, we will also obtain a right-going surface wave. The fields from the two semi-infinite arrays will have a phase difference that depends on the size of the finite array and the angle of incidence as shown in Fig. 4.12b. If we denote the width of the finite array by L and the angle of incidence by θ, the phase difference between the signals from the two semi-infinite arrays will be

$$\Delta = \beta L \sin \theta. \tag{4.4}$$
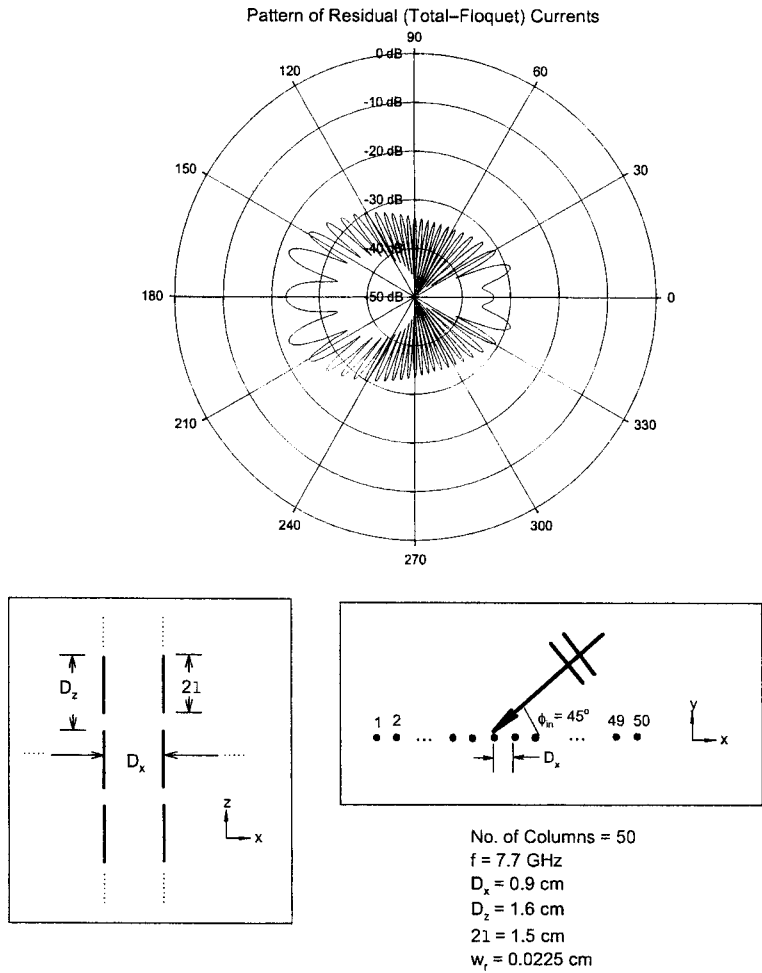
Fig. 4.9   *The bistatic scattering pattern of the residual currents (i.e., Total–Floquet's). Angle of incidence is 45°.*

Since L in general will be large in terms of wavelength, Δ can be substantial. However, it is of utmost importance that this phase difference is carried directly over in the two surface waves. In other words, the radiation pattern of the two surface waves will go in and out of phase as the angle of incidence θ changes. Let us consider an example.

Example 1   We assume a typical array consisting of 50 columns has an interelement spacing $D_x = 0.9$ cm. Then the total width of the finite array is $L = 50 \times 0.9 = 45$ cm. Thus, for an angle of incidence $\theta = 45°$ and frequency $f = 7.7$ GHz we obtain a phase difference between the left- and right-going surface wave equal to

$$\Delta = \beta L \sin \theta = 16.35\pi \; \text{(rad)}.$$

Polar Plot

No. of Columns = 50
f = 7.7 GHz
D_x = 0.9 cm
D_z = 1.6 cm
2ℓ = 1.5 cm
w_r = 0.0225 cm
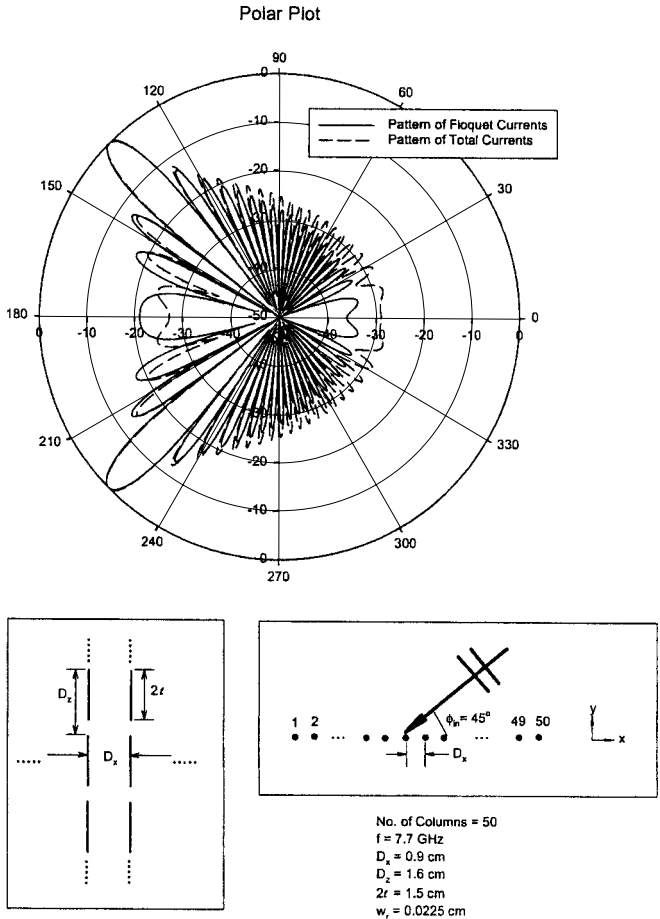
Fig. 4.10   The bistatic scattering pattern of the Total as well as the Floquet currents. Angle of incidence is 45°. Note the increase in sidelobe level when the residual currents are added.

We now reduce the angle of incidence by $\Delta\theta$ such that the phase difference between the two surface waves is reduced by π rad, that is,

$$\sin(\theta - \Delta\theta) = \frac{(16.35 - 1)\pi}{\beta L} = 0.665.$$

In other words, $\Delta\theta = 3.4°$ for a $180°$ phase change between the two surface waves.

We will illustrate this result in Fig. 4.13. We here show the calculated scattering pattern for an array of columns and vary the angle of incidence from $45.5°$ to $41.0°$ in steps of $0.2°$. We then selected the bistatic scattering pattern with the strongest residual pattern, namely Fig. 4.13a for $\theta = 45.2°$ and the weakest residual pattern as shown in Fig. 4.13c for $\theta - \Delta\theta = 41.8°$. Thus to obtain a
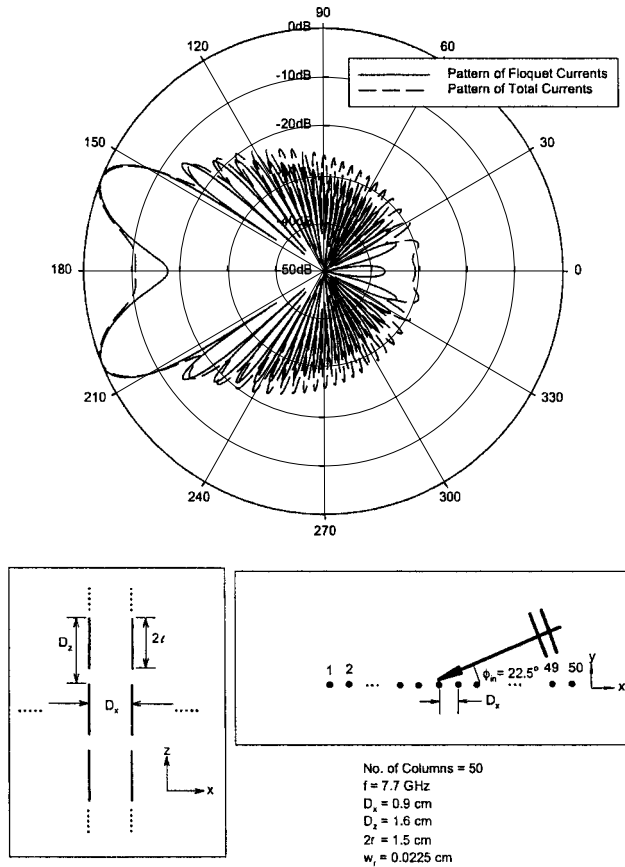
Fig. 4.11   The bistatic scattering pattern of the Total as well as the Floquet currents. Angle of incidence is 67.5°.

phase reversal of the two surface waves (including the end pattern), the angle of incidence should change by $\Delta\theta = 45.2 - 41.8 = 3.4°$, in complete agreement with the estimated value calculated above. As an extra check, we show a scattering pattern in between as illustrated in Fig. 4.13b.

4.9.2   Variation of the Array Size

Inspection of (4.4) above showed that the phase difference between the two semi-infinite arrays could be changed by variation of the angle of incident θ. Alternatively, a change in phase difference can also be obtained by variation of the width L of the finite array.

More specifically, let us change the original width L of the finite array to $L + \Delta L$ such that the phase difference Δ is changed by π; that is, by modification of (4.4) we find

$$\Delta + \pi = \beta(L + \Delta L) \sin\theta. \tag{4.5}$$
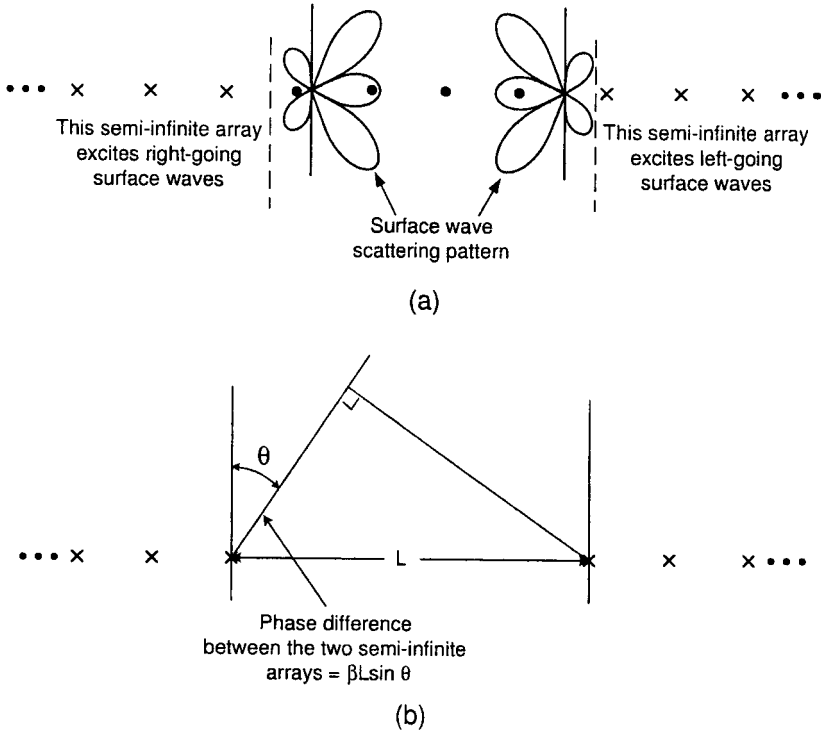
Fig. 4.12 (a) The two semi-infinite arrays excite right- and left-going surface waves as indicated in the figure. (b) Since the width L of the finite array usually is large in terms of wavelength, the phase difference between the two semi-infinite arrays will in general change strongly with angle of incidence θ. This phase difference is carried directly over into the two surface waves.

From (4.4) and (4.5) we obtain

$$\Delta L = \frac{\lambda}{2\sin\theta} \tag{4.6}$$

or the change ΔN in number of elements is

$$\Delta N \sim \frac{\Delta L}{D_x} = \frac{\lambda}{2D_x\sin\theta} \tag{4.7}$$

Example 2 Typically for $D_x = 0.9\,\text{cm}$, $\theta = 45°$, and $f = 7.7\,\text{GHz}$, we find from (4.7)

$$\Delta N \sim 3.1 \text{ column.} \tag{4.8}$$

Note: ΔN is independent of the width L of the array.

This estimate has been checked out by calculating the bistatic scattering pattern for arrays where the number of columns vary from 50 to 55 in increments of one. In Fig. 4.14a we show the case where the residual pattern is close to a maximum for $N = 51$ columns, and in Fig. 4.14b we show the case where it is close to a

Floquet Pattern and Residual Pattern   Floquet Pattern and Residual Pattern

(a)   **(b)**

Floquet Pattern and Residual Pattern

(c)

$\bar{E}^i = \hat{z}$ (1V/m)

ϕ_{in}=a:45.2°
b:43.6°
c:41.8°

1 2   49 50

D_x

No. of Columns = 50
f = 7.7 GHz
D_x = 0.9 cm
D_z = 1.6 cm
2ℓ = 1.5 cm
w_r = 0.0225 cm
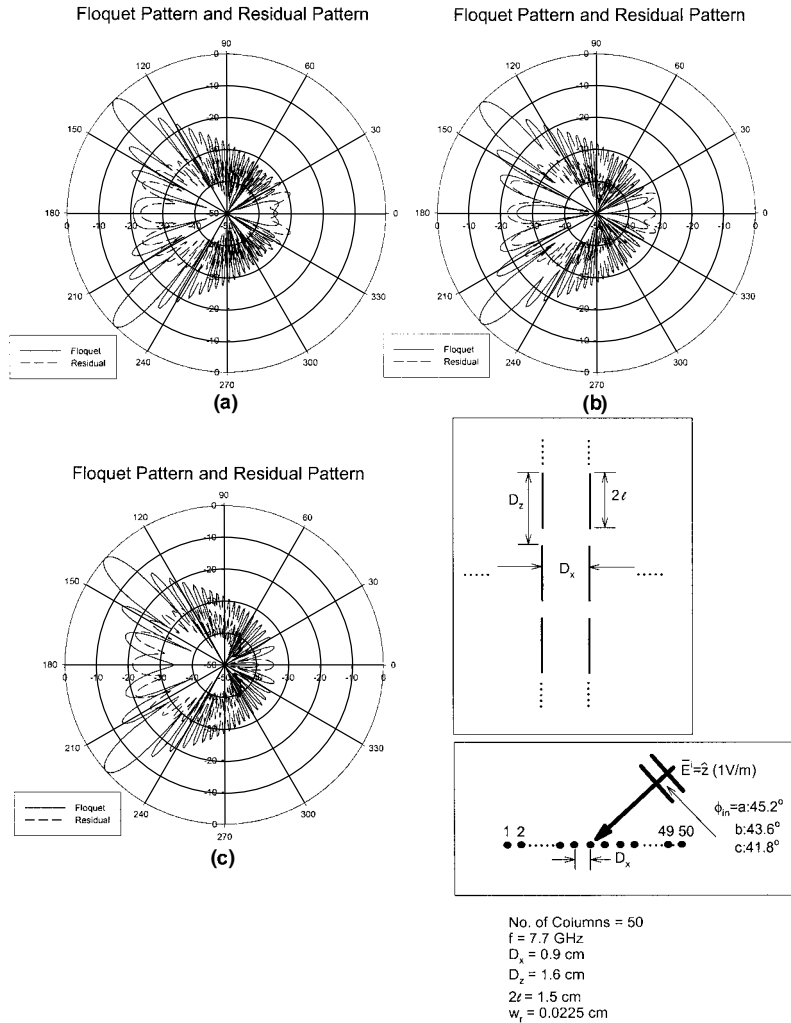
Fig. 4.13   The bistatic scattered fields for an array of 50 columns at f = 7.7 GHz. Floquet currents only (full line) and residual currents only (broken line). Angle of incidence: (a) 45.2°. Fields from the residual currents are maximum. (b) 43.6°. Fields from residual currents are medium. (c) 41.8°. Field from residual currents are minimum. The amplitude of the residual fields depends on the phase difference between the two semi-infinite arrays shown in Fig. 4.12.

minimum for 55 columns. Thus, $\Delta N = 55 - 51 = 4$ columns, which is in "fair" agreement with the estimate above. *Note*: The presence of the end current pattern makes "exact" comparison of the residual pattern somewhat blurred.

4.9.3   Variation of Frequency

All the examples presented so far have been at the frequency $f = 7.7$ GHZ. The effect of changing the frequency will be investigated next. The size of the array

Floquet Pattern and Residual Pattern

(a)

Floquet Pattern and Residual Pattern

No. of Columns (N)= a: 51
b: 55

f = 7.7 GHz
D_x = 0.9 cm
D_z = 1.6 cm
2ℓ = 1.5 cm
w_r = 0.0225 cm

(b)
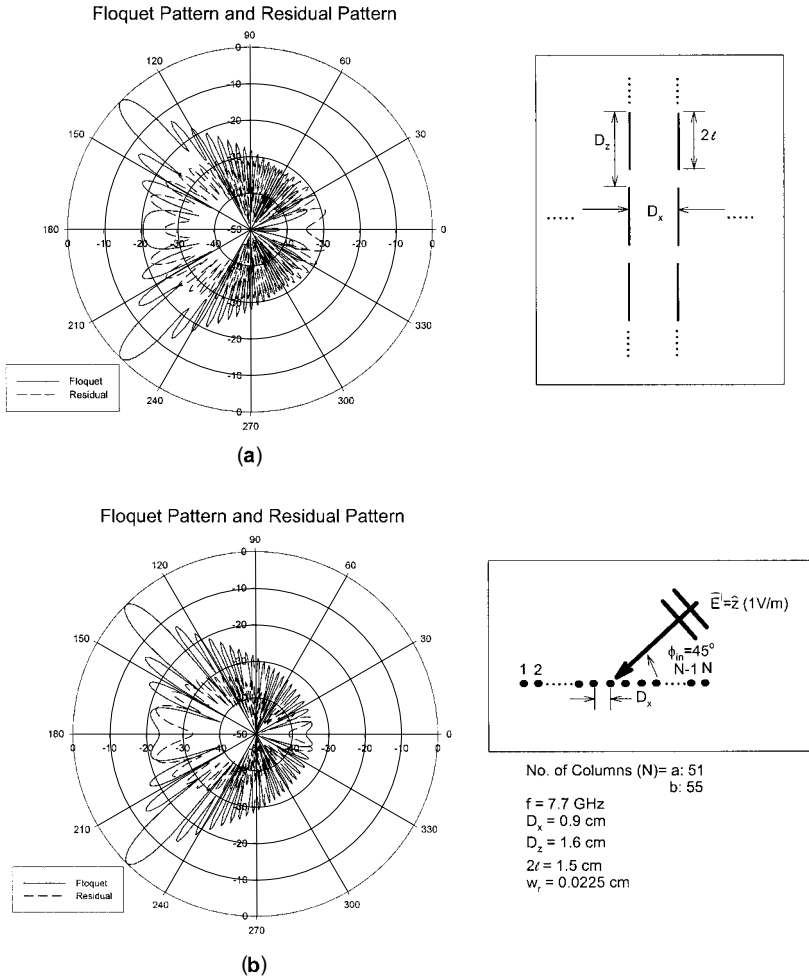
Fig. 4.14 The bistatic scattered field from arrays with (a) 51 columns and (b) 55 columns. Full line denotes field from Floquet currents only, and broken line denotes field from the residual currents only. Angle of incidence is 45°. Note that the fields from the residual currents are maximum for 51 columns and minimum for 55 columns.

is kept fixed at 25 columns, and a plane wave is incident at $67.5°$ from normal. We will calculate and plot the backscattered field in the complex plane as shown in Fig. 4.15. At the top of that figure we show the frequency range 2–6.2 GHz and at the bottom the range 6.3–12 GHz. We note that the low frequencies from 2 to 6.2 GHz rotate in the complex plane in a very regular and leisurely fashion as one would expect. However, in the frequency range 6.3–8.3 GHz shown at the bottom we observe a backscattered field that not only is significantly larger but also rotates much faster in the complex plane. Finally, from 8.4 to 12 GHz the backscattered field still has a large amplitude but has settled down and is rotating
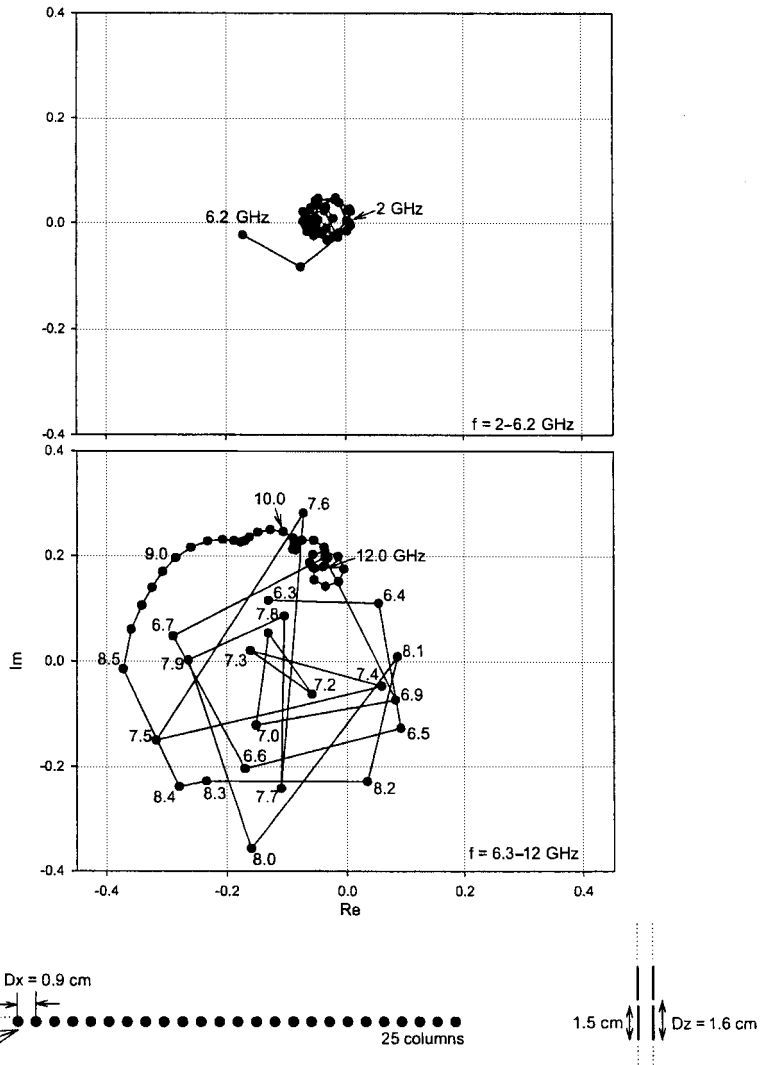
Fig. 4.15 The backscattered field plotted in the complex plane as a function of frequency. Angle of incidence is 67.5°. Number of columns is 25. Top: Frequency range 2–6 GHz. Bottom: Frequency range 6.3–12 GHz, where the surface waves are prevalent from 6.3 to 8.4 GHz. Called a backscattering diagram.

much slower. A closer investigation shows that the fast rotating range from 6.3 to 8.3 GHz is the frequency range where surface waves exist. We simply in that range observe column currents as shown earlier, for example, in Fig. 1.3 (more examples will be given later; see, for example, Figs. 4.17, 4.18, and 5.9). From 8.5 to 12 GHz the surface waves have essentially died out. There are two reasons for the higher values of the backscattered field in this frequency range.

1. We are closer to the resonant frequency ($\sim$10 GHz), resulting in a stronger column current and thus backscattered field.
2. The sidelobe level of the backscattered field is higher because we are getting closer to the onset of the first grating lobe ($\sim$18 GHz).

But how do we explain that surface waves are present only in a limited frequency range, namely $\sim$6.3–8.3 GHz? This is explained in Fig. 4.16 in a qualitative way. It shows the scan impedance Z_A plotted earlier in Fig. 4.2 but here plotted at three frequencies, namely 6, 7.7, and 10 GHz. Furthermore, these scan impedance curves are shown a bit more realistic by the fact that they for end-fire condition do no go to infinity but just to a large value depending on how large the array actually is. This point is easy to see by application of the mutual impedance concept. It simply tells that the magnitude $|Z_A|$ of the scan impedance can never exceed $\sum_{q=-Q}^{Q} |Z_{0,q}|$, where $Z_{0,q}$ is the mutual impedance between the reference element in column 0 and all the elements in column q (see Chapter 3 for details). Since $|Z_{0,q}|$ and Q are bounded, so is the finite sum $|Z_A|$. As already shown in Fig. 4.2 and repeated in Fig. 4.16 for easy comparison, we
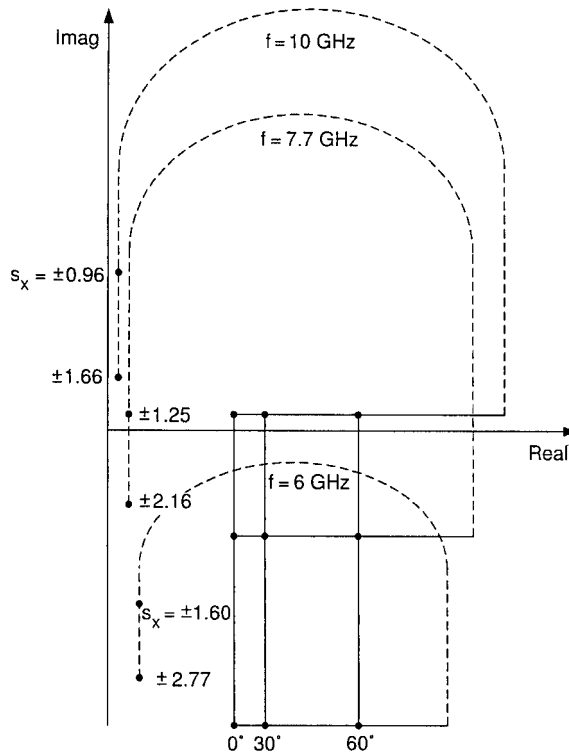
Fig. 4.16 *Typical complex scan impedance Z_A for a finite array at the following frequencies: 10 GHz, no surface waves since lowest point for $s_x = \pm1.66$ is too far from (0,0); 7.7 GHz, surface wave possible for $s_x \sim \pm1.25$; 6.0 GHz, no surface wave since too far from (0,0).*

see that at $f = 7.7$ GHz Z_A gets close to the origin for $s_x = \pm 1.25$; that is, a free surface wave can exist. However, at 10 GHz we are closer to resonance and Z_A will therefore in real space move closer to the real axis in the complex plane. Note that this upward motion is also taking place in imaginary space such that even for $s_x = \pm 1.66$ where Z_A turns around and moves upward along the imaginary axis, Z_A will not get close to the origin; that is, no free surface waves can exist at 10 GHz.

Similarly, at $f = 6$ GHz we drop too far down in the capacitive region for Z_A to get close to the origin; that is, no surface waves can exist here either. In other words: A finite array can only support surface waves in a limited frequency range as illustrated by the actual calculated curve in Fig. 4.15 and only for $D_x < \lambda/2$
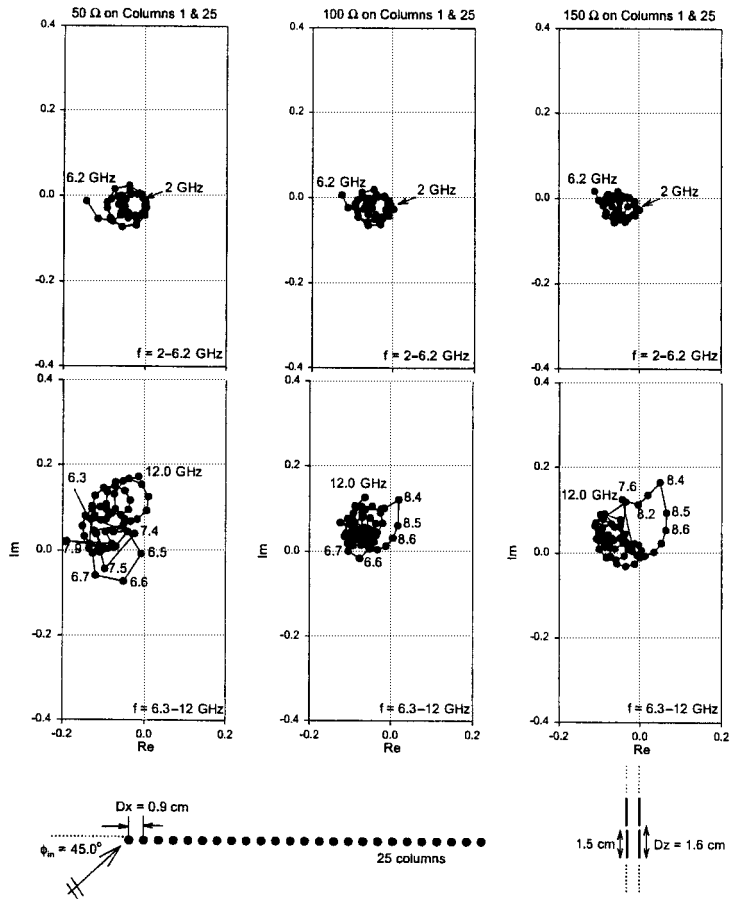
Fig. 4.17   The backscattered field (backscattering diagram) from an array of 25 columns plotted in the complex plane. Frequency range 2–6.2 GHz (top) and 6.3–12.0 GHz (bottom). Outer columns (i.e., numbers 1 and 25) are loaded with (left): 50 ohms; (middle) 100 ohms; and (right) 150 ohms.

(otherwise grating lobes will add a resistive component to the scan impedance and prevent the scan impedance from getting close to the origin). This presentation also shows that infinitely long wires cannot produce surface waves as discussed here. They have no resonance.

The curves shown in Fig. 4.16 are only typical. In reality the values of Z_A will vary from column to column and sometimes even have a small negative real part indicating that energy is absorbed. But the fundamental explanation stands. Note also that the cutoff frequencies will depend to some extent on the size of the array.
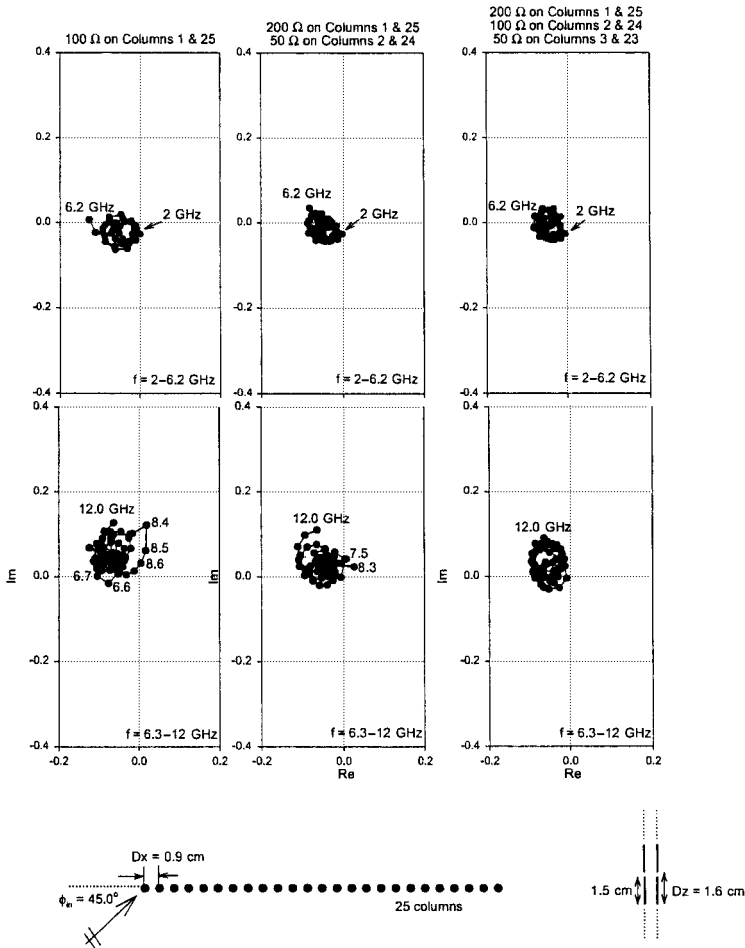
Fig. 4.18 *The backscattered field (backscattering diagram) from an array of 25 columns plotted in the complex plane at the frequencies 2–6.2 GHz (top) and 6.3–12.0 GHz (bottom). (left) Columns 1 and 25 loaded with 100 ohms; (middle) columns 1 and 25 loaded with 200 ohms and columns 2 and 24 loaded with 50 ohms; (right) columns 1 and 25 loaded with 200 ohms, columns 2 and 24 loaded with 100 ohms, and columns 3 and 23 loaded with 50 ohms.*

4.10 HOW TO CONTROL SURFACE WAVES

We saw earlier that surface waves radiate and can lead to a significant increase in the backscattered field. It is therefore of great interest to investigate ways to control them. We recall from Fig. 4.5d as well as Fig. 4.12 that the surface waves basically were driven by two semi-infinite arrays located on each side of the finite array. Thus, if we could somehow introduce a "barrier" between the two semi-infinite arrays and the finite array, we would expect a weaker excitation of the surface waves in the finite array. One such possible practical arrangement could consist of a finite number of columns between the semi-infinite and finite arrays where the column currents had been reduced by insertion of load resistors in each element. Such an arrangement could also serve as absorbers of the two surface waves as well as the Floquet waves incident upon the edges of the finite array.

Thus, in Fig. 4.17 we show three cases where the elements in the edge columns (one at each edge) of the array shown earlier in Fig. 4.15 have been loaded with 50, 100, and 150 ohms, respectively. We observe only minor changes at the low frequencies 2–6.2 GHz where surface waves do not exist. However, a significant reduction is obtained at the higher frequencies 6.3–12.0 GHz, where surface waves are prevalent from 6.3 to 8.5 GHz (see Fig. 4.15). Note further that the greatest reduction is obtained when the load resistors are 100 ohms (see Fig. 4.17, middle).

Furthermore, we show in Fig. 4.18 three cases where one, two, and three columns at each end of the finite array have been loaded with various resistors as indicated at the top of the figure. First, to the left we show the single column case, namely the optimum case shown earlier in Fig. 4.17, middle. Next follows the two- and three-column cases as shown in Fig. 4.18, middle and right, respectively. As we would expect, a steady improvement is observed as we increase the number of columns.

4.11 FINE TUNING THE LOAD RESISTORS AT A SINGLE FREQUENCY

In the last section we demonstrated how resistive loading of one or more columns located at the edges of the finite array could lead to a significant reduction of the surface waves. We considered the entire frequency range of interest, but our choice of a resistive profile was based on a combination of intuition and experience.

In this section we shall demonstrate a more systematic and also more precise approach. In general, it is performed only at a single frequency. However, experience has shown that the performance at the rest of the frequency band will in general be superior as well.

More specifically we show in Fig. 4.19a the column currents for an array comprised of 25 columns at $f = 7.8$ GHz. The angle of incidence is 45° as shown in the insert below in the figure. There are no resistive loads at all, and this case therefore serves as our baseline. Next we show in Fig. 4.19b the same array but where the three outer columns are loaded with 200, 100, and 50 ohms,
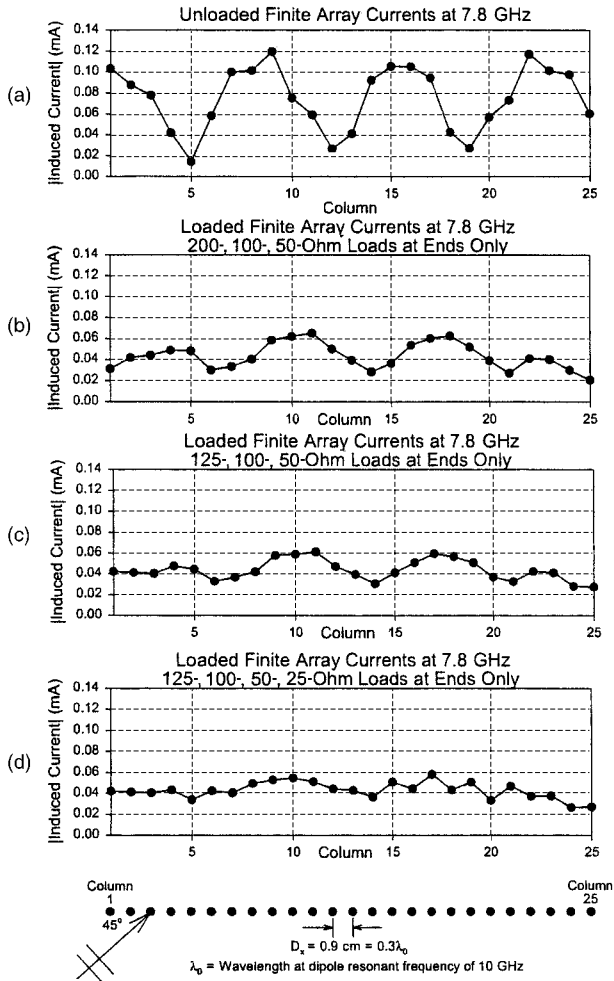
Fig. 4.19   *The column currents for an array of 25 columns under various load conditions: (a) No loads (baseline case); (b) columns 1 and 25, 200 ohms, columns 2 and 24, 100 ohms, columns 3 and 23, 50 ohms; (c) columns 1 and 25, 125 ohms, columns 2 and 24, 100 ohms, columns 3 and 23, 50 ohms, (d) columns 1 and 25, 125 ohms, columns 2 and 24, 100 ohms, columns 3 and 23, 50 ohms, columns 4 and 22, 25 ohms.*

respectively (actually the same case as shown earlier in Fig. 4.18, right). We observe a substantial reduction of the surface waves as compared with our baseline case in Fig. 4.19a. However, there is still a strong presence of surface waves as indicated by the rather strong variation of the column currents. Obviously the goal is to obtain as even column currents as possible. Close inspection of the currents in Fig. 4.19b reveals that the currents in the two outer columns (nos. 1 and 25) both are somewhat low. Using lower load resistors in these two columns should raise the current. Thus, we show in Fig. 4.19c the case where the load

resistors in the outer columns has been reduced from 200 ohms to 125 ohms. We observe that the currents in the three outer loaded columns are indeed fairly constant. However, the equalization of the currents in the rest of the array still needs improvement.

This observation suggests that more columns should be resistively loaded. Thus, we show in Fig. 4.19d a case where the four outermost columns have been loaded with 125, 100, 50, and 25 ohms, respectively. We observe a substantial improvement as compared to all the other cases in Fig. 4.19.

We finally show the backscattering diagram in Fig. 4.20 for the case in Fig. 4.19d. If we compare this case to the case in Fig. 4.18, right, we may at first glance be somewhat disappointed. However, a closer look reveals that a reduction has taken place at the lower frequency band 2–6.2 GHz. Furthermore, the higher values observed at 8.5–12 GHz is as we saw earlier not related to the surface waves. In fact they are "sidelobes" associated with the impending grating lobe about to pop up at $f \sim 18$ GHz. The higher values observed in Fig. 4.20 as compared to Fig. 4.18, right, is probably because the aperture is more tapered in the latter case than in the former (125 ohms compared to 200 ohms). In fact the

Fig. 4.20   The backscattered field from an array of 25 columns plotted in the complex plane (backscattering diagram). Frequency range: (a) 2–6.2 GHz and (b) 6.3–12 GHz. Load conditions like Fig. 4.19d: columns 1 and 25, 125 ohms; columns 2 and 24, 100 ohms; columns 3 and 23, 50 ohms; columns 4 and 22, 25 ohms.

frequency range from 6.3 to 8.5 GHz where surface waves typically reside looks "cleaner" and more deterministic than the case shown in Fig. 4.18, right.

4.12 VARIATION WITH ANGLE OF INCIDENCE

Periodic surfaces will often be exposed to signals where incidence varies from broadside to high angles. It is well known that the performance of any periodic structure may change considerable in such a scenario (see, for example, reference 81). Thus, it becomes important to check the cases considered above at other angles of incidence than merely $45°$.

As an example, let us consider the last case shown in Fig. 4.19d. We show this case again in Fig. 4.21a to facilitate the comparison to follow. Similarly, we show in Fig. 4.21b the same array configuration, but this time when the angle of incidence is equal to $67.5°$ (or $22.5°$ from grazing). Note that while the $45°$
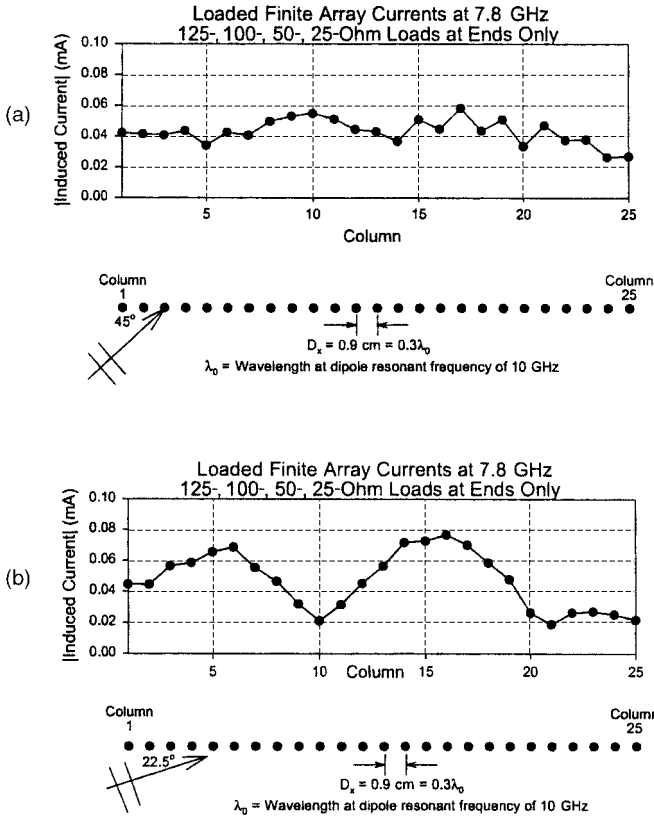
Fig. 4.21 The column currents for an array of 25 columns. Load conditions like Fig. 4.19d: columns 1 and 25, 125 ohms; columns 2 and 24, 100 ohms; columns 3 and 23, 50 ohms; columns 4 and 22, 25 ohms. (a) Angle of incidence is $45°$, (b) Angle of incidence is $67.5°$.
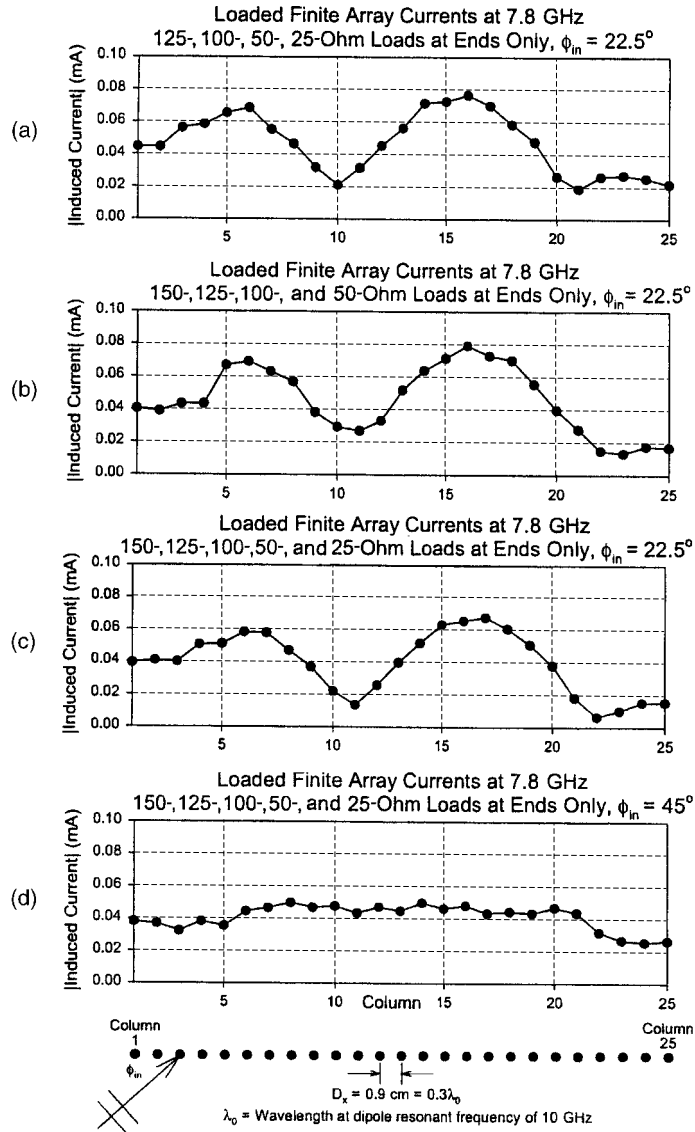
Fig. 4.22 The column currents for an array of 25 columns with various loads. (a) Angle of incidence is 67.5°. Columns 1 and 25, 125 ohms; columns 2 and 24, 100 ohms; columns 3 and 23, 50 ohms; columns 4 and 22, 25 ohms (like Fig. 4.21b). (b) Angle of incidence is 67.5°. Columns 1 and 25, 150 ohms; columns 2 and 24, 125 ohms; columns 3 and 23, 100 ohms; columns 4 and 22, 50 ohms. (c) Angle of incidence is 67.5°. Columns 1 and 25, 150 ohms; columns 2 and 24, 125 ohms; columns 3 and 23, 100 ohms; columns 4 and 22, 50 ohms; columns 5 and 21, 25 ohms. (d) Angle of incidence is 45°. Columns 1 and 25, 150 ohms; columns 2 and 24, 125 ohms; columns 3 and 23, 100 ohms; columns 4 and 22, 50 ohms; columns 5 and 21, 25 ohms.

Floquet Pattern

Total Pattern

(a)

(b)

Total Pattern with Loads

(c)

Column	Load
1,50	150 Ω
2,49	125 Ω
3,48	100 Ω
4,47	50 Ω
5,46	25 Ω

$\vec{E}^i = \hat{z}$ (1 V/m)

$\phi_{in} = 45°$

1 2   49 50

D_x

No. of Columns = 50
f = 7.7 GHz
D_x = 0.9 cm
D_z = 1.6 cm
2ℓ = 1.5 cm
w_r = 0.0225 cm
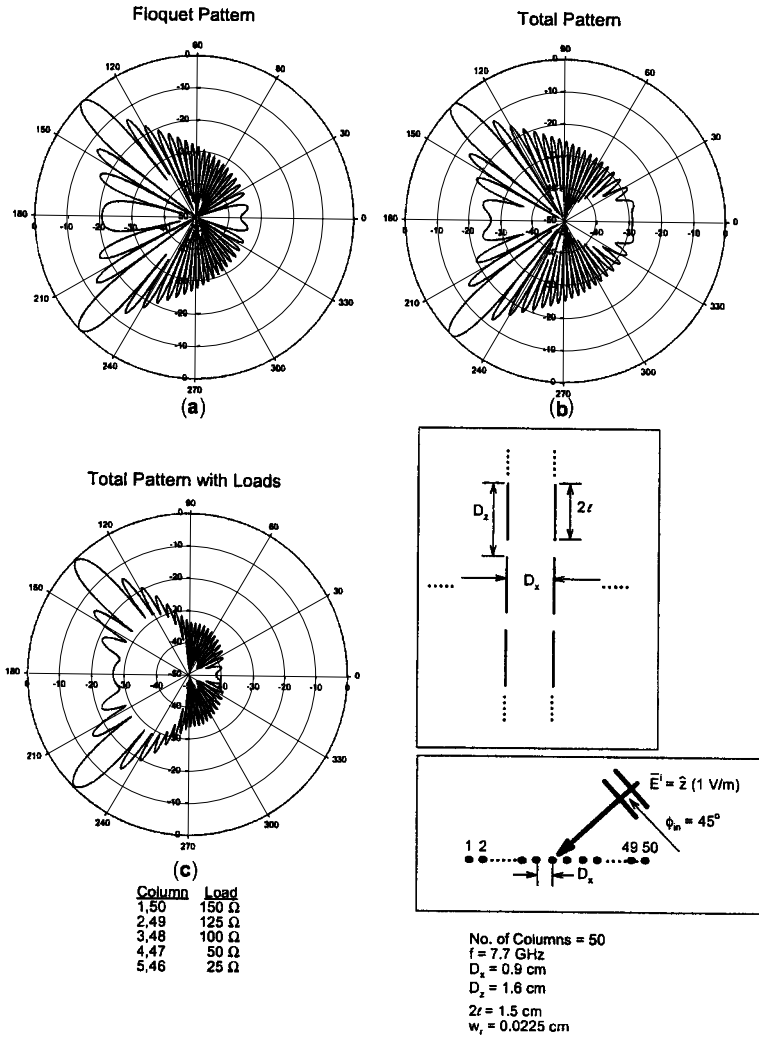
Fig. 4.23   The bistatic scattered field for an array of 50 columns for angle of incidence equal to 45°. (a) Assuming truncated Floquet currents only. No resistive loading. (b) Using the correct total column current as being equal to the sum of the Floquet, the left- and right-going surface waves and the end currents. No resistive loading. (c) Using the correct total column currents as being the sum of the Floquet, the left- and right-going surface waves, and the end currents. Resistive loading as indicated under (c) and same as in Figs. 4.22c and 4.22d. Note strong reduction of the backscatter lobes.

case basically exhibits ~4 humps (most clearly observed in the untreated array shown in Fig. 4.19a, we observe only ~2 humps in the 67.5° case shown in Fig. 4.21b. The reason for this difference is simply that while the phase velocities of the surface waves in the two cases are basically the same, the Floquet currents will move along the structure with a higher phase velocity in the 67.5°

case (i.e., closer to the velocity of the surface waves), resulting in a longer interference wavelength.

A most important consequence of this observation is simply that we need more columns to "sample" the array when the interference wavelength is longer (i.e., at high angle of incidence). As our baseline we show the four-column case already shown in Fig. 4.21b again in Fig. 4.22a in order to facilitate the comparison to follow. Next in Fig. 4.22b we show the case where we have increased all four column loads in an attempt to reduce the column currents. We observe in Fig. 4.22b that this is indeed the case, but there is a jump in column current between columns 4 and 5 and the currents in the rest of the array have not changed significantly.

However, if we load columns 5 and 20 with 25 ohms each, we obtain a notable improvement as shown in Fig. 4.22c.

We finally test the five-column case at angle of incidence equal to $45°$ as shown in Fig. 4.22d. We observe that the five-column case is quite a bit better than the four-column case shown earlier in Fig. 4.21a.

If the array is reasonably large, the energy lost in the end columns will be relatively minor in average. Thus, in that case the rule seems to be that adding a few extra resistively loaded columns is better than having too few. However, cost must also be considered.

4.13   THE BISTATIC SCATTERED FIELD

In the previous section we obtained an optimum load profile by simply observing the individual column currents in a finite array as illustrated, for example, in Fig. 4.22. We should, however, not lose sight of the fact that if the structure is to be used as a radome, it is the bistatic scattering pattern that must be the final proof of concept. Thus, although we are fairly sure that the optimum load profile arrived at in the above manner also constitutes the optimum profile for the bistatic scattered field, it should nevertheless be checked out. Thus, we show in Fig. 4.23 the bistatic scattering pattern for a *finite × infinite* array with $N = 50$ columns and angle of incidence equal to $45°$. More specifically we show in Fig. 4.23a the bistatic scattered field from the finite array by assuming that the column currents are simply of the Floquet types truncated to the size of the array. Similarly we showed in Fig. 4.23b the bistatic scattered field by assuming the correct column current comprised of the sum of the Floquet currents, the two surface waves as well as the end currents (denoted Total Pattern). We observed a significant increase in the sidelobe level for the total pattern as compared to the Floquet pattern, in agreement with earlier observations; see, for example, Figs. 4.10 and 4.11. Finally we show in Fig. 4.23c the same finite array as shown in Figs. 4.23a and 4.23b but where we use the same load profile as used in Figs. 4.22c and 4.22d. We observe that the sidelobe radiation level is significantly lower for the loaded total pattern in Fig. 4.23c than for the unloaded one in Fig. 4.23b (We should certainly expect that!). However, it is even lower than the truncated Floquet pattern in Fig. 4.23a. It seems fairly safe to state that this

is related to the fact that the aperture distribution in Fig. 4.23c is tapered as compared to Fig. 4.23a, which is uniform.

We finally show in Fig. 4.24 the same three cases as shown in Fig. 4.23 but where the angle of incidence is 67.5° rather than 45°. Again as in Fig. 4.23 we observe a significantly lower scattering level for the loaded case in Fig. 4.24c as compared to the total unloaded case in Fig. 4.24b (∼10 dB) but even up to several decibels below the scattering level in the Floquet case, Fig. 4.24a).

We finally remind the reader that the reduction level is not unique but depends on the size of the array as well as the angle of incidence (see Fig. 4.14 and Fig. 4.13, respectively).

4.14 PREVIOUS WORK

It is considered courteous and scholarly to present other researchers' contributions ahead of your own. However, if your subject is somewhat obscure and perhaps even controversial, this sequence often leads to a clouded relationship between new and old contributions. In fact, reference often end up being merely a litany of titles that "must be there" in order not to offend anyone. My own experience along those lines has often been that although I might have been referenced, it was doubtful whether my contribution was ever read or at least understood. Simply put, the references are simply not meaningful to the reader until after he has read most of the paper.

Thus, in an attempt to alleviate this problem I will review other contributions at this point. Please understand that this sequence in no way is an attempt to put other researchers' work in the background.

It would probably be safe to assume that the first researchers to consider a finite array of passive elements were the inventors of the Yagi–Uda array [82]. They excited these elements by a single active dipole being somewhat different than excitation by an incident plane wave. Besides, the surface wave concept apparently did not occur to them, nor did they actually need it to explain the radiation mechanism. That point of view appears first to have been introduced by Ehrenspeck [83] and later using a more theoretical approach by Mailloux [84]. It is interesting to note that a desirable radiation pattern is not obtained when we have a strong (i.e., free) surface wave, for example, at $s_x \sim 1.25$ as illustrated in Fig. 4.7. We observe that this leads to sidelobes larger than the mainlobe. Rather, the optimum antenna pattern for a Yagi–Uda array is obtained somewhere in the range $1.25 < s_x < 1.0$.

Recall that $s_x = 1.0$ corresponds to the endfire condition, leading to a gain significantly below that of a Yagi–Uda array tuned to maximum gain (it is close to the Hansen–Woodyard condition).

Further significant contribution to the theory of surface waves on Yagi–Uda arrays were given by Richmond and Garbacz [85] as well as by Damon [86].

Surface waves on finite periodic structures of the type discussed in this chapter seem not to have been treated in great detail until recently. That is not to say that

Floquet Pattern

Total Pattern

(a)

(b)

Total Pattern with Loads

(c)

Column	Load
1,50	150 Ω
2,49	125 Ω
3,48	100 Ω
4,47	50 Ω
5,46	25 Ω

$\widetilde{E}^i = \hat{z}$ (1 V/m)

$\phi_{in} = 22.5°$

No. of Columns = 50
f = 7.7 GHz
D_x = 0.9 cm
D_z = 1.6 cm
2ℓ = 1.5 cm
w_r = 0.0225 cm
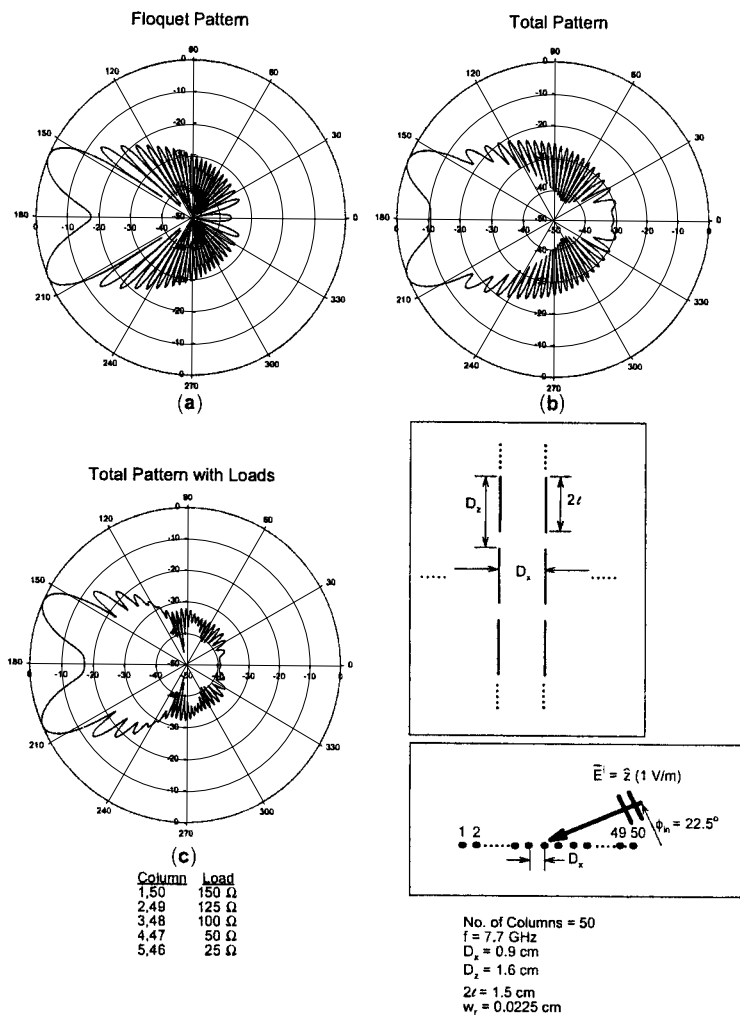
Fig. 4.24   The bistatic scattered field for an array of 50 columns for angle of incidence equal to 67.5° (similar to Fig. 4.23 except for angle of incidence). (a) Assuming truncated Floquet current only. No resistive loading. (b) Using the correct total column currents as being the sum of the Floquet, the left- and right-going surface wave, and the end currents. No resistive loading. (c) Using the correct total column currents as being the sum of the Floquet, the left- and right-going surface wave, and the end currents. Resistive loading as indicated under (c) and same as in Figs. 4.22c and 4.22d. Note strong reduction of the backscatter lobes.

surface waves on periodic structures never were suspected. In fact every time a curious (and often undesirable) effect on a periodic structure was encountered that could not be readily explained, it was often blamed on a mysterious "big bad surface wave." Many have eluded to such phenomena and reported them [3–5, 8–14], while probably even more have suspected them but not reported them. See also Section 1.5.3.

At any rate, the characterization of the surface waves on a finite FSS structure by their actual propagation constant appears not to have occurred until recently in papers by Munk et al. [87] and Janning and Munk [88], as well as in the dissertation by Janning [77] and the thesis by Pryor [76].

It is instructive to speculate on the reasons for this scant attention. Some of them appear to be related to the following:

1. Instead of finite wire sections, infinite long wires (or narrow strips) were used; that is, instead of a double periodic surface, only a single periodic one was used. These cannot support surface waves of the type discussed here (see Section 4.9.3).

2. The frequency band investigated was not sufficiently below the resonance of the structure (20–30%). For further discussion see Section 4.9.3.

3. The interelement spacings D_x were not less than $\lambda/2$; that is, grating lobes could occur as we move into imaginary space. As discussed in Section 4.9.3, that automatically rules out free surface waves.

4. The column currents were simply assumed to be truncated Floquet currents only. In other words the existence of any surface waves were simply ruled out from the onset. See also discussion in Section 4.8.

5. Finally, it should be pointed out that surface waves are naturally attached to planar surfaces. If these are curved, the surface waves will be naturally attenuated by shedding energy as they move along the curved surface. Since many practical applications of periodic structures are naturally curved (for example, such as bandpass radomes and subreflectors), it is easy to understand that the presence of surface waves simply went unnoticed.

4.15   ON SCATTERING FROM FACETED RADOMES

So far we have considered mostly scattering from planar *finite × infinite* arrays. They play an important role in helping us to understand the nature of surface waves on finite structures. They are, however, used rarely in practice. They may be curved, or planar sections may be put together in a faceted fashion such as shown, for example, in Fig. 4.25. Curving a surface leads to a natural attenuation of the surface waves by shedding energy. This case will not be treated here (if anyone out there has something to say about that subject, I would appreciate hearing about it).

The shape shown in Fig. 4.25 is characteristic for ship board applications. The incident signal is basically arriving in the horizontal plane. If the radome is opaque, the signal will be reflected upward or downward and thereby lead to a reduced RCS. When the radome is transparent, the incident signal will proceed to the antenna and be received. The RCS will in that case depend essentially on the antenna only. For a discussion of this subject, see Chapter 2. Also see Pryor [76].
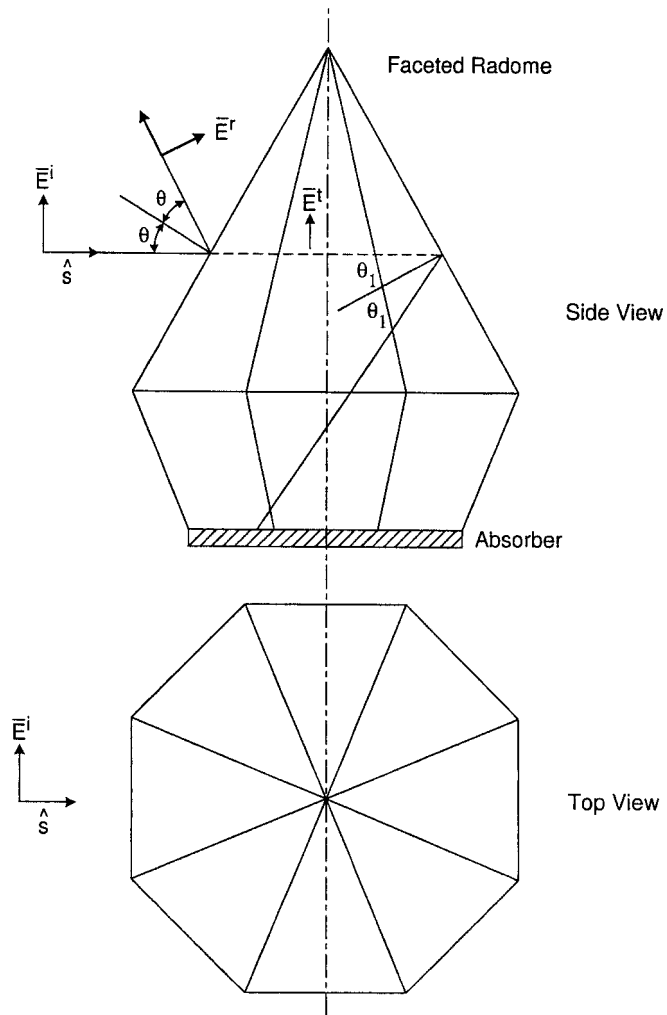
Fig. 4.25   A typical octagonal faceted radome. An incident signal in the horizontal plane will be reflected upward as shown if the radome is opaque. If part of the incident signal leaks through the front, it will essentially be reflected downward by the back. An absorber can be placed on the floor to prevent further scattering.

The situation becomes even more complicated if the frequency is somewhere in the transition range between being opaque and transparent. In that event, part of the incident signal may simply make it to the back wall where it will be partly reflected either down into the ground or upward. Although both of these signals will be reflected away from the horizontal plane, it is usually a good idea to cover the floor inside the radome with an absorber as indicated in Fig. 4.25.

We are at present unable to model a large faceted radome as shown in Fig. 4.25. However, we may combine eight *finite × infinite* flat panels

into an octagon shape as indicated in Fig. 4.26. There is a fundamental difference between the finite radome in Fig. 4.25 and the infinite long one in Fig. 4.26—namely, that in the latter case, reflections from the back wall will occur and can in that case obscure the reflections from the front. This problem can in our calculations be alleviated by covering the back wall with an absorber or, simpler yet, by removing the four back panels as indicated in Fig. 4.26. Thus, in the cases to follow we shall simply calculate the backscattered field from just the four front panels as also indicated in Fig. 4.26.

We note that the angles of incidence are 22.5° for the two front panels, while they are 67.5° for the two side panels. Based on our observations above (see Section 4.13), we may conclude that we should use at least five and most likely more loaded columns on each side of the corner columns. Furthermore, we would anticipate that the loading should be somewhat less severe than earlier since we are now talking about "bending" of the panels rather than a complete interruption.
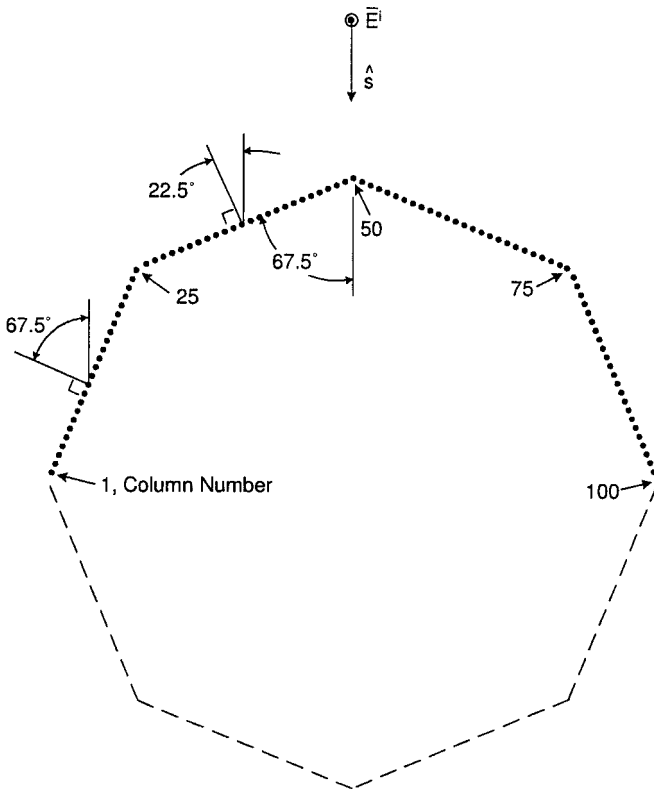
Fig. 4.26 Crude modeling of the faceted radome shown in Fig. 4.25. It is comprised of finite × infinite planar arrays. However, to avoid possible reflections from the back, only the four front panels are used to study the column currents in the front.

Element Currents
f = 7.8 GHz
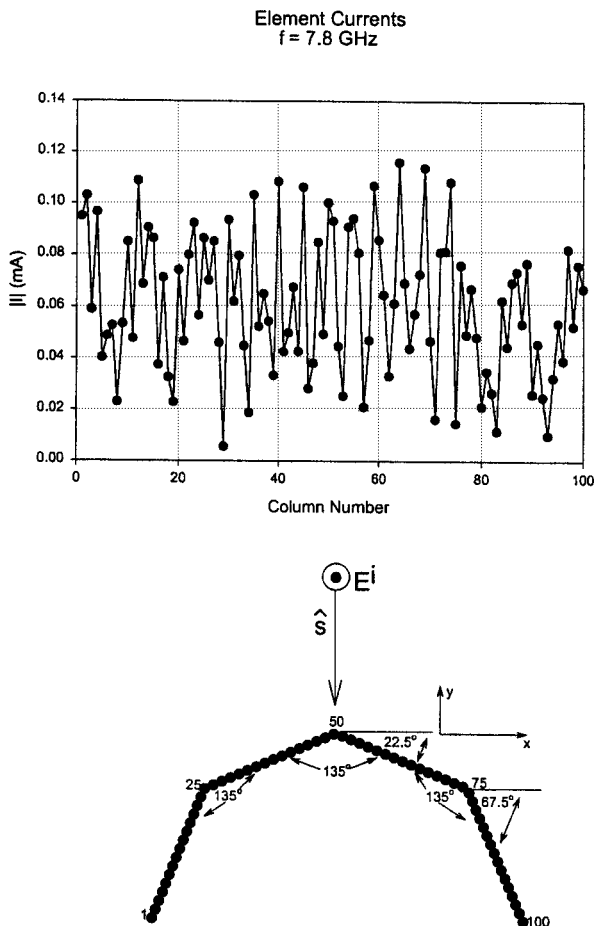
Fig. 4.27   The calculated column currents (from SPLAT) for the four front finite × infinite panels of an octagonal-shaped radome. Number of columns in each panel is 25, total number of four front panels is 100. There is no resistive loading; that is, this is the baseline case.

We shall present several practical examples obtained by use of the SPLAT program discussed earlier.

First we show in Fig. 4.27 the column currents at $f = 7.8$ GHz in the four front panels when no loads are present at all. This case constitutes our baseline. Note the very dramatic variation of the column currents as expected based on our investigation above (as discussed already in Chapter 1 and in this chapter as well, such a strong variation will only be expected in the frequency range where strong surface waves can exist, namely typically 6.3–8.5 GHz and not at other frequencies).

Next we show in Fig. 4.28 the same four front panels as shown above but now where five columns on each side of the corner columns have been resistively loaded as indicated in the figure (note the change of scale). We observe a very

Element Currents
f = 7.8 GHz
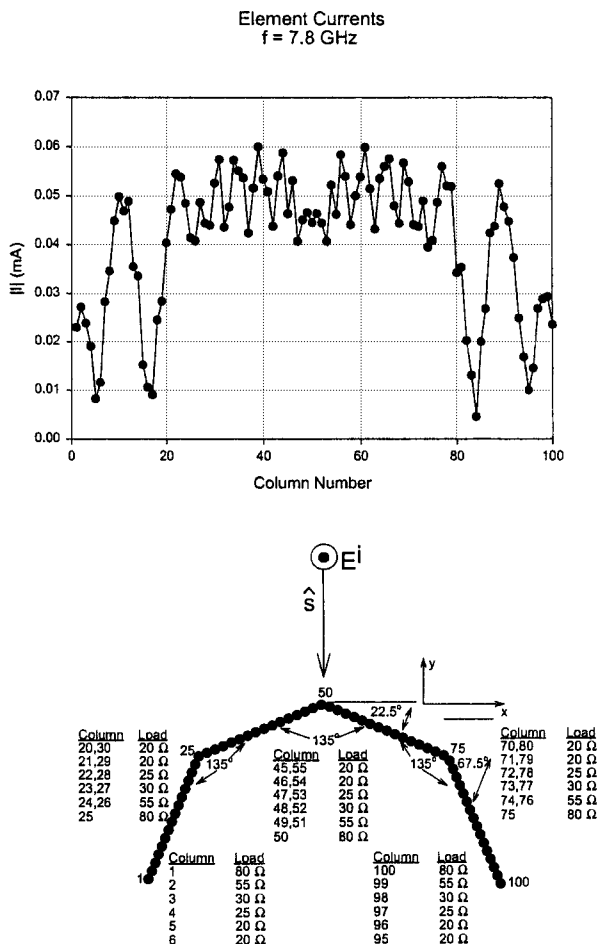
Fig. 4.28 *The calculated column currents (from SPLAT) for the four front finite × infinite panels of an octagonal-shaped radome, like those shown in Fig. 4.27. However, the corner and end columns have been loaded resistively at the center of each element as indicated in the insert. Note the dramatic reduction in variation of the element currents as compared to the unloaded case in Fig. 4.27. This indicates much lower amplitudes of the surface waves and thereby lower scattering. (Note the different scales in Figs. 4.27 and 4.28.).*

dramatic reduction of the column currents in the two front panels, while the variation in the two side panels still is significant but has been "cleaned up."

In Fig. 4.29 we show an interesting verification of some concepts developed earlier in this chapter. In Figs. 4.5 and 4.12 we described the surface waves as being excited by two imaginary semi-infinite arrays. We also demonstrated that this excitation could be reduced by insertion of barriers in the form of resistively loaded columns. Furthermore, we observed that the strongest surface wave would be excited at the corners at columns 25 and 75 and relatively weakly at columns
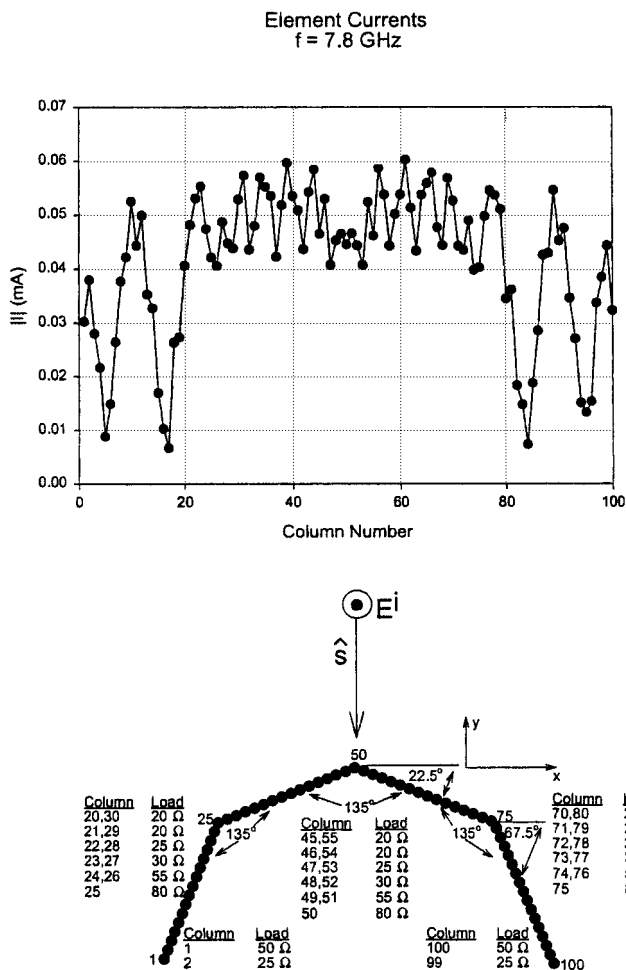
Fig. 4.29 The calculated column currents (from SPLAT) for the four front finite × infinite panels of an octagonal-shaped radome, like those shown in Figs. 4.27 and 4.28. However, only the two end columns have been resistively loaded as shown in the insert. Note the very little difference between the cases shown in Figs. 4.28 and 4.29.

1 and 100 (for illustration of this statement consult Fig. 4.5). Thus, the barrier at the open ends of the four panels need not be very wide. In fact, the main reason for having loaded columns at all in this case is simply to absorb the surface and Floquet waves incident upon the open edge.

Thus, we show in Fig. 4.29 a case where the number of loaded columns at the open ends has been reduced to just two columns. Sure enough, the two cases in Figs. 4.28 and 4.29 look very much alike except for the amplitudes of the column currents at the open ends. That could easily be adjusted by changing the load resistors at the open ends (if needed).

We may conclude from the examples above that surface waves become more prevalent at the higher angles of incidence. Also the interference wavelength between the Floquet and the surface waves becomes longer. This necessitates using more loaded columns at higher angles of incidence, which fortunately also leads to improved performance at the lower angles of incidence. Further good news is the fact that the backscatter is somewhat lower at the higher angles of incidence than at the lower ones because the sidelobe level of the scattering pattern is lower.

4.16   EFFECTS OF DISCONTINUITIES IN THE PANELS

Small faceted radomes can be made by flat panels containing no discontinuities. Larger ones will in general be constructed of large flat panels comprised of smaller panels. A pertinent question then becomes how precise must these small panels be joined together in order to avoid excitation of surface waves.

Considering the complexity of the typical periodic surfaces used today, we must state that a precise answer to this question is not possible, nor do we need it. Here we shall limit ourselves to investigating the effect of introducing discontinuities somewhere in the flat panels.

More specifically we show in Fig. 4.30 the case shown earlier in Fig. 4.28 but where a discontinuity has been introduced in each of the two front panels by simply removing one of the unloaded columns located in the middle of the two front panels. Similarly we show in Fig. 4.31 the case where two unloaded columns have been removed from each of the side panels. We note a considerable effect when the discontinuity is at the two front panels and very minor when it is at the sides. Part of the explanation for this observation might be that the surface waves are considerably stronger in the side panels already.

Based on our observations earlier in this chapter, we may conclude that the amplitudes of the surface waves in these examples are sufficiently low not to warrant any significant radiation and thereby raise the RCS level. Unfortunately, precise numbers of the RCS level cannot be reported.

4.17   SCANNING IN THE *E* PLANE

So far in this chapter we have considered plane waves incident in the *H* plane only. In general this is the plane where the most important phenomena occurs. However, one should be cognizant of the fact that surface waves characteristic for finite structures can also exist for *E*-plane incidence. We shall explore this case in some detail in the following.

In order to make meaningful comparisons between the two cases, we shall consider an array with the same element length $2l = 1.5$ cm as in the *H*-plane case above. However, the array will be slightly modified as explained in Fig. 4.32. First we show in Fig. 4.32a the original array used for the *H*-plane case. If
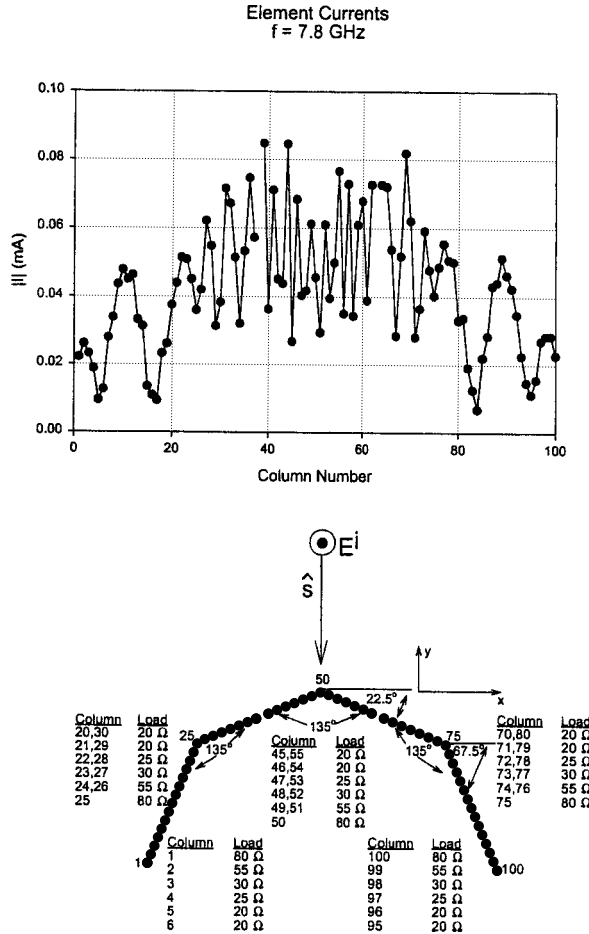
Fig. 4.30   *The effect of a discontinuity in each of the two front panels of radome in Fig. 4.28 by simply removing a complete column in the middle of each one as indicated in the figure. Note change of scale.*

we would scan this array in the E plane, we would readily observe that the first grating lobe for grazing incidence would occur at $\lambda_{G.L} = 2D_z = 3.2$ cm or $f_{G.L.} = 9.38$ GHz. Considering that the resonance frequency is around 10 GHz, this simply is too low even if surface waves typically occur at frequencies somewhat below resonance (see Sections 4.7 and 4.8).

However, early onset of grating lobes can in this case be easily prevented by interlacing the elements as shown in Fig. 4.32b. Note that array dimensions remain the same in the two cases except that adjacent columns have been shifted with respect to each other as shown.

Finally we recall that the SPLAT program is structured to have the finite dimension along the x axis and the infinite along the z axis. Thus, the array

Element Currents
f = 7.8 GHz
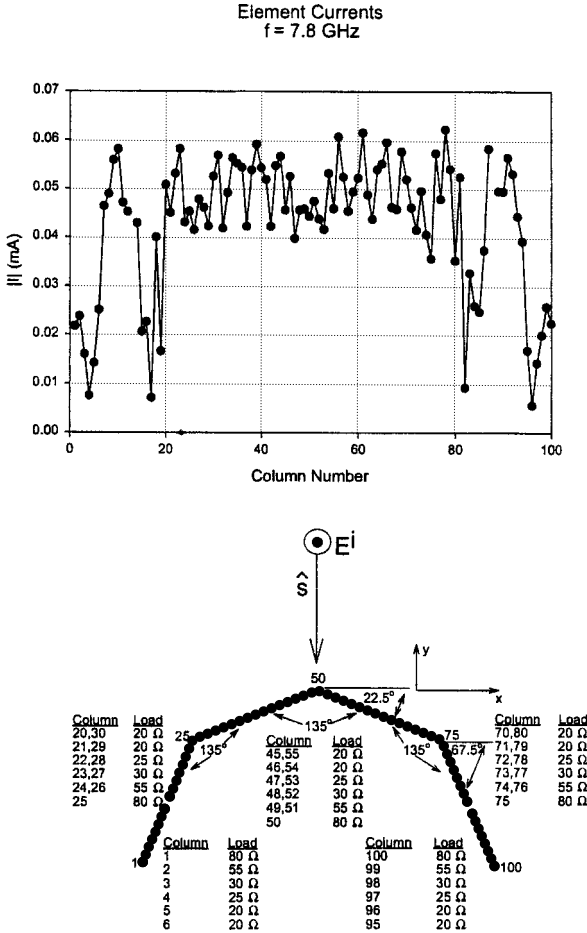
Fig. 4.31   The effect of a discontinuity in each of the two side panels of the radome in Fig. 4.28 by simply removing a complete column in the middle of each one as indicated in the figure.

in Fig. 4.32b must be rotated 90° as shown in Fig. 4.32c. Note that all array dimensions are the same in the two cases. Only the x and z axes have been interchanged. The dimensions in Fig. 4.32c will be used in the following.

We shall investigate the E-plane case analogous to the H-plane case above, namely by plotting the scan impedance from broadside ($s_x = 0$) and all the way into the "end" of imaginary space and back into real space.

A typical example of an E-plane scan impedance for an infinite array is shown in Fig. 4.33. We start at broadside at $\eta = 0°$ for $s_x = 0$ and proceed to grazing at $\eta = 90°$ for $s_x = 1$, which marks our entrance into the imaginary space. As s_x becomes larger than 1, we see that the scan impedance moves downward along the imaginary axis until it reaches its lowest level for $s_x = 1.12$ from where it starts moving upward and eventually crosses the real axis for $s_x = 1.65$. For
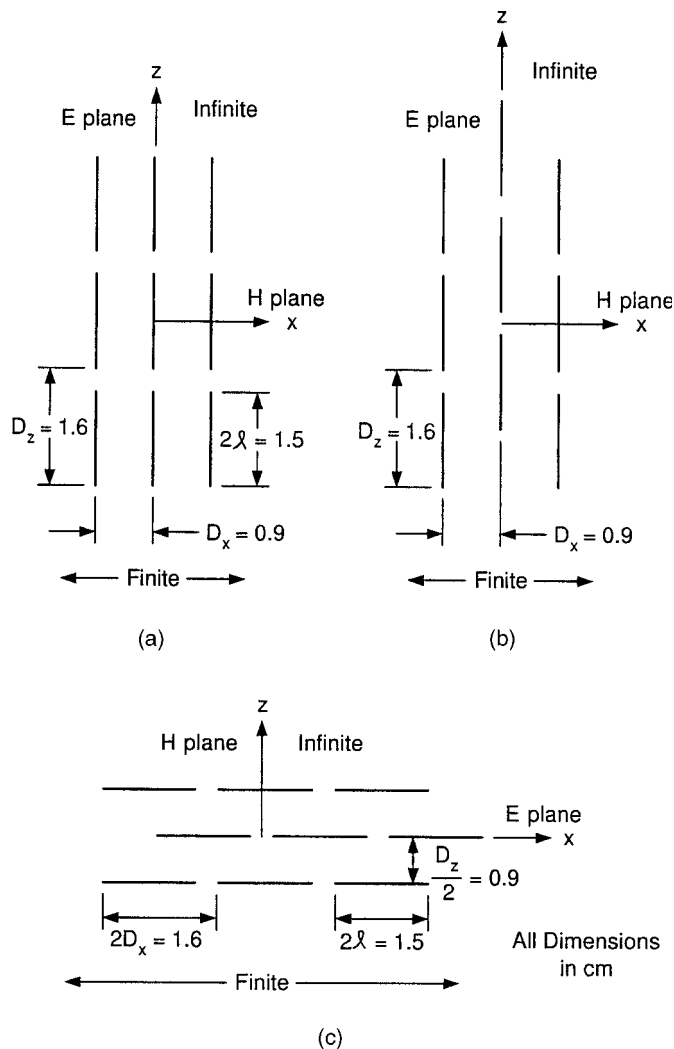
Fig. 4.32   Modification of the array when changing from H-plane to E-plane scan. (a) The original array used for H-plane scan. If we scan this array in the E plane, grating lobes will start too early, namely at 9.38 GHz. (b) By interlacing adjacent columns as shown, the onset of grating lobes can be delayed to a much higher frequency. (c) To comply with the structure of the SPLAT program the array in (b) is rotated 90° and the x and z axis interchanged as explained in the text.

$s_x = 2.08$ we reach the upper limit of the scan impedance. Increasing s_x beyond 2.08 produces the identical scan impedance on the way out of the imaginary space as on the way in until we reach $s_x = 2 \times 2.08 = 4.16$ or 0. The scan from $s_x = 4.16 - 1$ to 4.16 corresponds to $s_x = -1$ and 0; that is, the scan goes from $\eta = -90$ to $0°$ (see also Fig. 4.2).
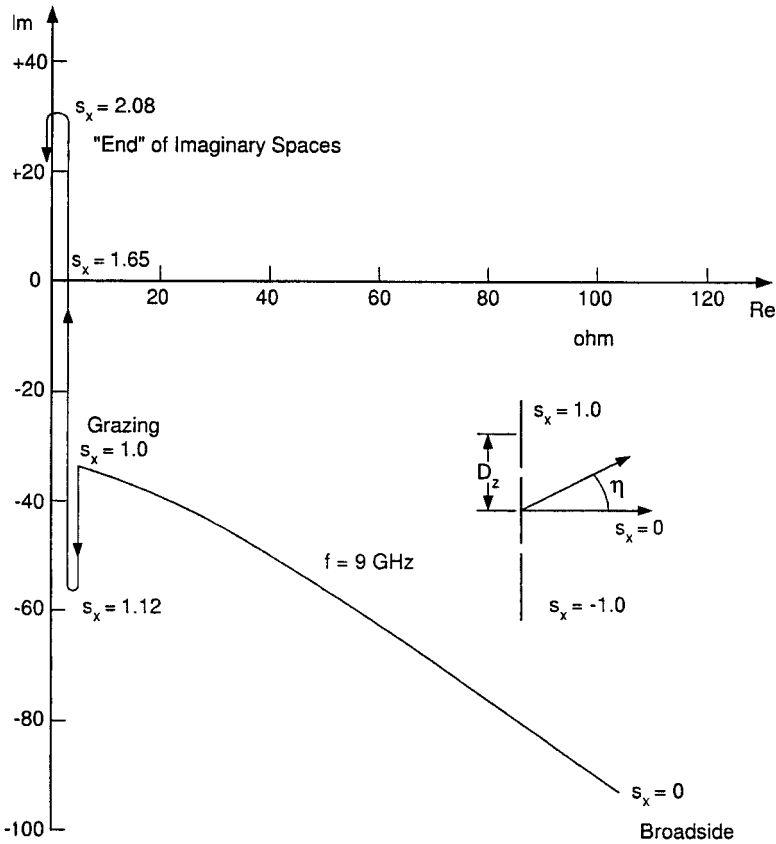
Fig. 4.33   *The scan impedance at f = 9 GHz when the array in Fig. 4.32c is scanned in the E plane. Broadside starts at $s_x = 0$ and grazing is at $s_x = 1.0$. Higher values of s_x correspond to scan in the imaginary space where the scan impedance is purely imaginary. It gets to the "end" of imaginary space for $s_x = 2.08$ from where it goes right back down the way it got in.*

The curve shown in Fig. 4.33 is an adaptation of data obtained from Janning's dissertation [77]. He used three current segments along each element since an asymmetric current distribution could be expected for *E*-plane scan. However, he also notes that good results could be obtained by using just a single current segment since the length of the elements in the present case is somewhat shorter than one-half λ.

There is a significant difference between the *H*-plane scan in Fig. 4.2 and the *E*-plane scan in Fig. 4.33—namely, that the former may only pass close to the origin for one value of s_x while the latter potentially can pass close to the origin for two values of s_x. At higher frequencies the impedance curves will move upward and vice versa at lower frequencies as shown specifically in Fig. 4.34 for the frequencies $f = 8$ GHz and 10 GHz. Obviously no strong surface wave can exist at either of these two frequencies, but at frequencies somewhere in between
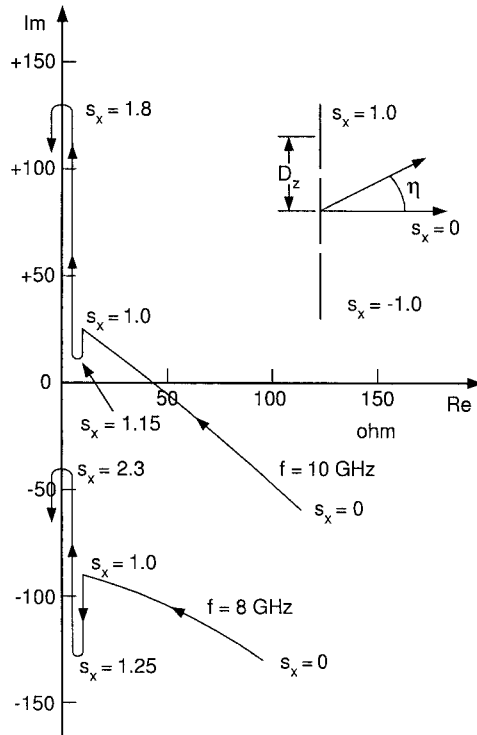
Fig. 4.34 *Same scan impedances as shown in Fig. 4.33 but at f = 8 and 10 GHz, respectively. Note how the higher frequencies move up toward the inductive region of the complex plane and vice versa for the lower frequencies. At some frequencies between 8 and 10 GHz we have the possibility to pass close to the origin once and even twice.*

we may pass close to the origin for one and even two values of s_x. That simply means that instead of one left- and one right-going surface wave we may have two left- and two right-going surface waves.

An example of actual calculated double surface waves are shown in Fig. 4.35. We clearly observe the Floquet current at $s_x = -0.707$ while we also observe a pair of right-going surface waves at $s_x = 1.015$ and 1.165 as well as left-going surface waves at $s_x = -1.015$ and -1.165. It is noteworthy that the column currents in Fig. 4.35 were produced by a simple Fourier transform of the actual calculated currents obtained directly from the SPLAT program. Thus, their validity can hardly be in doubt.[3] Therefore, even if one does not accept the physical explanation presented above, the facts speak fairly loudly. There will, however, always be those who refuse to believe anything they do not readily understand because things are explained somewhat differently than they are used to. And that is of course their right.

---

[3] The double surface waves were observed first by Janning (see his dissertation [77]) and are therefore often referred to as "Janning's Anomaly."
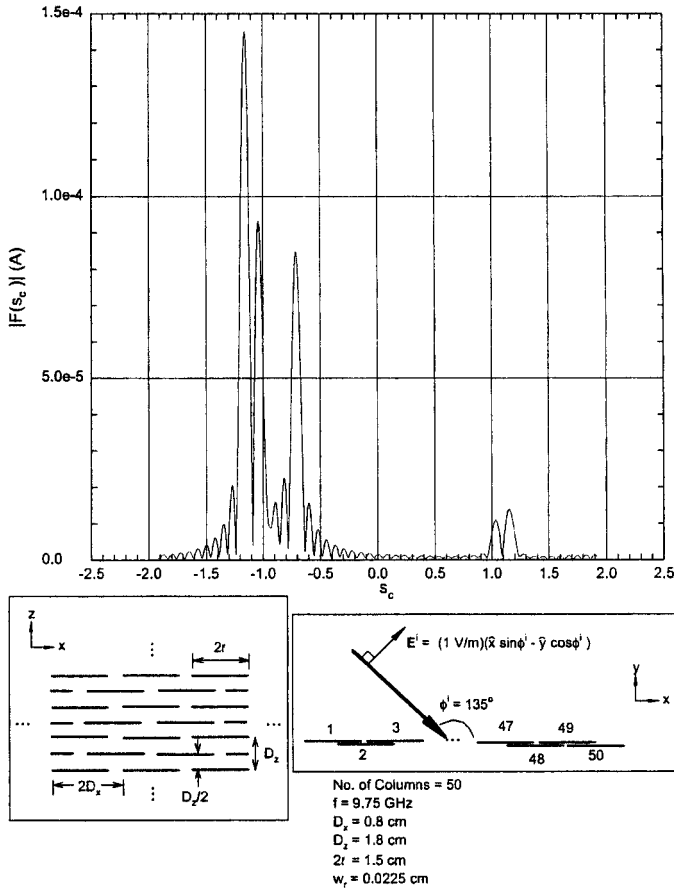
Fig. 4.35 *The column currents at f = 9.75 GHz for E-plane scan showing the Floquet currents at $s_x = -0.707$ and double surface waves at $s_x = \pm 1.015$ and $s_x = \pm 1.165$. The double surface waves were observed first by Janning (see his dissertation [77]) and are therefore often referred to as "Janning's Anomaly."*

But I would like to have these individuals explain these phenomena "their way."

4.18 EFFECT OF A GROUNDPLANE

So far we have considered surface waves only on finite periodic structures without a groundplane. When a groundplane is added to an array of dipoles, it is usually driven actively. This case is in practice somewhat different from the passive case considered above by the fact that all elements are connected to generators or amplifiers with impedances comparable to the scan impedances. As explained in Chapter 5, this leads to a highly desirable attenuation of any potential surface waves.

There is, however, a case where load resistors at each element are just not available, for example, when a slotted periodic surface is placed next to another slotted surface as is the case in a biplanar radome. In that event, surface waves can be excited on the finite slotted surface facing the incident signal while the second periodic surface essentially acts as a groundplane (at least in the frequency range where surface waves can potentially exist). Obviously the outer slotted surface does not enjoy the benefit of resistive loads connected to each slot.

The question then becomes, How will the second slotted surface affect the frequency range of the surface wave on the first?

From a physical point of view we note that the field associated with the surface wave on the latter is composed of an assembly of evanescent waves that is attenuated as we move away from the periodic structure. In fact these evanescent waves have fallen to rather low values at a distance of a quarter wavelength. Since this is about the typical spacing between adjacent slotted surfaces in many applications, we may conclude that the surface wave frequency for a single periodic surface is only lightly affected by the presence of a groundplane or a second slotted surface.

Janning examined in his dissertation [77] the effect of a groundplane upon arrays of dipoles. His approach was completely rigorous (actually he wrote a very fine dissertation that is highly recommended). His findings essentially verify the physical arguments put forth above.

4.19 COMMON MISCONCEPTIONS CONCERNING ELEMENT CURRENTS ON FINITE ARRAYS

4.19.1 On Element Currents on Finite Arrays

In Sections 4.6 and 4.7 we explained how the total currents of a finite array could be decomposed. Although the concept actually was quite simple, it often leads to some misconceptions. Some of these will be illustrated in Fig. 4.36 and discussed in the following.

In Fig. 4.36a we show the currents on an infinite array being exposed to an incident plane wave. As is well known, it results in currents of equal amplitude and phases matching that of the incident plane wave, namely based on the so-called Floquet Theorem. We next show in Fig. 4.36b how we can obtain a finite array, by superimposing two semi-infinite arrays with negative Floquet currents on the infinite array case in Fig. 4.36a. Obviously, that leads to zero current outside the finite array (exact). However, the finite array will itself have currents comprised of the original Floquet currents caused only by the incident plane wave plus some unknown currents caused only by the fields from the two semi-infinite arrays with negative Floquet currents. Note that the currents on the two semi-infinite arrays are defined very precisely as simply being equal to the negative of the original Floquet currents. This by no means implies that the currents on two semi-infinite arrays by themselves are simply of the Floquet

Infinite Array: Floquet Currents Only

(a)

Semi-Infinite Array	Finite Array	Semi-Infinite Array
Total Current =	Total Current =	Total Current =
Floquet - Floquet = 0	Floquet + ?	Floquet - Floquet = 0

(b)

Semi-Infinite Array	Finite Array	Semi-Infinite Array
Total Current =	Total Current =	Total Current =
Floquet + ?	Floquet – Floquet = 0	Floquet + ?

(c)

Semi-Infinite Array	Finite Array	Semi-Infinite Array
Total Current = 0	Total Current =	Total Current = 0
	Floquet	

(d)

Scenario (d) is possible only by feeding the
elements from constant current generators

Fig. 4.36   Some interesting finite and semi-infinite array configurations. (a) The amplitudes of the column currents on an infinite array being exposed to an incident plane wave. Consists of Floquet currents only. (b) Creating a finite array is done by adding two semi-infinite arrays with negative Floquet currents (exact) outside the finite array. The new currents in the finite array are complicated (see text). (c) Alternatively, the currents on two semi-infinite arrays can be obtained by superimposing a finite array with negative Floquet currents only upon the infinite array in (a). The new currents in the semi-infinite arrays are complicated (see text). (d) A finite array with Floquet currents is possible only when feeding the elements from constant current generators. An incident plane wave induces a voltage as a constant voltage generator and can therefore not produce Floquet currents only. The currents are then determined as in case (c).

type when exposed to an incident plane wave. In fact, this case is illustrated in Fig. 4.36c. Here a finite array with negative Floquet currents are superimposed on the original infinite array, case Fig. 4.36a. There are now no currents between the two semi-infinite arrays, while the currents on these consist of the original

Floquet current caused by the incident plane wave plus currents induced by the fields from the finite array between them and with negative currents.

Note again that the currents on neither the finite arrays in Fig. 4.36b nor the two semi-infinite arrays in Fig. 4.36c will in general ever consist of merely the Floquet currents. In fact, a finite array with only Floquet currents is shown in Fig. 4.36d. The only way a finite array can have constant element currents is by feeding them from constant current generators. While this is possible when feeding a finite structure as a phased array from man-made generators, an incident plane wave will merely induce a voltage in each element and not a constant current.[4] The fact that many researchers assume constant currents in finite arrays when exposed to an incident plane wave is simply an approximation that leads to erroneous conclusions. These cannot be remedied by application of more or less elaborate mathematical manipulations like, for example, Poisson's sum formula adapted to semi-infinite arrays with constant current. The starting point is simply too gross an approximation to obtain meaningful insight into a much more complex problem.

We finally remind the reader that the discussion above merely serves the purpose of explaining the mechanism of finite arrays. The actual decomposition into Floquet and surface wave currents as well as end currents is done by applying a Fourier analysis of the actual calculated currents obtained from the SPLAT program. Thus, whether one accepts the explanation above or not, the results speak for themselves.

4.19.2   On Surface Waves on Infinite Versus Finite Arrays

In this chapter much attention has been focused on surface waves that can exist only on finite arrays. The reactions to these findings are often sharply divided. Some deny that they actually exist. Other feel intuitively: "Yes, of course they can exist. But they will be there even on an infinite array, so why make all that fuss out of finite arrays?"

Although an extensive discussion of this subject was given in Section 4.6, it is nevertheless a fact that many readers do not quite understand our argument or simply do not have sufficient time to digest it. They would much prefer the following four-sentence contradiction.

Let us assume that a surface wave with a phase velocity depending only on the infinite structure was indeed present. Since the phase velocity of the Floquet currents depend only on the angle of incidence, the two waves would produce an interference wave with a wavelength unrelated to the periodicity of the array as shown, for example, in Fig. 4.19a. That would violate Floquet's Theorem, which is valid for an infinite array only, not a finite. Thus, the new kind of surface wave can exist only on the finite array.

---

[4] Only in the infinite array case is it immaterial how the elements are fed. Whatever the type of generator, we will always obtain merely Floquet currents.

4.19.3   What! Radiation from Surface Waves?

In our EM upbringing we have been inundated with numerous "facts" of life. One of these is, Surface waves do not radiate!

We can indeed agree with this "theorem," but only if the surface wave is attached to an infinite, straight structure. This point is stated very clearly in the discussion associated with Fig. 4.2. However, as also indicated in the same figure, we do indeed experience radiation when the periodic structure is finite. This phenomena is often interpreted as radiation emanating exclusively from the ends of the periodic structure while nothing comes from the rest of the structure. This is an observation, not an explanation. Even if it appears to come from the extremities of the structure, we should never lose sight of the fact that EM fields originate from electric and/or magnetic ($\overline{m} = \overline{E} \times \overline{n}$) currents. Thus, the total radiation from a finite periodic structure is obtained by integration of the currents present on the *entire* structure completely analogous to a classical antenna problem. See Section 4.8 for details.

However, once the total radiation is determined, it is of course a simple matter to assume that the radiation emanates entirely from the ends of the structure and then obtain some magic coefficients that potentially could be labor-saving, was it not for the fact that these are not invariant but change considerably with frequency and angle of incidence (see Section 4.9).

Thus, these "magic coefficients" should be traded among scientists with great reservation. And not like small boys trade baseball cards!

4.20   CONCLUSION

Much of the spotlight in this chapter has been focused upon surface waves on passive periodic structures. It appears that at this point in time we have two distinct groups, one of which is associated with the presence of a stratified medium placed in the immediate neighborhood of the periodic structure. It always requires a stratified medium to exist but is independent upon whether the structure is finite or infinite. It readily shows up in programs based on the infinite array approach like, for example, the PMM program.

The other group can exist whether a dielectric is presented or not, but the structure must be finite. Thus, it shows up only in programs based on finite array theory like, for example, the SPLAT program and not when using the PMM program.

The first type (Type I) can be viewed merely as grating lobes trapped inside the stratified dielectric medium. Therefore they typically occur at frequencies above resonance, namely such that grating lobes has started to emerge inside the stratified medium.

In contrast the second type usually occurs only in a band of frequencies considerably below the resonance frequency, like 20–30% for *H*-plane scan and 10% for *E*-plane scan and only when the interelement spacing is less than $\lambda/2$.

Both types can radiate and thereby lead to enhanced scattering. They are consequently in general not very desirable.

The first type can usually be avoided by simply making the interelement spacings sufficiently small in terms of wavelength. This approach usually leads to periodic structures of superior stability of the resonance frequency with angle of incidence. Thus, there is no conflict here.

The second type (Type II) is usually controlled by resistively loading the elements in one or more columns located at the edge of the finite structure. It is also possible to lightly load all elements in the entire periodic structure; however, this approach leads to reflection and transmission loss and is therefore in general not recommended (however, when dealing with active surfaces rather than passive ones, it is OK; see Chapter 5).

An important application of finite flat panels is for making faceted radomes. They must be treated at the edges resistively in order to attenuate the surface waves. Otherwise the RCS of such radomes will be larger than expected (in fact, this was how the presence of surface waves was first suspected).

Large faceted radomes are often made by joining smaller flat sections into larger flat sections. We demonstrated that the grooves between panels must be done very carefully in order not to create additional surface waves.

If the radome is curved rather than flat, there will be a natural attenuation due to shedding of energy along the surface. Since many radomes and dichroic surfaces in use today are in fact curved, this is probably the reason that this new type of surface wave has gone largely unnoticed.

PROBLEMS

4.1 The elements in Fig. 4.16 are encapsulated in dielectric tubing with wall thickness equal to the wire diameter and relative dielectric constant equal to 3. Without actually solving the problem, estimate and explain what will happen to the impedance curves in Fig. 4.16.

How will the frequency of the surface waves change?

This encapsulation can actually be done in the SPLAT program as written by Usoff [24].

4.2 Instead of encapsulating the elements in dielectric tubing, embed the elements in a dielectric slab (finite, please!) with a total slab thickness equal to the diameter of the dielectric tubes.

How will the new surface wave frequency compare with the values obtained in Problem 4.1?

To the best of the author's knowledge, this problem has not been solved rigorously for the finite dielectric slab.

If anyone out there pulls it off, I definitely would like to hear about it!

4.3 In this chapter we saw several examples where a finite periodic structure exposed to an incident plane wave of oblique angle of incidence could, due to surface waves, exhibit a backscatter several decibels higher than expected when based on simple Floquet currents only.

By inspecting several calculated bistatic scattering patterns in this chapter, discuss the loss of the reflection coefficient in the bistatic direction. Is this problem serious?

Similarly, if we instead consider an array of slots, discuss whether the loss in transmission coefficient in the forward direction would be of great concern.

<div align="right">*5*</div>

Finite Active Arrays

5.1 INTRODUCTION

In the previous chapter we studied surface waves on passive structures as for example finite FSSs. They were excited by an incident plane wave. We observed that a finite FSS in addition to the Floquet currents excited directly by the incident plane wave could also support surface waves. These would radiate and thereby lead to an increase in the scattered field; that is, the RCS could be larger than expected. The scattered field associated with the surface waves could be significantly reduced by resistively loading one or more columns at the edges of the finite FSS. This approach would leave the Floquet currents in the rest of the FSS unaffected; that is, the transmission and reflection properties of the FSS were basically left intact.

In this chapter we shall investigate the effect of surface waves on active periodic structures—like, for example, finite arrays. The most significant difference between the two cases is that while the first is excited by an incident plane wave, the second either is excited by a generator or is delivering the incident energy to a conjugate-matched amplifier, not just a reactive load. The important point here is that the generators as well as the amplifiers have impedances with a significant resistive component connected to the terminals of each element. This resistive component will as shown in Fig. 1.5a exhibit a significant attenuation on any potential surface wave. In fact, the amplitude of the surface waves on an active array is typically so low that the radiation from this component is of no great concern. However, as discussed in Section 1.4, even a small

amount of surface waves leads to some variation of the scan impedance of the individual elements. Thus, since it is desirable to use the same matching network for each element, precise matching can be a problem. This mismatch is typically so small that it does not adversely affect the received power. However, it may present a problem, if we are concerned with the RCS of the array as discussed in Chapter 2.

Another difference between the passive and active cases is worth mentioning. The first typically is comprised of FSS arrays with either slot and/or wire elements. They may be located in a stratified medium, but they will in general not directly contain a groundplane. In contrast, the active array will usually consist of a single array of either the wire or slot type, and they may also be located in a stratified medium but they are almost always provided with a groundplane.

The groundplane serves essentially two purposes. First of all it ensures that we have only a single mainbeam, not two. Second, as discussed in Chapter 2, the groundplane can lead to a significant reduction of the RCS of an active array. However, as discussed in Section 2.9, the area of the groundplane relative to the area of the active dipoles is crucial from an RCS point of view. Thus, the exact modeling of the finite groundplane becomes important. We shall discuss this issue in the next section.

5.2   MODELING OF A FINITE × INFINITE GROUNDPLANE

Our finite × infinite groundplane is comprised of an FSS with an area approximately matching the area of the active elements. It resonates at the center frequency, yielding a reflection coefficient equal to −1 like a perfect groundplane; however, some leakage will take place at other frequencies. Thus, it should be designed to have as broad a bandwidth as possible, or, alternatively, it may be retuned to other frequencies as deemed necessary.

Examples of FSS groundplanes are shown in Fig. 5.1. More specifically, we show a typical practical version in Fig. 5.1a. Each column consists of closely spaced straight wire sections interlaced as shown. Associated with the central part of each wire section is some inductance and associated with the small gap between them is some capacitance. Thus, the equivalent circuit will look approximately as shown in Fig. 5.1b. At resonance the reactance of such s sheet is zero; that is, it will act as a groundplane as noted already above.

Alternatively, the practical layout may also be executed by using actual lumped elements as shown in Fig. 5.1c. In fact, the inductances can consist of straight wire sections as shown in Fig. 5.1d. Similarly the capacitors may be partly lumped. They are simply in parallel with the end capacitors between adjacent element tips. This capacitance can be much more significant than many people expect (for further comments concerning this subject see references 89 and 90). Thus, the lumped capacitors act more like a fine-tuning device. See also Section 6.4.
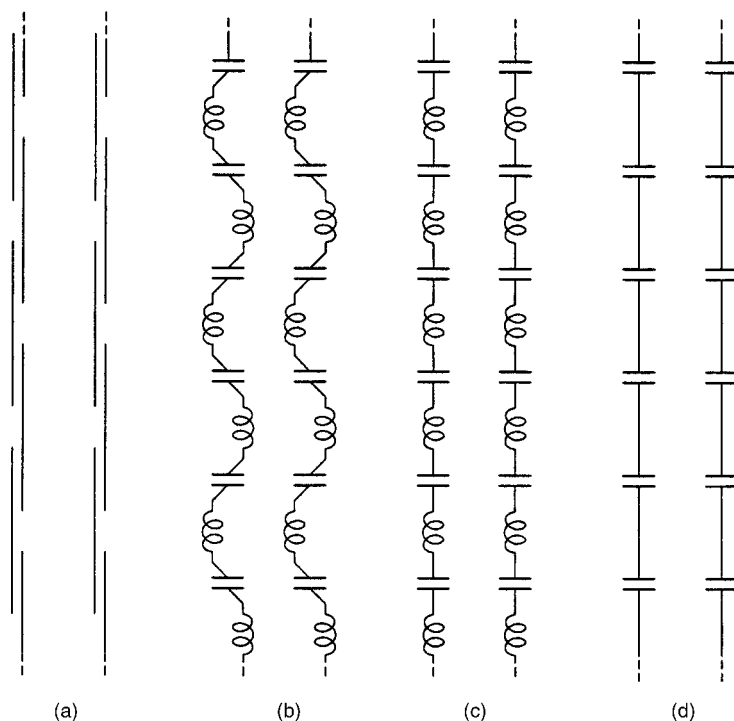
Fig. 5.1   Modeling of the reflecting groundplane by using FSS's of various forms.

5.3   FINITE × INFINITE ARRAY WITH AN FSS GROUNDPLANE

In Chapter 2 we discussed the backscatter from large arrays in general with-
out considering the possible effect of surface waves or edge scattering. We shall
investigate both of these phenomena in this chapter. As a simple but very instruc-
tive introduction to the latter, let us now consider the bistatic scattering pattern
for a finite × infinite array of active dipoles backed by a finite × infinite FSS
"groundplane" of the type discussed in Section 5.2. It illustrates many of the
ideas and concepts discussed in Chapter 2. The calculated curves were obtained
from the SPLAT program as were the curves in Chapter 4.

A top view of the array layout with the FSS groundplane is shown in the
insert of both Figs. 5.2 and 5.3. It is comprised of 20 columns of active elements
and twice as many FSS elements. The reason for more passive than active ele-
ments is simply to make the FSS groundplane more broadbanded. (In general,
the closer the elements, the greater the bandwidth; cf. the "Gangbuster" array in
reference 91.)

Putting the FSS elements closer together raises the resonance frequency some-
what. Since the elements cannot be made longer without disturbing the period-
icity, all the passive elements have instead been loaded with $Z_L = j208$ ohms
(*note*: Here we do not use interlaced elements of the type shown in Fig. 5.1a, just
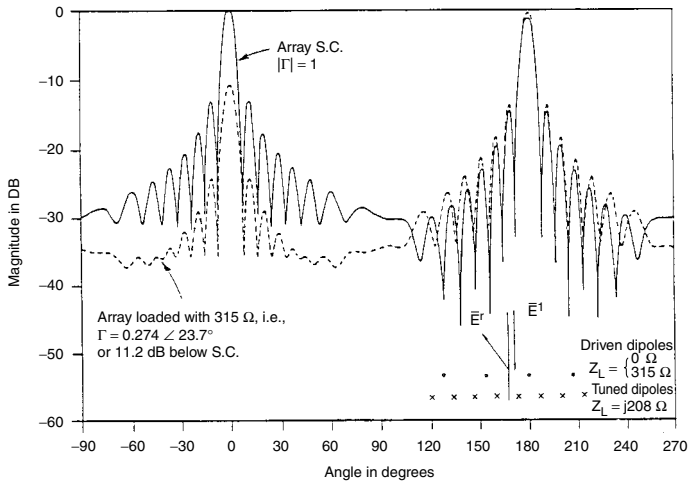
Fig. 5.2 Calculated bistatic scattered field obtained from the SPLAT program of a finite array of dipoles backed by a finite FSS ''groundplane'' for an incident plane wave arriving at broadside (0°). Two curves: One for the driven dipoles short-circuited (S.C.) and another when loaded with $Z_L = 315$ ohms.
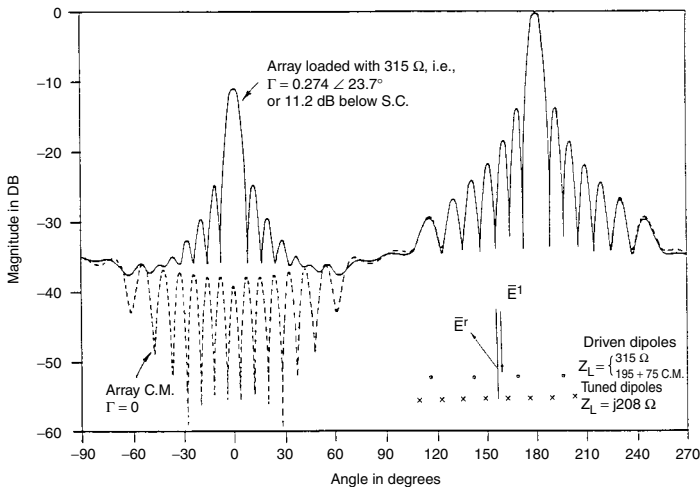
Fig. 5.3 Calculated bistatic scattered field of a finite array of dipoles backed by a finite FSS ''groundplane'' for an incident plane wave arriving from 0°. Two curves: One when loaded with $Z_L = 315$ ohms (like Fig. 5.2) and another when conjugate-matched. Obtained from the SPLAT program.

single straight elements). Actually this kind of tuning does not enhance the bandwidth, but we are here at present only concerned with one frequency (obviously these curves were obtained early on before we had reached our present level of sophistication).

A plane wave is incident broadside to this array—that is, at $0°$. The bistatic scattered field is obtained from the SPLAT program in the entire range from $-90°$ to $270°$. Furthermore, we show the bistatic fields for various load conditions of the active elements.

First in Fig. 5.2 we show two curves, one where the active elements are short-circuited and denoted S.C. and another where $Z_L = 315$ ohms. Note that for $Z_L = 0$ the backscattered field looks like it is coming from a groundplane the size of the array. Furthermore, for $Z_L = 315$ ohms and with $Z_A = 195 - j75$ ohms we obtain a reflection coefficient

$$\Gamma = \frac{Z_L - Z_A}{Z_L + Z_A} = \frac{315 - 195 + j75}{315 + 195 - j75} = 0.274\angle 23.7°,$$

or $11.2\,$dB below the short-circuited load as actually observed in Fig. 5.2.

Furthermore, in Fig. 5.3 we show the bistatic scattered field when $Z_L = 195 + j75$ ohms—that is, conjugate-matched. We also repeat the case $Z_L = 315$ ohms to facilitate comparisons.

The conjugate-matched case is particularly interesting. According to Section 2.9 and more precisely Fig. 2.12, Example II, we should expect the backscattered field to be approximately equal to zero. Inspection of Fig. 5.3 reveals a level of $\sim$38 dB below a flat plate and not ∞ dB. In the next section we will show that this discrepancy is caused by an edge effect. We shall in fact devise an approach that not only very precisely pinpoints where the excess scattering is coming from but also how to alleviate it. Finally we further note in Figs. 5.2 and 5.3 that the forward-scattered field at $\pm 180°$ is practically independent of the load impedance Z_L of the active elements as was predicted in Section 2.9.

This is also an excellent place to remind the reader that the *total* field in the forward direction is the sum of the incident field and the forward-scattered field. The former is merely a plane wave with an amplitude that is conceptually independent of its distance from the array in the forward direction. However, the latter will, as all fields scattered by an object of finite extent, be attenuated as we move away from the antenna. Thus, although the two components cancel each other approximately right behind the groundplane and produce "darkness" as one would expect, the incident field will soon dominate the scattered field. The result is that the "shadow" from the antenna will soon be blurred and eventually practically disappear. In other words, beating the stealth concept by observing the forward-scattered field might not be as easy as some individuals like to think.

5.4   MICROMANAGEMENT OF THE BACKSCATTERED FIELD

We are now going to show how we can pinpoint exactly any scattering anomalies in an array and how to alleviate it. To illustrate our approach, we are again going to consider a finite array of active dipoles backed by a finite FSS groundplane as shown in Fig. 5.4, top. It is being exposed to an incident plane wave at broadside.

Modeling and Approach
Two-Dimensional
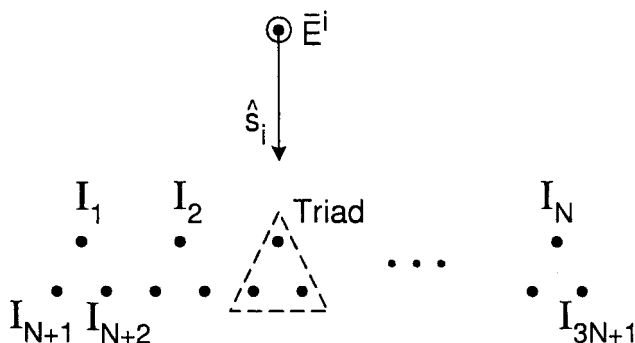
The finite groundplane is modeled by a
finite reflecting FSS (see Fig. 5.1)

Approach

1. Calculate all element currents including all
   mutual impedances (rigorous and exact).

2. Calculate all fields from each triad (see
   above figure) and plot in the complex plane;
   see Fig. 5.6.

Fig. 5.4   *Modeling of a finite array with a finite groundplane.*

We start by calculating all column currents in the *entire* array configura-
tion. Note that we take into account all mutual impedances between all wire
segments; that is, the calculated currents are exact within the accuracy of the
Method of Moments.

Most readers would at this point be tempted to obtain the entire scattered field
by simply adding the fields reradiated by each wire section. Although this would
be technically correct, it is precisely what not to do. Rather, the scattered fields
should be grouped together in a meaningful way.

More specifically, for the case shown in Fig. 5.4 we add the fields from each
active column to the fields from the two passive columns located right behind it

Radiation and Scattering Pattern for a Typical Triad
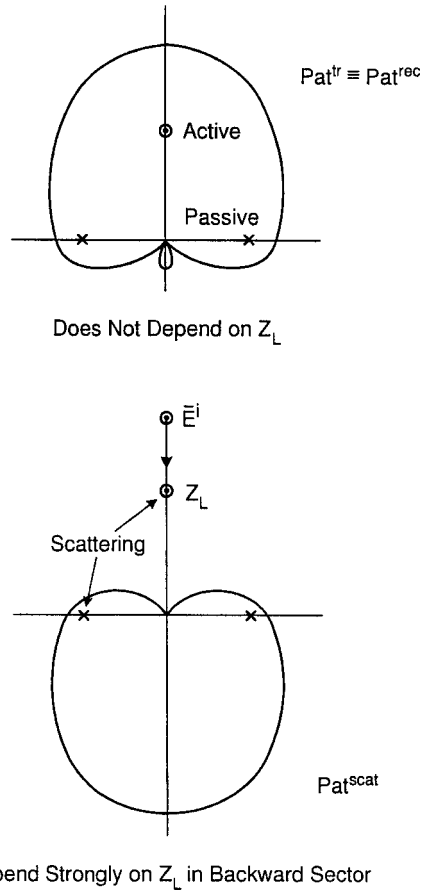
Fig. 5.5 Top: Typical transmitting or receiving pattern for a typical triad comprised of an active column of dipoles and two columns of passive FSS elements. Bottom: Typical scattering pattern from the same triad as above.

(we call such a configuration a triad). The reason for combining the fields in that way is illustrated in Fig. 5.5. At the top we show a typical radiation pattern for a single active column backed by two passive columns. This radiation pattern is similar to a cardioid pattern with the main beam pointing upward. At the bottom we show the scattered pattern for the same configuration when exposed to a plane wave incident from above. Note that the mainbeam is pointing downward. It is, however, not merely equal to the transmitting pattern rotated 180°. In particular we note that the transmitting pattern is completely independent of the load impedance Z_L while the scattering pattern in the backward sector is highly dependent on Z_L (see also the discussion in Section 2.9 as well as Problem 2.6).

Analyzing the Backscatter from a
Finite Array
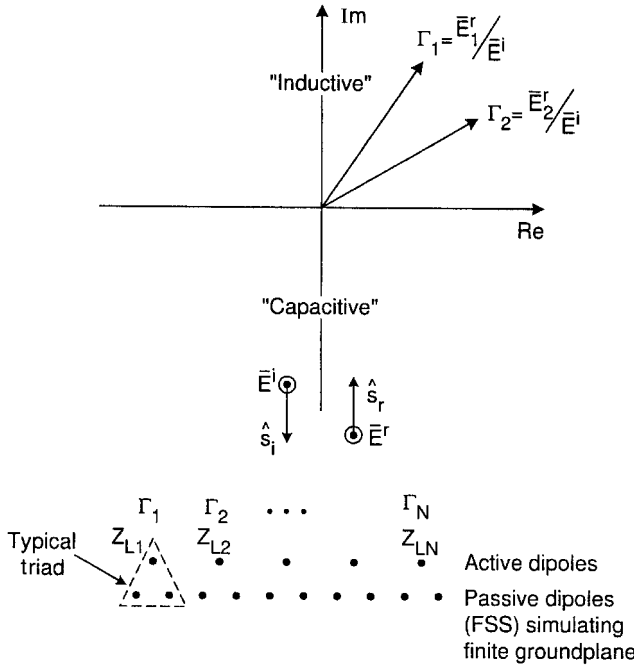
The individual loads Z_{Ln} can be adjusted to yield
$\Gamma_n \sim 0$ individually; see Fig. 5.8.

Fig. 5.6   A plane wave incident upon a finite array of triads produced the backscattered signals E_n^r. By plotting $\Gamma_n = E_n^r/E_i$ in the complex plane, each triad can be analyzed and adjusted separately.

Let us denote the field from each triad by $\overline{E}_n^r$. We then define the reflection coefficient for each triad as $\Gamma_n = E_n^r/E_i$, where E_i denotes the incident field. The "trick" is now to plot Γ_n in the complex plane as shown, for example, in Fig. 5.6. Note that the Γ_n's are different for each triad because Floquet's Theorem is no longer valid for a finite array.

Our next step is inspired by the Smith chart. (Some readers are happy to see this ingenious device "back in" in our curriculum. It was never "out" as far as I am concerned. See Chapter 6 and Appendices A and B and you will understand my devotion.).

Consider an infinite array of active dipoles loaded with Z_L and backed by an infinite FSS groundplane as shown in Fig. 5.7, bottom. Let us plot the reflection coefficient $\Gamma = \overline{E}^r/\overline{E}^i$ for the infinite array in a complex plane as, for example,

Backscatter from an Infinite Array
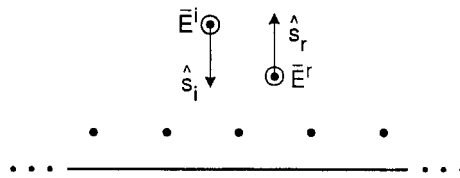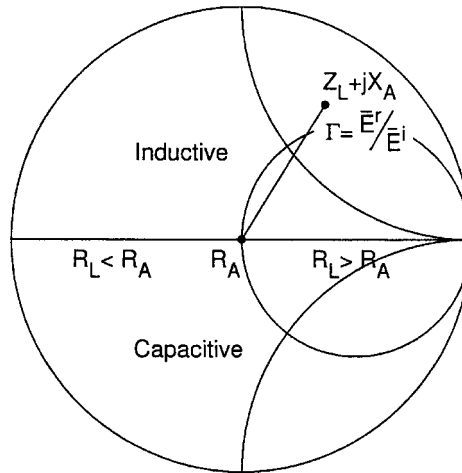
By adjusting Z_L we can obtain $\Gamma \sim 0$, i.e.,

$$\sigma_{tot} \sim 0.$$

Advantage of using Smith chart: It tells us
HOW to adjust Z_L to obtain $\sigma_{tot} \sim 0$.

Fig. 5.7   A plane wave incident upon an infinite array of active elements in front of an infinite groundplane. By plotting the reflected field in a complex plane (in this case a Smith chart) we can adjust the load impedances Z_L of the active dipoles such that the reflected field disappears in the backscatter direction.

a Smith chart normalized to R_A as shown in Fig. 5.7, top. The complex reflection coefficient Γ is then determined by the location of $Z_L + jX_A$ as shown in Figs. 2.3 and 2.6. (In fact, if $jX_A = 0$, the reflection coefficient Γ reduces to the ordinary reflection coefficient as explained in Fig. 2.3.)

The beauty of the Smith chart (one of many) is now that the location of $Z_L + jX_A$ will tell us how to adjust Z_L to obtain $\Gamma = 0$. For example, if $Z_L + jX_A$ is located in the upper right half of the Smith chart as shown in Fig. 5.7, we know

immediately that the inductance jX_L should be reduced and so should R_L in order to minimize $|\Gamma|$. The idea is now that we can at least in principle use a similar technique to reduce the individual reflection coefficients $|\Gamma_n|$ shown in Fig. 5.6.

However, while the adjustment of Z_L can be done precisely in the Smith chart, this is not quite the case for $|\Gamma_n|$ shown in Fig. 5.6. One reason being that the field reflected from the infinite array is a simple plane wave (we assume the evanescent waves have died out), while the fields from the triads are a combination of Hankel functions. Should we call this new chart a Hankel chart? Somebody could work it out and cover himself with fame and glory. See also comments in Section 5.8.
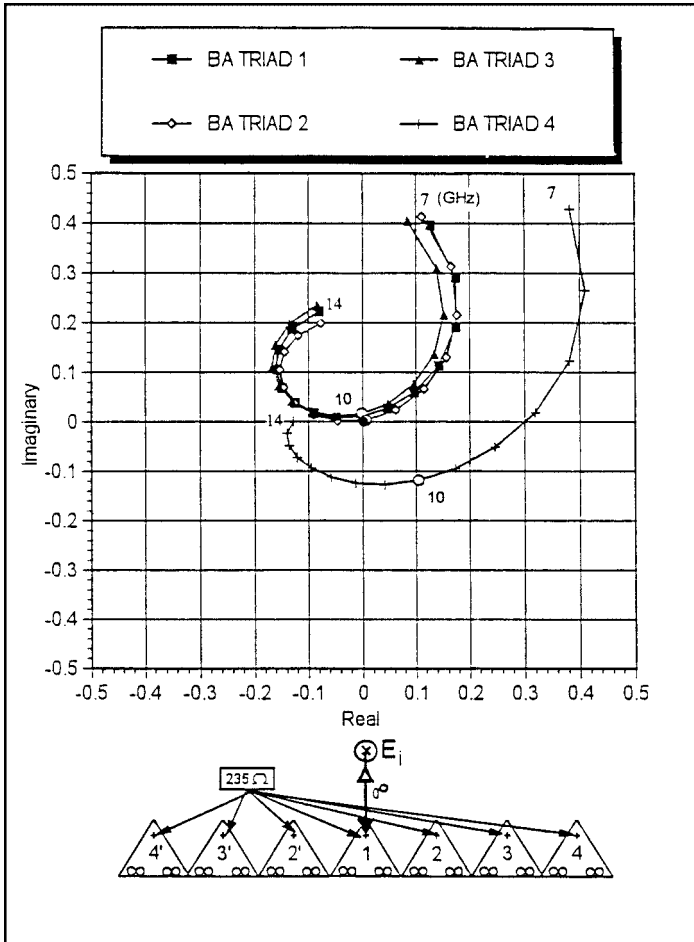
Fig. 5.8 The backscattered fields from a finite array of 7 triads plotted in the rectangular complex plane. All active dipoles are loaded with the same impedance equal to 235 ohms. This value leads to nearly no backscatter for all the triads at f = 10.0 GHz except for the edge columns 4 and 4'. By adjusting the loads for these two separately, the backscatter from these could also equal zero. (From Johnson [75].)

A typical plot of the fields from 7 triads is shown in Fig. 5.8. We immediately note the two most important problems in a finite array:

1. The fields scattered from each of the two outer columns (denoted 4 and 4′) are different and for the load impedance $Z_L = 235$ ohms larger than all the other triads at 10 GHz. However, if we change the load impedances for each of the outer columns by adding a little inductance and by lowering the real part, we can reduce the edge scattering that is so prominent in Fig. 5.3 for conjugate match. (Inspection of the scattering pattern in the figure with fine lobes of almost equal amplitudes is a strong indication that the scattering does originate on the edges.)

2. The second problem is somewhat more intriguing, namely the fact that the scattering from the various triads varies erratically ("jitters").

In principle we could match the individual columns with the proper but different load impedances and obtain zero total scattering. However, this approach is deemed too cumbersome and impractical.

We would prefer to solve this problem in a more elegant and universal way. We suspect that the impedance variation from column to column is related to surface waves (or at least a degenerate form of a surface wave). In the next sections we shall identify the problem and show how to reduce their effect.

5.5 THE MODEL FOR STUDYING SURFACE WAVES

We shall next study surface waves on active arrays with a finite FSS groundplane. Our model will be similar to the one used in the previous section—except that in order to properly study surface waves, the model must be considerably wider.

The fundamental problem is now that all finite periodic structures may exhibit strong presence of surface waves at least at some frequencies as discussed in Chapter 4. We may envision that the finite FSS groundplane alone shows surface waves in one frequency band and the active array possibly in another. However, when the active array is placed adjacent to the FSS groundplane, we would expect both of these frequency bands to change and, possibly, to degenerate into a single frequency band. From a practical point of view, it is of course the surface waves on the combined structure that are most important.

Although it is feasible that an actual practical array could be built as modeled here namely by using a finite FSS groundplane, it is more likely that the groundplane will consist of just a finite piece of perfectly conducting sheet metal with holes so small that no surface wave can exist. In that case the possible surface waves will depend only on the active array elements and is therefore less complex. More specifically, if we can learn to control the surface wave phenomena on arrays with finite FSS groundplanes, there is good reason to expect that we can do the same when using a finite perfectly conducting groundplane.

Calculating the effect of a finite conducting groundplane may not be as simple as some individuals think. Merely using the scattering mechanisms of a semi-infinite groundplane may be jeopardized by the presence of the active array (simply "trading" these coefficients as baseball cards should not be encouraged). Also, use of plates as is ordinarily done in the Method of Moments often leads to leaks behind the groundplane which are avoided completely at the resonant frequency of the FSS groundplane.

Thus, in the following we shall use the finite FSS groundplane and accept the greater complexity due to the more intricate presence of surface waves.

In the next section we shall examine these surface waves in more detail and also ways to alleviate them.

5.6 CONTROLLING SURFACE WAVES ON FINITE FSS GROUNDPLANES

In this section we shall investigate surface waves on finite FSS groundplanes without any active dipoles. Typically they are comprised of interlaced wire elements each of length 1.35 cm as shown schematically in the insert of Fig. 5.9, bottom. The frequency scattering diagram is also shown in Fig. 5.9, top, for angle of incidence equal to 45°. To the left we show the frequency range 2.0–6.7 GHz, and to the right we show the range 6.8–12.0 GHz. It is obvious by inspection that surface waves are significant in the lower frequency range but not in the upper range, in accordance with our observations in Chapter 4, Section 4.9.3.

By inspection of Fig. 5.9 we chose the frequency 5.7 GHz (more or less arbitrarily) as a representative of a range of frequencies with strong surface waves. The actual column currents obtained from the SPLAT program are shown in Fig. 5.10. Indeed, we observe very strong surface waves at that frequency.

We shall attempt to suppress these surface currents similarly as we did in Chapter 4, namely by loading the edge columns only with resistors located at the center of each element. Two examples are shown in Figs. 5.11 and 5.12, respectively. In the first case we have loaded the three outermost columns with the load resistors 200, 100, and 50 ohms, respectively, as shown in the insert of Fig. 5.11, bottom. Similarly, the example in Fig. 5.12 has the seven outermost columns loaded with resistors as indicated in the figure. In the following we shall refer to these as the lightly and heavily loaded cases, respectively.

We observe a significant reduction of the surface waves as compared to the "wild" case shown in Fig. 5.10, in particular for the heavily loaded case shown in Fig. 5.12. Neither of these two cases represents in any way the optimum. Undoubtedly, further improvement is possible. However, we should not lose sight of the fact that our "final" product in reality is the finite FSS groundplane including the active loaded columns in front. Since such a combination can be expected to have strong surface waves in a frequency range somewhat different from what we saw in Figs. 5.9 and 5.10, we shall postpone further investigation of this subject until the next section.
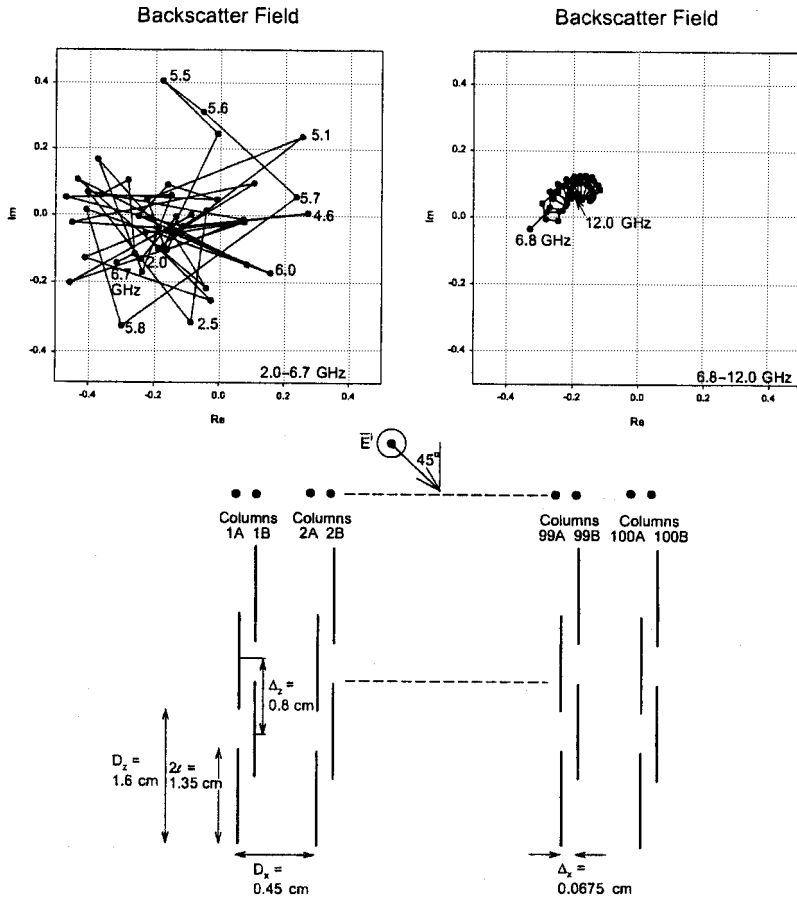
Fig. 5.9 The field reflected from the finite FSS array shown in the middle and plotted in the complex plane as a function of frequency (scattering diagram). Top left: The frequency range 2.0–6.7 GHz where surface waves are prevalent. Top right: The frequency range 6.8–12.0 GHz shows no sign of strong surface waves.

Finally we should remind ourselves that a practical antenna probably will be made with a groundplane comprised of a finite perfectly conducting groundplane rather than using a finite FSS (except perhaps at the edges; see later). Thus, in that event our interest in surface waves associated with the finite FSS groundplane has been reduced to be of merely academic interest.

5.7 CONTROLLING SURFACE WAVES ON FINITE ARRAYS OF ACTIVE ELEMENTS WITH FSS GROUNDPLANE

In the previous section we found surface waves on the FSS groundplane most prevalent below 6.7 GHz. Let us now examine the more complicated problem
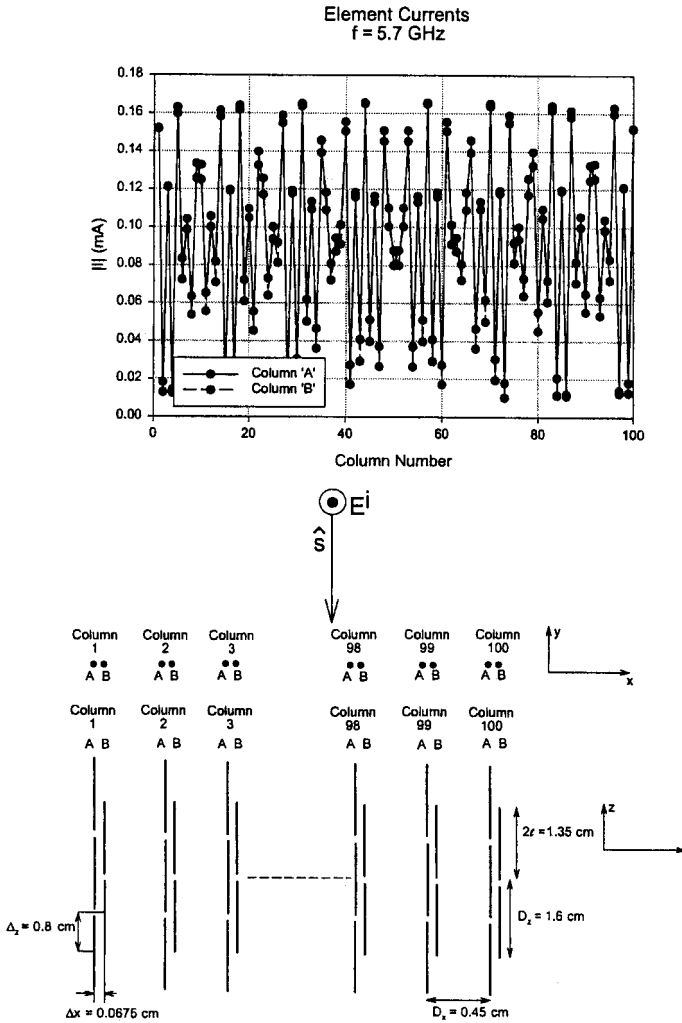
Fig. 5.10 The element currents (column) for the finite FSS array without loading shown at the bottom. Incident field at broadside. Frequency 5.7 GHz where strong surface waves are present.

where our structure consists of the same finite FSS groundplane as above but with active elements placed in front of it.

This structure will be tested for surface waves at three frequencies: the same low frequency as before, $f_L = 5.7$ GHz; a frequency in the middle, $f_M = 7.8$ GHz; and the highest frequency, $f_H = 10$ GHz.

5.7.1 Low Test Frequency $f_L = 5.7$ GHz

We show in Fig. 5.13 the column currents on the lightly loaded FSS groundplane shown earlier in Fig. 5.11. The active elements are loaded with $R_L = 100$ ohms,
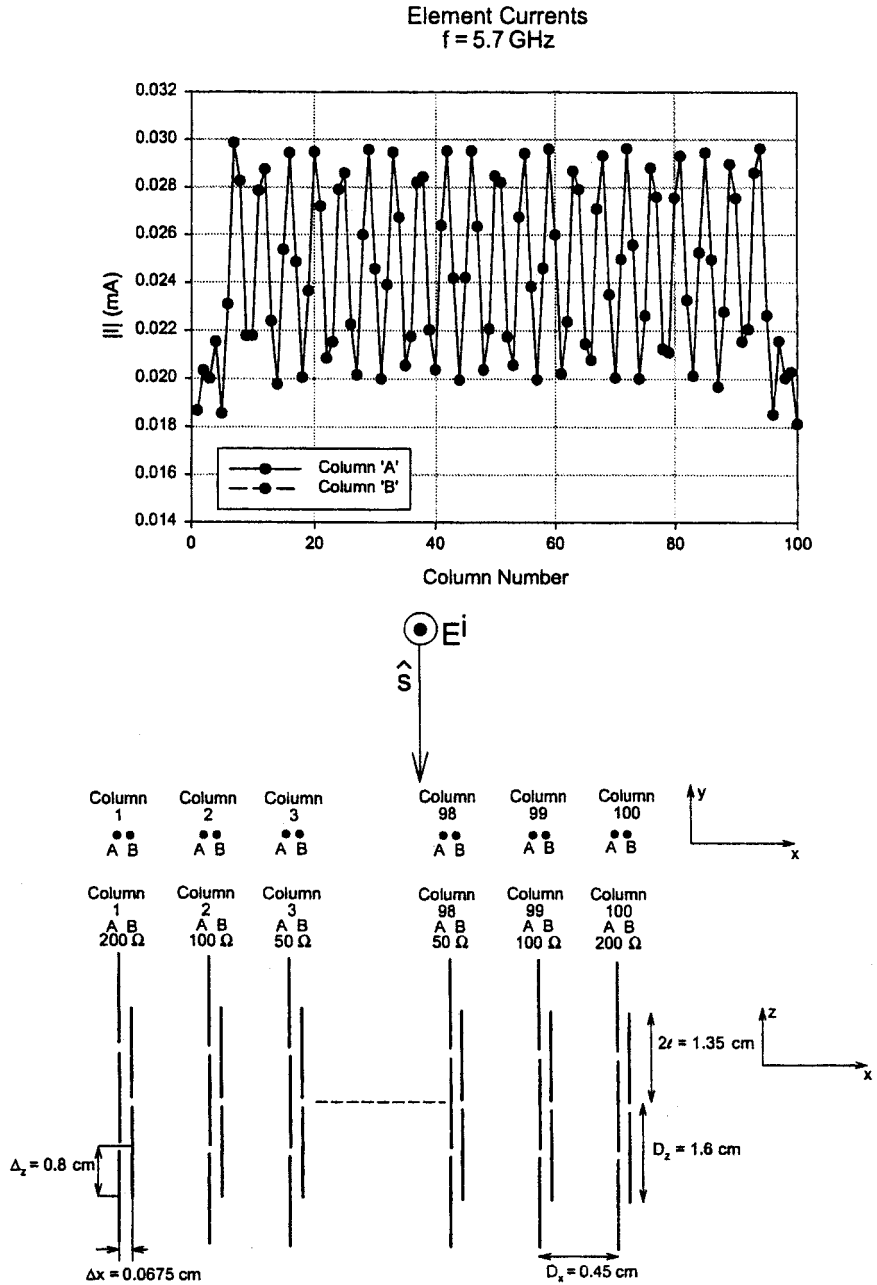
Fig. 5.11   *The element currents for the same finite FSS array as shown in Fig. 5.10, but with light loading as shown at the bottom. Note the dramatic reduction of current oscillations — that is, weaker surface waves. Also note the change of scale compared to Fig. 5.10.*

Element Currents
f = 5.7 GHz
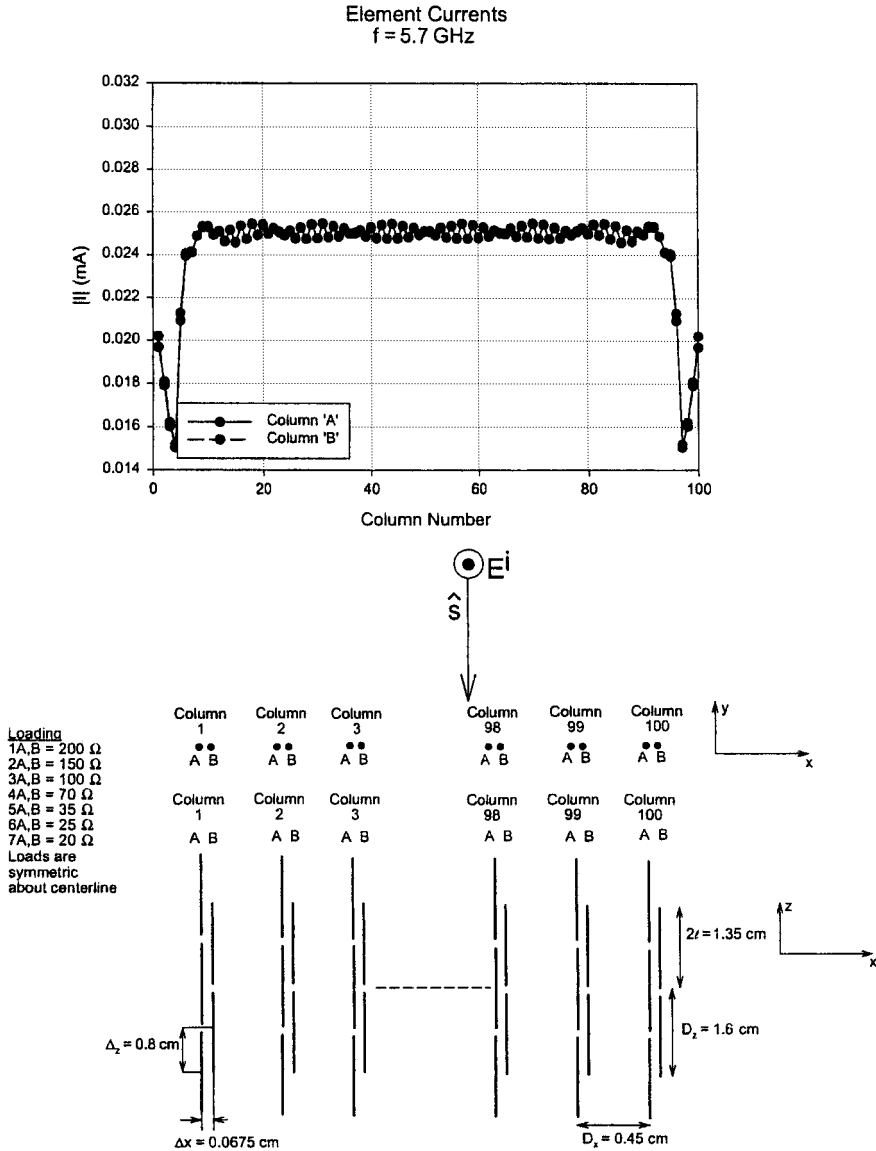
Fig. 5.12   The element currents for the same finite FSS array as shown in Figs. 5.10 and 5.11, but heavily loaded as shown at the bottom. Note the further reduction of the surface waves.

which is actually rather low considering that the antenna resistance R_A is ~235 ohms (see later). Thus, we also show in Fig. 5.14 the lightly loaded FSS groundplane case but where the active elements are now loaded with $R_L = 200$ ohms. We note that the current variations from element to element are of approximately the same magnitude in both cases and although small, it

Element Currents
f = 5.7 GHz
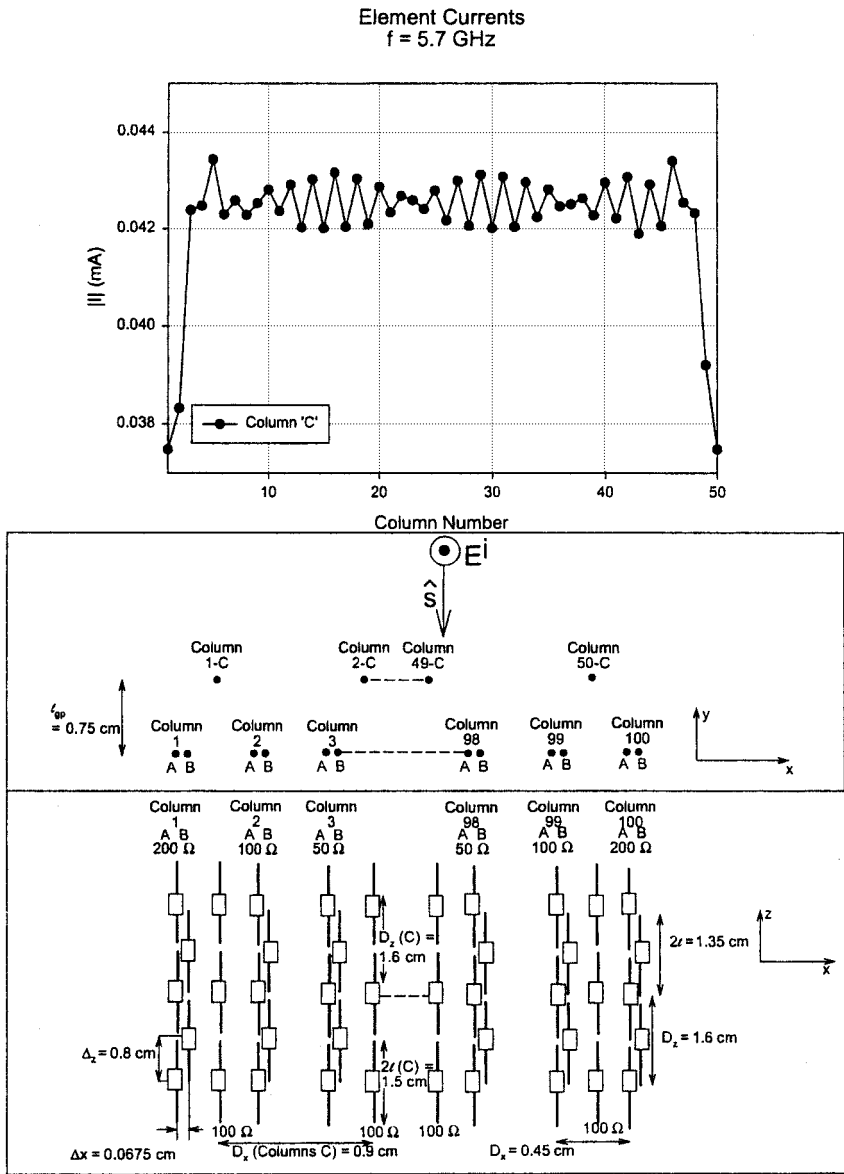
Fig. 5.13 The element currents of the active dipoles placed in front of the lightly loaded FSS array shown in Fig. 5.11. The active dipoles are all loaded with 100 ohms. Frequency is 5.7 GHz.

would be desirable to have them even lower. Note also that the average current is reduced from ∼0.043 to ∼0.032 as expected (see Section 1.4).

Thus, we show in Fig. 5.15 the heavily loaded FSS groundplane case and where the active elements again are loaded with $R_L = 200$ ohms. We observe
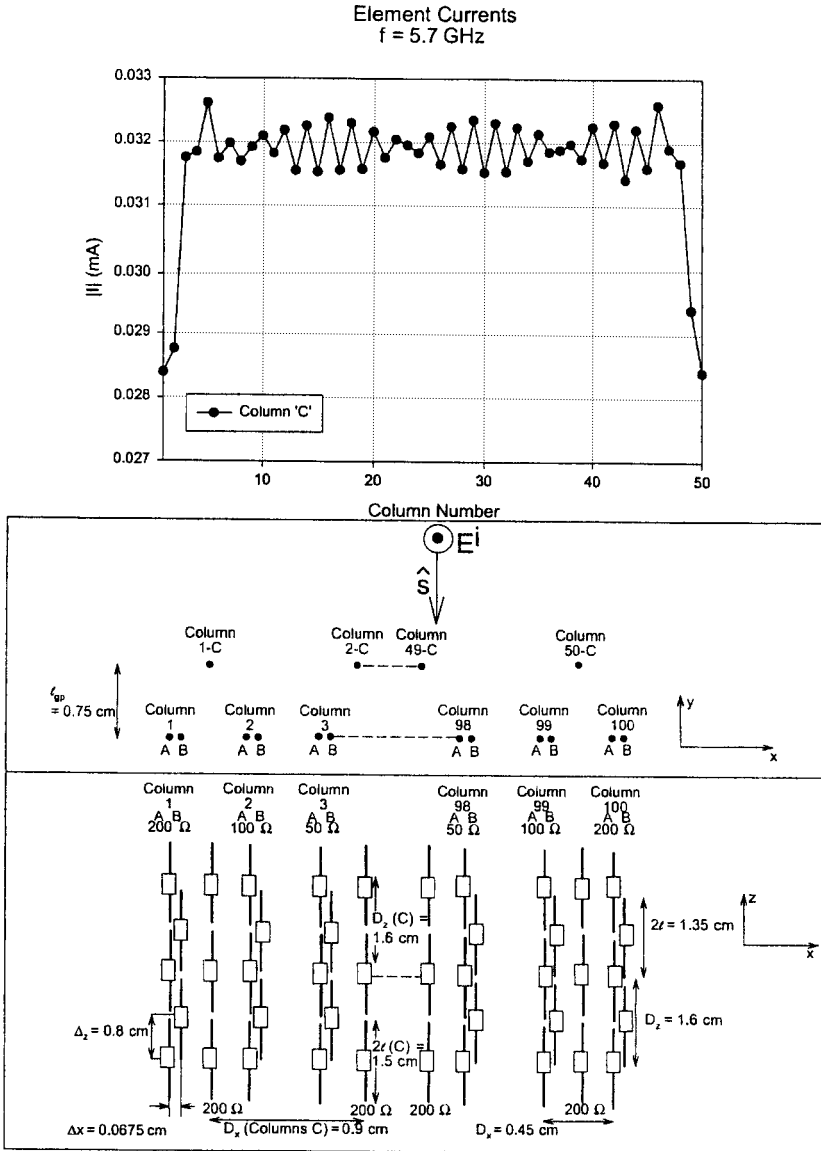
Fig. 5.14   The element currents of the active dipoles placed in front of the lightly loaded FSS array shown in Fig. 5.11. The same case as shown in Fig. 5.13, but this time all the active dipoles are loaded with 200 ohms. Frequency is 5.7 GHz.

a significant reduction of the current variations as expected. This experiment seems to show rather conclusively that it is the finite FSS groundplane that is the "troublemaker."

However, this hypothesis must be tested at other frequencies.

Fig. 5.15   The element currents of the active dipoles placed in front of the heavily loaded FSS array shown in Fig. 5.12. The active dipoles are loaded with 200 ohms. Frequency is 5.7 GHz.

5.7.2   Middle Test Frequency $f_M = 7.8$ GHz

We next show the same three cases as in Figs. 5.13, 5.14, and 5.15, but at the middle frequency $f_M = 7.8$ GHz. More specifically, Figs. 5.16 and 5.17 show the lightly loaded FSS groundplane with active load impedances $R_L = 100$ ohms and 200 ohms, respectively. This time we observe a significant reduction of the

Fig. 5.16   The element currents of the active dipoles placed in front of the lightly loaded FSS array shown in Fig. 5.11. Active dipole loading is 100 ohms — that is, same case as Fig. 5.13 except frequency is equal to 7.8 GHz.

surface wave for 200 ohms as we would expect but did not observe in Figs. 5.13 and 5.14. Furthermore, we show the heavily loaded FSS case in Fig. 5.18 for load impedance $R_L = 200$ ohms. Curiously, we do not observe much of an improvement except at the edge region.
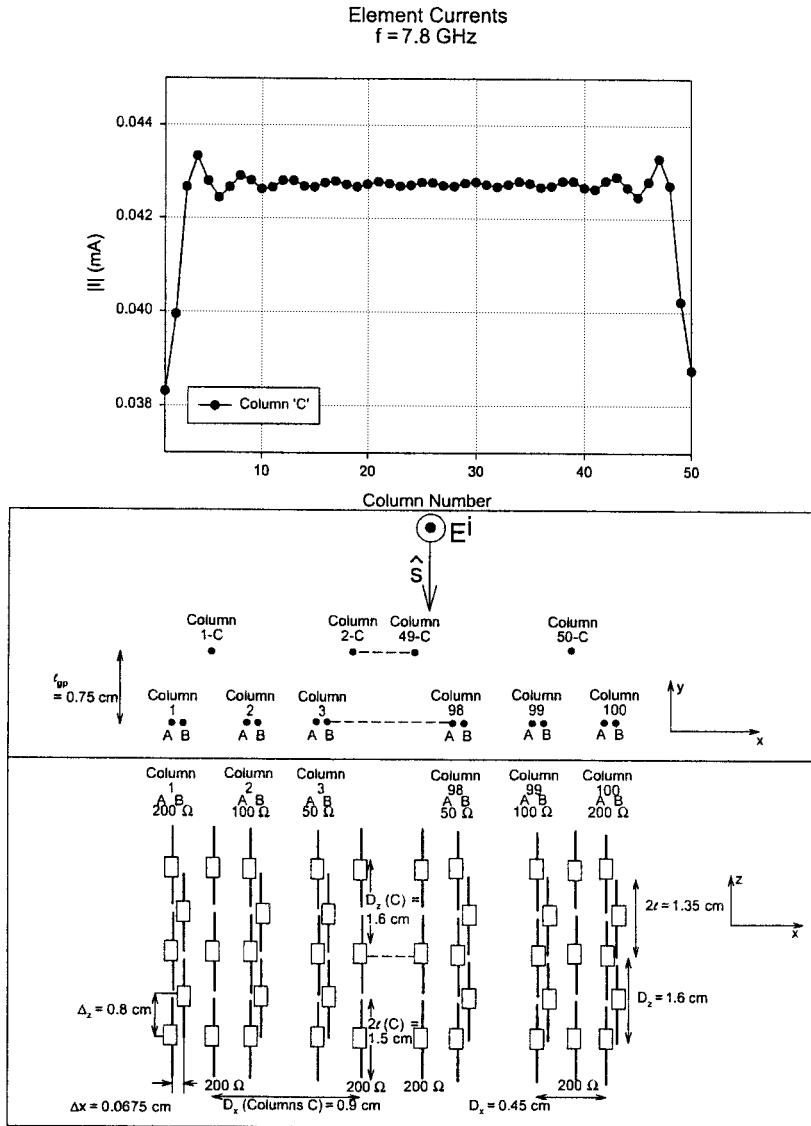
Fig. 5.17   The element currents of the active dipoles placed in front of the lightly loaded FSS array shown in Fig. 5.11. Active dipole loading is 200 ohms — that is, the same case as Fig. 5.14 except frequency is equal to 7.8 GHz.

5.7.3   High Test Frequency $f_H = 10$ GHz

In Figs. 5.19, 5.20, and 5.21 we finally show the same three test cases as above but at the high test frequency $f_H = 10.0$ GHz. Again, we show the lightly loaded cases in Figs. 5.19 and 5.20 with active loads being equal to $R_L = 100$ ohms and

Element Currents
f = 7.8 GHz
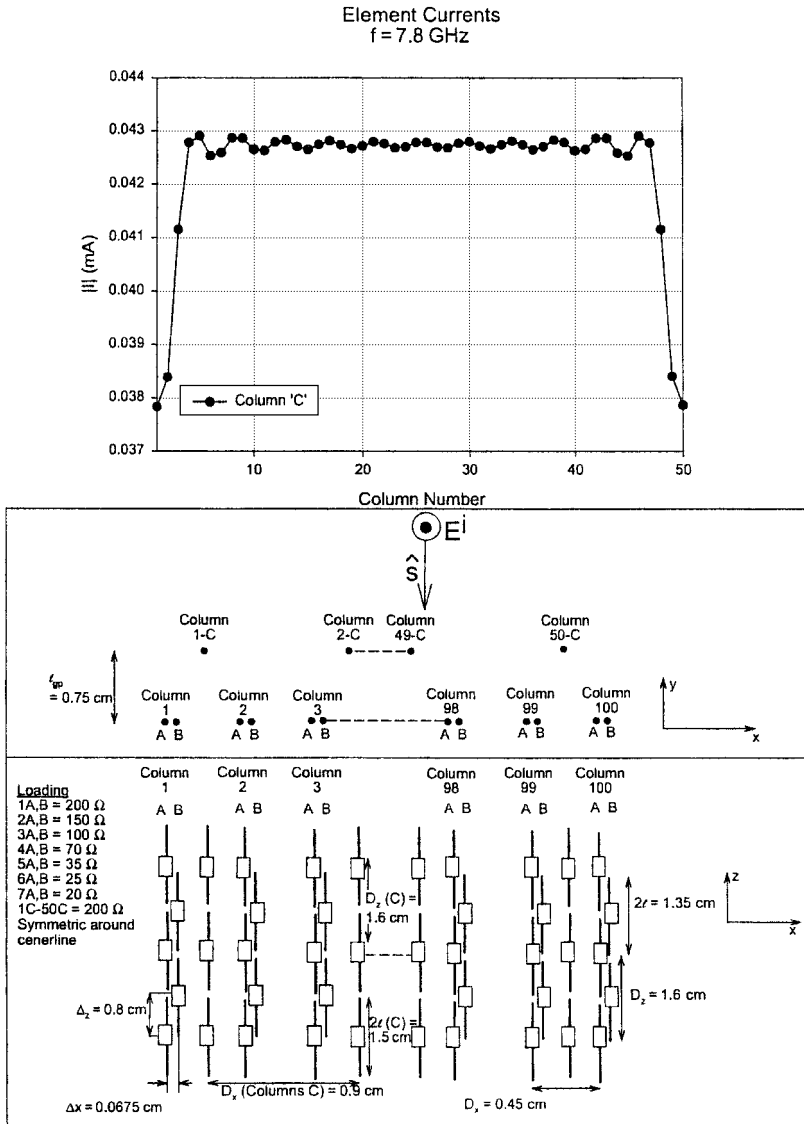
Fig. 5.18   The element currents of the active dipoles placed in front of the heavily loaded FSS array shown in Fig. 5.12. Active dipole loading is 200 ohms — that is, the same case as Fig. 5.15 except frequency is equal to 7.8 GHz.

200 ohms, respectively. As expected, we observe the most significant reduction of the surface waves when the active load resistance R_L is highest. Similarly, we show in Fig. 5.21 the heavily loaded FSS case when the load resistance R_L is 200 ohms. As we saw earlier above, the oscillations have not been reduced in the largest part of the array, only in the edge region.
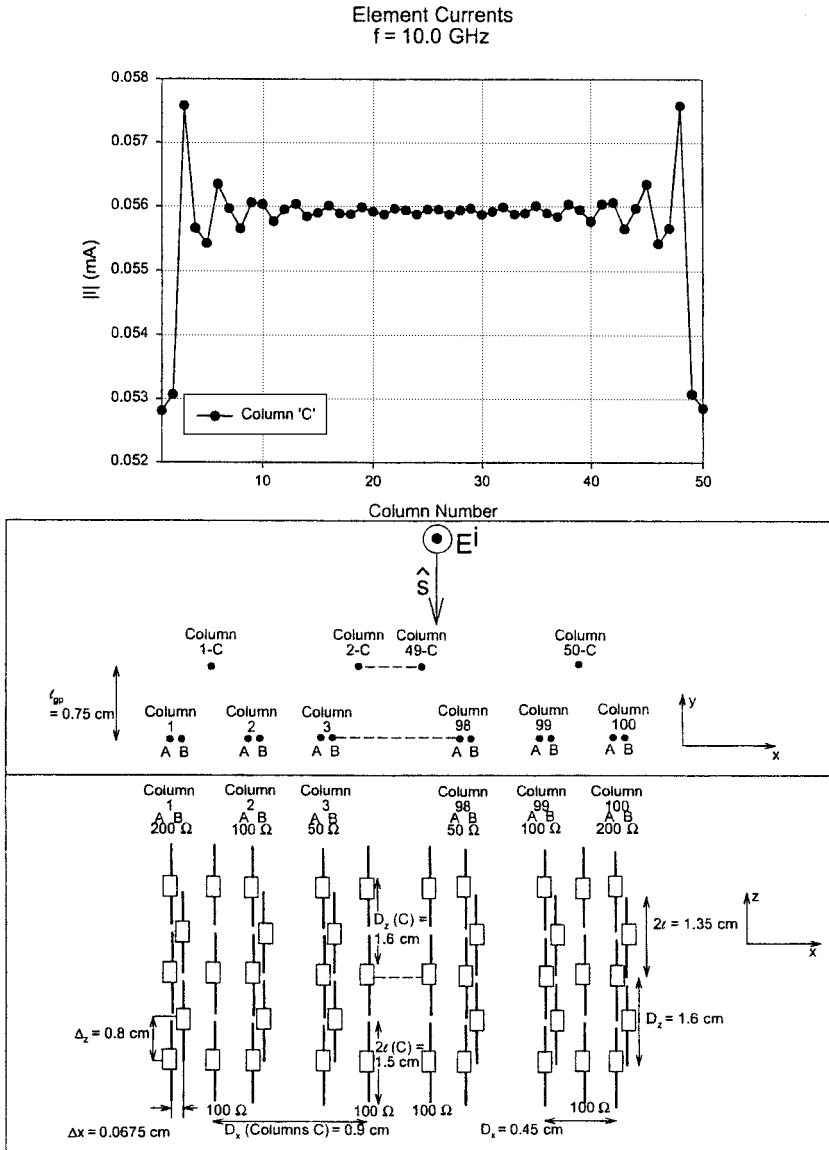
Fig. 5.19   Same case as shown in Figs. 5.13 and 5.16 except frequency is 10.0 GHz.

5.8   THE BACKSCATTERED FIELDS FROM THE TRIADS IN A LARGE ARRAY

The scattering diagrams at normal angle of incidence from an array consisting of 7 triads was shown in Fig. 5.8. All the active dipole elements in front of the FSS groundplane were loaded with identical resistors $R_L = 235$ ohms. We observed
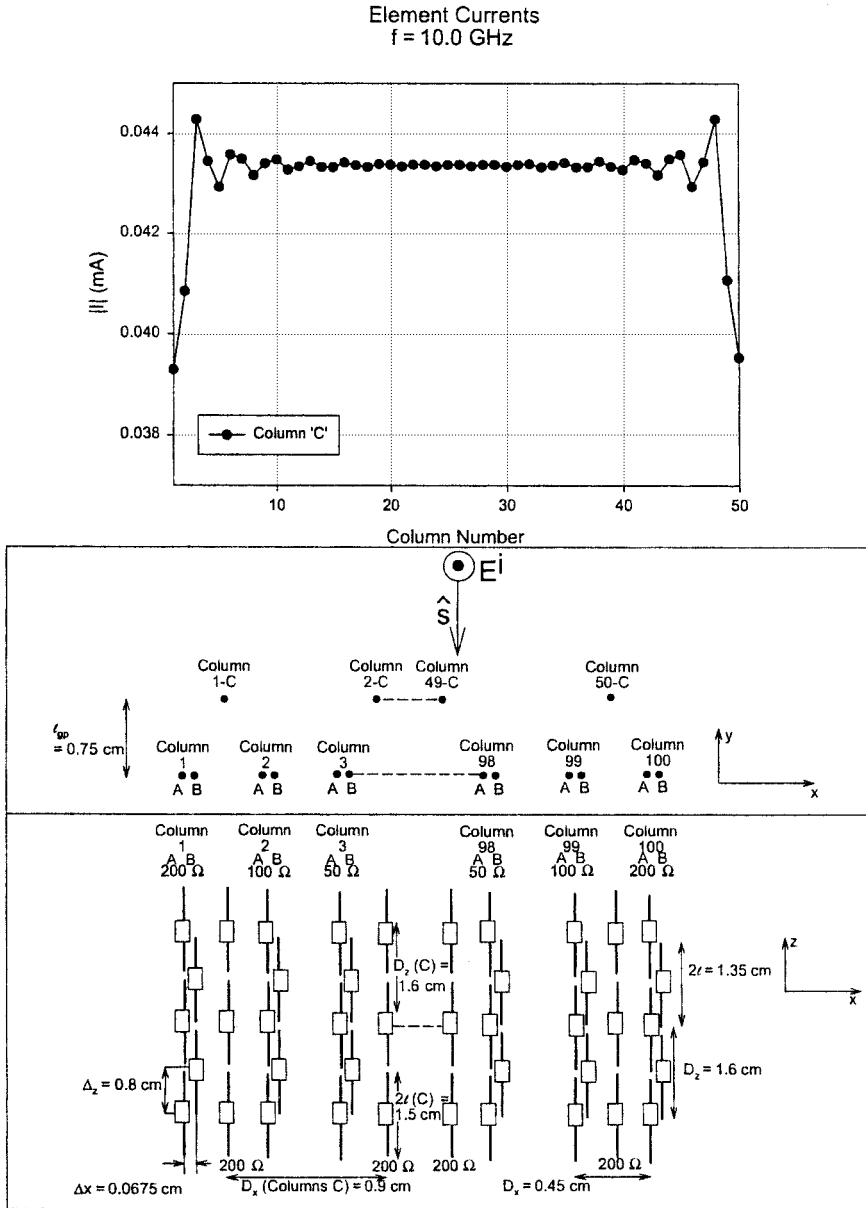
Fig. 5.20   Same case as shown in Figs. 5.14 and 5.17 except frequency is 10.0 GHz.

that the backscattered fields from the two edge triads differed significantly from the other triads. These, however, looked basically alike except for some minor deviations, often referred to as "jitter." This phenomenon appears to be typical for all finite periodic structures regardless of their extent. It has long been a source

Element Currents
f = 10.0 GHz
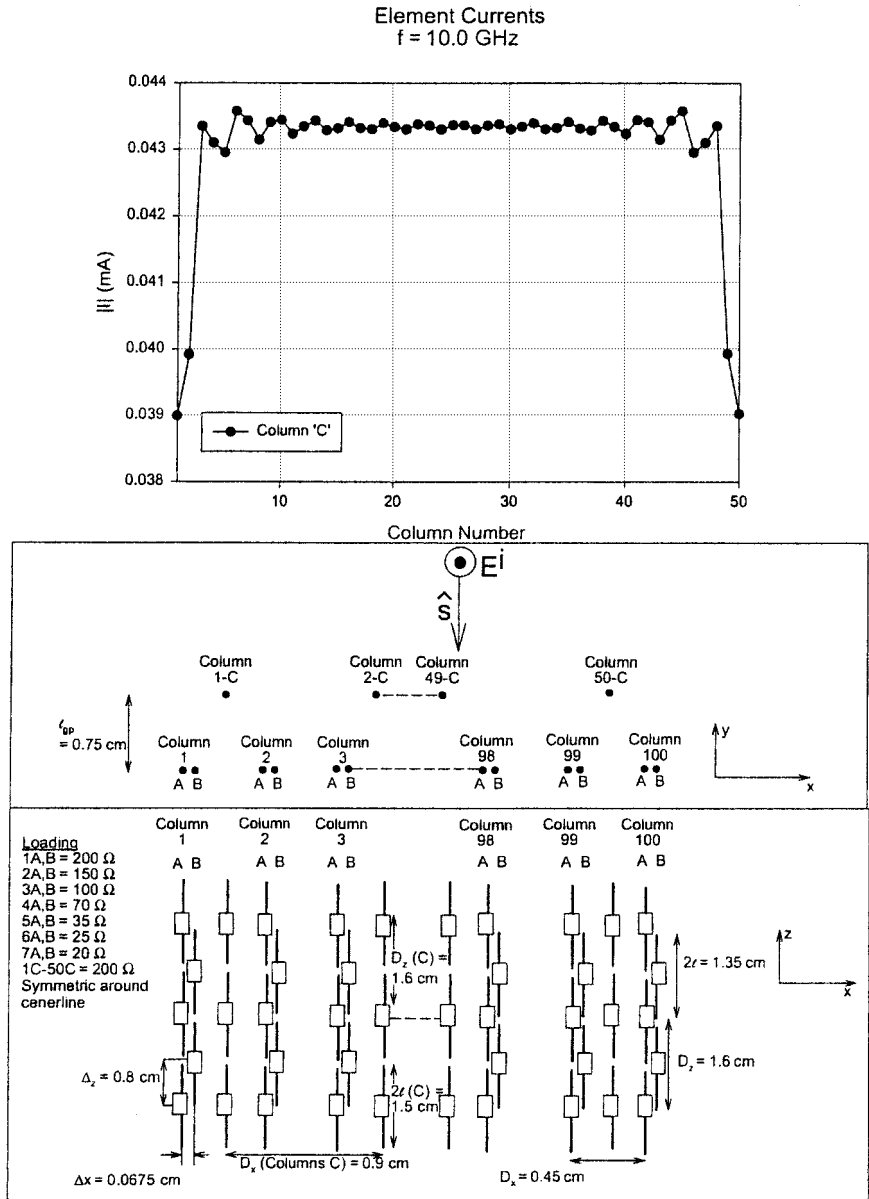
Fig. 5.21 Same case as shown in Figs. 5.15 and 5.18 except frequency is 10.0 GHz.

of irritation to designers of practical arrays since it makes precise matching of each triad with identical matching networks problematic. And as discussed in Chapter 2, superior matching is crucial if a low RCS at normal angle of incidence is desirable.

We postulated that this problem was associated with the presence of surface waves characteristic for finite structures. Thus, to reduce the jitter our aim should be to suppress these surface waves as much as possible.

We shall test this hypothesis on an array backed by the heavily loaded FSS groundplane shown in Figs. 5.15, 5.18, and 5.21. Thus, we show in Fig. 5.22 the scattering diagrams of 5 typical triads in an array of 50 triads. Each of the active elements are loaded with identical loads $R_L = 235$ ohms, and the distances between the active elements and the FSS groundplane are all equal to 0.68 cm. These values bring the backscatter at 10 GHz to the center of the scattering diagram; that is, we experience no backscatter at that frequency. However, we do at all other frequencies. To determine how much, we introduce the VSWR circles in the following way. We choose a VSWR equal to say m_1 and load the active elements with R_L/m_1 and $R_L m_1$ ohms, respectively (where as noted above $R_L = 235$ ohms). From the SPLAT program we then obtain the reflection coefficients for each of these values and plot them in the complex plane as shown in Fig. 5.22. These two reflection coefficients are located diametrically opposite in the complex plane and will consequently determine the circle corresponding to VSWR $= m_1$. For easy reference we also show in Fig. 5.22 the reflection coefficients (in decibels) corresponding to the respective VSWRs.

The triads depicted in Fig. 5.22 are nos. 10, 15, 23, 24, and 25—that is, typical specimens removed somewhat from the edges of the array. We observe that the reflected fields from all 5 triads in the frequency range 7–12 GHz are so close to each other that they practically melt together into single points. However, below 7.0 GHz this is certainly not the case. In fact, we show the scattering diagram for triad no. 23, 24, and 25 in Fig. 5.23 for the frequency range 5.0–7.0 GHz. Obviously, similarity between any of these 3 triads would be a complete coincidence. We strongly suspect that this phenomenon is directly related to the very strong presence of surface waves below 6.7 GHz in the FSS groundplane as observed clearly in the scattering diagram shown in Fig. 5.9. In other words, even heavy loading is not sufficient to completely eradicate the surface waves in the finite FSS groundplane at these lower frequencies.

However, we should by no means despair and conclude that operating a phased array with precision at the lower frequencies is a real problem. Recall that we are using the FSS groundplane merely to model a finite groundplane. When actually building a practical array, we would most likely use an ordinary piece of sheet metal of finite length and with holes so small that surface waves would be unlikely.

Which brings us right up to the very important question: What actually happens at the very edges of the finite array?

To answer that question we show in Fig. 5.24 the scattering diagram for the 5 triads closest to the edge, namely nos. 1, 2, 3, 4, and 5, respectively. Recall now that these triads, besides being at the edge, have the FSS portion right behind the active elements loaded heavily with resistors in order to attenuate potential surface waves (see Fig. 5.21). Thus, we would expect the scattering diagrams to differ somewhat from the "inner" triads shown in Fig. 5.22. Obviously, we

Partial Field Backscattered from Triads

VSWR	|Γ| (dB)
1.05	32.2
1.10	26.4
1.20	20.0
1.30	17.7
1.40	15.6
1.50	14.0

50 Triads
Distance from Array to Ground Plane = 0.68 cm
R_L = 235 Ω on All Active Array Elements

Active Elements Loaded with R_L = 235 Ω
Heavily Loaded FSS shown in Fig 5.15
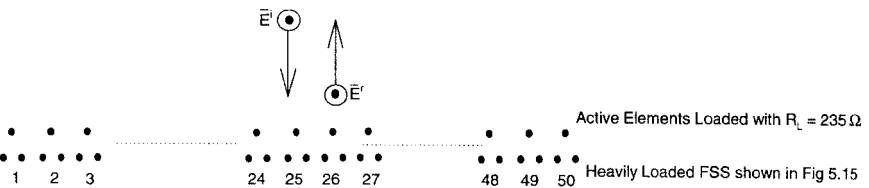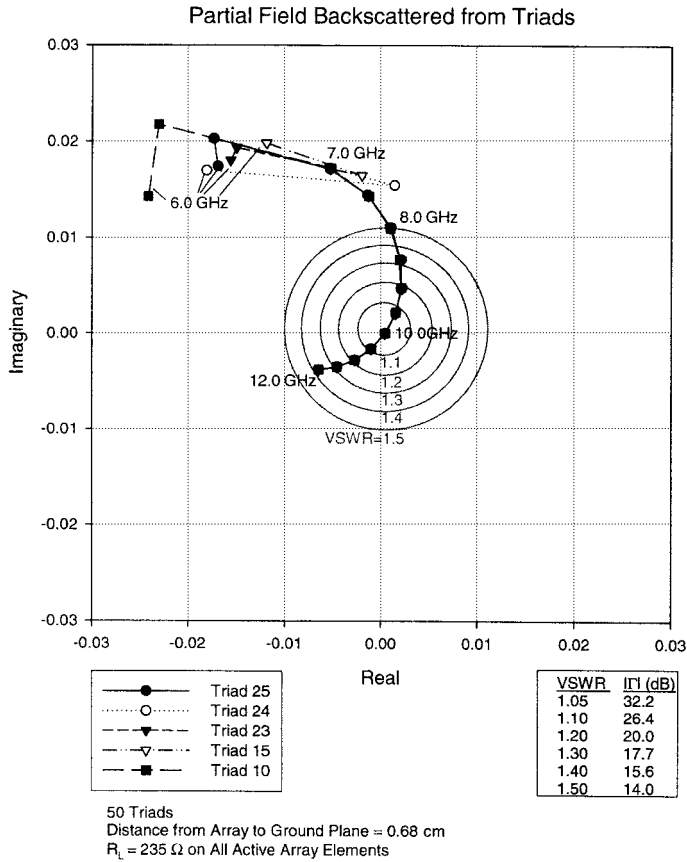
Fig. 5.22   The scattering diagrams for 5 typical triads as shown in an array of 50 triads. Note how the scattering from all 5 triads is virtually identical in the frequency range 7–12 GHz without any jitter as was the case in the untreated array in Fig. 5.8. Below 7 GHz we observe strong jitter as shown in detail in Fig. 5.23.

would like to reduce the backscatter from these outer triads as well. However, we are (or should be) prepared to use special R_L's and design special matching networks for these triads that differ from the ones designed for the majority. This would just be considered part of the edge treatment we would expect to do for any finite structure.

Partial Field Backscattered from Triads

Fig. 5.23   *The scattering diagram for the 3 triads in the enter of the same array as in Fig. 5.22 but in the frequency range 5–7 GHz. The strong jitter is attributed to surface waves present in the FSS groundplane as shown in Fig. 5.9.*

More specifically, we observe in Fig. 5.24 that triads 1 and 2 show the greatest deviation while triads 3, 4, and 5 more closely follow the majority shown in Fig. 5.22.

Furthermore, if triad 1 is loaded with 220 ohms rather than $R_L = 235$ ohms and the spacing between the active element and the FSS groundplane is decreased
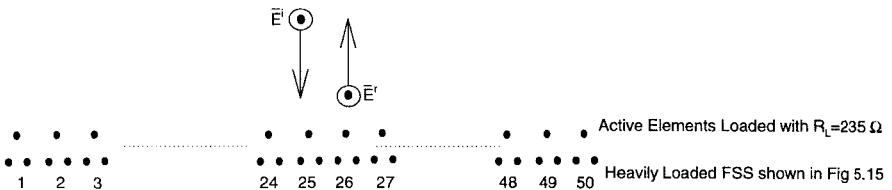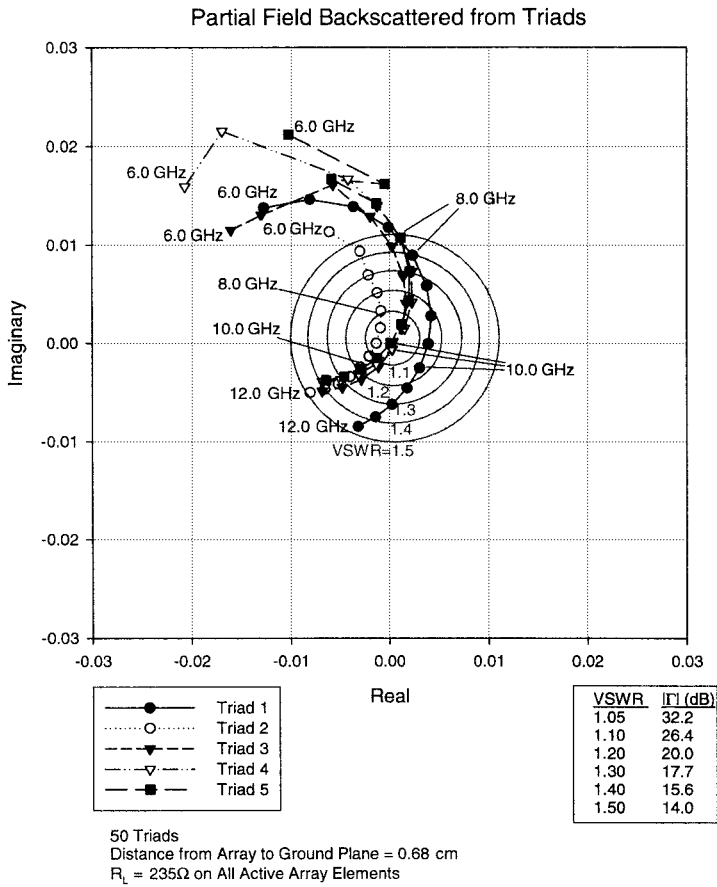
Fig. 5.24 The scattering diagram for the 5 triads closest to the edge of the same array as shown in Figs. 5.22 and 5.23. Note how the jitter is reduced as we move away from the edges for frequencies above 7 GHz but not below.

to 0.62 cm rather than 0.68 cm, we can as shown in Fig. 5.25 bring the 10-GHz point to the center while the other frequencies are now much closer to each other. Similarly, triad 2 can be brought closer to the center by increasing the load resistor to 280 ohms while we leave the spacing between dipole and FSS unchanged at 0.68 cm.
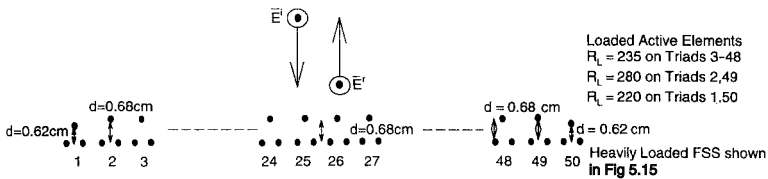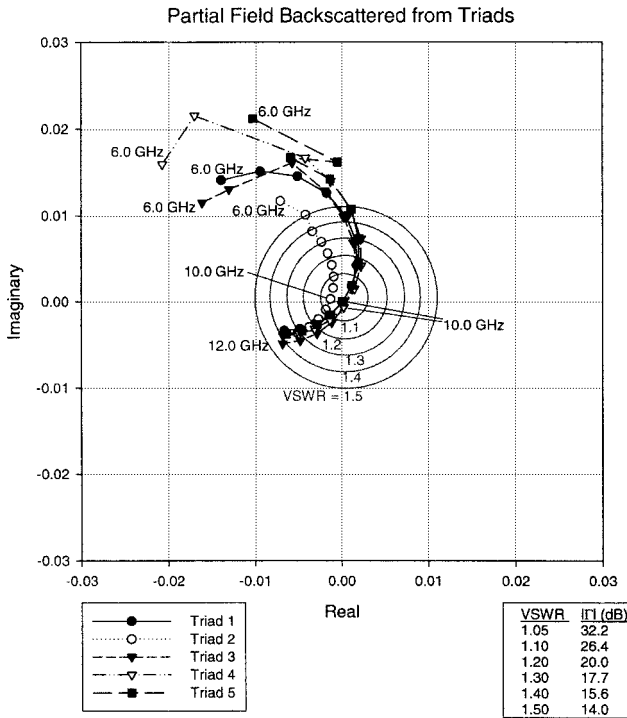
Fig. 5.25 *By decreasing the load resistor to 220 ohms and reducing the spacing between dipole and the FSS to 0.62 cm, triad 1 can be moved close to the center. Similarly, triad 2 is loaded with 280 ohms.*

5.9 ON THE BISTATIC SCATTERED FIELD FROM A LARGE ARRAY

In the previous section we determined the backscattered fields from the individual triads at normal angles of incidence. This information yields the RCS at boresight and is very important from a practical point of view.

It is, however, very instructive to observe how the field is scattered in all directions when the incident field is arriving from a fixed direction. Thus, we show at the top of Figs. 5.26 through 5.29 the bistatic scattered field at $f = 5.7$, 7.8, 10.0, and 12.0 GHz, respectively, for a typical triad (no. 25).
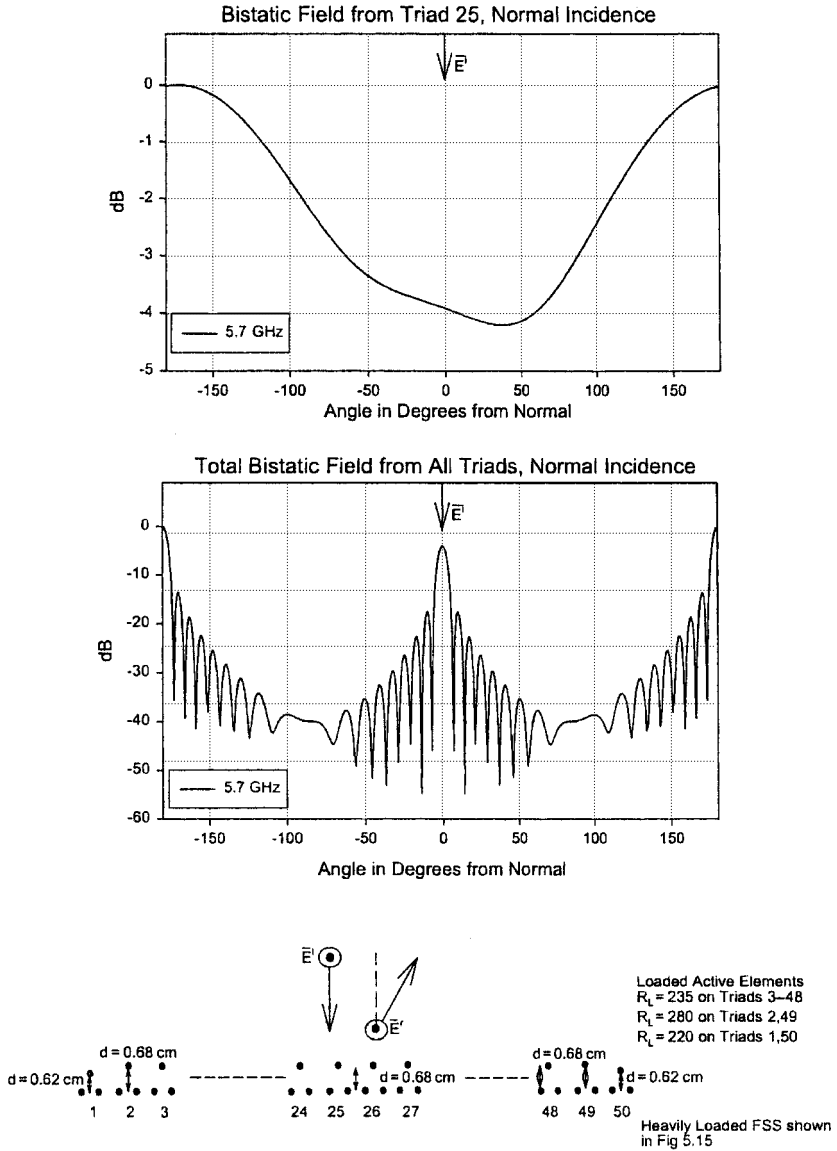
Fig. 5.26 Top: The bistatic scattered field from a single typical triad (no. 25). Bottom: The bistatic scattered field from the entire array of 50 triads. Normal angle of incidence. f = 5.7 GHz.

The direction of the incident wave is normal to the array. Note that the backscatter at the lowest frequency (5.7 GHz) is relatively high due to the inferior matching as observed in Figs. 5.22 and 5.23. However, at the design frequency 10 GHz the backscatter is very low as expected due to the superb matching as illustrated in Fig. 5.22.

Bistatic Field from Triad 25, Normal Incidence

Total Bistatic Field from All Triads, Normal Incidence

Loaded Active Elements
R_L = 235 on Triads 3–48
R_L = 280 on Triads 2,49
R_L = 220 on Triads 1,50

Heavily Loaded FSS shown in Fig. 5.15
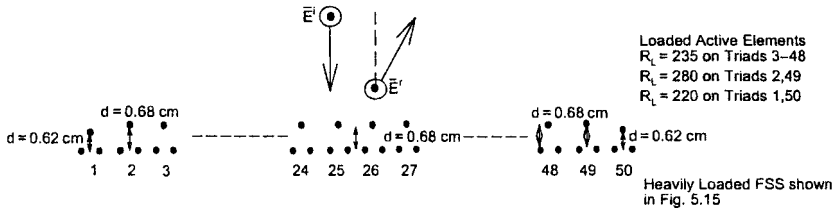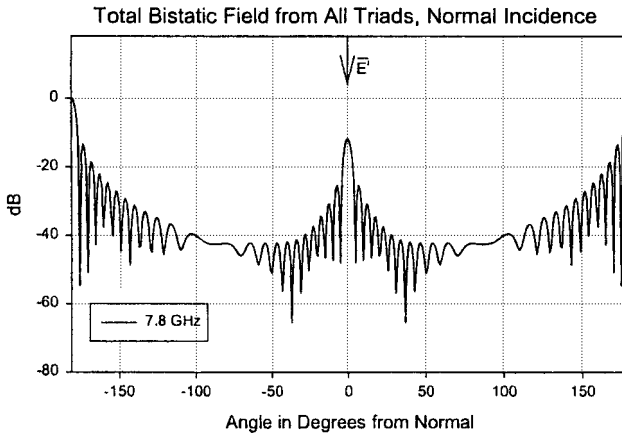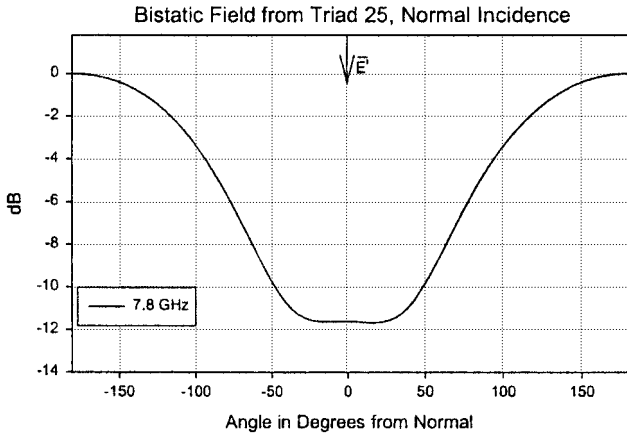
Fig. 5.27 Top: The bistatic scattered field from a single typical triad (no. 25). Bottom: The bistatic scattered field from the entire array of 50 triads. Normal angle of incidence. f = 7.8 GHz.

If all the triads had identical bistatic scattering patterns, we could next obtain the total bistatic scattered field for the entire array by multiplication with the array factor. A typical example of this factor at 10 GHz is shown in Fig. 5.30. At other frequencies they look similar except for the beamwidth and are therefore not shown.
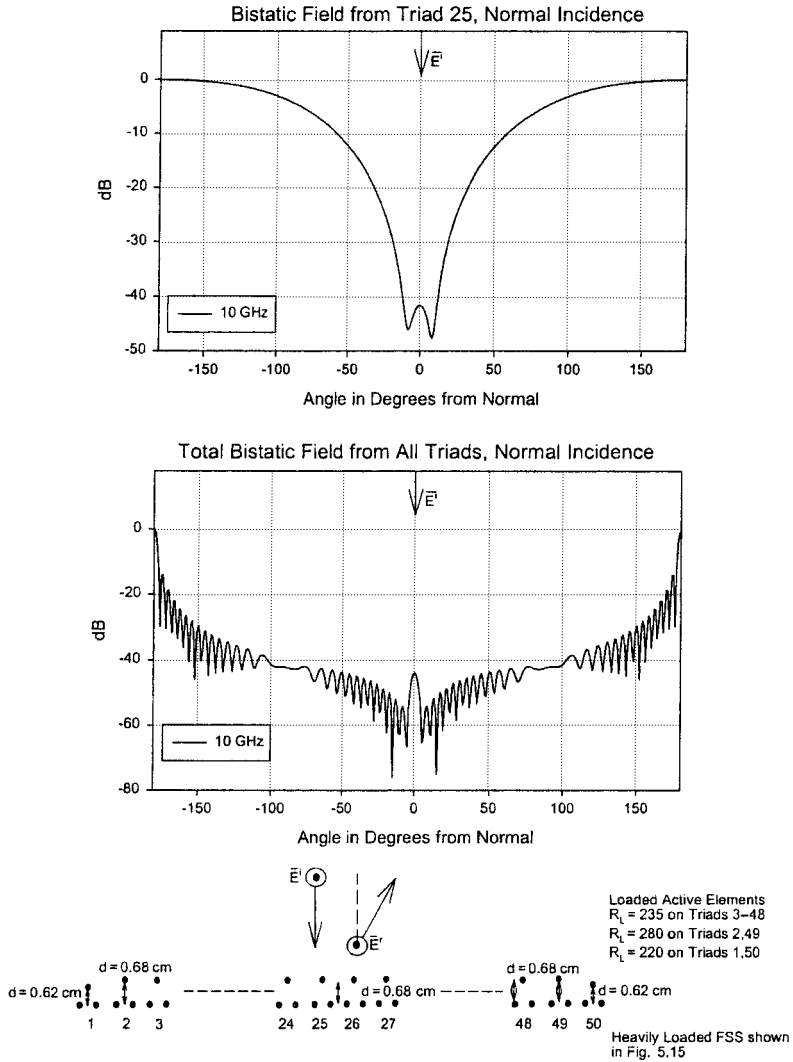
Fig. 5.28 Top: The bistatic scattered field from a single typical triad (no. 25). Bottom: The bistatic scattered field from the entire array of 50 triads. Normal angle of incidence. f = 10.0 GHz.

However, the bistatic scattering patterns are as implied earlier not quite the same for the triads located close to the edges (see Figs. 5.22 and 5.25). Thus, simple array theory strictly speaking does not apply, although it is actually fairly accurate for large arrays with compensated edges as noted later.

We will therefore obtain the bistatic scattered field from the entire array by simply adding the bistatic scattered field from all the individual triads. Typical examples are shown at the bottom of Figs. 5.26 through 5.29 at the same frequencies as above, namely 5.7, 7.8, 10.0, and 12.0 GHz, respectively.

Bistatic Field from Triad 25, Normal Incidence

Total Bistatic Field from All Triads, Normal Incidence

Loaded Active Elements
R_L = 235 on Triads 3–48
R_L = 280 on Triads 2,49
R_L = 220 on Triads 1,50

d = 0.68 cm

d = 0.62 cm

d = 0.68 cm

d = 0.68 cm

d = 0.62 cm

1   2   3   24 25 26   27   48 49 50

Heavily Loaded FSS shown
in Fig 5.15
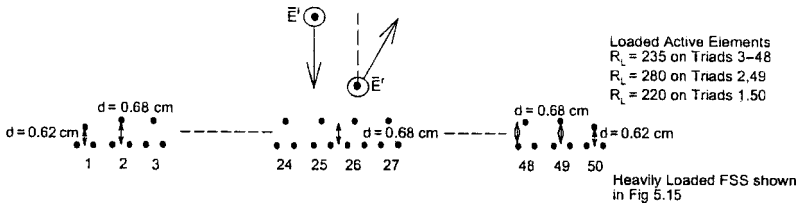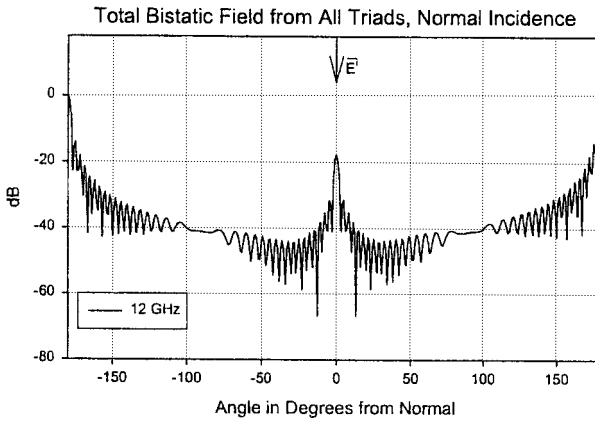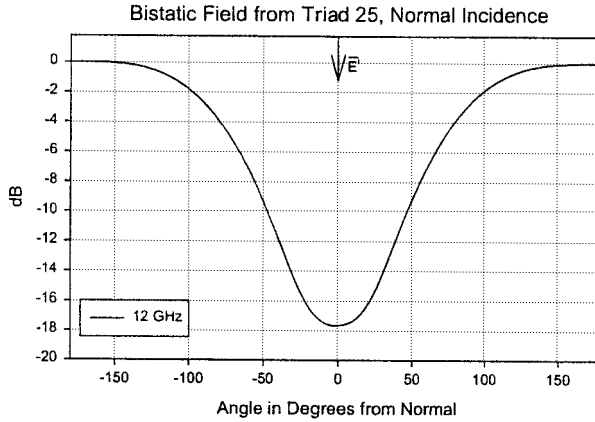
Fig. 5.29   Top: The bistatic scattered field from a single typical triad (no. 25). Bottom: The bistatic scattered field from the entire array of 50 triads. Normal angle of incidence. f = 12.0 GHz.

Again, as expected, we note a very high backscatter at the lowest frequency 5.7 GHz while we observe a very low backscatter at the design frequency 10 GHz.

Furthermore, we observe that the forward scattered field is at the same level as the backscatter of a perfectly conducting groundplane at the same size as the finite array. This is in agreement with our observations in Figs. 5.2 and 5.3.

Next, in Figs. 5.31 through 5.34 we show the bistatic scattered field for the same array as above but for angle of incidence equal to $-30°$. At the top we

Array Factor, Normal Incidence
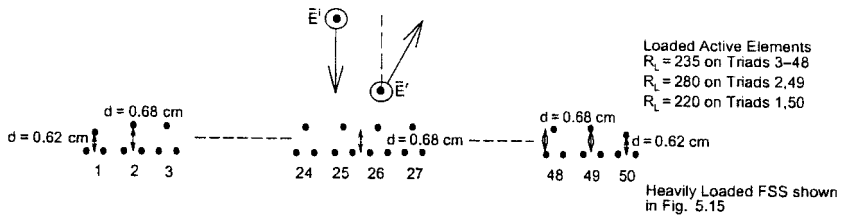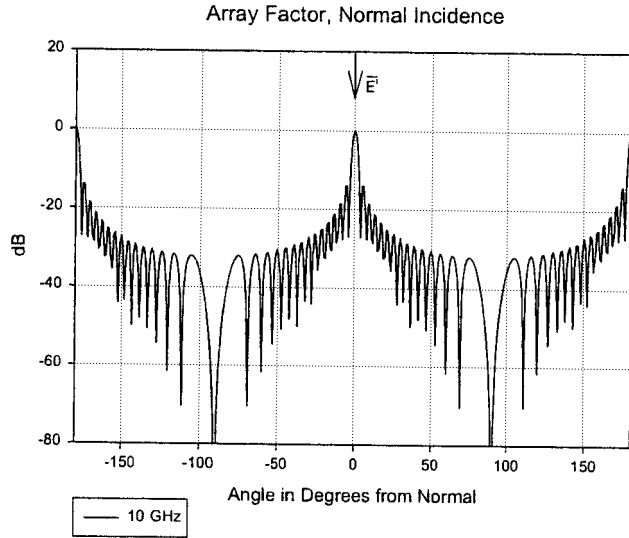
Fig. 5.30   The array factor for the entire array of 50 triads. Normal angle of incidence.
f = 10.0 GHz. The factors at the other frequencies look quite similar except for beamwidths.

show the pattern for a single typical triad (no. 25), and at the bottom we show the bistatic scattered pattern for the entire array. Furthermore, in Fig. 5.35 we show a typical array factor for the entire array at $f = 10$ GHz and angle of incidence equal to $-30°$. The patterns at other frequencies look similar.

It is interesting to note that the backscatter level for oblique incidence is considerably lower than that for normal incidence due to the array factor.

Again we note that the level in the forward direction ($150°$) is 0 dB as it was for normal angle of incidence.

Finally we observe that the specular scattered field is quite closely equal to the normalized scattering value of a single triad only. Similarly, the backscattered field can be obtained as the sum of the backscatter from a triad and the array factor. This shows that for a large array with adjusted edge triads the total scattered field could have been obtained quite accurately by simple pattern multiplication of a typical triad and the array factor.
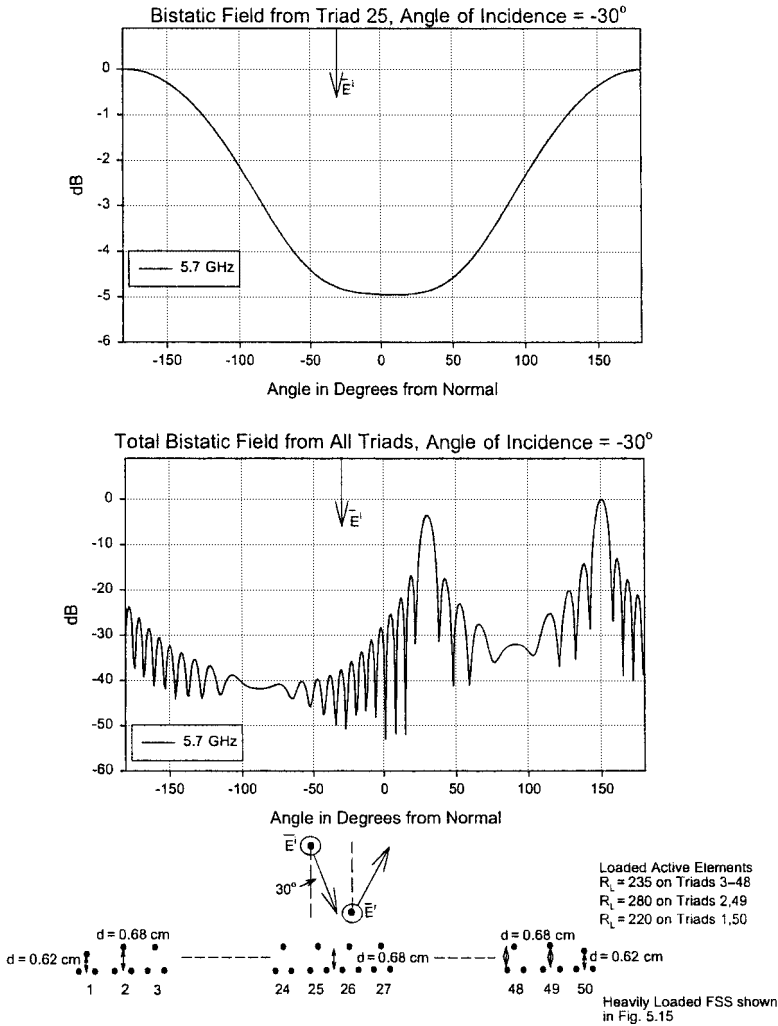
Fig. 5.31   Top: The bistatic scattered field from a single typical triad (no. 25). Bottom: The bistatic scattered field from the entire array of 50 triads. Angle of incidence is $-30°$. $f = 5.7$ GHz.

We may also state that the backscatter from a large array looks similar to that of an equal-sized groundplane from where we subtract the triad scattering.

To summarize: At broadside the backscattered field for a large array with compensated edges depends essentially on the scattering level of a typical triad. At oblique angle of incidence the total backscatter is given as the sum of the array factor and the triad scattering. Thus, even if the scattering pattern for a typical triad deteriorates somewhat for oblique incidence, the lower sidelobe level of the array factor can still be quite instrumental in producing a low backscatter for the entire array.
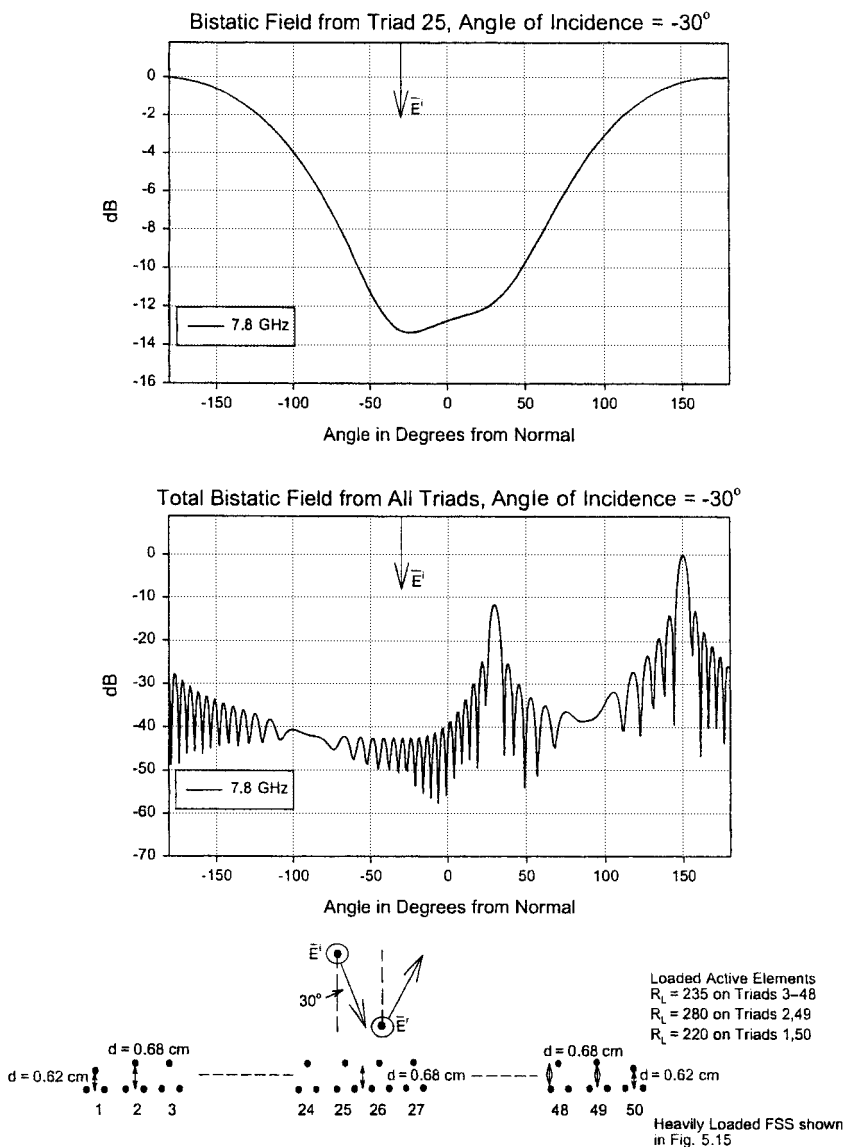
Fig. 5.32   Top: The bistatic scattered field from a single typical triad (no. 25). Bottom: The bistatic scattered field from the entire array of 50 triads. Angle of incidence: $-30°$. $f = 7.8\,GHz$.

5.10   FURTHER REDUCTION: BROADBAND MATCHING

We demonstrated above that the backscatter is proportional to the reflection coefficient Γ. The array was matched at 10 GHz. At other frequencies Γ was larger, resulting in a stronger scattering from the individual triads.
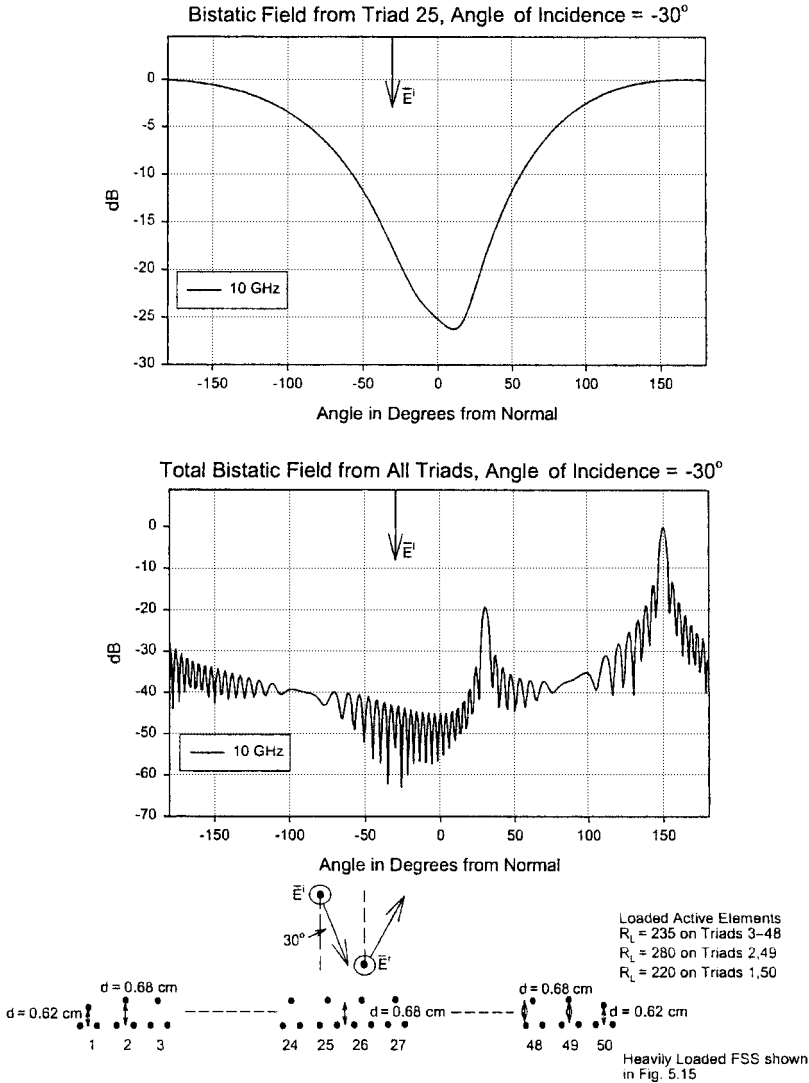
Fig. 5.33   Top: The bistatic scattered field from a single typical triad (no. 25). Bottom: The bistatic scattered field from the entire array of 50 triads. Angle of incidence is −30°. f = 10.0 GHz.

Thus, by better matching at all frequencies the backscatter could be further reduced. In other words we need to add a carefully designed matching network at the terminals of all the dipole elements. This network can be designed to be identical for all the typical triads since the array can be made free from jitter as seen earlier.

The active input impedance for triad 25 is shown in Fig. 5.36, bottom. It will be observed that the VSWR is ~1.02 at 10 GHz. In Fig. 5.36, top, we observe

Bistatic Field from Triad 25, Angle of Incidence = -30°

Total Bistatic Field from All Triads, Angle of Incidence = -30°
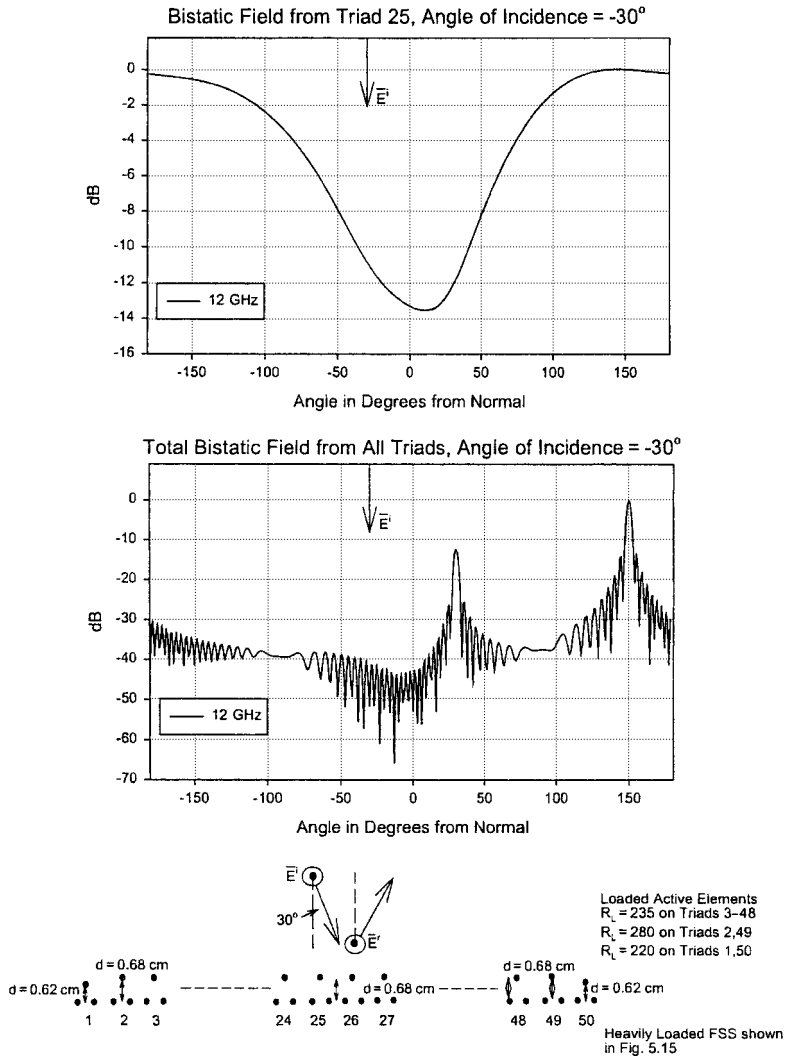
Fig. 5.34 Top: The bistatic scattered field from a single typical triad (no. 25). Bottom: The bistatic scattered field from the entire array of 50 triads. Angle of incidence is −30°. f = 12.0 GHz.

that the backscattered field at 10 GHz has a reflection coefficient corresponding to a standing wave ratio equal to ~1.01. Considering that these calculations were obtained using only one mode, this agreement is quite satisfactory. See also Problem 5.3.

In Appendix B we review the principles for broadband matching, and in Chapter 6 we apply them to broadband arrays. In Problem B.3 you are invited to design a broadband matching network for the active input impedance shown in Fig. 5.36, bottom.
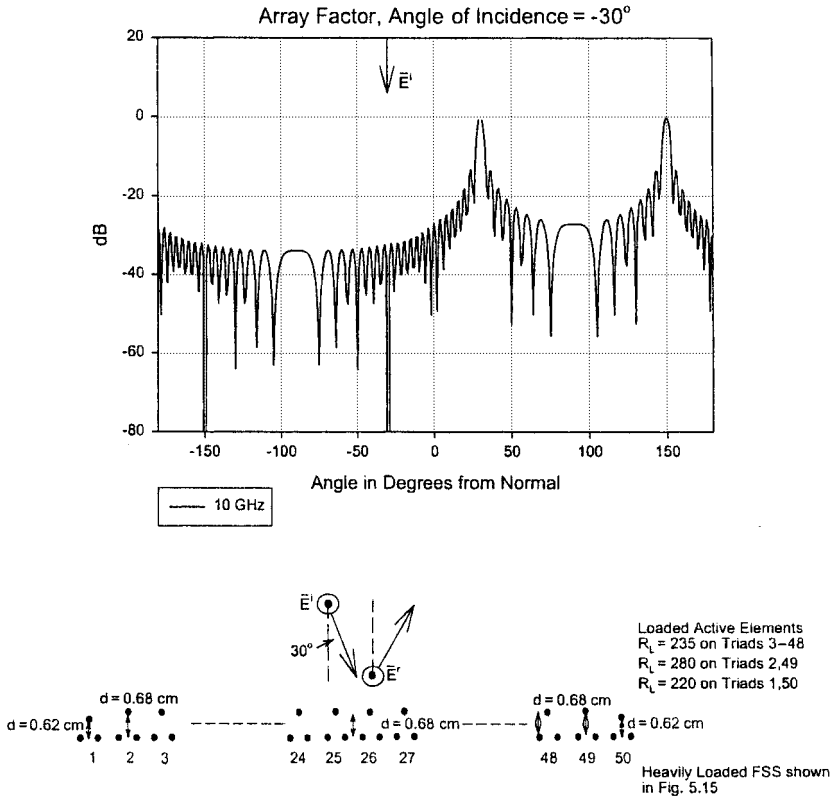
Fig. 5.35   The array factor for the entire array of 50 triads. Angle of incidence is −30°.
f = 10.0 GHz. The factors at the other frequencies look quite similar except for beamwidth.

5.11   COMMON MISCONCEPTIONS

5.11.1   On Minimizing the Backscattering by Optimization

It is often suggested to minimize the backscattering from a finite array by a computerized optimization process. (Some people will go to great length to avoid any involvement with the physics of their problem. Some have no choice.)

While such an approach is feasible, it should be applied with great care. A very simple example will illustrate what can easily go wrong and undetected by operators whose intellectual capacity is limited to comparing numbers. In Fig. 5.37a we show the typical backscattered fields in vector form from each triad similar to the case in Fig. 5.8. Recall that the fields scattered from the two edge triads are quite different from the rest if all the triads are loaded with identical load resistors R_L. This was simply because the terminal impedances of the edge triads were in a different element environment, resulting in terminal impedances different from the rest.
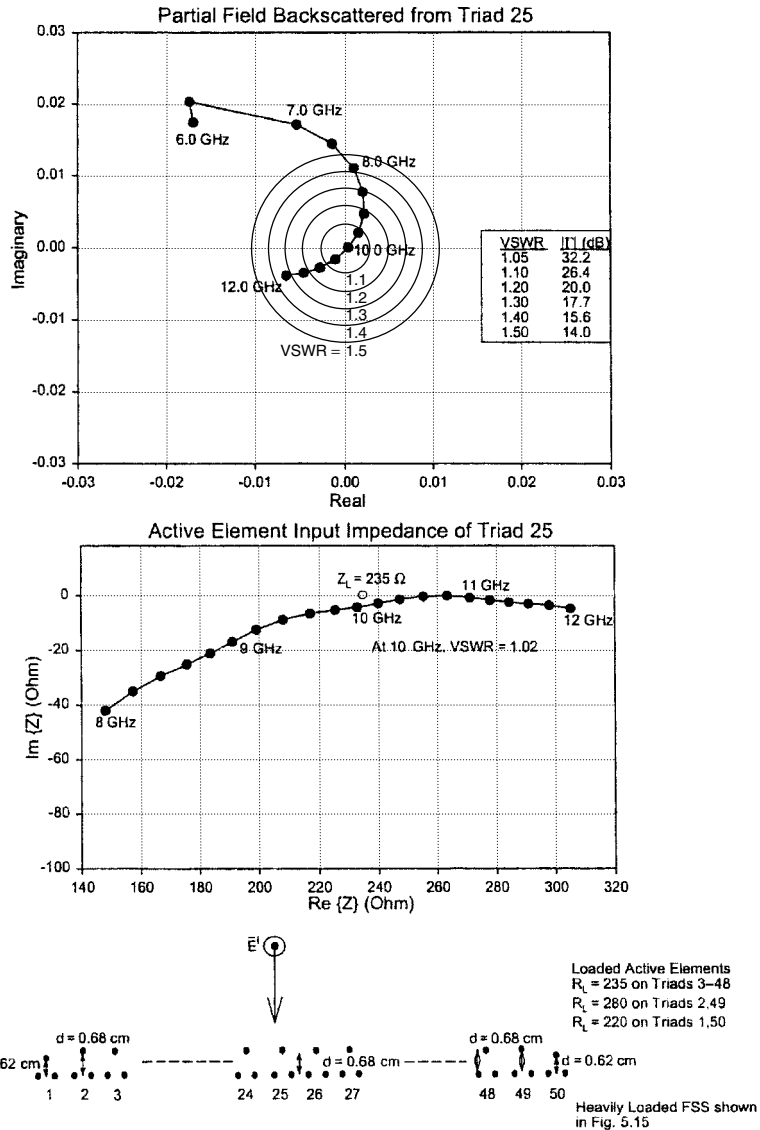
Fig. 5.36   Top: The backscattered field for triad 25 in an array of 50 triads. Bottom: The active input impedance for triad 25. Note that the incident field reflected from the outside very closely matches the magnitude of the reflection coefficient as seen at terminals from the inside. This shows that the residual scattering is ~0.

When applying a computerized approach, we would most likely calculate the total backscattered field—that is, the sum of the triad fields. Typically a computer would then in all likelihood find the simple solution shown in Fig. 5.37b. By variation of the identical load impedances Z_L, the computer would produce a

(a) Typical backscattering from each triad.

(b) Total backscattering equal to zero.
But narrow banded.

(c) Backscattering from each triad ~ 0.
Conceptually broadbanded.
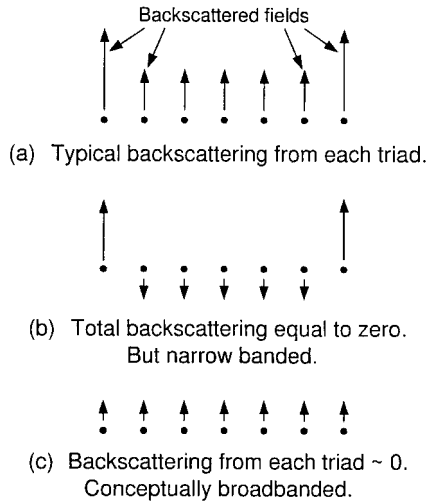
Fig. 5.37   Reducing the backscatter by an unguided optimization program typically produces inferior results. (a) Typical backscattering from the individual triads—in this case, strong at the edges and smaller elsewhere (see Fig. 5.8). (b) By varying the load impedances Z_L an optimization program calculating the total backscattered field will typically find a solution where the strong edge scattering simply cancels the weaker scattering from the triads elsewhere. However, the solution is not very broadbanded and is very sensitive to angle of incidence. (c) A much better solution is to reduce the backscatter from all triads and make them as close to zero as possible as discussed in Sections 5.4 and 5.9.

solution where the strong scattering from the two edge triads would simply cancel the sum of the much smaller fields from all the other triads. Thus, the total backscattered field could certainly easily be zero, but the result is obtained by simple cancellation which is in principle risky unless done with care. In this case the solution will be narrow-banded and highly sensitive to the angle of incidence.

A better solution is shown in Fig. 5.37c. Here the fields from *each* triad have been forced to be zero by the process discussed earlier in this chapter. It does not rely on simple cancellation and will consequently be more broadbanded and less sensitive to angle of incidence.

Oh yes, there is more to design than just run a computer, or worse yet, let the computer run itself without any interference from the human brain.

5.11.2   Can the RCS be Reduced by Treating the Dipole Tips?

In Problem 5.1 we address the fact that the backscatter does not always even appear to originate from the edges of a reflecting surface.

A related misconception is the notion that the backscatter from an array is originating at the very tips of the dipoles. Thus, it is often reasoned that if the tips could somehow be treated in some magic fashion, the backscatter from the array could possibly be reduced.

A common attack along this idea is to simply place resistors at the very tips of the dipoles. However, since there is basically no conducting current in this area, anything placed here will be practically ineffective (except possibly a small change in resonance frequency due to a slight increase in the end capacitance of the dipoles).

In order for a resistive loading to be effective, it must be inserted at a place where there is a current. And there must be a groundplane.

And that happens to be precisely what we do when we place load resistors in the middle of the dipoles as amply demonstrated in this chapter.

Asymptotic methods and way of thinking work fine at high frequencies when applied correctly. But they should not blindly and religiously be carried into the *resonance* region. They may "work" in some cases, but often merely due to luck and by coincidence.

5.12 CONCLUSION

In Chapter 2 we introduced the reader to the fundamentals of the RCS of antennas in general. We demonstrated how the scattering from any antenna could be decomposed into two components, namely the antenna mode component proportional to the mismatch at the terminals of the elements and another component today usually referred to as the residual scattering component. (For further discussion on this subject see Section 2.2.)

Array antennas with groundplane were of particular interest since they turned out to have no residual scattering component, at least potentially. Thus, to obtain zero backscatter we merely would have to match each element perfectly.

While this sounds conceptually simple, there are practical problems to be solved.

First, the triads in the edge area will have terminal impedances significantly different from all the other triads. This is simply related to the fact that the elements at the edge are in a different environment as far as mutual impedances are concerned. Thus, if the inside triads are conjugate-matched and the edge triads loaded with the same impedances, mismatch will occur, causing a significant amount of scattering from the edge columns.

The second problem is actually more complex. When considering an infinite array, the terminal impedance will be the same from element to element in accordance with Floquet's Theorem. However, when the array is finite, it is well known that the terminal impedance will differ from element to element in an oscillating way around the infinite array value (sometimes denoted as jitter). We postulated that this phenomenon was related to the presence of surface waves of the same type as encountered in Chapter 4. However, there is a significant difference in amplitude of these surface waves in the passive and active cases. This is due to the fact that the elements in the former case in general are loaded with pure reactances (if any), while the elements in the latter case are (or should be) connected to individual amplifiers or generators containing substantial resistive components (as encountered when conjugate matched).

These resistive components cause significant attenuation of potential surface waves along the structure. In fact, they will in general be so weak that the surface wave radiation from active arrays can be ignored in contrast to the FSS case discussed in Chapter 4. However, they may be strong enough to produce jitter of the terminal impedance.

Furthermore, one more component will complicate the situation, namely the groundplane that in our investigation is modeled in the form of a finite FSS surface. Potential surface waves on such a structure cannot be attenuated by simple resistive loading all the elements across the entire surface since such an approach would lead to excessive reflection loss as a groundplane. Thus, possible surface waves must in this case be controlled in the same manner as was done in Chapter 4, namely by resistively loading just a few columns in the edge areas.

By monitoring the column currents as a function of the loading in the edge areas, we were able to obtain a significant reduction of the surface waves in the finite FSS groundplane. By further loading the active element of each triad everywhere with load resistors R_L equal to $R_A = 235$ ohms as discussed already above, we were able to eliminate all visible jitter in all triads at least between nos. 10 and 40 in the frequency range 7–12 GHz (and most likely significantly beyond 12 GHz). However, below 7 GHz we did indeed experience a significant amount of jitter. We attributed this almost entirely to the finite FSS groundplane. Thus, we could avoid this problem by lowering the resonant frequency of the FSS groundplane. Or better yet, simply realize that when building an actual array, we would most likely use a finite solid groundplane rather than a finite FSS groundplane. Thus, there would be no surface wave attached to the finite groundplane per se. At any rate, if we can avoid jitter when using a "nervous" FSS groundplane, we should be able to handle quite a few options.

Some deviations in scattering was observed from a few triads in the edge area. However, by adjusting the load resistors as well as the spacing to the groundplane, it was possible to reduce the scattering at the center frequency 10 GHz to zero while the scattering at the rest of the frequencies were sufficiently close to the triads in the rest of the array.

Let us summarize: It is possible by careful design to obtain large arrays of dipoles with a groundplane that are virtually free from jitter over a significant frequency range.

And once demonstrated for dipoles, it is generally recognized that it should be possible for other types of phased arrays as well.

The designs presented in this chapter have not been optimized for greater bandwidth essentially for two reasons:

1. We wanted primarily to demonstrate that jitter-free arrays simply exist.
2. Most practical arrays will be blended into an airframe or ship structure and should consequently be designed with this in mind.

Super-broadbanded infinite arrays will be discussed in Chapter 6.

PROBLEMS

5.1 It has often been noted that the scattering from a flat plate appears to emanate from the edges. This observation is certainly true when considering a perfectly conducting plate and to some extent a dielectric slab.

However, reflecting flat plates in general can be considerably more complicated than just that, and great care should be observed.

Discuss how it is possible to design flat finite reflectors that:

- Scatter strongly from the edges and absorb everywhere else.

- Absorb at the edges and reflect strongly everywhere else.

- Absorb at the edges and everywhere else.
  So much for simplistic concepts.

5.2 Based on the curves given in Figs. 5.26 through 5.35, estimate the backscattered field for the entire array for angle of incidence equal to $-15°$.

5.3 From Fig. 5.36, bottom, calculate the VSWR at $f = 8, 9, 10, 11,$ and 12 GHz. Compare these values with the standing wave ratio shown in Fig. 5.36, top, for the field reflected from the front of the array in the backscatter direction. Considering that only a single current mode is used, you will find the agreement quite satisfactory.

6

Broadband Wire Arrays

6.1 INTRODUCTION

It was pointed out in Chapter 2 that arrays possess unique features from a radar cross section point of view. To reduce the RCS outside the operating band of an antenna in general, a bandpass radome is often placed in front of it (see Chapter 2, Fig. 2.1). In the case of an array we recall from Chapter 2 that a low RCS is obtained when the terminal reflection coefficient is low; in other words, the bandwidth of the array should ideally exceed that of the radome. Furthermore, due to the high price tag of arrays in general, it is desirable to pass on as much information through them as possible. Thus, we shall in this chapter consider the principles for broadband arrays, which is of interest to the communication community.

Quite often arrays are expected to be rather narrowbanded. This is usually rooted in the fact that a single dipole has a rather limited bandwidth (10–20% unless broadband-compensated; see Appendix B). However, when placed in an array the mutual coupling between the individual dipoles can as shown here be designed to increase the bandwidth substantially rather than reduce it (see also Appendix D). Furthermore, addition of a groundplane in the back and dielectric compensation slabs in the front can lead to designs where the bandwidth is approaching a decade rather than an octave. However, it should be emphasized that merely using a couple of dielectric slabs laying around in the shop will not do. Proper design is of utmost importance.

It should also be pointed out at the beginning of this chapter that frequent use will be made of rather simple equivalent circuits. These are intended only

to explain the physics of the problem and guide us in our design effort. At no time do we rely on these to obtain actual calculated values. These are obtained rigorously by use of either the PMM (infinite $\times$ infinite array) or the SPLAT program (finite $\times$ infinite array).

Everybody can learn to run somebody else's program. Only a minority is capable of making the correct interpretation. But a simple equivalent circuit certainly helps.

6.2 THE EQUIVALENT CIRCUIT

The key to the equivalent circuit for an array of dipoles backed by a groundplane and with one or more dielectric slabs in the front is obtained from Problem 5.2 in reference 92. For easy reference it has been reproduced in Fig. 6.1. The circuit is strictly speaking only valid for the E and H planes, and for no grating lobes. Furthermore, the elements must be short as stated in the original problem [92]. In the intercardinal planes some cross-polarization will occur as is in general the case with dipole arrays. However, that should not deter us from developing our designs guided by this equivalent circuit since we ultimately would use the PMM code for verification of the concept for all scan planes.

Furthermore, R_{A0} denotes the radiation resistance of the array when located in an infinite free space and with no groundplane. Similarly, R_{A1} denotes the radiation resistance of the same array without a groundplane and located in an infinite medium with intrinsic impedance Z_1.
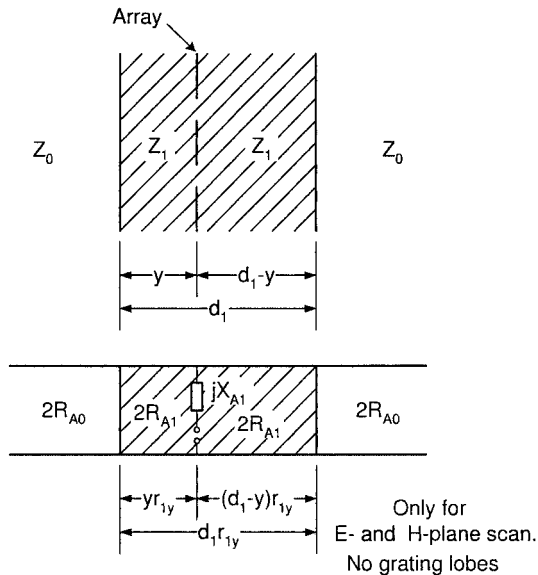
Fig. 6.1 *This problem is taken from reference 92 and constitutes the entire basis for this chapter about broadband wire arrays. The elements are assumed to be short in terms of wavelength.*

We see no reason to reveal the solution to Problem 5.2 (of reference 92) and thereby deprive the reader of a great opportunity to enlighten himself.

6.3   AN ARRAY WITH GROUNDPLANE AND NO DIELECTRIC

To start, let us consider an array of dipoles with a groundplane and no dielectric slabs in front. From Fig. 6.1 we readily obtain the equivalent circuit for this case as shown in the insert of Fig. 6.2. We shall point out various impedance
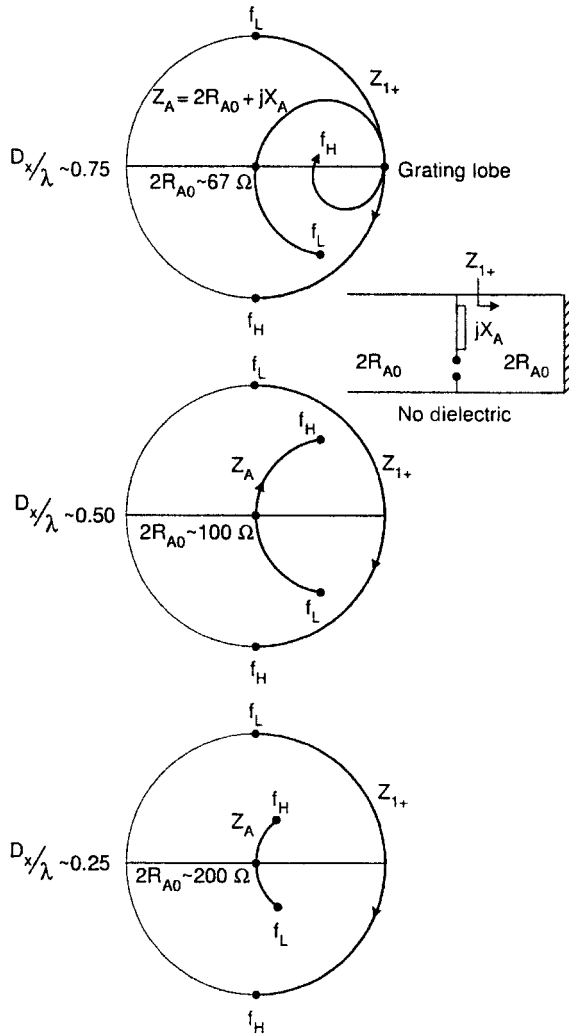
Fig. 6.2   *Typical terminal impedance* $Z_A = 2R_{A0} + jX_A$ *in the negative direction. The interelement spacing is varied from* $D_x/\lambda = 0.75$ *to 0.25. The groundplane impedance* Z_{1+} *is purely imaginary; that is, it is located on the rim of the Smith charts as shown.*

components. First, the impedance Z_{1+} denotes the input impedance of the equivalent transmission line looking in the positive direction from the array and terminated in a short (namely the groundplane). This impedance will always be purely imaginary; that is, it will be located on the rim of the Smith chart as also shown for various cases in Fig. 6.2 to be discussed later. Quite often it is suggested that this impedance ideally should be infinite (see *Common Misconceptions*, Section 6.12). This will happen when the spacing between the elements and the groundplane is one-quarter wavelength (for broadside radiation). At a lower frequency f_L, it becomes inductive and similarly it is capacitive at the higher frequency f_H. Looking in the negative direction we observe an infinite transmission line with characteristic impedance $2R_{A0}$. Finally, the reactive part jX_A of the antenna impedance $Z_A = 2R_{A0} + jX_A$ in the negative direction is obtained only from the evanescent waves surrounding the elements on both the positive and negative sides of the array elements, see reference 93.

Let us now examine the typical effect of the interelement spacing D_x as illustrated for three cases in Fig. 6.2. At the top we show a typical impedance Z_A for $D_x/\lambda \sim 0.75$. This is followed by cases for $D_x/\lambda \sim 0.50$ and 0.25 as shown in the middle and the bottom, respectively. Note that $2R_{A0}$ is approximately inverse proportional to D_x/λ and also that more bandwidth is obtained for smaller interelement spacings. The latter observations are counterintuitive to many people since the mutual impedance certainly will increase with smaller interelement spacings. (Note that the real part of the impedance does indeed increase as D_x decreases while the imaginary part does not.)

One physical explanation for this fact is that the imaginary part of the mutual impedances start canceling each other as we move away from the reference element, provided that the interelement spacings are small ($<0.4\lambda$), while they add up (eventually to disastrous grating lobes) if D_x/λ is larger than ~ 0.5. For further discussion of this subject see Section 6.12 and also Appendix D.

6.4 PRACTICAL LAYOUTS OF CLOSELY SPACED DIPOLE ARRAYS

When laying out the elements of a broadband dipole array without a groundplane, one should keep in mind that the ideal aperture is really a continuous current sheet as suggested by Wheeler [94]. It has no reactance (when there is no groundplane), only a radiation resistance that is scan-dependent, but can be compensated to a degree with dielectric slabs [95–97]. The question then becomes how best to make an approximation to such a current sheet. One approach is shown in Fig. 6.3. It basically consists of long closely spaced wires fed periodically along the wires as shown. This approach will ensure a current distribution between the feedpoints that is sinusoidal, but with a strong DC component. Thus, the current distribution is significantly different from that of isolated short dipoles that essentially go to zero at the ends (with a somewhat blunt "nose" caused by the end capacity). However, since short wires are associated with inductances, we have inserted series capacitors with the same periodicity as the feed
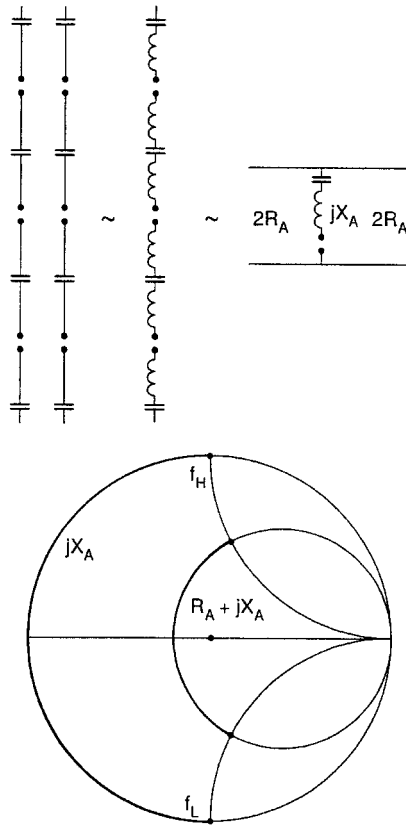
Fig. 6.3 *One possible implementation of a current sheet aperture by using infinitely long wires periodically fed and with their inductance compensated by periodically inserting series capacitors. Note: Our goal is to obtain reasonable constant currents along the wires to imitate a current sheet.*

points. The resulting equivalent circuit is shown in the insert of Fig. 6.3; and by consulting Appendix B, we readily obtain the locus for the antenna impedance $Z_A = R_A + jX_A$ as shown in the Smith chart in Fig. 6.3. Note that the value of the capacitors is not critical since they are actually in parallel with the tip capacitance between the elements (that can be more substantial than many expect; see also Section 6.12.2 and the discussion concerning circuit analog absorbers [98] as well as Weber [89]).

An alternate approach is shown in Fig. 6.4, left, where the capacitance between the element tips has been increased by tilting the elements as shown. This layout was first presented in Tom Kornbau's dissertation [99] and resulted in an FSS with extreme bandwidth, commonly referred to as the "gangbuster surface" [91]. It was the result of a brainstorm that Tom and the author had one day. However, somebody missed the deadline for the patent applications (some lawyers are fast, others are not).
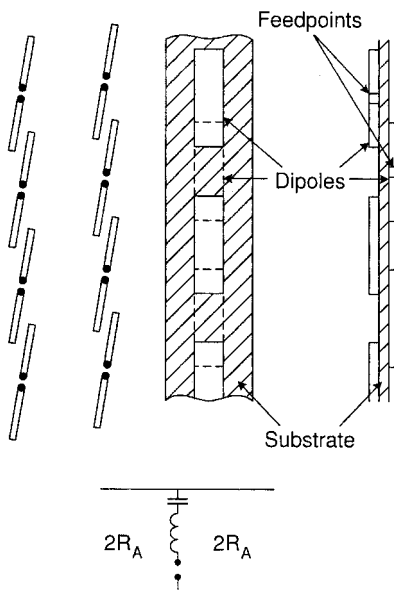
Fig. 6.4 Alternative approaches for designing a current sheet aperture. Left: Tilted and closely packed dipoles. Right: Dipoles alternating between the two sides of a dielectric substrate.

Still another variation is shown in Fig. 6.4, right. There the elements are placed on both sides of a thin dielectric substrate in one interlacing pattern, as shown. That approach is currently being used by Mission Research Corporation, Dayton, Ohio. Harris uses elements loaded with finger capacitors (see Fig. 10.4 and associated comments).

6.5 COMBINATION OF THE IMPEDANCE COMPONENTS

We next show in Fig. 6.5 how the various impedance components are combined. First we connect Z_{1+} in parallel with $2R_{A0}$. Since Z_{1+} is purely reactive, the parallel combination $2R_{A0} \parallel Z_{1+}$ will be located somewhere on a circle going through $2R_{A0}$ and the origin (0,0) of the Smith chart (for a comprehensive introduction to impedance matching in general and broadband matching in particular, see Appendix B). Finally, we add the reactance jX_A in series with $2R_{A0} \parallel Z_{1+}$. Since jX_A is purely imaginary, all the new impedances will lie somewhere on the circles going through the respective impedances $2R_{A0} \parallel Z_{1+}$ and the infinity point in the Smith chart (again consult Appendix B). From Fig. 6.2 we recall that jX_A typically is negative at frequencies below the center frequency f_0. Thus, the impedances $2R_{A0} \parallel Z_{1+}$ will be dragged downward toward the capacitive region. Similarly, the impedances $2R_{A0} \parallel Z_{1+}$ will be pushed upward when the frequency is above f_0. The net result is that we obtain a total impedance that is clustered in a smaller area than the impedances of the various impedance components
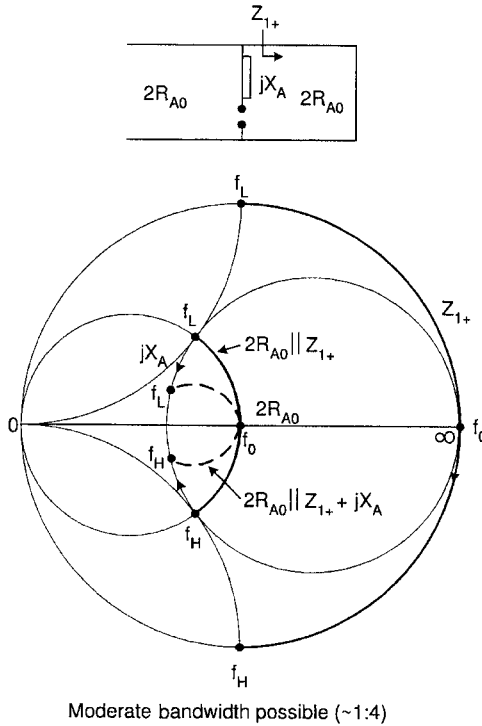
Fig. 6.5 Top: The equivalent circuit for an array of wire dipoles backed by a groundplane. Bottom: The groundplane impedance Z_{1+} at the rim of the Smith chart is being connected in parallel with $2R_{A0}$ to the left and denoted $2R_{A0}\|Z_{1+}$. Finally, adding the antenna reactance jX_A in series is seen to produce a more compact terminal impedance $2R_{A0}\|Z_{1+} + jX_A$ than without a groundplane.

individually. If we at the same time can land this cluster at the correct impedance, we have indeed obtained a broadband array. Obviously the terminal impedance curve can be compressed further than is shown.

6.6 HOW TO OBTAIN GREATER BANDWIDTH

An array of dipoles with small interelement spacings and backed by a ground-plane can be designed to have a bandwidth of around 4:1 with a VSWR <2. In order to obtain a greater bandwidth (or a lower VSWR), several ideas come to mind. First, it is desirable that the level of the groundplane impedance Z_{1+} should be high. (This does not mean that it should be infinite at all frequencies; in fact, that is not even desirable in order to compensate other impedance components as shown above. See also Section 6.12 for further discussion.) One approach often suggested is to somehow make a groundplane that would move electrically as a function of frequency with respect to the dipole array. Since that

idea turns out to be a "bad" one, it is merely discussed in *Common Misconceptions*, Section 6.12.1.3.

Another approach would be to fill the space between the dipole array and the groundplane with a material having a higher intrinsic impedance than that of free space. This would automatically lead to a higher groundplane impedance Z_{1+} and thereby a potential for larger bandwidth. Unfortunately, material with a higher relative μ than relative ε are rare; and if encountered at all, they are usually narrow banded, heavy, and lossy. Thus, this approach does not hold much promise either at this point in time. In fact, based on a fair amount of experience, it seems safe to state that a high groundplane impedance Z_{1+} being independent of frequency has so far eluded us. (If anyone out there somehow engineers such a material, don't write a paper about it—just see me.)

However, what we might do is to lower the impedance Z_{1-} relative to Z_{1+}, where Z_{1-} denotes the input impedance of the equivalent transmission line looking left; see insert at the top of Fig. 6.6. If such a manipulation would leave
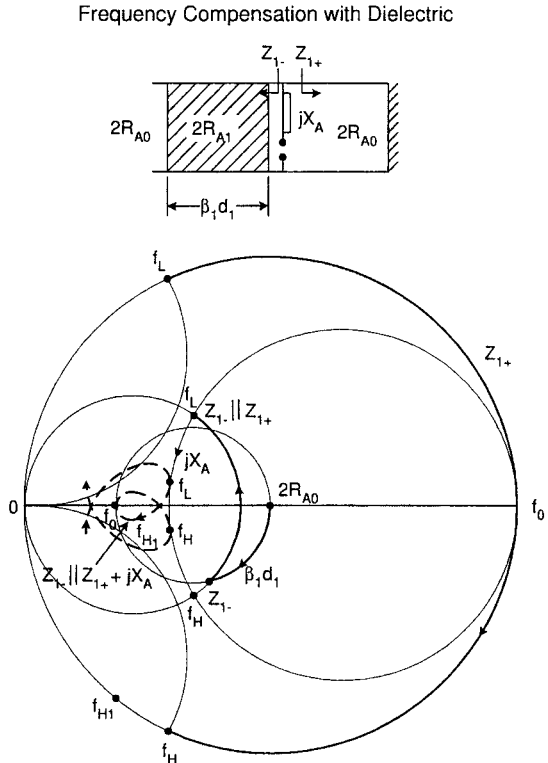
Fig. 6.6 Top: The equivalent circuit for an array of wire dipoles with a dielectric slab in front and a groundplane in the back. Bottom: From the array we look left through the dielectric slab and see Z_{1-}. Then we connect the groundplane impedance Z_{1+} in parallel and obtain $Z_{1-} \| Z_{1+}$. Finally, we connect the antenna reactance jX_A in series and obtain the compensated terminal impedance curve $Z_{1-} \| Z_{1+} + jX_A$.

the groundplane impedance Z_{1+} unaffected, it would be equivalent to making Z_{1+} relatively higher and thereby lead us to a potentially larger bandwidth.

One possible execution of that idea is discussed next.

6.7   ARRAY WITH A GROUNDPLANE AND A SINGLE DIELECTRIC SLAB

In Fig. 6.6 we show an array comprised of a groundplane and a dielectric slab in front of the dipoles. Again, we shall examine the various impedance components and their combinations. First of all, the impedance Z_{1-} denotes the input impedance of the equivalent transmission line at the plane of the array looking in the negative direction. It is seen merely to be the input impedance of a transmission line with characteristic impedance $2R_{A1}$ and terminated in $2R_{A0}$. The Smith chart at the bottom of Fig. 6.6 is normalized to $2R_{A0}$; that is, the transforming circle will for $\beta_1 d_1 = 0$ start from the center of the Smith chart. Furthermore, when the slab is equal to $\lambda_1/4$ at the center frequency f_0, the input impedance will be determined by the point $(2R_{A1})^2/2R_{A0}$ (for details consult Appendix B). Since $2R_{A1} < 2R_{A0}$ because of the presence of the dielectric, it is clear that the quarterwave point of the transforming circle will be located at a point denoted f_0 to the left of the center of the Smith chart, as shown in Fig. 6.6. Furthermore, the distance between the array and the groundplane is typically chosen also to be equal to one quarter-wavelength at the center frequency f_0. Thus, $Z_{1+} = \infty$ and will consequently not change Z_{1-} when connected in parallel. Finally, we must according to the equivalent circuit at the top of Fig. 6.6 add jX_A to $Z_{1-} \parallel Z_{1+}$. Typically, $jX_A \sim 0$ at the center frequency f_0; that is, the entire terminal impedance $Z_{1-} \parallel Z_{1+} + jX_A$ is essentially given by point f_0 at the center frequency.

Let us next examine the terminal impedance at a typical lower frequency f_L. Again we observe that the impedance Z_{1-} will be located on the same transformation circle as for f_0 above. However, since the electric thickness of the dielectric slab now is smaller than a quarter-wavelength, we will transverse a shorter path than above as indicated by Z_{1-} in the Smith chart in Fig. 6.6. Next, we add the impedance Z_{1+} in parallel with Z_{1-}. Since the frequency f_L is lower than f_0, Z_{1+} is inductive and will consequently push Z_{1-} up toward the inductive part of the Smith chart along the circle going through Z_{1-} and point (0,0) as indicated by point $Z_{1-} \parallel Z_{1+}$ (for details see Appendix B). Finally, we must add jX_A. At the lower frequency f_L it is capacitive and will consequently push $Z_{1-} \parallel Z_{1+}$ downwards when added in series. It will move along a circle going through $Z_{1-} \parallel Z_{1+}$ and the infinity point to the point denoted f_L (again, see Appendix B for details).

The performance of a typical high frequency f_H is obtained completely analogous to the f_L case. If jX_A is symmetric around f_0 (which is idealized), we will simply find that the terminal impedance is given by the point f_H located symmetrically to f_L. The typical terminal impedance curve as a function of frequency is denoted by $Z_{1-} \parallel Z_{1+} + jX_A$ in Fig. 6.6.

It is interesting to compare the nondielectric case in Fig. 6.5 with the dielectric case shown in Fig. 6.6. A casual inspection indicates that the latter has a greater potential for yielding a wider bandwidth or lower VSWR than the former. The reason is of course that the groundplane impedance Z_{1+} is partly canceled by the reactive part of Z_{1-} at higher as well as lower frequencies. In contrast to the nondielectric case in Fig. 6.5, the Z_{1-} impedance remains equal to $2R_{A0}$ without any reactive part at any frequency and will consequently not reduce the effect of the variation of Z_{1+} as a function of frequency.

The discussion above has been somewhat idealized; for example, $2R_{A0}$ will vary some with frequency and jX_A is not completely symmetric around f_0.

Input impedance renormalized to $Z_o = 100\ \Omega$ for:dip$_g$p41
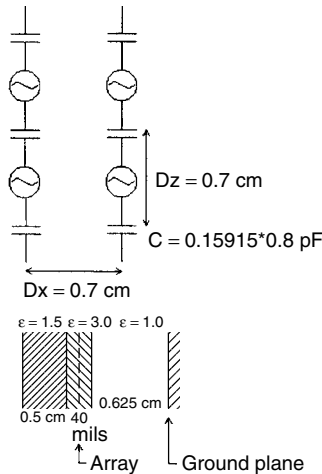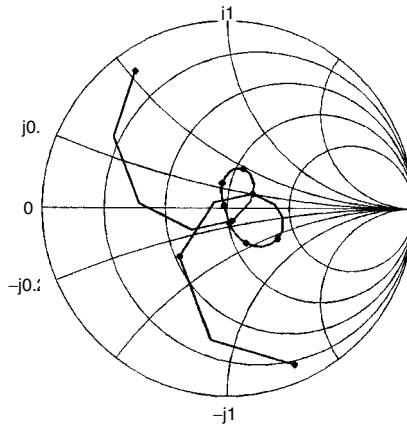
Fig. 6.7 *Calculated terminal impedance at broadside obtained from the PMM code based on the dimensions shown in the insert. The values include a small matching section comprised of a transmission line of length 0.13 cm and characteristic impedance 200 ohms.*

Nevertheless, it has served our main purpose, namely, to develop a concept yielding a broadband array. The final test will be trying our design using the PMM program. This is the subject of the next section.

6.8 ACTUAL CALCULATED CASE: ARRAY WITH GROUNDPLANE AND SINGLE DIELECTRIC SLAB

In the insert of Fig. 6.7 we show the pertinent dimensions of an array of dipoles with a groundplane and essentially a single dielectric slab (*Note*: The dielectric "underwear" [100] next to the dipole elements serve primarily as protection. It
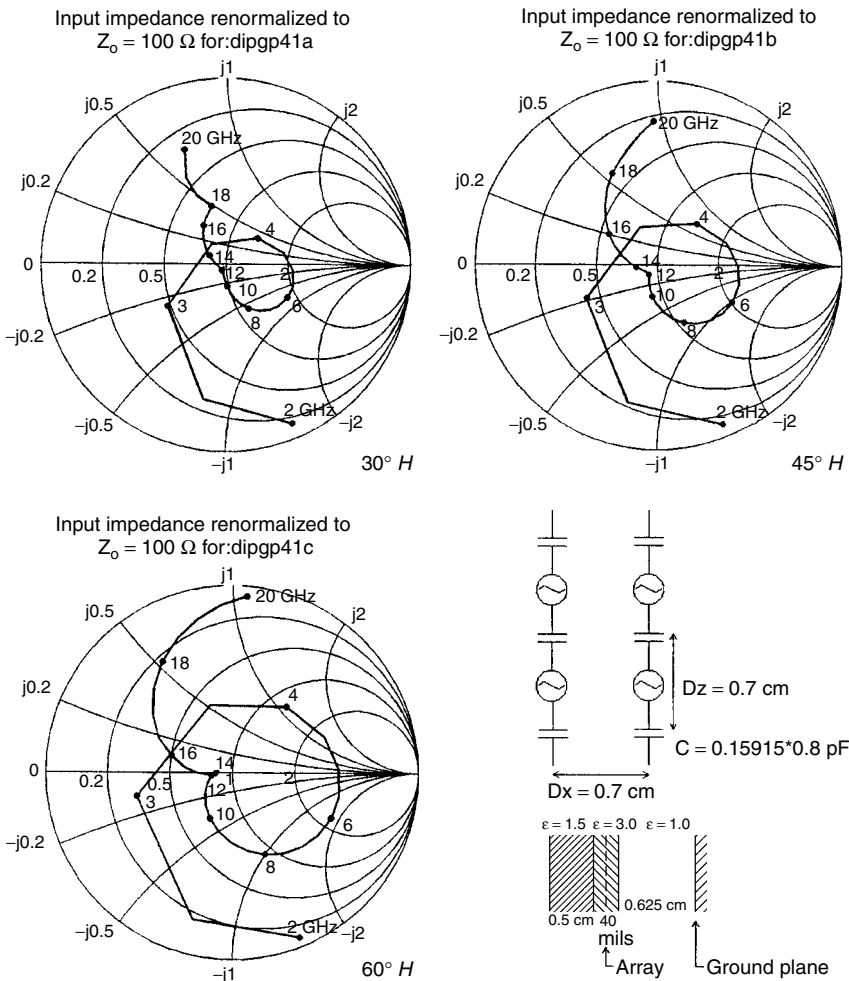
Fig. 6.8   Same array configuration as shown in Fig. 6.7 but for scan angles 30°, 45°, and 60° in the H plane.

is so thin that its transforming contribution is minimal. It is, of course, included exactly in the PMM calculations). The terminal scan impedance as obtained from the PMM program is shown in the Smith chart in Fig. 6.7. Several points should be emphasized when compared to the qualitative case in Fig. 6.6. First the calculated curve in Fig. 6.7 has been normalized to 100 ohms, which centers the impedance curve fairly well. Furthermore, the calculated curve actually is the input impedance of a transmission line with characteristic impedance 200 ohms, length 0.13 cm, and termination in the actual scan impedance. This transmission line serves the sole purpose of improving the matching as explained in Appendix B. Although short (the electric length amounts to 0.009λ at 2 GHz
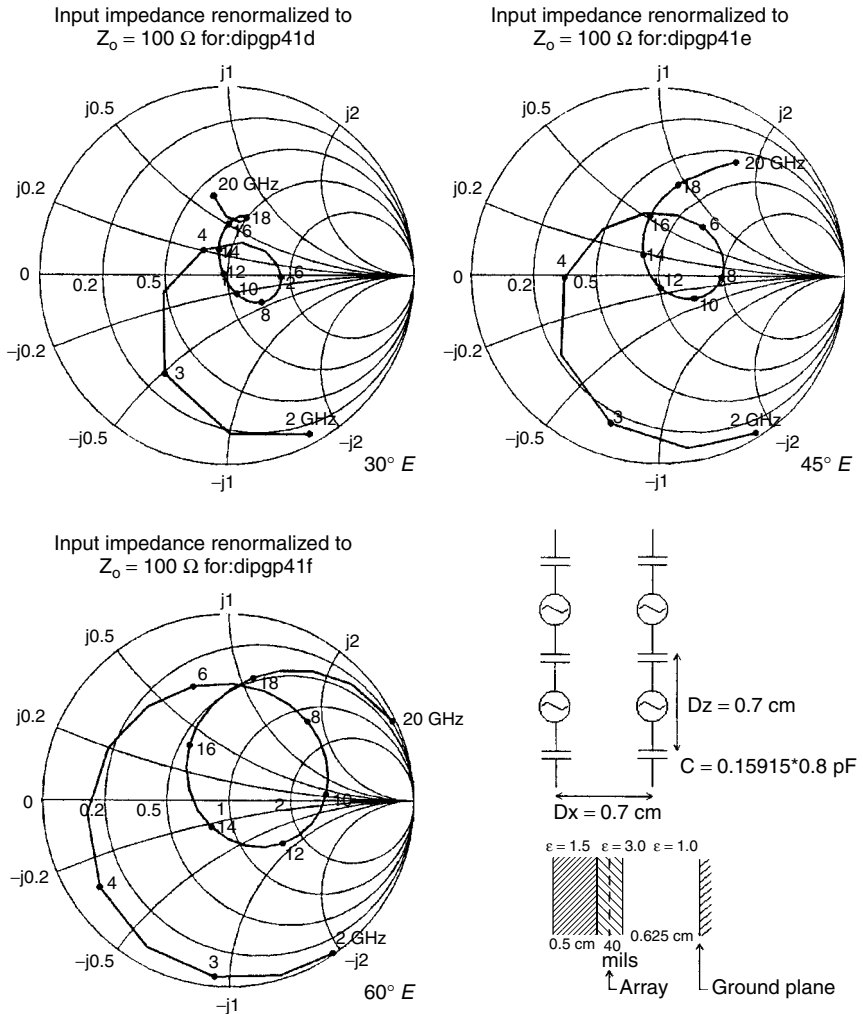
Fig. 6.9   Same array configuration as shown in Figs. 6.7 but for scan angles 30°, 45°, and 60° in the E plane.

and $\sim 0.09\lambda$ at 20 GHz), this section nevertheless plays an important role in obtaining the best match. It is simply a correction of the idealized situation shown in Fig. 6.6. It is also worth mentioning that the calculated curve is somewhat tighter than the qualitative one in Fig. 6.6. The reason for this is primarily that jX_A is somewhat more capacitive at the lower frequencies and more inductive at the higher; that is, jX_A is made somewhat more *narrowbanded* by itself in order to obtain greater bandwidth of the total scan impedance. This is counter to many people's intuition and is discussed further in Section 6.12.

Finally, we show in Fig. 6.8 the scan impedance for 30°, 45°, and 60° in the H plane. Similarly, Fig. 6.9 shows the scan impedances in the E plane for the same scan angles.

Note that the computed case has not been optimized for either bandwidth or scan compensation. This would be a good place to start. But please don't write a paper about it. It is simply left as an exercise for the students.

And by the way: Once you get this close to a good design, the winner among the various optimization programs is probably more a matter of coincidence than substance.

6.9   ARRAY WITH GROUNDPLANE AND TWO DIELECTRIC SLABS

In the previous section we demonstrated how an increase in bandwidth and/or reduction in VSWR could be obtained by placing a single dielectric slab in front of the array. It would be natural to expect further improvement if we used two or more slabs instead of a single slab. This is indeed the case. However, to obtain the potential improvement we shall need some design guidance, and for this purpose we will next show the transformations for one and two dielectric slab cases as seen in the rectangular coordinate system rather than the Smith chart. The reason for this choice is simply that it allows us to depict quite complicated transformations on a single piece of paper leading to a better overview. Thus, for the sake of comparison we show first in Fig. 6.10 the rectangular transformation of a single dielectric slab similar to the case shown earlier in the Smith chart in Fig. 6.6. We have chosen a dielectric constant for the slab equal to $\varepsilon_1 = 2$, leading to a transformation of $2R_{A0}$ into R_{A0} at the center frequency f_0. Thus, the transformation circle for all frequencies at broadside is given by the circle going through these two points as shown in Fig. 6.10. A typical input impedance of the transmission line looking left is as shown in the schematic denoted Z_{1-}. We next add the groundplane impedance Z_{1+} in parallel and obtain the point $Z_{1-} \parallel Z_{1+}$ located in the upper half of the complex plane. Finally, we add the antenna reactance jX_A and obtain the total scan impedance denoted $Z_{1-} \parallel Z_{1+} + jX_A$.

Next we show in Fig. 6.11 a typical two-layer case. Again, we have chosen the dielectric constants such that the impedance $2R_{A0}$ will be transformed into R_{A0} at the center frequency f_0 like in the single slab case. However, we must in the double-layer case choose still another parameter. We have chosen the impedance level between the two slabs to be midway between $2R_{A0}$ and R_{A0}; that is, it is
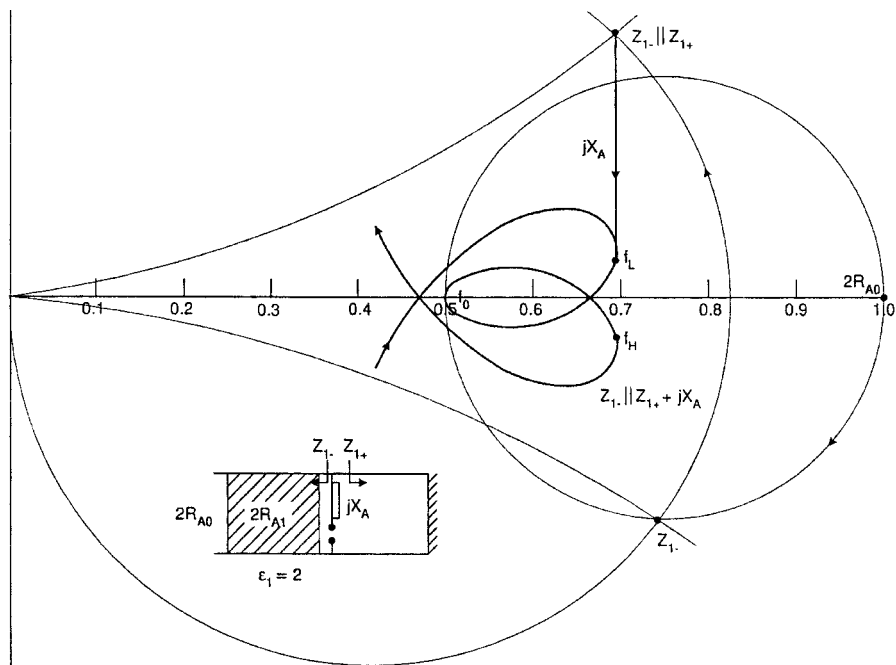
Fig. 6.10 *Single dielectric slab. The input impedance as seen through the dielectric slab at the array in the negative direction is denoted Z_{1-}. As shown in the schematic, we then connect the groundplane impedance Z_{1+} in parallel and obtain $Z_{1-} \| Z_1$. Finally, we add the antenna reactance jX_A in series and obtain the compensated terminal impedance curve $Z_{1-} \| Z_{1+} + jX_A$.*

fixed at $1.5R_{A0}$. That completely determines the characteristic impedances of both dielectric slabs as indicated in Fig. 6.11 as well as the relative dielectric constants shown in the insert. More precisely, the transformation circles for the outer slab Z_1 will be determined as having a diameter going from $2R_{A0}$ to $1.5R_{A0}$, while the transformation circle for the second slab Z_2 will span over R_{A0} and $1.5R_{A0}$. The input impedance of the outer slab looking in the negative direction is denoted Z_{1-}. At a typical frequency f_L lower than f_0 it will be located on the lower half of the transformation circle for the first slab as indicated in the figure. We must next use this impedance Z_{1-} as the load impedance for the second slab. Since we also know the characteristic impedance Z_2 for the second slab, we can determine the transformation circle as shown in Appendix A, Case III (in particular, consult Fig. A.3). The pertinent construction lines are shown dashed in Fig. 6.11. Next, we determine the position of the input impedance Z_{2-} for the second slab as explained in Appendix A, Section A.2, Case III, in conjunction with Fig. A.3. Similar to the single-slab case we now add the groundplane impedance Z_{2+} in parallel and obtain in that way the point $Z_{2-} \| Z_{2+}$ in the upper part of the complex plane as shown. Finally, we add the antenna reactance jX_A in series and obtain the total scan impedance denoted as $Z_{2-} \| Z_{2+} + jX_A$.
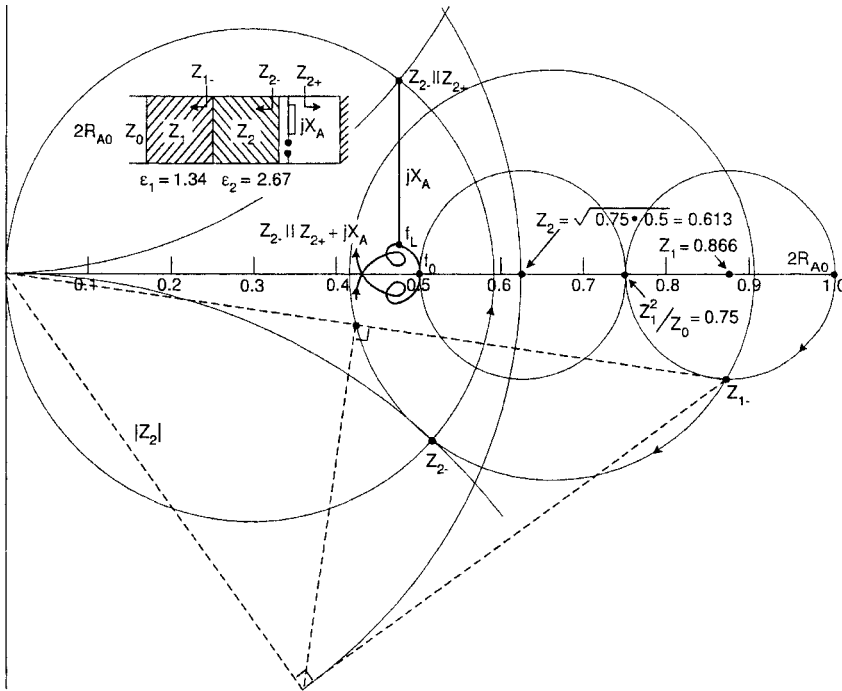
Fig. 6.11 Double dielectric slab. We first obtain the input impedance Z_{1-} of slab 1 looking left. Next, we find the input impedance Z_{2-} of the second slab when terminated in Z_{1-}. From the schematic we then see that the groundplane impedance Z_{2+} should be added in parallel yielding $Z_{2-} \| Z_{2+}$. Finally, we add the antenna reactance jX_A in series and obtain the compensated terminal impedance $Z_{2-} \| Z_{2+} + jX_A$.

6.10 COMPARISON BETWEEN THE SINGLE- AND DOUBLE-SLAB ARRAY

The determination of the locus for the scan impedance for a single slab in Fig. 6.10 and a double slab in Fig. 6.11 is only qualitative. However, the reduction of VSWR and to some extent an increase in bandwidth in the double-slab case is quite obvious. Inspection of the figures of the two cases shows that the primary reason is that the double-slab case produces a smaller variation of the real part of the scan impedance while the imaginary part must be balanced very carefully with the groundplane reactance Z_{2+} and the antenna reactance jX_A. In other words, a parametric study of actual calculated curves should be undertaken. A typical example will be given in the next section.

6.11 CALCULATED SCAN IMPEDANCE FOR ARRAY WITH GROUNDPLANE AND TWO DIELECTRIC SLABS

Undoubtedly, many readers have not felt too comfortable being "dragged around" the complex plane as was just demonstrated above. For those who prefer exact

Input impedance renormalized to $Z_o = 100\ \Omega$ for:dipgp68o
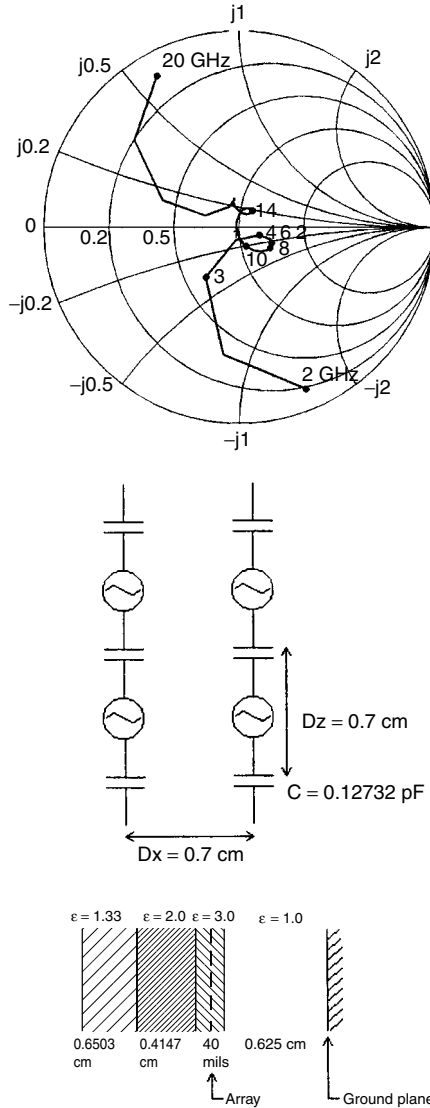
Fig. 6.12   Calculated impedance of a double-slab array as obtained from the PMM code with dimensions as shown in the insert. This curve also incorporates a small matching section comprised of a transmission line of length 0.12 cm and characteristic impedance 200 ohms. Note: This case has not been optimized.

calculated impedance curves, a typical calculated scan impedance curve is shown in Fig. 6.12. It is the result of an exploratory parametric study that showed that minimum VSWR is obtained by choosing the impedance level at the elements slightly higher than R_{A0} as was the case in Fig. 6.11. Rather, it should be chosen

around $1.32R_{A0}$. Similar to the single dielectric case in Fig. 6.7, it makes use of a short transmission line of length 0.12 cm and characteristic impedance 200 ohms in order to better center and compress the impedance curve.

As stated in the previous section, it clearly leads to a lower VSWR rather than increasing the bandwidth. However, it must be pointed out that no formal optimization for either one of these two features was performed.

Finally, we show in Fig. 6.13 the scan impedance for scanning at 30°, 45°, and 60°, respectively, in the H plane, while Fig. 6.14 shows the E-plane scan at the same scan angles. Compared to the single-slab cases shown in Figs. 6.8 and 6.9, we observe that the double-slab case continues to be superior to the single-slab
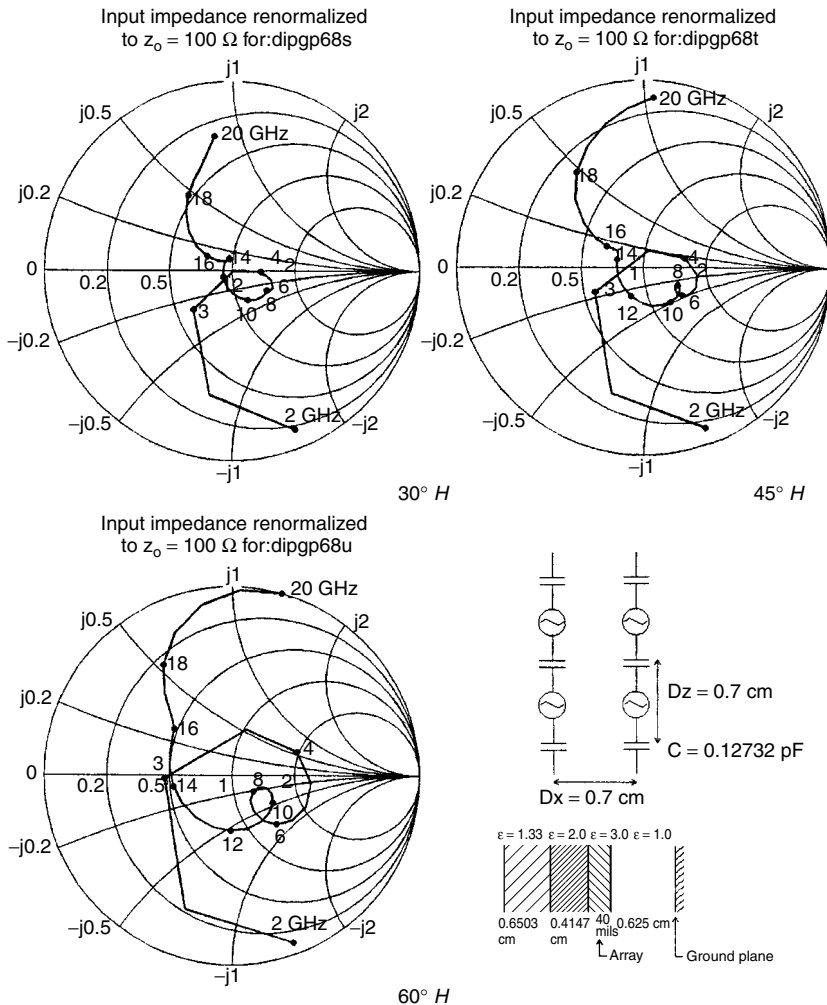
Fig. 6.13   The scan impedance for the same case as shown in Fig. 6.12 but for scan angles equal to 30°, 45°, and 60° in the H plane.
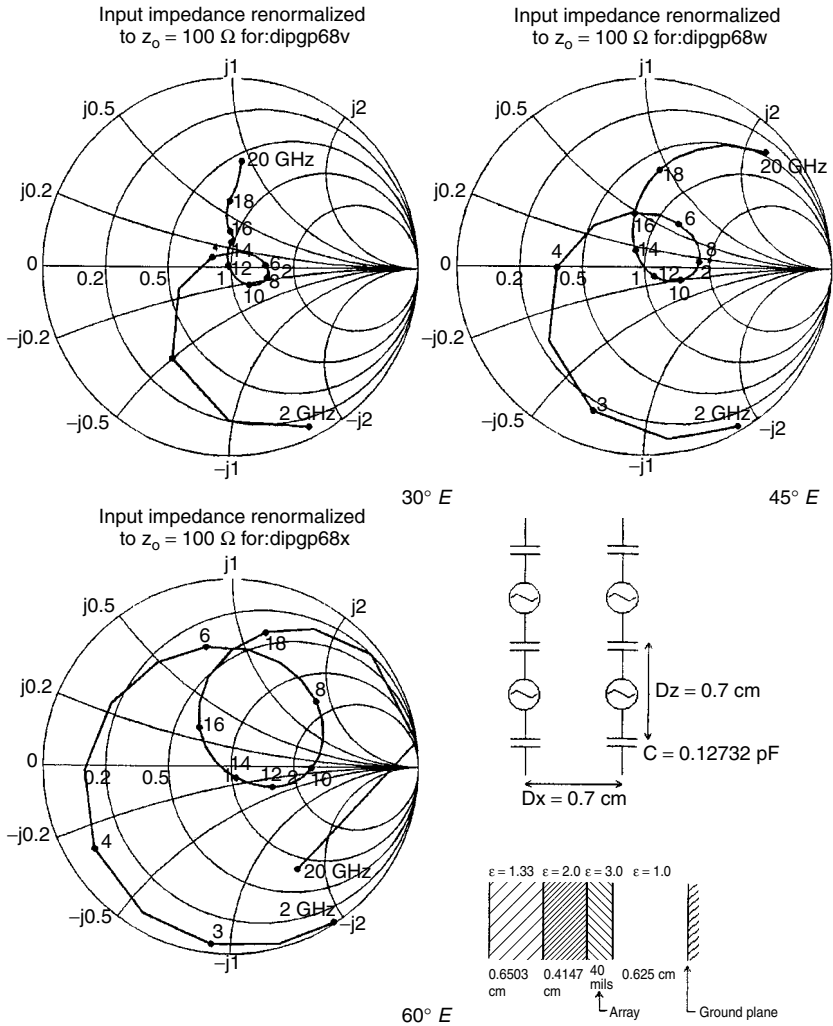
Fig. 6.14   The scan impedance for the same case as shown in Figs. 6.12 and 6.13 but for scan angles 30°, 45°, and 60° in the E plane.

case. However, we emphasize that no parametric study has been undertaken to determine a better design from a scan angle point of view. This could perhaps be worthy of a paper.

6.12   COMMON MISCONCEPTIONS

6.12.1   Design Philosophy

6.12.1.1   Array Versus Element   It is often suggested that design of a broadband array starts with the development of a single element with large bandwidth.

Certainly, an element with an inherently small bandwidth is not very likely to yield a much wider bandwidth when placed in an array environment. The patch element would fall in that category. But a single short dipole is not particularly broadbanded either, although it is better than the typical patch (see also Appendix D). Still, when dipoles are placed in an array environment, a significant increase in bandwidth can be obtained as demonstrated by several examples earlier in this chapter. The trick consists of placing the dipoles close to each other as shown in Figs. 6.2 and 6.4 while the patches in general will be too large to do the same. To many designers, placing dipoles closer to each other runs counter to their intuition since it definitely increases the mutual coupling between elements. The physical explanation of this dilemma is simply to note that the stored energy associated with a single element removed from the array occupies the space reaching from the surface of the element to infinity. In contrast, the stored energy associated with a single element in an array reaches only from the element surface and midway to the next neighbor elements—that is, less space resulting in less stored energy. And that simply in general means more bandwidth (and for the record, this is also the reason "fat" dipoles have more bandwidth than the thin ones). See also Sections 6.3 and 6.12.2.

This argument does in no way contradict the fact that most stored energy is located in the immediate vicinity of the elements. Recall (see Sections 4.8–4.10 in reference 1) it is directly associated with the evanescent waves that decrease exponentially but are still "felt" at a typical distance of $\sim\lambda/4$ from the elements. Thus, if the interelement spacing typically is 0.3λ, the "storage space" is limited to 0.15λ.

[It is more complicated to examine the field from a single elements where the near field falls off like $1/r^2$ and $1/r^3$.]

Finally, the designer should be reminded that the element spacing should always be sufficiently small to avoid grating lobes and surface waves in dielectric slabs adjacent to the dipole elements.

6.12.1.2 *Array Versus Groundplane*   Another misconception concerning a design approach is that one should first attempt to design a broadband array without a groundplane and then later battle the effect of adding a groundplane. Typically, that philosophy might lead to an array of closely wound flat spiral elements. Such an array without a groundplane can indeed have a reasonably low VSWR over a significant bandwidth as indicated in Fig. 6.15. However, note that the antenna impedance rotates several times around the Smith chart, in sharp contrast to the variation of a dipole array that goes slowly and monotonically from the capacitive to the inductive region (see Figs. 6.2 and 6.3). As we saw earlier in this chapter, this simply means that the antenna reactance jX_A and the groundplane impedance Z_{1+} could be designed to partly cancel each other and thereby yield a larger bandwidth as shown earlier. In contrast, the spiral array as well as other antennas, like the Vivaldi, can improve only when it happens to be in the capacitive region when Z_{1+} is inductive; otherwise the VSWR will get worse.

The fast variation with frequency as observed in the spiral array is typical for elements consisting of long wires (namely in this case the two arms of the

Long Wires vs. Short End-Loaded Dipoles
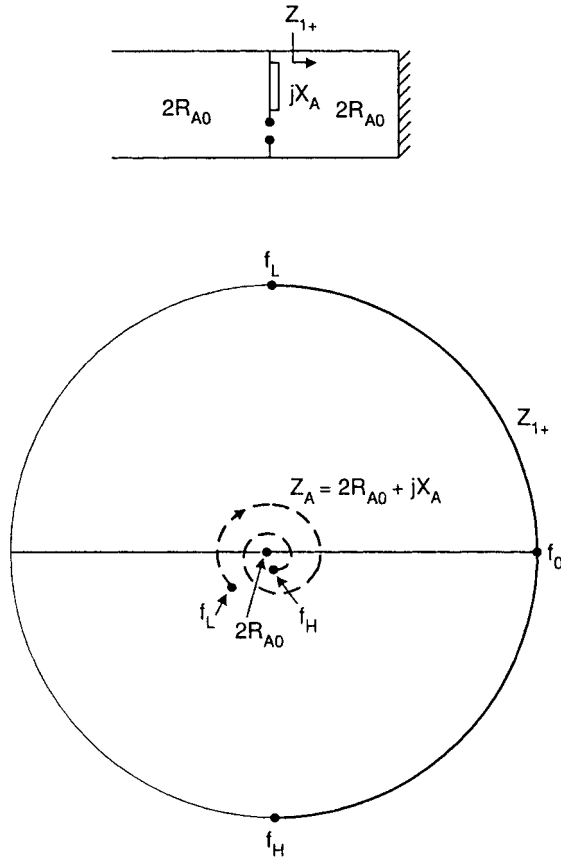
Fig. 6.15 *Typical antenna impedance $Z_A = 2R_{A0} + jX_A$ in the negative direction for a long wire antenna like a flat spiral without the effect of a groundplane. At lower frequencies the groundplane impedance Z_{1+} is inductive as shown on the rim of the Smith chart. The total antenna may improve if jX_A is capacitive but get worse if inductive. Thus, no broadband compensation will take place.*

spirals). It is quite similar to the input impedance of a long transmission line terminated in a load. However, in the spiral array case the loss should come primarily from radiation and not from actually terminating the arms in resistive loads (moderate loading might be acceptable to improve the performance of the spiral array at the lowest frequencies).

6.12.1.3 The "Moving Groundplane" (That Moves Too Fast!) We considered above an array of spirals in front of a groundplane. We observed how the antenna reactance X_A was incompatible with the groundplane impedance Z_{1+} and therefore would not lead to a consistently lower VSWR. However, one may

ask, Would it be possible to just make the groundplane impedance Z_{1+} very large over a large frequency range, if not infinite. In other words, could we somehow manage to keep the electrical spacing between groundplane and array equivalent to one quarter-wavelength at *all* frequencies?

One scheme often suggested to accommodate such an approach is shown in Fig. 6.16. We have placed an array of dipoles in front of a groundplane at a distance of one-quarter wavelength at the lowest operating frequency, for instance at $f_1 = 1$ GHz. In between the array and the groundplane is an FSS resonating at a higher frequency, such as $f_2 = 2$ GHz. The distance between the array and the FSS is one-quarter wavelength at f_2 as indicated in the figure.

We may further assume that the FSS is *transparent* at $f_1 = 1$ GHz (this is a gross approximation, but since this scheme is a scam anyway, so what!). Under that assumption we obtain $Z_{1+} = \infty$ at $f_1 = 1$ GHz as indicated in the Smith chart in Fig. 6.16. (A more rigorous calculation will show that the distance between the array and the groundplane should be somewhat less than $\lambda_1/4$ when we take into account the capacitive effect of the FSS at $f_1 = 1$ GHz.)
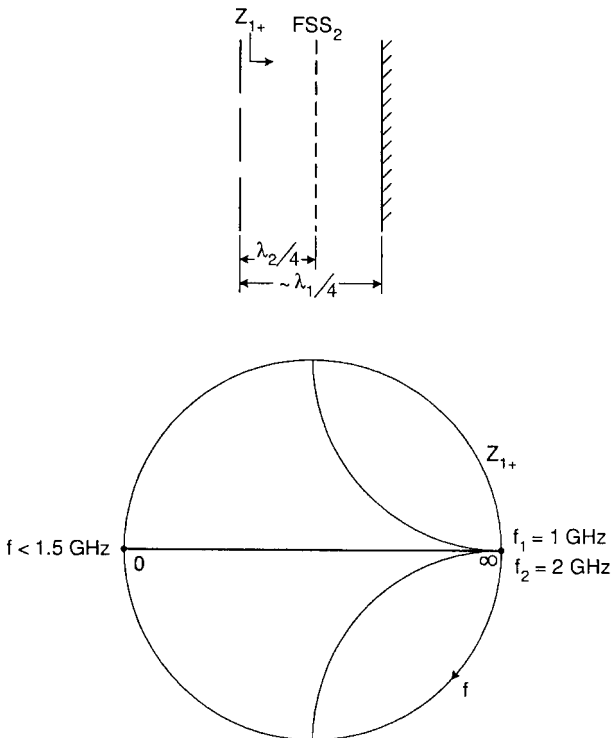
Fig. 6.16   The ''moving'' groundplane that moves too fast! An FSS resonating at 2 GHz will produce $Z_{1+} = \infty$ if the spacing between array and FSS is $\lambda_2/4$. Similarly, $Z_{1+} = \infty$ at $f = 1$ GHz, if the array and the groundplane is spaced slightly less than $\lambda_1/4$ from the array (see text). However, $Z_{1+} = 0$ somewhere between 1 and 2 GHz (Foster's Reactance Theorem [101]).

Similarly, $Z_{1+} = \infty$ at $f_2 = 2\,\text{GHz}$ as also indicated in the same Smith chart. So far we have obtained our objective: Z_{1+} is infinite at 1 and 2 GHz. The question now is, What will happen at other frequencies? First of all we note that all components to the right of the array are lossless. Thus, Z_{1+} must be purely imaginary—that is, located somewhere on the rim of the Smith chart. It is now a well-established fact that all impedances at the *rim* of a Smith chart will move clockwise with increasing frequency (it cannot just stop!). Thus, when going from 1 to 2 GHz we simply must follow the rim of the Smith chart; that is, at some frequency between 1 and 2 GHz, Z_{1+} must pass through zero in the Smith chart, which of course is a clear disaster. (For those who need a more rigorous proof, consult *Foster's Reaction Theorem* [101].)

Thus, it may be safe to state that a groundplane that moves with frequency such that the spacing between the moving groundplane and the array is $\sim\lambda/4$ simply violates fundamental physical laws. It is not that the groundplane does not move; rather, it moves about twice as fast as we want! Then of course there are those who would turn that feature into a multiband affair!

6.12.1.4 A Little Loss Can Cure Anything!

If one's main objective is to avoid going through zero in the Smith chart, it is certainly possible using the approach shown in Fig. 6.17. We have now added a load resistance R_L to the terminals of the FSS (or call it an array of loaded dipoles). This will result in an impedance of this sheet alone denoted by Z_{absorber} as indicated in the Smith chart in Fig. 6.17. If the spacing between the loaded FSS and the groundplane is $\lambda/4$ at the center frequency, the groundplane impedance Z_g as seen at the loaded array will look like also shown in the same Smith chart. Combining Z_{absorber} and Z_g in parallel yields the impedance Z_{2+}. Finally, if the spacing between Z_{absorber} and the actual array is $\lambda/4$ at the center frequency, the loaded groundplane impedance Z_{1+} is readily obtained by appropriate transmission line transformation of Z_{2+} in the Smith chart (see Appendix B).

Certainly, we have produced a loaded groundplane impedance Z_{1+} that does not go through zero over a considerable frequency range. However, we have in effect merely produced an absorber, or more precisely a circuit analog absorber. For an in-depth discussion about this type, see Chapter 9 in reference 102.

Typically, about half the input power will be absorbed and converted into heat (i.e., about a 3-dB loss). Thus, this is not a solution that is recommended in general—that is, unless you have a couple of hundred watts (or more) of transmitting power available and want to make an omelet (works best if you point the antenna toward nadir).

6.12.2 On the Controversy Concerning Short Dipoles

The self-impedance of a short dipole is indeed comprised of a low radiation resistance in series with a high capacitive reactance. Thus, when it is suggested to use these elements to build a broadband array, it is quite often discarded as being a bad idea.
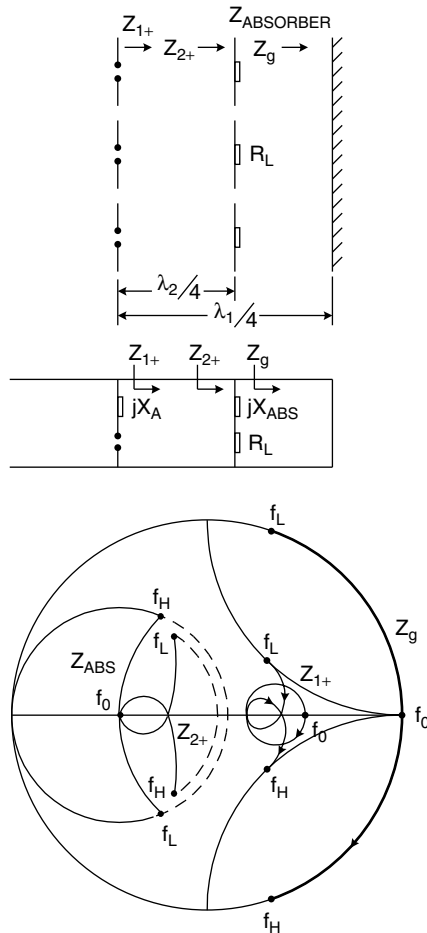
Fig. 6.17   *By adding loss to the FSS in Fig. 6.16 either in the form of lumped resistors or otherwise, we can avoid going through (0,0). However, we have merely produced an absorber, resulting in losses that usually are unacceptable.*

And when it subsequently is suggested to add an extra capacitance across the tips of the dipoles, many (or at least some) instantly assume that "Voodoo Physics" has made its entrance into the world of phased arrays.

Not withstanding the fact that numerous examples to the contrary were given earlier in this chapter, there are nevertheless many readers that would appreciate a more direct physical discussion of this apparent dilemma.

Thus, to accommodate this segment of our readers, let us consider the development depicted in Fig. 6.18. First to the far left (Fig. 6.18a) we show an array comprised of $\lambda/2$ dipoles. It resonates at the frequency f_0. The equivalent circuit of this array is shown in Fig. 6.18b. Note that it is comprised of equivalent inductances L_0 near the terminals and equivalent capacitances C_0 between the
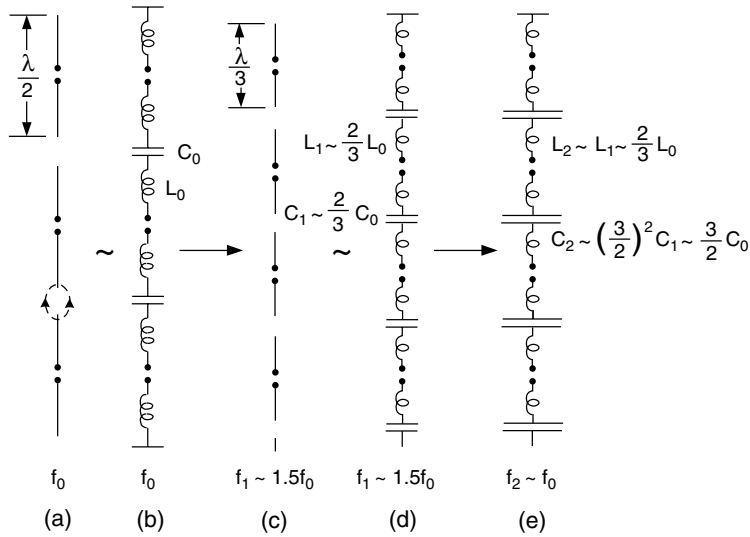
Fig. 6.18 *Self-impedance of a short dipole is indeed capacitive. However, it contains no "big bad capacitance." In fact, a dipole is comprised of an inductive wire L_0 near its terminals and a capacitance C_0 at the tips. Thus, if L_0 is reduced, C_0 must be increased to maintain resonance. Any conclusion to the contrary is based on voodoo physics. This figure explains why the capacitance between dipole tips must be increased if the dipoles are shortened and the resonance frequency is to be maintained.*

dipole tips (that a short wire is essentially an inductance should be well known to even inexperienced antenna engineers, and the formula for tip capacitance is given by Weber [89]).

Next, in Fig. 6.18c we scale the entire array downward by the factor $\lambda/3$: $\lambda/2 \sim 0.67$; that is, this scaled array resonates at $f_1 = 1.5 f_0$. In Fig. 6.18d we indicate that the new equivalent inductance is now $L_1 \sim 2/3 L_0$ while the new equivalent capacitance is $C_1 \sim 2/3 C_0$. Thus, based on these equivalent values, the array resonates at the correct frequency $f_1 = 1.5 f_0$.

Finally, in Fig. 6.18e we show the same array as in Fig. 6.18d, but in Fig. 6.18e we have added an extra capacitance from tip to tip (i.e. in parallel with C_1) such that we obtain a new larger total capacitance equal to $C_2 \sim (3/2)^2 C_1 \sim 3/2 C_0$.

Thus, the resonant frequency for this new array with augmented tip capacitance is equal to f_0.

Finally we remind the reader that the radiation resistance R_A of an array of dipoles without a groundplane is given by [103]

$$R_A = \frac{Z_0}{2 D_x D_z} \frac{1}{r_y} [_\perp P_\perp P^t + {}_\parallel P_\parallel P^t], \qquad (6.1)$$

where D_x, D_z denotes the interelement spacings, r_y denotes the direction cosine of the beam direction with respect to the boresight axis, $_\perp P, {}_\parallel P$ are the orthogonal

and parallel pattern components under scattering condition, respectively, and $_\perp P^t, {}_\parallel P^t$ are the orthogonal and parallel pattern components under transmitting conditions, respectively.

When an array is scaled, everything in (6.1) remains essentially constant except of course the interelement spacings D_x and D_z.

Thus, if D_x and D_z are reduced, the radiation resistance R_A will increase; in fact for close spacings it may easily reach several hundred ohms.

The fallacy with the short dipole argument alluded to above is simply that many readers do not fully appreciate how dominating a role the mutual coupling can play. Historically, it is rooted in the fact that the classical phased array approach typically would start by considering only a single element of whatever type. It was then hoped that the mutual coupling would be so low that the features of a single element would not be "masked" too badly in the array environment. Otherwise it became necessary to calculate the entire array which was in general frowned upon.

Today we know that it is actually easier to calculate the terminal impedance of an infinite array than it is to calculate it for a single element. And the mutual coupling should not be viewed as an evil to be avoided. On the contrary, when handled properly, it can be a true blessing to be enjoyed. And you certainly cannot outlaw it.

P.S.: The mutual coupling between adjacent dipoles in the typical arrays considered here is very large. We do not know how large because we do not care! And there is not much you can do with it anyway except marvel at it.

6.12.3   Avoid Complexities

6.12.3.1   On Array Gain   Some readers may by now have noticed that very little attention has been given to the gain of the array. This should not be interpreted as lack of interest in that subject. Rather it reflects the fact that it can be obtained in a forward and simple manner.

It was already pointed out in Chapter 2, Section 2.6.2, that a large array with groundplane, uniform illumination, and physical area A also has a receiving area equal to A. Thus, if the array is designed to have no grating lobes and no significant surface waves, we may conclude from one of the most fundamental laws in antenna theory that the directivity D of the array is

$$D = \frac{4\pi}{\lambda^2} A. \tag{6.2}$$

If the aperture illumination is tapered, the directivity in (6.2) should be multiplied by the aperture efficiency. That depends only on the aperture distribution [104].

Finally, the gain G is obtained from (6.2) by multiplication of the loss efficiency. Most commonly we are here talking about transmission line loss in the feeding harness and possibly some from the dielectric substrate supporting the elements.

Also, we must add the mismatch loss. If the antenna has a *VSWR* < 2 (as typical for the arrays discussed here), the mismatch loss will be less than 0.5 dB.

We emphasize that our derivation fails if there are grating lobes or a strong presence of surface waves. Both of these calamities are usually recognized by their adverse impedance behavior. Again we remind the reader that the most dangerous surface waves are the ones that show up only in the finite arrays (see Chapters 4 and 5). However, as also explained there, these surface waves can be greatly attenuated by feeding the elements from voltage generators with realistic generator impedances.

Thus, it is possible to get a relatively quick handle on the gain of a large and well-designed array. However, not all designers see it that way. Confusion often occurs if one tries to obtain the "gain" of a single element in the array. This can be made into a highly complex endeavor and will therefore often be the source of controversial results. The author remembers in particular a case where it was claimed that the gain of an array was low because the "element currents were low."

This is quite a common misconception. The amplitude of the element currents has nothing to do with the gain. Usually it just means that the element impedances are high. However, if the array impedance is properly matched, the field strength observed in the far field will be determined entirely by the total gain of the array that is dominated by the array factor and not the element pattern as discussed in *Common Misconceptions*, Section 2.14.3. See also Section 6.12.3.2.

For those who still prefer to marvel over the element pattern and gain, just take the total array gain as calculated above and divide it by the number of elements. At some point down the road, they will most likely ask for the total array gain. Well, just multiply the element gain by the number of elements!

6.12.3.2 Will More Elements Increase the Gain? It is sometimes implied that adding more elements to a large array of a given aperture will increase the gain. Well, under some circumstances it will and under others it won't. Let us examine this phenomena in a little more detail.

Consider first an array where the density of the elements is so low that grating lobes can exist. Since energy is lost in the grating lobe(s) (obviously we are transmitting), we will have less power going into the mainbeam and consequently a lower gain in that direction. Thus, if grating lobes can exist, adding more elements will increase the gain (the author can think of only a few cases where the presence of a grating lobe has been any blessing to mankind).

Let us now look at the case where the element density is so large that no grating lobe can exist. In that case the radiation resistance R_A of each element is given by [103]

$$R_A = \frac{Z_0}{2D_x D_z} \frac{1}{r_y} P^t P, \tag{6.3}$$

where D_x and D_z are the interelement spacings in the X and Z directions, respectively, r_y is the direction cosine along the y axis of the main beam, and P^t and

P are the radiation patterns under transmitting and receiving conditions, respectively.

Let us further denote the number of elements per meter along the X and Z directions by

$$N_x = \frac{1}{D_x} \quad \text{and} \quad N_z = \frac{1}{D_z}, \tag{6.4}$$

respectively.

From (6.3) and (6.4) we then obtain the following equation for the energy being supplied to the array per square meter:

$$P_A = N_x N_z R_A I_A^2 = (N_x N_z)^2 \frac{Z_0 P^t P}{2r_y} I_A^2, \tag{6.5}$$

where I_A denotes the effective element currents.

The far field E_{far} in the mainbeam must be proportional to I_A, N_x and N_z, that is,

$$E_{far} = C N_x N_z I_A, \tag{6.6}$$

where C is merely a proportionality factor. Substituting in (6.6) for I_A obtained from (6.5), we obtain

$$E_{far} = C \sqrt{\frac{2 P_A r_y}{Z_0 P^t P}}. \tag{6.7}$$

Thus, for no grating lobes and no surface waves we observe that E_{far} is completely independent of the total number $N_x N_z$ of elements. Obviously so is the gain. That should come as no surprise.

Remember that the antenna pattern is dominated completely by the array factor (see Section 2.14.3). The elements are merely there to approximate a continuous aperture. Once they reach a certain density, we are in a sense just oversampling.

But isn't anything happening when we increase the number of elements? Certainly, namely the radiation resistance R_A increases [see (6.3)] while the element currents I_A are reduced [see (6.5)]. And most importantly, the stored energy is being reduced, which means more bandwidth.

Of course, this is what this chapter is all about.

It is sometimes implied that a weak element current I_A results in a low far field and thus a low gain. It is hoped that this section will put this notion to sleep. See also Section 6.12.3.1. And by the way, adding more elements to produce endfire elements does not help either!

6.12.4 What Is So Special About λ/4 Anyway?

This author has been known to state that in microwave technology good things happen if you move in one-quarter time (unless you are in Vienna of course, where it should be in three-quarter time).

More specifically, is there something special going on when the distance between an array and a groundplane is one-quarter wavelength? Well, everyone can quickly convince themselves that with a space delay of $2 \times 90°$ and a $180°$ phase reversal in the perfectly electric conducting groundplane, the direct and the reflected signal will be in perfect phase in the forward direction. Apparently, many will assume that this is where the antenna gain is maximum. However, this is just another common misconception. To clarify this, consider the radiation pattern for a single column of dipoles in front of a PEC groundplane as shown in Fig. 6.19 at different frequencies. First of all we note that since the image in the groundplane is always $180°$ out of phase with the original, we will always observe a null along the groundplane. Furthermore, at the lowest frequency where the spacing to the groundplane is 0.06λ, the radiation pattern for the dipole column and the groundplane will be almost a perfect circle as shown. At the higher frequency where the groundplane spacing is 0.25λ, the radiation pattern deviates slightly
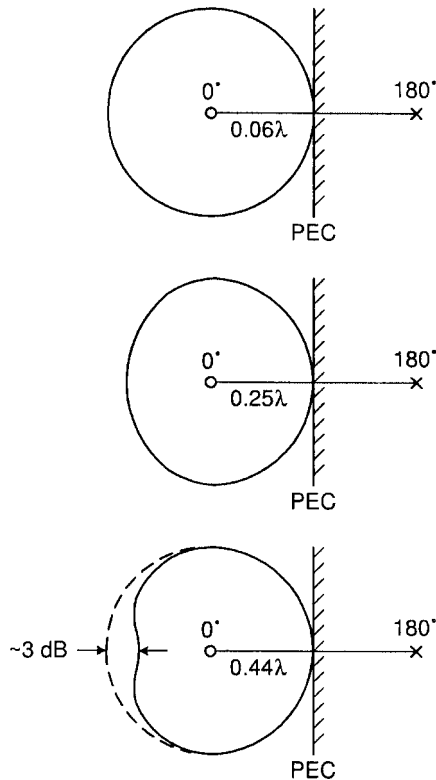
Fig. 6.19   Radiation pattern for a column array in front of a PEC groundplane seen end-on. By pattern integration we easily see that the directivity is largest at the lowest frequencies where the groundplane spacing is very small (but not too close to zero). At higher frequencies we obtain lower directivity. Note in particular that nothing special happened when the spacing is equal to $\lambda/4$.

from a circle, being a little broader. And when the spacing finally is ∼0.44λ, the radiation pattern is about 3 dB lower in the forward direction than the maximum value. (To be sure, for a groundplane spacing of 0.5λ we would observe a null in the forward direction.) The directivities of those three patterns can be obtained by simple pattern integration. Without actually doing that, any seasoned antenna engineer would agree that the difference between these three cases would be a couple of decibels or so—that is, about the same over a frequency range of $0.44/0.06 = 7.3{:}1$. While it would be unwise to go up in frequency, no great problem would be encountered at a groundplane spacing of, for example, 0.04λ; that is, we would then cover a frequency range of $0.44/0.04 = 11.0{:}1$. If we were to go further down in frequency, the radiation resistance would eventually get so low that ohmic losses could diminish the efficiency. However, noticing that the surface resistance for a good conductor (copper) is only 0.024 ohm per square at 10 GHz, that is usually not as significant a problem as many expect. (While working as an antenna engineer in industry in the early 1960, the author designed and built a communication antenna for the Titan missile system. The distance between the vertical dipoles and a very heavy mast was only ∼0.01λ at the lowest frequency.[1] It was with some anxiety that he watched the customer fly in a 1-kW transmitter and meticulously measure the temperature rise at seven agreed-upon checkpoints on the dipoles and the mast. While he does not remember the exact temperature rise, it simply turned out to be a non-event, much to everyone's surprise.) For further comments consult Kraus and Marhefka [104].

Finally, we should point out that when the individual elements are arranged into an array, the array pattern is so domineering compared to the element pattern that the directivity of the individual elements becomes almost of pure academic interest only. So what can we conclude? Simply that if you can match your antenna and stay away from the ohmic losses, you are probably OK! See also Sections 2.14.3 and 6.12.3.1.

P.S.: Actually, it is (or should be) well known that maximum directivity and gain are not necessarily obtained for the in-phase condition. For example, an endfire array of dipoles attains maximum endfire gain when the phases of the elements are delayed ∼$3/N$ radians per element in addition to the simple end-fire condition. This is called the Hansen–Woodyard condition [105]. The W8JK antenna by Kraus is another example [106].

6.12.5   Would a Magnetic Groundplane Be Preferable to an Electric One (If It Were Available)?

The notion discussed above—namely, that *good things will happen* when the groundplane spacing is ∼λ/4—sometimes erupts into other ingenious ideas. What about if we instead of a PEC groundplane would use one made of a perfect *magnetic* conductor (PMC)? In that case the image would be in phase with the

---

[1] The antenna had to fit into a silo during storage.
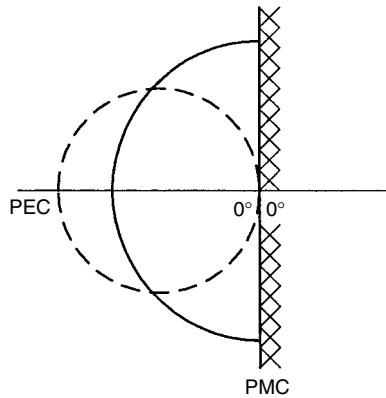
Fig. 6.20 *Radiation pattern for a column array seen from the top mounted directly in front of a perfectly magnetic conducting (PMC) groundplane and, for comparison, the same if using a PEC groundplane at some distance (see Fig. 6.19). By pattern integration we observe that the former has lower directivity than the latter.*

original if the latter were placed directly on the PMC as shown in Fig. 6.20. Consequently, the potential bandwidth could reach from DC to broad daylight!

However, before being carried away, let us consider the pattern of an electric dipole mounted in front of a PMC groundplane. Since the image always is in phase with the original, the total pattern would be the same as that of a single dipole—that is, a circle without a null as shown in Fig. 6.20. Also shown for comparison is the typical antenna pattern for the PEC groundplane considered above. Pattern integration will readily reveal that the *ideal* magnetic groundplane actually leads to lower directivity than the PEC counterpart.

But for those who still think that a Nobel prize is just around the corner, I must report about my most recent visit to RadioShack. Although not staffed with EE candidates, they nevertheless employ people with reasonably good technical knowledge and they do fairly well what they are supposed to do, namely, "move the merchandise." One of them, however, was a little bit cocky and in one of my mischievous moments I decided to have a little fun. "Could I also have a roll of magnetic conductor?" I inquired. "Certainly," came the quick answer as the young man disappeared into a back room. After a few minutes he reappeared and with great regret confided, "Sorry sir, we just ran out of it." Too bad. I would have taken a couple of rolls.

But could we somehow by artificial means produce an equivalent magnetic groundplane? There has certainly been several attempts to do just that. However, everything this author has seen so far has in effect been merely an electric groundplane where the distance between the array and groundplane has been shortened by a more or less elaborate use of capacitive loading. This technique is actually well known to seasoned antenna engineers. So is the price: You pay in the form of a reduced bandwidth. You are in general much better off just staying with a plain electric groundplane as discussed earlier in this chapter.

6.12.6   Will the Bandwidth Increase or Decrease When a Groundplane Is Added to an Array?

It is quite common to hear statements to the effect that when a groundplane is added to an array the bandwidth is reduced. Apart from the fact that we have seen several examples earlier in this chapter where just the opposite was the case, it is interesting to shortly explore the reasons for this conclusion.

The most common argument is simply that when the distance between array and groundplane is one-quarter electrical wavelength, the signals from the array and the groundplane will be in phase in the forward direction (see also Section 6.12.4). Thus, it is concluded that this must constitute the *optimum!* And when the frequency deviates, it goes *downhill*; that is we will lose bandwidth.

This conclusion is wrong on several accounts. First of all, as discussed earlier in this chapter, there is no particular spacing that constitutes an optimum condition but rather a very broad range of frequencies where the directivity is almost independent of the distance to the groundplane as long as the distance does not get too close to one-half wavelength or zero. Second, since the groundplane impedance Z_{1+} is inductive at the lower frequencies while the array reactance X_A (for dipoles) is capacitive, the two components can as demonstrated earlier in this chapter by numerous examples be designed to partly cancel each other and thereby yield a greater bandwidth.

But what if we considered an array of slots rather than dipoles? Well, that would result in several interesting differences. First of all there would be only the signal coming directly from the slots, none would be coming directly from the groundplane (see Chapter 7 in reference 107). Thus, there would be no *optimum* groundplane spacing as far as radiation is concerned, although we could of course not make it equal to one-half wavelength or zero for matching reasons. However, as far as bandwidth is concerned, the most noteworthy would be the fact that the impedance of a slot array[2] is inductive at the lower frequencies and capacitive at the higher, which is, as we saw earlier, precisely the same way the groundplane impedance Z_{1+} behaves with frequency. Thus, the two impedance components will no longer cancel each other as in the dipole case but rather reinforce each other, leading to a narrower bandwidth when adding a groundplane to a slot array.

Interesting to note how it often is possible to arrive at the right conclusion by using the wrong argument! Or we may use intuition, which is great as long as it has been honed by experience and knowledge that conform to reality.

6.13   CONCLUSIONS

We have considered arrays of short dipoles with capacitors between their tips. By making the interelement spacing D_x small (typically 0.7 cm for the frequency range 2–18 GHz) it was possible to obtain an array impedance with basically just

---

[2] We assume that the total length of the slots is $\sim\lambda/2$.

one resonant frequency, a fairly constant real part R_A, and an imaginary part jX_A being capacitive below resonance and inductive above. Adding a groundplane was equivalent to adding a pure reactance Z_{1+} in parallel with jX_A. Since this reactance was inductive at the lower frequencies and capacitive at the higher, it could partly compensate for the frequency variations of jX_A and Z_{1+} leading to an increase of the bandwidth.

Further improvement in bandwidth could be obtained by placing a dielectric slab in front of the dipole array. When it was one-quarter wavelength thick, it acted merely as a transformer. However, at lower frequencies we experienced in addition to some resistive transformation also a reactive capacitive component. Thus, the reactance associated with the slab would be pulling in the same direction as the array reactance X_A; that is, they would both pull in the opposite direction of the groundplane impedance Z_{1+}. Since the latter is the most domineering in the frequency range of interest here, it is possible to obtain just the right balance to achieve a very large bandwidth ($>7.0:1$).

Use of two or more dielectric slabs, each of which was approximately one-quarter wavelength thick (electrically), at the center frequency could lead to further improvement in bandwidth or lowering of the VSWR. However, a systematic optimization of the dielectric constants of the slabs and of the antenna as a whole was not done.

When this concept is presented for the first time, many would expect this design to be distinctly narrowbanded. It is usually based on the performance of a single, very short dipole that is known to be highly capacitive and very narrowbanded when tuned to resonance with an inductance. However, the most noteworthy point here is that it is the performance in the array environment that is important and not the individual elements. And due to a very strong mutual coupling between the elements, the array performance may differ vastly from the individual elements. In other words, while mutual coupling between elements historically has been treated as an evil, it can be a blessing when used correctly (see also Appendix D and Section 6.12.2).

Similarly, when thicknesses or spacings are prescribed to be one-quarter-wavelength at the center frequency, the performance is often expected to be mediocre at frequencies below and above the center frequency. While this often may be the case, we have demonstrated that it is indeed possible to play the various components out against each other and thereby obtain greater bandwidth.

Pursuit of this analytic design approach is in this writer's opinion where antenna engineers might demonstrate their foremost skill. It is not an art and is not necessarily based on years of experience. To the contrary, it is based on sound and fundamental engineering principles. Unfortunately, much design work today is turned over to a computer and eventually assisted by an optimization program, but is otherwise completely untouched by the human brain. While that approach can lead to some success, there is plenty of evidence to suggest that the truly optimum solution might be missed. The problem is that many designers today really do not have much of a clue of what should be optimized. A meaningful

optimization should merely be checking out minor tedious perturbations after you have a concept and a fundamental design. And that is precisely what it originally was intended to do.

It should finally be mentioned that the concept for this antenna as well as certain practical details are covered by US patent no. 6512487.

7

An Omnidirectional Antenna with Low RCS

7.1 INTRODUCTION

In Chapter 2, 5, and 6 we considered arrays backed by a groundplane. Such configurations typically produced pencil beams. There is, however, also considerable interest in antennas with omnidirectional radiation patterns. The principles for these will be presented in this chapter. It should be emphasized, however, that we shall limit ourselves to designs with inherently low RCS. That rules out the common simple dipole and monopole—in fact, most omnidirectional antennas.

Furthermore, in Chapter 8 we will show that in order to design a parabolic antenna with a low RCS, it is crucial to use a feed with low RCS. Such a feed is readily obtained by a relatively simple modification of the omnidirectional antenna presented in this chapter. Note that no power is lost in the omnidirectional antenna or in the low RCS feed when transmitting. See also Section 7.6.

We should point out that the RCS level of a parabolic antenna never can attain the low levels possible with an array. They are, however, popular in some camps and will therefore be discussed in Chapter 8.

7.2 THE CONCEPT

In Chapter 2, Section 2.6 we investigated planar arrays of dipoles without a groundplane as shown in Fig. 7.1a. Such configurations have a transmitting
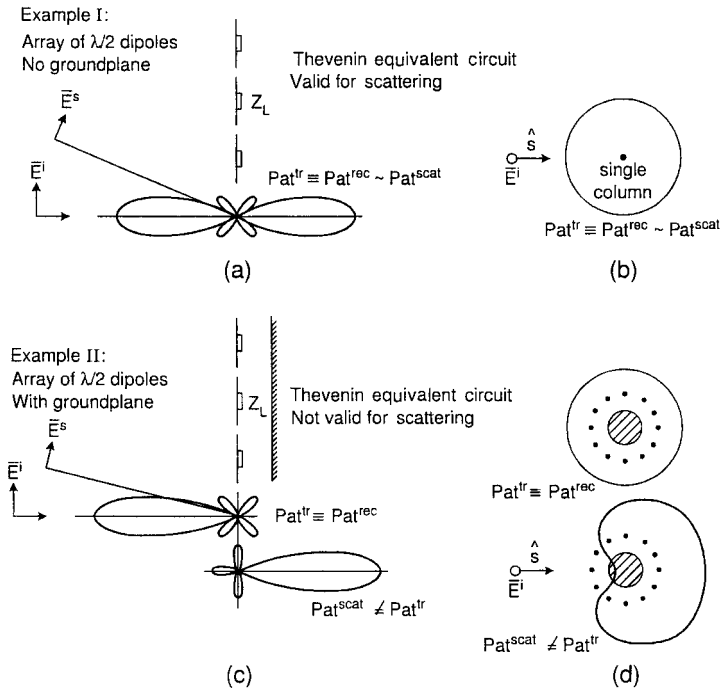
Fig. 7.1   The transmitting, receiving, and scattering pattern Pat^{tr}, Pat^{rec}, and Pat^{scat}, respectively, for various antenna configurations: (a) Array of dipoles without a groundplane, (b) single column of collinear dipoles, top view, (c) array of dipoles with a groundplane, (d) columns of vertical dipoles arranged in a circle around a conducting rod or pipe, top view.

pattern Pat^{tr} comprised of two pencil beams in directions opposite each other (we assume all elements are fed in phase). If we instead consider a single column of dipoles as shown in Fig. 7.1b, the transmitting pattern Pat^{tr} will be omnidirectional. When either one of those two configurations are exposed to an incident plane wave, the RCS will for conjugate match be only ~6 dB below the maximum value obtained when the antenna terminals are essentially short-circuited. This is simply not low enough to be of any practical interest.

Let us instead consider an array of dipoles backed by a groundplane as shown in Fig. 7.1c. From Chapter 2, Section 2.6, we know that the backscattered signal can in principle be "infinitely" low. (For edge effect and fine-tuning see Chapter 5.)

The omnidirectional version of the planar array with a groundplane is shown in Fig. 7.1d. It consists of a conducting rod or pipe surrounded by dipoles arranged in columns. It is well known that if these elements are fed in phase, we will obtain an omnidirectional transmitting pattern Pat^{tr} that essentially can be described as a circle with ripples. The depth and number of these ripples (not shown in Fig. 7.1d) depend on the density of the columns. The closer they are to each

other, the smaller the ripples. In fact, when the columns in the limit form a continuous current sheet around the pipe, the transmitting pattern Pat^{tr} simply becomes a pure circle with no ripples at all.

Any antenna exposed to an incident plane wave will receive a signal at its load impedance Z_L. The receiving pattern Pat^{rec} will, according to the reciprocity theorem, always be identical to the transmitting pattern Pat^{tr} as discussed in depth in Chapter 2, Section 2.9. We also there define the scattering pattern Pat^{scat} as the bistatic scattered field reradiated from the antenna when exposed to an incident plane wave. It is obtained by calculating the radiation pattern based on the antenna current under receiving (i.e., scattering) conditions. Many readers will expect this pattern to merely be equal to the receiving pattern (and thus identical to the transmitting pattern). While this may be approximately true for the two examples shown in Figs. 7.1a and 7.1b, it is far from true in general. As an example, consider Fig. 7.1c, as discussed in detail in Chapter 2, Section 2.9. The scattering pattern had its mainbeam pointing in the forward direction and not in the backward direction as does $Pat^{tr} \equiv Pat^{rec}$; see the radiation pattern in Fig. 7.1c. Furthermore, we remind the reader that the transmitting and receiving pattern always are completely independent of the load impedance Z_L (or the generator impedance Z_G). In contrast, the scattering pattern is extremely dependent upon Z_L in the back sector but hardly in the forward direction as illustrated by direct calculations shown in Chapter 5, Figs. 5.2 and 5.3. We finally emphasize that the forward mainbeam of the scattering pattern is not merely equal to the mainbeam of the transmitting pattern rotated $180°$. They may in some cases be similar, but in general they are not that simply related. Again, consult Figs. 5.2 and 5.3.

A typical scattering pattern of the omnidirectional antenna is shown in the lower part of Fig. 7.1d. We observe a "main beam" in the forward direction and a low backscattered signal in the back sector. Note that the forward scattering changes little with the load impedance Z_L while the backscatter is very sensitive. For further discussion as well as calculated scattering pattern see Sections 7.4 and 7.6.1.

7.3   HOW DO WE FEED THE ELEMENTS?

As mentioned earlier, we will obtain an omnidirectional transmitting (and thus also receiving) radiation pattern if all the elements are fed in phase. Basically this can be done by using an ordinary harness with simple T connectors as shown for example in Chapter 2, Section 2.12. However, as also shown there, we must prevent coupling between the elements through the feed network since this could lead to high backscatter return. Use of hybrids is a proven way to avoid the calamity.

An example of this approach is shown in Fig. 7.2. Note that due to the hybrids each element will always see the same resistive load regardless of the nature of the incident field.
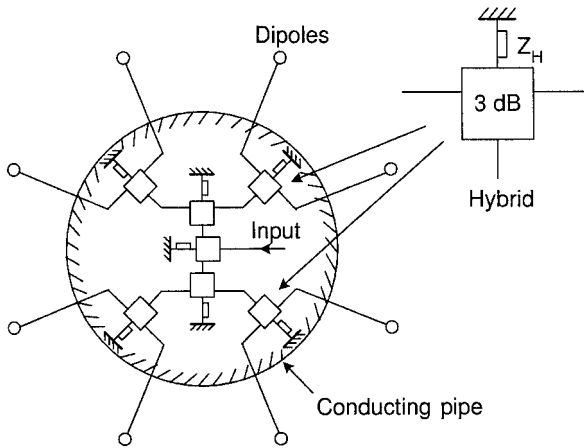
Fig. 7.2 Columns of vertical dipoles arranged in a circle around a conducting pipe, inside which is the harness feeding the dipoles. Use of hybrids ensures that all dipoles are seeing the same load regardless of how the dipoles are excited by the incident field. In other words, the hybrids prevent any coupling between elements through the harness.

Thus, when calculating the scattering patter, we shall model the antenna as a circular array of dipoles loaded with the same load resistances.

7.4 CALCULATED SCATTERING PATTERN FOR OMNIDIRECTIONAL ANTENNA WITH LOW RCS

In Figs. 7.3 and 7.4 we show the calculated bistatic scattering pattern for an omnidirectional infinitely long low RCS array [108]. The diameter of the pipe was around 0.5λ at the center frequency, while dipoles were located on a circle with diameter around 0.75λ. The load resistors were not conjugate-matched but close to it (remember, only planar arrays become invisible for conjugate matching). The scattering pattern at $f = 4, 6$, and $8\,\text{GHz}$ are shown in Fig. 7.3, and similarly the patterns at 10, 12, and $14\,\text{GHz}$ are shown in Fig. 7.4. We note that the forward-scattered field changes very little with frequency. However, as we would expect, the field scattered in the backward sector varies significantly with frequency and matching.

7.5 MEASURED BACKSCATTER FROM A LOW RCS OMNIDIRECTIONAL ANTENNA

The patterns above were first calculated in a thesis by Jeff Hughes [108], a former student and now very successfully working for the U.S. Air Force. While there never was any doubt in the author's mind about the validity of Jeff's results, there are always those who refuse to believe anything contrary to their
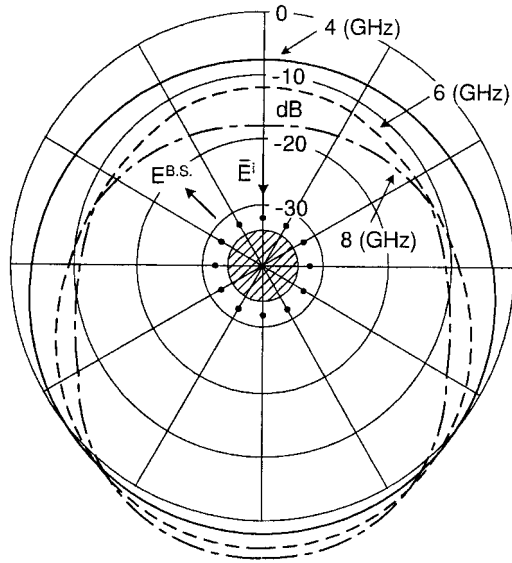
Fig. 7.3 *The calculated bistatic scattering pattern Pat^{scat} for a circular array of dipole columns arranged around a conducting rod or pipe. Frequencies 4, 6, and 8 GHz [108].*
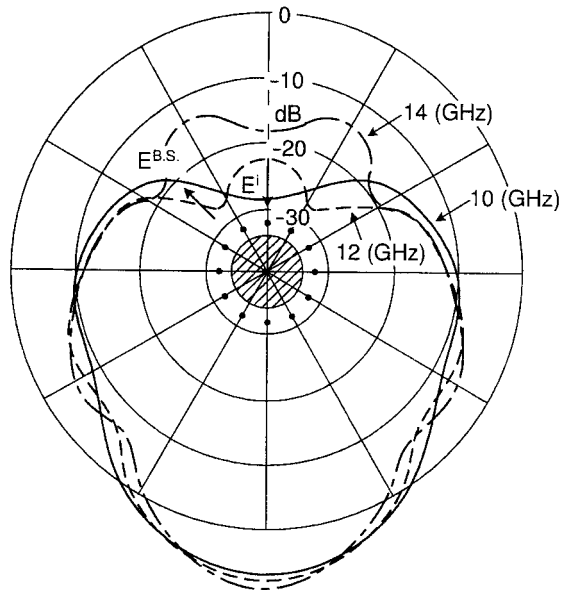
Fig. 7.4 *The calculated bistatic scattering pattern Pat^{scat} for a circular array of dipole columns arranged around a conducting rod or pipe. Frequencies 10, 12, and 14 GHz [108].*

"intuition" (often misguided by insufficient training). They simply demand to see actual measurements.[1]

Thus, the investigation was continued and greatly extended in the dissertation by Jay Simon [109]. He, assisted by other students, designed, built, and measured an actual antenna. Because the elements at X-band frequencies were rather small, it was for tolerance reasons decided to change the frequency band to the S-band region. Jay very carefully calculated the optimum loads to be placed at the terminals of each dipole (this would simulate the input impedance of receivers, amplifiers, or the generator impedances of the transmitters; see also Chapter 2, Sections 2.10 through 2.12). Again, note that the optimum value of the load impedance was slightly different than the conjugate match. The reason for this is simply that this antenna is nonplanar. It implies that the residual scattering no longer is zero but small.

The measured array consisted of a conducting pipe with diameter 4 cm while the vertical dipoles were photoetched on a thin sheet of substrate rolled up in a cylinder with 6.7-cm diameter. The length of each of the vertical dipoles were 3.6 cm, and there were 20 of them in each of the 10 columns. That corresponds to a total array length of 87 cm.

The measured monostatic RCS of this finite array as a function of frequency is shown in Fig. 7.5. We show three RCS curves where the field is incident in the equatorial plane.

  a. One where the entire circular array is covered with a layer of foil fitting snugly around all dipoles.
  b. Also, as a further verification, the backscattered signal from the center pipe alone without any dipoles or foil.
  c. And finally, the backscattered field when all the loaded dipoles are placed around the center pipe simulating the actual antenna.

We note that the measured RCS level is as much as 40 dB below the foil-covered antenna at one frequency. That is in fact fairly close to what Jay calculated. Furthermore, the relative 13-dB bandwidth is about $5.2/2.8 = 1.9$—that is, approximately an octave wide. Note that this result is obtained for fixed load impedances without any broadband matching as discussed in Appendix B. Further increase in bandwidth can be obtained by using more elements.

We also show in Fig. 7.6 the return from the same antenna but for horizontal polarization with and without foil. As one would expect, the return is similar to the pipe alone for vertical polarization.

Finally, in Fig. 7.7 we show the backscattering from an antenna with horizontal curved elements. The pipe diameter was 4 cm, and the diameter of the circle with the dipoles was 6.7 cm with a total array length of 87 cm. The depth of the null is similar to the vertical case, but it is more narrowbanded. Again, we emphasize

[1] Jeff's approach was completely rigorous in that he expanded everything including the field from the pipe into Hankel functions with origins at the center.
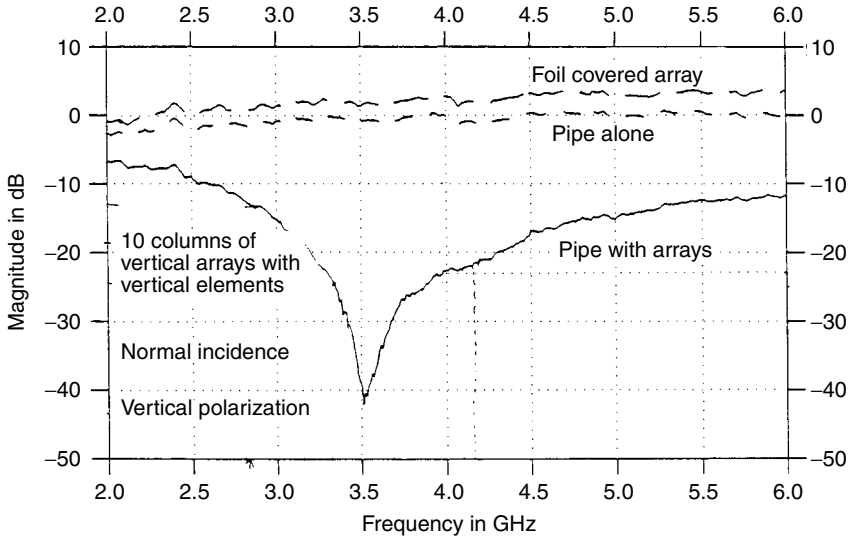
Fig. 7.5   The measured backscattering from an array of resistively loaded vertical dipoles arranged around a conducting pipe as shown in Figs. 7.3 and 7.4. Three curves are shown: one where the entire array is covered with foil (baseline) one of only the pipe without dipoles, and one where the pipe is surrounded by resistively loaded dipoles. Polarization of incident and reflected field: vertical [109].
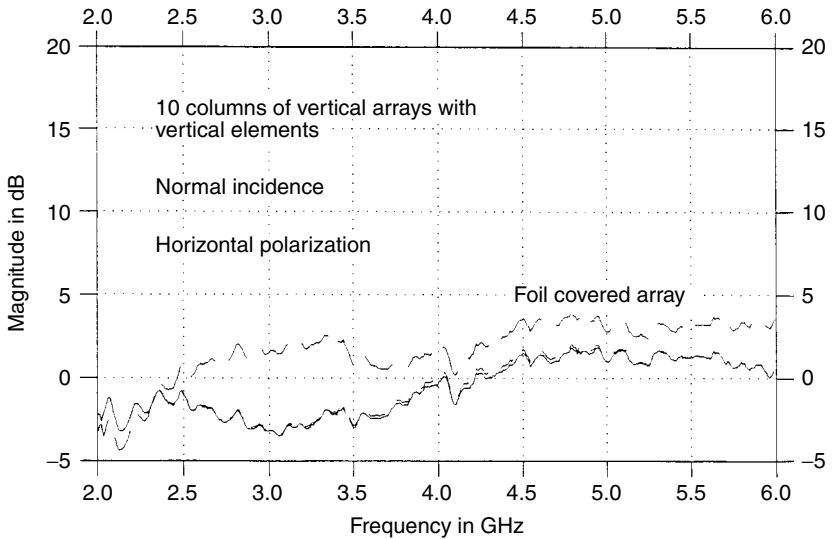
Fig. 7.6   Same case as shown in Fig. 7.5 but where the incident and reflected fields are horizontally polarized [109].
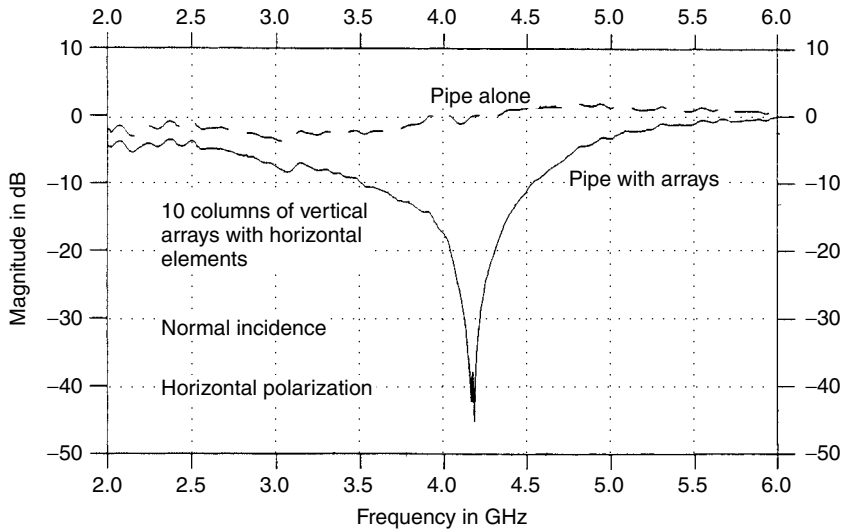
Fig. 7.7   The measured backscattering from a circular array of horizontal resistively loaded dipoles photoetched on a thin substrate curved around a conducting pipe. Two curves are shown: one of the pipe alone without dipoles and another with the resistively loaded dipoles. Polarization of incident and reflected field: horizontal [109].

that these results were obtained for constant load resistors without the use of a broadband matching technique.

Incidentally, both array models can still be viewed in the author's office. However, some ravage from rough handling over the years is observable.

7.6   COMMON MISCONCEPTIONS

7.6.1   On the Differences and Similarities of the Radiation Pattern

The transmitting, receiving, and scattering patterns are often the subject of some misunderstanding. Let us consider the omnidirectional low RCS antenna in particular.

Actually, the transmitting pattern is straightforward to comprehend. All elements are fed with the same in-phase currents via the harness including the hybrids. Surely the radiation pattern will basically be omnidirectional with ripples as discussed earlier. The receiving pattern is more complicated. When a plain wave is incident upon the antenna, there will be stronger currents on the lit side in the front than on the shadow side in the back. This imbalance might cause some power to go into the hybrid loads rather than the receiver load. Furthermore, the elements on the shadow side will deliver less power than those at the front. All of this can lead one to believe that the antenna is less efficient when receiving than when transmitting.

This is not the case. We merely have to apply the reciprocity theorem between the main terminals of our omnidirectional antenna and an external test antenna. When transmitting from the array and receiving at the test antenna, no loss will occur in any of the hybrid loads. Conversely, if we transmit from the test antenna and receive on the array terminals, we will certainly lose some power in the hybrid loads, but the total transmission loss must be unchanged whether we transmit or receive. What happened is simply that the elements on the lit side combine into an antenna with higher directivity but the same gain as the omnidirectional case. Remember, the reciprocity theorem deals only with the *terminal* voltages and currents. It says absolutely nothing about the current *distribution* under receive and transmit conditions. While they may be the same in some cases, they are radically different in this case. When this asymmetric receiving current is integrated over all the elements, we will obtain the asymmetric scattering pattern shown in Figs. 7.3 and 7.4.

Finally, there are those who wonder how the scattered field in the forward direction can be maximum when everyone knows that we have a "shadow" there. Well, as explained already in Chapter 2, Section 2.2, and Chapter 5, Section 5.3, these individuals are simply thinking about the *total* field. Recall that this is the sum of the scattered and the incident fields. They will partly cancel each other in the forward sector and create a shadow as expected. In other words, the incident field will primarily be absorbed by the antenna when matched, and a relatively weak *total* field will be observed in the forward scattering sector. See also Chapter 5, Figs. 5.2 and 5.3.

7.6.2   How You Can Lock Yourself into the Wrong Box

A highly respected professor in electromagnetics once told the author that pursuing the development of a low RCS omnidirectional antenna most likely was a waste of time.

He based his statement on the following argument: Consider a dipole. When a load impedance is connected to its terminals, a current will flow through the load and thus also through the antenna wire (at least in the vicinity of the terminals). And since that current will reradiate, we will observe a significant RCS.

His argument was flawless in every respect except one: He limited himself at the onset to a simple dipole. It might have been the first time the author replied: "If you have a problem you cannot solve, change the problem!"

Today we know of course that a circular array placed around a pipe acting as a groundplane can be designed to have a low RCS without any significant loss. And where did that come from? Well, it came from the planar arrays with a groundplane, as discussed in great length in Chapters 2 and 5. And where did this seemingly hopeless idea come from? From the fundamental antenna concept that a large aperture backed by a groundplane can absorb *all* the incident energy; that is, *nothing* will be left to be reflected in the back direction (concerning edge effect; see Chapter 5). Oh, if we could just get our young engineers to study fundamentals again!

7.7 CONCLUSIONS AND RECOMMENDATIONS

Many readers intuitively assume that it is inherently impossible to design an omni-directional antenna with low backscatter.[2] This assumption is based upon considering only a simple dipole as discussed in Common Misconceptions, Section 7.6.2. However, we have shown in this chapter that just as a planar array of dipoles backed by a groundplane has a very low backscatter, see Chapters 2 and 5, so can a circular array of dipoles placed around a conducting pipe. It was remarkable that the measured RCS at one frequency was ∼40 dB below the same array covered by foil. A 13-dB reduction was obtained over a bandwidth of almost an octave. It should also be noted that the load resistors were somewhat different than conjugate match. This is simply because the curved surface has a small residual scattering component in contrast to the planar surface which has none (in principle). No broadband technique as illustrated in Chapter 6 and Appendices A and B was applied.

It is recommended to further investigate the effect of the "groundplane" in the form of the central pipe just as we did in the planar case discussed in Chapter 6. No doubt, with our increased knowledge about design today, we could surely obtain a better and more broadbanded cancellation of the element and the groundplane reactances.

Finally, just like a dielectric slab placed in front of a planar dipole array can increase the bandwidth (see Chapter 6, Sections 6.5 through 6.11), we strongly expect the same to be true when a dielectric sleeve of proper thickness and dielectric constant is placed around the dipole elements on the outside. In fact, Simon [109] already incorporated the effect of dielectric on the outside, but no attempt was done to design for an increase of the bandwidth. After all, dissertations should be unclassified (although the author's dissertation was classified for many years).

---

[2] All antennas receiving real energy from an incident wave will have a strong scattered field in the forward direction. However, the total field being the sum of the incident and the scattered field is weak.

The RCS of Two-Dimensional Parabolic Antennas

8.1 THE MAJOR SCATTERING COMPONENTS

The following investigation is limited to the parabolic cylinder with a feed placed at the focal line. However, the scattering mechanism of a parabolic dish with a typical feed is easily understood by simple extension of the cylindrical case.

The backscatter of a parabolic antenna consists essentially of two components:

a. The scattering coming directly from the reflector itself without any involvement from the feed. We shall call it the *reflector scattering*.

b. The scattering from the feed as the incident signal is focused upon it and reradiated via the reflector. We will denote this the *feed scattering*.

8.1.1 The Reflector Scattering

In Fig. 8.1 we show the bistatic scattering pattern for a parabolic cylinder with aperture width equal to 14λ and without any object at the focal line. In other words, this constitutes the reflector scattering alone. The cylindrical reflector is modeled by placing 96 columns of reactively loaded dipoles along a parabolic surface. Thus, the surface acts like an FSS surface similar to our approach shown in Figs. 5.2 and 5.3. This will ensure minimal leakage through the reflecting surface as opposed to using just infinitely long rods (see Sections 5.2 and 5.3). The SPLAT program was eminently well-suited for calculating these configurations.
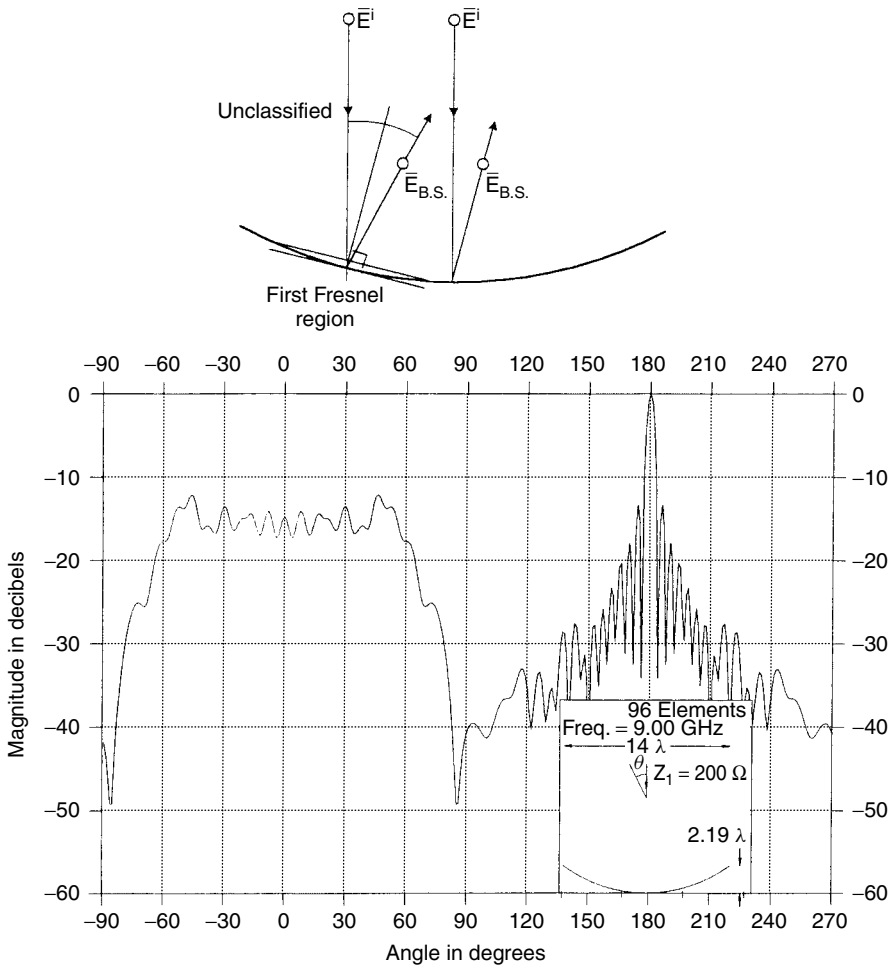
Fig. 8.1 *The bistatic scattered field from a parabolic cylinder for an incident plane wave along boresight; that is, at θ = 0°. There is no feed; that is, this shows the scattering from the parabolic surface itself referred to as reflector scattering.*

The general shape of the bistatic pattern in the back sector is readily understood by noting that the scattered field is essentially coming from the first Fresnel zone associated with the particular bistatic directions as shown at the top of Fig. 8.1.

The field in the forward sector can basically be obtained approximately by integration of the incident field over the aperture width as discussed in Section 2.9.2. Note, however, that the entire pattern in Fig. 8.1 was obtained from the SPLAT program and therefore is as exact as the method of moments. In other words, the effect of edge currents is rigorously observed. See also Section 8.5.

8.1.2   Total Scattering from a Parabolic Reflector with a Typical Feed

The total scattering from a parabolic reflector with a typical feed is more complicated. As we shall see, it depends very much on the type of feed being used as well as upon the circumstances. Basically we can assume that one of the strongest backscatter cases is obtained when the feed deteriorates into a single column of resonating lossless dipoles placed at the feed line. This case is shown in Fig. 8.2 for incidence along the boresight axis. We clearly recognize the main beam at $\theta = 0°$ while the reflector scattering in Fig. 8.1 has been broken up by interference from the feed scattering.
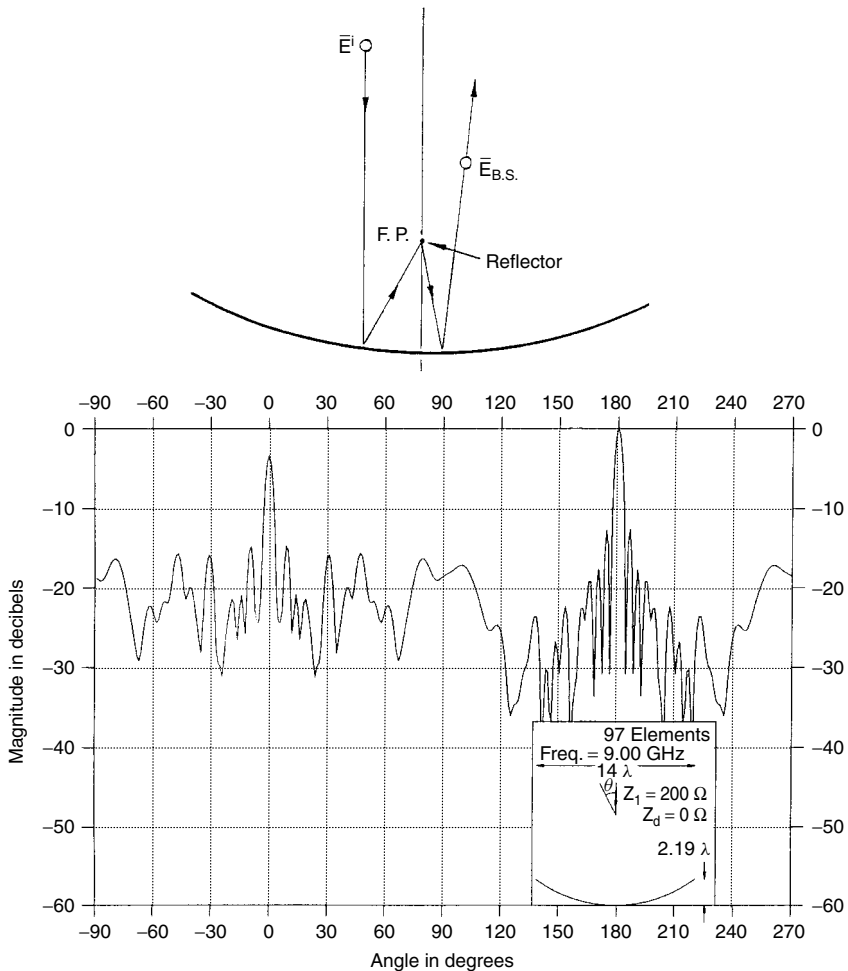
Fig. 8.2   *The bistatic scattered field from a parabolic cylinder for an incident plane wave along boresight — that is, at $\theta = 0°$. There is a collinear array of short-circuited dipoles at the focal line, resulting in a large backscatter in the boresight direction.*

If an actual feed in the form of a flared parallel plate waveguide is used, the backscatter can be significant but in general not as strong as the resonating dipole case in Fig. 8.2—that is, as long as we are incident along the boresight axis. If we are obliquely incident upon the reflector such that the incident field is focused on one of the edges of the horn we will, for the E field parallel to the edges, obtain a very strong return similar to the resonating dipole case in Fig. 8.2. Such a case is shown in Fig. 8.3. We clearly see a main beam in the bistatic pattern a few degrees to the right. At this angle of incidence the monostatic return coincides with the bistatic return as indicated in Fig. 8.3, top. This situation is of more than theoretical interest. It is typically encountered in practice during acquisition, leading to large RCS values on each side of the boresight axis. It therefore is of utmost importance to design a new type of feed without edges. This can be accomplished by simple modification of the omnidirectional antenna discussed earlier in Chapter 7.
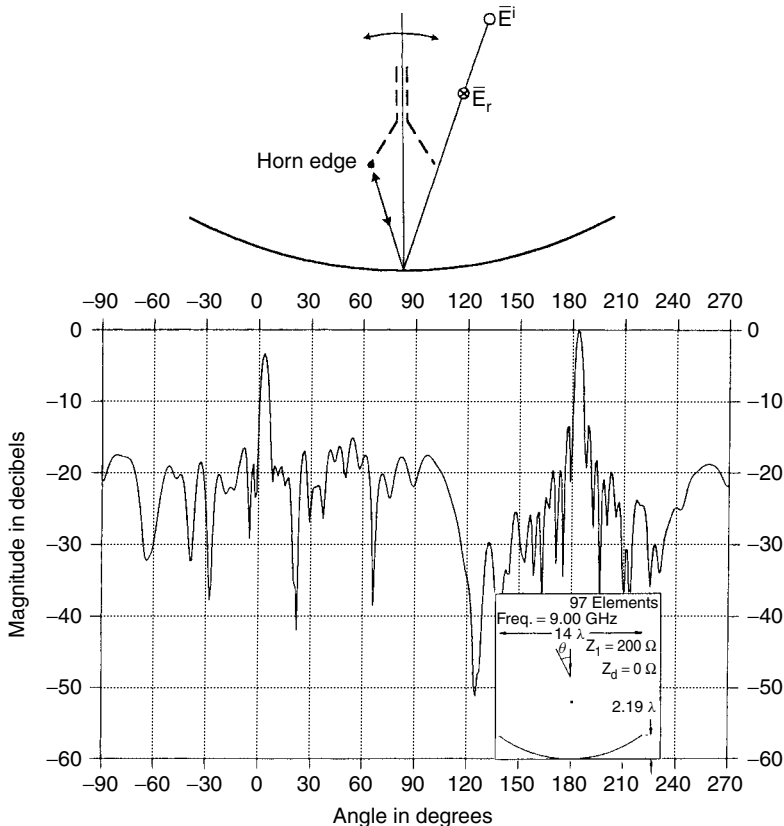
Fig. 8.3 *The bistatic scattered field from a parabolic cylinder with a wedge-shaped "horn." When the incident field is slightly off boresight, the incident energy will focus at the edge of the feed, resulting in a large backscatter as shown.*

8.2   TOTAL SCATTERING FROM A PARABOLIC REFLECTOR WITH LOW RCS FEED

Horn antennas have long been popular in the microwave community, and rightly so. They can simply be considered natural extensions of waveguides. However, the walls in horns are not necessarily needed to direct the energy in the forward direction as some intuitively might expect. This job can be handled in a number of other ways—for example, by using arrays. The beauty of this approach is simply that unwanted scattering from the walls can be avoided. To this end we shall start with the omnidirectional antenna discussed in Chapter 7 by simply exciting only part of the elements such that a suitable illumination of the reflector is obtained. The rest of the elements (or at least part of them) would be resistively loaded and serve to absorb the incident energy either directly or via the reflector.

The active elements would of course be fed from hybrids as explained in Section 2.12 and in detail in Section 8.3. Thus, from a scattering point of view we merely have to consider an omnidirectional antenna placed at the focal line with all the elements resistively loaded.

It should be admitted that some energy could be lost in the passive element because they may be excited by the active elements. However, we intend to excite the active elements in a tapered fashion, which should lead to minimum loss in the passive elements. For practical execution of such a feed, see Section 8.3.

A typical bistatic scattering pattern for a cylindrical parabolic reflector with a low RCS feed is shown in Fig. 8.4. The incidence is along the boresight axis at the center frequency 9.0 GHz. Also shown for comparison is the bistatic scattering pattern for the same reflector but without any feed—that is, the same as shown earlier in Fig. 8.1. Much to many readers' surprise, we observe that the scattering with the low RCS feed is about 6 dB lower than that with no feed at all. An explanation for this apparent paradox is illustrated in Fig. 8.4, top. In the no-feed case to the left, the incident signal will be focused on the focal line from where it continues into the back sector and will thus be incorporated into the reflector scattering, whereas the low RCS feed will simply absorb the energy converging into the focal area and thus not be incorporated into the reflector scattering.

As stated earlier, the results shown in Fig. 8.4 are obtained for incidence along the boresight axis and at the center frequency 9.0 GHz. Obviously our suggested low RCS feed should be tested at other frequencies as well as at other angles of incidence. This will be the subject of discussion in the next two sections.

8.2.1   The Bistatic Scattered Field as a Function of Angle of Incidence

Figures 8.5 through 8.9 show the bistatic scattered field for a parabolic cylinder with a low RCS feed. The frequency is fixed at the center frequency 9.0 GHz
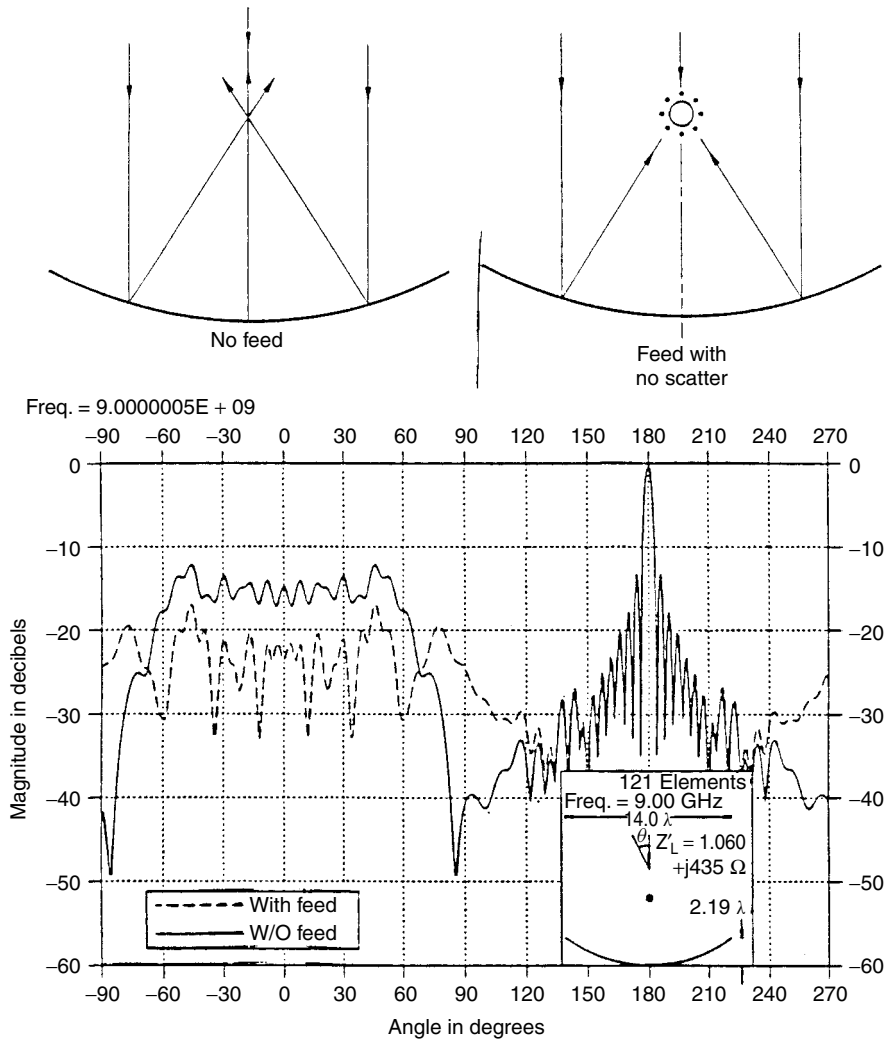
Fig. 8.4   The bistatic scattered field from a parabolic cylinder for an incident plane wave along boresight; that is, $\theta = 0°$. Shown with and without a low RCS feed. Frequency is 9.0 GHz.

while the angles of incidence are $\theta = 1.25°, 2.5°, 3.75°, 5.0°$, and $10.0°$, respectively. These angles were chosen based on certain criteria. At $\theta = 1.25°$ the central ray is just clearing the central pipe of the low RCS feed as indicated in the drawing at the top of Fig. 8.5. Note that the angles are not drawn to scale, nor is the size of the low RCS feed. This enables us to better assess the relationship among the incident field, the scattering, and the feed itself. This "distortion" of the figures will be observed in all the subsequent figures to follow.

Freq. = 9.0000005E + 09
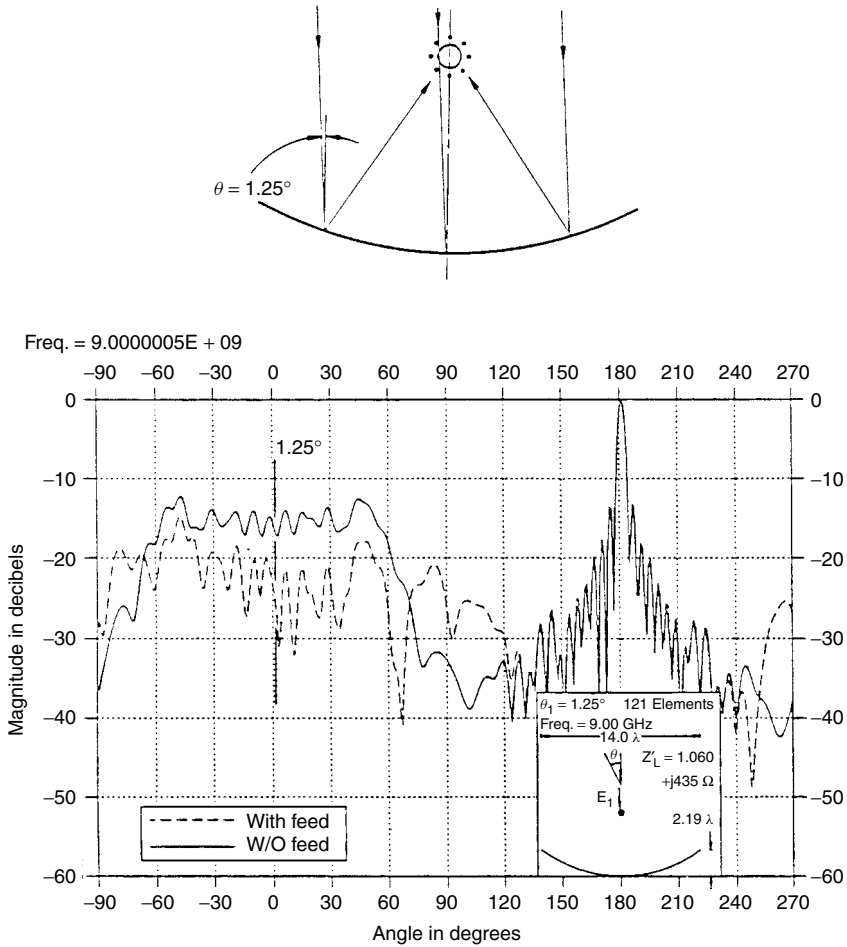
Fig. 8.5   *The bistatic scattered field from a parabolic cylinder for an incident plane wave arriving at $\theta = 1.25°$. Shown with and without low RCS feed. Frequency is 9.0 GHz.*

Similarly, we show in Fig. 8.6 the bistatic scattered field when the incident signal is at $2.5°$ from boresight. We observe in this case that the incident direction just clears the location circle of the dipoles while we in Fig. 8.7 with $\theta = 3.75°$ are well outside this circle. At $\theta = 5.0°$ and $10.0°$ shown in Figs. 8.8 and 8.9, respectively, we clear the feed to the extent that we basically obtain reflector scattering only. All in all this "movie" shows a gradual change from $\theta = 0°$ to $\theta = 10°$ without any particular surprises.

8.2.2   The Bistatic Scattered Field as a Function of Frequency

We next show a series of calculated bistatic scattered patterns where the angle of incidence is fixed at $0°$ along the boresight axis while we vary the frequency
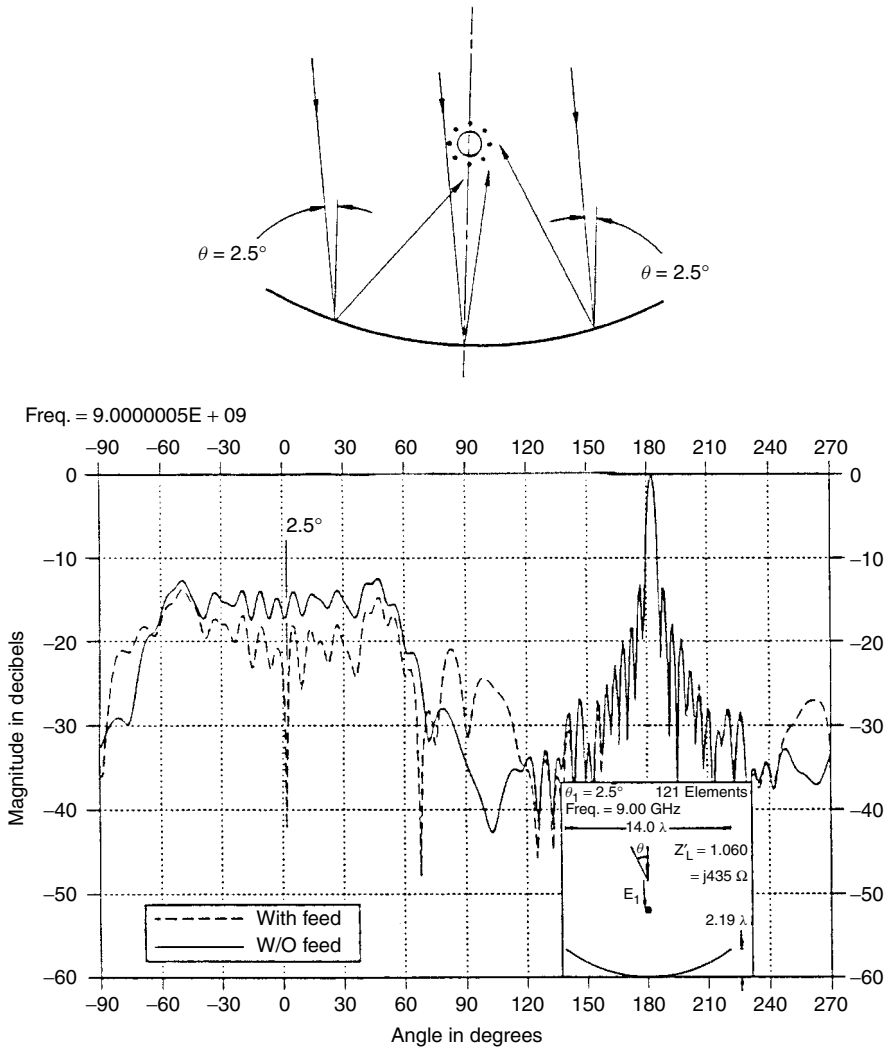
Fig. 8.6 The bistatic scattered field from a parabolic cylinder for an incident plane wave arriving at $\theta = 2.5°$. Shown with and without low RCS feed. Frequency is 9.0 GHz.

downward as well as upward from the center frequency 9.0 GHz. More specifi-cally, we show in Figs. 8.10 through 8.13 the bistatic scattered pattern at the fre-quencies 8.5, 8.0, 7.5, and 7.0 GHz, respectively. Similarly, we show in Figs. 8.14 and 8.15 the pattern at 9.5 and 10.0 GHz, respectively. We note that for all of these patterns the scattering with the low RCS feed is consistently below that of the parabolic reflector without feed. In other words, the low RCS feed works very efficiently over a significant band.
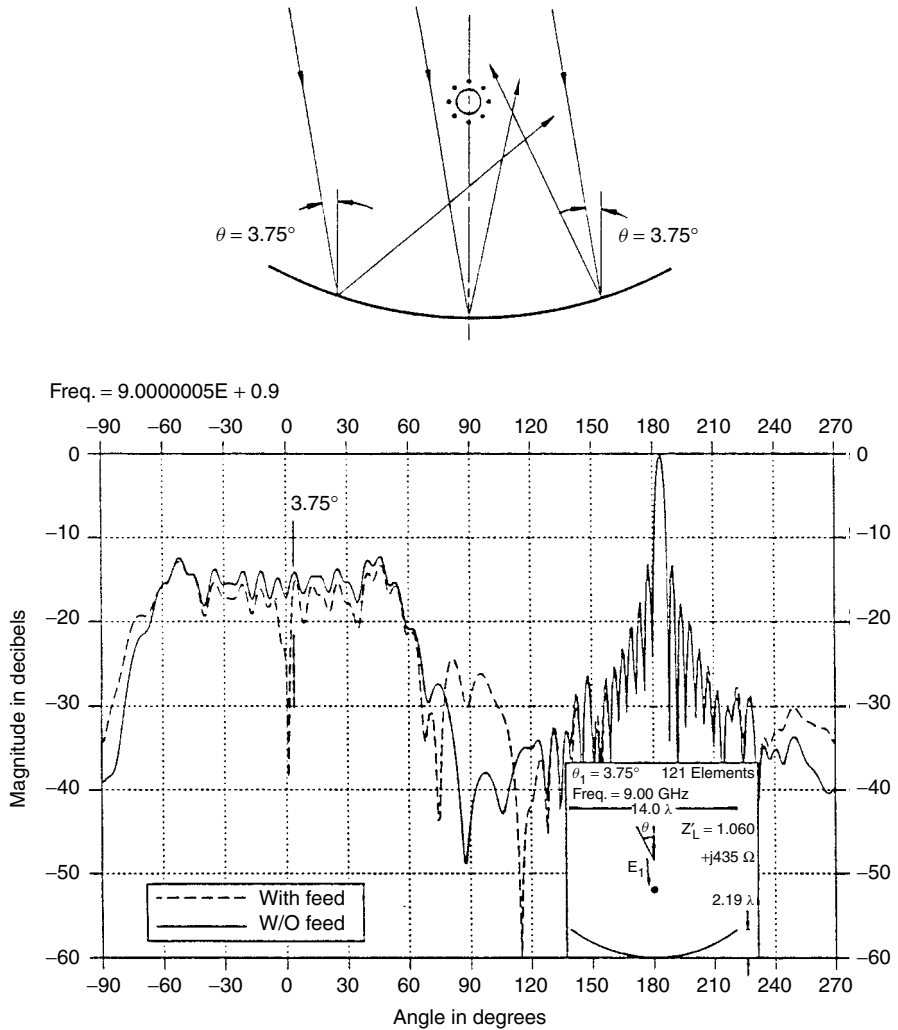
Fig. 8.7   The bistatic scattered field from a parabolic cylinder for an incident plane wave arriving at $\theta = 3.75°$. Shown with and without low RCS feed. Frequency is 9.0 GHz.

8.3   PRACTICAL EXECUTION OF THE LOW RCS FEED

A possible execution of a low RCS feed arrangement is shown in Fig. 8.16. To the left we show the transmitting case and to the right the receiving case. We show four dipoles being feed via hybrids with power division ∼2−4 dB. This will under transmitting condition produce a tapered aperture distribution as desired. (In reality, more dipoles and stronger taper may be needed.) However, when receiving, all dipoles are basically being exposed to the same power level. The tapered illumination will again be created by the hybrids with the excess

Freq. = 9.0000005E + 09
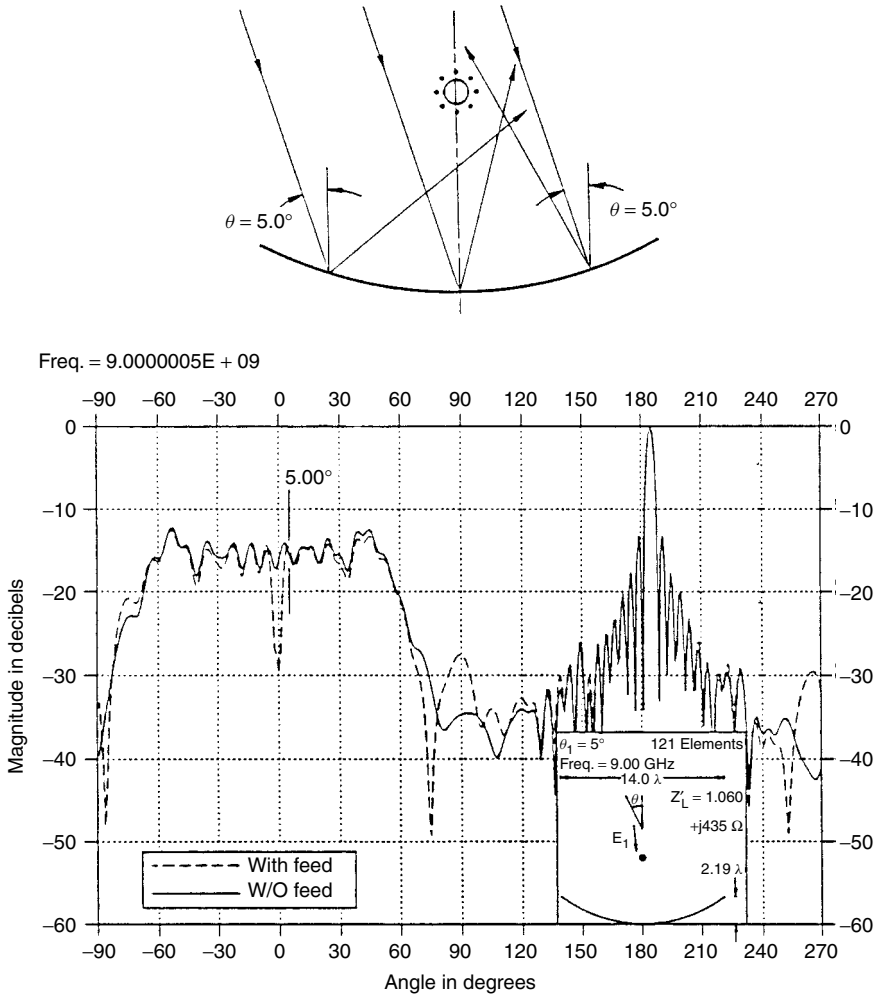
Fig. 8.8 *The bistatic scattered field from a parabolic cylinder for an incident plane wave arriving at $\theta = 5.0°$. Shown with and without low RCS feed. Frequency is 9.0 GHz.*

received power being absorbed by the hybrid loads. That is, no power will be reradiated. Further discussion about this mechanism is given in Section 2.12 under planar arrays.

8.4   OUT-OF-BAND REDUCTION

We have so far considered RCS in-band reduction only. The success of this approach depends strongly upon how well the antenna is matched to the load (i.e., the terminal impedances of receivers or transmitters). Since a good match

Freq. = 9.0000005E + 09
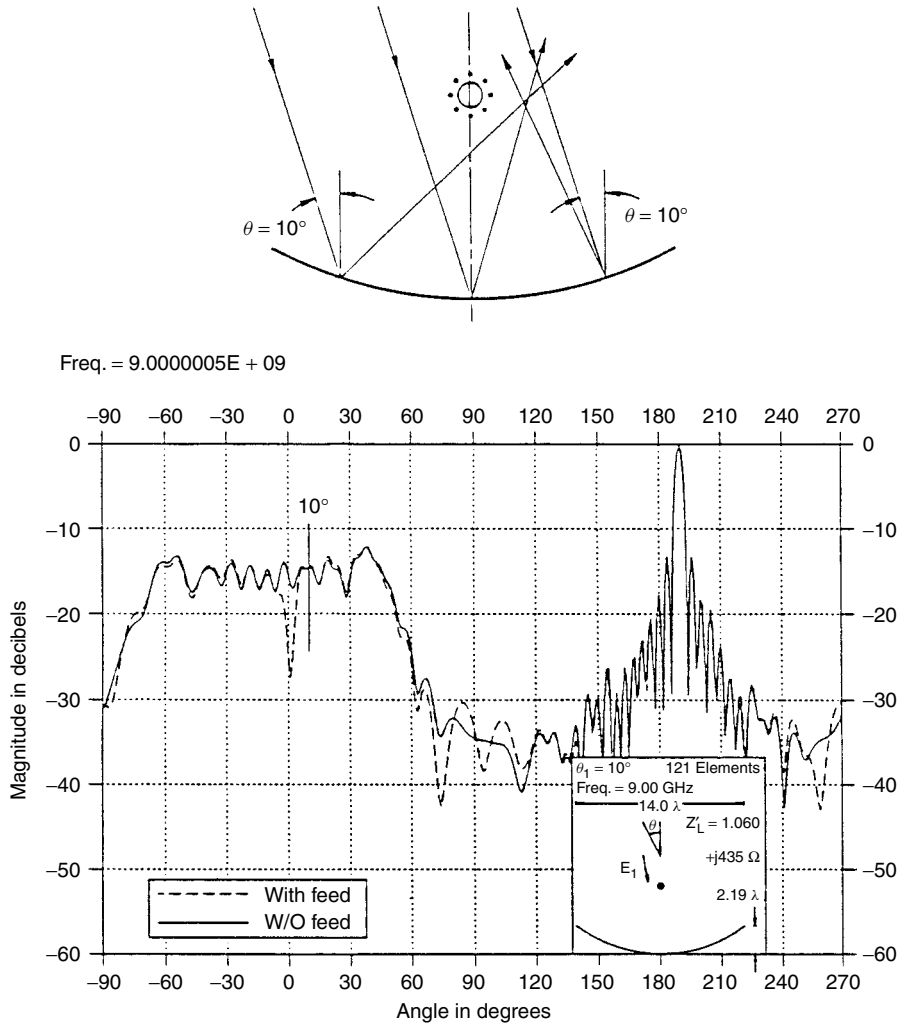
Fig. 8.9   The bistatic scattered field from a parabolic cylinder for an incident plane wave arriving at $\theta = 10.0°$. Shown with and without low RCS feed. Frequency is 9.0 GHz.

is difficult to maintain over a large frequency band, we often resort to other approaches outside the operating band like the use of bandpass radomes (see Fig. 2.1).

One design covers the entire reflector. An example is given in Fig. 8.17. It is extremely effective but it requires a large, heavy, and expensive radome. The good news is that it in general also reduces the wind resistance.

Another design covers only the feed itself. An example is shown in Fig. 8.18. It is important that the wedge angle (or cone angle) is correct such that energy is not reflected back toward the reflector nor in the backscatter direction. Also, the

Input file = [.BDISH]BDISH85.PLT
Number of arrays = 96
Freq. = 8.5000003E + 09
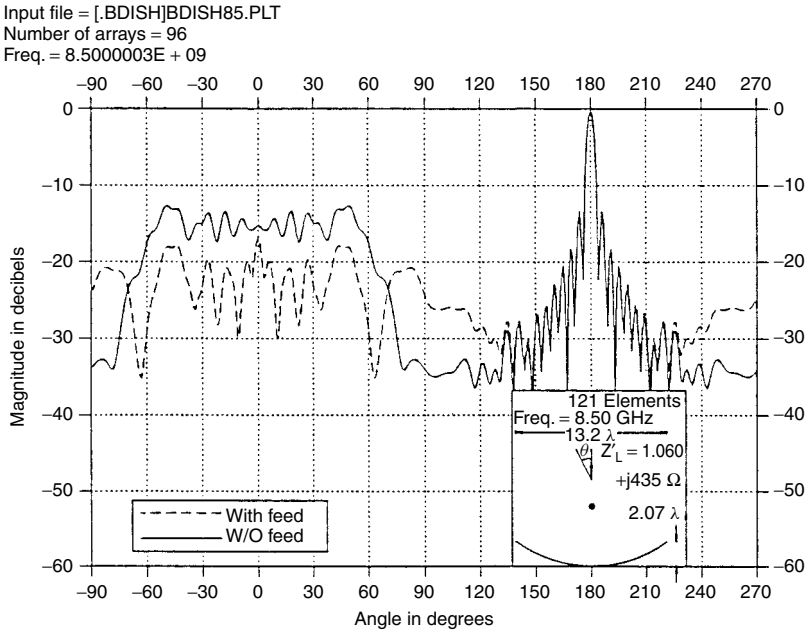
Fig. 8.10 *The bistatic scattered field from a parabolic cylinder for an incident plane wave along boresight; that is, $\theta = 0°$. Shown with and without a low RCS feed. Frequency is 8.5 GHz.*

Input file = [.BDISH]BDISH8.PLT
Number of arrays = 96
Freq. = 8.0000000E + 09
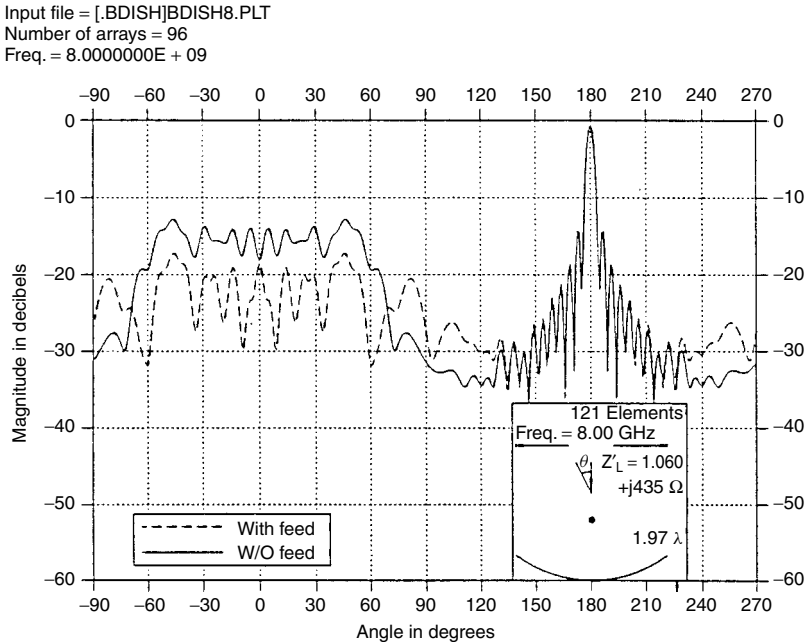
Fig. 8.11 *The bistatic scattered field from a parabolic cylinder for an incident plane wave along boresight; that is, $\theta = 0°$. Shown with and without a low RCS feed. Frequency is 8.0 GHz.*

Input file = [.BDISH]BDISH75. PLT
Number of arrays = 96
Freq. = 7.5000003E + 09
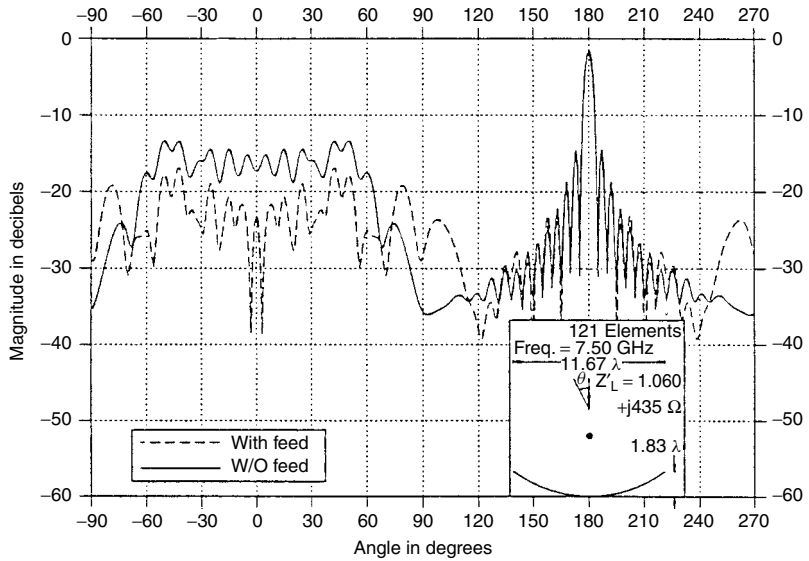
Fig. 8.12   The bistatic scattered field from a parabolic cylinder for an incident plane wave along boresight; that is, $\theta = 0°$. Shown with and without a low RCS feed. Frequency is 7.5 GHz.

Input file = [.BDISH]BDISH7.PLT
Number of arrays = 96
Freq. = 7.0000000E + 09
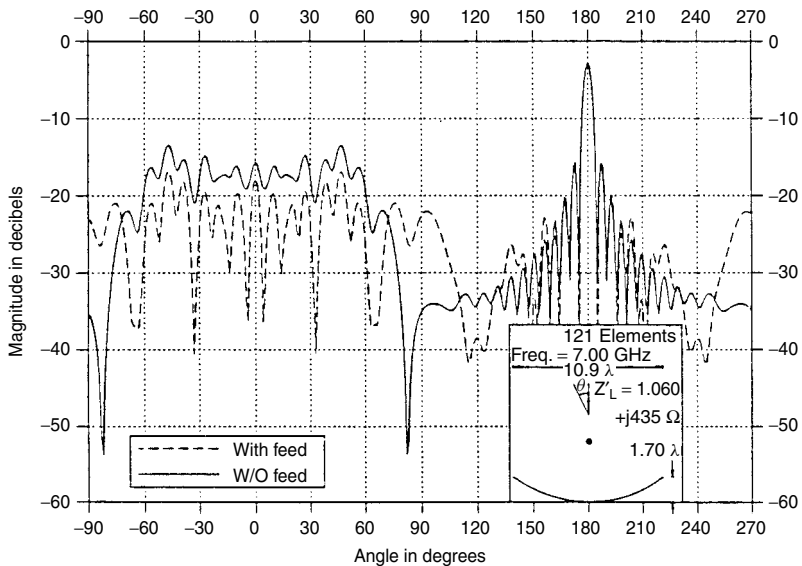
Fig. 8.13   The bistatic scattered field from a parabolic cylinder for an incident plane wave along boresight; that is, $\theta = 0°$. Shown with and without a low RCS feed. Frequency is 7.0 GHz.

Input file [.BDISH]BDISH95.PLT
Number of arrays = 96
Freq. = 9.5000003E + 09

121 Elements
Freq. = 9.50 GHz
14.8 λ
θ Z'_L = 1.060
+j435 Ω

2.31 λ

With feed
W/O feed
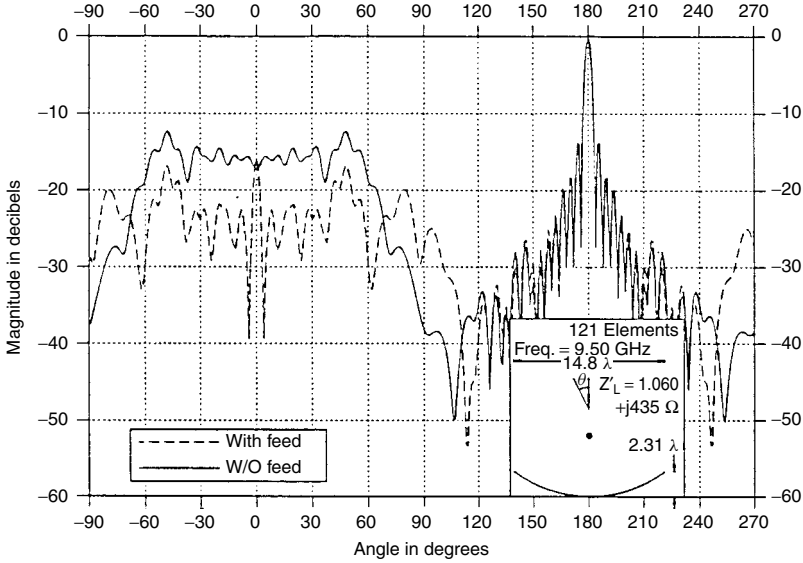
Fig. 8.14   The bistatic scattered field from a parabolic cylinder for an incident plane wave along boresight; that is, $\theta = 0°$. Shown with and without a low RCS feed. Frequency is 9.5 GHz.

Input file [.BDISH]BDISH10.PLT
Number of arrays = 96
Freq. = 1.0000000E + 09

121 Elements
Freq. = 10.00 GHz
15.6 λ
θ Z'_L = 1.060
+j435 Ω

2.43 λ

With feed
W/O feed
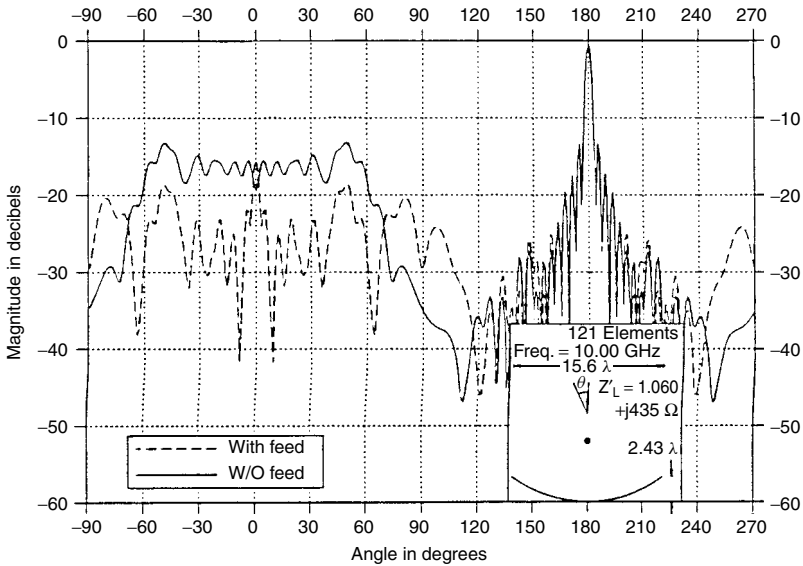
Fig. 8.15   The bistatic scattered field from a parabolic cylinder for an incident plane wave along boresight; that is, $\theta = 0°$. Shown with and without a low RCS feed. Frequency is 10.0 GHz.
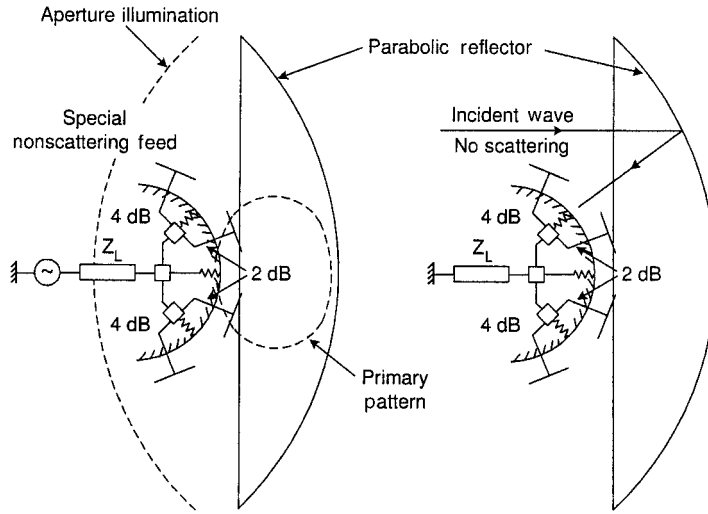
Fig. 8.16   A practical design of a low RCS feed comprised of dipoles in front of a circular groundplane and being fed via hybrids. Left: Transmitting case. The special 2/4 dB hybrids will provide a tapered aperture distribution as desired. Right: Receiving case. All dipoles will be exposed to approximately the same power level. However, the hybrid will deliver the energy to the load impedance Z_L in a tapered fashion while excess power is being dissipated in the hybrid loads.
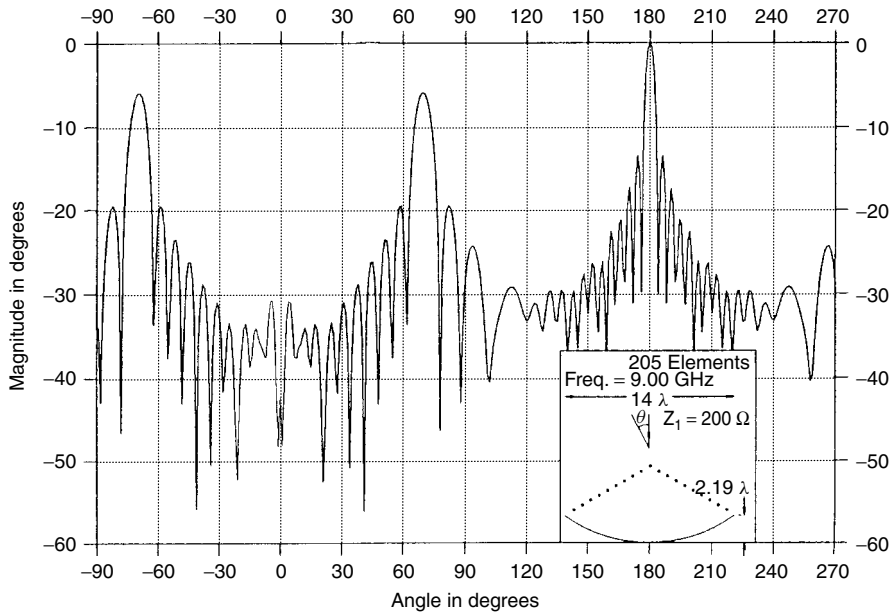
Fig. 8.17   Out-of-band reduction. An FSS radome covering the entire reflector aperture. The bistatic scattered field is obtained when the radome is opaque.
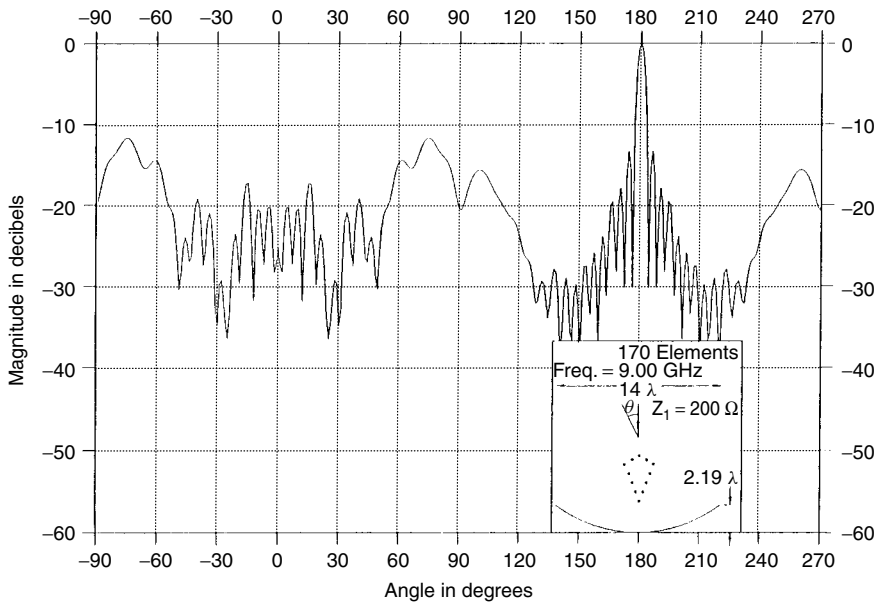
Fig. 8.18   Out-of-band reduction. An FSS radome surrounding the feed only. The bistatic scattered field is obtained when the radome is opaque. The wedge (or cone) angle is quite critical and so is the length of the radome. See text.

cone must be sufficiently long such that a convergent bundle of rays is reflected from it and not just a "big fat dipole pattern." The reader is also reminded that the total transmitting energy will pass through the radome. Thus, consideration must be given to the power handling capacity in particular if the small feed radome is chosen. See also reference 110.

8.5   COMMON MISCONCEPTIONS ON EDGE CURRENTS

When discussing scattering from a parabolic antenna the question is often asked, "Did you incorporate the edge currents?" Our answer is, "Certainly!"

And the next question is, "Where was that done?"

Actually we calculated the bistatic scattering by direct application of the method of moments. It is therefore very accurate and includes everything. Other researchers may take a somewhat different approach. Basically they study the exact solution (like ours) and observe that it "looks like" one component is coming, for example, from the vertex of the dish, another from the edges, and still another from the feed itself, and so forth. These observations might indeed be correct and can even lead to a computationally very fast approach. However, one may also arrive at some erroneous conclusions. For example, it is often suggested that since a significant part of the reflector scattering seems to come from the

edges of the reflector, some form of edge treatment could reduce the reflector scattering. Although some minor change may be observed by attacking the edges only, it must be emphasized that any radiated field from any structure is derived from electrical (and/or magnetic) currents only and integrated over the *entire* body. As an illustration, consider our reflector model made of infinitely long FSS sticks located on a parabola (see Section 8.1.1). Any modification of the outermost FSS sticks would hardly change the currents in the rest of the reflecting elements and thus not the reflected field. In fact, if we ultimately simply removed the outermost sticks we would simply end up with a reflector slightly smaller than the original and we would be right back to square one. A tapered approach might be slightly better.

However, edge treatment is an entirely different matter if we instead of a single FSS surface had considered an array of conjugate-matched dipoles located in front of a groundplane as was the case in Chapter 5, Sections 5.3 and 5.4. If the edge columns were loaded with the same load as the rest of the array, namely the conjugate matched, we would indeed observe no reflection from the surface itself and observe a relatively strong scattering from the edge columns (see Figs. 5.2 and 5.3). This is simply because these columns are in an "outside" environment and thus have an antenna impedance quite different from the rest of the columns in the array. We can in that case load the outer columns with a load impedance being basically conjugate-matched to the outer columns. Note that these facts should not be interpreted as edges are always scattering. In fact, we can engineer surfaces that do not scatter at the edges but everywhere else. See Chapter 5 for details, as well as Problem 5.1.

8.6 CONCLUSION

We have demonstrated that the scattering from a parabolic cylindrical reflector consists essentially of two components: One is reflected from the reflector directly without the feed, and another is reflected from the feed via the reflector.

The first of these components, namely the reflector scattering, in general cannot be reduced significantly in band. Out of band a suitably designed radome placed either over the entire reflector or over the feed itself was as shown in Section 8.4 an effective way to reduce the frontal RCS.

The other component, namely the feed scattering, could be greatly reduced by using a new specially designed feed. It consisted, in principle, of dipole elements placed around a circular pipe acting as a "groundplane." In fact, the bistatic return of the entire antenna was about 6 dB lower with the new feed than was the reflector scattering without any feed at all. The reason for this apparent paradox was that the field being reflected from the reflector would pass unperturbed through the focal area and thus be added to the field coming directly from the reflector. If these two components were approximately in phase, an increase in the total backscattered field is observed. If we instead use the low RCS feed, the field in the focal area would simply be absorbed and not continue through to the backscatter sector.

The RCS for a parabolic reflector cannot be as low as the planar array backed by a groundplane, see Chapters 2 and 5. However, they are discussed here because of their popularity in some camps.

Cassegrain antennas have also been investigated but are not reported here. The reason being that they exhibit certain problems relating to standing waves between the sub and main reflector. That makes the control of the backscatter difficult and they are therefore in general not recommended.

Our investigation here has primarily been focused around the two-dimensional cylindrical parabola. This case could be solved exactly and efficiently by using the SPLAT program. However, it is readily extended to explain the scattering mechanism for the parabolic disk as well.

Finally, I would like to point out that one of my former students, John Mehr, was extremely active in this investigation. Thank you John.

9

Aperiodicity: Is It a Good Idea?

9.1 INTRODUCTION

When working with periodic structures, someone will sooner or later ask the question, "Can new, improved, and innovative designs be obtained by variation of the periodicity?"

For example, what would happen if we in an array of simple straight dipoles made every other dipole a little longer and the rest a little shorter? Since the longer dipoles would resonate at a lower frequency and the shorter at a higher, many designers would expect to obtain a staggered tuning effect, possibly leading to a somewhat broader resonance curve and perhaps with a little luck (and "tweaking"!) a flat top. A highly desirable feature indeed.

However, before we delve into a detailed analysis of this very interesting subject, let us briefly present a typical example as shown in Fig. 9.1. It was obtained from the PMM program for normal and 60° angle of incidence.

We first show the resonant curve for an unperturbed array with total element length $2l = 1.5\,\text{cm}$, $d_x = 0.6\,\text{cm}$, and $D_z = 1.7\,\text{cm}$, as seen in the insert of Fig. 9.1. In the same figure we also show the resonant curve for the same array as above but where the length of every other dipole has been increased to $1.65\,\text{cm}$ and the rest have been shortened to $1.35\,\text{cm}$ as also shown in the insert in Fig. 9.1.

We observe a double resonance as expected but we also observe a null between them. An inexperienced designer might think that the null could be at least "toned down" if the two resonances were moved closer to each other. Typically

Reflection Coefficient
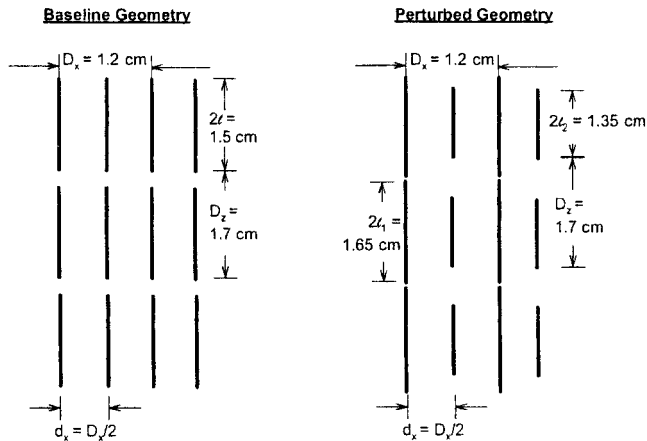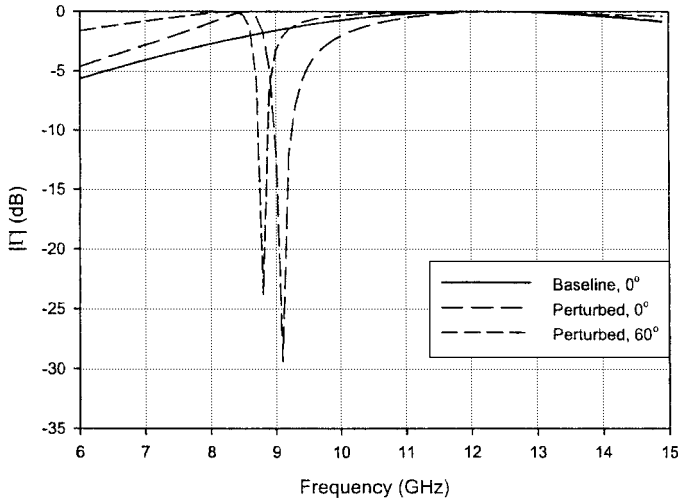
Fig. 9.1   The resonant curve for an array with identical element length (left insert) and also where every other element is longer and the others are shorter (right insert). This may not be particularly useful, but it is interesting.

he would most likely embark on a computational approach backed up by an optimization routine or perhaps just a parametric study. After some praying to the great computer god, he might even arrive at the right conclusion: A flat top without loss just seems impossible for such a configuration. Or maybe we just did not run the program long enough?

However, in the author's opinion a better approach is to analyze the general problem in a classical analytic way. It will be presented in detail below.

But if variation of periodicity in general is somewhat disappointing from an application point of view (not from a theoretical), why spend time on the subject at all? Primarily for two reasons:

1. Even experienced designers sometimes come up with "innovative" designs where the optimizer somehow does not deliver an acceptable design, for the simple reason that none exist.
2. From time to time the periodicity can be disturbed unintentionally. Typically, that might happen if the modes in the PMM calculation are applied improperly. The designer should therefore be familiar with these symptoms if encountered.

However, if the structure is finite, interesting results can be obtained by variation of the periodicity. This case will be investigated in Section 9.6.

We shall next analyze periodic structures in detail when we vary either the element loads, the interelement spacings, or both at the same time.

9.2 GENERAL ANALYSIS OF PERIODIC STRUCTURES WITH PERTURBATION OF ELEMENT LOADS AND/OR INTERELEMENT SPACINGS

The structure to be investigated is shown in Fig. 9.2. It is comprised of two subarrays, each with interelement spacings D_x and D_z. They are interlaced into each other such that array 1 has its reference element located at the origin while the reference element for array 2 is located at $(d_x, 0, 0)$. We denote the element loads by jX_{L1} and jX_{L2} for arrays 1 and 2, respectively. However, we assume that the elements in both arrays have the same length $2l$. That simplifies our analysis by the fact that the self-impedances $Z^{1,1}$ and $Z^{2,2}$ for the two arrays are identical. Thus, the perturbation of the elements is obtained purely by variation of the load resistances jX_{L1} and jX_{L2} and/or d_x. This corresponds approximately to variation of the element length. Furthermore, we denote the mutual impedances between the two arrays by $Z^{1,2}$ and $Z^{2,1}$.

The structure is being exposed to an incident plane wave propagating in the direction $\hat{s}$. It induces the voltages $V^{(1)}$ and $V^{(2)}$ as well as the currents $I^{(1)}$ and $I^{(2)}$ in the two reference elements, respectively.

From the generalized Ohm's Law we thus obtain

$$V^{(1)} = (Z^{1,1} + jX_{L1})I^{(1)} + Z^{1,2}I^{(2)}, \tag{9.1}$$

$$V^{(2)} = Z^{2,1}I^{(1)} + (Z^{2,2} + jX_{L2})I^{(2)}. \tag{9.2}$$

From (9.1) and (9.2) we obtain from Cramer's rule

$$I^{(1)} = \frac{1}{D}[(Z^{2,2} + jX_{L2})V^{(1)} - Z^{1,2}V^{(2)}], \tag{9.3}$$

$$I^{(2)} = \frac{1}{D}[-Z^{2,1}V^{(1)} + (Z^{1,1} + jX_{L1})V^{(2)}], \tag{9.4}$$
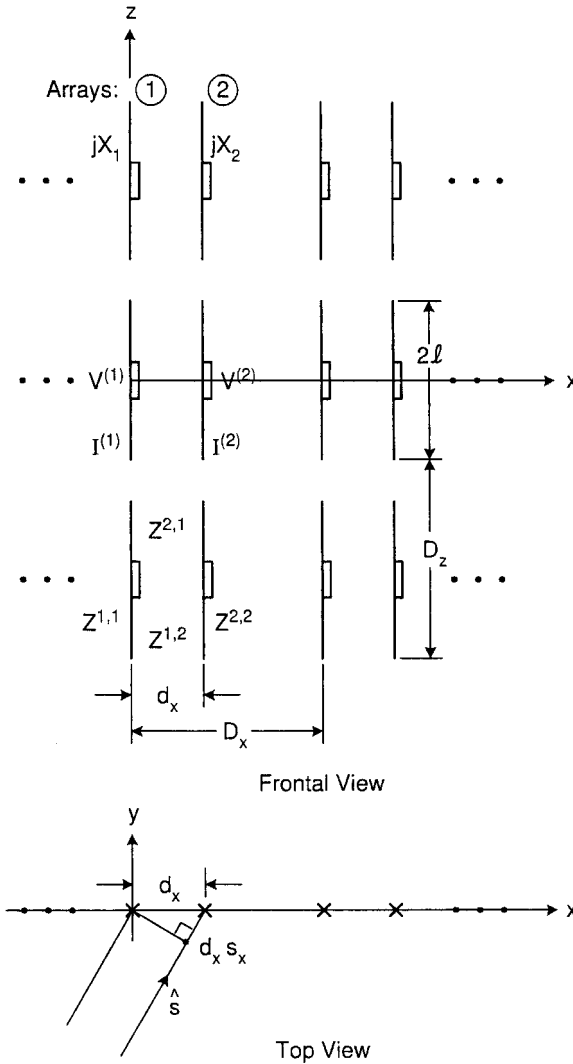
Fig. 9.2 Two arrays 1 and 2 with interelement spacing D_x and D_z interlaced into each other with array spacing d_x. Array 1 is loaded with jX_{L1} and array 2 with jX_{L2}. The element lengths of both arrays are identically equal to 2l.

where the determinant D is

$$D = \begin{vmatrix} Z^{1,1} + jX_{L1} & Z^{1,2} \\ Z^{2,1} & Z^{2,2} + jX_{L2} \end{vmatrix}. \qquad (9.5)$$

Furthermore, we assume that the plane of incidence is the xy plane while the incident field $\overline{E}^i$ is oriented along the z axis. Then the voltage induced in the

reference element for array 1 is then given by [111]

$$V^{(1)} = E^i P^t(0, 0), \tag{9.6}$$

where $P^t(0, 0)$ is the pattern factor under transmitting condition for $(k, n) = (0, 0)$.

Furthermore, the voltage $V^{(2)}$ induced in the reference element for array 2 has the same amplitude as $V^{(1)}$ (the elements are identical), but the phase is adjusted for its displacement d_x, that is,

$$V^{(2)} = V^{(1)} e^{-j\beta d_x s_x}, \tag{9.7}$$

The element currents $I^{(1)}$ and $I^{(2)}$ are now completely determined by equations (9.3) through (9.7).

Furthermore, we recall that the propagating field $\overline{E}^{(j)}(\overline{R})$ for a single array is given by [63]

$$E^{(j)}(\overline{R}) = I^{(j)}(\overline{R}^{(j)}) \frac{Z}{2D_x D_z} \frac{e^{-j\beta(\overline{R}-\overline{R}^{(j)}) \cdot \hat{r}_\pm}}{r_y} \overline{e}_\pm(0, 0) P^{(j)}(0, 0), \tag{9.8}$$

for no grating lobes, where $\overline{R}^{(j)}$ denotes the reference point for array "j," $\overline{e}_\pm = (\hat{z} \times \hat{r}_\pm) \times \hat{r}_\pm$ (see [63]), and $P^{(j)}$ is the pattern factor under scattering conditions. The total bistatic scattered field from the two subarrays is now obtained by addition of the fields from the two arrays given by (9.8), just like an ordinary antenna problem.

Substituting the values for $I^{(1)}$ and $I^{(2)}$ as calculated above and noting that

$$R_A = \frac{Z}{2D_x D_z} \frac{1}{s_y} P(0, 0) P^t(0, 0), \tag{9.9}$$

we readily obtain the following equation for the total reflection coefficient for the two arrays:

$$\Gamma = -R_A \frac{(Z^{1,1} + jX_{L1}) - Z^{1,2} e^{-j\beta d_x s_x} - Z^{2,1} e^{+j\beta d_x s_x} + (Z^{2,2} + jX_{L2})}{(Z^{1,1} + jX_{L1})(Z^{2,2} + jX_{L2}) - Z^{1,2} Z^{2,1}}. \tag{9.10}$$

9.2.1 No Grating Lobes from Subarrays

When no grating lobes from the subarrays exist, we have

$$Z^{1,1} = Z^{2,2} = R_A + jX_A. \tag{9.11}$$

Furthermore, based on the general plane wave expansion, Hill has obtained a general expression for the mutual impedances [112]:

$$Z^{1,2} = (R_A - R_M + jX_M) e^{+j\beta d_x s_x} \tag{9.12}$$

for no grating lobes and

$$Z^{2,1} = (R_A + R_M + jX_M)e^{-j\beta d_x s_x} \tag{9.13}$$

for no grating lobes. Note that $R_M = 0$ for $d_x = D_x/2$ and also for normal incidence. However, we always have $Z^{1,2} \neq Z^{2,1}$ except if the two subarrays are displaced right behind each other—that is, along the y axis only.

After straightforward but somewhat tedious calculations, substituting (9.11), (9.12), and (9.13) into (9.10) yields

$$\Gamma = -\cfrac{1}{1 + j\cfrac{X_A^2 - R_M^2 - X_M^2 + X_A(X_{L1} + X_{L2}) - X_{L1}X_{L2}}{R_A(2X_A - 2X_M + X_{L1} + X_{L2})}}. \tag{9.14}$$

Without any loss of generality except a simple frequency shift, we now assume asymmetric loading (i.e., $X_{L1} = -X_{L2} = X_L$), which reduces (9.14) to

$$\Gamma = -\cfrac{1}{1 + j\cfrac{X_A^2 - R_M^2 - X_M^2 - X_L^2}{2R_A(X_A - X_M)}}. \tag{9.15}$$

Inspection of (9.15) readily shows that we obtain $\Gamma = -1$ (resonance) for

$$X_A = \pm\sqrt{R_M^2 + X_M^2 + X_L^2} \tag{9.16}$$

and a null ($\Gamma = 0$) for

$$X_A = X_M. \tag{9.17}$$

In Fig. 9.3 we show a typical general resonance curve as a function of X_A for a structure comprised of two subarrays with reactive loads $jX_{L1} = -jX_{L2} = jX_L$ and with interelement spacing D_x and D_z. The reference elements of the second array are shifted d_x along the x axis only.

Also shown is the baseline curve for $d_x = D_x/2$ and $X_L = 0$.

Note that since $R_M = 0$ in that case, we obtain at resonance from (9.16) $X_A = \pm X_M$. However, only the negative value is correct since the positive value is canceled by the null at $X_A = +X_M$ [see (9.17)].

Based on the plane wave expansion, Hill derived an expression for X_M [112]. He found that for a straight dipole, X_M would in general be negative (it appears that positive X_M could only occur if the current distributions were odd; for tripoles, see Section 9.3).

Thus, in Fig. 9.3 the baseline resonance at $-X_M$ will be located to the right of $X_A = 0$. Furthermore, by inspection of (9.16) we observe that the highest resonance is always higher than the baseline resonance at $X_A = -X_M$, depending on X_L and R_M.
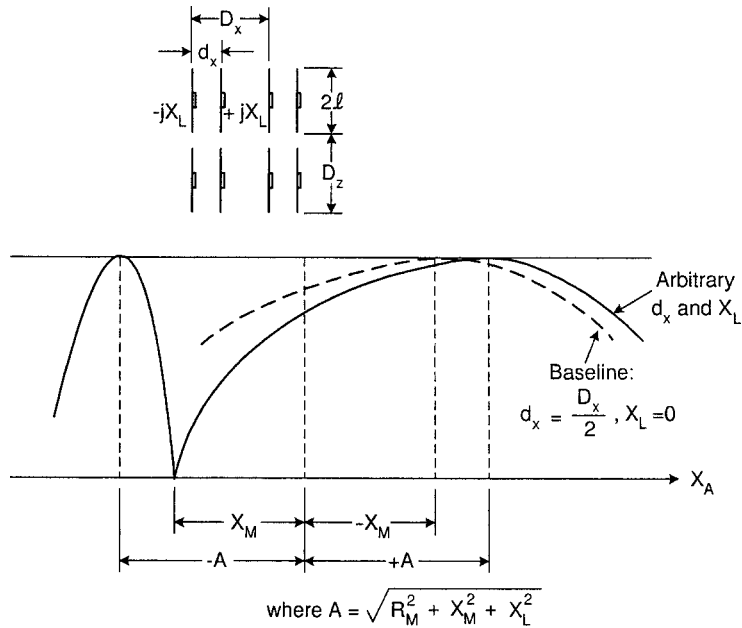
Fig. 9.3   The resonance curve as a function of X_A for two arrays with interelement spacings D_x and D_z interlaced into each other with array separation d_x. The element lengths are the same for both arrays, but one array is loaded with jX_L and the other with $-jX_L$. Note that regardless of spacing $d_x \neq D_x/2$ and $jX_L \neq 0$, we always obtain a null at $X_A = X_M$ and a main resonance slightly higher than the unperturbed configuration.

Furthermore, the lowest resonance is always lower than the null at $X_A = X_M$; that is, the null will always be located between the two resonances, in agreement with Foster's reactance theorem [101].

It is also interesting to note that the null is independent of d_x as well as X_L while the two resonances depend strongly on both of these parameters.

Finally note that the highest resonance for the perturbed case is as much above the baseline resonance at $X_A = -X_M$ as the lowest resonance frequency is below the null at $X_A = X_M$.

9.2.2   Grating Lobe from Subarrays

So far we have assumed that the interelement spacings D_x and D_z were so small that no grating lobes would emerge from the two subarrays. However, if this is not the case, the expressions above must be modified. More specifically, (9.11) becomes

$$Z^{1,1} = Z^{2,2} = R_A + R_G + jX_A \qquad (9.18)$$

when grating lobes are present. R_G denotes a resistance representing the extra energy disappearing in the direction of the grating lobe(s).

Similarly, if the elements are regularly spaced (i.e., $d_x = D_x/2$), (9.12) and (9.13) should according to Hill [112] be modified to

$$Z^{1,2} = (R_A - R_G + jX_{MG})e^{+j\beta d_x s_x} \tag{9.19}$$

for grating lobes and modified to

$$Z^{2,1} = (R_A - R_G + jX_{MG})e^{-j\beta d_x s_x} \tag{9.20}$$

for grating lobes. If unevenly spaced, (9.19) and (9.20) become more complicated.

Substituting (9.18), (9.19), and (9.20) into (9.10) yields the reflection coefficient Γ where grating lobe(s) can emerge from the two subarrays as evaluated by Hill [112].

However, in this chapter it will be sufficient to state the overall effect of grating lobes:

1. The upper resonance—that is, the one slightly higher than the resonance of the unperturbed structure—will exhibit a slight loss due to the extra energy that must be diverted to the grating lobe directions. The loss typically ranges from a few tenths to a few decibels.
2. The lower resonance as well as the null in the resonance curve will be more or less washed out, depending on the onset frequency of the grating lobes.

9.2.3   Concluding Remarks for Section 9.2

Variation of the inter element spacing and/or the reactive tuning loads of a periodic structure will result in a new resonance slightly above the unperturbed resonance and without loss, provided that no grating lobes exist. If grating lobes from the two subarrays do exist, we will experience loss at resonance.

There will also be a lower and narrower first resonance without loss, provided that no grating lobes exist. A perfect null is located between the two resonant frequencies. It too will partly disappear when grating lobes occur.

Thus, a resonance curve with a flat top and without loss appears not to be obtainable from a single surface. However, it is possible if the two arrays are cascaded behind each other (see reference 113).

9.3   PERTURBATION OF ARRAYS OF TRIPOLES

We have so far considered perturbations of arrays of just straight parallel dipoles. Although they are indicative of what may happen when we apply more complicated elements instead, we shall now specifically investigate arrays of tripoles. (Taken from Hill's dissertation [112].)

From the PMM program we obtain the resonance curve for an array of tripoles arranged in a regular equilateral triangular grid as shown in Fig. 9.4
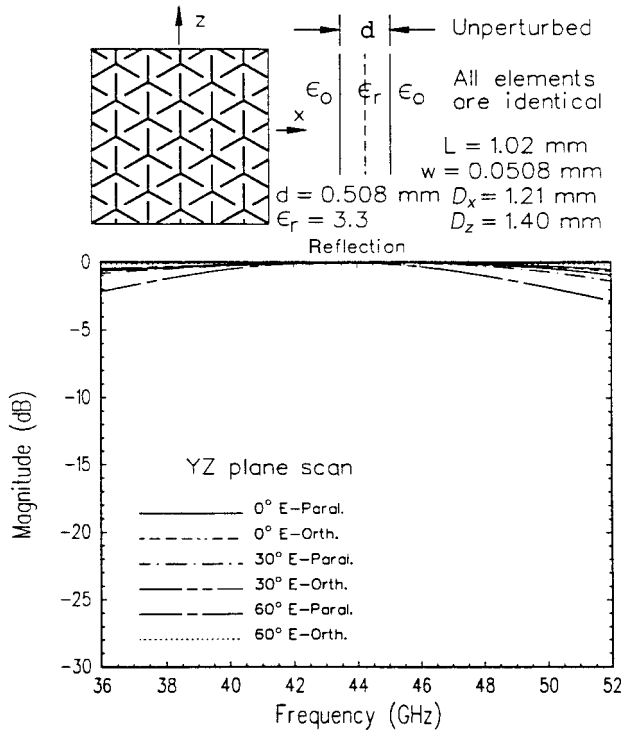
Fig. 9.4   Calculated reflection response of a tripole array with no perturbations.

(our baseline). We next show in Fig. 9.5 the same array except that each fourth element has been reduced 20% in size. Similarly we show in Fig. 9.6 the case where the same elements have been increased by 20% instead. Inspection of these curves clearly shows that the shorter elements push the resonance frequency of the array upwards and vice versa for the longer case. While that in itself is both expected as well as acceptable, we also observe a number of deep dips in the resonance curve that would make such an arrangement less than desirable. Finally in Fig. 9.7 we show the extreme case where each 4*th* element is completely missing. Although that configuration could be used for some less demanding application, it is obviously not an approach that should be pursued seriously, not even if we observe no loss at resonance in spite of the fact that we have fewer elements. In other words, to obtain a quality periodic surface, we must observe periodicity in the strictest sense.

9.4   MAKING USE OF OUR OBSERVATIONS

The investigation above can be highly instructive. We shall illustrate this statement by several examples.
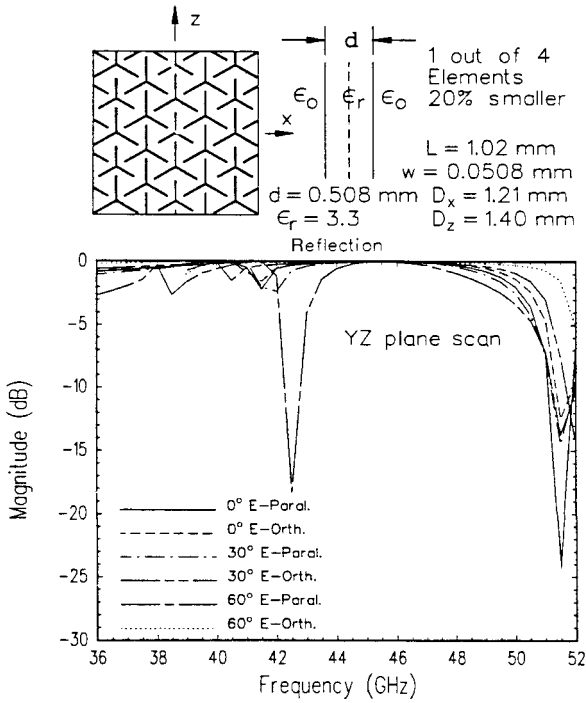
Fig. 9.5   *Calculated reflection response of a tripole array with every fourth element 20% smaller.*
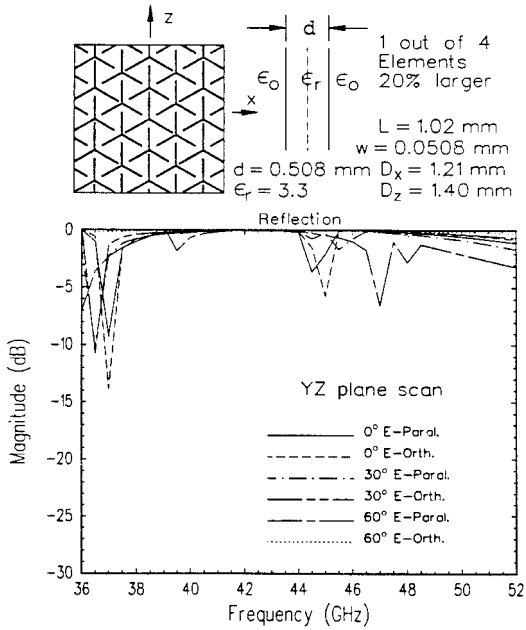
Fig. 9.6   *Calculated reflection response of a tripole array with every fourth element 20% larger.*
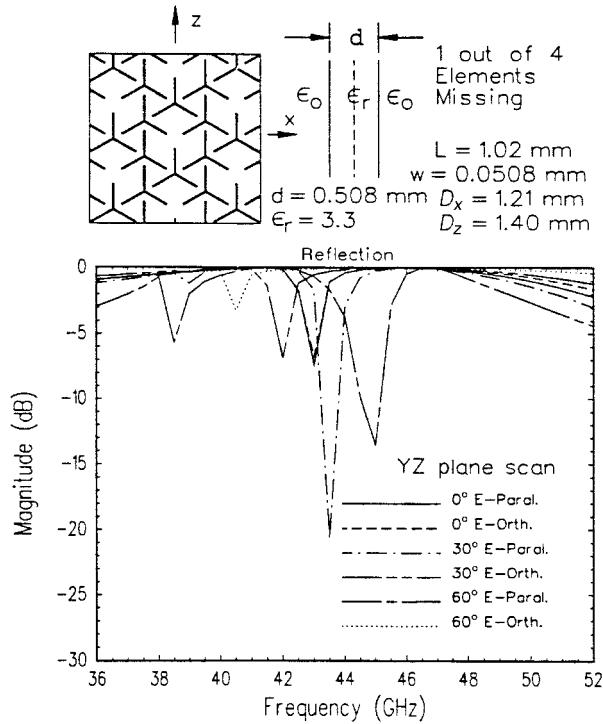
Fig. 9.7   Calculated reflection response of a tripole array with every fourth element missing.

9.4.1   Multiband Designs

Every so often, dual-band designs are called for—as, for example, two reso-
nances separated by a null or valley. The approach to this problem depends to a
high degree on the ratio between the two bands. If it is low, one possibility is to
use concentric loops as illustrated in Fig. 9.8. Recalling that the circumference of
a resonating loop element is about one wavelength, we readily conclude that the
largest loop should have a diameter $\sim\lambda_L/3$, which also is the smallest interele-
ment spacing in a rectangular grid. At the high frequency the interelement spacing
should be no more than $\lambda_H/2$ to avoid grating lobes for all scan angles, that is,
$f_H < 1.5 f_L$. This constitutes about the largest frequency ratio that can be used
for concentric loops. However, if we instead of loops use hexagons embedded
in dielectric, the frequency ratio could be driven up to as high as $\sim$1.8:1.

   If higher frequency ratios are called for, we must resort to other approaches.

   One possibility shown in Fig. 9.9 is comprised of large Jerusalem crosses
interlaced with smaller ones (not recommended, read on). At the lowest fre-
quency only the large elements will be strongly excited, yielding as good a
performance as one can expect of the Jerusalem cross (the small elements are
only weakly excited).
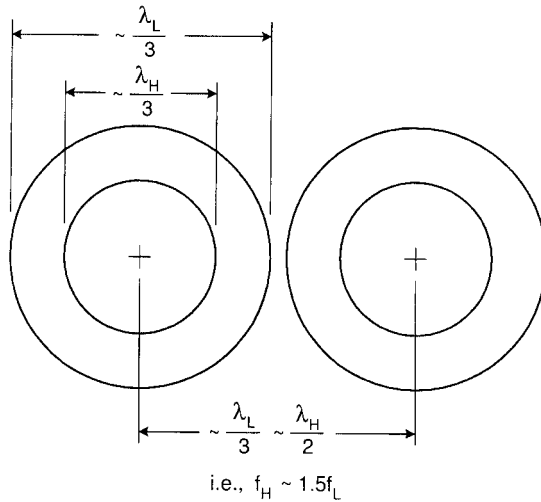
Fig. 9.8   *An array of concentric loops will have two resonances. However, the ratio between the two should not exceed 1.5:1 unless "distorted" into hexagons and embedded in dielectric. See text.*

Not recommended !
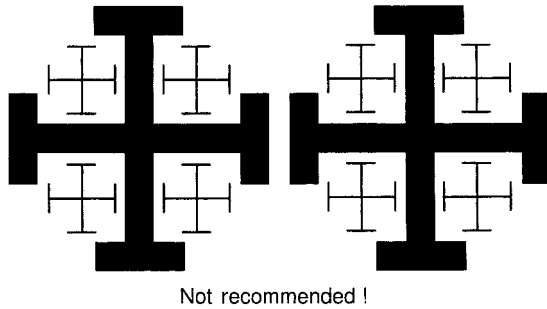
Fig. 9.9   *An array of large Jerusalem crosses interlaced with small ones. In the low-frequency band, only the large elements will be excited, resulting in satisfactory performance. However, in the high-frequency band the small element will be in an irregular environment, resulting in mediocre performance in general.*

At the higher frequency band there is always the possibility that a higher resonance will be excited on the larger elements—in particular, at an oblique angle of incidence. However, even if we luck out in that respect, we do observe that the "periodicity" of the small elements has been violated on several accounts. For example, one end of the small elements is close to the large elements, while the other end is not. Thus, even if the small elements were arranged with the "proper" element spacings, the uneven end loading would produce undesirable nulls, similar to what is seen for example in Fig. 9.3. Thus, the design shown in Fig. 9.9 is not recommended.
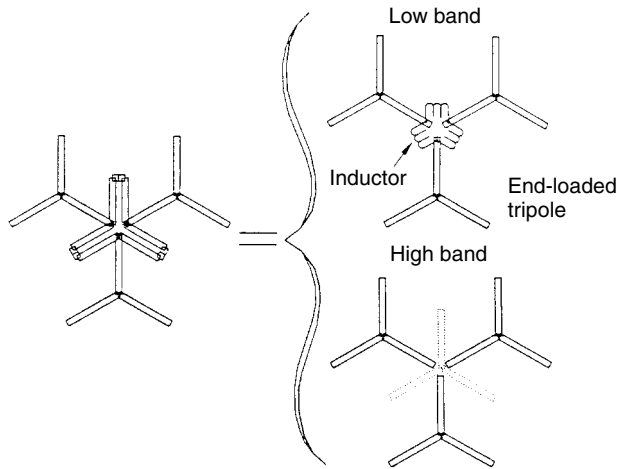
Fig. 9.10 A sketch of the original ''snowflake'' element showing the equivalent structures for the low and high bands. Each leg in the three-legged trap is about $\lambda_H/4$ long, leading to separation of the three tripoles.

9.4.2 The Original "Snowflake" Element

We saw above how seemingly sound arrangements of elements were deemed undesirable because the periodicity was violated. An attempt to rectify this situation is to use an alternative element—as, for example, the snowflake element shown in Fig. 9.10. It is basically made of three tripoles joined together by three traps in parallel and each having a length of $\sim\lambda_H/4$ at the high frequency. Thus the three tripoles are basically disconnected at the high frequency band while they are joined together by inductive loading at the low frequency band such that they basically form an end-loaded and center-loaded tripole. Furthermore, the three-armed trap acts like the fourth tripole at the high band that should be there in order not to disturb the periodicity. A typical performance is shown in Fig. 9.11. We observe satisfactory performance at normal angle of incidence in both bands and also for oblique incidence in the low band as well. However, the E-plane polarization at the high band is not satisfactory.

One of the fundamental problems with this type of element is that the optimum length when acting as traps may not coincide with the correct resonant frequency of the mid-element. And as we saw in Figs. 9.5 and 9.6, this leads to undesirable resonances. Some improvement in that respect can be obtained by modification of the original snowflake element as will be described next.

9.4.3 The Modified "Snowflake" Element

The modified snowflake element is shown in Fig. 9.12. We use three traps as earlier, but this time connected to the three tripoles via series capacitors as shown in the insert. This gives us an extra degree of freedom. We typically start the
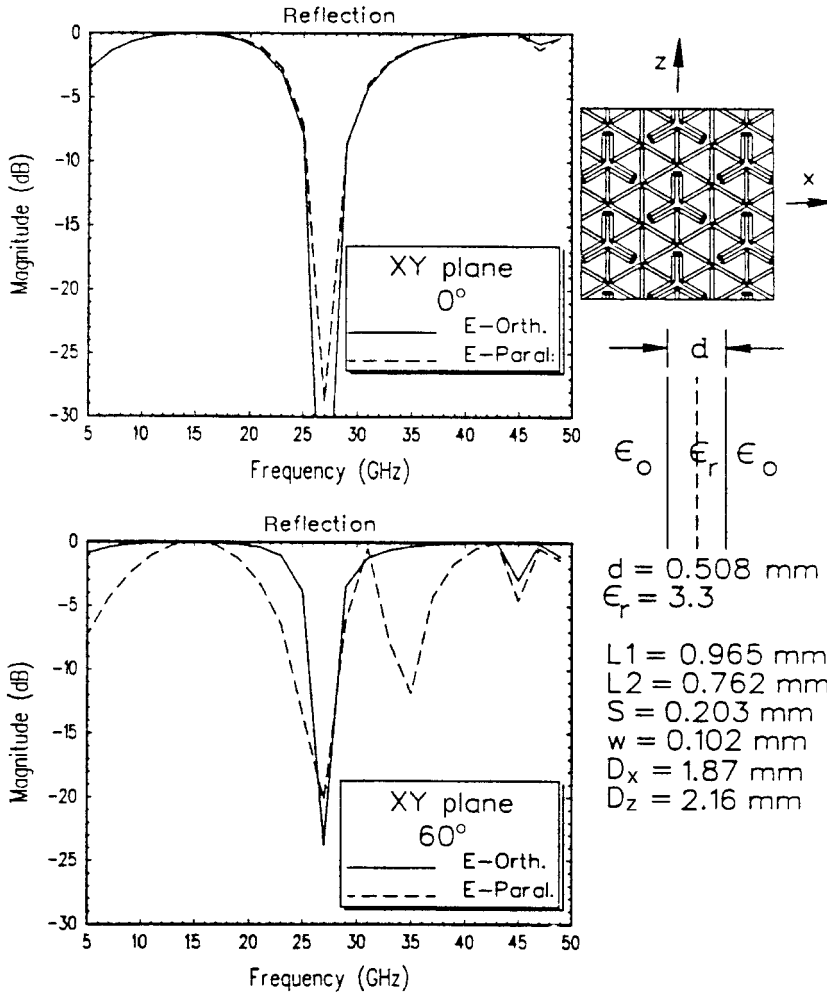
Fig. 9.11 Calculated response for an array of original "snowflake" elements at normal and oblique incidence.

design procedure by choosing the tripoles to resonate at the high-frequency band. Next, we design the traps to also isolate at that frequency. And finally we adjust the capacitors such that we obtain resonance in the low band.

Typical calculated resonant curves for both the low and high bands are shown in Fig. 9.13. The low band is seen to be entirely satisfactory while the high band barely "squeaks" by in a very narrow frequency range. The problem is simply that the three traps do not perform well as a fourth element at the high band. Consequently, we will experience the type of resonances illustrated in Figs. 9.5, 9.6, and 9.7. The element has been deemed satisfactory when used in radomes for communication purposes. We would not recommend it for precision purposes.
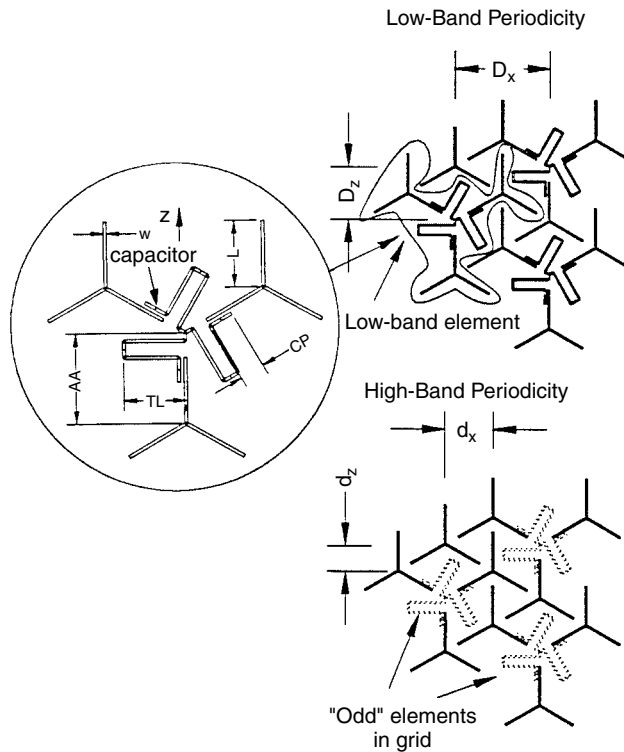
Fig. 9.12   Demonstration of the periodicity of the modified ''snowflake'' element. Consists of three tripoles joined together with traps with series capacitors.

9.4.4   Elements with Mode Suppressors

At this point the reader is entitled to a design that really works! Well, here it is.

It was demonstrated above that periodicity must be preserved and the interelement spacing be small to obtain stability of the resonant frequency with angle of incidence. Fundamentally, that requires elements that are not only small but also of such a shape that close packing is possible. Tripoles are particularly strong candidates in that respect. However, we must also make sure that the low-band elements do not have a second resonance somewhere in the high band. And this is precisely where the tripole has a problem if the frequency ratio is around 2:1. In fact, by inspection of Fig. 2.10 in reference 114 we observe a typical strong second resonance for oblique angle of incidence in the *E* plane. In other words, it may be desirable to move the fundamental and the second harmonic somewhat apart from each other.

One approach is to use so-called suppressors as shown in Fig. 9.14 in the case of a simple straight dipole. We show the current and voltage distribution for the fundamental (top) as well as the second harmonic (bottom). If we place capacitors either in the form of plates or just wires at the ends of the dipoles
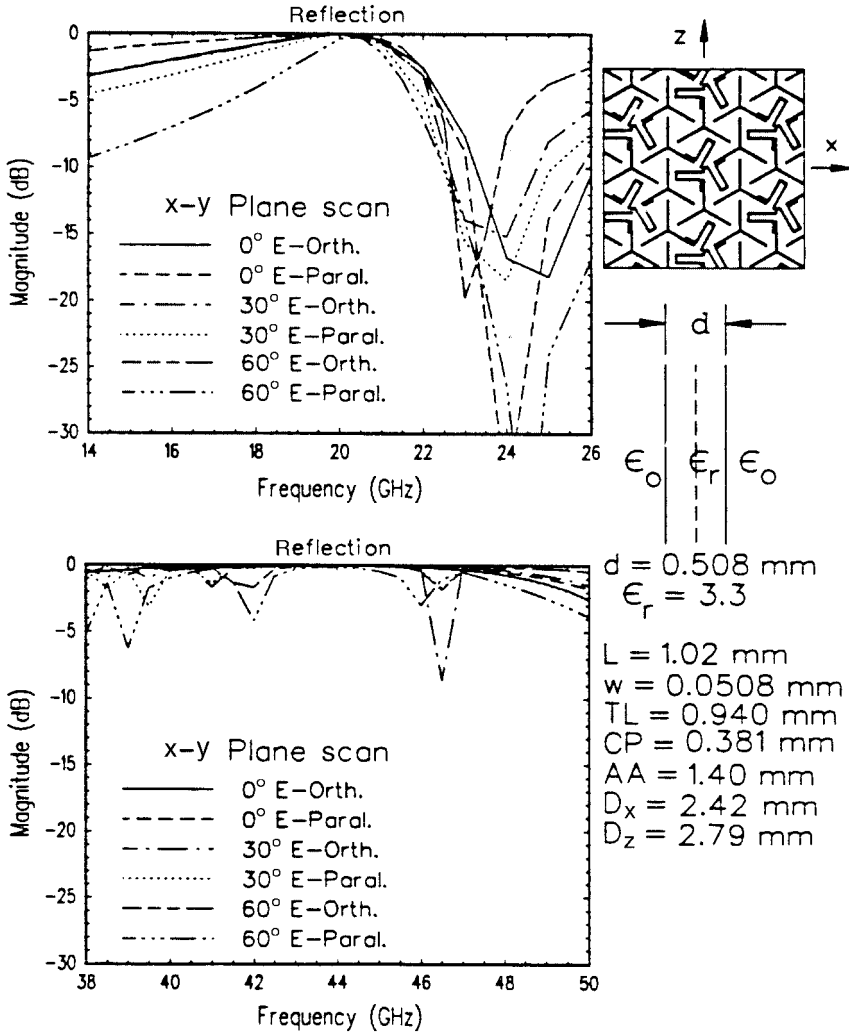
Fig. 9.13 Calculated reflection curves for an array of modified "snowflake" elements in the low (top) as well as the high (bottom) bands.

when the voltage is maximum, it is clear that the fundamental as well as harmonic resonances will be moved strongly downward in frequency.

However, if we place the capacitors at points on the dipole where the voltage for the second harmonic is zero, no change of resonant frequency will take place for this mode. But we will see a considerable shift downward for the fundamental.

The net effect is that we have increased the ratio between the harmonic and the fundamental to be significantly larger than 2:1 as desired.

An example of a dual-band structure made of large tripoles interlaced with small ones is shown in Figs. 9.15 and 9.16. The large tripoles are provided with
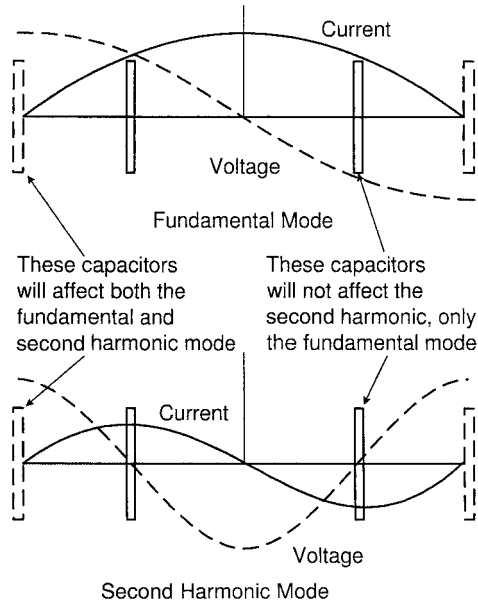
Fig. 9.14 Current and voltage distributions along a straight dipole for the fundamental and second harmonic modes. Capacitive plates placed at the ends will detune both modes downward in frequency. However, if placed where the voltage of the second harmonic is zero, no change in resonant frequency will take place. However, the fundamental mode will still be tuned somewhat downward.

capacitive suppressors as described above, and the periodicity of both kinds of elements has been maintained rigorously. Scans in both the *YZ* and the *XY* planes are shown. The results speak for themselves (well done Roger!).

9.4.5 Alternative Design

We saw in the previous section how the fundamental and the second harmonic of a tripole element could be moved apart from each other by use of suppressors. We could in that way avoid excitation of the second harmonic of the low-frequency elements. However, by inspection of the resonance curve for the loaded three-legged element shown in Fig. 2.23 in reference 114 we observe a distinct null at a frequency twice the fundamental. Thus, the tripole loop element is already suitable for a dual-band surface with the ratio 2:1 between the two bands.

Although this idea has not been tried (it emerged after Roger H. graduated), the author would be very much interested in hearing why it would not work.

9.5 ANOMALIES DUE TO INSUFFICIENT NUMBER OF MODES (THE UNNAMED ANOMALY)

In this section we shall present an example of an anomaly caused by insufficient number of modes on the elements.
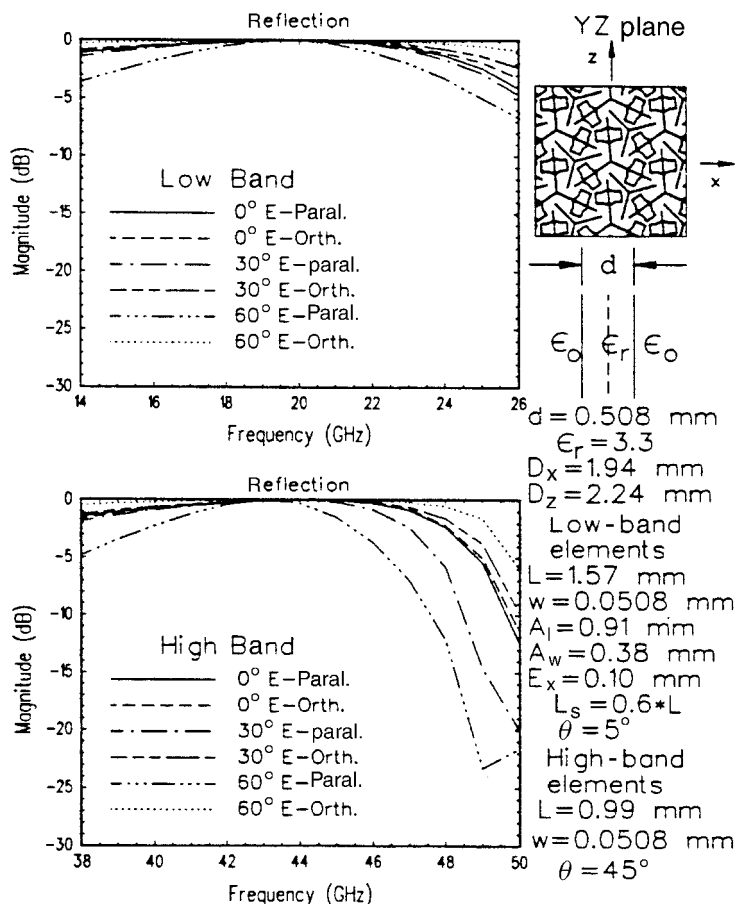
Fig. 9.15   *Calculated low and high band YZ plane response for a mid-arm loaded multiple tripole element array.*

Consider the array of four-legged loaded elements shown in Fig. 9.17. As indicated in the insert to the right, we have used four modes to obtain the resonant curve shown for oblique angle of incidence ($\eta = 45°$). However, if the incident E field is vertically polarized, it appears that the current across the top and bottom of the elements should be zero. Thus, one could argue that only the two modes shown in the insert to the left are sufficient. However, although the resonance curve in that case basically "agrees" with the four-mode case, we do observe a particular anomaly around $f = 7.2$ GHz. What has happened?

Well, in the two-mode case the two modes simply act as the reference elements in two interlaced arrays with interarray spacing $d_x \neq D_x/2$. Thus, we will obtain an effect analogous to the phenomena shown in Fig. 9.3. Not before we add the connector modes at the top and bottom will the two arrays be joined into *one* array with the proper phases on the left and right halves of the elements.

Reflection

Magnitude (dB)

Low Band

—————— 0° E–Paral.
– – – – – 0° E–Orth.
– · — · — 30° E–Paral.
– – – – – 30° E–Orth.
– · · · — · · · 60° E–Paral.
· · · · · · · · 60° E–Orth.

Frequency (GHz)

XY plane

z

x

d

ϵ_o ϵ_r ϵ_o

$d = 0.508$ mm
$\epsilon_r = 3.3$
$D_x = 1.94$ mm
$D_z = 2.24$ mm
Low-band
elements
$L = 1.57$ mm
$w = 0.0508$ mm
$A_l = 0.91$ mm
$A_w = 0.38$ mm
$E_x = 0.10$ mm
$L_s = 0.6*L$
$\theta = 5°$
High-band
elements
$L = 0.99$
$w = 0.0508$ mm
$\theta = 45°$

Reflection

Magnitude (dB)

High Band

—————— 0° E–Paral.
– – – – – 0° E–Orth.
– · — · — 30° E–Paral.
– – – – – 30° E–Orth.
– · · · — · · · 60° E–Paral.
· · · · · · · · 60° E–Orth.

Frequency (GHz)
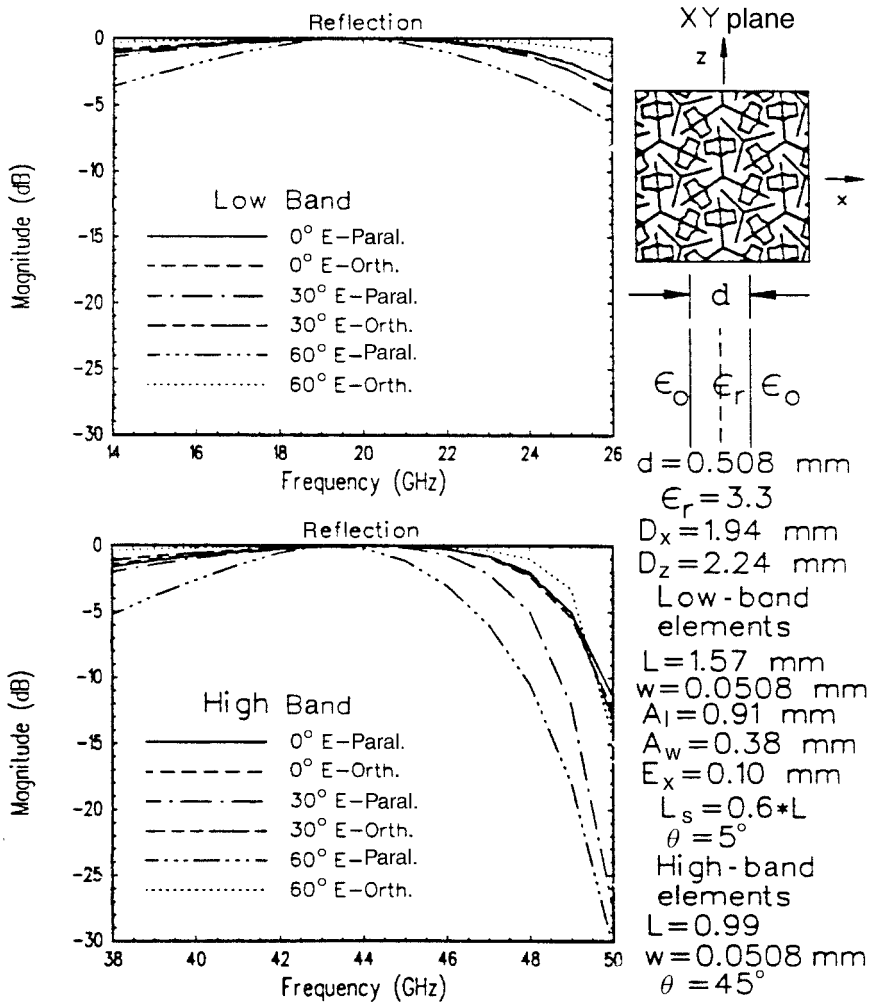
Fig. 9.16 Calculated low- and high-band XY plane response for a mid-arm loaded multiple tripole element array.

Thus, even if computer time can be saved, don't be too stingy with the number of modes. On the other hand, putting on too many can lead to problems too, as discussed in reference 115.

Note that no anomaly of this type is observed for normal angle of incidence.

This anomaly was first observed more than a dozen years ago. A highly respected researcher and friend at first refused to believe the explanation given above. To tease him, the rest of us named this anomaly after him. He eventually asked that his very good name be "crossed out." Actually, he should not be embarrassed: This is the one and only time I can ever remember where he "missed it."
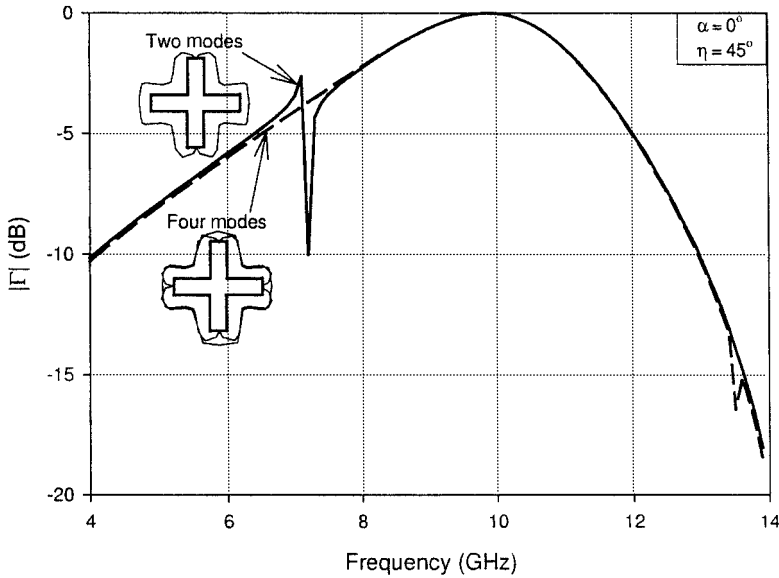
Fig. 9.17 The resonant curves for a single array of four-legged loaded elements at 45° angle of incidence in the H plane. One curve shows the correct response when using four modes (minimum). The other curve (full line) shows the response when using only two modes corresponding to two interlaced arrays with d_x different from $D_x/2$ as shown in Figure 9.3.

9.6   TAPERED PERIODIC SURFACES

9.6.1   Introduction

A tapered periodic surface (TPS) is an array of wire or slot type elements with element sizes and interelement spacings that vary as a function of position over the array[1]. Many different applications of TPS come to mind. Most of these applications involve a smooth electrical transition to terminate the finite edge of an FSS or phased array. A TPS could also be used to transition from one FSS design to another in a radome with multiband window areas. Another application is as a building block for broad band and low side lobe antenna designs. Tapered Periodic Surfaces exhibit two fundamental properties:

1. **Diffraction Control:** A TPS provides a tapered impedance surface similar to a tapered resistive surface or tapered R-card. The difference is that a TPS is a tapered reactive surface and could be thought of as a tapered "jX" card.

2. **Frequency Compensation:** A TPS effectively behaves as an electrical conductor that changes size as a function of frequency. This property

---

[1] English, Errol K, and Leeper, William J., "Periodic Surfaces for Selectively Modifying the Properties of Reflected Electromagnetic Waves," United States Patent Number 5,606,335 Patent Date February 25, 1997.

enables the design of radiating elements and/or apertures that become effectively smaller with increasing frequency. Thus a TPS maintains a constant electrical size, resulting in electrical performance that is very constant over a large bandwidth.

9.6.2 Physical Description

The majority of this discussion will be limited to tapered periodic surfaces used to smoothly terminate a finite edge of a periodic surface. Typically, the element sizes become progressively (monotonically) smaller along the length of the taper. The periodic surface elements may be of any type: linear, four-legged-unloaded, four-legged-loaded, three-legged, etc. The elements may be spaced in a relatively sparse grid or an extremely dense grid depending on the application. A TPS is normally produced by printed circuit methods where the elements reside on a dielectric substrate.

Slot and Wire Type TPS Figure 9.18 shows a TPS of simple straight wire segments. This example is referred to as a parallel type because the wire segments are parallel to the direction of the taper. The edge with the long elements is the baseline or low impedance edge while the edge with the short elements is the terminal or high impedance edge. In an analogous manner, an orthogonal type TPS has wire segments oriented orthogonal to the direction of taper. Note that the TPS of Fig. 9.18 is designed only for linear polarization. If a wire TPS for arbitrary polarization is desired, an element type such as three legged or four legged might be used rather than the simple linear elements. However, the greatest bandwidth is obtained by very tight packing of the elements in the grid, and straight wire elements can be packed extremely tight. Therefore, the largest bandwidth (for arbitrary polarization) is achieved by superimposing a parallel type and an orthogonal type TPS, one behind the other.

In the case of a slot TPS, the edge with the short elements is the baseline or low impedance edge while the edge with the long elements is the terminal or
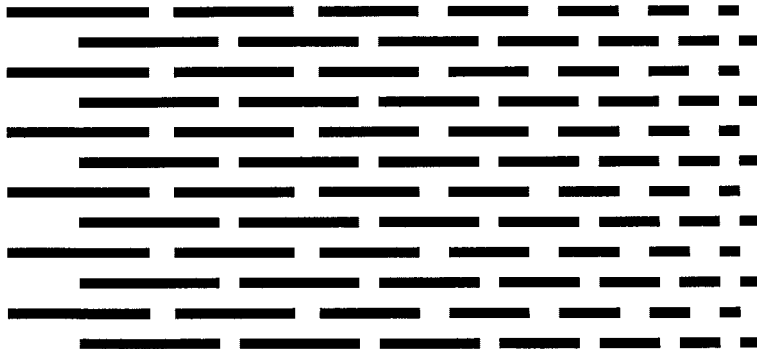
Fig. 9.18 Parallel type Tapered Periodic Surface of linear wire segments.

high impedance edge. As in the case of the wire TPS, the parallel and orthogonal descriptions refer to slot element orientation relative to the direction of taper. An orthogonal slot TPS and a parallel slot TPS may not be superimposed one behind the other. The use of one precludes the other. If a taper for arbitrary polarization is desired, slot elements such as three legged or four legged must be used in a single surface.

General TPS dimensions depend greatly on the specific application and the frequency range of operation. Typically, for applications in the microwave frequency band (2 to 18 GHz), the length of the taper may be anywhere from 2 to 24 inches. Also, the element width and the gap width are typically in the vicinity of 0.002 inches to 0.020 inches for broad band applications.

The length of the longest segments of the TPS is typically chosen to be approximately $\lambda/2$ or less at the center of the operating frequency band. The length of the shortest segments at the terminal edge is chosen to be a vanishingly small fraction of a wavelength at the highest operating frequency.

The thickness of the substrate supporting the TPS is application dependent but is typically between 0.002 inches to 0.020 inches. Good substrate materials have a fairly low dielectric constant and loss tangent. Typical substrate materials include glass/epoxy (such as FR4), glass/PTFE, quartz/polyimide, quartz/cyanate-ester, as well as kapton or mylar film.

9.6.3 Purpose and Operational Description

Diffraction Control One purpose of a tapered periodic surface is to provide a gradual transition from a good conductor (i.e. metal) to free space. Abrupt termination of a conducting edge gives rise to a very strong diffracted field when illuminated by an externally impressed EM wave. A tapered periodic surface provides a gradually tapered surface impedance, eliminating the abrupt termination and thereby significantly reducing diffracted fields. Figure 9.19 illustrates the use of a TPS at a metal edge.

Functionally, a tapered periodic surface performs in a fashion similar to a tapered resistive film (sometimes referred to as an R-card or edge card). Ideally,
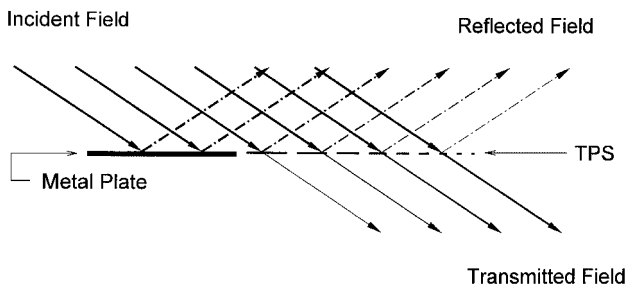
Fig. 9.19 An edge-view of a Tapered Periodic Surface used to gradually transition from metal to free space.

a tapered resistive film transitions impedance from $Z = 0 \, \Omega/sq$ to $Z = \infty \, \Omega/sq$ assuming real (resistive) values. TPS tapers provide similar impedance transitions assuming imaginary (reactive) values. A wire TPS transitions from $Z = 0 \, \Omega/sq$ to $Z = -j\infty \, \Omega/sq$ along a path of increasing capacitive reactance. A slot TPS transitions from $Z = 0 \, \Omega/sq$ to $Z = +j\infty \, \Omega//sq$ along a path of increasing inductive reactance.

A periodic surface of closely spaced wire segments will be highly reflective (almost identical to solid metal) over a wide frequency range centered at the frequency where the segments are approximately a half wavelength long. When the periodic surface is highly reflective, its surface impedance is very close to $0\Omega/sq$ (the same as a perfect conductor). This is the situation at the baseline edge of a wire TPS. As the wire segments are gradually shortened (along the length of the taper), the wire segments are increasingly below resonance and the surface impedance (purely capacitive reactance) increases, and the electromagnetic wave reflection gradually decreases as the transmission gradually increases. This gradual transition from total reflection to total transmission eliminates the hard reflection and transmission shadow boundaries and therefore results in significantly reduced levels of diffracted fields.

The following example illustrates an example of diffraction control using a wire TPS. A parallel type TPS of straight wire elements was designed for broad band use (2 to 18 GHz). At the baseline edge, the elements are 0.295 inches long, 0.002 inches wide, and spaced in a skewed grid with a side-by-side periodicity of 0.004 inches. The lengths of the elements are linearly tapered to zero over a 12-inch distance. Figure 9.20 shows this TPS attached to the edge of a solid sheet of copper. The solid copper and the TPS are supported by a thin glass/epoxy substrate and backed by foam (0.25 inches thick). This is incorporated into a test article for radar cross section (RCS) testing.

The RCS testing was conducted with the illumination at normal incidence to the metal edge. Also, the polarization is parallel to the plane of incidence (orthogonal to the metal edge, i.e. the hard diffraction case). Figure 9.21 shows the monostatic RCS at 30° above grazing for the TPS attached to the trailing metal edge. The RCS of an abruptly terminated trailing metal edge is also shown in Figure 9.21 for comparison. Note that the TPS reduces the diffracted field in the monostatic direction by approximately 25 dB over the entire 2 to 18 GHz band.

Frequency Compensation   Frequency compensation is a very important property of the TPS that is not shared by the tapered R-Card. Since the TPS is a periodic surface, it is frequency sensitive, a property that may be exploited on a variety of broad band antenna applications.

If we think of a TPS as being highly opaque (conductive) at one end and highly transparent (nonconductive) at the other end, then there is some point in between where the transmission is at its halfway point or 3 dB point. The position along the taper of this 3 dB point varies with frequency. Therefore, we may conclude that the TPS effectively behaves like a conductor from its conductive end to the 3 dB point of the taper. The equivalent conductive length of the TPS varies monotonically with frequency. This is true for both wire and slot TPS.
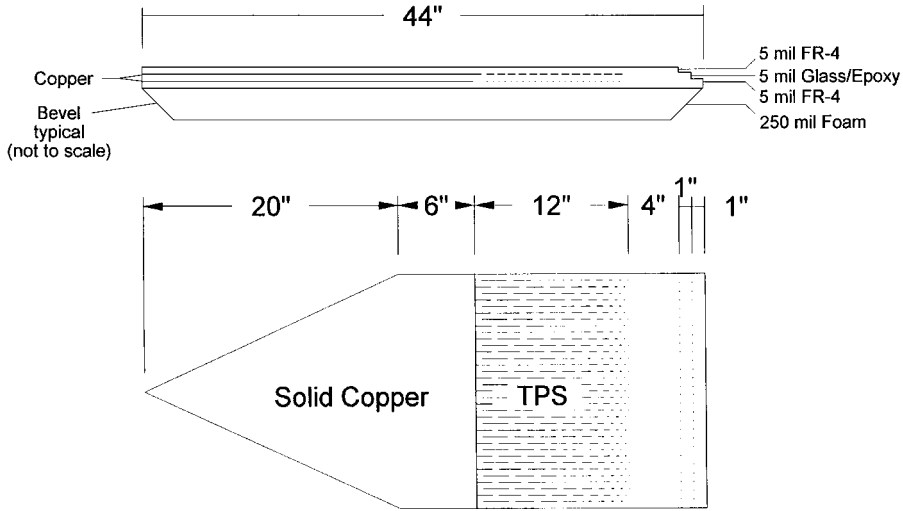
Fig. 9.20   RCS test article used to evaluate the diffraction reduction effectiveness of a TPS.
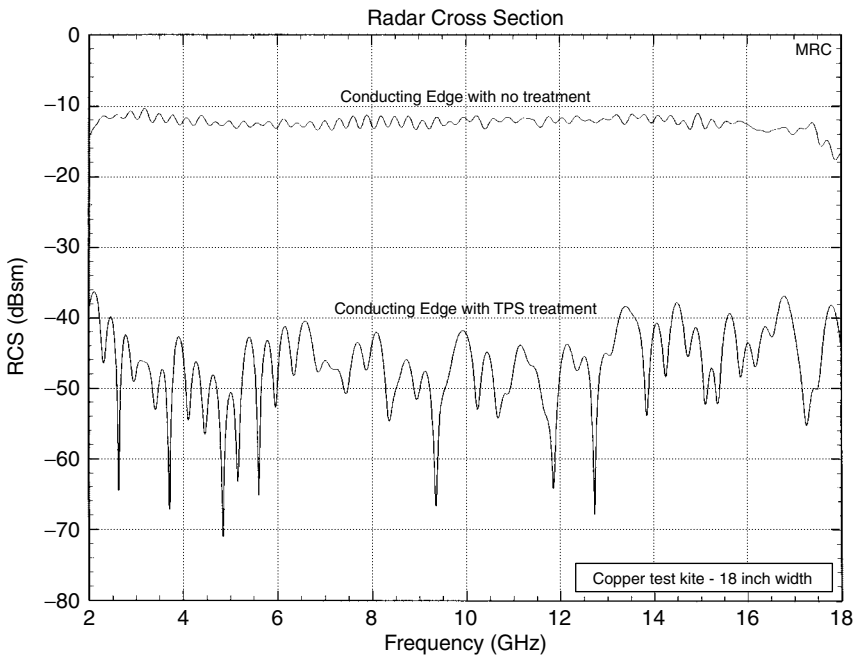
Fig. 9.21   RCS spectrum of an 18-inch wide metal edge terminated with a 12 inch long broad band Tapered Periodic Surface, 30° above grazing, E-parallel. (bare metal edge case also shown).
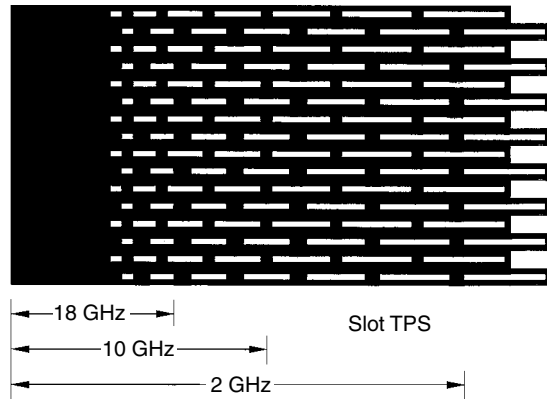
Fig. 9.22 *The equivalent conductive length of a slot Tapered Periodic Surface decreases with increasing frequency.*

The equivalent conductive length of a wire TPS increases with increasing frequency while that of a slot TPS decreases with increasing frequency. Figure 9.22 depicts this situation for a slot TPS. This "equivalent conductor" with its frequency dependent length can be used as a basic building block for many broad band antenna applications.

9.6.4 Application of TPS to a Pyramidal Horn Antenna

TPS may be used as extensions to the walls of a horn antenna. A conventional pyramidal horn antenna has relatively high side lobes and back lobes in the E-plane due to the strong edge diffraction at the aperture. TPS applied to the edges of the solid metal walls greatly reduces this diffracted energy. A slot TPS could also be designed such that the effective length (as well as the effective aperture size) of the horn decreases with increasing frequency thereby maintaining a frequency independent gain and beam width as well as low side lobes.

Figure 9.23 shows measured E-Plane patterns of two horn antennas. Both horns have the same flare angle and the same "effective length" producing approximately the same half power beam width. The pattern with higher side lobes is of a typical horn with metal walls. The other pattern in Fig. 9.23 is of a horn with walls terminated by TPS. Notice the vastly improved side and back lobe performance of the TPS horn.

9.6.5 Conclusions

It has been demonstrated that by gradually changing the size and/or spacing of the elements of an otherwise periodic surface, a smooth and continuous electromagnetic transition may be obtained. Not only does this transition exhibit very low EM field diffraction, but it also has the inherent ability to be frequency
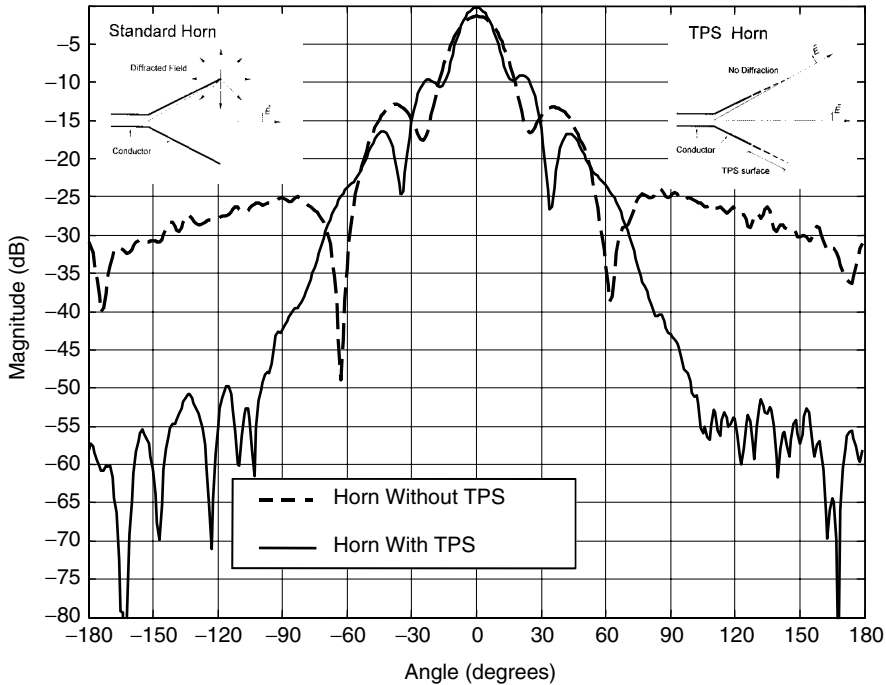
Fig. 9.23   E-plane pattern (at 6 GHz) of a horn antenna with and without Tapered Periodic Surface treatment of the E-plane walls.

independent. Other applications of TPS include reflector antenna edge treatment, aperture antennas with constant electrical dimensions (i.e. frequency independent performance), and low RCS test bodies with low diffracting edges.

9.7   CONCLUSIONS

Periodic structures are usually composed of identical elements positioned at equal spacings. In this chapter we have investigated surfaces made of two or more similar subarrays interlaced into each other in an arbitrary way. The subarrays were loaded with different load impedances, resulting in different resonance frequencies for the various subarrays.

For arrays of straight dipoles, this perturbation typically resulted in a slight upward shift of the original (unperturbed) resonant frequency. Furthermore, we obtained a lower, usually narrower, resonance frequency and a null located between the two resonant frequencies. No loss was observed at either resonant frequencies as long as no grating lobes were present in any of the subarrays. If that was not the case, we observed loss at both resonant frequencies and the null was more or less washed out.

These observations were typical for relatively small ratios between the two resonant frequencies (10–20%). For larger ratios like an octave or more, we demonstrated that arrays of large and small elements could be interlaced into each other and we could indeed obtain a dual-band structure, provided that;

1. Any harmonic resonance of the large elements should be moved away from the resonance region of the small elements.
2. Periodicity should be observed in the strictest of sense for both the small and the large elements.

In other words: Successful designs of dual- or multiband periodic surfaces is highly unlikely to occur by just leaving a computer to its own devices. A trained human brain is essential (as it is most of the time for even single-band structures).

We also demonstrated that insufficient modes on the elements could be troublesome. For example, if a four-legged loaded element did not incorporate the connector modes at the top and bottom (vertical polarization), we would observe anomalies for oblique angle of incidence. The two remaining modes would simply act as the reference elements for two subarrays with array spacings $d_x \neq D_x/2$, where D_x denotes the element spacings in the subarrays.

However, as illustrated in Section 9.6, kindly provided by Errol K. English, Mission Research Corporation, Dayton, Ohio, finite arrays where element length and spacing vary can be highly beneficial with many interesting applications.

10

Summary and Final Remarks

10.1 SUMMARY

As of this writing, the author is not quite sure what the title of this book will be. Many well-meaning friends have suggested that it be short and snappy (and rightly so). The problem is of course that so many seemingly diverse subjects have been investigated. It is hoped that the reader will realize that there is a common thread holding them all together. To facilitate this process, the following comprehensive summary is presented next.

10.1.1 Broadband Arrays

Of all the subjects considered in this book, none has turned out to be more controversial than the broadband array treated in Chapter 6. Actually, it started quite innocently. Two of my old friends from the Harris Corporation, Bill Crosswell and Bob Taylor, stopped by my office in the OSU ElectroScience Laboratory and said, "Ben, we need a broadband array. Our ideas so far have not panned out. Do you have any suggestions?"

In fact, the fundamental principles for broadband arrays had been known not only to the author but also to several of his students for a good many years. I think it was Kornbau who in his dissertation first put in writing that a closely spaced array of dipoles without a ground plane can be designed to be very broadband (this observation was a by-product of our investigation of the Gangbuster element discussed in reference 91).

The effect of a ground plane was also well understood, but no particular interest was ever visible in the technical community. In fact, when the author mentioned the concept to a group of engineers, he was politely laughed out of the room with comments like "We do not need an overpopulated array!" Which of course would drive the price tag up. And nothing can make tears run down faster over the fat cheeks of managers than a frontal attack on their billfold.

For years there was (and in some camps still is) the unrealistic hope that grating lobes could be dealt with in some magic fashion for example by "rattling around" the interelement spacings (that may help in some scan planes but will sure make it worse in others).

Today it is probably prudent to state that there is no real alternative to the fact that the element spacings in a quality broadband array should not exceed $\sim 0.6\lambda$ at the highest frequency (for moderate scan). And that again demands hardware such as amplifiers and phase shifters that are small in size. The author is aware and extremely pleased to know that strong efforts in that respect is underway at several places in the industry. If at the same time we could design the amplifiers with balanced input terminals to be connected directly to the balanced dipoles, a classical problem would be overcome, namely designing the baluns. Although these can be made very broadband indeed (see, for example, reference 116), it is expected that a balanced amplifier can do an even better job.

It cannot be emphasized enough that the success of designing a broadband array depends largely on how well the reactive groundplane impedance is being compensated by the reactive part of the antenna impedance. At this point in time it appears that not much can be done to increase the groundplane reactance for example by using materials with higher intrinsic impedance than that of free space. If that was possible, it could lead to larger bandwidth.

Thus, the groundplane impedance will typically remain infinite at the center frequency and inductive and capacitive at the lower and higher frequencies, respectively. Consequently, only certain types of elements are suitable for broadband arrays. The flat spiral, for example, is not a good choice because its impedance changes repeatedly as a function of frequency between the inductive and capacitive region (this is typically for all long wire antennas like the two arms in a flat spiral).

Note in particular that we are not interested in an array that without a groundplane has a constant impedance over a broad band. On the contrary, we need an array impedance with a reactive part that can at least partly cancel the groundplane reactances at the upper and lower frequencies, respectively.

An array of dipoles with a groundplane can typically be designed to have a bandwidth of around 4:1 (with VSWR < 2). Further increase in bandwidth can be obtained by placing one or more dielectric slabs directly in front of the dipole elements as shown schematically in the equivalent circuit shown in Fig. 10.1.

This increase of bandwidth is explained (not calculated) in the following way:

1. The impedance $2R_{A0}$ in free space to the left is transformed into a lower value Z_{1-} via the dielectric slab with intrinsic impedance $2R_{A1} < 2R_{A0}$.
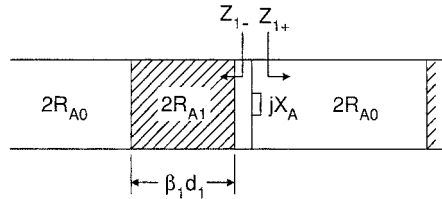
Fig. 10.1 The equivalent circuit for an array of dipoles backed by a groundplane (right) and with a dielectric slab of thickness d_1 in front. For further details see Chapter 6.

The groundplane reactance Z_{1+} is obviously not affected by the dielectric. Thus, we have in effect a lower array impedance in parallel with the same groundplane reactance which is equivalent to a larger bandwidth.

2. Furthermore, when transforming $2R_{A0}$ through the dielectric slab, we will observe a capacitive component of Z_{1-} at the lower frequencies (try it out in the complex plane and you will see it). This component will be added to jX_A in parallel, and they will both "fight" the groundplane reactance that normally has the "upper hand."

In addition, it is well known that a dielectric slab reduces the variation of the scan impedance with scan angle (see reference 117).

This type of array has a bandwidth of about 9:1. However, optimization could increase it further. It is covered by US patent no. 6512487

10.1.2 On Antenna RCS and Edge Effect

For a number of years the author taught a graduate antenna course at Ohio State University. In the very first lecture he would usually remind the students that there are three important issues in an antenna's life:

1. The impedance
2. The radiation pattern (from where we can obtain the directivity by integration).
3. And finally the antenna radar cross section (RCS).

The first two items got plenty of attention. However, not much time could be devoted to the antenna RCS, which was a shame since the RCS of some antennas can potentially be larger than that of an airplane.

In Chapter 2 we presented the theoretical background for antenna scattering in general. However, typically our examples were primarily aimed toward antennas with low RCS. (The demand for antennas with high RCS appears to be rather limited! There are plenty of them out there anyway.) Arrays were of particular interest by the fact that their residual scattering is basically equal to zero. More precisely, this means that if an array is conjugate-matched, not only will we

receive maximum energy (true for all antennas) but the RCS of the array will at the same time also be zero (unique for arrays).

Furthermore, in Chapter 5 we expanded our investigation to also include edge effects and showed that zero RCS is still possible. It was done rigorously by calculating the bistatic scattered field from each triad composed of a column of active elements and two columns of passive elements acting as reflectors. When conjugate-matched, the backscatter from such a triad was equal to zero.

In addition, we also found the backscattered field at other frequencies where we no longer had conjugate match. We found that the reflected field was proportional to the magnitude of the reflection coefficient for the signal incident upon the array. Furthermore, the magnitude of the reflection coefficient observed at the terminals looking out was practically identical to the one observed from the outside. This is further proof that the residual scattering in the backscatter direction for even a finite array is basically zero (normal angle of incidence).

Finite arrays will often exhibit strong variation of the scan impedance from element to element. This phenomenon is often referred to as *jitter*. This makes it difficult to obtain precise matching, which is important to obtain a low RCS (see Chapters 2 and 5). In the latter chapter we show that by connecting each element to an amplifier (conjugate-matched), we obtain a strong attenuation of any potential type II surface wave over a significant frequency band (see also Section 5.7). An additional edge treatment is sometimes recommended for perfection. Knowing that it is possible to design arrays free of jitter is extremely important.

So far we have considered planar arrays with a pencil beam. However, there is also interest in antennas with omnidirectional pattern and low RCS. Intuitively, many designers feel that such an antenna is inconsistent with the fundamentals of physics. Usually this conclusion is based on the facts associated with a simple dipole or monopole. However, we show in Chapter 7 that if we instead consider a circular array of dipoles arranged around a conducting cylinder, we can indeed obtain an omnidirectional pattern and very low RCS for signals incident anywhere in the equatorial plane. A substantial reduction was obtained over a frequency range of one octave.

It should be noted that these results were obtained with merely lumped load resistors connected directly to the dipole terminals without any matching network to improve the bandwidth as discussed in Appendix B. Application of that technique is expected to increase the bandwidth further. Further improvement is expected if dielectric sheets are placed around the dipoles analogous to the dielectric slabs in front of a planar array.

Parabolic reflector antennas cannot compete with arrays in respect to low RCS. However, by using a newly designed feed, it can be reduced substantially. Since this type of antenna still is popular in some camps, it is discussed in Chapter 8.

10.1.3 Surface Waves: Types I and II

Nothing strikes more fear in some people's minds than dielectric slabs placed next to a periodic surface. Are we not inviting one of these terrible surface waves
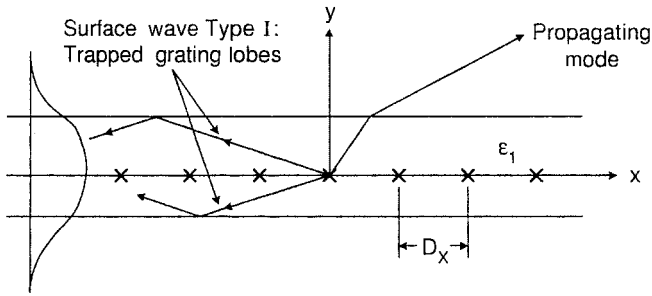
Fig. 10.2   *An array of dipoles located in a dielectric slab can support a surface wave of Type I if the frequency is sufficiently high to form grating lobes inside the dielectric slab. It can exist on finite as well as infinite periodic structures.*

right into our lives? We are indeed. However, once we learn to properly design periodic structures of the active as well as passive types, we can avoid many of these potential disasters.

First of all, there are basically at least two kinds of surface waves associated with periodic structures. The first kind can exist only on periodic surfaces in conjunction with a stratified medium regardless of whether the structure is infinite or finite. Thus, this type will readily be encountered when using computer codes based on infinite array theory such as the PMM program. It has therefore been known for some time and is discussed in detail in reference 118. We shall refer to this kind as Type I. As illustrated in Fig. 10.2, this surface wave consists merely of a pair of grating lobes trapped inside the dielectric slab. Only the propagating mode is incident upon the dielectric interface from within at an angle lower than the critical and will therefore make it out into free space. The trapped grating lobe will occur only at the higher frequencies where D_x/λ_1 is sufficiently large to launch grating lobes. Associated with this type of surface wave will be a field that is sinusoidal inside the slab and evanescent outside as shown in Fig. 10.2. If the structure including the dielectric slab is finite, this field will radiate in the X direction.

The second kind of surface wave denoted Type II can exist only on finite periodic structures with or without dielectric slabs. It will therefore not show up in computer codes based on infinite array theory such as the PMM program. But it does show up in the SPLAT code that incidentally can model only dielectric shells around the elements and not dielectric slabs. This kind has been investigated in this book but is less documented than Type I. In contrast to Type I, Type II can exist only for $D_x/\lambda < 0.5$ and if we also typically are 20–30% below resonance (for simple straight elements).

The important question now is, Which of the two types of surface waves is most likely to cause trouble? Well, whether we are talking about broadband arrays or FSS's the interelement spacings D_x should not exceed 0.5λ in order to obtain a good design. In other words, onset of the Type I surface wave will in general not occur before we are well above the normal operating frequency

band. However, the Type II surface wave will as stated earlier occur if $D_x <$ 0.5λ and if the frequency typically is 20–30% below resonance. In other words, there is a strong likelihood, if not certainty, that the Type II surface wave will be excited in a finite array operating over a broad band. If this is the case, it must be dealt with, and the treatment depends on whether the structure is active or passive.

If we are working with an active array, the good news is that in the future each element will most likely be connected to its own amplifier or generator having impedances with substantial resistive components. That is one of the most effective ways to eradicate potential Type II surface waves. An additional light edge treatment could be useful.

However, in cases where we are working with FSS's, the element loads, if there are any, will in general be entirely reactive; that is, no attenuation of a potential surface wave will take place. Nor is it a good idea to place even small resistors in each element since that would lead to reflection and transmission loss of the principal mode. In that case only a small number of edge columns should be resistively loaded. This is not as effective a way to control surface waves as resistors placed in each element, but then again FSS's are more forgiving in that respect than are the active arrays.

We finally note that curving an FSS will greatly reduce the presence of surface waves by shredding energy. Since radomes and subreflectors for example typically are nonplanar, this is probably one of the reasons that it has not been noted very much in practical applications.

10.1.4   On Broadband Matching (Appendix B)

Most engineers are quite familiar with how to design a matching network that will bring an arbitrary impedance into the center of a Smith chart at a single frequency. However, if the impedance varies with frequency (and in general it will), and they still have to place all the impedance points close to the center of the Smith chart, it will soon become clear that the conventional matching tools such as the single, the double, and even the triple stub tuner in general do a very poor job: You will lose bandwidth.

Since precision matching is an important tool for controlling the RCS of antennas in general and arrays in particular, it becomes important to be able to match the antenna over a wide band, see Chapters 2 and 5 as well as Section 10.1.2 for details. In fact, many of the author's friends have strongly suggested that this subject should be treated in a regular chapter rather than an appendix (Appendix B). My decision was guided by the fact that the subject is by no means new.[1]

Thus, Appendix B should be considered more an overview of principles rather than going into every detail. You will find this in reference 119 and you might also find Appendix A useful to better understand the "tricks."

---

[1] It appears that the subject grew out of an effort to produce broadband antennas for countermeasure purposes during World War II. The best, if not the first, treatment appears to be given in *Very High-Frequency Techniques*. If you find a copy, grab it! [119].

10.1.5   A Broadband Meanderline Polarizer (Appendix C)

Every so often it is desirable to transform linear polarization into circular or vice versa. A meanderline polarizer is an excellent choice for such a task; and since it is a periodic structure, we have investigated it in Appendix C.

When a well-designed polarizer is exposed to an incident linear polarized field, we should first of all expect to obtain a circular polarized field of great purity. Furthermore, we should maintain a high quality over a broad band. But the real challenge is to design a polarizer where these qualities exist over a wide range of angles of incidence.

The last feature can be controlled by use of dielectric slabs on each side of the polarizer, similar to what was done earlier for scan compensation [117]. The large bandwidth (approximately an octave) was the result of careful calculation of the two orthogonal polarizations in amplitude as well as phase. It was finally finished off by a parametric study leading to a design with a bandwidth approaching an octave and angles of incidence ranging from normal up to $60°$.

10.1.6   Aperiodic and Multiresonant Structures (Chapter 9)

The effect of variation of the resonant frequency of the individual elements as well as the interelement spacings was also investigated. In general, this resulted in resonance curves with extra nulls. Thus, unless such a feature is desirable for whatever reason, such a treatment is in general not recommended. However, if the structure is finite × finite instead of infinite × infinite, the nulls would disappear, leading to interesting applications.

Multiband FSS were also investigated. The complexity of such surfaces depends to a very high degree upon the frequency ratio between the desired bands.

10.1.7   The Theory

Periodic structures of finite extent are often analyzed by dividing them into infinitely long column arrays (stick arrays) with either longitudinal or transverse elements. Thus, in Chapter 3 we examined both of these types of arrays in some detail.

In the *longitudinal* case we determined the fields, being parallel as well as orthogonal to the elements. Furthermore, we obtained the mutual impedance in the spectral domain between a stick array with longitudinal elements and an outer longitudinal element as an infinite series containing products of Hankel functions and two pattern functions. Similarly, the mutual impedance between a longitudinal array and an outer orthogonal element could be obtained in the spectral domain by numerical integration of the orthogonal field along the outer orthogonal element. The orthogonal field could be expressed in the spectral domain by an infinite series containing products of Hankel functions and a single pattern function.

The beauty of the Hankel functions is that their argument $\beta r_\rho \rho$ becomes negative imaginary when $r_\rho = \sqrt{(s_z + n\frac{\lambda}{D_z})^2 - 1}$ does. In that case the Hankel

functions will fall off faster than an exponential as n increases (see Fig. 3.7). Thus, fast convergence of the infinite series is assured. This feature is quite analogous to the double infinite case where r_y goes negative imaginary, forcing the exponential term $e^{-j\beta r_y r}$ to fall off extremely fast.

The *transverse* case was somewhat more complicated as we would expect. For the field parallel with the elements, we found that it could be expressed in the spectral domain by an infinite series with terms comprised of three Hankel functions with arguments $\beta r_\rho \rho_\pm$ and $\beta r_\rho \rho_0$. Here $\rho_\pm$ and ρ_0 denotes the distance from the point of observation to the two endpoints and the midpoint of the array reference elements, respectively. The mutual impedance between the array and an outer parallel element is then obtained by numerical integration of the field along the outer parallel element.

Again as in the longitudinal case above, the argument of the Hankel function would go negative imaginary with r_ρ ensuring fast convergence. When the outer element is orthogonal to the transverse array elements, it appears at this point in time that two numerical integrations are necessary. First the orthogonal field from the array is determined by numerical integration along the array element in an infinite series containing Hankel functions. The mutual impedance is then obtained by numerical integration of the field along the outer orthogonal element. Again, the Hankel functions should insure fast convergence.

Due to these problems for the transverse array in the spectral domain, Usoff decided to write his program SPLAT primarily in the spatial domain as part of his doctoral dissertation [24]. It is extremely fast, accurate, and versatile. It simply became and currently is the workhouse for our research of finite periodic structures. It has over the years been extended and improved by several in the author's group; in particular, Dan Janning made it more user-friendly among other things.

Still, if anyone out there ever decides to try his or her hand in the spectral domain, the author would very much like to hear about it.

10.2   ARE WE GOING IN THE RIGHT DIRECTION?

Very few readers of a book pay much attention to the Preface. However, those who did may recall that I struck a somewhat critical chord concerning numerical approaches applied without appreciation of the physics. Nothing would have pleased me more than to be proven wrong. However, in the face of de facto observations getting within my range as of late, I am saddened by the fact that my pessimism was justified.

One paper in particular was investigating a combination of circuit analog and Jaumann absorbers. It was the result of a computer optimization process apparently without any consideration of physics. In less than 10 minutes I spotted the first fundamental and disastrous design flaw: The interelement spacings were larger than a full wavelength! For the author such an observation is an extremely emotional affair. It simply means that grating lobes are present in some bistatic

directions. And for some angles of incidence at some frequencies, these directions may coincide with the backscatter directions where they may produce a significant return signal. In other words, the absorber can in some cases become just the opposite: an RCS enhancer.

Another design had placed a circuit analog sheet less than 0.01λ in front of the groundplane. Even an inexperienced designer should know that a groundplane that close to a CA sheet basically shorts it out, leaving it virtually ineffective (try it out in a Smith chart and you will soon understand).

Sure, unconventional designs can sometimes lead to new superior designs. Not this time. The bandwidth was typically 25% of what should be expected from a design that complex (read Chapter 9 in reference 120).

In another paper the RCS of an array of conjugate-matched slots were calculated. I deliberately did not say investigated because only a minimum of physical insight was displayed. It should therefore surprise no one that the resulting RCS was 6 dB higher than that of a flat plate with an area equal to the total aperture! It should have been "infinitely" many decibels below (see Chapter 2). A simple sign error? Yes, but designers with physical insight would catch such a mistake almost instantly.

While the list of indiscretions goes on, let us stop here and just ask the simple question, How can researchers of even great repute ever fall into traps like these? And furthermore, How is it possible that papers of such quality can pass through the review process associated with the world's most prestigious journals?

Let us try to answer the second question first.

There are basically two reasons for anyone to undertake a review:

1. You are genuinely interested in reading about the latest in your field of interest. If you feel that you are inadequate, you simply pass the paper on to a more competent colleague. This is the proper procedure for reviewing a paper.
2. You are merely doing it because you are asked and it is expected of you in order to tip the promotion scale to the next level in the academic world. You may even secretly enjoy the power you hold over another person's reputation. Chances are you are really not well-suited to review the paper. You are reviewing it for the wrong reasons.

There is no unique answer to the first question. However, a common thread seems to be that the designer has put an almost blind trust into mindless computations only. There is often a single-minded belief that the computer will eventually find the optimum solution based entirely on its superior speed. No physical insight is necessary, or so it is thought.

However, as already shown above by several examples, this is far from the case. More specifically: If Boeing starts designing airplanes without involving their vast practical experience and know-how, my flying days will come to an end!

We should of course have an open mind for those who want to experiment with new ideas in their own backyard. But please do not publish these designs

unless they are sound. Most people expect papers written in accredited journals to be not only correct but also superior in quality. Again, the review process is often hampered because many reviewers have a minimum of engineering knowledge, only the mathematical insight. Later it then becomes almost impossible for a straight-thinking competent designer to convince the public otherwise.

And please do not try to extract money from those with limited technical knowledge that nevertheless control vast pools of money. Many of them are easily taken in by imaginative notions and fairy tales. Note that the number of publications may not mean much. As we have seen, they may be right, wrong, significant, or so what. Unfortunately it often appears that the further "out" a proposal, the more some potential sponsors might like them.

The conclusion of our discussion above is that a numerical optimization process must be treated very carefully. If the end product has to be manufactured or is important in any other way (not just for writing a paper!), it is strongly recommended to work side by side with a designer well-versed in the physics of the problem, which brings us right to the center of my deepest concern: We are not educating enough young engineers with solid knowledge of fundamentals. It sounds almost unbelievable that some professors advise their students not to take any classes where real engineering is taught (heaven forbid that the students should get smarter than their professors!).

10.3   LET US MAKE UP!

The author has several times expressed concern over using purely numerical approaches without sufficient physical insight.

But it would be unfair and biased to finish this chapter without applauding some of the remarkable results that can be obtained only by a numerical approach (short of measurements, of course). Particularly appreciated by the author is the investigation of the so-called *feed organizer* shown in Fig. 10.3.[2] The purpose of this device is twofold: It provides a precise and robust way of feeding two sets of orthogonal dipoles. And at the same time it appears to prevent excitation of the so-called push–push or common mode. In that case, in addition to the desired feed current to the dipoles (push–pull mode), we observe a mode where a pair of feed lines is excited like monopoles orthogonal to the groundplane and where the dipoles act simply as top-loading. If that is the case, an undesirably high sidelobe level will occur. And the terminal impedance will also be adversely affected. A detailed discussion is given, for example, in the dissertation by S.J. Lin [121].

The phenomenon is often blamed on faulty baluns. This may or may not be the case. In fact, even with perfect baluns the phenomenon can occur. What happened is simply that either the incident field or the field from the array itself will at oblique scanning have a field component along the feed lines that may

---

[2] This ingenious device was invented by Robert Taylor from the Harris Corporation, US Patent no. 6483464.
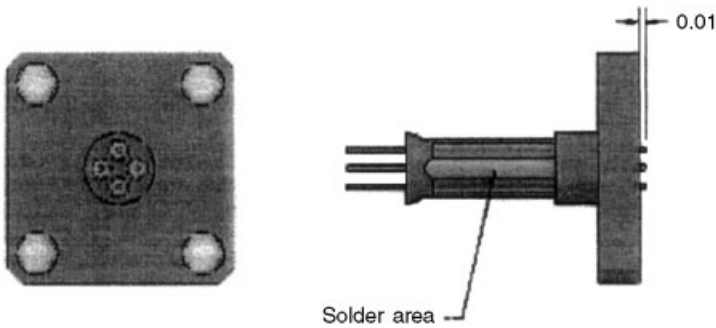
Fig. 10.3   The feed organizer comprised of a step with four holes to accommodate four coaxial cables for feeding the two sets of orthogonal dipoles. Originally intended to merely provide mechanical support, it apparently also suppresses the common or the push–push mode.

readily excite the common mode if conditions are right. What happens when we use a feed organizer is apparently that the casing of the feed organizer almost becomes part of the ground plane and consequently remains "cool."

A detailed examination of these conditions are obtained by one of several finite element method programs like for example the HFSS code. Details of this examination will be given in forthcoming reports by Harris Melbourne, Florida. It shows the finite element method in its finest hour. Bravo!

Finally we show in Fig. 10.4 a practical execution of an array comprised of two orthogonal sets of dipoles fed at the points of their intersections. We also clearly see the finger capacitors. These should be sufficiently large to ensure proper performance at the lower frequencies. However, the length of the fingers
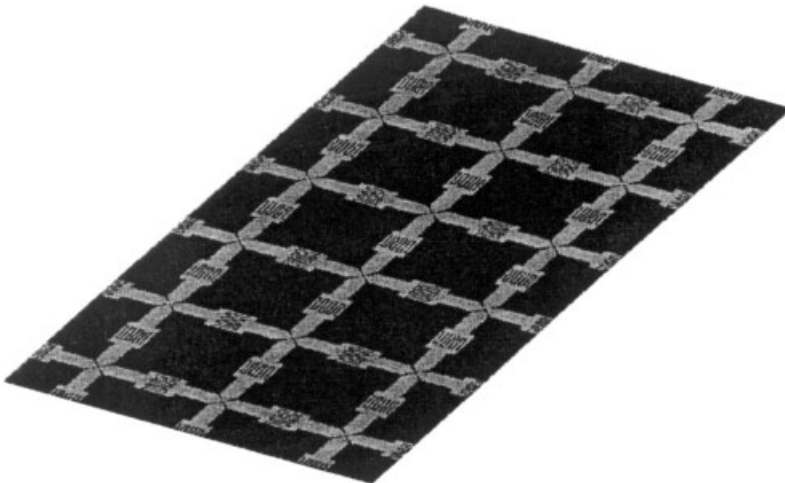
Fig. 10.4   Array of two sets of orthogonal dipoles fed at their crosspoints. Note also the finger capacitors between the feedpoints.

should not be too long since it might lead to undesirable resonances at the higher frequencies. The example shown here is made by the Harris Corporation. Measurements showed excellent agreement with the calculated curves. See also the back cover of this book.

Mission Research Corporation Dayton, Ohio has also built broadband arrays based on the principle presented in Chapter 6.

References

1. B. A. Munk, *Frequency Selective Surfaces, Theory and Design*, New York: John Wiley and Sons, 2000.

2. L. W. Henderson, The Scattering of Planar Arrays of Arbitrary Shaped Slot and/or Wire Elements in a Stratified Dielectric Medium, Ph.D. Dissertation, Ohio State University, Department of Electrical Engineering, Columbus, OH, 1983.

3. L. W. Henderson, Introduction to PMM, Technical Report. 715582-5, Ohio State University Electroscience Laboratory, Department of Electrical Engineering, prepared under contract No. F33615-83-C-1013 for the Air Force Avionics Laboratory, Wright Aeronautical Laboratories, Air Force Systems Command, Wright-Patterson Air Force Base, OH, February 1986.

4. D. R. Denison and R. W. Scharstein, Decomposition of the Scattering by a Finite Linear Array into Periodic and Edge Components, *Microwave Opt. Tech. Lett.*, Vol. **9**, August 1995, pp. 338–343.

5. K. A. Shubert and B. A. Munk, Matching Properties of Arbitrarily Large Dielectric Covered Phased Arrays, *IEEE Trans. Antennas Propag.*, Vol. **AP-31**, January 1983, pp. 54–59.

6. J. P. Skinner and B. A. Munk, Mutual Coupling Between Parallel Columns of Periodic Slots in a Ground Plane Surrounded by Dielectric Slabs, *IEEE Trans. Antennas Propag.*, Vol. **AP-40**, November 1992, pp. 1324–1335.

7. J. P. Skinner, C. C. Whaley, and T. K. Chattoraj, Scattering from Finite by Infinite Arrays of Slots in a Thin Conducting Wedge, *IEEE Trans. Antennas Propag.*, Vol. **AP-43**, April 1995, pp. 369–375.

8. H. Steyskal, Mutual Coupling Analysis of a Finite Planar Waveguide Array, *IEEE Trans. Antennas Propag.*, Vol. **AP-22**, July 1974, pp. 594–597.

9. V. Galindo, Finite Arrays, Edge Effects, and Aperiodic Arrays, in *Theory and Analysis of Phased Array Antennas*, N. Amitay, V. Galindo, and C. P. Wu, eds., Wiley-Interscience, New York, 1972, Chapter 8.

10. S. Fukao et al., A Numerical Consideration on Edge Effect of Planar Dipole Phased Arrays, *Radio Sci.*, Vol. **21**, January–February 1986, pp. 1–12.

11. R. C. Hansen, Formulation of Echelon Dipole Mutual Impedance for Computer, *IEEE Trans. Antennas Propag.*, Vol. **AP-20**, February 1972, pp. 780–781.

12. A. D. Gallegro, Mutual Coupling and Edge Effects in Linear Phased Arrays, M.S. Thesis, Polytechnic Institute of Brooklyn, 1969.

13. A. Ishimaru et al., Finite Periodic Structure Approach to Large Scanning Array Problems, *IEEE Trans. Antennas Propag.*, Vol. **AP-33**, November 1985, pp. 1213–1220.

14. R. C. Hansen, Finite Array Scan Impedance Gibbsian Models, *Radio Sci.*, Vol. **31**, November–December 1996, pp. 1631–1637.

15. R. C. Hansen and D. Gammon, Standing Waves in Scan Impedance of Finite Scanned Arrays, *Microwave Opt. Tech. Lett.*, Vol. **8**, March 1995, pp. 175–179.

16. R. C. Hansen and D. Gammon, Standing Waves in Scan Impedance: *E*-Plane Finite Array, *Microwave Opt. Tech. Lett.*, Vol. **11**, January 1996, pp. 26–32.

17. R. C. Hansen and D. Gammon, A Gibbsian Model for Finite Scanned Arrays, *IEEE Trans. Antennas Propag.*, Vol. **AP-44**, February 1996, pp. 243–248.

18. R. C. Hansen and E. Raudenbush, Modulated Oscillations in Finite Array Scan Impedance, in *Proceedings of the IEEE Symposium on Phased Array Systems*, Boston, 1996.

19. A. A. Oliner and R. G. Malech, Mutual Coupling in Finite Scanning Arrays, in *Microwave Scanning Antennas*, Vol. II, R. C. Hansen, ed., Academic Press, New York, 1966 [Peninsula Publishing, Los Altos, CA, 1985], Chapter 4.

20. A. A. Oliner and R. G. Malech, Mutual Coupling in Infinite Scanning Arrays, in *Microwave Scanning Antennas*, Vol. II, R. C. Hansen, ed., Academic Press, New York, 1966 [Peninsula Publishing, Los Altos, CA, 1985], Chapter 3.

21. D. M. Pozar, Analysis of Finite Phased Arrays of Printed Dipoles, *IEEE Trans. Antennas and Propag.*, Vol. **AP-33**, October 1985, pp. 1045–1053.

22. D. M. Pozar, Finite Phased Arrays of Rectangular Microstrip Patches, *IEEE Trans. Antennas Propag.*, Vol. **AP-34**, May 1986, pp. 658–665.

23. R. C. Hansen, *Phased Array Antennas*, John Wiley and Sons, New York, 1998.

24. J. M. Usoff, Scattering from a Collection of Periodic Linear Arrays of Arbitrarily Shaped Thin Wire Elements Emphasizing Truncation Effects of Planar Periodic Surfaces, Ph.D. Dissertation, Ohio State University, Department of Electrical Engineering, Columbus, OH, 1993.

25. J. M. Usoff and B. A. Munk, Edge Effects of Truncated Periodic Surfaces of Thin Wire Elements, *IEEE Trans. Antennas Propag.*, Vol. **AP-42**, July 1994, pp. 946–953.

26. M. G. Floquet, Sur les equations différentielles linéaires a coefficients périodiques, *Annale École Normale Superieur*, 1883, pp. 47–88.

27. J. M. Usoff and B. A. Munk, *op. cit.*

28. P. Y. Ufimtsev, Comments on Diffraction Principles and Limitations of RCS Reduction Techniques, *Proc. IEEE*, Vol. **84**, No. 12, December 1996.

29. W. W. Hansen and J. R. Woodyard, A New Principle in Directional Antenna Design, *Proc. IRE*, Vol. **26**, March 1938, pp. 333–345.

30. T. Nguyen and A. Dominek, An Edge Wave Reflection Coefficient, Technical Report 721929-22, The Ohio State University Electroscience Laboratory, March 1990.

31. R. C. Hansen and D. Gammon, A Gibbsian Model for Finite Scanned Arrays, *IEEE Trans. Antennas Propag.*, Vol. **44**, No. 2, February 1996, p. 243.

32. R. C. Hansen, Anomalous Edge Effect in Finite Arrays, *IEEE Trans. Antennas Propag.*, Vol. **47**, No. 3, March 1999, p. 549.

33. R. C. Hansen, *Phased Array Antennas*, John Wiley and Sons, New York, 1997, Chapter 8.

34. B. A. Munk, *op. cit.*, Chapters 7 and 8.

35. B. A. Munk, *Frequency Selective Surfaces, Theory and Design*, New York: John Wiley and Sons, 2000, Section 1.7.

36. J. D. Kraus and R. J. Marhefka, *Antennas for All Applications*, McGraw-Hill, New York 2002, pp. 27–30.

37. R. J. Garbacz, Basic Relations Between Antennas and Scattering Parameters, from short course, *Antenna and Scattering Theory: Recent Advances*, Ohio State University, Columbus, OH, 1966.

38. R. B. Green, The General Theory of Antenna Scattering, Ph.D. Dissertation, Ohio State University, Department of Electrical Engineering, Columbus, OH, 1963.

39. J. A. McEntee, A Technique for Measuring the Scattering Aperture and Absorption Aperture of an Antenna, Ohio State University Electroscience Laboratory, Contract AF 30(635)-2811, Rome Air Development Center, 1957.

40. R. C. Hansen, Relationship Between Antennas as Scatterers and as Radiators, *Proc. IRE*, Vol. **77**, No. 5, May 1979, pp. 659–662.

41. R. J. Garbacz, Determination of Antenna Parameters by Scattering Cross-Section Measurements, *Proc. IEE*, Vol. **111**, No. 10, October 1964, pp. 1679–1686.

42. J. Appel-Hansen, Accurate Determination of Gain and Radiation Patterns by Radar Cross-Section Measurements, *IEEE Trans. Antennas Propag.*, Vol. **AP-27**, No. 5, September 1979, pp. 640–646.

43. J. J. H. Wang, C. W. Choi and R. L. Moore, Precision Experimental Characterization of the Scattering and Radiation Properties of Antennas, *IEEE Trans. Antennas Propag.*, Vol. **AP-30**, No. 1, January 1982, pp. 108–112.

44. D. D. King, Measurement and Interpretation of Antenna Scattering, *Proc. IRE*, Vol. **35**, December 1947, pp. 1451–1467.

45. E. Heidrich and W. Wiesbeck, Features of Advanced Polarimetric RCS-Antenna Measurements, *IEEE AP-S International Symposium & URSI Radio Science Meeting*, Conference Proceedings, Vol. II, San Jose, CA, June 1989, pp. 1026–1029.

46. E. Heidrich and W. Wiesbeck, Bestimmung der polarisationsabhängigen Strahlungs- und Streueigenschaften von Antennen, ITG-Fachtagung Antennen, ITD-Fachbericht 111, 217–221, Wiesbaden, March 1990.

47. E. Heidrich and W. Wiesbeck, Wideband Polarimetric RCS-Antenna Measurement, *Seventh International Conference on Antennas and Propagation*, Conference Proceedings, University of York, UK, April 1991.

48. E. Heidrich and W. Wiesbeck, Application of RCS-Antenna-Measurements to Multiport Antennas, *Thirteenth Antenna Measurement Techniques Association (AMTA) Meeting and Symposium*, Conference Proceedings 9-35–9-40, Boulder, CO, October 1991.

49. E. Heidrich, Theoretiche und Experimentelle Charakterisierung der Polarimetrischen Strahlungs und Streneigenschaften von Antennen, Ph.D. Dissertation, University of Karlruhe, Germany, 1992.

50. B. A. Munk, *op. cit.*, Chapter 4.

51. J. Kraus, *Antennas*, McGraw-Hill, New York, 1950, Chapter 3.

52. S. A. Schelkunoff and H. T. Friis, *Antenna Theory and Practice*, first edition, John Wiley and Sons, 1952, p. 600.

53. B. A. Munk, *op. cit.*, Problem 5.2.

54. B. A. Munk, *op. cit.*, Section 9.9.2.

55. C. G. Montgomery, R. H. Dicke, and E. M. Purcell, *Principles of Microwave Circuits, Radiation Laboratory Series*, Vol. 8, McGraw-Hill, New York, 1948, p. 333.

56. R. B. Green, The Echo Area of Small Rectangular Plates with Linear Slots, *IEEE Trans. Antennas Propag.*, Vol. **AP-12**, No. 1, January 1964, pp. 101–104.

57. W. K. Kahn and H. Kurss, Minimum-Scattering Antenna, Adelphi University, Department of Graduate Mathematics, AGM Report No. 121, March 1965.

58. R. B. Green, Scattering from Conjugate-Matched Antennas, *IEEE Trans. Antennas Propag.*, Vol. **AP-14**, No. 1, January 1966, pp. 11, 17–21.

59. D. C. Jeun and V. Flokos, In-Band Scattering from Arrays with Parallel Feed Network, *IEEE Trans. Antennas Propag.*, Vol. **44**, No. 2, February 1996, p. 172.

60. B. A. Munk, *op. cit.*, Chapter 4, equations (4.49) and (4.50).

61. B. A. Munk, *op. cit.*, Chapters 4 and 5.

62. B. A. Munk, *op. cit.*, Chapter 3.

63. B. A. Munk, *op. cit.*, Sections 4.4 and 4.5.

64. B. A. Munk, *op. cit.*, Sections 4.7.1 and 4.7.2.

65. B. A. Munk, *op. cit.*, Section 4.12.3.

66. E. K. English, Electromagnetic Scattering from Infinite Periodic Arrays of Arbitrarily Oriented Dipole Elements Embedded in a General Stratified Medium, Ph.D. Dissertation, Ohio State University, Department of Electrical Engineering, Columbus, OH, 1983.

67. B. M. Kent, Impedance Properties of an Infinite Array of Non-planar Rectangular Loop Antennas Embedded in a General Stratified Medium, Ph.D. Dissertation, Ohio State University, Department of Electrical Engineering, Columbus, OH, 1984.

68. K. T. Ng, Admittance Properties of a Slot Array with Parasitic Wire Arrays in a Stratified Medium, Ph.D. Dissertation, Ohio State University, Department of Electrical Engineering, Columbus, OH, 1985.

69. S. J. Lin, On the Scan Impedance of an Array of V-Dipoles and the Effect of the Feedlines, Ph.D. Dissertation, Ohio State University, Department of Electrical Engineering, Columbus, OH, 1985.

70. H. K. Schuman, D. R. Pflug, and L. D. Thompson, Infinite Planar Array of Arbitrarily Bent Thin Wire Radiators, *IEEE Trans. Antennas Propag.*, **AP-32**(4), April 1984, pp. 364–477.

71. R. Andre, An Analysis Method for Doubly Periodic Nonplanar Antenna Arrays, M.Sc. Thesis, Ohio State University, Department of Electrical Engineering, Columbus, OH, 1985.

72. B. A. Munk, *op. cit.*, Chapters 5 and 6.

73. R. F. Harrington, *Time-Harmonic Fields*, McGraw-Hill, New York, 1961, pp. 163–168.

74. E. C. Saladin, The Termination and Bending of the Infinite Array in an Effort to Create a Low RCS Phased Array with 270 Degree Scan Angle, M.Sc. Thesis, Ohio State University, Department of Electrical Engineering, Columbus, OH, 1997.

75. B. L. Johnson, Proper Design for Uniform Scattering from a Semi-Infinite Dipole-Element Phased Array, M.Sc. Thesis, Ohio State University, Department of Electrical Engineering, Columbus, OH, 1995.

76. J. B. Pryor, Suppression of Surface Waves on Arrays of Finite Extent, M.Sc. Thesis, Ohio State University, Department of Electrical Engineering, Columbus, OH, 2000.

77. D. Janning, Surface Waves in Arrays of Finite Extent, Ph.D. Dissertation, Ohio State University, Department of Electrical Engineering, Columbus, OH, 2000.

78. J. P. Skinner, Scattering from a Finite Collection of Transverse Dipole and Axial Slot Arrays with Edge Effects, Ph.D. Dissertation, Ohio State University, Department of Electrical Engineering, Columbus, OH, 1988.

79. J. A. Hughes, Impedance Properties of Cylindrical Arrays and Finite Planar Arrays, M.Sc. Thesis, Ohio State University, Department of Electrical Engineering, Columbus, OH, 1988.

80. R. C. Hansen, *Phased Array Antennas*, John Wiley and Sons, New York, 1998, Chapter 8.

81. B. A. Munk, *op. cit.*, Chapter 7.

82. S. Uda and Y. Mushioke, *Yagi–Uda Antenna*, Tohoku University, Sandai, Japan, 1954.

83. H. W. Ehrenspeck and H. Poehler, A New Method for Obtaining Maximum Gain from Yagi Antennas, *IRE Trans. Antennas Propag.*, Vol. **AP-7**(4), October 1959, pp. 379–386.

84. R. J. Mailloux, Antennas and Wave Theories of Infinite Yagi–Uda Arrays, *IEEE Trans. Antennas Propag.*, Vol. **AP-13**, July 1965, pp. 499–506.

85. J. H. Richmond and R. J. Garbacz, Surface Waves on Periodic Arrays of Imperfectly Conducting Dipoles Over the Flat Earth, *IEEE Trans. Antennas Propag.*, Vol. **AP-27**(6), November 1979, pp. 783–787.

86. E. K. Damon, The Near Fields of Long End-Fire Dipoles, *IRE Trans. Antennas Propag.*, Vol. **AP-10**, September 1962, pp. 511–523.

87. B. A. Munk, D. S. Janning, J. B. Pryor, and R. J. Marhefka, Scattering from Surface Waves on Finite FSS, *IEEE Trans. Antennas Propag.*, Vol. **49**, No. 12, December 2001, pp. 1782–1793 .

88. D. S. Janning and B. A. Munk, Effect of Surface Waves on the Current of Truncated Periodic Arrays, *IEEE Trans. Antennas Propag.*, Vol. **AP-50**(9), September 2002, pp. 1254–1265.

89. E. Weber, *Electromagnetic Fields*, John Wiley, and Sons, New York, 1950, pp. 111–115 and p. 337.

90. B. A. Munk, *op. cit.*, Appendix E.

91. B. A. Munk, *op. cit.*, Section 2.2.1.

92. B. A. Munk, *op. cit.*, pp. 187–188.

93. B. A. Munk, *op. cit.*, pp. 100–105.

94. H. A. Wheeler, Simple Relations Derived from a Phased Array Antenna Made of an Infinite Current Sheet, *IEEE Trans. Antennas Propag.*, **AP-13**(4), 506–514, July 1965.

95. B. A. Munk, *op. cit.*, pp. 143–149.

96. P. Munk, On Arrays that Maintain Superior CP and Constant Scan Impedance for Large Scan Angles, to be published in *IEEE Trans. Antennas Propag.*, February 2003.

97. P. Munk, Scan Independent Array for Circular Polarization, Reception and Transmission, U.S. Patent 6,346,918 B1.

98. Munk, *op. cit.*, pp. 333–334.

99. T. W. Kornbau, Analysis of Periodic Arrays of Rotated Linear Dipoles, Rotated Crossed Dipoles, and of Biplanar Dipole Arrays in Dielectric, Ph.D. Dissertation, Ohio State University, Department of Electrical Engineering, Columbus, OH, 1984.

100. B. A. Munk, *op cit.*, pp. 10–14, 185, 393–396.

101. R. M. Foster, A Reactance Theorem, *Bell Syst. Tech. J.*, Vol. **30**, April 1924, pp. 259–267.

102. B. A. Munk, *op. cit.*, pp. 315–335.

103. B. A. Munk, *op. cit.*, (4.70) on p. 105.

104. J. D. Kraus and R. J. Marhefka, *Antennas for All Applications*, McGraw-Hill, New York, 2002, Section 2.9.

105. W. W. Hansen and J. R. Woodyard, A New Principle in Directional Antenna Design, *Proc. IRE*, Vol. **26**, March 1938, pp. 333–345.

106. J. D. Kraus and R. J. Marhefka, *Antennas for All Applications*, McGraw-Hill, New York, 2002, pp. 183–187.

107. B. A. Munk, op. cit., pp. 227–240.

108. J. A. Hughes, Impedance Properties of Cylindrical Arrays and Finite Planar Arrays, M.Sc. Thesis, Ohio State University, Department of Electrical Engineering, Columbus, 1988, and private communication.

109. J. I. Simon, Impedance Properties of Periodic Linear Arrays Conformal to a Dielectric-Clad Infinite PEC Cylinder, Ph.D. Dissertation, Ohio State University, Department of Electrical Engineering, Columbus, OH, 1989.

110. B. A. Munk, op. cit., Chapter 10.

111. B. A. Munk, op. cit., Section 4.7, equation (4.62).

112. R. A. Hill, The Design of a Dual Band Frequency Selective Surface and the Effect of Perturbing the Elements and the Interelement Spacing, Ph. D. Dissertation, Ohio State University, Department of Electrical Engineering, Columbus, OH, 1991.

113. B. A. Munk, op. cit., Chapter 8.

114. B. A. Munk, op. cit., Chapter 2, Figs. 2.10 and 2.23.

115. B. A. Munk, op. cit., p. 75.

116. J. D. Kraus and R. J. Marhefka, *Antennas for All Applications*, McGraw-Hill, New York, 2002, Chapter 23.

117. B. A. Munk, op. cit., Section 5.10.

118. B. A. Munk, op. cit., Chapter 5, Section 5.13.

119. Radio Research Laboratory, *Very High-Frequency Techniques*, Harvard University, Boston Technical Publishers, Boston, 1965.

120. B. A. Munk, op. cit., Chapter 9.

121. S. J. Lin, On the Scan Impedance of an Array of V-Dipoles and the Effect of the Feedlines, Ph. D. Dissertation, Ohio State University, Department of Electrical Engineering, Columbus, OH, 1985.

122. B. A. Munk, *op. cit.*, p. 371.

123. B. A. Munk *op. cit.*, Appendix A.

124. V. H. Rumsey, The Design of Frequency-Compensating Matching Section, *Proc. IRE*, Vol. **38**, pp. 1191–1196, October 1950.

125. W. N. Caron, *Antenna Impedance Matching*, American Radio Relay League, 1994.

126. H. Jasik, ed., *Antenna Engineering Handbook*, first edition, McGraw-Hill, New York, 1961.

127. J. D. Kraus and R. Marhefka, *Antennas for All Applications*, McGraw-Hill, 2002, pp. 891–892.

128. J. J. Pakan, Antenna Polarizer Having Two Phase Shifting Mediums, U.S. Patent No. 2,978,702, April 1961.

129. D. S. Lerner, A Wave Polarization Converter for Circular Polarization, *IEEE Trans. Antennas Propag.*, **AP-13**(1), January 1965, pp. 3–7.

130. L. Young, L. A. Robinson, and C. A. Hacking, Meander-Line Polarizer, *IEEE Trans. Antennas Propag.*, **AP-21**(3), May 1973, pp. 376–378.

131. J. J. Epis, Broadband Antenna Polarizer, U.S. Patent No. 3,754,271, August 1973.

132. C. Terret, J. R. Levrel, and K. Mahdjoubi, Susceptance Computation of a Meander-Line Polarizer Layer, *IEEE Trans. Antennas Propag.*, **AP-32**(9), September 1984, pp. 1007–1011.

133. R. S. Chu and K. M. Lee, Analytical Model of a Multilayered Meander-Line Polarizer Plate with Normal and Oblique Plane-Wave Incidence, *IEEE Trans. Antennas Propag.*, **AP-35**(6), June 1987, pp 652–661.

134. R. A. Marino, Accurate and Efficient Modeling of Meander-Line Polarizers, *Microwave J.*, November 1998, pp 22–34.

135. B. A. Munk, *op. cit.*, Section 4.11.3.

136. B. A. Munk, *op. cit.*, pp. 185, 354–357–.

137. E. H. Newman, A User's Manual for the Electromagnetic Surface Patch Code; Preliminary Version ESP 5.0, Ohio State University Electroscience Laboratory, Columbus, OH, 1998.

Determination of Transformation and Position Circles

A.1   INTRODUCTION

The input impedance Z_{in} of a transmission line with a given characteristic impedance Z_1 and length d_1 and terminated in a load impedance Z_L (as shown in the insert of Fig. A.1) is usually determined either by use of an appropriate computer program or by use of a Smith chart. In view of the fact that the computer program is usually faster and more accurate than the Smith chart, one is entitled to pose the simple question, "Why consider a graphical approach at all?" The answer is simple: To guide us in our design procedure by better pinpointing where the problems are and, in particular, which components should be used or avoided. Illustrations of these concepts are given in Chapter 6 and Appendix B.

The Smith chart is well-suited for handling transmission line problems when normalized to the characteristic impedance of the transmission line in question. However, when working with several transmission line sections with different characteristics impedances, for example, we must renormalize the Smith chart each time a change is made to a new characteristic impedance. Since all Smith charts "look alike" after normalization, we can easily lose track of just exactly where we are when dealing with a complex matching problem.

One way to overcome this shortcoming is to stay in the same classical rectangular coordinate system regardless of the characteristic impedance. Although this leads to *transformation circles* that are no longer concentric and *position circles* that are no longer straight lines through the center of the normalized Smith chart, the advantage is that an entire complex problem can be kept on *one* single piece
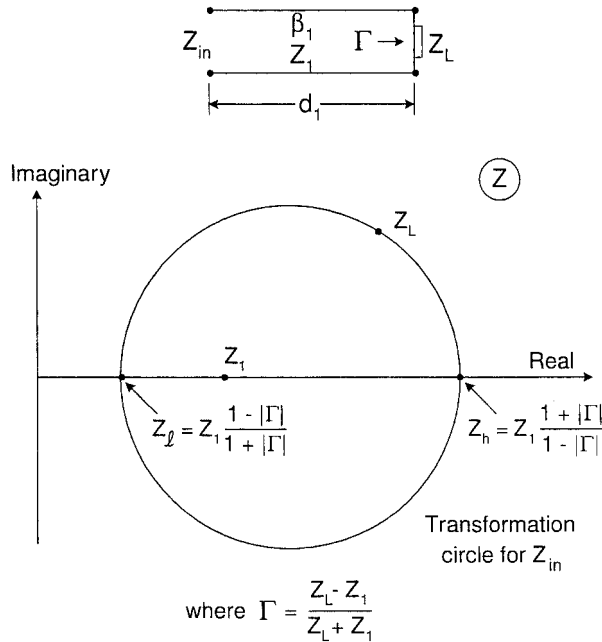
Fig. A.1 *Case I: Given the load impedance Z_L and characteristic impedance Z_1, numerically calculate Γ, Z_l and Z_h from the formulas in the figure. This completely determines the transformation circle going through Z_L. Note: This approach is valid for Smith charts as well, as long as we read all the impedances in the Smith chart.*

of paper. The next step is that this technique can also be used in a single Smith chart normalized to whatever impedance one prefers. It is emphasized that the approach is recommended primarily to develop a concept. The actual calculations should be executed on a computer.

A.2 CASES DEMONSTRATING HOW TO CONSTRUCT TRANSFORMATION CIRCLES

In the following, several cases will demonstrate how to construct the transformation circles given various parameters.

Case I: Given Load Impedance Z_L and Characteristic Impedance Z_1

We seek the input impedance Z_{in} of a transmission line with length d_1, characteristic impedance Z_1, and propagation constant β_1, and that terminates at an arbitrary load impedance Z_L (as shown in the insert of Fig. A.1).

It is shown in reference 122 that

$$Z_{in} = Z_1 \frac{1 + \Gamma \, e^{-j2\beta_1 d_1}}{1 - \Gamma \, e^{-j2\beta_1 d_1}}, \qquad (A.1)$$

where the reflection coefficient Γ is given by

$$\Gamma = \frac{Z_L - Z_1}{Z_L + Z_1}. \tag{A.2}$$

Furthermore, it is shown in the same reference that Z_{in} will be located on a circle determined by the two extreme points

$$Z_h = Z_1 \frac{1 + |\Gamma|}{1 - |\Gamma|} \quad \text{and} \quad Z_l = Z_1 \frac{1 - |\Gamma|}{1 + |\Gamma|}, \tag{A.3}$$

as shown in Fig. A.1.

If the load impedance Z_L and the characteristic impedance Z_1 are known numerically (i.e., as simple complex numbers), one can readily determine Γ from (A.2) and subsequently Z_h and Z_l from (A.3). Thus, the locus circle for Z_{in} is readily given by Z_h and Z_l as shown in Fig. A.1. However, there are cases when Z_L as well as Z_1 are merely known by their geometric location in the complex plane.

Thus we will next show how to determine the locus circle for Z_{in} by purely geometrical means. *Note*: This approach holds for Smith charts as well, as long as all the impedances are read in the Smith chart.

Case II: Both Z_L and Z_1 Located on the Real Axis

Here the locus circle for Z_{in} is sought when both Z_L and Z_1 are located on the real axis, as shown in Fig. A.2.

Solution: Draw a circle with center at the origin O and radius $|Z_1|$. Next, draw the tangent from Z_L to this circle touching at point A. Draw a line from A that is orthogonal to the real axis which determines the intersection point B. Point B is the point Z_l that together with $Z_h (Z_L = Z_h)$ determines the locus circle.

Proof: The two triangles OAB and OB_1A are similar. Thus,

$$\frac{OB}{OA} = \frac{OA}{OB_1}$$

or

$$OB \cdot OB_1 = (OA)^2 = |Z_1|^2; \tag{A.4}$$

that is, B is harmonic related to B_1 with $OB_1 = Z_L = Z_h$ and therefore $OB = Z_l$. The locus circle for Z_{in} is simply drawn through Z_l and Z_h.

Note: This approach is valid for only the rectangular coordinate system.
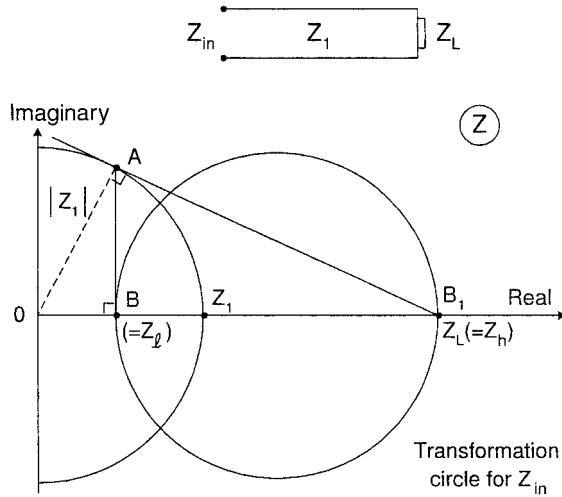
From the similar triangles OAB and OB_1A: $\frac{OB}{OA} = \frac{OA}{OB_1}$ or $Z_l \cdot Z_h = |Z_1|^2$.

Fig. A.2   Case II: Given the load impedance Z_L and the characteristic impedance Z_1 as points in the complex plane (both real). The low impedance Z_l is obtained by drawing the tangent from Z_L to the circle $z = |Z_1| e^{j\phi}$. Next, project the touching point A upon the real axis to obtain point B, which determines Z_l. The points Z_l and $Z_h = Z_L$ completely determine the transformation circle going through Z_L. Note: Only valid for the rectangular coordinate system.

Case III: Load Impedance Z_L Anywhere in the Complex Plane. Characteristic Impedance Z_1 on the Real Axis

For the third case, we seek the locus circle for Z_{in} when the load impedance Z_L is located anywhere in the complex plane and the characteristic impedance Z_1 is on the real axis, as shown in Fig. A.3.

Solution: Draw a circle with center at the origin O and radius $|Z_1|$. Draw the tangent from Z_L to that circle touching at point A. Next, draw a line from A orthogonal to the line through O and Z_L to determine the intersection point B. The locus point for Z_{in} is the circle going through B and Z_L with its center on the real axis (we assume Z_1 is real). The same circle intersects the real axis at points C and C_1 when $OC = Z_l$ and $OC_1 = Z_h$.

Proof: The two triangles OAB and OB_1A are similar. Thus,

$$\frac{OB}{OA} = \frac{OA}{OB_1}$$

or

$$OB \cdot OB_1 = (OA)^2 = |Z_1|^2.$$
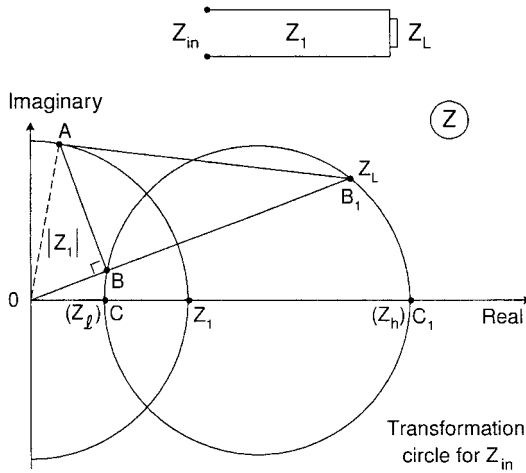
Fig. A.3 *Case III: Given Z_L (arbitrary) and the characteristic impedance Z_1 on the real axis. Draw a tangent from Z_L to the circle $z = |Z_1| e^{j\phi}$ and project it onto the line OB_1 producing point B. The transformation circle for Z_{in} will go through B and B_1 with center on the real axis (for Z_1 real). This approach is only valid in the rectangular coordinate system.*

Furthermore, from the "Power of the Circle" [123] we also have

$$OC \cdot OC_1 = OB \cdot OB_1, \tag{A.5}$$

so by using (A.4) we obtain

$$OC \cdot OC_1 = |Z_1|^2; \tag{A.6}$$

that is, C and C_1 are harmonic related with respect to $|Z_1|$ [and so are B and B_1, as in (A.4)]. Again, this is valid only for the rectangular coordinate system.

Case IV: Two Arbitrary Points B_2 and B_3 on the Locus Circle for Z_{in}

For the fourth case, given two arbitrary points B_2 and B_3 on the locus circle for Z_{in}, find the characteristic impedance Z_1 (real).

Solution: Draw a circle through B_2 and B_3 with its center on the real axis (we assume Z_1 is real). As shown in Fig. A.4, this circle intersects the real axis at the extreme impedances Z_l and Z_h. Next, draw a tangent to the above circle from the origin O. The "touching point" is denoted "T." Finally, draw a circle with center at O and radius OT. It intersects the real axis at point T_1. OT_1 is the desired characteristic impedance Z_1.

Proof: Again, from the "Power of the Circle" [123], $Z_l \cdot Z_h = (OT)^2 = Z_1^2$ (Z_1 is real), which proves our claim. This result is valid only in the rectangular
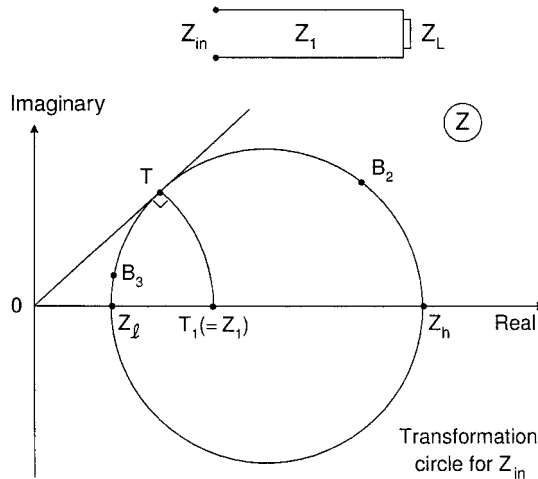
Fig. A.4   Case IV: Given two arbitrary points B_2 and B_3, the transformation circle for Z_{in} can be drawn immediately with center on the real axis assuming that the characteristic impedance Z_1 is real. Next draw a tangent from the origin O touching the transformation circle at point T. The length of $OT = |Z_1|$. This approach is only valid in the rectangular coordinate system unless actual numbers are read in the Smith chart.

coordinate system unless we read the actual numbers in the Smith chart. See Problem B.2.

A.3   WHERE IS Z_{in} LOCATED ON THE TRANSFORMATION CIRCLE? DETERMINATION OF THE POSITION CIRCLES

So far we have concentrated merely on determining the transformation circle for Z_{in}. In this section we discuss how to determine where on that circle Z_{in} is located. Since this subject is thoroughly described in reference 123, only a brief overview of the approach is given.

First, draw a circle through Z_L and Z_1 with its center on the imaginary axis as showed in Fig. A.5. Draw the tangent to this circle at point Z_1. Next draw another line through Z_1 intersecting the first one at the angle $2\beta_1 d_1$ (clockwise direction) where β_1 is the propagation constant of the line and d_1 is the length. Finally, draw the position circle through Z_1 having the second line as a tangent and its center located on the imaginary axis. The intersection between this position circle and the transformation circle determines Z_{in} as indicated in Fig. A.5.

PROBLEMS

A.1   Given a load impedance $Z_L = 100 + j50$ ohms, find the characteristic impedance Z_1 and the shortest cable length d_1 that produces an input impedance Z_{in} equal to

Fig. A.5   *Determination of Z_{in} on the transformation circle. Draw a circle with center on the imaginary axis and going through Z_L and Z_1 as shown. Draw the tangent to this circle at point Z_1. Draw a line, making an angle $2\beta_1 d_1$ with the above tangent (clockwise direction). Draw the position circle with its center on the imaginary position axis and going through Z_1 and with the second line as a tangent. The intersection between this position circle and the transformation circle determines Z_{in} as shown.*

    (a)   50 ohms

    (b)   100 ohms

    (c)   150 ohms

You are of course welcome to use a graphical approach. The brightest student usually knows what goes on in 10 minutes or less. If you use a computational approach, be prepared to spend a "bit" more time. And don't get too frustrated about case (b) or a few other values in that neighborhood.

    Computer power is wonderful. However, it is a supplement, not a substitute, for brain power.

Appendix B

Broadband Matching

B.1 INTRODUCTION

Most students who have taken a course in fundamental antenna and transmission line theory consider themselves well-versed in matching an arbitrary load impedance Z_L into a resistive load. When challenged, they usually with some indignation will let it be known that they certainly know the workings of not only the single-stub tuner but also the double-stub tuner and perhaps even the triple stub. The sad facts are, however, that although all of these schemes will give us perfect match at *one* frequency, they will typically create a tremendous mismatch at others. In fact, it is sometimes stated even in reputable textbooks that the matching of an antenna always leads to a narrowband design; however, this is not necessarily so. In order to repudiate this notion, we shall in this appendix examine matching in general and, in particular, broadband matching. This has been necessitated by the realization that broadband matching is taught very superficially at most universities today, if it is mentioned at all.

This should not be interpreted as stating that broadband matching has been given insufficient time to mature. In fact, the author still remembers how he as a young engineer in the mid-1950s studied Chapter 3 in *Very High-Frequency Techniques* [119]. In his opinion, it still today remains the most authoritative text written on that subject. (He always made sure that his students in his first antenna course got a copy since the book, to the best of his knowledge, is out of print.)

Much of the broadband matching technique was developed during World War II for the purpose of countermeasures. One simply did not know where

in the frequency range the enemy could pop up. Further interest in broadband matching was fueled by the emerging TV industry. Ideally, the industry required transmitting antennas with VSWR <1.05 over most of a TV channel (see also Section B.9.1). Expertise in that area appeared to have resided at a few antenna "houses." They were in no particular hurry to share their knowledge with the rest of the world. (Industry sometimes exhibits a remarkable degree of modesty when it comes to products of commercial interest.) You simply had to go there and learn from the inside. The author himself joined the company "Rohde and Schwartz" in Münich, Germany, in the late 1950s. Beside being a well-known powerhouse in the area of measurement equipment (they were often compared to Hewlett Packard), they had an antenna department that probably was the most advanced in Europe in the VHF and UHF range at that time. Typically, they would match their antenna systems to have a VSWR <1.05 not only in the operating TV channel but actually in an entire band—that is, such as 47–68 MHz and 174–224 MHz for the European Band I and Band III antenna systems, respectively. The author not only had the great fortune of participating in the design of several very challenging projects but also had several mentors, one in particular being Mr. L. Thomanek. When it came down to matching, his vision and experience were phenomenal.

Some papers were written on this subject. One in particular was by V. H. Rumsey and appeared in 1950 [124]. In spite of the fact that it was published later than reference 119, it mostly treated special cases as compared to the more general approach described in the earlier reference; however, there are indications that Rumsey actually did his work in England in the early part of World War II. Furthermore, reference 125 addresses primarily *amateurs*, but many *professionals* could benefit from reading it. Finally, Chapter 31 of reference 126 gives a general introduction and additional references on the subject of broadband matching.

B.2 MATCHING TOOLS

The fundamental tools used to match an arbitrary load impedance Z_L into another arbitrary impedance are shown schematically in Fig. B.1. At the very top we show from left to right:

(a) Load impedance Z_L in series with a pure reactance jX.
(b) Load impedance Y_L in parallel with a pure susceptance jB.
(c) Transmission line with characteristic impedance Z_1, length d, and termination in the load impedance Z_L.

Although some improvement in matching can be obtained by using lossy elements, it is in general not recommended since the possible reduction in mismatch loss in general is more than canceled by deterioration of the efficiency. Only at frequencies lower than ~100 MHz should this be considered since most of the noise at these frequencies comes from the outside through the antenna in the form
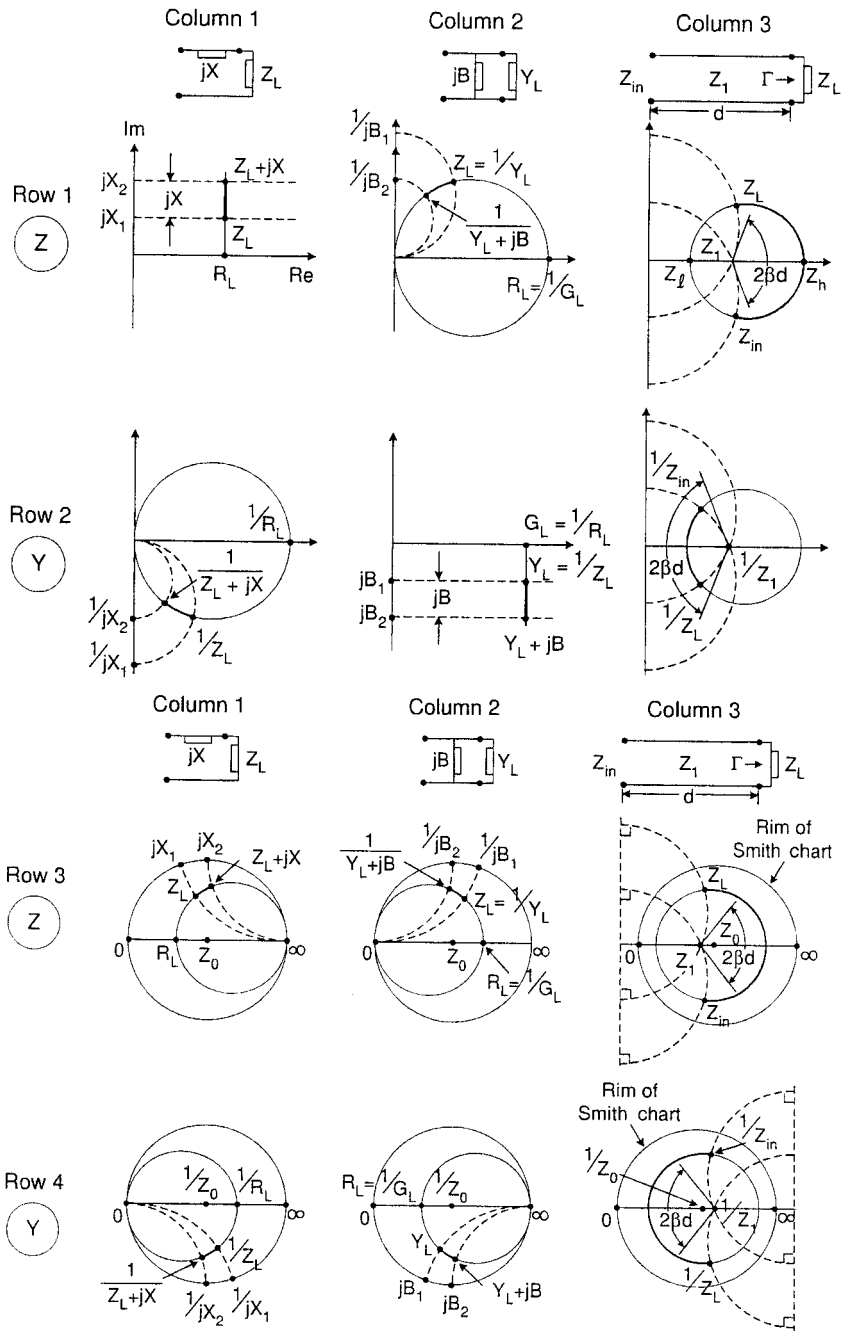
Fig. B.1 Basic tools for matching and their depiction in the complex plane: Pure reactances connected in series, column 1, or parallel, column 2, and a transmission line of length d and characteristic impedance Z_1, column 3.

of Galactic or man-made noise. In other words, the signal and the noise are attenuated to the same degree, leaving the signal-to-noise ratio basically unchanged. Thus, since we are mostly interested in the general case, we shall in the following assume that all matching elements are idealized to be purely imaginary.

Figure B.1 is organized as follows. In row 1 we show the three cases depicted at the top in the impedance plane Z in rectangular coordinates. Next, in row 2 we show the same three cases in the admittance plane Y in rectangular coordinates. Similarly, we show in row 3 the impedance plane Z like row 1, but this time depicted in a Smith chart normalized to an arbitrary impedance Z_0. Finally, row 4 shows the admittance plane Y, as in row 2, but depicted in a Smith chart normalized to an arbitrary admittance $Y_0 = 1/Z_0$.

More specifically, we show in column 1 what happened in any of the complex planes when we add a pure reactance jX in series with an arbitrary load impedance Z_L. As jX varies, we readily see how the series combination in row 1 moves along the vertical line going through Z_L. Furthermore, the admittance plot in row 2 is obtained from the case in row 1 by noticing that

$$Y = \frac{1}{Z}.\tag{B.1}$$

Since (B.1) constitutes a bilinear transformation, we know from reference 123 that a general circle will be transformed into a general circle. In particular, we note that the real and imaginary axes will be transformed into themselves while the vertical line through Z_L in the Z plane will have its infinity point transformed into $(0, 0)$ in the Y plane and the point R_L into $1/R_L$. By further noting that the bilinear transformation is conformal [123], we see that the angle between the real axis and the locus in the Y plane must remain $90°$; that is, the center of the locus circle must be located on the real axis. That completely determines the locus circle in the Y plane as shown.

Finally, the horizontal lines $X = jX_1$ and jX_2 will have their infinity point in the Z plane transformed into point $(0, 0)$ in the Y plane while the two points jX_1 and jX_2 on the imaginary axis in the Z plane will be transformed into $1/jX_1$ and $1/jX_2$, respectively, on the imaginary axis in the Y plane. Again, noting that the bilinear transformation preserves angles we reason that the two horizontal lines $X = jX_1$ and jX_2 will be circles in the Y plane with their centers on the imaginary axis as shown. That completely determines the locus in the Y plane when adding a series reactance to an arbitrary impedance Z_L.

In row 3 we show the impedance plot from row 1 but now plotted in a Smith chart normalized to Z_0. Again, we notice that the transformation from row 1 to row 3 is bilinear [123]; that is, general circles will be transformed into general circles. In particular, the imaginary axis in row 1 will be transferred into the rim of the Smith chart in row 3 while the real axis will be transformed into itself. Furthermore, the two lines $X = jX_1$ and jX_2 will have their infinity point transformed into ∞ in the Smith chart and the two points jX_1 and jX_2 are located on the rim of the Smith chart. We further note in row 1 that the angle between the two horizontal lines and the real axis is zero; that is, the center for

the circle arcs connecting ∞ and jX_1 and jX_2 must be located on the vertical line going through ∞ in the Smith chart. Finally, the vertical line going through R_L in row 1 is readily seen to be transformed into the circle going through ∞ and point R_L in the Smith Chart, row 3. That completely determines the locus in a Smith chart when adding a pure reactance jX in series with the arbitrary impedance Z_L. Finally the admittance case in row 4 is obtained as shown.

We next examine the case in column 2 of Fig. B.1 where we have connected a pure susceptance jB in parallel with the admittance $Y_L = 1/Z_L$. In that case it is most convenient to start with the admittance plane Y as shown in row 2. Adding a pure susceptance jB to the load admittance $Y_L = 1/Z_L$ will produce a locus that simply is the vertical line passing through Y_L. By arguing analogous to the case where we went from row 1 to row 2 in the series case (column 1), we readily observe that the locus in the impedance plane (Z of row 1) must be a circle with its center on the real axis and going through (0, 0) and the point $R_L = 1/G_L$. Similarly, the two horizontal lines going through jB_1 and jB_2 in the admittance plane (row 2) will in the impedance plane (row 1) be two circles with centers on the imaginary axis and going through (0, 0) and the two points $1/jB_1$ and $1/jB_2$, respectively, as shown. Finally, the Smith chart presentations in row 3 and row 4 are obtained by using the bilinear transformation features of the Smith chart transformation just as was done in column 1 when going from row 1 to 2 and from row 3 to 4, respectively.

Column 3, row 1, illustrates how to obtain the input impedance Z_{in} of a cable with characteristic impedance Z_1, length d, and termination in the impedance Z_L. As explained in Appendix A, the input impedance Z_{in} will lie on a transformation circle going through the extreme points Z_h and Z_l on the real axis where

$$Z_h = Z_1 \frac{1 + |\Gamma|}{1 - |\Gamma|}, \qquad Z_l = Z_1 \frac{1 - |\Gamma|}{1 + |\Gamma|} \tag{B.2}$$

and the reflection coefficient

$$\Gamma = \frac{Z_L - Z_1}{Z_L + Z_1}. \tag{B.3}$$

All the position circles will go through Z_1 and have their centers located on the imaginary axis [123]. Furthermore, the first is uniquely determined by also going through Z_L. We next draw the tangent to this position circle point through Z_1. This is followed by drawing a second line through Z_1, making an angle with respect to the first line equal to $2\beta d$ in the clockwise direction. The second line is a tangent to the position circle that determines the input impedance Z_{in} as shown.

The admittance case is shown in row 2. It follows directly from the impedance case in row 1 by the simple inversion $Y = 1/Z$, that is, circles will be transformed into circles. More specifically, the characteristic admittance is $Y_1 = 1/Z_1$ while the transformation circle is determined by the extreme points

$$Y_h = \frac{1}{Z_l} \quad \text{and} \quad Y_l = \frac{1}{Z_h}. \tag{B.4}$$

The position circles are obtained completely analogous to the impedance case in row 1.

We next move to row 3 where we show the impedance plane but this time depicted in a Smith chart normalized to the arbitrary impedance Z_0 (i.e., $Z_0 \neq Z_1$ in general). Again, recalling that the Smith chart transformation from row 1 to row 3 is bilinear, we can immediately conclude that the transformation circles in row 1 will be transformed into similar circles in row 3. However, only if the Smith chart is normalized to Z_1 (i.e., $Z_1 = Z_0$) will the transformation circles in the Smith chart be concentric. The position circles are obtained completely analogous to the rectangular impedance case in row 1. Only if $Z_1 = Z_0$ will the position circle be straight lines going through the enter of the Smith chart. Finally, the admittance case in row 4 is obtained from row 2 completely analogous to the impedance transformation above.

One might at this point wonder: "Why consider the general Smith chart case where $Z_1 \neq Z_0$?" Let us emphatically state that actual detailed calculations in a Smith chart should not in general be performed unless $Z_1 = Z_0$. However, as will be illustrated later, a typical situation occurs when Z_L is not a single point in the Smith chart but actually a given curve obtained by measurements (or otherwise) and plotted in a Smith chart normalized to Z_0. It is in that case quite convenient to quickly draw the transformation circle for the extreme points of Z_L for various test values of Z_1. See Appendix A. As discussed later, that will tell us what the smallest possible VSWR can be for a given curve for Z_L. See Section B.6.

One might be tempted to assume that the presentation above terminates our education in matching. Actually, it is just about to begin. The real challenge is to combine any of the three tools above in a design that transforms the arbitrary impedance curve Z_L into a small cluster of impedance points located anywhere in the complex plane. There is in general no simple unique approach. In the author's opinion the best approach appears to be the graphical approach, as will now be illustrated with examples. (Oh yes, I admit for once, a little bit of experience is helpful as well.)

B.3 EXAMPLE: THE SINGLE SERIES STUB TUNER (NOT RECOMMENDED FOR BROADBAND APPLICATIONS)

Given: The load impedance Z_L as a function of frequency is shown in a Smith chart normalized to both 200 ohms and 100 ohms as shown in Fig. B.2. We are required to design a single series stub tuner as shown in the insert that transforms Z_L at the center frequency $f = 250\text{MHz}$ into 50 ohms. Based on that design at the center frequency we are next required to find the input impedance Z_{in} at the other frequencies.

Customarily one chooses the characteristic impedance Z_0 of the transmission line to be equal to the match impedance—that is, 50 ohms in our case. However, to illustrate a more general case for this type of matching we choose to use a characteristic impedance equal to 100 ohms. Thus we start with Z_L normalized
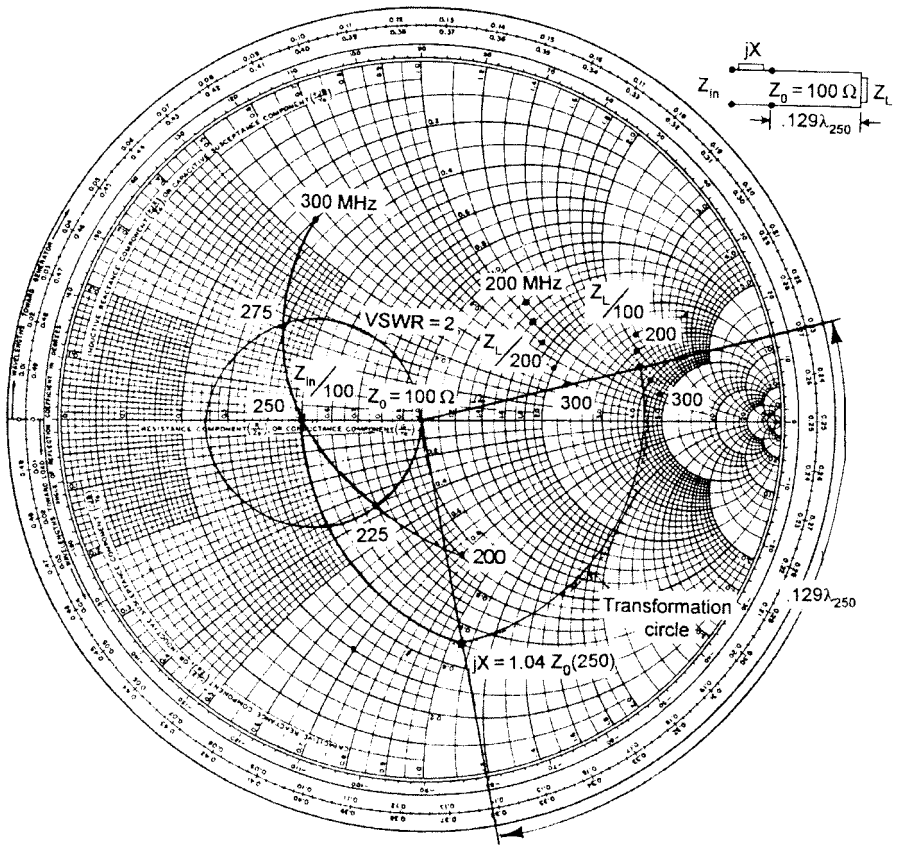
Fig. B.2 A load impedance Z_L is matched at the center frequency (250 MHz) to 50 ohms. The impedance Z_{in} is next obtained at the other frequencies as explained in the text. Not recommended for broadband applications.

to 100 ohms and rotate the value at $f = 250$ MHz until we intersect the constant resistance circle that goes through $\frac{1}{2} \cdot 100 = 50$ ohms (see Fig. B.1, column 1). As indicated in Fig. B.2, at the rim of the Smith chart this equals $0.129\lambda_{250}$. Finally, adding an inductance $jX = 1.04Z_0$ will bring the center frequency to $0.5Z_0 = 50$ ohms.

The other frequencies are determined by noting that their rotation in the Smith chart is proportional to the frequency—that is, $0.129 \cdot [(f/250\lambda)]$. Furthermore, we shall assume that the series reactance jX varies with frequency like an ideal lumped load; that is, it is also proportional to the frequency (stubs of transmission lines do not behave quite that simply). The final result is seen in the Smith chart normalized to $Z_0 = 100$ in Fig. B.2. The VSWR circle corresponding to 2 with respect to 50 ohms is also shown (see Problem B.2). Needless to say, broadbanded it ain't!

B.4 EXAMPLE: BROADBAND MATCHING

We are next going to match the same load impedance Z_L as shown in Fig. B.2 earlier. However, this time we will use a more sophisticated matching. A schematic of the network in question is shown at the bottom of Fig. B.3. (An example of a practical execution is shown later in Fig. B.8.)
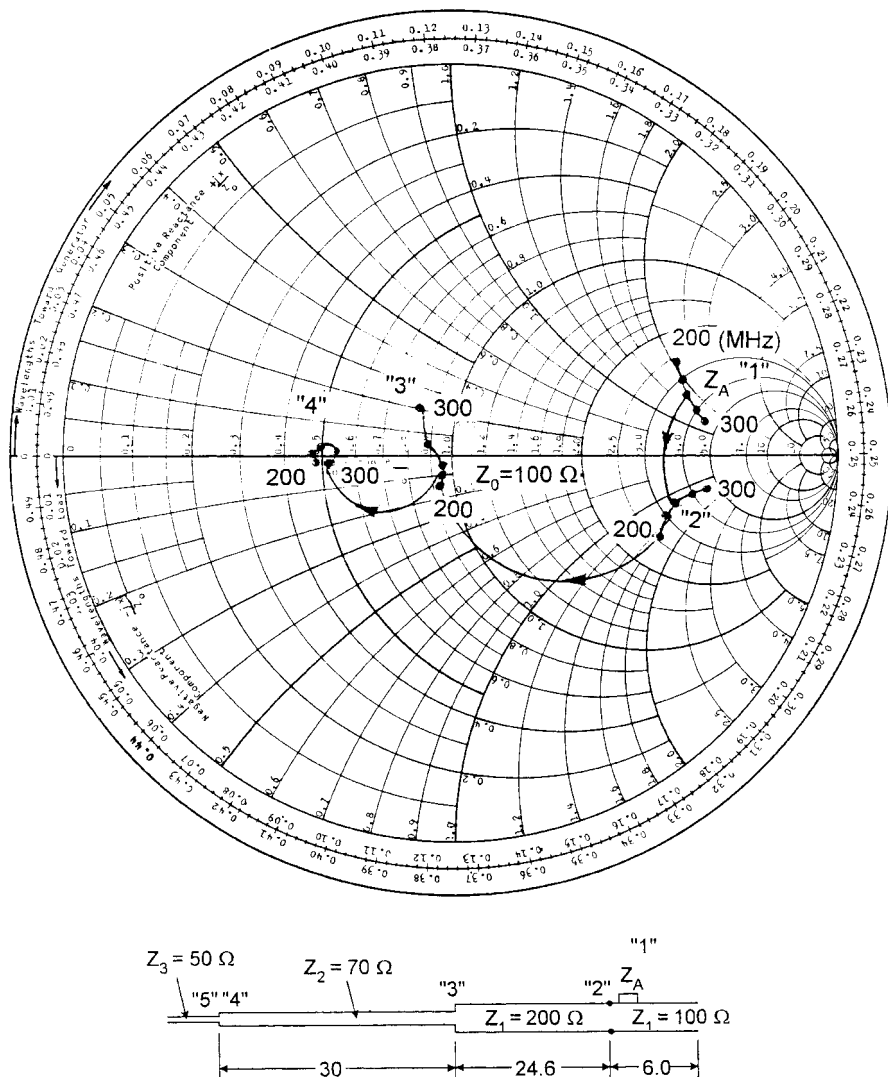
Fig. B.3 *The same load impedance Z_L as given in Fig. B.2 but this time matched by a broadband matching scheme shown in the insert below. Curve 4 denotes the desired input impedance. Compared to the curve obtained in Fig. B.2, the improvement is quite noticeable.*

Table B.1   Impedance Values for Fig. B.3

Frequency (MHz)	Z_A ("1") (ohms)	"2" (ohms)	"3" (ohms)	"4" (ohms)
200	$260 + j220$	$260 - j169.5$	$93.42 - j15.9$	$49.49 - j2.23$
225	$300 + j200$	$300 - j144.2$	$99.49 - j10.5$	$48.21 - j0.62$
250	$340 + j180$	$340 - j127.8$	$98.22 - j4.4$	$49.79 + j2.23$
275	$400 + j140$	$400 - j137.8$	$86.93 + j5.7$	$55.72 + j0.36$
300	$440 + j120$	$440 - j132.6$	$82.86 + j20.9$	$51.19 - j4.21$

We start calculating the input impedance Z_{stub} of the open-ended stub to the far right in the schematic. We have

$$Z_{\text{stub}} = j100 \cot \beta l_{\text{stub}}. \qquad (B.5)$$

When added in series with the load impedance Z_L curve 1, we obtain curve 2 (see Fig. B.1, column 1). We next transform curve 2 along a transmission line of length 24.6 cm and obtain curve 3, which again is transformed along a transmission line of length 30 cm yielding the final curve 4 (see Fig. B.1, column 3). Clearly, curve 4 in Fig. B.3 is far superior to the impedance curve in Fig. B.2 obtained earlier for a single series stub tuner (for details, see Table B.1). The obvious question is of course, Why the big difference?

The broadband concept was developed graphically. The fine-tuning was performed on the computer by Jonothan Pryor (like so many other items in this book). This would be a good place to start an optimization process.

B.5   THE "TRICKS"

When broadband matching, it is a fundamental rule that the original impedance curve 1 should as soon as possible be "reversed," which basically means that it should run the wrong way in the Smith chart—that is, counterclockwise. Statements to that effect will in general be met with strong objections, and they should! However, while it is true that an impedance curve will run clockwise as a function of frequency on the **average**, it is nevertheless possible for it to run backwards over a limited but still extensive frequency range. In fact, if we watch curve 2 in Fig. B.3 we observe that it does indeed run counterclockwise when watched from the center of the Smith chart (not if you watch it from a higher impedance to the right of the curve. Also note that curve 2 will run clockwise over a broader frequency range; that is, curve 2 merely has a loop).

The beauty of this situation becomes clear when we rotate curve 2 along the transmission line of length 24.6 cm. Since the rotations along the transformation circles are proportional to the frequency, the higher frequencies will travel further. However, since they are *behind* the lower frequencies (by virtue of reversing Z_L into curve 2), it becomes clear that curve 2 might be clustered together as they arrive at point 3. We observe this to be the case indeed; however, curve 3

has not landed at 50 ohms as desired and is also overcompensated (see later). For that reason we are inserting still another transmission line of length 30 cm and characteristic impedance 70 ohms. It serves two purposes: One is to transform curve 3 down to 50 ohms, the other is to obtain compression into the final impedance curve 4.

B.6   DISCUSSION

B.6.1   Overcompensation

Many questions remain to be answered. First of all, why don't we merely lower the characteristic impedance of the 24.6-cm transmission line from 200 ohms to, say, 160 ohms. That would land curve 3 closer to 50 ohms as illustrated in principle in Fig. B.4.

The typical problem with that suggestion might be that although the new transformation circles based on 160 ohms may appear in the figure to be as much apart from each other as the ones associated with 200 ohms, they might in effect lead to a curve 3 that is relatively wider than before because of the nature of the Smith chart (see also Problem B.2). But a more severe problem might be that the
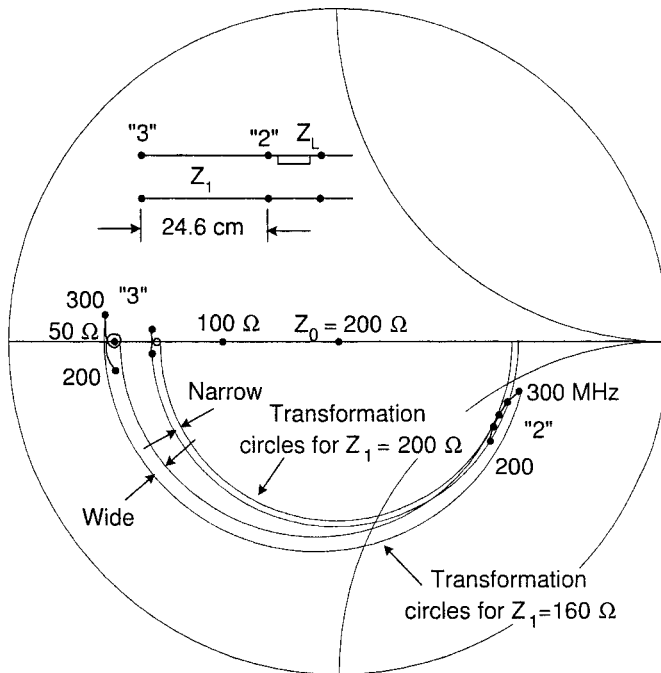
Fig. B.4   *By changing the characteristic impedance Z_1 from 200 ohms to 160 ohms, we can land "3" closer to 50 ohms but the curve is wider and more stretched out than the original. Note: Not to scale.*

higher frequencies now are too far ahead of the lower frequencies as shown in somewhat exaggerated fashion in Fig. B.4. Thus, this overcompensation must be corrected either by using an additional transmission line as already demonstrated or by using other matching tools from Fig. B.1.

Alternatively, as shown in Fig. B.5, one might suggest to keep the characteristic impedance equal to 200 ohms and then instead move curve 2 somewhat outward from the center along the constant resistance circles as illustrated in Fig. B.1, row 3, column 1. This could be accomplished by increasing the reactance of the open-ended stub for example by making it slightly shorter. The limitation of this approach is that curve 2 eventually will start bending the wrong way, leading to a wider spacing between the transforming circles and ultimately leading to a wider curve 3. In addition, curve 3 might end up being overcompensated as we saw earlier in Fig. B.4.

The conclusion of the discussion above is that curve 2 should be manipulated to produce transforming circles as close to each other as possible. That is not likely to land curve 3 at the right impedance level. This can subsequently be corrected by use of one or more transformations as explained above. Alternatively, other tools from Fig. B.1 can be used as discussed next.
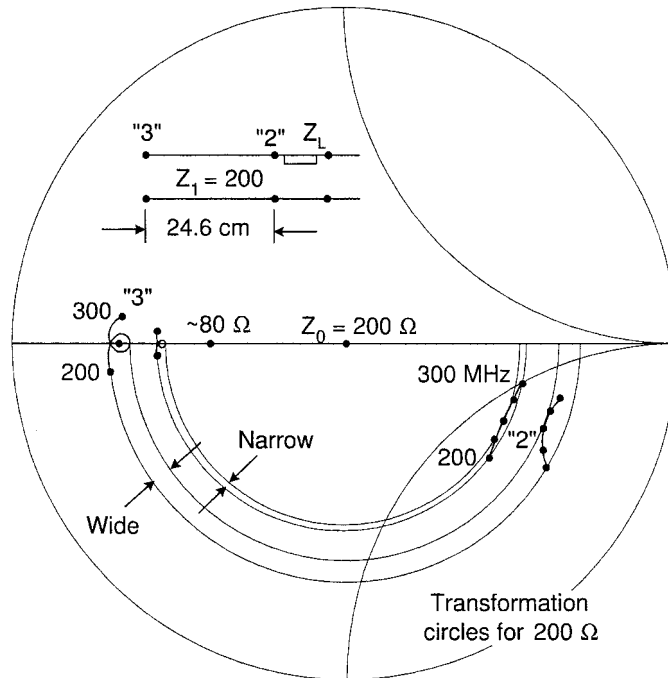
Fig. B.5   By increasing the reactance of the open stub to the far right in the schematic above, we typically bend curve ''2'' too much resulting in a new curve ''3'' closer to 50 ohms but too wide. Note: Not to scale.

Fig. B.6 If the high frequencies are behind the low ones, the impedance curve can be compressed by transformation through a transmission line with high characteristic impedance Z_1 as shown. Note: Not to scale.

B.6.2   How to Correct for Undercompensation

We saw above an example where the higher frequencies were ahead of the lower (overcompensation). The opposite might also be the case as shown in Fig. B.6. To correct for this dilemma, we may transform curve 3 through a transmission line with a characteristic impedance Z_1 that is higher than curve 3. If that does not land us in the desired area, more subsequent transformations might be necessary.

B.6.3   Alternative Approaches

An undercompensated curve 3 can also be compressed by an insertion of a series circuit or equivalent as shown in Fig. B.7 to the left. At the lower frequencies the series circuit is capacitive, which will move the lower frequencies of curve 3 toward the capacitive part of the Smith chart along the constant resistance circles (see Fig. B.1, row 3, column 1).

Similarly, an overcompensated curve 3 can be treated by placing a parallel LC circuit in parallel with the impedance curve 3 as shown in Fig. B.7, right. At the lower frequencies the LC circuit is inductive, which will push the lower frequencies of impedance curve 3 up toward the inductive part of the Smith chart. They will move along the circles going through (0, 0) in the Smith chart as shown in Fig. B.1, row 3, column 2.

Fig. B.7   *Undercompensation, shown to the left, can also be corrected by a series insertion of a series LC circuit or equivalent like an open-ended transmission line. Similarly, overcompensation, shown to the right, can be treated by insertion of a parallel circuit in parallel with "3".*

B.7   ON THE LOAD IMPEDANCE Z_L

So far not much has been said about the load impedance Z_L. However, after a couple of tries into the fine art of broadband matching, it soon becomes clear that Z_L just cannot be any impedance willy-nilly. The fundamental discovery is that since all the matching tools shown in Fig. B.1 or combinations thereof varies with frequency in a monotonic and predictable fashion, so must Z_L in order to obtain a final impedance confined to a small area in the complex plane. Thus, Z_L should vary in a *smooth* fashion with frequency; that is, there should be no sudden accelerations or de-accelerations as a function of frequency.

Furthermore, Z_L itself should have as much bandwidth as possible. When working with wire elements, this is typically accomplished by using a large wire diameter (remember the "Fat is beautiful" doctrine).

The physical explanation for this fact is simply that by using thick elements we are displacing or reducing the energy stored around the elements and that translates directly into a larger bandwidth (see also Section 6.12.1.1 and Appendix D).

Furthermore, the curve depicting Z_L should be shaped or curved the proper way. More precisely, after it is reversed (for example) as illustrated above, it should ideally follow a transformation circle as close as possible. This turns out to be one of the more intriguing tasks in broadband matching. Typically, the

antenna in question might be a single row of dipoles mounted side by side in the H plane; that is, the mutual coupling is strong. Recall now that the leading term in the mutual coupling between two elements with interelement spacing d is

$$Z_m \sim C \frac{e^{-j\beta d}}{d} \tag{B.6}$$

(C is a complex constant); that is, the mutual impedance can in principle be located anywhere in the complex plane. Consequently, when added to the self-impedance of a single element, it can for the proper spacing d actually bend the curve Z_L the "wrong" way in a limited band. The element spacing d must be chosen primarily for impedance reasons (typically around 0.5λ) and not for either maximum gain (0.7–0.8λ) or very small spacings as recommended in Chapter 6 for ultra-wide band but with higher VSWR. However, the author can recall an interesting case where six vertical dipoles each with their own separate reflector grids were mounted axially; that is, the mutual coupling was rather weak. In that case it was simply not possible to obtain an ideal Z_L. The problem was eventually solved in a somewhat unusual way. As stated above, each dipole was backed by an individual reflector grid made of four closely spaced vertical rods interconnected by four widely spaced horizontal runners. Normally, one must be careful that the grid openings are small enough that they do not start to resonate at the operating frequencies. In that event the overcoupled impedance from the grid openings can produce highly undesirable loops in the impedance curve for Z_L. In this case we did precisely that. By cutting away part of one of the horizontal runners, some reflector loops of twice the normal size were produced. As a result of that "undesirable" resonance, the curve for Z_L could be bent just enough to clear the spec (because we anticipated problems, we had agreed to a VSWR <1.05 only over 11% bandwidth).

Finally, it should be pointed out that Z_L also might be adjusted to the proper magnitude. In fact, Z_L as given in the example above is a bit too high, leading to a characteristic impedance of the first transformer equal to 200 ohms. While this value is fine when working with twin leads, it leads in general to an inner conductor too thin to be practical when we use a coaxial cable as shown in Fig. B.8. This is in general a relatively easy to fix when we recall that while the radiation resistance of a $\lambda/2$ dipole varies relatively little with its diameter, a full-wave dipole has a radiation resistance amounting to several thousand ohms for thin wire radii while it might be as low as a couple of hundred ohms for large wire radii [127]. Although our dipole is neither a half- nor a full-wave dipole but more somewhere around 0.7λ, its radiation resistance can easily be manipulated by the wire radius as well.

We may conclude from the discussion above that quite a considerable time and effort is often spent to manipulate the load impedance to be just right, or as it is sometimes expressed in the matching jargon, "Make sure it is born right." No question about it, experience plays a significant role in that development and there is no better way than to fight it out partly by hand in a Smith chart. Once a concept is developed, the fine-tuning can be done on the computer.

The load impedance Z_L is customarily obtained by measurement. In industry, nobody believes the calculations of thick dipoles except the guy who did them. Everybody believes measurements, except the guy who took them.

B.8 EXAMPLE OF A PRACTICAL EXECUTION

Many possibilities exist when reducing the matching scheme above to practice. One is shown in Fig. B.8. First of all the dipole has, as mentioned earlier, a total length of $\sim$0.7λ. If we plot the voltage (or potential) along such a long element, we observe that it is zero somewhere in the middle of each dipole half (see Fig. B.8). We may support these two halves at the neutral point and essentially leave the current and voltage distribution on the dipole unchanged. In addition, we can feed the dipole through one of these support structures (such an arrangement belongs to a class of baluns called "natural baluns;" see reference 116).

We further note that the open-ended stub to the far right in the schematic is placed inside the right dipole half (the length can be adjusted by moving a sleeve with a tool inserted through a hole in the end of the right dipole half). We next follow with the transmission lines of lengths 24.6 and 30 cm, respectively. They are executed in the form of coaxial lines placed inside the left dipole half. Typically one might, as in this case, resort to folding one (or more) of the cable sections in order to obtain a length sufficiently long to accommodate the required transformations.
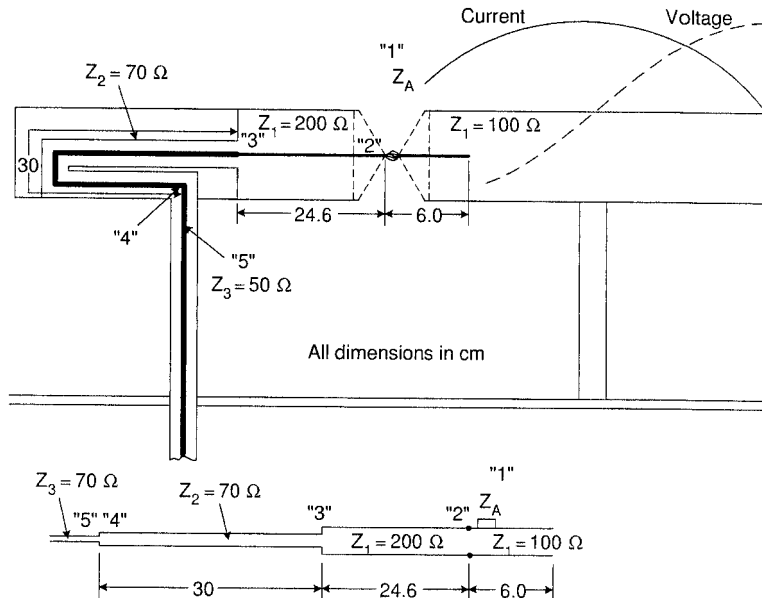
Fig. B.8 A practical execution of the broadband matching schematic shown in the insert. Consists of a dipole with total length $\sim$0.7λ and built-in matching network.

B.9   COMMON MISCONCEPTIONS

B.9.1   Should One Always Conjugate Match?

Many readers assume that two devices connected to each other should always be conjugate-matched. This is not necessarily the case. One should reflect upon the fact that conjugate matching means that the reactive parts of the two impedances simply cancel each other (in order to transfer maximum power) while the real parts are equal. As any fundamental textbook in circuit theory shows, this condition leads to maximum transfer of real power between the two impedances. What is not always pointed out is that since the two real parts are equal, the same amount of power will be lost in the generator resistance as is delivered to the receiver resistance. In other words, the efficiency is only 50% when we conjugate match. The reason for this omission is basically that nobody actually cares as long as we merely consider transfer of power at low levels as, for example, a receiving antenna connected to a receiving load. All we care about in that case is simply how to get maximum power into the receiver, not if some power is lost in the form of heat or reradiation in the process (there is no significant heat developed, nor is there a bill to be payed for energy lost or otherwise).

It is quite a different story if we work at high power levels. Take a typical power generator where we get paid for energy delivered to the users out there. If the combined resistance of these amounts to R_{user} and the generator resistance is denoted R_{gen}, then the power being paid for is $R_{\text{users}}I_{\text{gen}}^2$ while $R_{\text{gen}}I_{\text{gen}}^2$ represents loss that will not be paid for (at least not directly). Obviously it will be the aim of the generator designers to make R_{gen} as low as possible, and it is strongly recommended not even to attempt to conjugate match such a well-designed power generator. For one, you probably could not pay the bill and you most certainly would be arrested for attempted sabotage.

Admittedly, most readers of this book will in general have a limited interest in power generation (it is just a plug in the wall that is there when you need it). However, it becomes considerably more interesting if you must connect your antenna to a high-power transmitter. You will then find that the transmitter designers are quite interested in efficiency and as a result produce transmitters with internal impedances of just a few ohms. Any suggestion on your part of conjugate matching will be met with a stern lecture by the transmitter designers that the load connected to their transmitter better be just what they tell you and within rather narrow limits at that. In other words, a high-power transmitter can be somewhat temperamental and should not be tampered with (for one it is a nonlinear device and quite sophisticated).

As a result, there is in general a severe "mismatch" between a high-power transmitter and the antenna cable. The next question then becomes, "Is this of any relevance?:" The answer is, "Absolutely." Take, for example, a TV transmitting antenna that is connected to a high-power transmitter via a long cable of length l. Denoting the reflection coefficients between the cable and the antenna for Γ_{A} and between the cable and transmitter for Γ_{Tr} we readily see that the

relative level of the first ghost is given by $\Gamma_A \Gamma_{Tr} e^{-2j\beta l}$. In order not to see this ghost, it should be sufficiently low, depending on the time delay through the cable. For a typical cable length of a couple of hundred meters, it has been found to be around 38 dB. Furthermore, because of the poor match between transmitter and cable, we typically have $\Gamma_{Tr} \sim 2$ dB. Also, the single way cable loss may be ~ 2 dB; that is, we must require Γ_A to be ~ 32 dB corresponding to a VSWR ~ 1.05. Quite a responsibility on the frail shoulders of the antenna engineer. (For a receiving antenna with a much shorter cable the ghost level drops to typically ~ 26 dB. Furthermore, the reflection coefficient at the receiver with VSWR < 2 leads to $\Gamma_{Rec} < 10$ dB; that is, we must require a VSWR < 2 also for the antenna.)

But the most interesting situation for most readers is probably how to control the RCS of an antenna array. As explained in Chapter 2, Section 2.12, we must simply require the reflection coefficient between antenna and transmitter impedance to be as low as possible, which is in direct contradiction to the low transmitter impedance as discussed above. The problem is solved, for example, by use of circulators as explained in Section 2.12.2. An incident signal will in that case be perfectly absorbed by the load in port 3, while the transmitter independently is delivering power to the antenna without loss of power.

B.9.2   Can New Exotic Materials Be Churned Out by Running Backwards?

An impedance curve that runs counterclockwise in the Smith chart is likely to produce quite a commotion. In fact, this author is known for having thrown students out of his office on that account. However, one should be very careful to distinguish between an impedance curve that goes the wrong way at all frequencies and one that just exhibits a loop in a limited frequency range.[1] See also Section B.5.

If an impedance curve is shown over a reasonably large frequency range, a competent antenna engineer will usually size up the situation very quickly (here we have another good reason for plotting our impedance curve in the complex plane). However, if only a small frequency range is at hand, an inexperienced engineer or a computer could be misled into "thinking" we had discovered something new. The interpretation of this discovery appears to depend somewhat on one's background. Engineers may think they have discovered negative inductances and capacitances while physicists may interpret their observations as a new material with negative μ and $\in$. Many wonder if backward running "materials" can be designed at optical frequencies. Answer: Certainly! How: Left as an exercise for the student. Does the "material" really have negative μ and $\in$? Answer: No.

---

[1] This situation in no way violates Foster's reaction theorem [101], which applies only to *lossless* reactances while antenna impedances of radiating antennas are (or should be) lossy to represent radiated power.

B.10 CONCLUDING REMARKS

We have presented three basic matching tools as shown in Fig. B.1. We illustrated how to use these tools in a case where we matched a given impedance first by a single stub tuner and next by a broadband matching scheme where the given impedance was inverted, which basically means that it was running counterclockwise in the Smith chart over a limited frequency range. The improvement in VSWR amounted to more than an order of magnitude.

This presentation makes no claim to be complete. It was only intended to introduce the reader to the concept. In fact, the number of combinations of the matching tools is actually infinite. And like good music, the real beauty comes out when the various voices are blended together.

PROBLEMS

B.1 Prove that

$$Z_1 = \sqrt{Z_l \cdot Z_h}$$

where Z_l and Z_h are given by (B.2).

B.2 Prove that the voltage standing wave ratio is determined by the extreme impedances Z_l and Z_h (B.2) as

$$\text{VSWR} = \sqrt{\frac{Z_h}{Z_l}}$$

B.3 Design a broadband matching network for the terminal impedance shown in Fig. 5.36, bottom. This can actually be done simpler than the example treated in Fig. B.3. You may "land" the matched impedance anywhere on the real axis between 150 and 260 ohms.

Meander-Line Polarizers for Oblique Incidence

C.1 INTRODUCTION

A polarizer is a device that transforms a linear polarized wave into a circular polarized wave, or vice versa. The common principle is simply to decompose the incident field into two components where the phase of one is advanced and the other is delayed such that their difference is 90° while their amplitudes are the same. It appears that Pakan [128] was the first to utilize this principle. Later improvements were introduced by Lerner [129]. These devices were not of the meander-line type, as will be discussed here. These seem to appear first in a paper by Young et al. [130] and were subsequently improved by Epis [131]. Later, a paper by Terret et al. [132] discussed how to calculate the susceptance of a meander line. All of these contributions were primarily focused on normal angle of incidence while Chu and Lee [133] extended the calculation to include oblique angle of incidence. A recent contribution was supplied by Marino [134]. It was apparent that meander-line polarizers gradually deteriorate for higher angles of incidence. The present appendix will demonstrate that introduction of a "dielectric profile" can greatly improve this calamity.

   The general principle for a meander-line polarizer is illustrated in Fig. C.1, top. It consists of one (or more) sheet(s) of meander-line-shaped conductors usually printed on a circuit board. The E vector $\overline{E}^i$ of an incident plane wave is tilted 45° with respect to the principal axis of the meander line. It is decomposed into a vertical component $\overline{E}_v^i$ and a horizontal component $\overline{E}_h^i$. The equivalent circuit for the vertical component is a transmission line with a shunt inductance
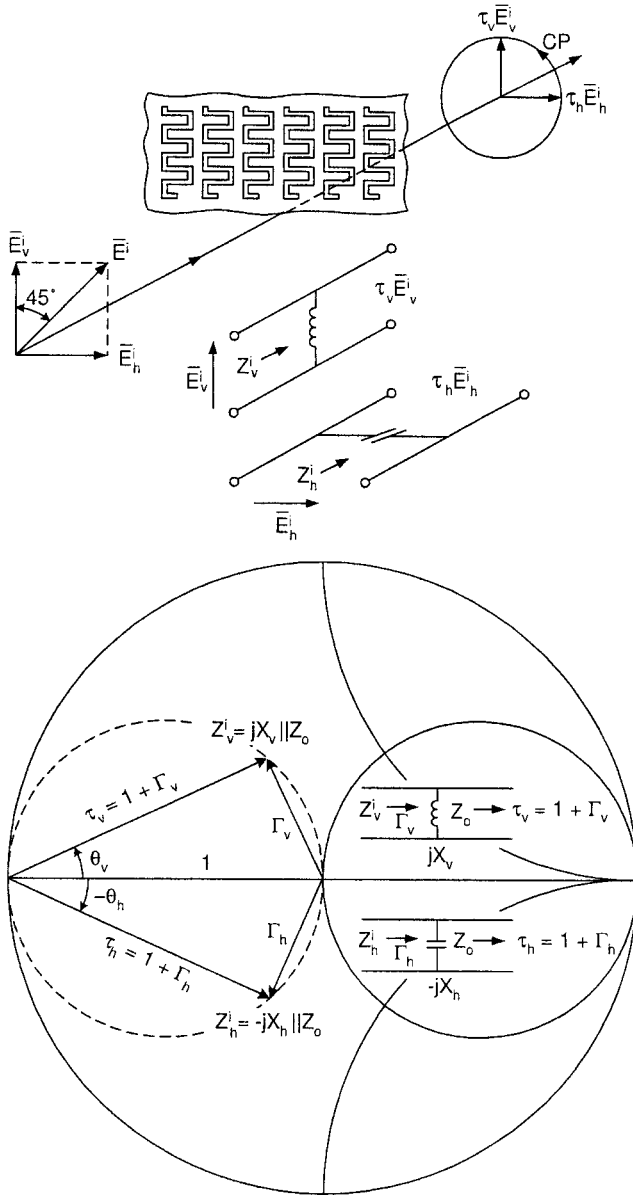
Fig. C.1   The workings of a singe meander-line polarizer. Top: A meander-line sheet acts as a shunt inductance for the vertical components and as a shunt capacitance for the horizontal components of an incident signal. Bottom: The vertical component of the incident field is reflected with reflection coefficient Γ_v and transmitted with the transmission coefficient $\tau_v = 1 + \Gamma_v$ as shown in the Smith chart. Similarly, the horizontal component is reflected and transmitted with reflection coefficient Γ_h and transmission coefficient $\tau_h = 1 + \Gamma_h$, respectively.

as illustrated in Fig. C.1, middle, while the equivalent circuit for the horizontal component is a transmission line with a shunt capacitor, as also illustrated in the same figure.

Let us denote the reactance of the equivalent inductance by jX_v and that of the equivalent capacitance by $-jX_h$ as indicated in the insert of the Smith chart, Fig. C.1, bottom. Then the input impedances for the two components are going to be $Z_v^i = jX_v \parallel Z_0$ and $Z_v^i = -jX_h \parallel Z_0$, respectively. These two values are also indicated in the Smith chart, and we note that they are located on the great circle passing through $(0, 0)$ and the center of the Smith chart (for details consult Appendix B). We now further remind the reader that one of the many beautiful features of the Smith chart is that the distance from the center to the respective input impedances located in the Smith chart simply constitute the reflection coefficients Γ_v and Γ_h, respectively, as also indicated in the same Smith chart (the phase is measured from the horizontal line going right). Finally, the transmission coefficients $\tau_v = 1 + \Gamma_v$ and $\tau_h = 1 + \Gamma_h$ are obtained by simple vector addition of the respective reflection coefficients and "1," namely, the radius of the Smith chart as also indicated. Again, the phase angles θ_v and $-\theta_h$ of the respective transmission coefficients are measured from the horizontal line. The total phase difference between these two transmitted components is seen to be $\theta_v + \theta_h$. When the difference is 90° and if $|\tau_v| = |\tau_h|$, the total transmitted field will be circular polarized.

There will also be a reflected field. The vertical and horizontal components have amplitudes and phases given simply by Γ_v and Γ_h, respectively. In general this reflected field will be elliptic polarized. What is of concern, however, is the fact that when a single meander-line sheet transmits a perfect circular polarized field, we readily see from the Smith chart that $|\Gamma_v| = |\tau_v| = |\Gamma_h| = |\tau_h|$. In other words: A single meander-line sheet will produce a reflected field of the same amplitude as the transmitted field; that is, the efficiency is only 50%. The remedy for this calamity is to use several meander-line sheets cascaded after each other as will be discussed in the next section. See also Problem C.1, where you are asked to consider a two-sheet meander-line polarizer.

C.2   MULTILAYERED MEANDER-LINE POLARIZERS

Use of two or more meander-line sheets can, if designed correctly, result in much improved performance. An example consisting of three sheets is shown in Fig. C.2, middle, where we show the equivalent circuit for the vertical component only. We shall start our analysis from the back, where the impedance at point 1 is equal to $jX_3 \parallel Z_0$ as indicated in the Smith chart at the top. This point is now rotated to point 2, corresponding to the sheet separation d_3. We next add the sheet impedance jX_2 in parallel and arrive at point 3. Note that in order to preserve "symmetry" we choose $jX_2 \sim \frac{1}{2}jX_3$. This will bring point 3 to a position similar to point 1 (in general all "inside" sheets should have a susceptance twice as large as the two "outside" sheets). This simply means that the transmission angle θ_{v2}
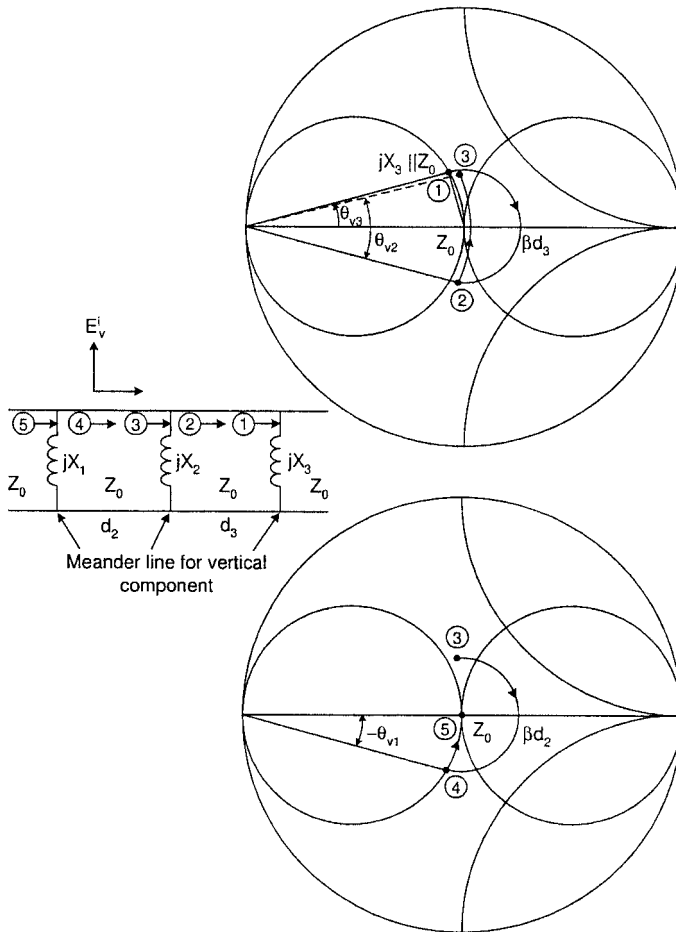
Fig. C.2 *By cascading two or more meander-line sheets, we may obtain broader bandwidth and lower reflection. The Smith charts show the input impedances at the various locations as indicated in the schematic.*

of sheet 2 is about twice as large as the transmission angles $\theta_{v1} = \theta_{v3}$ of sheets 1 and 3, respectively.

We next rotate point 3 into point 4, corresponding to the sheet separation d_2 as shown in the Smith chart, bottom. Finally, adding sheet reactance jX_1 in parallel brings us to point 5 located at the center of the Smith chart; that is, we should now have practically nothing reflected from this three-layered design, in contrast to the single meander-line case discussed above.

In order to obtain a phase advance of $45°$ for the vertical component only, we must require

$$\theta_{v1} + \theta_{v2} + \theta_{v3} = 45°,$$

where $\theta_{v2} \sim 2\theta_{v1} \sim 2\theta_{v3}$, that is,

$$\theta_{v1} = \theta_{v3} = \frac{45°}{4} = 11,25°,$$

$$\theta_{v2} = 22.5°.$$

Note: In addition to the phase advance of 45° for the vertical component, there will also be a delay from the sheet separations d_2 and d_3. However, this delay will also be experienced by the horizontal component (that is, also delayed 45° due to the capacitive effect). Thus, the net phase difference between the two components is still going to be 90° as desired. In the following we shall show various designs. They differ essentially by the distance between the sheets as well as by the dielectric constant of the spaces that typically ranges from air to $\varepsilon_r \sim 2$.

C.3   INDIVIDUAL MEANDER-LINE IMPEDANCES

The impedance of the outer meander-line sheet including the free space Z_0 behind the individual sheets is shown in the Smith chart in Fig. C.3 for the vertical as well as the horizontal components. Similarly, we show the impedances for the inner meander-line sheets including Z_0 in the Smith chart shown in Fig. C.4. We observe that both the vertical and horizontal components vary with frequency; however, the angular difference between the transmission coefficients for the two components remains reasonably constant with frequency. This feature is quite essential for producing polarizer designs with a large frequency range.

We also note that the angles of the transmission coefficient for the inner meander lines are approximately twice that for the outer meander lines, as they should be (see discussion above). The meander-line dimensions are given in the respective Smith charts. We observe that both of these designs have the same dimensions D_x and D_z, and so on. This is done so as not to violate Floquet's Theorem (see reference 26). The differences in impedances are obtained by using different line widths w in the two cases.

We further note that all the meander lines are encapsulated by dielectric sheets ("underwear") of thickness 2×20 mils and relative dielectric constant $\varepsilon_r = 2.2$.

To assist in designing the proper meander-line sheets, we show in Fig. C.5 the typical impedance variance as a function of the strip width w and meander-line spacings D_x. Note that the variation is one-sided as a function of the strip width w and symmetric with meander-line spacing D_x.

C.4   DESIGN 1

Meander-Line Sheet Separation: $\sim\lambda_0/4$
Dielectric: Air
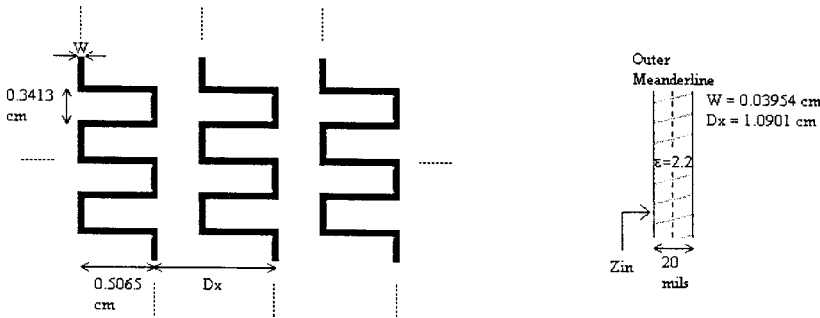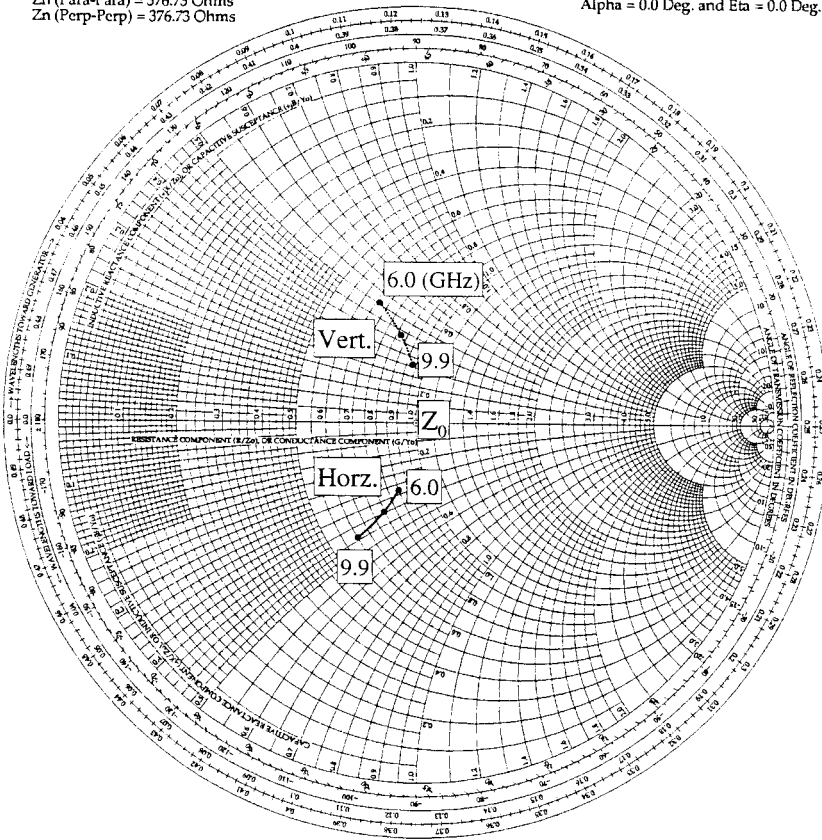
Fig. C.3 The input impedance of a single encapsulated meander line (outer) including free space Z_0 behind. Vertical as well as horizontal cases.

This design is comprised of three meander-line sheets separated by air of thickness 0.8657 cm, as shown at the bottom of Fig. C.6. At $f = 8.7$ GHz this corresponds to a separation of $\sim\lambda_0/4$. However, when incorporating the dielectric substrate around the meander lines, an effective quarter-wave separation is obtained at

Para-Para Pol. (Solid) / Perp-Perp Pol. (Dashed)
Zn (Para-Para) = 376.73 Ohms
Zn (Perp-Perp) = 376.73 Ohms

Frequency Range: 6.0 GHz - 9.9 GHz
Alpha = 0.0 Deg. and Eta = 0.0 Deg.
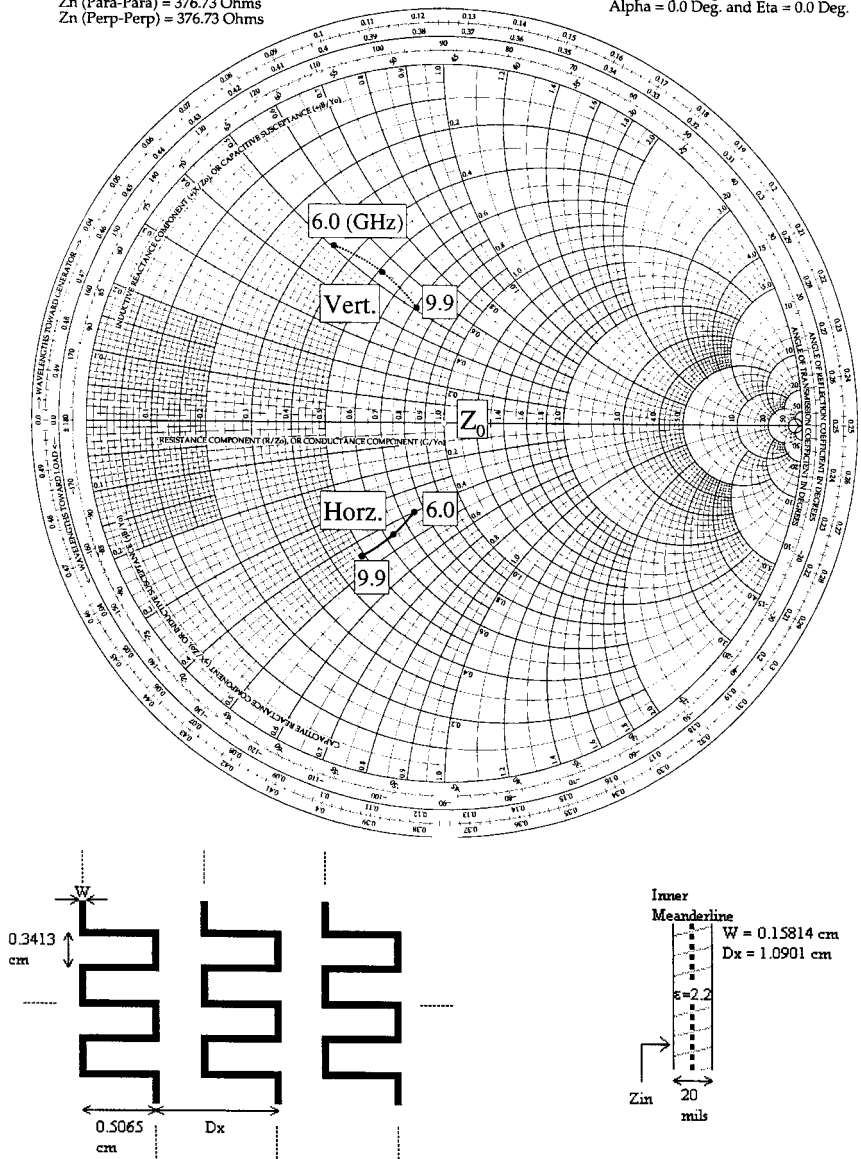
Fig. C.4   The input impedance of a single encapsulated meander line (inner) including free space Z_0 behind. Vertical as well as horizontal cases.

$f \sim 7.4$ GHz. At the top of Fig. C.6 we show the ratio between the vertical and horizontal components of the transmitted field as a function of frequency for various angles of incidence. Similarly, we show the phase difference between the two components in the middle of Fig. C.6.
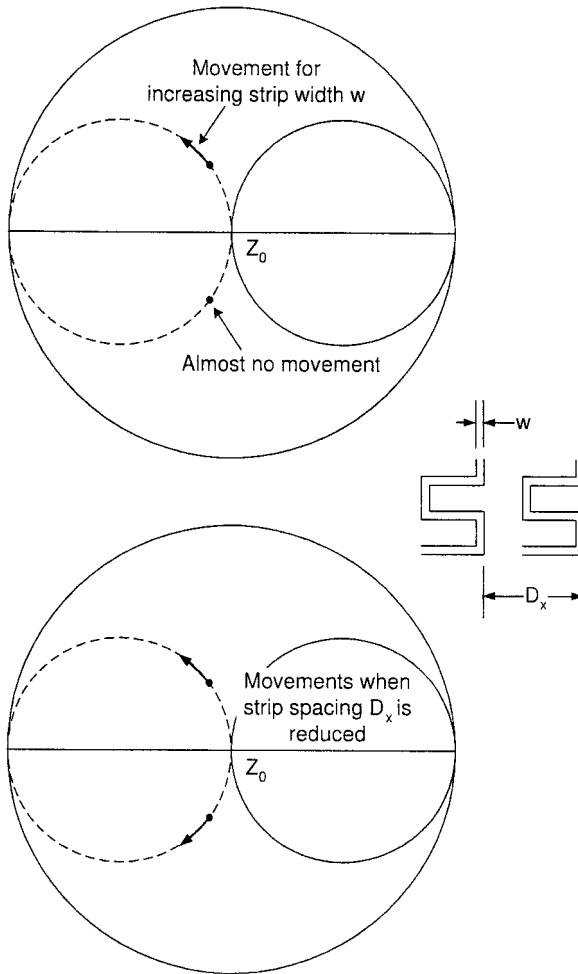
Fig. C.5 Typical movement of the meander-line impedance including free space Z_0 for: Top: Variation of line width w; Bottom: Variation of line spacing D_x.

We observe a variation in amplitude ratio of less than 1.12 and a phase variation of less than $15°$ for normal angle of incidence. This corresponds to a cross polarization of less than ~ 17 dB.

However, at $60°$ angle of incidence we observe a serious deterioration of the amplitude ratio toward the lower frequencies, although it held up quite well at the higher frequencies.

The reason for this dilemma is simply that the electrical separation between the meander-line sheets typically is given by $\beta_0 \, d r_{0y}$ (d is the physical separation). Thus, at $60°$ the electrical separation will be reduced by a factor of $1/\cos 60° = 2$, making the electrical separation approximately correct at the higher frequencies
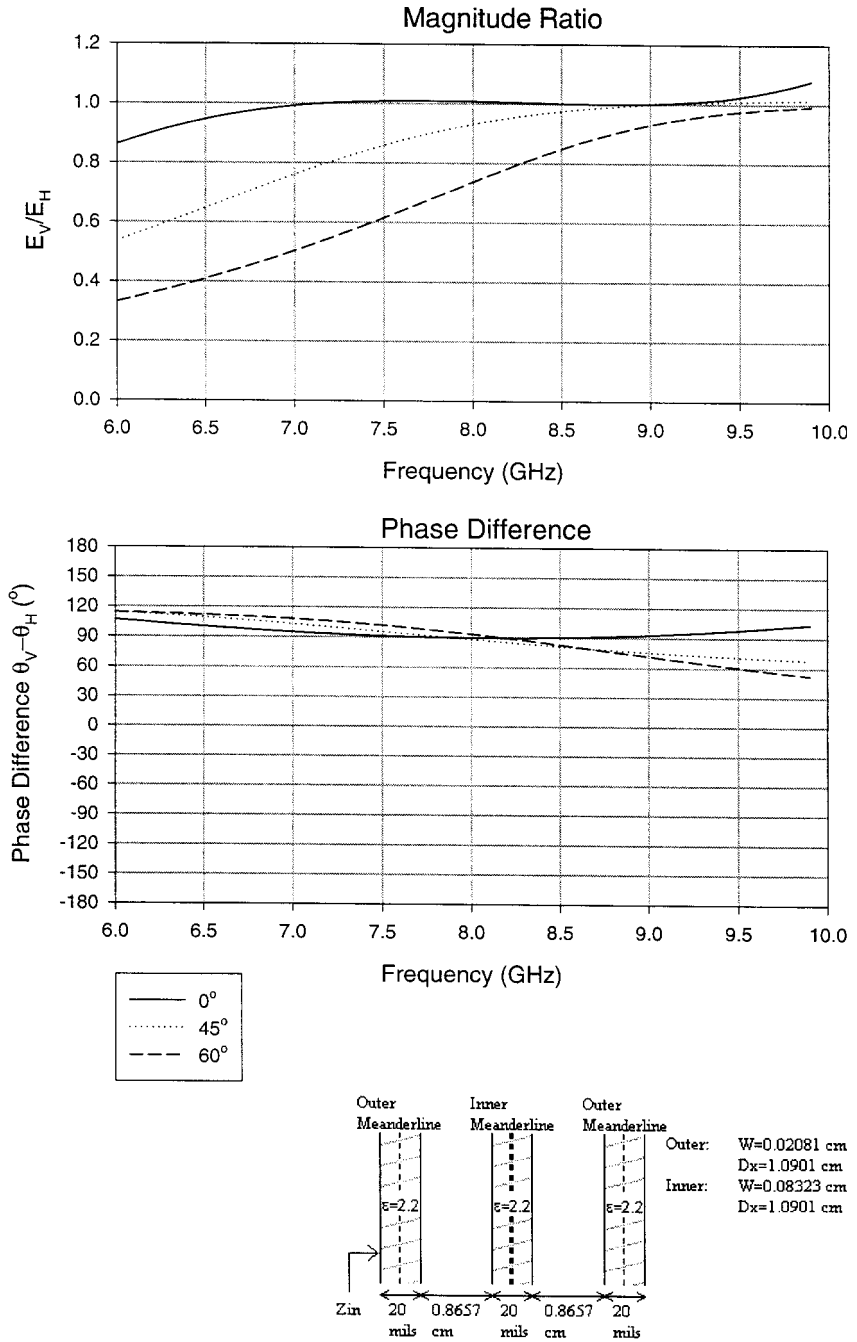
Fig. C.6   Design 1. Three encapsulated meander-line sheets without dielectric. Top: The magnitude ratio E_v/E_h as a function of frequency. Bottom: The phase difference $\theta_v - \theta_h$ as a function of frequency.
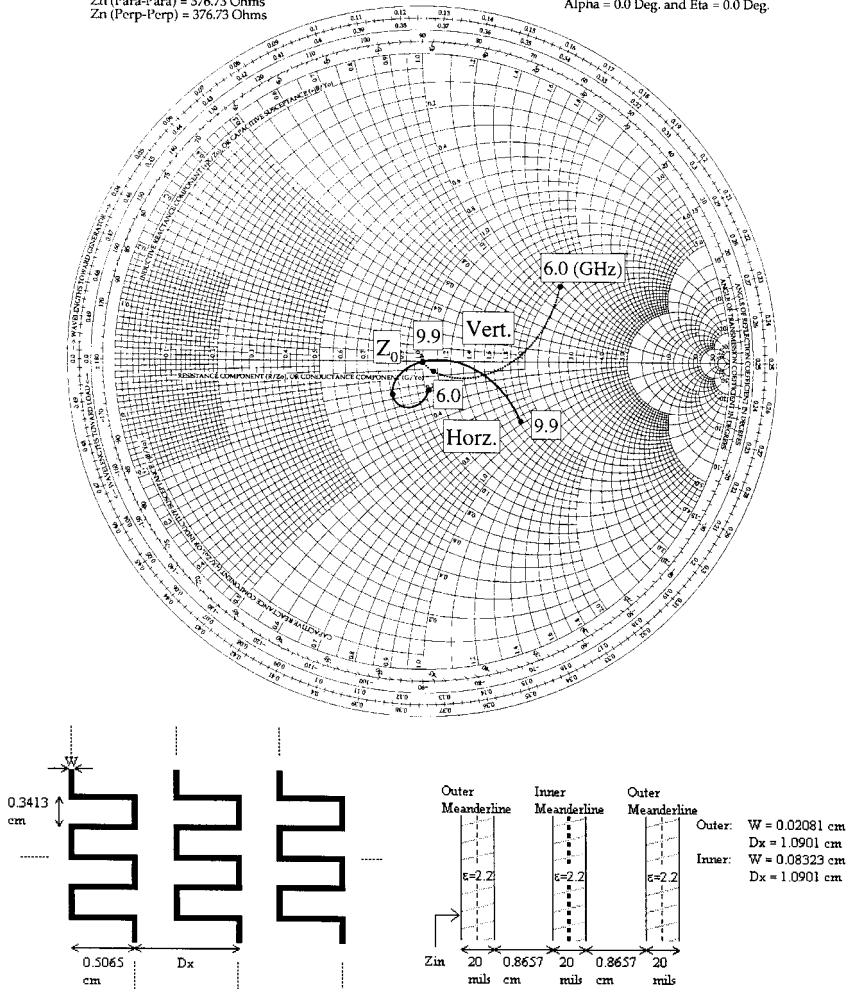
Fig. C.7 Design 1. Three encapsulated meander-line sheets without dielectric. Input imped-ances for the vertical as well as the horizontal field component.

but much too small at lower frequencies. Finally we show in Fig. C.7 the input impedances of the vertical and horizontal field components for the entire polarizer at normal angle of incidence.

C.5   DESIGN 2

Meander-Line Sheet Separation: $>\lambda_0/4$
Dielectric: Air

We just observed how Design 1 fails at the lower frequencies at higher angles of incidence because the factor r_{0y} becomes less than one. In Design 2 we shall attempt to correct for this discrepancy simply by increasing the meander-line sheet separation.

More specifically, the meander-line sheet separation is increased from 0.8657 cm to 0.9996 cm. It does indeed lead to some improvement in phase response at the lower frequencies but also to some degradation at the higher frequencies for normal angle of incidence. Thus, it is clear that a more radical treatment is needed. Since space is limited in this book, we have chosen simply not to show the results for this design.

C.6   DESIGN 3

Meander-Line Sheet Separation: $\sim\lambda/4$ in Dielectric
Dielectric Constant of Spacers: $\varepsilon_{r1} = \varepsilon_{r2} = 2.0$

In this design we will use dielectric slabs, rather than air, between the meander-line sheets as shown in Fig. C.8, bottom. The idea is simply that the electrical spacing in that case will be given by $\beta_2 d_2 r_{2y}$, where r_{2y} is the cosine to the angle of incidence inside the dielectric slab d_2. Thus as a consequence of Snell's law r_{2y} will vary considerably less than r_{0y} in free space. In other words, We expect to obtain a more stable design with angle of incidence when using dielectric slabs instead of air. Indeed, the amplitude ratio shown in Fig. C.8, top, shows a significant improvement compared with nondielectric design 2, not shown. However, we also note that the phase difference shown in Fig. C.8, middle, is about $15°$ short of $90°$, although it is very constant as a function of frequency.

The reason for this "shortage" of phase difference is that when we use dielectric spacers, we lower the intrinsic impedance by $\sqrt{\varepsilon_r}$. This simply implies that the meander-line impedances must also be lowered accordingly as will be demonstrated in the next design.

Finally, we show the input impedances for the vertical and horizontal field components in Fig. C.9. Note that the "center of gravity" is somewhat below Z_0, which supports the statements made above.

C.7   DESIGN 4

Meander-Line Sheet Separation: $\sim\lambda/4$ in Dielectric
Dielectric Constant of Spacers: $\varepsilon_{r1} = \varepsilon_{r2} = 2.0$
Meander-Line Impedances Lowered

Magnitude Ratio
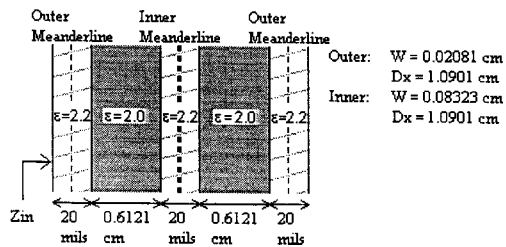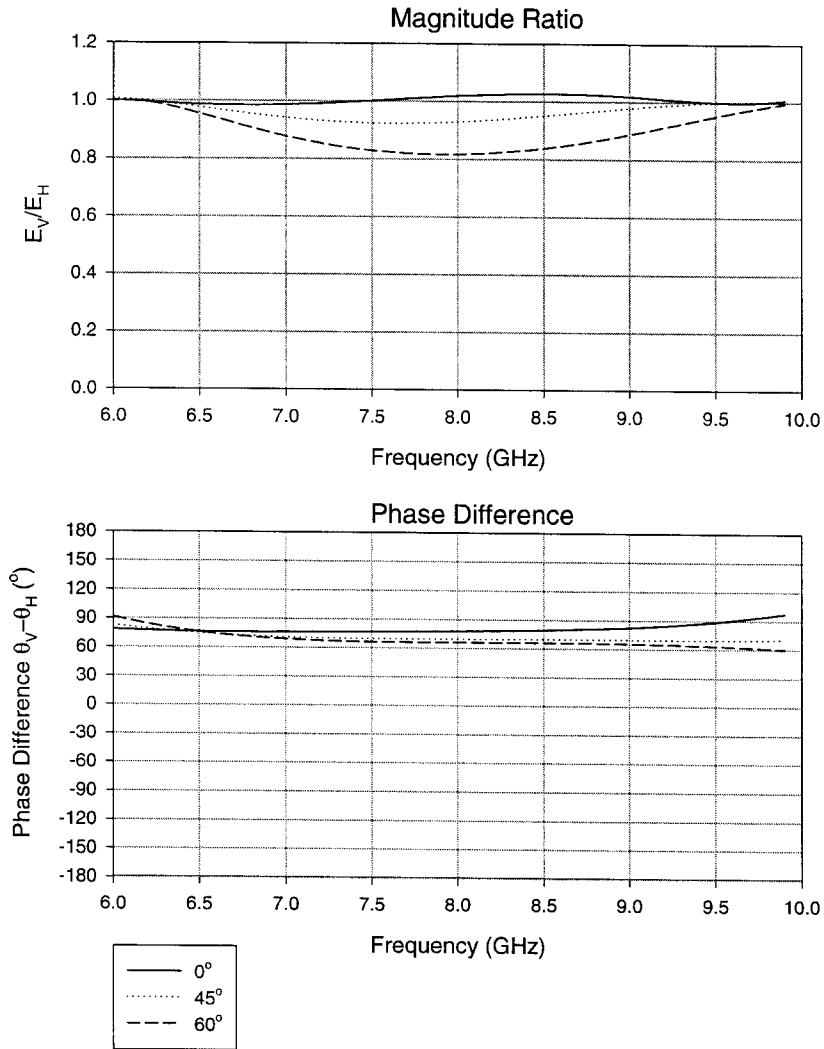
Phase Difference

Fig. C.8 Design 3. Three encapsulated meander-line sheets with dielectric separation. Top: The magnitude ratio E_v/E_h as a function of frequency. Bottom: The phase difference $\theta_v - \theta_h$ as a function of frequency.
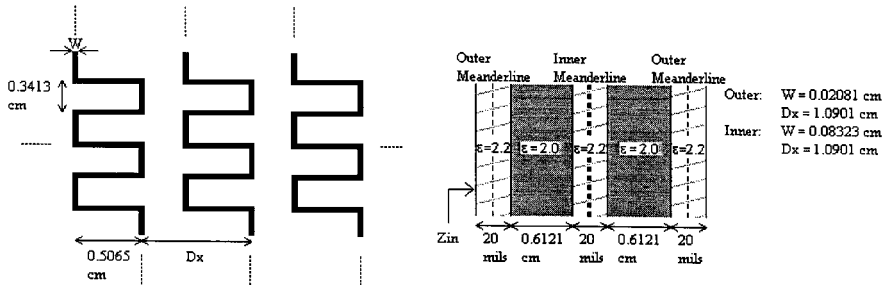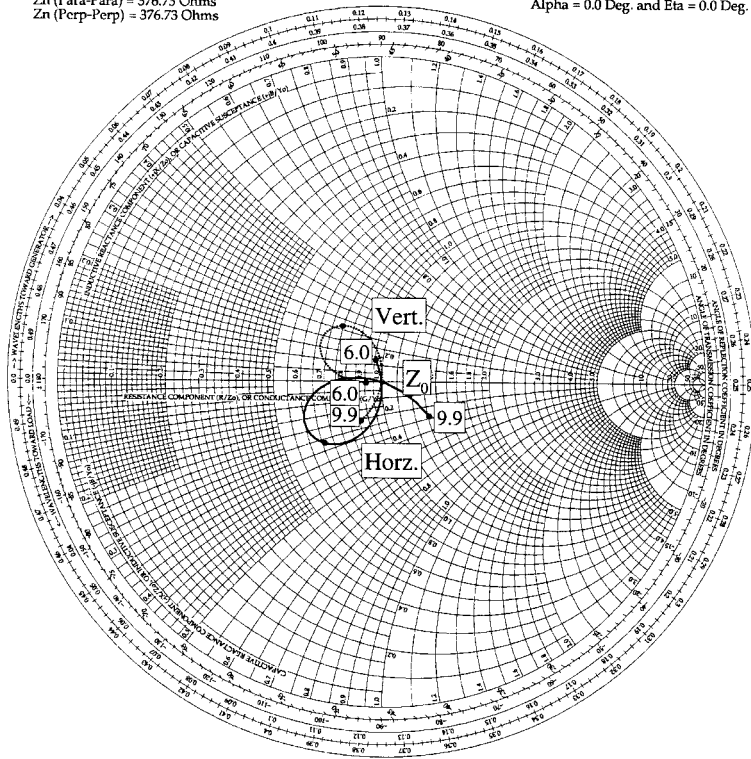
Fig. C.9   Design 3. Three encapsulated meander-line sheets with dielectric separation. Input impedances for the vertical as well as the horizontal field components.

This design has the same dielectric profile as Design 3, but the meander-line impedances have been reduced. This has been accomplished for the outer meander lines by simply increasing the line width *w* of the meander lines from 0.02081 cm to 0.03954 cm while all other dimensions remain the same. A plot of the outer meander-line sheet incorporating a dielectric slab is shown in Fig. C.10. It should be compared with the original meander-line sheet in Fig. C.3 except that the dielectric slab rotates the impedance approximately 90° clockwise (on the
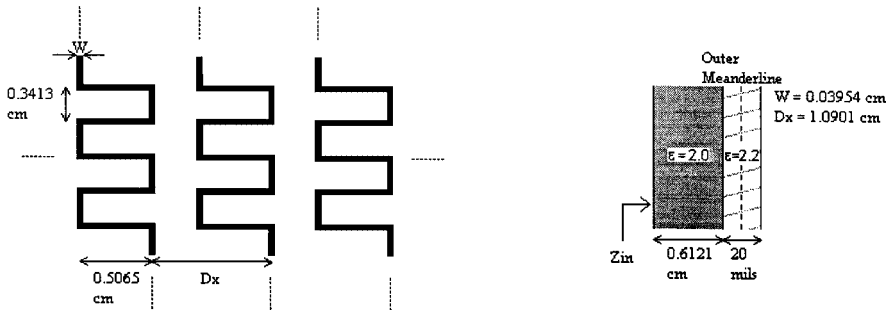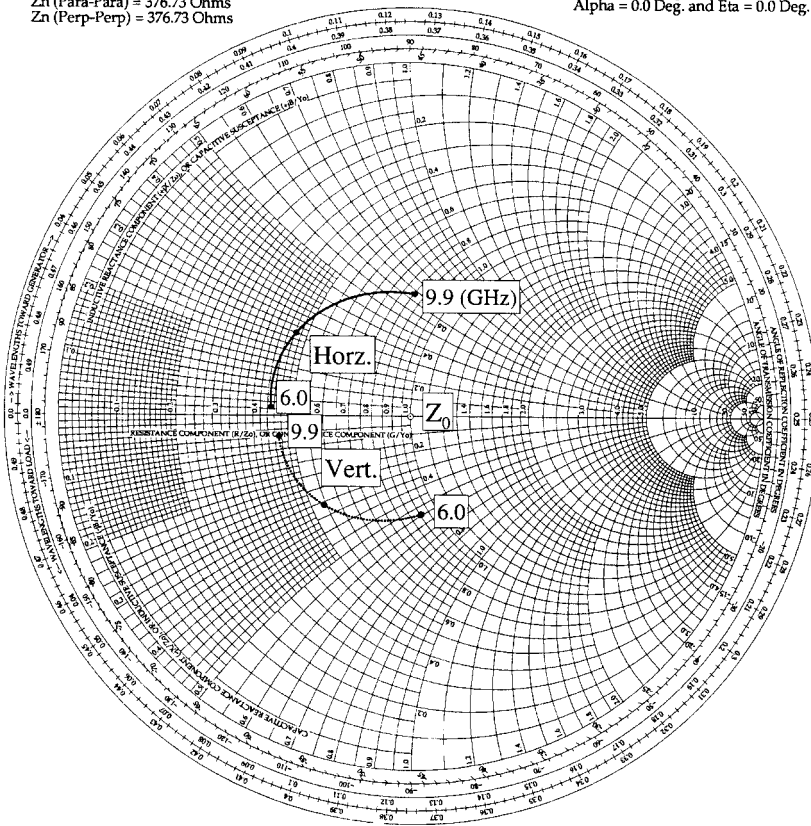
Fig. C.10   Design 4. Input impedances (vertical and horizontal) of a single meander line (outer) including free space Z_0 behind and a dielectric slab in front.

average). Similarly, the impedance of the inner meander-line has been lowered by increasing its line width from 0.08323 cm to 0.15814 cm while all other dimensions remain the same. The input impedances of the outer and an inner meander line are shown in Fig. C.11, while the addition of the next dielectric slab is

Para-Para Pol. (Solid) / Perp-Perp Pol. (Dashed)
Zn (Para-Para) = 376.73 Ohms
Zn (Perp-Perp) = 376.73 Ohms

Frequency Range: 6.0 GHz - 9.9 GHz
Alpha = 0.0 Deg. and Eta = 0.0 Deg.
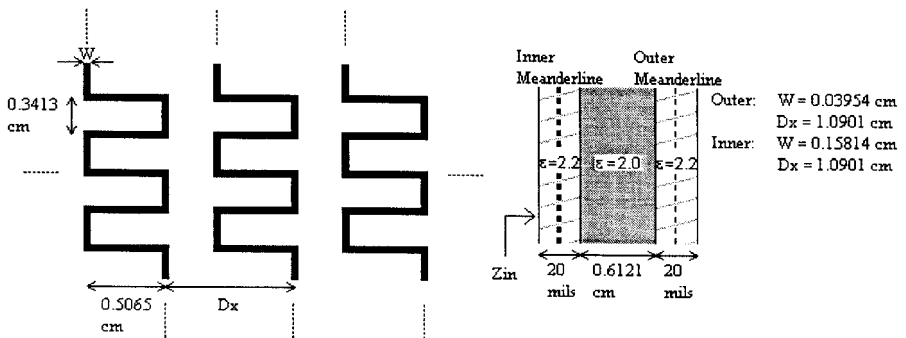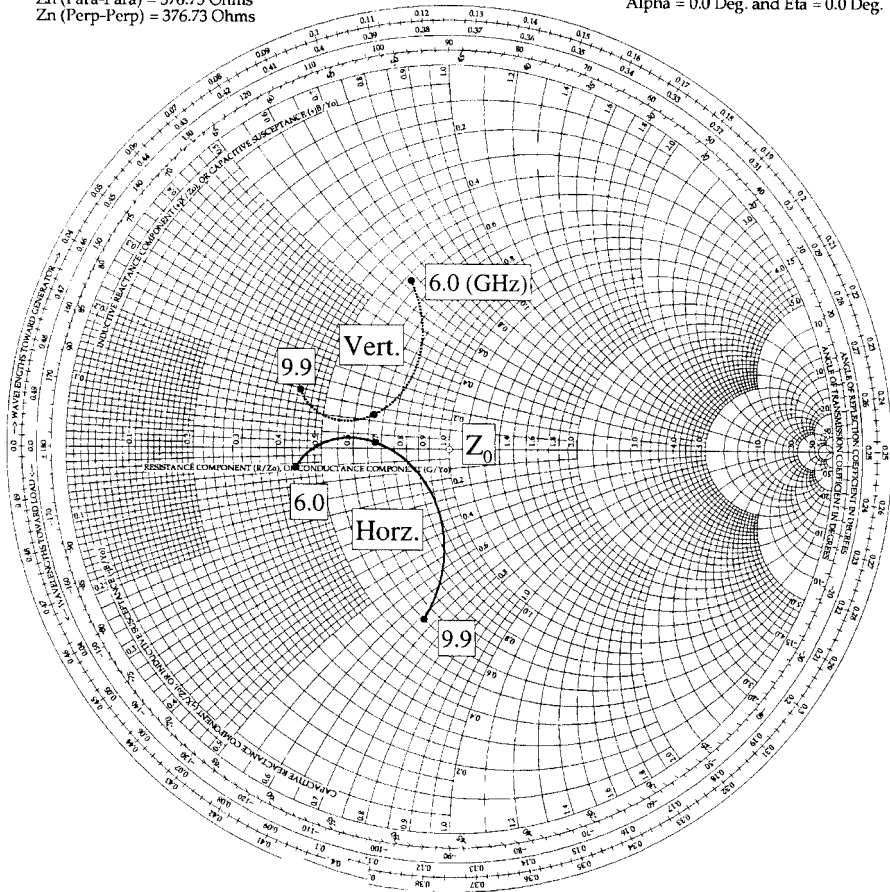
Fig. C.11 *Design 4. Input impedances (vertical and horizontal) of two meander lines separated by a dielectric slab.*
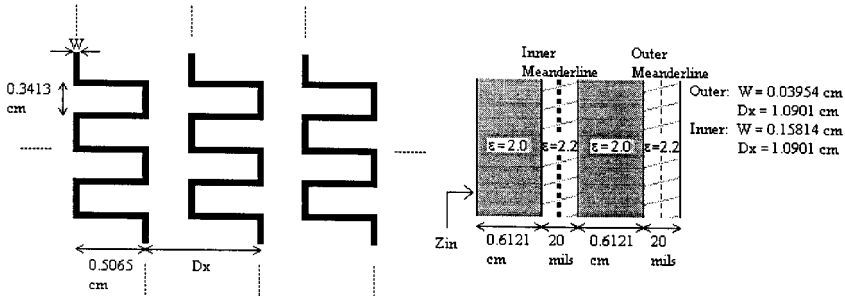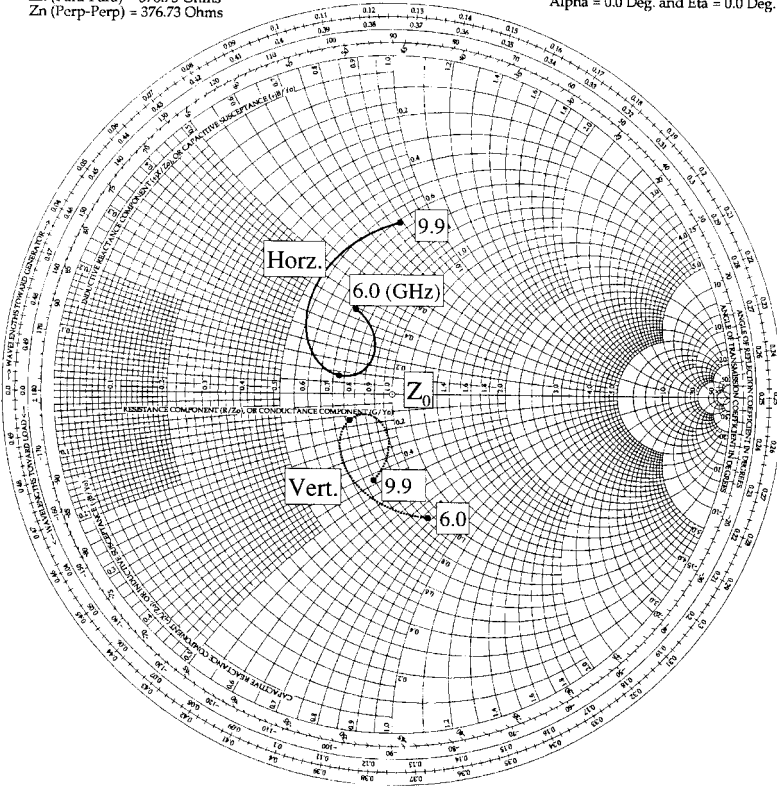
Fig. C.12   Design 4. Input impedances (vertical and horizontal) for two cascaded meander-line sheets and two dielectric slabs as shown.

shown in Fig. C.12. Finally, in Fig. C.13 we have added the last outer meander line. Note here the input impedance remains close to Z_0 over a considerable bandwidth. Thus, it should not surprise us that the amplitude ratio as well as the phase difference shown in Fig. C.14 looks almost perfect for normal angle of incidence and "not bad" for oblique angle of incidence.

However, further improvement is possible, as we shall see next.
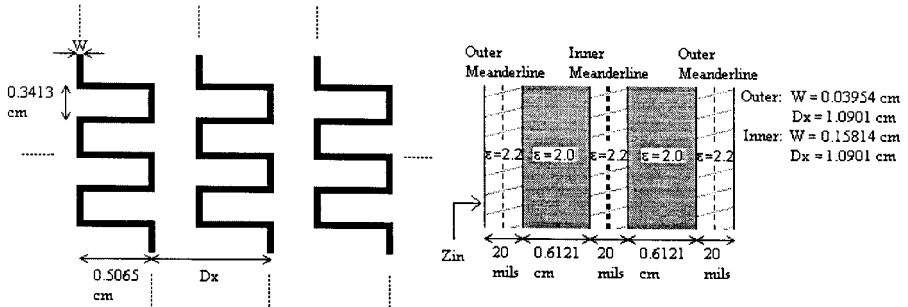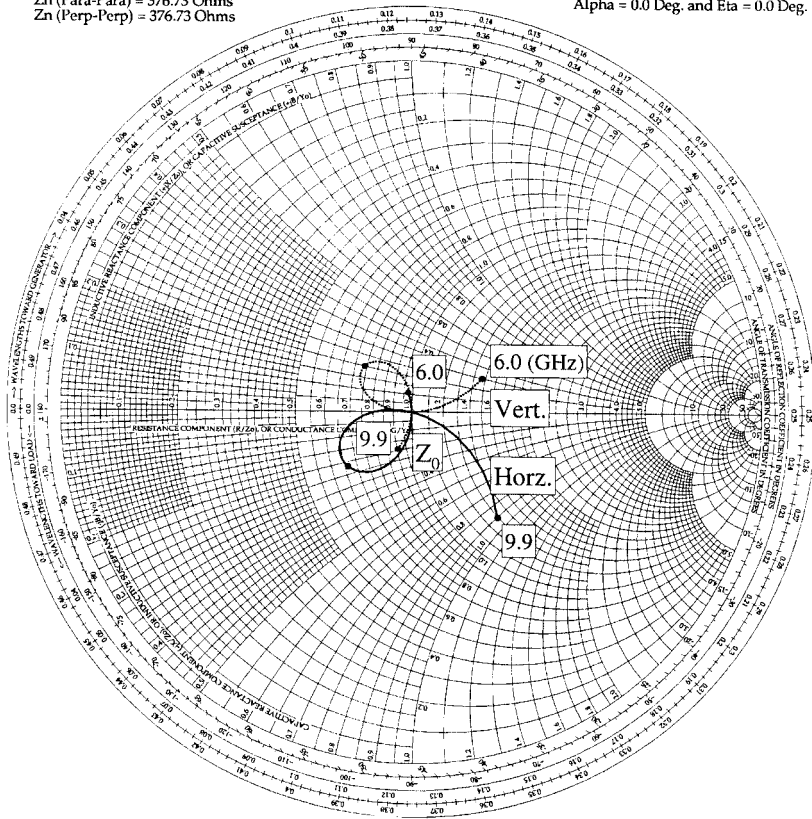
Fig. C.13 Design 4. Input impedances (vertical and horizontal) for three cascaded meander-line sheets separated by dielectric spacers as shown.

C.8 DESIGN 5

Meander-Line Sheet Separation: $\sim\lambda/4$ in Dielectric

Dielectric Constant of Spacers: $\varepsilon_{r1} = \varepsilon_{r2} = 2.0$

Magnitude Ratio
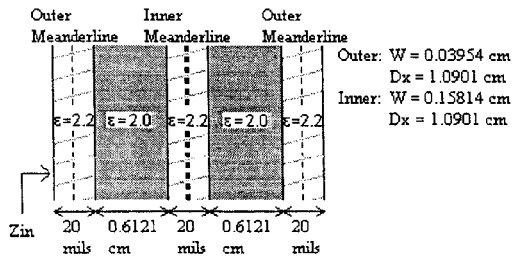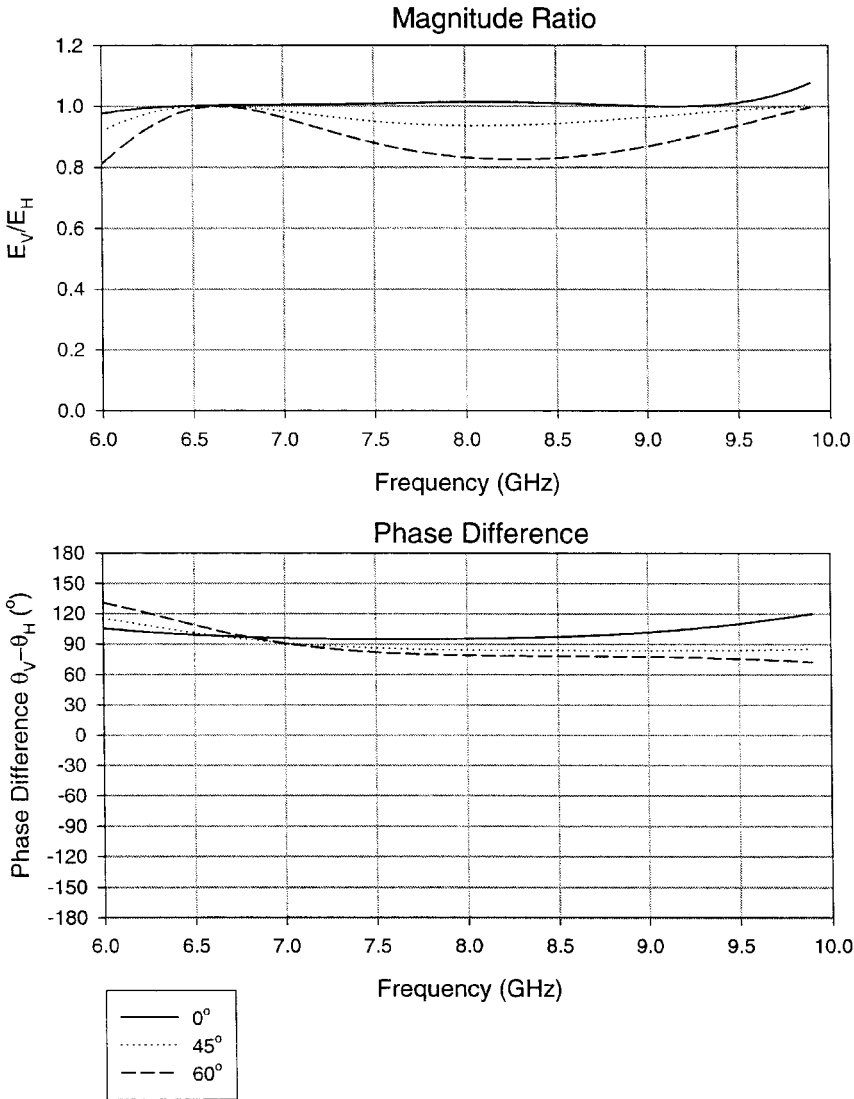
Phase Difference

Fig. C.14 *Three meander-line sheets separated by dielectric slabs. Top: The amplitude ratio E_v/E_h as a function of frequency. Bottom: The phase difference $\theta_v - \theta_h$ as a function of frequency.*
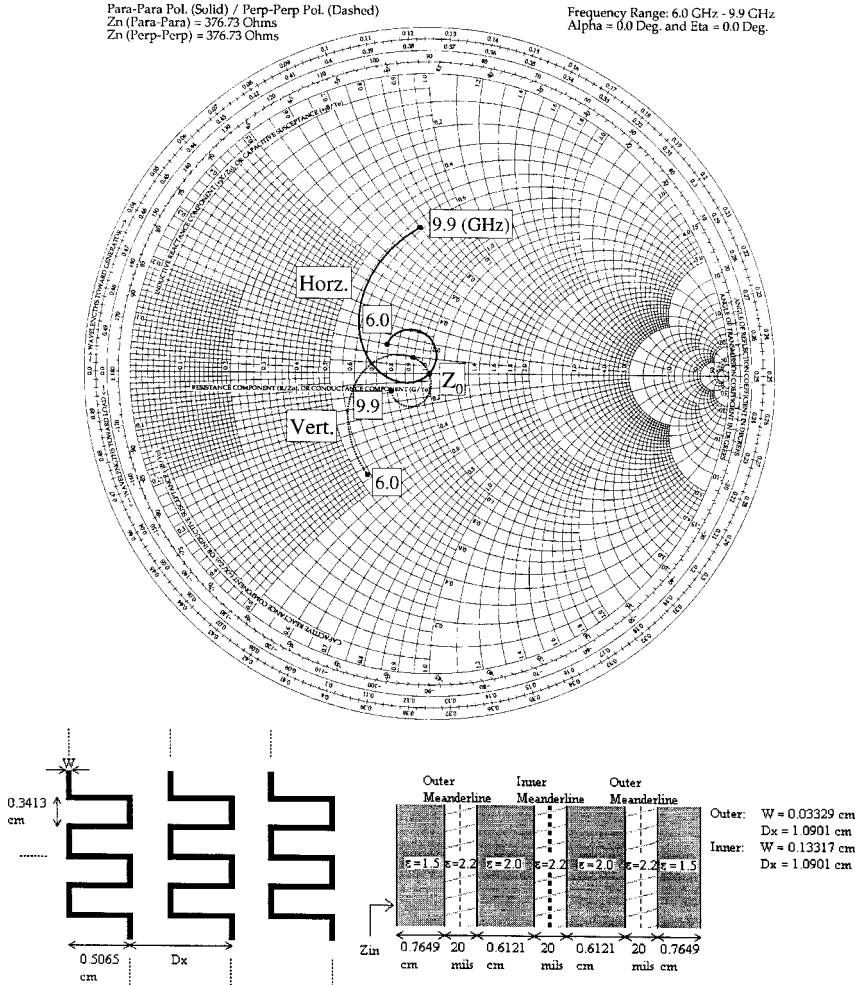
Fig. C.15   Design 5. Three meander-line sheets separated by dielectric slabs and further provided with outer matching transformers. The input impedances (vertical and horizontal).

Meander-Line Impedances Lowered
Outer Matching Plate at Each End

It is by now well known that the variation with angle of incidence of the scan impedance of phased arrays as well as the bandwidth of hybrid radomes can be reduced by using dielectric slabs placed between free space and the device in question. To be sure, the dielectric constant should in general be less than 2 (for a single slab) and the thickness should be somewhat thicker than $\lambda/4$ in the dielectric. An example of applying this technique is shown in Fig. C.15. Compared to the uncompensated case in Fig. C.13, we observe some improvement

Magnitude Ratio
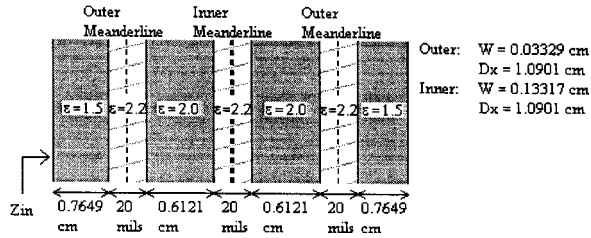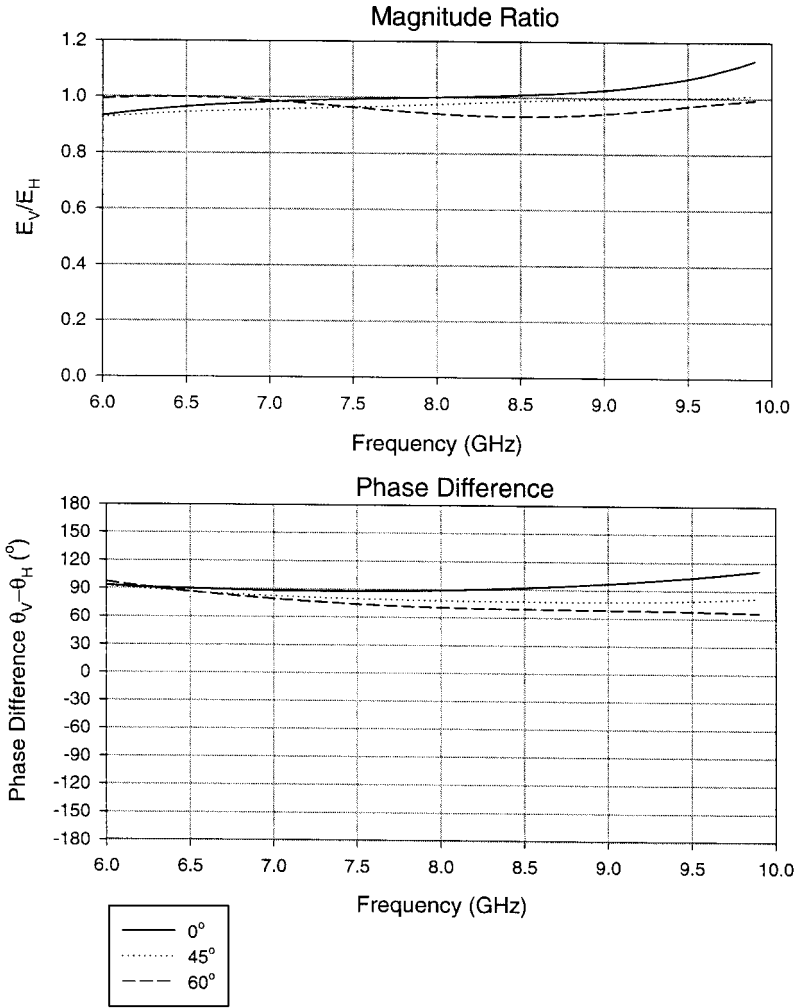
Phase Difference

Fig. C.16 Design 5. Three meander-line sheets separated by dielectric slabs and further provided with outer matching transformers for wide angle scanning. Top: The amplitude ratio E_v/E_h as a function of frequency. Bottom: The phase difference $\theta_v - \theta_h$ as a function of frequency.

for horizontal polarization at the lower frequencies and for vertical at the higher frequencies. Note, however, we only show normal angle of incidence.

Furthermore, we show in Fig. C.16 the amplitude ratio as well as the phase difference as a function of frequency. Compared to the uncompensated Design 4 shown in Fig. C.14, we observe a significant improvement in amplitude ratio, less so in the phase difference. It should be pointed out, however, that neither Design 4 nor Design 5 has been optimized.

C.9   CONCLUSION

Examination of Design 6 comprised of four meander-line sheets with dielectric spacers both inside and outside showed that some improvement compared to Design 5 was possible. However, since the differences between these specific designs were minor, it was decided not to show Design 6. It is the opinion of the author as well as his right-hand man, Jonothan Pryor, that further improvement is possible by a simple optimization process (which algorithm is used is of less importance). We shall leave this as an exercise for the student.

PROBLEMS

C.1   Consider a polarizer comprised of two meander-line sheets.

Design it to yield perfect circular transmission at the center frequency. Determine the reflection coefficient at that frequency.

What percentage of the incident field is being transmitted and how much is being reflected?

Compare it to a polarizer of a single meander-line sheet.

On the Scan Versus the Embedded Impedance

D.1 INTRODUCTION

When working with phased arrays, it is of particular interest to compare the scan impedance with the embedded impedance, in particular whether one can be derived from the other.

The first of these, namely the scan impedance, is the impedance observed at the element terminals when the proper voltages are applied to *all* the elements. These voltages may all have the same amplitude corresponding to uniform aperture illumination or they may be tapered across the aperture. When we vary the phases of these terminal voltages in a linear fashion across the aperture, the beam will scan in different directions and the scan impedance will in general vary considerably with scan angle.

The embedded impedance, on the other hand, is the terminal impedance observed at just one element usually located somewhere in the middle of the array and with all the other elements terminated in loads (usually resistive). Thus, a terminal voltage is only applied to a single element, while all the other elements are excited parasitically.

It is also of interest to consider the case where we excite a single column or row with identical voltages while all the other elements are terminated in loads like before. The impedance measured at the terminals of the column of elements in question is often called the embedded stick impedance $Z_{\text{emb stk}}$. We shall see that it often makes more sense to consider the embedded stick impedance rather than the embedded impedance of a single element.

Although there are similarities between the scan and embedded impedances, they are distinctly different. Only the scan impedance can be associated with the direction of the beam, while the embedded impedance can be associated with only one direction. (Actually the pattern looks more like an element pattern with ripples.) However, not even for broadside scan do we obtain more than an occasional similarity between the two types of impedance.

Needless to say, the embedded impedance for a single element is by far the simplest of the three types of impedance to implement. You only need a single connector at one element in the middle of the array, while all the others are terminated by resistors that can be either soldered in place or simply printed. In contrast, measurements of the scan impedance may require a connector or equivalent at each element, and, most importantly, we must be able to apply voltages at each terminal and be able to control these voltages in phase as well as amplitude.

For these reasons there has long been a strong tendency to measure just the embedded impedance of a single element. While this may be a good way to check certain fundamental features of the array and in some cases the presence of surface waves, it cannot be emphasized enough that it is *not* a substitute for measuring the scan impedance, not even at broadside. And of these two impedances, the latter is by far the most important. In fact the embedded impedance has always reminded the author of an honorable degree. There is not much you can do with it except marvel at it!

But let us now look at the facts of the scan and the embedded impedances.

D.2   THE SCAN IMPEDANCE

The scan impedance has been discussed extensively in reference 135. Thus, only the highlights will be given here for easy reference.

Consider Fig. D.1, where we show two infinite stick arrays q and q'. We denote the mutual impedance between the reference element in array q and element m in array q' by $Z_{q,q'm}$. The mutual impedance between the reference element in array q and all the other elements in array q' is then defined as

$$Z^{q,q'} = \sum_{m=-\infty}^{\infty} Z_{q,q'm} e^{-j\beta m D_z s_z}. \tag{D.1}$$

Let us now consider a finite $\times$ infinite array as shown in Fig. D.2 consisting of $2Q + 1$ stick arrays. The current in the reference elements are denoted I_q. Writing Ohm's Law for the reference element in stick array number 0 yields

$$V^{0,0} = \sum_{q=-Q}^{Q} Z^{0,q} I_q. \tag{D.2}$$

We now let $Q \to \infty$ such that the array becomes infinite $\times$ infinite. In that event the array is truly periodic in the X direction as well as in the Z direction and
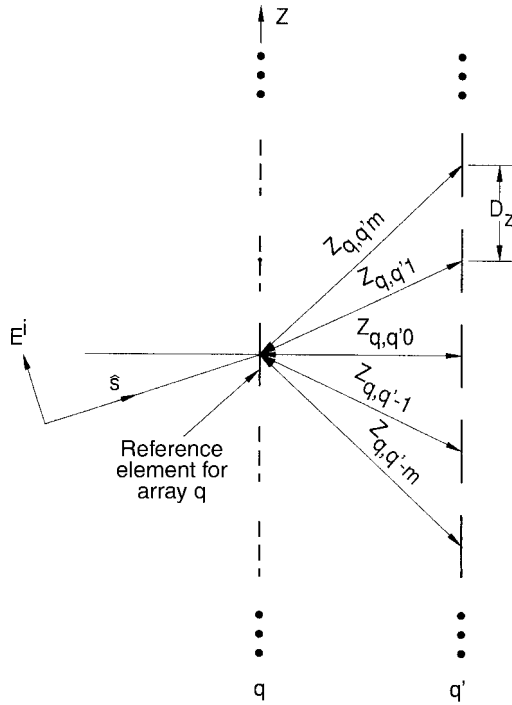
$$Z^{q,q'} = \sum_{m=-\infty}^{\infty} Z_{q,q'm} \; e^{-j\beta m D_z s_z}$$

Fig. D.1 Evaluation of the array mutual impedance $Z^{q,q'}$ between the reference element in array q and all the other elements in array q' by using the mutual impedance approach.
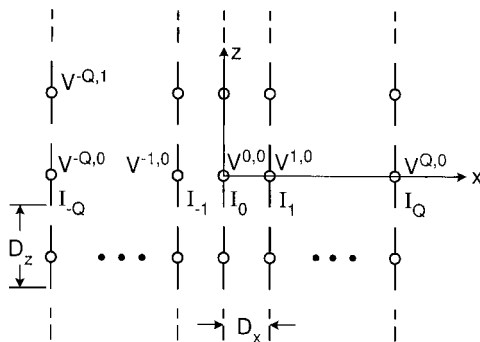
Fig. D.2 A finite $\times$ infinite array comprised of $2Q + 1$ infinitely long stick arrays. All elements are driven with voltage generators $V^{q,m}$, and the currents in the reference elements in row 0 are denoted I_q. For $Q \to \infty$ we obtain an infinite $\times$ infinite array where Floquet's Theorem yields $I_q = I_0 e^{-j\beta q D_x \, s_x}$.

Floquet's Theorem applies [26], yielding

$$I_q = I_0 e^{-j\beta q D_x s_x}. \tag{D.3}$$

Substituting (D.3) into (D.2), we obtain

$$V^{0,0} = I_0 \sum_{q=-\infty}^{\infty} Z^{0,q} e^{-j\beta q D_x s_x}. \tag{D.4}$$

Thus, the scan impedance for an infinite array without a groundplane is

$$Z_A = \frac{V^{0,0}}{I_0} = Z^{0,0} + 2 \sum_{q=1}^{\infty} Z^{0,q} \cos(\beta q D_x s_x). \tag{D.5}$$

A plot of the scan impedance Z_A for an infinite $\times$ infinite array without a groundplane and with the same interelement spacings as used in Chapter 6 as obtained from the PMM code is shown in Fig. D.3. The impedance is plotted in a Smith chart normalized to 100 ohms. Furthermore, the impedance in Fig. D.3 as well as in later figures includes the matching of a short transmission line with characteristic impedance 200 ohms and length 0.13 cm. This was typically true in the cases shown in Chapter 6, which should make comparisons between the various curves more meaningful. We remind the reader that the purpose of this transmission line (also referred to as a "pigtail") was to better center the impedances as well as compress them (for details see Chapter 6 and Appendix B).

D.3 THE EMBEDDED STICK IMPEDANCE

The embedded stick impedance is perhaps best illustrated by considering just three stick arrays as shown in Fig. D.4. Each element in the center column is fed by voltage generators with voltages $V^{0,m}$, where m refers to the row number. The two outer stick arrays are not fed but only loaded with identical load impedances Z_L.

By writing Ohm's Law for each reference element in row 0, we obtain

$$\begin{bmatrix} 0 \\ V^{0,0} \\ 0 \end{bmatrix} = \begin{bmatrix} Z^{-1,-1} + Z_L & Z^{-1,0} & Z^{-1,1} \\ Z^{0,-1} & Z^{0,0} & Z^{0,1} \\ Z^{1,-1} & Z^{1,0} & Z^{1,1} + Z_L \end{bmatrix} \begin{bmatrix} I_{-1} \\ I_0 \\ I_1 \end{bmatrix}. \tag{D.6}$$

Applying Cramer's rule, we obtain from (D.6)

$$I_0 = \frac{1}{D} \begin{vmatrix} Z^{-1,-1} + Z_L & 0 & Z^{-1,1} \\ Z^{0,-1} & V^{0,0} & Z^{0,1} \\ Z^{1,-1} & 0 & Z^{1,1} + Z_L \end{vmatrix}, \tag{D.7}$$

Input impedance renormalized to Z_o=100 Ω for:dipgp74a
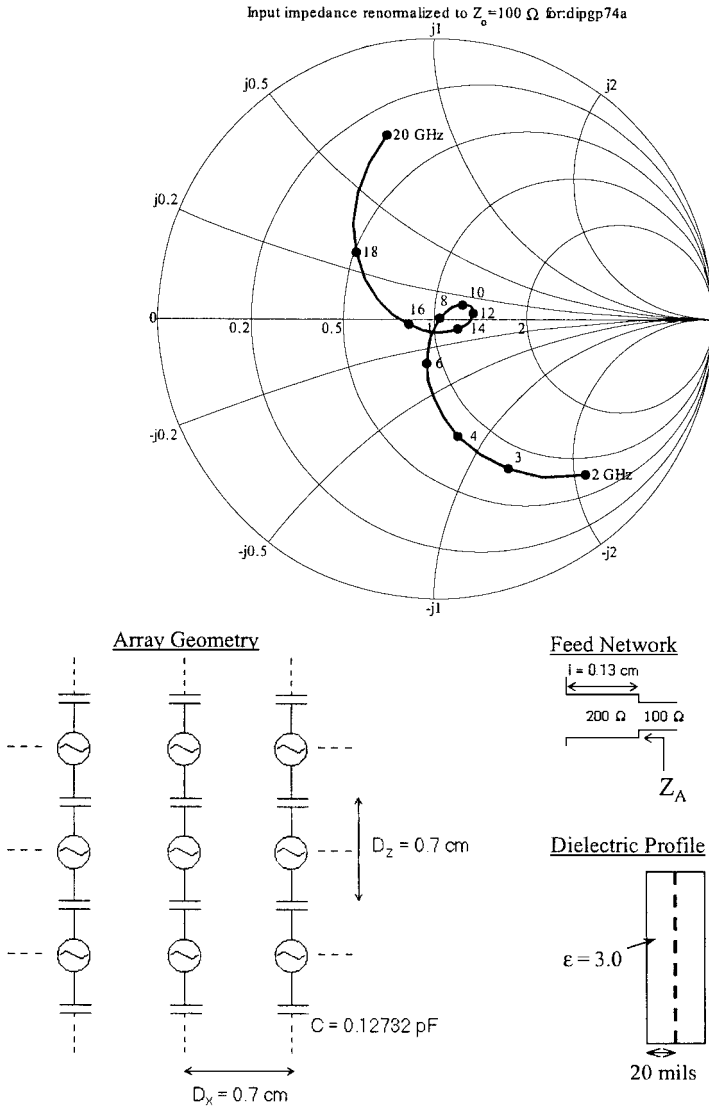
Fig. D.3   The scan impedance Z_A for an infinite × infinite array without a groundplane obtained from the PMM program. The array dimensions are identical to the broadband array in Chapter 6 (see insert) but includes only the ''underwear'' (see ''Dielectric Profile'' above). Also included is a small transmission line matching section as was the case in Chapter 6 (see text).

where D denotes the determinant of (D.6). Expanding (D.7) along the second column yields

$$I_0 = \frac{V^{0,0}}{D}[(Z^{-1,-1} + Z_L)(Z^{1,1} + Z_L) - Z^{-1,1}Z^{1,-1}]. \qquad (D.8)$$
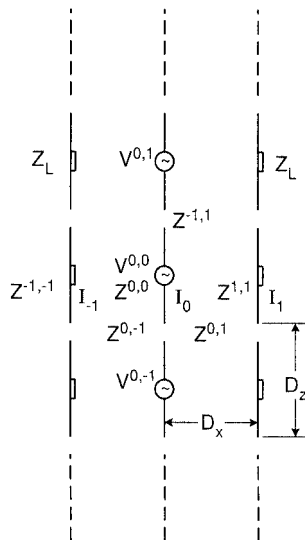
Fig. D.4   *The embedded stick impedance $Z_{\text{emb stk}}$ is the terminal impedance observed in the center stick array when all terminals in the center array are fed with voltages $V^{o,m}$ and all other stick arrays are loaded with identical load impedances and merely excited parasitically.*

Furthermore, we obtain for the determinant D of (D.6) by expanding along the second column

$$
\begin{aligned}
D = {}& -Z^{-1,0}[Z^{0,-1}(Z^{1,1} + Z_L) - Z^{0,1}Z^{1,-1}] \\
& + Z^{0,0}[(Z^{-1,-1} + Z_L)(Z^{1,1} + Z_L) - Z^{-1,1}Z^{1,-1}] \\
& - Z^{1,0}[(Z^{-1,-1} + Z_L)Z^{0,1} - Z^{-1,1}Z^{0,-1}].
\end{aligned}
\tag{D.9}
$$

Substituting (D.9) into (D.8) finally yields for the embedded stick impedance

$$
\begin{aligned}
Z_{\text{emb stk}} = {}& \frac{V^{0,0}}{I_0} \\
= {}& -Z^{-1,0}\frac{Z^{0,-1}(Z^{1,1} + Z_L) - Z^{0,1}Z^{1,-1}}{(Z^{-1,-1} + Z_L)(Z^{1,1} + Z_L) - Z^{-1,1}Z^{1,-1}} + Z^{0,0} \\
& - Z^{1,0}\frac{(Z^{-1,-1} + Z_L)Z^{0,1} - Z^{-1,1}Z^{0,-1}}{(Z^{-1,-1} + Z_L)(Z^{1,1} + Z_L) - Z^{-1,1}Z^{1,-1}}.
\end{aligned}
\tag{D.10}
$$

Inspection of (D.10) shows that the embedded stick impedance $Z_{\text{emb stk}}$ consists of the stick self impedance $Z^{0,0}$ for the center array plus two terms representing the overcoupled impedances from the two outer arrays.

It can be shown that the embedded stick impedance for any size finite array is structured the same way—that is, as a sum of the stick self-impedance $Z^{0,0}$ plus overcoupled terms associated with all the other parasitically excited stick arrays.

D.3.1 Example

We have calculated the stick self-impedance $Z^{0,0}$ for an array without ground-plane with dimensions as used in Chapter 6 as obtained from the SPLAT program. This program cannot handle dielectric slabs; however, it will approximate the effect of the dielectric "underwear" [136] by placing cylindrical dielectric shells around each element. The thickness of these dielectric coatings should be approximately equal to the thickness of the "underwear."

Thus, we show in Fig. D.5 an example of the stick self-impedance $Z^{0,0}$ with dimensions as shown in the insert and as obtained from the SPLAT program (includes a matching transmission line).

Furthermore, we show in Fig. D.6 the embedded stick impedance $Z_{\text{emb stk}}$ as given by (D.10) as also obtained from the SPLAT program and with dimensions as given in the insert (includes matching transmission line).

Comparing $Z^{0,0}$ in Fig. D.5 and $Z_{\text{emb stk}}$ in Fig. D.6 shows that they are in fact very similar except that the latter has a larger loop at the middle frequencies as caused by the overcoupled terms observed in (D.10). At the lower and upper frequencies, $Z^{0,0}$ and $Z_{\text{emb stk}}$ are practically identical. More comments about this subject will be given in the conclusion section. [A parametric study (not shown) reveals that the impedance loop of $Z_{\text{emb stk}}$ becomes larger for smaller values of Z_L and vice versa. See also comments in the Postscript section of this chapter.]

D.4 THE EMBEDDED ELEMENT STICK IMPEDANCE

In the previous section we considered the impedance properties when an entire column array was fed at all its terminals. However, as was pointed out already in the Introduction, the embedded impedance will in general be obtained by exciting only one pair of terminals while all other terminals are just loaded.

It is therefore of interest to investigate just a single stick array when we feed only a single pair of terminals while the rest are loaded with the same load impedances Z_L. We have denoted the terminal impedance for this case for the embedded element stick impedance $Z_{\text{emb ele stk}}$. Examples are shown in Fig. D.7. The array has the same dimensions as used in the previous section (see insert). The calculations were obtained from the method of moment program ESP [137]. Similar to the SPLAT program used to obtain the results in Figs. D.5 and D.6, it uses dielectric cylinders placed around each element.

Finally we show in Fig. D.8 the self-impedance of a single dipole without capacitors or any other elements present but includes matching sections (see text earlier). As we would expect, the real part is low and the reactance is capacitive and high. Obviously, this is what sticks in peoples' minds when they say that the type of array discussed in Chapter 6 will never have a chance for yielding a broad bandwidth (no pun intended). Note how the impedance "shrinks" as more elements are added and excited as observed in Fig. D.7.

It is of course the mutual coupling that comes to our rescue. We will elaborate on this subject in the next section.

Input impedance renormalized to $Z_o = 100 \ \Omega$ for:dipgpl column

Array Geometry

$\epsilon = 3.0$
Shell thickness = 20 mils

$D_z = 0.7$ cm

$C = 0.12732$ pF

Feed Network

$I = 0.13$ cm

$200 \ \Omega$ $100 \ \Omega$

$Z^{0,0}$
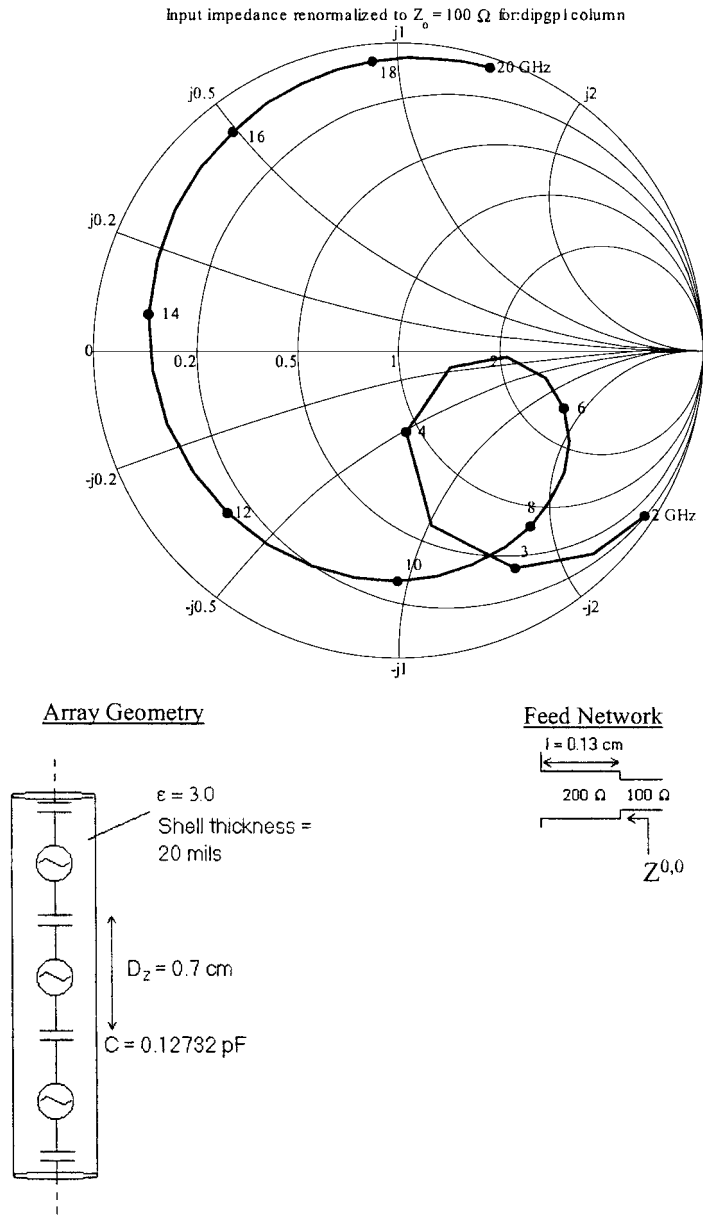
Fig. D.5   The stick self-impedance $Z^{0,0}$ for an array without a groundplane. Element dimensions identical to the case in Fig. D.3 (see insert). Obtained from the SPLAT program. The dielectric "underwear" is modeled by placing dielectric shells around the elements. Diameter approximately equal to total thickness of the underwear. Includes a matching transformer (see text).
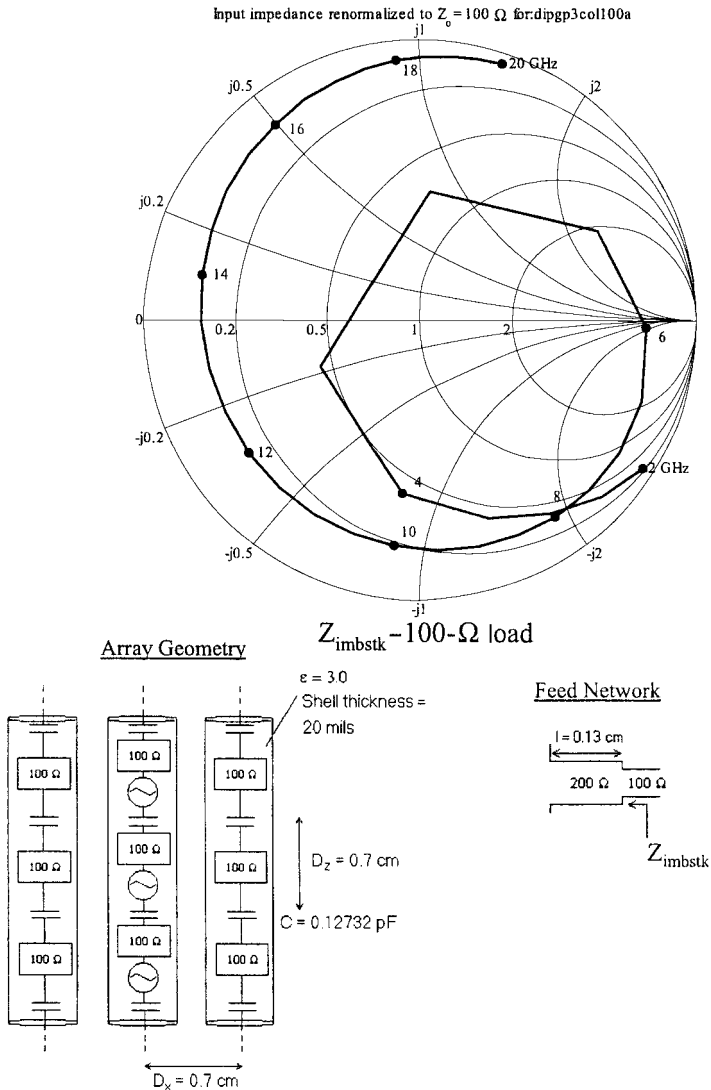
Fig. D.6   *The embedded stick impedance $Z_{emb\ stk}$ as given by (D.10) (no groundplane). The center stick array is driven while the two outer stick arrays are just loaded with $Z_L = 100$ ohms. Array dimensions as in Figs. D.3 and D.4 (see insert). From the SPLAT program. Includes matching transformer (see text).*

D.5   ON THE SCAN IMPEDANCE OF A FINITE ARRAY

In the previous sections we observed that the effect of the parasitic columns was practically nil at the lower and upper frequencies while it had a deteriorating effect at the middle frequencies. However, we already know that the scan impedance
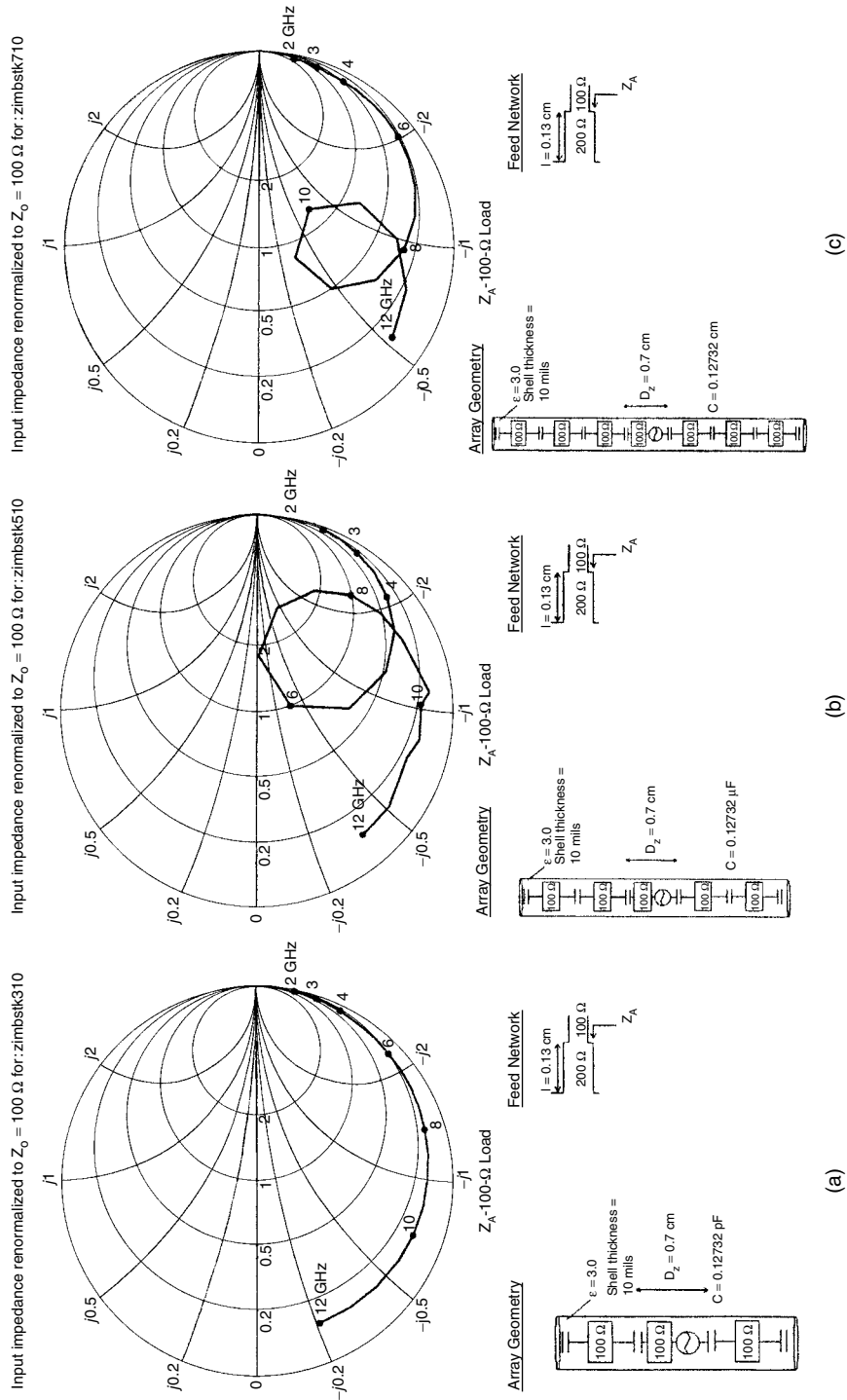
Fig. D.7 The embedded element stick impedance $Z_{emb\,ele\,stk}$ for element dimensions identical to Fig. D.6. From the ESP program. Dielectric "underwear" modeled by dielectric cylinder around the elements. (a) With one parasitically excited dipole on top and bottom. Loaded with $Z = 100\,ohms$. (b) With two parasitically excited dipoles on the top and two on the bottom. Loaded with $Z_L = 100\,ohms$. Includes matching section (see text). (c) With three parasitically excited dipoles on the top and bottom. Includes matching section (see text).

Input impedance renormalized to $Z_o = 100 \, \Omega$ for:zimbsingle10

$$Z_A - 100\text{-}\Omega \text{ load}$$
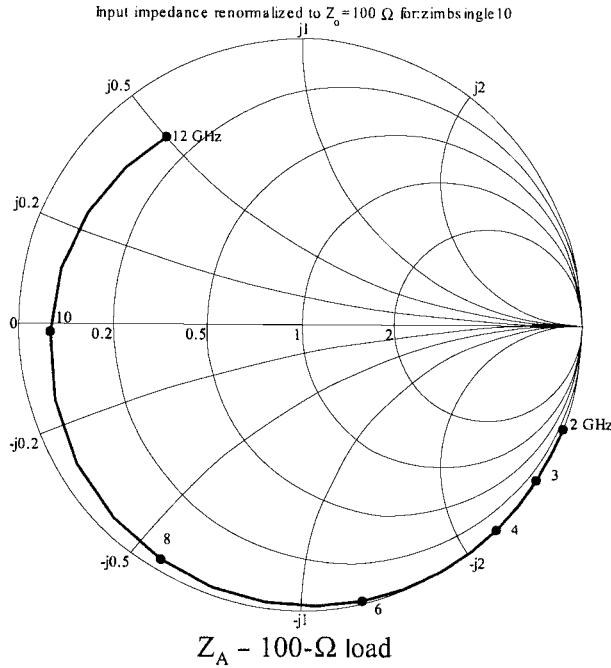
Array Geometry   Feed Network

$\varepsilon = 3.0$
Shell thickness
10 mils

$l = 0.13$ cm

$200 \, \Omega$ $100 \, \Omega$

Z_A

100 Ω

C = 0.12732 pF
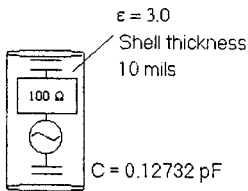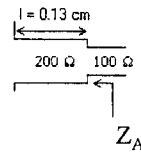
Fig. D.8   The self-impedance of a single dipole with total length equal to the element section used in Fig. D.7 (see insert). A dielectric cylinder was placed around the element to model the "underwear." Includes a matching section (see text).

Z_A for an infinite array is considerably "better" in the entire frequency range (see Fig. D.3). It is therefore pertinent to ask the question, Would it not be better to excite the parasitic columns with voltage generators like the center column rather than parasitically?

Thus, we therefore show the scan impedance for the center column in Fig. D.9 when the two outer columns are excited as well. Similarly we show the scan impedance for the two outer columns in Fig. D.10. Comparing the scan impedances in Figs. D.9 and D.10 with the embedded impedance $Z_{\text{emb stk}}$ in Fig. D.6 readily shows a significant improvement in particular at the **lower frequencies**. In the midrange we observe the presence of a surface wave. It has been suppressed by feeding each element with a voltage generator that includes a

Input impedance renormalized to $Z_o = 100 \; \Omega$ for:dipgp3col3vol100$_2$

$Z_{imbstk} - 100 - \Omega$ load

Array Geometry

$\varepsilon = 3.0$
Shell thickness = 20 mils

Feed Network

$D_z = 0.7$ cm

$C = 0.12732$ pF

$l = 0.13$ cm

200 Ω 100 Ω

Z_{imbstk}

$D_x = 0.7$ cm
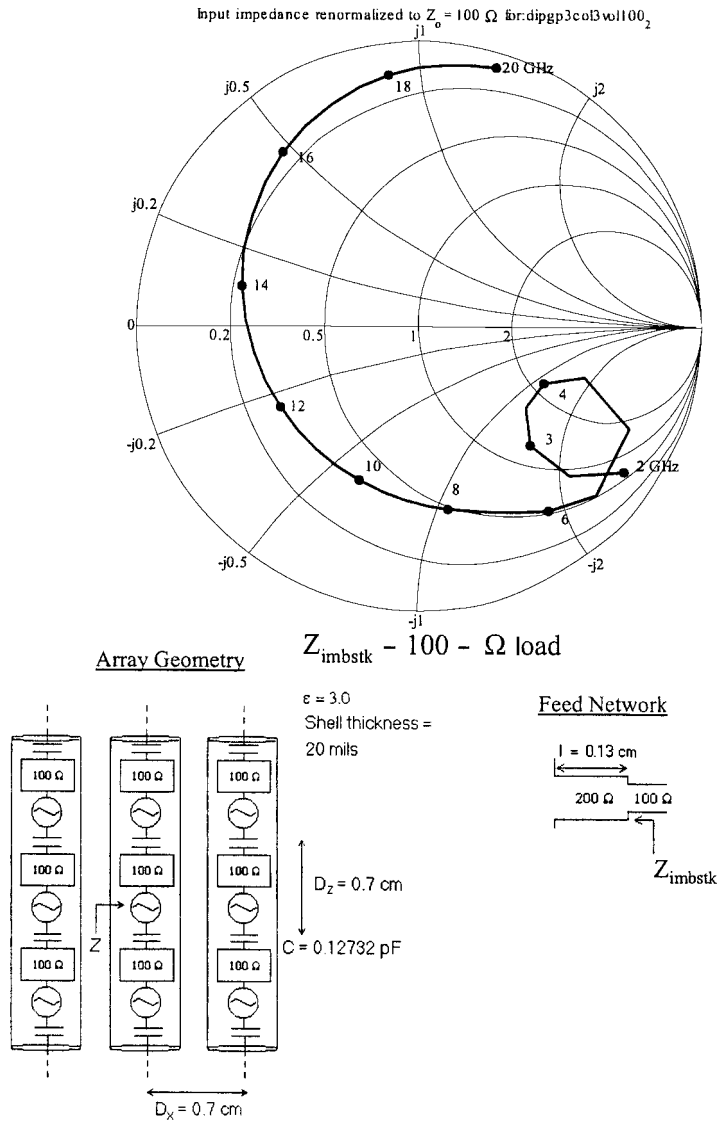
Fig. D.9 The scan impedance for the center column when all three columns are fed with identical voltage generators with generator impedances equal to 100 ohms (to suppress surface waves). Dielectric cylinders are placed around the elements to model the "underwear." Includes matching section (see text). From the SPLAT program.

generator impedance equal to 100 ohms as discussed in detail in Chapter 4. This resistor is subtracted in the figure.

We have further verified this observation for the case when we are using five columns rather than three (not shown).

Input impedance renormalized to $Z_o = 100 \, \Omega$ for:dipgp3col3vol100

$Z_{imbstk} - 100\text{-}\Omega$ load

Array Geometry

$\varepsilon = 3.0$
Shell thickness =
20 mils

$D_z = 0.7$ cm

$C = 0.12732$ pF

$D_x = 0.7$ cm

Feed Network

$l = 0.13$ cm

$200 \, \Omega$ $100 \, \Omega$

Z_{imbstk}
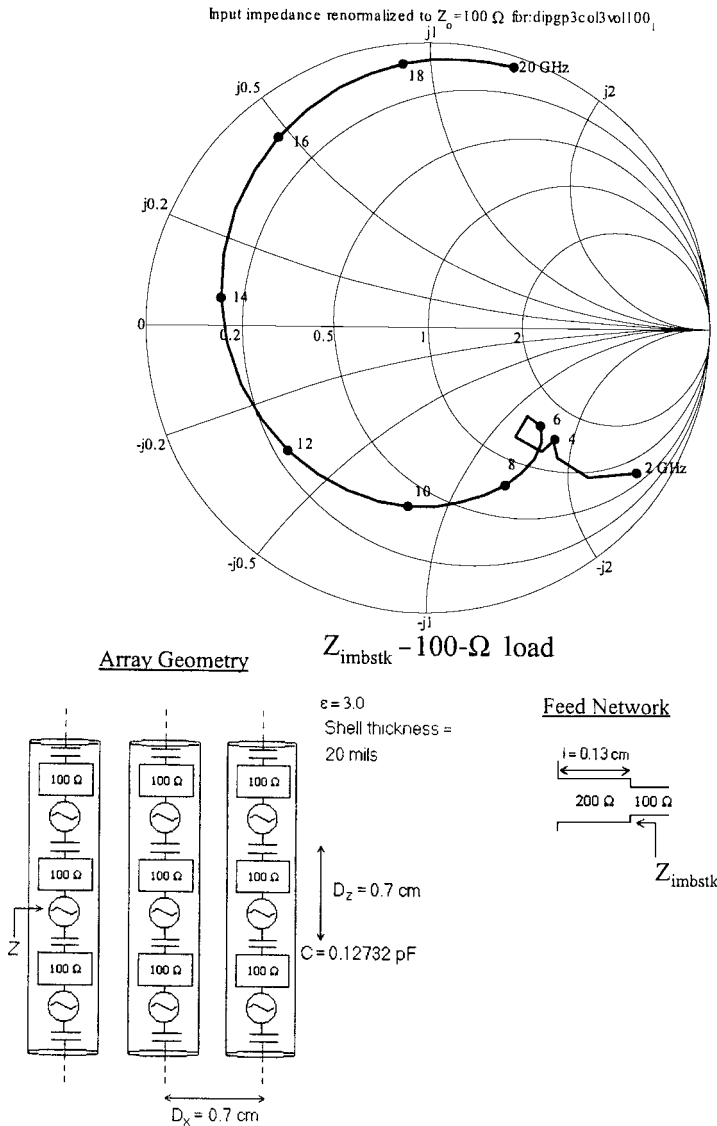
Fig. D.10 *The scan impedance for the outer columns when all three columns are fed with identical voltage generators with generator impedance equal to 100 ohms to suppress surface waves. Dielectric cylinders are placed around the elements to model the "underwear." Includes matching section (see text). From the SPLAT program.*

We may conclude that use of parasitic columns either is ineffective or simply makes things worse. It appears prudent to recommend to excite all columns in a finite array and not try to improve upon the impedance by garnishing the active part of the array with all kinds of dummy elements located next to them.

We finally show in Fig. D.11 the terminal impedance as seen from the center element with two parasitic sections at the top and two below like Fig. D.7b but also flanked on each side with parasitically excited columns comprised of five segments. Dimensions are given in the insert, and the ESP program was used with a 10-mil dielectric sheet. As usual, the impedance curves include the small transmission line section. Note the poor performance at the lower frequencies compared to the scan impedance in Fig. D.3.

D.6   HOW TO MEASURE THE SCAN IMPEDANCE Z_A

It does not seem possible to obtain the scan impedance Z_A from any embedded impedance. Thus, let us discuss how to obtain Z_A by measurement. Two schemes come to mind.

The first and most direct is shown in Fig. D.12. Here all elements are fed via a harness as shown. The impedance Z_A of a typical element is determined by insertion of an appropriate reflectometer or impedance measuring device. Neither of these devices should have any attenuation, and their electrical length must be incorporated in the feed cable. From the complex reflection coefficient Γ at the element terminal we find

$$Z_A = Z_0 \frac{1 + \Gamma}{1 - \Gamma}. \tag{D.11}$$

The second scheme is shown in Fig. D.13. Here all elements are loaded directly with the same load impedances Z_{L1} and exposed to an incident plane wave $\overline{E}^i$ (*note*: no connectors are necessary, strictly speaking). From the Thevenin equivalent circuit shown in the insert we then have

$$V_{L1} = V \frac{Z_{L1}}{Z_{L1} + Z_A}, \tag{D.12}$$

where V is the induced generator voltage from the incident field (is independent of Z_L) and V_{L1} is the voltage across the load impedance Z_{L1}.

Similarly, for another load impedance Z_{L2} we have

$$V_{L2} = V \frac{Z_{L2}}{Z_{L2} + Z_A}. \tag{D.13}$$

Division of (D.12) and (D.13) yields

$$\frac{Z_A + Z_{L2}}{Z_A + Z_{L1}} = \frac{Z_{L2}}{Z_{L1}} \frac{V_{L1}}{V_{L2}}. \tag{D.14}$$

Knowing Z_{L1} and Z_{L2}, along with determination of the complex ratio V_{L1}/V_{L2} by measurements, enables us to find Z_A from (D.14).

Input impedance renormalized to $Z_o = 100 \, \Omega$ for:zimbstk1510

j1

j0.5   j2

j0.2

0   0.2   0.5   1   2

6

2 GHz

-j0.2

12 GHz   3

4

10   8

-j0.5   -j2

-j1

Z_A–100-Ω load

Array Geometry

100 Ω   100 Ω   100 Ω $\varepsilon = 3.0$
Shell thickness =
10 mils

100 Ω   100 Ω   100 Ω

100 Ω

100 Ω   100 Ω $D_z = 0.7 \text{ cm}$

100 Ω   100 Ω   100 Ω

100 Ω   100 Ω   100 Ω $C = 0.12732 \text{ pF}$

$D_x = 0.7 \text{ cm}$

Feed Network

$l = 0.13 \text{ cm}$

200 Ω   100 Ω

Z_A
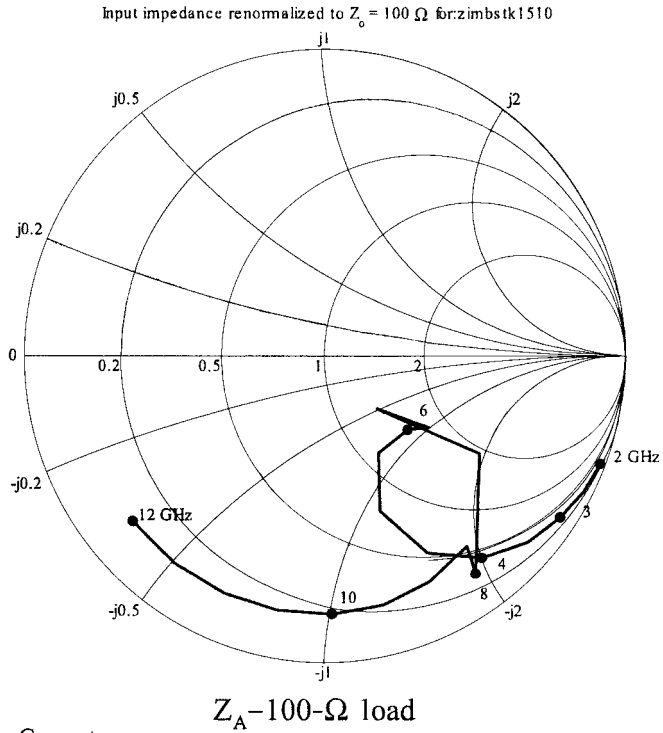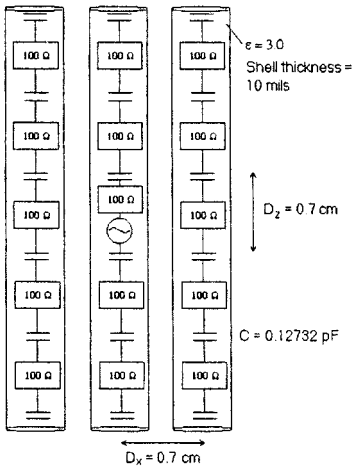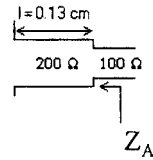
Fig. D.11   The impedance as seen from the center element with two parasitic sections at the top and two at the bottom like Fig. D.7b but flanked with parasitically excited columns of 5 segments as each side as shown in insert. From the ESP program; 10-mil dielectric. Includes matching sections (see text).
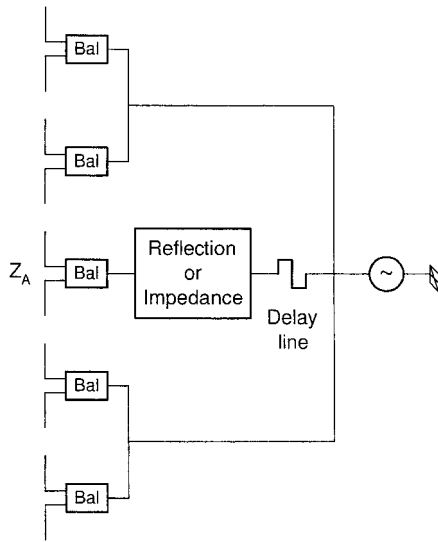
Fig. D.12 *Determination of Z_A in a finite array by feeding all elements with the same voltages from "behind." The individual impedance Z_A of a selected element is determined by an appropriate impedance measuring device as shown.*

$$V_{L1} = V \frac{Z_{L1}}{Z_{L1} + Z_A}$$

$$V_{L2} = V \frac{Z_{L2}}{Z_{L2} + Z_A}$$

by division

$$\frac{V_{L1}}{V_{L2}} = \frac{Z_{L1}}{Z_{L2}} \frac{Z_{L2} + Z_A}{Z_{L1} + Z_A}$$
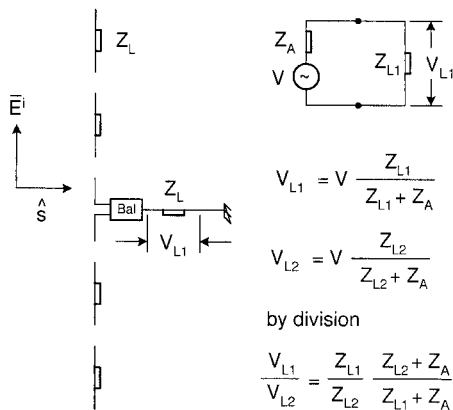
Fig. D.13 *Determination of Z_A in a finite array by exposing all elements to the same incident field from the "front." By knowing the load impedances Z_L in at least two cases and determination of V_L across the loads, we can determine Z_A (see insert).*

The second approach does not require a harness or actual connectors as does the first approach. But we must use at least two different load impedances. Furthermore, measurement of the V_{L1}/V_{L2} takes sophisticated equipment. If any one out there "pulls it off," the author would appreciate to hear from you. Congratulations would be in order.
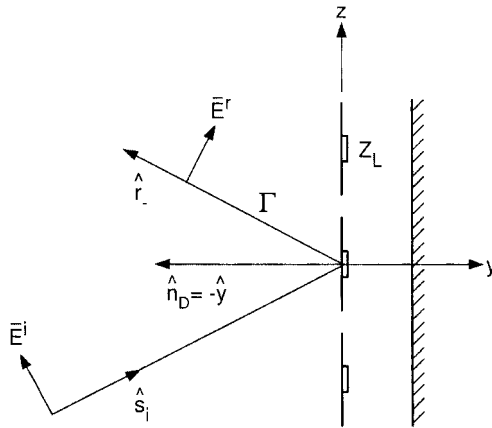
Fig. D.14 A plane wave incident upon an array of loaded dipoles in front of a groundplane.

Finally we show in Fig. D.14 a variation of the "frontal approach." Here all elements in the array backed by a groundplane are simply terminated in the same load impedance Z_L (this requires no connectors). A plane wave $\overline{E}^i$ with direction of propagation $\hat{s}_i$ is incident upon this aperture. It is being reflected in the specular direction $\hat{r}_-$ with reflection constant Γ. The reflection coefficient observed from the terminals looking in the direction of $\hat{r}_-$ (or $\hat{s}_i$) has the same magnitude as Γ (not phase in general).

D.7 CONCLUSIONS

The investigation in this appendix clearly shows that the scan impedance and the embedded impedance are *not* the same, not even for broadside scan.

The fundamental reason for this is actually well known but practiced very little. In fact the embedded impedance is often demanded of the sponsors primarily for no other reason than "we have always done it that way in the past."

If we merely plot the VSWR of the two impedances, they might exhibit some similarities, in particular for mediocre VSWR. This is by no means a proof of similarity. Impedance curves should preferably be plotted in the complex plane that always tells the complete story (and in particular what to do about matching; see Chapter 6 and Appendix B).

Thus, we have plotted all impedances in Smith charts normalized to the same impedance, namely 100 ohms. We can then compare the scan impedance Z_A as given by (D.5) in Fig. D.3 with the stick self-impedance $Z^{0,0}$ as shown in Fig. D.5. Although some similarities are found at the middle to higher frequencies, the difference at the lower frequencies is simply enormous. One could then wonder whether that difference could be reconciled if we instead of the stick self-impedance $Z^{0,0}$ would consider the embedded stick impedance $Z_{\mathrm{emb\ stk}}$ as

given by (D.10) and depicted in Fig. D.6. That is obviously not the case. The reason is simply that $Z_{\text{emb stk}}$ according to (D.10) is the sum of $Z^{0,0}$ and two overcoupled terms from the parasitically excited arrays. These overcoupled terms reach their largest value when the outer stick self-impedances $Z^{-1,-1} + Z_L$ and $Z^{1,1} + Z_L$ including Z_L reach their minimum, namely around resonance at the middle frequencies. At the lower and higher frequencies, $Z^{-1,-1}$ and $Z^{1,1}$ are large, resulting in low values of the overcoupled impedances—that is, resulting in small deviations from $Z^{0,0}$.

To summarize: Using the embedded stick impedance $Z_{\text{emb stk}}$ instead of the stick self-impedance $Z^{0,0}$ may lead to even greater deviation from the scan impedance Z_A at the middle frequency range. At the lower frequencies, $Z^{0,0}$ and $Z_{\text{emb stk}}$ are similar but both differ substantially from the scan impedance Z_A.

An even greater difference is observed if we consider the embedded element stick impedance $Z_{\text{emb ele stk}}$ as shown in Fig. D.7. Here we excite only the center element of a single stick while all the other elements in the stick array are parasitically excited.

We finally demonstrated that a better approximation (in particular at the lower frequencies) to the scan impedance Z_A was obtained if we excited all columns in the finite array with voltage generators similar to the center columns and without any dummy elements whatsoever. To summarize, it seems that parasitic elements do more harm than good (at least for the type of array considered here).

D.8   POSTSCRIPT

Part of this appendix was written while I was recuperating at the Beth Israel hospital in Boston after some very delicate heart operations. I was consequently without my trusted associate Jonothan Pryor and his computer. Thus, I had to rely entirely on graphical approaches and my sliderule to verify my conclusions.

A typical example was to estimate the overcoupled impedance as given by the first and last term in (D.10). Making the rather gross approximation that

$$Z^{-1,1} = Z^{1,-1} \sim 0$$

reduces the overcoupled impedances in (D.10) to

$$-\frac{Z^{-1,0}Z^{0,-1}}{Z^{-1,-1} + Z_L} \quad \text{and} \quad -\frac{Z^{1,0}Z^{0,1}}{Z^{1,1} + Z_L}, \quad \text{respectively.} \tag{D.15}$$

Further choosing $Z_L \sim 100\,\text{ohms}$ and making the rough approximation (at least at the middle frequencies) that

$$Z^{-1,-1} = Z^{1,1} \sim 100 + jC\frac{\Delta f}{f_0}\,\text{ohms} \qquad (C \text{ is a scaling constant}),$$
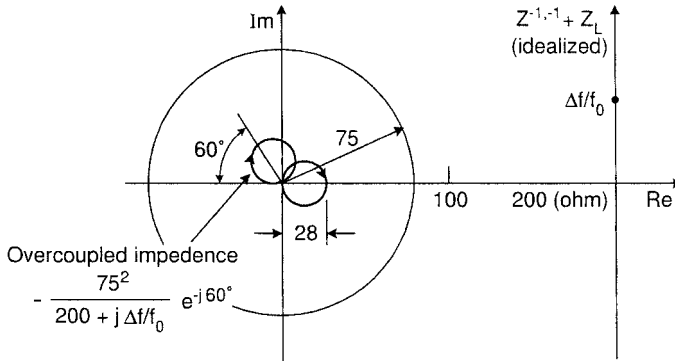
Fig. D.15 *How to estimate the overcoupled impedance from the two outer stick arrays. See text for details.*

we find that

$$Z^{-1,-1} + Z_L = Z^{1,1} + Z_L \sim 200 + jC\frac{\Delta f}{f_0} \quad \text{ohms}, \qquad (D.16)$$

that is, a straight vertical line through the point 200 ohm as shown in Fig. D.15.

Furthermore, it was estimated that

$$Z^{-1,0} = Z^{0,-1} \sim 75e^{-j30°}. \qquad (D.17)$$

Substituting (D.16) and (D.17) into (D.15) yields

$$-\frac{Z^{-1,0}Z^{0,-1}}{Z^{-1,-1} + Z_L} \sim -\frac{75^2}{200 + jC\dfrac{\Delta f}{f_0}}e^{-j60°}. \qquad (D.18)$$

Inspection of (D.18) readily shows that it merely is an inversion of the vertical line going through 200 ohms into a circle with diameter $75^2/200 = 28$ ohms [123]. It is followed by the simple rotation $-e^{-j60°}$. The inverted circles before and after rotation are also shown in Fig. D.15.

When the overcoupled impedances (remember we have two) are added to $Z^{0,0}$ as suggested by (D.10), we readily see that the embedded stick impedance $Z_{\text{emb stk}}$ will have a larger loop than the one present in $Z^{0,0}$ (see Fig. D.5). This is of course exactly what Jonothan later calculated (see Fig. D.6).

We may also conclude from (D.18) that a larger Z_L produces a smaller over-coupled impedance and vice versa.

Estimates as above are typically what I usually do before my students get the "right" values on the computer. Thus, I am ready to take a critical look at their results. It is just amazing to me when I think about the time and trouble some of them will go through to confuse and mislead a senile old professor.

Index